Artificial Radionuclides in the Environment

2021

環境における人工放射能の研究（2021 年版）

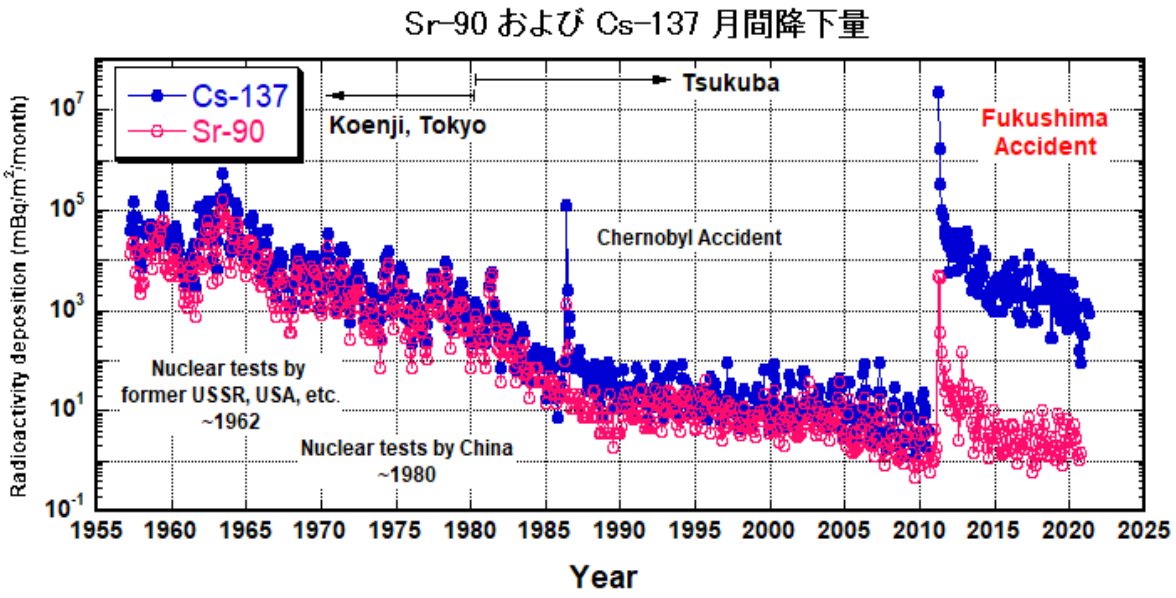

Meteorological Research Institute

JMA

March 2022

気象庁　気象研究所

最終ページに図の詳しい説明があります。

See figure caption at the end page of this publication.

「環境における人工放射能の研究（2021 年版）」について

気象研究所では、1954 年以来、主に現在の原子力規制庁放射能調査研究費により、大気及び海洋の環境放射能の研究を実施してきました。特に人工放射性核種の降下量を 60 年余りの長期にわたり、毎月、東京・高円寺で、そして気象研究所の筑波研究学園都市移転後（1980 年～）は同地で、精密に測定してきました。この長期モニタリング観測は、世界でも最長の人工放射性核種の定点観測です。この観測期間に、1950 年代から 1960 年代にかけては、旧ソ連や米国などによる大気圏核実験が行われ、その後 1986 年には旧ソ連のチェルノブイリ原子力発電所で爆発事故が発生するなどがありましたが、この長期にわたる精密観測によって、それらの影響を含めたバックグラウンドの人工放射性核種の長期的変動を明らかにし、国民の安全・安心に寄与してきました。2011 年には不幸にして東日本大震災に伴う福島第一原子力発電所事故が発生し、それによって放出された放射性核種の推移を調査するという課題も担うこととなりました。今後も長期的な視点に立って、人工放射性核種の変動を監視する必要があります。

長寿命の放射性核種を含む物質の濃度や分布は、その物質の性質に応じて再飛散・輸送・沈着といった複雑なメカニズムにより変動しています。そのため、それらの長期的な変動を予測するためには、長期観測や再飛散観測、サンプルの分析等による変動メカニズムの理解に基づいた、数値計算モデルの開発が必要です。気象研究所では、気候変動や降水予測の研究のため、大気中の微粒子の動きを表現する数値モデルを開発してきましたが、そのような数値モデルの技術を利用して、 バックグラウンド放射能の変動メカニズムを解析する研究も行ってきました。

これまでの研究から、長期的変動に対しては、降水などにより一旦地面などに沈着した人工放射性核種が、土壌粒子や生物由来の粒子等を通じて空気中へ再飛散する過程が重要であることがわかりました。福島事故直前の人工放射能の降下量は、黄砂等による再浮遊放射能の長距離輸送が関与していたと推定されます。また現在の降下量は、主に事故後に降水などとともに地面に沈着した放射能が、土壌粒子や生物活動によって空気中に再浮遊するフラックス（流速）によって決まっていると推定されます。

本論文集「環境における人工放射能の研究（2021 年版）」 は、その研究成果を、関係省庁の担当者の方々及び大学や試験研究機関の研究者の方々に広く知って頂くために、2019 年から 2021 年までの期間に出版された論文（主に英語論文）を、過去から現在までの成果と最近のトピックスに関するテーマ毎に分類し、各テーマの冒頭に簡単な日本語の解説を加えて、一冊にまとめたものです。

令和 4年 3月

気象研究所 研究総務官　石井　雅男

Contents

目次

0. はじめに

気象研究所（2021 年 1 月現在は予報気象研究部および全球大気海洋研究部）では、1954 年以来、環境放射能の観測・測定法の開発、放射能汚染の実態の把握、大気や海洋における物質輸送解明のトレーサーとしての利用を目的として、60 年余にわたって環境放射能の研究を実施してきた。1957 年以降、各省庁がそれぞれの所掌で実施してきた環境放射能調査研究関連業務は、まず旧科学技術庁、その後文部科学省が所管してきた。さらに原子力規制委員会と原子力規制庁の発足に伴って 2013 年からは、原子力規制庁が所管することとなった。このような長期にわたり多数の研究者が係わり、観測・研究を継続してきた結果、環境放射能について世界的にも他に類を見ない貴重な時系列データが内外に提供され、また様々な気象学・海洋学的発見をもたらしてきた。この間の研究成果は 200 編以上の原著論文や解説資料として内外の雑誌や成書で公表されている。

1954 年 3 月 1 日に米国によりビキニ環礁で行われた水爆実験により、危険水域外で操業していた第五福竜丸乗組員が放射性物質を含む降灰（いわゆる死の灰）による被ばくを受けた事件を契機にして、日本における環境放射能研究が本格的に始まった。当時の気象研究所地球化学研究室は環境の放射能の分析・研究において日本で有数の研究室であり、海洋及び大気中の放射能汚染の調査・研究に精力的に取り組んだ。その結果、当時予想されていなかった海洋の放射能汚染、さらに大気を経由した日本への影響など放射能汚染の拡大の実態を明らかにすることができた。1958 年には、放射能調査研究費による特定研究課題の一つである「放射化学分析（落下塵・降水・海水中の放射性物質の研究）」を開始し、以降、地点の変動はあるが、札幌、仙台、東京、大阪、福岡の五つの管区気象台、秋田、稚内、釧路、石垣島の 4 地方気象台、輪島、米子の 2 測候所の全国 11 気象官署及び観測船で採取した海水中の人工放射性核種（^{90}Sr、^{137}Cs、^{3}H 及びプルトニウム）の分析を実施してきた。

東京・つくばにおける大気中の人工放射性核種の降下量は 1961 年から 1962 年に行われた大規模な大気圏核実験の翌年である 1963 年に最大値を観測した。その後、「部分的核実験禁止条約」の締結により米ソの大気圏核実験が中止された結果、降下量はおよそ 1 年の半減時間で減少した。この放射性核種の降下量の減少率は成層圏にまきあげられた物質の滞留時間を反映している。その後も、中国及びフランスにより大気圏核実験は続けられ、人工放射性核種の降下量は増減を繰り返した。1980 年の中国による最後の大気圏核実験の後、フォールアウトは再度 1 年の半減期間で減少し、1985 年には 1957 年の観測開始以降最も低いレベルになった。しかし、1986 年の旧ソ連のチェルノブイリ原子力発電所事故により、大気中の人工放射性核種濃度（特に揮発性の高い ^{131}I、^{134}Cs、^{137}Cs など）は日本でも 1963 年に近いレベルに達するほど著しく増加した。大部分の放射性核種は対流圏の滞留時間（25 日）で減少したが一部 ^{137}Cs は成層圏にも輸送されていることが分かった。1988 年以降は低いレベルで推移しているが、明瞭な減少の傾向は見られなかった。この原因は一度地上に降下した放射性核種の再飛散に由来すると考えている。さらに、再飛散がどこで起るかについて研究を進め、東アジアの砂漠域で発生する黄砂が有力な候補であることを明らかにした。黄砂の発生は大陸域の環境変化と関連しており、降下物中の人工放射性核種は、砂漠化や関連する植生変化など大陸域の環境変化の指標となりうることが分かった。

大気フォールアウトの研究とともに、海洋における放射性核種の挙動も長期的に調査研究を実施してきた。日本周辺海域ばかりでなく、太平洋の広域に亘って海水試料の採取を実施し、放射能汚染の実態を明らかにした。1960 年代後半から 1970 年代の調査で、海洋表面水中の放射能が北半球の中緯度で高いことを明らかにし、フォールアウトの緯度分布を反映していることが分かった。その後、海洋表面水中の放射性核種は海洋の物質循環に支配されていることを

明らかにした。さらに、海水中の人工放射性核種の分析法の高度化を実現し少量の試料で分析可能にし、海洋の ^{137}Cs 濃度の精密鉛直断面を描き、核実験由来の ^{137}Cs の主な部分は北太平洋の亜熱帯中層に存在していることを明らかにした。フォールアウトによる人工放射性核種の海洋への主な降下以来、数 10 年以上経過し、その広がりは北太平洋から、インド洋など他の海盆に及んでいる。これに関連して 2003－4 年に実施された BEAGLE2003 の航海で採取された海水について人工放射性核種の分析を行って、その広がりについて知見が得られた。1993 年旧ソ連/ロシアによる放射性廃棄物の日本海等への海洋投棄の実態が明らかにされ、それに伴う日本海の放射能調査の実施に参加した。放射性廃棄物による影響は検出されなかったが、調査の結果を踏まえ、日本海における固有水の生成過程及び生成場所（ウラジオストック沖）についての知見を得ることができた。これらは、海洋放射能のデータベースとして公開されている。

1990 年以降の環境放射能汚染として、1997 年の旧動力炉核燃料開発事業団「アスファルト固化処理施設」の火災爆発事故や 1999 年の JCO ウラン燃料工場の臨界事故があるが、いずれも環境中に放出された放射能は極めて低いレベルで、その影響は殆どなかった。しかしながら、2011 年 3 月に起きた東日本大震災にともなう東京電力福島第一原子力発電所事故により、^{137}Cs の総量だけで 10 PBq（ペタベクレル）以上という過去日本では経験したことのない大量の人工放射性核種が環境中に放出され、その 2 割程度が日本の国土に降下し、残りの 8 割は北太平洋に降下したと考えられている。これらの影響評価やその後の環境中での拡散状況の把握のためにも、環境放射能調査・研究は今後とも重要である。

2006 年 4 月より 2011 年 3 月まで、気象研究所では放射能調査研究費による特定研究課題として「放射性降下物の長期変動と再浮遊に関する研究」及び「海洋環境における放射性核種の長期挙動に関する研究」の二課題で環境放射能研究に取り組んできた。また、2011 年 8 月からは、「大気を通じた人工放射性核種の陸圏・水圏への沈着およびその後の移行過程の解明研究」の課題のもと、過去の知見を十分に活用しながら、同年 3 月 11 日に発生した東日本大震災にともなう福島第一原子力発電所の事故以降の新たな事態に対応し、放出された大量の人工放射性核種の挙動を解明する研究を行った。目の前の大気に加えて、北太平洋におけるこれらの核種による汚染実態の把握やその動態の解明に取り組んだ。

過去 60 年余にわたり実施されてきたこうした研究成果を踏まえ、2015 年 4 月からは「人工放射性核種のバックグラウンド大気監視と数値解析に関する研究」を新たに開始した。本報告書では、この研究課題で得られた成果を含め、最新の成果やトピックスをテーマ毎に記述した。関係各位の今後の研究や業務に役立つ資料とすべく、編集作業を行った。我が国における環境放射能研究や大気科学研究に多少なりとも寄与できたとすれば、著者一同の望外の喜びである。

1. Sr-90 と Cs-137 の降下量の長期変化について

1) 福島事故由来以前の長期変化

気象研究所では、東京（高円寺；1957-1980）とつくば（気象研究所；1980-）で人工放射性同位体の月ごとの降下量（乾性沈着と湿性沈着の総量）のモニタリングを継続している。図１に、これまで測定された 90Sr と 137Cs の降下量の変化を示す。1945 年より前には、人工の放射性物質は環境中に存在しなかったが、核実験等により大気中に放出された。1963 年までの降下量は、核実験により成層圏に巻き上げられた放射能が、徐々に対流圏へ降下する過程（グローバルフォールアウト）により、高い値が継続していたが、1963 年に部分的核実験禁止条約が発効してから減少し始めた。減少速度は、中国とフランスが大気中の核実験を終了してから速まった。1986 年にチェルノブイリで事故が起こると、降下量は一時的に大きく増加した。その後、1990 年頃から降下量の減少速度は再び低下した。これは、一旦地面に沈着した放射性同位体が、ローカルダストと長距離輸送ダスト（黄砂）を担体として再浮遊するプロセスが、グローバルフォールアウトよりも相対的に重要になったためと考えられる。

2) 福島事故由来の 3 つのフェーズ

2011 年 3 月の福島の原発事故により、大量の人工放射性同位体が環境中に放出された。環境中の放射性同位体は、壊変と環境要因による除去プロセスにより減少するが、90Sr と 137Cs の壊変速度(半減期)は、どちらも約 30 年と非常に長いため、減少速度を決めるのは主に環境要因である。しかし、そのプロセスは、気象や担体の物理化学的性質、生物活動、人間活動等に依存し、非常に複雑である。福島事故直後につくばで観測された 137Cs の月間降下量は、2.31×104Bqm-2 であり、核実験が行われていた頃、例えば 1963 年 6 月(548 Bqm-2)よりもずっと高い。しかし、90Sr に関しては、福島事故直後の値(5.2 Bqm-2)は、1960 年 6 月(170 Bqm-2)と比べて低い。これは、福島事故により放出された 90Sr の総放射能量が 137Cs に比べて非常に少なかった（90Sr/137Cs=0.02 と見積もられている）ことで説明される。つくばと榛名山で観測された月間降下量の変化曲線から、期間を３つのフェーズに分類可能である。第１は、事故直後の 2011 年 3 月の期間で、原発からの直接の放出が効いているフェーズである。第２は、2011 年 4 月から 11 月の期間で、放出された物質がまだ空気中に残っており、対流圏での循環や除去プロセスが重要になるフェーズである。第 3 は、2012 年以降であり、再浮遊が重要になるフェーズである。2021 年 5 月につくばで測定された 137Cs の月間降下量は、ピーク時の 1/26000 まで減少したが、事故前のレベルと比較すると 130 倍にもなる。一方 90Sr については、事故前のレベルと同等まで低下している。

3) 環境中に 137Cs の減少率（回帰による推定）

事故前後の 137Cs 降下量について指数関数による回帰を行った。事故前の 1990 年 1 月から 2010 年 7 月の期間については１個の指数関数を、事故後の 2012 年から 2018 年(フェーズ３)の期間について、２つの指数関数（短寿命、長寿命の核種に対応）を用いて回帰を行った。事故後の実効半減期は、つくばについては、195 日と 4.7 年、榛名山については、148 日と 5.9 年であった。つくばにおける事故前の実効半減期は 8.5 年であったのでそれより短い。137Cs が事故前と同レベルに戻るには、計算上、2011 年から 42 年を要すると推定される。

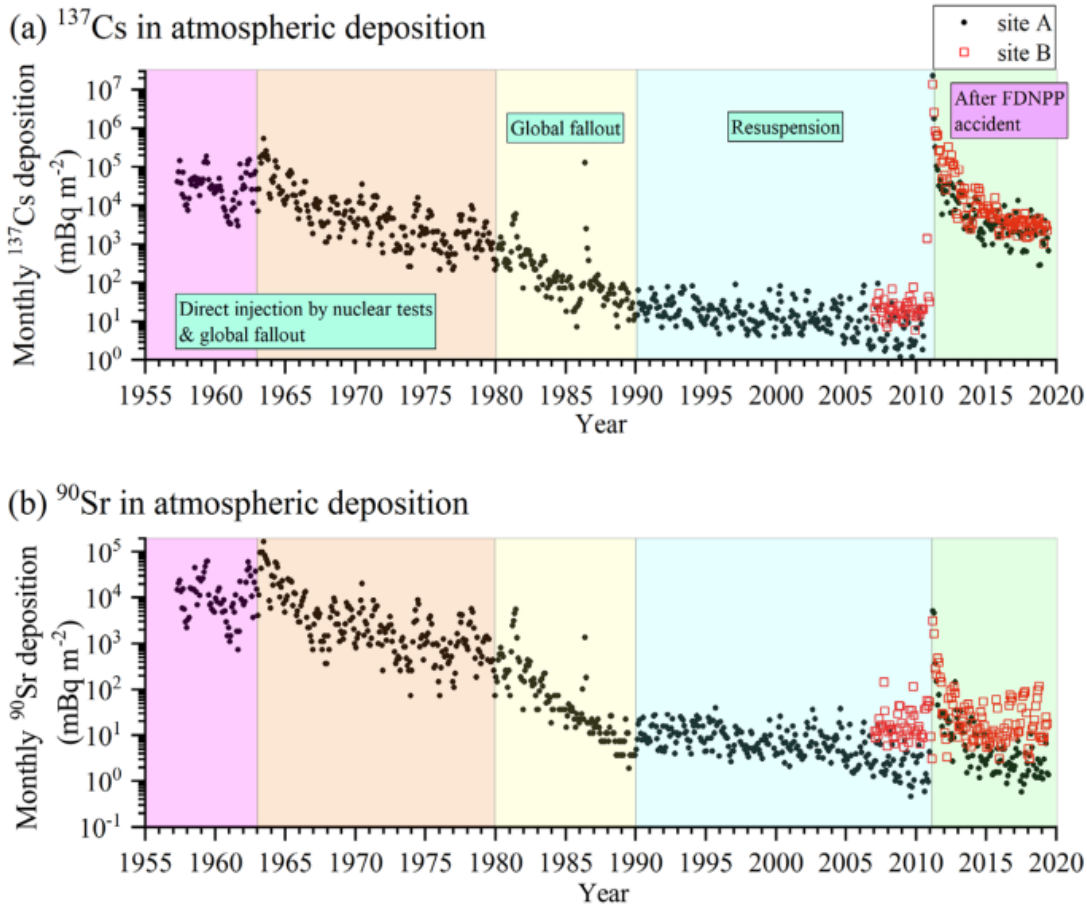

図１． Cs-137(a)と Sr-90(b)の月間降下量。2007 年以降の赤い四角は榛名山での観測データを示す。

参考文献

Kinase, T., Adachi, K., Sekiyama, T. T., Kajino, M., Zaizen, Y., & Igarashi, Y. (2020). Temporal variations of 90 Sr and 137 Cs in atmospheric depositions after the Fukushima Daiichi Nuclear Power Plant accident with long-term observations. Scientific reports, 10(1), 1-8.

2. 放射性物質の再浮遊の再評価

1） 福島原子力事故由来の放射性セシウムの地表面からの再浮遊過程の再評価

Kajino et al. (2016) もしくは前報（環境における人口放射能の研究（2018 年版）第 3 章）で報告した再浮遊の試算は、^{137}Cs の担体エアロゾルの仮定が誤っていたために、再浮遊量を過小評価した。具体的には、2013 年の計算において ^{137}Cs の担体エアロゾルを 2011 年 3 月の一次放出（原子炉からの直接放出）と同様に、サブミクロン粒子（直径 1 μm より小さい）と仮定した。しかし、その後の研究から再浮遊は土壌粒子やバイオエアロゾルなど、スーパーミクロン（直径 1 -10 μm）の粒子が主たる担体粒子である可能性が指摘されて来た。スーパーミクロン粒子は、サブミクロン粒子に比べて乾性沈着速度（v_d）や湿性沈着率（E_c）が 1 桁もしくはそれ以上に高い可能性があり、実際、福島市における ^{137}Cs の沈着量を大幅に過小評価していた（Watanabe et al., 2021）。そこで本研究（Kajino et al., 2021）では、福島県浪江町津島地区、福島県福島市（福島大学）、および茨城県つくば市（気象研究所）、の 3 か所における大気濃度と沈着量を整合的に説明する粒径分布を仮定した計算（Fig.1）により、再浮遊量と再沈着量の再評価を実施した。Fig. 1 は、大気濃度の月平均値と月間降下量をそれぞれ対数軸でとったプロットであり、傾きが 1 に近ければ縦軸の切片が沈着速度の次元となる。Kajino et al. (2016) は、観測値（紫）や本研究（緑）と比べて沈着速度が 1 桁以上過小評価していることが分かる。また紫と緑が近いことから、本研究の見積もりが現実と整合的であることも見てとれる。

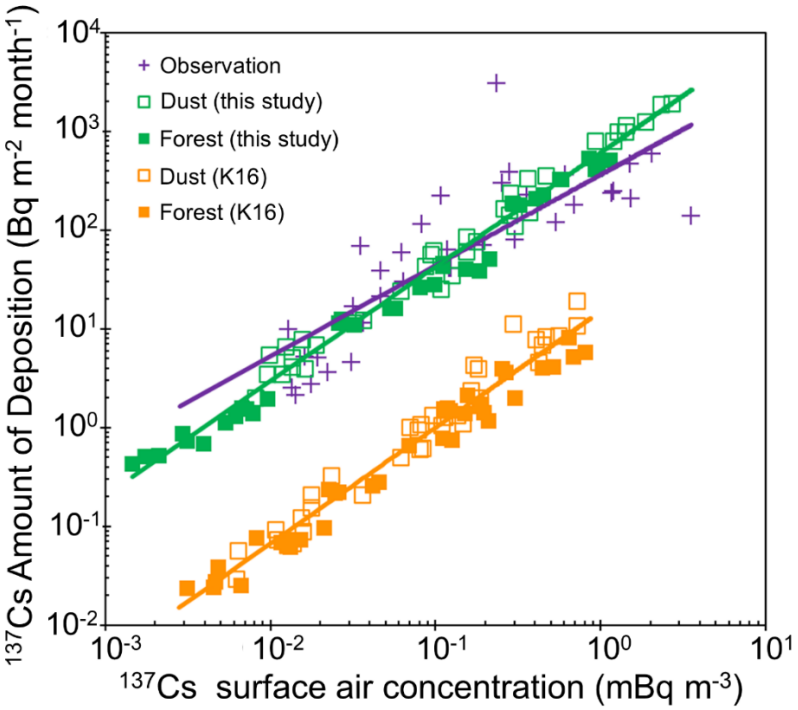

Figure 1: Scatter diagram of the depositions of ^{137}Cs over the monthly mean (purple crosses) observed surface concentrations at Namie (Tsushima), Fukushima, and Tsukuba in 2013 and those simulated by Kajino et al., 2016 (K16) ($\underline{E_c}$ and $\underline{v_d}$ are 0.04 and 0.1 cm s^{-1}, respectively) considering different emission sources: the open orange squares represent mineral dust particles from bare soil (dust aerosols), and the closed orange squares denote bioaerosols emitted from forest ecosystems (forest aerosols). The green open and closed squares are the same as the orange squares but are simulated by this study ($\underline{E_c}$ and $\underline{v_d}$ are 0.4 and 10 cm s^{-1}, respectively). The purple, orange, and green lines indicate the regression lines of the purple crosses, orange squares (open plus closed), and green squares (open plus closed), respectively.

Figure 2 に年間再浮遊・再沈着量を旧評価（上）と新評価（下）に分けて示す。新評価では、^{137}Cs の年間再浮遊量は 25.7 TBq であり、これは初期沈着量（2.68 PBq）の 0.96%に相当した。また沈着率が速いため、年間の再沈着量も 10.6 TBq と大きく、再浮遊した ^{137}Cs のうち 40%は再び地上に沈着した（残り 60%は系外に流出）。この年間再浮遊率（0.96% y^{-1}（=2.6×10^{-5} d^{-1}））は一見小さく見えるが、実際の福島県で得られた空間ガンマ線量率の減少率と比較すると、無視できないかもしれない。2013 年の ^{137}Cs と ^{134}Cs の放射性壊変を除外した減少率（つまり、陸面過程や除染などによるものと考えられる）は 1.0 – 7.9×10^{-4} d^{-1} であり、再浮遊はそれらの 1-10%程度を占める可能性がある。

依然、本研究もまた Kajino et al. (2016)と同様、再浮遊のメカニズムを解明した研究ではなく、実際の観測結果と整合的になるように領域収支（発生・輸送・沈着）を算出した結果であり、そのメカニズムはまだ未解明のままである。今後も、メカニズム解明の実験的研究に基づいた影響評価を継続していく必要がある。

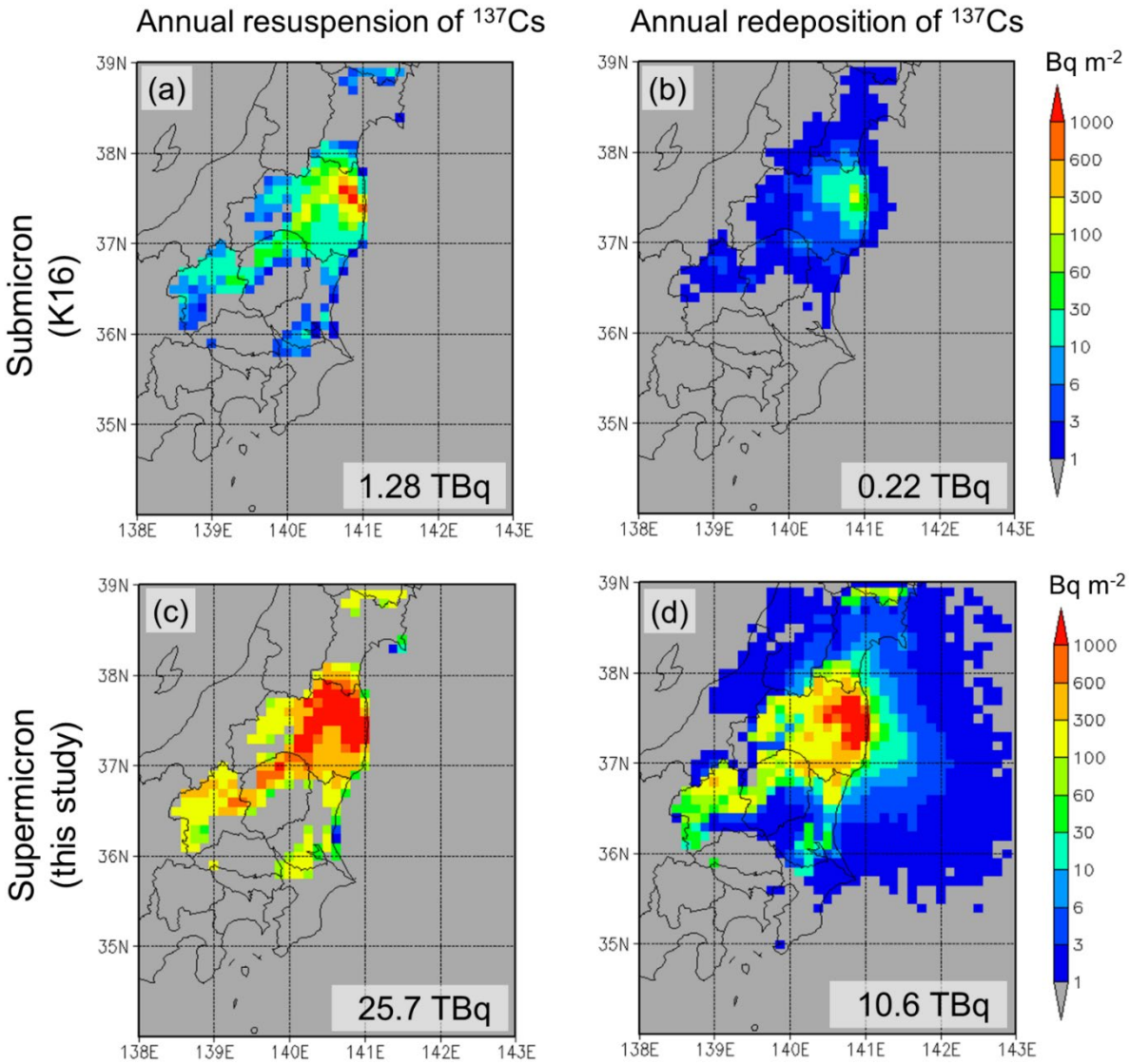

Figure 2: Horizontal distributions of (a,c) the annual total amounts of resuspended ^{137}Cs (Bq m^{-2}) and (b,d) redeposited amounts of resuspended ^{137}Cs (Bq m^{-2}) obtained from the simulations assuming (a,b) submicron (K16; $\underline{E_c}$ and $\underline{v_d}$ are 0.04 and 0.1 cm s^{-1}, respectively) and (c,d) supermicron (this study; $\underline{E_c}$ and $\underline{v_d}$ are 0.4 and 10 cm s^{-1}, respectively) sizes of ^{137}Cs-bearing particles. The areal total amounts are embedded at the bottom right of each panel.

参考文献

Kajino, M., M. Ishizuka, Y. Igarashi, K. Kita, C. Yoshikawa, M. Inatsu. Long-term assessment of airborne radiocesium after the Fukushima nuclear accident: Re-suspension from bare soil and forest ecosystems, Atmos. Chem. Phys., 16, 13149-13172, https://doi.org/10.5194/acp-16-13149-2016, 2016.

Watanabe, M., M. Kajino, K. Ninomiya, Y. Nagahashi, and A. Shinohara, Eight-year variations in atmospheric radiocesium in Fukushima city, Atmos. Chem. Phys. Discuss. [preprint], https://doi.org/10.5194/acp-2021-591, in review, 2021.

Kajino, M., A. Watanabe, M. Ishizuka, K. Kita, Y. Zaizen, T. Kinase, R. Hirai, K. Konnai, A. Saya, Y. Shiroma, H. Hasegawa, N. Akata, M. Hosoda, S. Tokonami, and Y. Igarashi, Reassessment of the radiocesium resuspension flux from contaminated ground surfaces in East Japan, submitted to Atmos. Chem. Phys.

3. Publications 2019-2021

出版論文 2019-2021

Progress in Earth and Planetary Science

RESEARCH ARTICLE Open Access

Widespread distribution of radiocesium-bearing microparticles over the greater Kanto Region resulting from the Fukushima nuclear accident

Yoshinari Abe[1,2*], Seika Onozaki[1], Izumi Nakai[1], Kouji Adachi[3], Yasuhito Igarashi[4,5], Yasuji Oura[6], Mitsuru Ebihara[6,7], Takafumi Miyasaka[3,8,9], Hisashi Nakamura[8], Keisuke Sueki[10], Haruo Tsuruta[11] and Yuichi Moriguchi[12]

Abstract

The Fukushima Daiichi Nuclear Power Plant (FDNPP) accident in March 2011 emitted a considerable amount of radioactive materials. This study isolated radiocesium-bearing microparticles (CsMPs), a form of radioactive materials emitted from the FDNPP at the early stage of the accident, from aerosols collected hourly on filter tapes at seven monitoring stations at the greater Kanto Region, including the Tokyo metropolitan area, on 15 March 2011. The aerosols had a spherical shape ~ 1 μm in diameter with activity of less than 1 Bq of ^{137}Cs per particle. Their physical and chemical characteristics, including radioactivity ratio ^{134}Cs/^{137}Cs as well as chemical composition and state, are essentially the same as previously reported CsMPs. This study demonstrated that air parcels containing CsMPs emitted from the FDNPP were widespread over the greater Kanto Region, more than 250 km away from the FDNPP, during the daytime of 15 March. Trajectory analysis indicated that these particles were emitted from the reactor No. 2 of FDNPP between 14 March evening and 15 March early morning. The information obtained on the widespread distribution of CsMPs can be useful for assessing the actual impacts of radioactive contamination from the FDNPP accident on the environment and human health.

Keywords: Fukushima Daiichi Nuclear Power Plant accident, Radiocesium-bearing microparticle, Suspended particulate matter, Synchrotron radiation X-ray analysis, Trajectory analysis

1 Introduction

Considerable amounts of radioactive materials were released into the environment following the Fukushima Daiichi Nuclear Power Plant (FDNPP) accident caused by tsunamis associated with the Tohoku Earthquake on 11 March 2011 (e.g., MEXT 2020; Steinhauser et al. 2014). To reveal the time evolution of atmospheric radionuclide concentrations immediately after the accident, Tsuruta et al. (2014, 2018) and Oura et al. (2015) investigated suspended particulate matter (SPM) collected on filter-tape at automated air pollution monitoring stations across Eastern Japan. More than 400 stations in Eastern Japan were in operation during the initial period of the FDNPP accident. Analyzing atmospheric radiocesium concentrations at 99 of those SPM monitoring stations, these studies revealed that radioactive materials emitted into the air from the FDNPP were transported over Eastern Japan via several major plumes during 12–23 March (Tsuruta et al. 2014, 2018).

* Correspondence: y.abe@mail.dendai.ac.jp
[1]Department of Applied Chemistry, Faculty of Science, Tokyo University of Science, 1-3 Kagurazaka, Shinjuku-ku, Tokyo 162-8601, Japan
[2]Division of Material Science and Engineering, Graduate School of Engineering, Tokyo Denki University, 5 Senju Asahi-cho, Adachi-ku, Tokyo 120-8551, Japan
Full list of author information is available at the end of the article

As a form of radioactive materials emitted from the FDNPP at the early stage of the accident, radiocesium-bearing microparticles (CsMPs) have been investigated by numerous researchers in recent years (Igarashi et al. 2019). They were solid particles and not easily dissolved into water, which first discovered by Adachi et al. (2013) from aerosols collected at the Meteorological Research Institute (MRI) in Tsukuba, 170 km south-southwest of FDNPP, during 2110 JST 14 March and 0910 JST 15 March 2011. After the discovery of the CsMP, many studies focused on their physical and chemical characteristics as well as their environmental distributions (Igarashi et al. 2019). While several types of CsMPs have been reported, almost CsMPs examined previously were nearly spherical, several μm in diameter, and had relatively high specific radioactivity, i.e., ~ 1 Bq per particle as ^{137}Cs (Adachi et al. 2013; Furuki et al. 2017). Their main matrices were silicate glass (Satou et al. 2016) with Fe and Zn (Adachi et al. 2013; Abe et al. 2014), and trace amounts of various heavy elements associated with nuclear fuel and fission products (FPs) were detected (Abe et al. 2014). Physical and chemical characterizations of radioactive materials, including their water solubility, shape, size, and chemical composition and state, are critical factors that determine their behavior within the environment and human body. CsMPs and other particulate radioactive materials have previously been identified in various environmental samples collected in Fukushima Prefecture as follows: soils collected around the FDNPP (e.g., Satou et al. 2016, 2018, Ono et al. 2017, Furuki et al. 2017, Martin et al. 2019, 2020), a non-woven fabric cloth laid on an agricultural field (Yamaguchi et al. 2016), and river sediments (Miura et al. 2018). Similar radioactive microparticles were also found on masks worn during cleaning work in residential areas near the FDNPP 5 years after the accident (Higaki et al. 2017). As mentioned above, these CsMPs found previously consist primarily of silicate glass. It is thus concerned that they have a long-term impact on the environment compared to water-soluble radioactive materials, whereas some recent investigations indicate a very slow rate of dissolution of CsMP into pure-water or seawater (Okumura et al. 2019; Suetake et al. 2019). Meanwhile, some CsMPs containing chloride as a water-soluble compound had been recently found from aerosols collected near the FDNPP after the hydrogen explosion of the reactor No. 1 of the FDNPP (Onozaki et al. 2019). Comprehensive investigations of CsMPs with various physical/chemical properties are therefore vitally important in accurately assessing the impacts of radioactive contamination from the FDNPP accident on the environment and human health.

Among the major polluted plumes identified by Tsuruta et al. (2014), the second plume (P2) carried the aerosols collected at the MRI on 14 and 15 March 2011 (Adachi et al. 2013). After being observed at SPM monitoring stations in the vicinity of the MRI (Tsukuba) during the morning of 15 March, P2 was then spread into the Kanto Plain, including the Tokyo metropolitan area, one of the most populated areas in the world. The southward spread of P2 was due to low-level northerlies associated with an eastward-moving low-pressure system located south of the Kanto Region (Takemura et al. 2011). Hypothesizing that CsMPs were the major carrier of radioactive Cs in P2, this study aims to verify the widespread distribution of CsMP in P2 over the greater Kanto Region (in and around the Kanto Region) on 15 March, focusing on how far CsMPs were transported southwest from the FDNPP by the local wind system. We examined radioactive aerosol particles from the SPM filter-tape samples collected hourly on 15 March at several stations in the greater Kanto Region to compare their physical/chemical characteristics with those of previously reported CsMPs isolated from various environmental samples. To investigate detailed chemical characteristics of the radioactive aerosols isolated from the SPM filter-tape samples, we applied multiple X-ray analytical techniques using a synchrotron radiation microbeam (SR-μ) X-ray in a nondestructive manner. The SR-μ-X-ray analysis is an analytical technique that is commonly used for microscopic chemical characterization of various materials in the nondestructive manner and is quite suitable for CsMPs as demonstrated by several previous studies (Abe et al. 2014; Ono et al. 2017; Onozaki et al. 2019; Miura et al. 2020; Kurihara et al. 2020a). This study has implications for the impacts of radioactive materials on the environment and human health as well as the reactor condition during the early stage of the accident.

2 Methods/experimental

2.1 SPM filter-tape samples and separation method of particles

The SPM monitors within the Japan air pollution monitoring network are routinely operated by local governments (prefectures and municipalities designated by ordinance). Particulates less than 10 μm in diameter were automatically collected on the filter tape installed in the SPM monitors as a sample spot (11 or 16 mm in diameter) for 1 h at a flow rate of 15.0, 16.7, or 18.0 l/min. The filter tape was made of glass fiber or polytetrafluoroethylene. Detailed information of the SPM filter-tape samples has been described in previous studies (Tsuruta et al. 2014, 2018; Oura et al. 2015). Seven pieces of the filters sampled at seven monitoring stations designated as A, B, C, D, E, F, and G within the greater Kanto Region (see Table 1 and Fig. 1) were used in this study. Each piece was selected which had the highest

Table 1 Information of seven monitoring stations (A~G) and SPM filter-tape samples investigated in the present study

Station	Latitude	Longitude	Distance from FDNPP	Sampling time (JST)	^{137}Cs/Bq m^{-3}
A	35.85	140.25	189 km	15 March 0800–0900	22.1
B	36.19	139.13	218 km	15 March 1200–1300	59.1
C	35.78	139.62	229 km	15 March 1000–1100	81.9
D	35.65	139.59	236 km	15 March 1000–1100	29.4
E	35.37	139.22	280 km	15 March 1400–1500	29.3
F	36.33	138.44	261 km	15 March 1600–1700	22.1
G	36.41	138.24	273 km	15 March 1600–1700	32.8

^{137}Cs concentration on March 15 at each station under the direct influence of P2. We cut these filters into four or eight portions in collecting radioactive particles. An imaging plate (GE Measurement and Control, CR × 25P computed radiography scanner) and micromanipulator (AP-xy-01; Micro Support Corp.) were used to detect and separate radioactive particles from the filters. The amount and distribution of radioactive particles on the filter was observed in a process similar to previous studies (Adachi et al. 2013; Abe et al. 2014). Prior to the SR experiments, a low-vacuum scanning electron microscope (SEM; SU 3500; Hitachi High-Technologies) was used to observe the shapes of individual particles isolated from the filters. The radioactivity of ^{134}Cs and ^{137}Cs in each particle was determined by using a Ge semiconductor detector (GC4018; CANBERRA) coupled with a multichannel analyzer (Lynx Digital Signal Analyzer; CANBERRA). The gamma-ray spectrum was collected for more than 400,000 s per particle. Two standard radioactive sources, ^{134}Cs standard by Japan Radioisotope Association and ^{137}Cs standard by Amersham plc, were measured in the same manner to

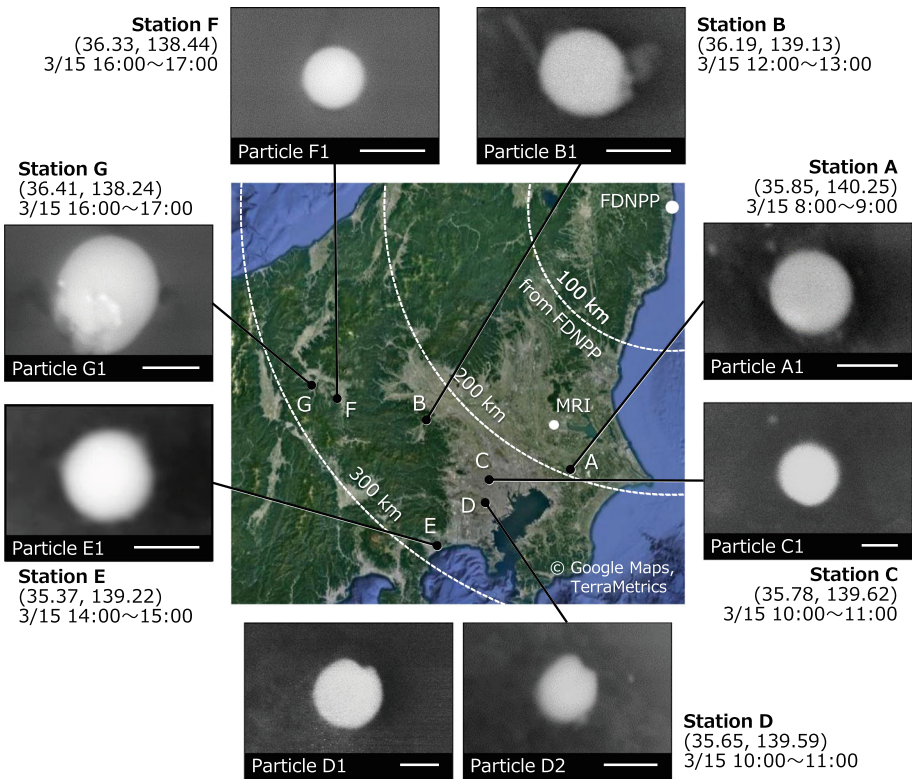

Fig. 1 Locations of monitoring stations A~G in the greater Kanto Region and radioactive particles isolated in this study. Coordinates and collection time of the filters are shown for each station. White dashed lines on the map indicate distance from the FDNPP. Eight CsMPs were isolated from these seven filters as displayed by SEM images around the map. They are nearly spherical in shape with a diameter of 1.3 μm (particle A1), 1.3 μm (B1), 1.4 μm (C1), 1.5 μm (D1), 1.2 μm (D2), 1.3 μm (E1), 0.9 μm (F1), and 1.8 μm (G1). The scale bars under the SEM images show a length of 1 μm

calibrate radioactivity of the particles. Absolute value and statistical error of radioactivity of ^{134}Cs and ^{137}Cs in individual particles were calculated as decay-corrected data at the time of 1446 JST 11 March 2011. After these analyses, the radioactive particles on carbon tape fragments were removed and then placed on a flat Kapton tape with a plastic holder for the SR-μ-X-ray analyses.

2.2 Synchrotron radiation X-ray analyses of CsMPs

The SR experiments using an X-ray microbeam were carried out at the BL37XU (Terada et al. 2004, 2010), a hard X-ray undulator beamline at SPring-8, located at the Japan Synchrotron Radiation Research Institute (JASRI). The sample was placed on an automatic XY stage in the experimental hatch. Monochromatic X-rays were obtained with a Si (111) double crystal monochromator, and the X-ray microbeam with the size of ~ 1 μm (V) × ~1 μm (H) was produced by focusing Kirkpatrick–Baez mirrors. We applied three X-ray analytical techniques: SR-μ-X-ray fluorescence (XRF) analysis, SR-μ-X-ray absorption near edge structure (XANES) analysis, and SR-μ-X-ray powder diffraction (XRD) analysis. The measurement conditions of the SR-experiments were the same as in our previous investigations (Abe et al. 2014; Ono et al. 2017; Onozaki et al. 2019).

The SR-μ-XRF analysis was carried out using 37.5 keV X-rays that enable to excite K-edges of Cs (36.0 keV) and Ba (37.4 keV). Three types of energy-dispersive X-ray detectors were used depending on the beamtime: a Si (Li) detector for the beamtimes until 2017, and eight-elements silicon drift detectors or a Ge semiconductor detector for the beamtimes in 2018 and 2019. The SR-μ-XRF spectrum was measured for 200 s in live time per sample. The intensity of each spectrum was normalized to that of the Thomson scattering peak detected at 37.5 keV. The SR-μ-XANES spectra of the particles and the reference samples were measured in fluorescence mode for the following absorption edges: Fe-K edge (7111 eV), Zn-K edge (9661 eV), Mo-K edge (20,000 eV), and Sn-K edge (29,200 eV). The intensity of Kα line of each target elements in individual particles was scanned with a measurement step of ~ 1 eV/step, integration times of 3.0~10.0 s/step, and an energy range of ~ 100 eV from the lower to the higher energy sides of the absorption edge. To normalize the Kα intensity of the target elements, an intensity of the incident X-ray beam (I_0) was monitored using an ionization chamber. Reference materials (powders of metals, typical oxides, sulfides, silicates, and synthesized glass samples) containing each target elements were also measured as a same manner. In the SR-μ-XRD analysis, the X-ray diffraction patterns of the samples were measured with a Debye–Scherrer optical system using a two-dimensional detector (CMOS flat panel) placed 200 mm behind the sample. The energy of the incident X-ray was set to 15.0 keV with an exposure time of 440 ms and an integration of 100 times/sample.

2.3 Trajectory analysis for the radioactive plume transport

A meteorological trajectory analysis was conducted to evaluate air parcel positions every 10 min based on wind fields from the Japan Meteorological Agency mesoscale-model objective analysis. The analysis has a horizontal resolution of 0.0625 × 0.05° with 50 vertical levels up to 21,800 m. Three-hourly analysis data of wind on model levels were used, as well as 3-hourly analysis and 1-hourly forecast data of 10 m surface wind. The three-dimensional wind data cannot resolve small-scale turbulence that is most vigorous within the mixed layer. Air parcels were initially placed at 50 m intervals from 50 m to 1000 m above the surface. For each parcel, the trajectory calculation was terminated if it hit the surface.

3 Results and discussion

3.1 Physical/chemical characteristics of CsMPs isolated from SPM filter-tape

In total, eight CsMPs were successfully isolated from seven pieces of SPM filter-tape samples. As illustrated in Fig. 1, the eight CsMPs were labelled as A1, B1, C1, D1, D2, E1, F1, and G1 in corresponding to the seven SPM monitoring stations. The particles were spherical with diameters of ~ 1 μm, and their radioactivity was less than 1 Bq of ^{137}Cs per particle (Fig. 2). The radioactivity ratios between ^{134}Cs and ^{137}Cs (^{134}Cs/^{137}Cs) were ~ 1.0, suggesting that these particles were emitted from either reactor No. 2 or 3 of FDNPP (Nishihara et al. 2010) (see additional data Table S1 online). As first pointed out by Satou et al. (2018), CsMPs from the FDNPP can be categorized into two major types, type A and type B, based on the ^{134}Cs/^{137}Cs ratio of individual particles. Type A particles are characterized by ^{134}Cs/^{137}Cs ratio of ~ 1.0, in contrast to type B particles with ^{134}Cs/^{137}Cs ratio of ~ 0.9.

As a result of the SR-μ-XRF analyses of individual particles, A1~G1 were found to have qualitatively-similar chemical compositions. The SR-μ-XRF spectra of four representative particles (A1, B1, C1, and E1) are shown in Fig. 3 with that of a type A CsMP collected at the MRI in a previous study (Abe et al. 2014). Note that all these spectra were measured using the same Si (Li) detector in several beamtimes. The XRF analysis using a monochromatic SR-μ-X-ray with high-energy (37.5 keV) for the excitation can detect trace amounts of heavy elements within individual particles, although lighter elements (such as Si) that are major components of the particle could not be detected in the spectrum. In addition to sharp K-line peaks of Cs which had been identified by the gamma-ray spectroscopy, the following eight heavy elements were detected in all particles: Fe,

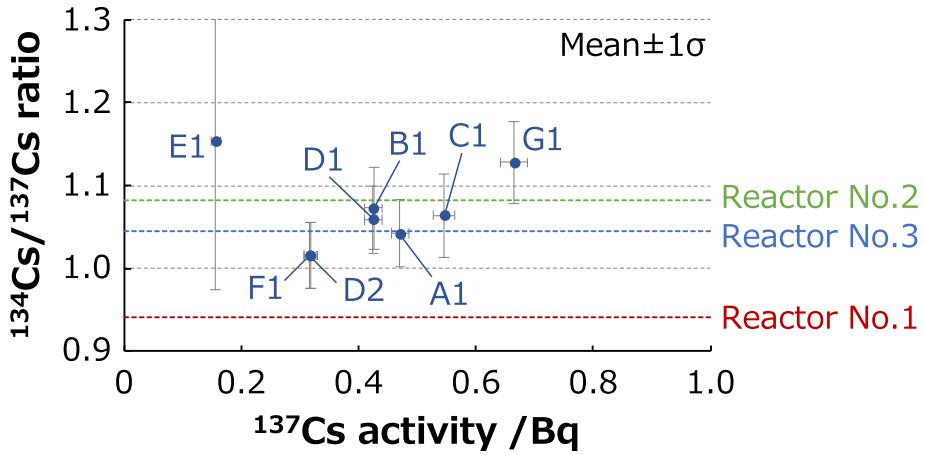

Fig. 2 Radioactivity of ^{137}Cs and ^{134}Cs/^{137}Cs activity ratio of individual particles. The radioactivity of ^{137}Cs (± 1 × standard deviation, σ) of eight particles (A1~G1) are as follows: 0.471 ± 0.016 Bq (particle A1), 0.426 ± 0.015 Bq (B1), 0.546 ± 0.019 Bq (C1), 0.425 ± 0.014 Bq (D1), 0.318 ± 0.011 Bq (D2), 0.156 ± 0.008 Bq (E1), 0.317 ± 0.011 Bq (F1), and 0.665 ± 0.023 Bq (G1). The three dashed lines show estimates of the ^{134}Cs/^{137}Cs ratio of nuclear fuel in FDNPP reactors No. 1, 2, and 3, respectively, at the time of the accident, as calculated using ORIGEN2 Code (Nishihara et al. 2010). Activity values shown here were decay-corrected as of 11 March 2011

Zn, Rb, Mo, Sn, Sb, Te, and Ba. Several trace elements specific to certain particles were also found: Zr from seven particles except for particle B1; Nb from particle C1; Ag from particle F1, Cd from particles C1 and G1; Pb from particles A1, B1, C1, E1, F1, and G1; and U from particles A1, B1, and F1.

The SR-μ-XANES analysis examined the chemical states of four metal elements (Fe, Zn, Mo, and Sn) and indicated that these elements exist as cations in silicate glass with high oxidation numbers (see additional data Fig. S1 online). SR-μ-XRD analysis of individual particles showed no diffraction peaks caused by crystal structure for any of the particles (see additional data Fig. S2 online), confirming that these particles have glass bodies.

As discussed above, physical/chemical characteristics obtained for the eight CsMPs (A1~G1) collected at the seven SPM monitoring stations in the greater Kanto Region are essentially the same as those of type A CsMPs found in the previous studies (e.g., Abe et al. 2014; Igarashi et al. 2019). As first reported by Utsunomiya et al. (2019), it is already-known fact that air parcels containing type A CsMPs passed over Tokyo City at some point on 15 March. Our results strongly support their pioneering report. At the same time, this paper first demonstrated that CsMPs emitted from the FDNPP were widespread over the greater Kanto Region, including West side of Tokyo metropolitan area, during the daytime of 15 March with a temporal resolution of an hour.

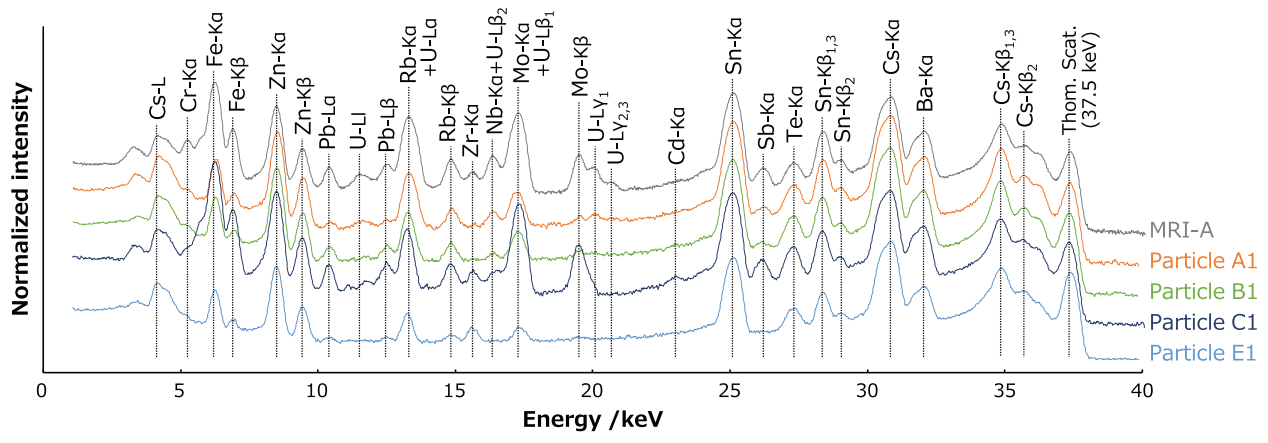

Fig. 3 SR-μ-XRF spectra of four representative CsMPs (A1, B1, C1, and E1) isolated from the SPM filter-tape samples, showing the heavy elemental composition of individual particles. The intensity of each spectrum is displayed on a logarithmic scale and shifted in a longitudinal direction. The spectrum of MRI-A shows datum obtained for one of type A CsMPs (particle A) collected at the MRI in the previous study (Abe et al. 2014)

3.2 Transport pathway of CsMP from FDNPP to greater Kanto Region

To estimate the emission time of the CsMPs and identify their transport pathway(s) from the FDNPP to the greater Kanto Region, we conducted trajectory analysis of air parcels that passed over the seven monitoring stations A~G. As an example, Fig. 4 shows backward trajectories for air parcels situated at different heights over station B starting at 1200 JST 15 March, where the SPM aerosols including particle B1 were collected during 1200–1300 JST. The trajectories are color-coded to distinguish parcel heights at station B in Fig. 4a and also color-coded by parcel height at each time step in Fig. 4b. Figure 4a, b suggests that the air parcels situated at 150–600 m above station B at 1200 JST were likely to be located below the 500 m level within 20 km range from the FDNPP sometime between 0040 and 0330 JST on the same day. The vertical profile of potential temperature at station B (Fig. 4c) indicates that the atmospheric mixed layer was as deep as 800 m above the surface, suggesting that air parcels within the layer should have experienced vigorous turbulent mixing and thus be well-mixed down to near-surface levels. Likewise, air parcels from the FDNPP were released into the night-time mixed layer. Advected by low-level northerlies, these air parcels then travelled along the coast mostly within the marine mixed layer (Fig. 4b), which was probably well developed in the early morning given the cool offshore northerlies over the relatively warm ocean.

Results of our backward trajectory analysis for the seven monitoring stations are summarized in Table 2. Although the estimated emission times have ranges that span several hours, we concluded that polluted air parcels containing CsMPs that passed over the greater Kanto Region on 15 March were emitted from the FDNPP between the evening of 14 March and early morning 15 March. After being released into the mixed layer, these polluted air parcels were advected southward by low-level northerlies and later by northeasterlies. The parcels very likely underwent vigorous mixing down to near-surface levels, within the mixed layer above the stations. The earliest emission time is estimated for the parcels above station E, as the trajectories detoured far offshore under the northwesterlies shortly after emitted. Our trajectory analysis implies that individual aerosol particles that were emitted locally from the FDNPP subsequently spread widely over the greater Kanto Region within a relatively short period of time (within 18 h at the longest) under time-varying flow conditions. Based on the results of our backward trajectory analysis, we calculated forward trajectories for air parcels over the FDNPP starting at 0100 JST 15 March 2011 and showed them on the map with the seven monitoring stations A~G (Fig. 5). The air parcels situated above the FDNPP at that time moved southward and then widespread over the greater Kanto Region within a day.

3.3 Possible source of CsMPs distributed over greater Kanto Region

The chemical composition of particles emitted primarily from the FDNPP could reflect the reactor condition during the early stages of the accident. As indicated by Okumura et al. (2019), we cannot ignore the possibility that CsMP collected from soils years after the accident was altered physically or chemically in the environment even if they are hardly soluble into the water. Unlike such field samples, there would be little change in physical and chemical properties of the CsMPs as they were sampled on the SPM filter-tape shortly after emission. The

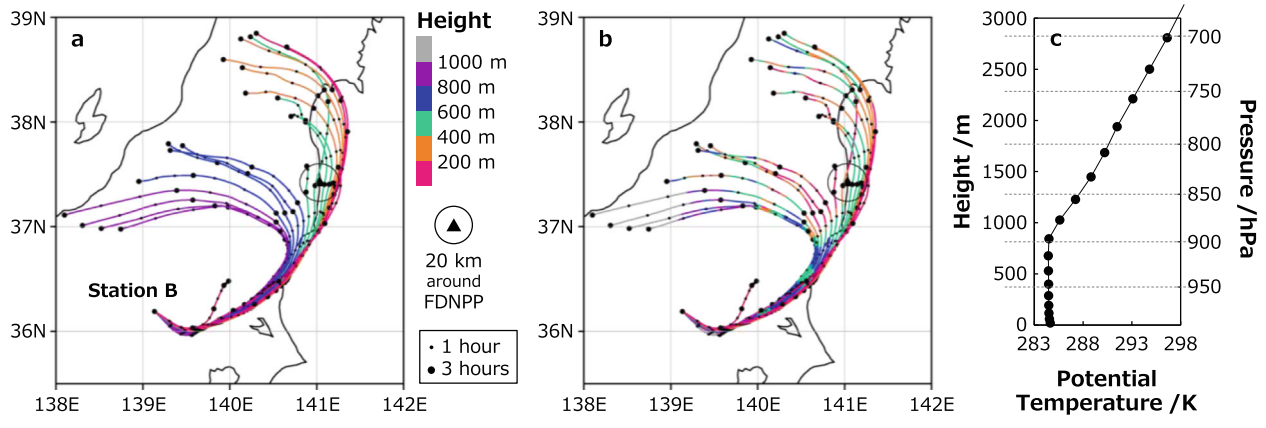

Fig. 4 Backward trajectories calculated for air parcels placed above station B at 1200 JST 15 March 2011. The trajectories are color-coded (**a**) to distinguish heights (m) of the parcels at station B and (**b**) according to their heights at each time step. Small and large dots on the trajectories indicate intervals of every hour and 3 h, respectively, after the calculation start time. **c** Vertical profile of potential temperature (K) above station B at the trajectory start time

Table 2 Summary of the backward trajectory analysis for seven monitoring stations (A~G)

Station	Starting time (JST) of backward trajectories	Depth of atmospheric mixed layer above the station	Estimated paths of air parcels between the station and 20 km range from FDNPP		
			Height above the station	Height above 20 km range from FDNPP	Estimated emission time (JST) from FDNPP
A	15 March 0800	~500 m	750-800 m	0-600 m	15 March 0000-0220
B	15 March 1200	~800 m	150-600 m	0-500 m	15 March 0040-0330
C	15 March 1100	~900 m	800-900 m	100-700 m	15 March 0210-0340
D	15 March 1100	~900 m	850-900 m	50-650 m	15 March 0120-0310
E	15 March 1400	~700 m	750-850 m	100-650 m	14 March 2000- 15 March 0130
F	15 March 1600	~200 m	50-650 m	50-550 m	15 March 0040-0340
G	15 March 1600	~200 m	50-300 m	100-300 m	14 March 2330- 15 March 0200

chemical compositions of the CsMPs discussed in this study are thus likely to be preserved except for radioactive decay effects. Therefore, our analysis offers important information regarding raw materials and the generation process of CsMP in the reactor. All elements identified in the CsMPs can be associated with materials in the FDNPP. As a result of the nuclear fission reaction of ^{235}U, the FPs yielded 11 elements (Rb, Zr, Nb, Mo, Ag, Cd, Sn, Sb, Te, Cs, and Ba) (Crouch 1977, Burns et al. 2012, Yamamoto 2012). It is also possible that Zr and Sn in the CsMPs originate to Zr–Sn alloy used for fuel cladding within the reactors. On the other hand, vaporous elements, such as Rb (e.g., the boiling points of RbOH and RbI are about 1660 K and 1577 K under 1 atm, respectively) and Cs (e.g., the boiling points of CsOH and CsI are about 1263 K and 1553 K under 1 atm, respectively), in the CsMPs were richer than the original composition of FPs derived from U fuel. Therefore, condensation of these elements by vaporization in the reactor pressure vessel (RPV) could happen during the particle generation process. Moreover, the amounts of Cs in the particles would be higher than those of Mo even considering the difference in excitation efficiency from monochromatic X-rays (37.5 keV). Although Cs_2MoO_4 was suggested as one possible source for the vapor phases carrying Cs at high temperature (Kissane and Drosik 2006; Gouello et al. 2013; Do et al. 2018), our result indicates that the volatilization and condensation of Cs_2MoO_4 were not predominant processes of the generating of the CsMPs. Do et al. (2018) have pointed out that CsOH is the predominant cesium species when the damaged fuel temperature is higher than 2000 K at higher steam pressures, but Cs_2MoO_4 would become more important at lower temperature. In this connection, Imoto et al. (2017) reported the presence of nanoparticles of $CsFeSi_2O_6$ within CsMP and pointed out that the material could be formed by the CsOH chemisorption onto Si-bearing stainless steel. Iron, Cr, Mn, Ni, and Mo could originate from stainless steel, which composed RPV and FDNPP buildings. Regarding a possible source for Zn, we previously identified an additive agent of primary cooling water (Abe et al. 2014), but a thin plating of steel and inorganic paint on RPV and buildings could be other potential sources (Itou et al. 2018). Lead metal and Pb-containing materials are commonly used for shielding of radiation. To make a more detailed interpretation of the generation process of the CsMPs, it is indispensable to carry out further scientific investigation using other analytical methods to reveal more quantitative chemical composition and isotopic features of individual particles, such as secondary ion mass spectrometry (Imoto et al. 2017; Kurihara et al. 2020a; Kurihara et al. 2020b).

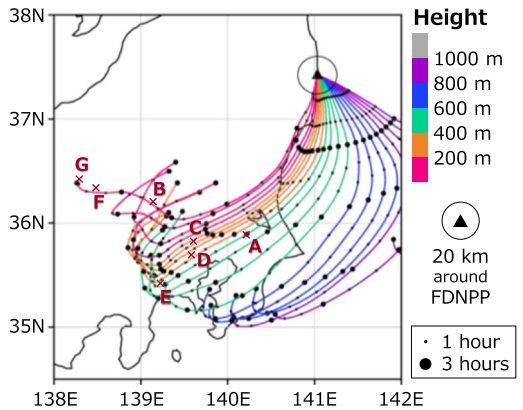

Fig. 5 Forward trajectories calculated for air parcels placed above the FDNPP at 0100 JST 15 March 2011. The trajectories are color-coded to distinguish heights (m) of the parcels at FDNPP. Small and large dots on the trajectories indicate intervals of every hour and 3 h since the calculation start time, respectively

As described above, type A CsMPs including eight particles investigated in this study have been thought to be originated to either reactors No. 2 or No. 3 of the FDNPP based on their $^{134}Cs/^{137}Cs$ ratio: there are two opinions about from which the type A CsMPs were emitted (e.g., Igarashi et al. 2019; Ikehara et al. 2020). We therefore consider the source of the type A CsMPs in relationship to the accident progress, making use of high time-resolution of the SPM filter-tape samples. Our trajectory analysis suggests that the emission time for the

type A CsMPs isolated from the greater Kanto Region was between midnight and early morning 15 March, although emission time could have been as early as the evening of 14 March for parcels that reached station E (Table 2). Consistent with these estimated emission times, pressure inside the RPV in reactor No. 2 decreased after the usage of a safety relief valve around 1903 JST on 14 March, followed by three sharp RPV pressure peaks around 2100 and 2300 JST 14 March and 0100 JST 15 March (TEPCO 2015). Around 0300 JST on 15 March, the pressure inside the primary containment vessel of reactor No. 2 exceeded its designed value (TEPCO 2015). In contrast, no incident was reported for reactor No. 3 during the same period except for a hydrogen explosion at 1101 JST 14 March. We therefore hypothesized that the incident(s) in reactor No. 2 were the most likely cause of the type A CsMPs, rather than reactor No. 3. Our hypothesis is strongly supported by recent investigation of isotopic ratios of U and Cs in CsMPs (Kurihara et al. 2020b).

4 Conclusions

Eight CsMPs were isolated successfully from aerosol particles collected hourly on filter tapes at seven monitoring stations in the greater Kanto Region, including the Tokyo metropolitan area, on 15 March 2011. Our finding demonstrates clearly that air parcels containing CsMPs emitted from the FDNPP were widespread over the greater Kanto Region, farther than 250 km away from the FDNPP, during the daytime of 15 March. Detailed physical and chemical properties of individual CsMPs were investigated by SR-μ-X-ray analyses. As a result, it was concluded that the incident(s) in reactor No. 2 of FDNPP were the most likely cause of CsMPs distributed over the greater Kanto Region. Our trajectory analysis also suggests that air parcels containing the CsMPs as water-insoluble microparticles with radionuclides likely passed over the greater Kanto Region including Tokyo metropolitan area on 15 March. Some of those particles could have been deposited on the ground or suspended in the near-surface air, although most of them were transported to the ocean. Further investigation is necessary to estimate the environmental and health impacts from the CsMPs that travelled into the metropolitan area. Information regarding widespread distribution of CsMPs can be useful toward calculating an inhalation dose of radionuclides during the early stage of the accident.

5 Supplementary Information

The online version contains supplementary material available at https://doi.org/10.1186/s40645-020-00403-6.

Additional file 1: Table S1. ^{134}Cs and ^{137}Cs radioactivities and $^{134}Cs/^{137}Cs$ activity ratio of eight particles (A1~G1). **Figure S1.** SR-μ-XANES spectra of four representative CsMPs (A1, B1, C1, and E1) isolated from the SPM filter and reference materials. (a) Fe-K edge, (b) Zn-K edge, (c) Mo-K edge, and (d) Sn-K edge. **Figure S2.** SR-μ-XRD patterns of four representative radioactive particles (A1, B1, C1, and E1) isolated from the SPM filter and reference material. (a) Particle A1, (b) particle B1, (c) particle C1, (d) particle E1, and (e) silicon powder (NIST SRM 640c). In contrast to sharp diffraction peaks detected in silicon powder, no obvious peaks were detected in four radioactive particles.

Abbreviations

FDNPP: Fukushima Daiichi Nuclear Power Plant; SPM: Suspended particulate matter; CsMP: Radiocesium-bearing microparticle; JST: Japan Standard Time; MRI: Meteorological Research Institute; FP: Fission product; SR-μ-X-ray: Synchrotron radiation microbeam X-ray; JASRI: Japan Synchrotron Radiation Research Institute; XRF: X-ray fluorescence; XANES: X-ray absorption near edge structure; XRD: X-ray powder diffraction; SEM: Scanning electron microscope; RPV: Reactor pressure vessel

Acknowledgements

We thank all local governments for allowing us to investigate the SPM filter-tape samples. We are deeply grateful to Dr. Y Terada, Dr. K Nitta, and Dr. O Sekizawa (SPring-8/JASRI) for their assistances in the SR experiment at BL37XU, SPring-8. The synchrotron radiation experiments were performed with the approval of the SPring-8 Program Advisory Committee (proposal numbers 2016A1705, 2016B1811, 2017A1719, 2017B1757, 2018A1704, 2018B1748, and 2019B1308).

Authors' contributions

YA performed the SR measurements, data analysis, and wrote the manuscript. SO performed the separation of particles and SR measurements. IN and YI conceived the study idea. KA conducted the SEM analysis. YO and ME controlled the SPM filter-tape samples. TM and HN performed the trajectory analysis. KS conducted the gamma-ray spectrometry. HT and YM helped to devise the study idea and assisted with cooperation and coordination with local governments. All authors read and approved the final manuscript.

Funding

This work was supported by MEXT/JSPS KAKENHI Grants (24110003, 15H00978, 19H05702), in collaboration with projects of Environment Research and Technology Development Fund of the Environmental Restoration and Conservation Agency, Japan (JPMEERF20155001, JPMEERF20181002, and JPMEERF20192004). This work was also supported by Joint Research on Risk Evaluation and Management in Nuclear Technology (Japan-U.K.), the Collaborative Laboratories for Advanced Decommissioning Science, JAEA (JPJA18F18072860).

Availability of data and materials

Data sharing not applicable to this article as no datasets were generated or analyzed during the current study. Please contact corresponding author for data requests.

Competing interests

The authors declare that they have no known competing financial interests or personal relationships that could have appeared to influence the work reported in this paper.

Author details

[1]Department of Applied Chemistry, Faculty of Science, Tokyo University of Science, 1-3 Kagurazaka, Shinjuku-ku, Tokyo 162-8601, Japan. [2]Division of Material Science and Engineering, Graduate School of Engineering, Tokyo Denki University, 5 Senju Asahi-cho, Adachi-ku, Tokyo 120-8551, Japan. [3]Meteorological Research Institute, 1-1 Nagamine, Tsukuba-shi, Ibaraki 305-0052, Japan. [4]Institute for Integrated Radiation and Nuclear Science, Kyoto University, 2-chome, Asashiro-Nishi, Kumatori-cho, Sennan-gun, Osaka 590-0494, Japan. [5]College of Science, Ibaraki University, 2-1-1 Bunkyo, Mito-shi, Ibaraki 310-8215, Japan. [6]Graduate School of Science, Tokyo Metropolitan University, 1-1 Minami-Osawa, Hachioji-shi, Tokyo 192-0397, Japan. [7]Department of Earth Sciences, School of Education and Integrated Arts & Sciences, Waseda University, 1-6-1 Nishi-waseda, Shinjuku-ku, Tokyo 169-8050, Japan. [8]Research Center for Advanced Science and Technology, The University of Tokyo, 4-6-1 Komaba, Meguro-ku, Tokyo 153-8904, Japan.

[9]Japan Meteorological Business Support Center, 1-1 Nagamine, Tsukuba-shi, Ibaraki 305-0052, Japan. [10]Faculty of Pure and Applied Sciences, University of Tsukuba, 1-1-1 Tennodai, Tsukuba-shi, Ibaraki 305-8571, Japan. [11]Remote Sensing Technology Center of Japan, 3-17-1 Toranomon, Minato-ku, Tokyo 105-0001, Japan. [12]Department of Urban Engineering, The University of Tokyo, 7-3-1 Hongo, Bunkyo-ku, Tokyo 113-8656, Japan.

Received: 23 September 2020 Accepted: 21 December 2020
Published online: 26 January 2021

References

Abe Y, Iizawa Y, Terada Y, Adachi K, Igarashi Y, Nakai I (2014) Detection of uranium and chemical state analysis of individual radioactive microparticles emitted from the Fukushima nuclear accident using multiple synchrotron radiation X-ray analyses. Anal Chem 86:8521–8525. https://doi.org/10.1021/ac501998d

Adachi K, Kajino M, Zaizen Y, Igarashi Y (2013) Emission of spherical cesium-bearing particles from an early stage of the Fukushima nuclear accident. Sci Rep 3:2554. https://doi.org/10.1038/srep02554

Burns PT, Ewing RC, Navrotsky A (2012) Nuclear fuel in a reactor accident. Sci 225:1184–1188. https://doi.org/10.1126/science.1211285

Crouch EAC (1977) Fission-product yields from neutron-induced fission. At Data Nucl Data Tables 19:417–532. https://doi.org/10.1016/0092-640X(77)90023-7

Do TM, Sujatanond S, Ogawa T (2018) Behavior of cesium molybdate, Cs_2MoO_4, in severe accident conditions. (1) Partitioning of Cs and Mo among gaseous species. J Nucl Sci Technol 55:348–355. https://doi.org/10.1080/00223131.2017.1397560

Furuki G, Imoto J, Ochiai A, Yamasaki S, Nanba K, Ohnuki T, Grambow B, Ewing RC, Utsunomiya S (2017) Caesium-rich micro-particles: a window into the meltdown events at the Fukushima Daiichi Nuclear Power Plant. Sci Rep 7:42731. https://doi.org/10.1038/srep42731

Gouello M, Mutelle H, Cousin F, Sobanska S, Blanquet E (2013) Analysis of the iodine gas phase produced by interaction of CsI and MoO3 vapours in flowing steam. Nucl Eng Des 263:462–472. https://doi.org/10.1016/j.nucengdes.2013.06.016

Higaki S, Kurihara Y, Yoshida H, Takahashi Y, Shinohara N (2017) Discovery of non-spherical heterogeneous radiocesium-bearing particles not derived from Unit 1 of the Fukushima Dai-ichi Nuclear Power Plant, in residences five years after the accident. J Environ Radioact 177:65–70. https://doi.org/10.1016/j.jenvrad.2017.06.006

Igarashi Y, Kogure T, Kurihara Y, Miura H, Okumura T, Satou Y, Takahashi Y, Yamaguchi N (2019) A review of Cs-bearing microparticles in the environment emitted by the Fukushima Dai-ichi Nuclear Power Plant accident. J Environ Radioact 205–206:101–118. https://doi.org/10.1016/j.jenvrad.2019.04.011

Ikehara R, Morooka K, Suetake M, Komiya T, Kurihara E, Takehara M, Takami R, Kino C, Horie K, Takehara M, Yamasaki S, Ohnuki T, Law GTW, Bower G, Grambow B, Ewing RC, Utsunomiya S (2020) Abundance and distribution of radioactive cesium-rich microparticles released from the Fukushima Daiichi Nuclear Power Plant into the environment. Chemosphere 241:125019. https://doi.org/10.1016/j.chemosphere.2019.125019

Imoto J, Ochiai A, Furuki G, Suetake M, Ikehara R, Horie K, Takehara M, Yamasaki S, Nanba K, Ohnuki T, Law GTW, Grambow B, Ewing RC, Utsunomiya S (2017) Isotopic signature and nano-texture of cesium-rich micro-particles: release of uranium and fission products from the Fukushima Daiichi Nuclear Power Plant. Sci Rep 7:5409. https://doi.org/10.1038/s41598-017-05910-z

Itou K, Suzuki A, Ohishi Y, Nakamori F, Hikida S, Nozaki K, Honda T, Mizokami S (2018) Investigation of in-reactor cesium chemical behavior in TEPCO's Fukushima Daiichi Nuclear Power Station accident (10) Phenomenological generation mechanisms of spherical cesium bearing particle. In: Oral presentation in Atomic Energy Society of Japan 2018 Annual Meeting, held on 27 March 2018 at Osaka University Suita Campus

Kissane MP, Drosik I (2006) Interpretation of fission-product transport behaviour in the Phébus FPT0 and FPT1 tests. Nucl Eng Des 236:1210–1223. https://doi.org/10.1016/j.nucengdes.2005.10.012

Kurihara E, Takehara M, Suetake M, Ikehara R, Komiya T, Morooka K, Takami R, Yamasaki S, Ohnuki T, Horie K, Takehara M, Law GTW, Bower W, Mosselmans JFW, Warnicke P, Grambow B, Ewing RC, Utsunomiya S (2020a) Particulate plutonium released from the Fukushima Daiichi meltdowns. Sci Total Environ 743:140539. https://doi.org/10.1016/j.scitotenv.2020.140539

Kurihara Y, Takahata N, Yokoyama TD, Miura H, Kon Y, Takagi T, Higaki S, Yamaguchi N, Sano Y, Takahashi Y (2020b) Isotopic ratios of uranium and caesium in spherical radioactive caesium-bearing microparticles derived from the Fukushima Dai-ichi Nuclear Power Plant. Sci Rep 10:3281. https://doi.org/10.1038/s41598-020-59933-0

Martin PG, Jones CP, Cipiccia S, Batey DJ, Hallam KR, Satou Y, Griffiths I, Rau C, Richards DA, Sueki K, Ishii T, Scott TB (2020) Compositional and structural analysis of Fukushima-derived particulates using high-resolution X-ray imaging and synchrotron characterisation techniques. Sci Rep 10:1636. https://doi.org/10.1038/s41598-020-58545-y

Martin PG, Louvel M, Cipiccia S, Jones CP, Batey DJ, Hallam KR, Yang IAX, Satou Y, Rau C, Mosselmans JFW, Richards DA, Scott TB (2019) Provenance of uranium particulate contained within Fukushima Daiichi Nuclear Power Plant Unit 1 ejecta material. Nat Commun 10:2801. https://doi.org/10.1038/s41467-019-10937-z

MEXT (2020) Japanese Ministry of Education, Culture, Sports, Science and Technology. https://www.mext.go.jp/en/. Accessed 22 Nov 2020

Miura H, Kurihara Y, Sakaguchi A, Tanaka K, Yamaguchi N, Higaki S, Takahashi Y (2018) Discovery of radiocesium-bearing microparticles in river water and their influence on the solid-water distribution coefficient (K_d) of radiocesium in the Kuchibuto River in Fukushima. Geochem J 52:145–154. https://doi.org/10.2343/geochemj.2.0517

Miura H, Kurihara Y, Yamamoto M, Sakaguchi A, Yamaguchi N, Sekizawa O, Nitta K, Higaki S, Tsumune D, Itai T, Takahashi Y (2020) Characterization of two types of cesium-bearing microparticles emitted from the Fukushima accident via multiple synchrotron radiation analyses. Sci Rep 10:11421. https://doi.org/10.1038/s41598-020-68318-2

Nishihara K, Iwamoto H, Suyama K (2010) Estimation of fuel compositions in Fukushima-Daiichi nuclear power plant. In: JAEA-Data/Code 2012-018, Japan Atomic Energy Agency, 2010.

Okumura T, Yamaguchi N, Dohi T, Iijima K, Kogure T (2019) Dissolution behaviour of radiocaesium-bearing microparticles released from the Fukushima nuclear plant. Sci Rep 9:3520. https://doi.org/10.1038/s41598-019-40423-x

Ono T, Iizawa Y, Abe Y, Nakai I, Terada Y, Satou Y, Sueki K, Adachi K, Igarashi Y (2017) Investigation of the chemical characteristics of individual radioactive microparticles emitted from reactor 1 by the Fukushima Daiichi Nuclear Power Plant accident by using multiple synchrotron radiation X-ray analyses. Unseki Kagaku 66:251–261. https://doi.org/10.2116/bunsekikagaku.66.251

Onozaki S, Abe Y, Nakai I, Adachi K, Igarashi Y, Oura Y, Ebihara M, Miyasaka T, Nakamura H, Sueki K, Tsuruta H, Moriguchi Y (2019) Investigation of physical and chemical characteristics of radioactive aerosols emitted from reactor unit 1 by Fukushima Daiichi Nuclear Power Plant accident. BUNSEKI KAGAKU 68:757–768. https://doi.org/10.2116/bunsekikagaku.68.757

Oura Y, Ebihara M, Tsuruta H, Nakajima T, Ohara T, Ishimoto M, Katsumura Y (2015) Determination of atmospheric radiocesium on filter tapes used at automated SPM monitoring stations for estimation of transport pathways of radionuclides from Fukushima Dai-ichi Nuclear Power Plant. J Radioanal Nucl Chem 303:1555–1559. https://doi.org/10.1007/s10967-014-3662-4

Satou Y, Sueki K, Sasa K, Adachi K, Igarashi Y (2016) First successful isolation of radioactive particles from soil near the Fukushima Daiichi Nuclear Power Plant. Anthropocene 14:71–76. https://doi.org/10.1016/j.ancene.2016.05.001

Satou Y, Sueki K, Sasa K, Yoshikawa H, Nakama S, Minowa H, Abe Y, Nakai I, Ono T, Adachi K, Igarashi Y (2018) Analysis of two forms of radioactive particles emitted during the early stages of the Fukushima Dai-ichi Nuclear Power Station accident. Geochem J 52:145–154. https://doi.org/10.2343/geochemj.2.0514

Steinhauser G, Brandl A, Johnson TE (2014) Comparison of the Chernobyl and Fukushima nuclear accidents: a review of the environmental impacts. Sci Total Environ 470:800–817. https://doi.org/10.1016/j.scitotenv.2013.10.029

Suetake M, Nakano Y, Furuki G, Ikehara R, Komiya T, Kurihara E, Morooka K, Yamasaki S, Ohnuki T, Horie K, Takehara M, Law GTW, Bower W, Grambow B, Ewing RC, Utsunomiya S (2019) Dissolution of radioactive, cesium-rich microparticles released from the Fukushima Daiichi Nuclear Power Plant in simulated lung fluid, pure-water, and seawater. Chemosphere 233:633–644. https://doi.org/10.1016/j.chemosphere.2019.05.248

Takemura T, Nakamura H, Takigawa M, Kondo H, Satomura T, Miyasaka T, Nakajima T (2011) A numerical simulation of global transport of atmospheric particles emitted from the Fukushima Daiichi Nuclear Power Plant. SOLA 7:101–104. https://doi.org/10.2151/sola.2011-026

TEPCO (Tokyo Electric Power Co.) (2015) Examination into the reactor pressure increase after forced depressurization at Unit-2, using a thermal-hydraulic code. In: TEPCO reports latest findings of technical inquiry into how accident at Fukushima unfolded (2015) https://www.tepco.co.jp/en/press/corp-com/release/2015/1250927_6844.html. Accessed 22 Nov 2020

Terada Y, Goto S, Takimoto N, Takeshita K, Yamazaki H, Shimizu Y, Takahashi S, Ohashi H, Furukawa Y, Matsushita T, Ohata T, Ishizawa Y, Uruga T, Kitamura

H, Ishikawa T, Hayakawa S (2004) Construction and commissioning of BL37XU at SPring-8. AIP Conf Proc 705:376–379. https://doi.org/10.1063/1.1757812

Terada Y, Yumoto H, Takeuchi A, Suzuki Y, Yamauchi K, Uruga T (2010) New X-ray microprobe system for trace heavy element analysis using ultraprecise X-ray mirror optics of long working distance. Nucl Instrum Meth Phys Res A 616:270–272. https://doi.org/10.1016/j.nima.2009.12.030

Tsuruta H, Oura Y, Ebihara M, Moriguchi Y, Ohara T, Nakajima T (2018) Time-series analysis of atmospheric radiocesium at two SPM monitoring sites near the Fukushima Daiichi Nuclear Power Plant just after the Fukushima accident on March 11, 2011. Geochem J 52:103–121. https://doi.org/10.2343/geochemj.2.0520

Tsuruta H, Oura Y, Ebihara M, Ohara T, Nakajima T (2014) First retrieval of hourly atmospheric radionuclides just after the Fukushima accident by analyzing filter-tapes of operational air pollution monitoring stations. Sci Rep 4:6717. https://doi.org/10.1038/srep06717

Utsunomiya S, Furuki G, Ochiai A, Yamasaki S, Nanba K, Grambow B, Ewing RC (2019) Caesium fallout in Tokyo on 15th March, 2011 is dominated by highly radioactive, caesium-rich microparticles. https://arxiv.org/abs/1906.00212. Accessed 22 Nov 2020

Yamaguchi N, Mitome M, Akiyama-Hasegawa K, Asano M, Adachi K, Kogure T (2016) Internal structure of cesium-bearing radioactive microparticles released from Fukushima nuclear power plant. Sci Rep 6:20548. https://doi.org/10.1038/srep20548

Yamamoto T (2012) Radioactivity of fission product and heavy nuclides deposited on soil in Fukushima Dai-Ichi Nuclear Power Plant accident. J Nucl Sci Technol 49:1116–1133. https://doi.org/10.1080/00223131.2012.740355

Publisher's Note

JGR Atmospheres

RESEARCH ARTICLE
10.1029/2020JD033460

Deposition and Dispersion of Radio-Cesium Released due to the Fukushima Nuclear Accident: 2. Sensitivity to Aerosol Microphysical Properties of Cs-Bearing Microparticles (CsMPs)

Mizuo Kajino[1,2,3], Kouji Adachi[1], Yasuhito Igarashi[4,5], Yukihiko Satou[6], Morihiro Sawada[7], Tsuyoshi Thomas Sekiyama[1], Yuji Zaizen[1], Akane Saya[1], Haruo Tsuruta[8], and Yuichi Moriguchi[9]

[1]Meteorological Research Institute (MRI), Japan Meteorological Agency (JMA), Tsukuba, Ibaraki, Japan, [2]Faculty of Life and Environmental Sciences, University of Tsukuba, Tsukuba, Ibaraki, Japan, [3]Institute of Radiation Emergency Medicine (IREM), Hirosaki University, Hirosaki, Aomori, Japan, [4]Institute for Integrated Radiation and Nuclear Science (KURNS), Kyoto University, Kumatori, Osaka, Japan, [5]College of Science, Ibaraki University, Mito, Ibaraki, Japan, [6]Collaborative Laboratories for Advanced Decommissioning Science (CLADS), Japan Atomic Energy Agency (JAEA), Tomioka, Fukushima, Japan, [7]Graduate School of Life and Environmental Sciences, University of Tsukuba, Tsukuba, Ibaraki, Japan, [8]Remote Sensing Technology Center of Japan (RESTEC), Minato, Tokyo, Japan, [9]Graduate School of Engineering, University of Tokyo, Bunkyo, Tokyo, Japan

Key Points:

- The regional impacts of two types (A and B) of Cs-bearing solid microparticles (CsMPs) were numerically examined for the first time
- Type B CsMPs could partly explain the underestimation of simulated total deposition over land
- The environmental behaviors of type A CsMPs could vary substantially depending on size

Correspondence to:
M. Kajino,
kajino@mri-jma.go.jp

Citation:
Kajino, M., Adachi, K., Igarashi, Y., Satou, Y., Sawada, M., Thomas Sekiyama, T., et al. (2021). Deposition and dispersion of radio-cesium released due to the Fukushima nuclear accident: 2. Sensitivity to aerosol microphysical properties of Cs-bearing microparticles (CsMPs). *Journal of Geophysical Research: Atmospheres*, *126*, e2020JD033460. https://doi.org/10.1029/2020JD033460

Received 7 JUL 2020
Accepted 5 DEC 2020

Abstract The dispersion and deposition of radio-cesium (^{137}Cs) carried by two types (type A and type B) of water-insoluble Cs-bearing solid microparticles (CsMPs) released due to the Fukushima nuclear accident were simulated for the first time. The presence of type B CsMPs (70–400 μm found in soil and 1–5 μm found in air), associated with the hydrogen explosion of Unit 1 in the afternoon of March 12, could partly explain the simulated underestimation of total deposition over land by assuming that 100% of the Cs carriers were water-soluble submicron particles (WSPs). Type A CsMPs (0.1–10 μm), released from Units 2 or 3 in the midnight between March 14 and 15, traveled over the Kanto Plain, the most populated plain in Japan. Differences in the size distribution of type A CsMPs altered the surface air concentration over Kanto substantially, by up to more than one order of magnitude. The major deposition mechanisms varied among dry, wet, and fog (and/or cloud) depositions depending on the size distribution and locations. The simulated activity fractions due to the CsMPs in the total deposition were compared to those observed in surface soil for the first time. The observations could be explained by the simulations for the locations under the influence of type B CsMPs. However, the simulations were substantially underestimated for the locations influenced by type A CsMPs. There could be more fractions of type A CsMPs emission in the source term and/or the simulated deposition rates of type A CsMPs were underestimated.

1. Introduction

The Fukushima Daiichi Nuclear Power Plant (F1NPP or FDNPP) accident released substantial amounts of fission products into the atmosphere (Chino et al., 2011; Hirao et al., 2013; Katata et al., 2015; Saunier et al., 2013; Stohl et al., 2012; Terada et al., 2020, 2012; Winiarek et al., 2014; Yumimoto et al., 2016). The contaminated air mass traveled over Japan and the radionuclides were deposited into and contaminated terrestrial ecosystems; this phenomenon was discovered by field measurements (Igarashi et al., 2015; Ikehara et al., 2020; NRA [Nuclear Regulation Authority], 2012; Oura et al., 2015; Sanada et al. 2014, 2018; Torii et al., 2012; Tsuruta et al., 2014, 2017, 2018, 2019) and has been investigated by numerical simulations (Kajino et al., 2018, 2019a; Morino et al, 2011, 2013; Nakajima et al., 2017; Sekiyama & Iwasaki, 2018; Sekiyama & Kajino, 2020; Saya et al., 2018; Sekiyama et al, 2015, 2017; Terada et al., 2020). The radionuclides were transported and deposited over the ocean (Aoyama et al., 2016) and further to North America (Wetherbee et al., 2012) and Europe (Masson et al., 2011, 2013). Radio-Cs (^{134}Cs and ^{137}Cs) is among the key radioisotopes due to its abundance and relatively long half-lives (2.06 and 30.1 years, respectively).

Thanks to extensive field measurements and numerical simulations, knowledge has been accumulated (Mathieu et al., 2018). Between 7 and 20 PBq of ^{137}Cs was released to the atmosphere (Mathieu et al., 2018)

and ~3 PBq was deposited in terrestrial areas in Japan (NRA, 2012; Torii et al., 2012). Nakajima et al. (2017) identified the transport pathways of radio-Cs over Japan by using numerical simulations together with hourly surface air activity concentration measurements from one hundred stations in Japan (Oura et al., 2015; Tsuruta et al., 2014). Deposition mechanisms over land were systematically investigated by the altitudinal analysis of aircraft measurements and a numerical simulation by Sanada et al. (2018). To better simulate the atmospheric behaviors of radio-Cs, multimodel ensemble studies have been conducted (Draxler et al., 2015, Kitayama et al., 2018; Kristiansen et al., 2016; Sato et al., 2018, 2020; SCJ [Science Council of Japan], 2014). However, although the properties of radio-Cs in the atmosphere are relatively easy to predict, that is, it is chemically inert and has an extremely low vapor pressure, there are still significant uncertainties in multimodel simulations, especially for deposition.

Several issues remain regarding the accurate simulation of radio-Cs, such as (1) deposition modeling, (2) horizontal resolution, and (3) aerosol microphysical properties. Due to the large uncertainty in deposition modeling, even using the same meteorological field and the same source term, different transport models have predicted very different deposition fields and relative magnitudes of different deposition mechanisms (i.e., dry or wet depositions) (Sato et al., 2018). Most models do not include the fog and cloud droplet deposition process, which could play a key role in radio-Cs depositions over the mountain forests of Japan (Hososhima & Kaneyasu, 2015; Imamura et al., 2020; Katata et al., 2015; Kajino et al., 2019a; Sanada et al., 2018). There is also considerable uncertainty in meteorological modeling, which was indicated from Part 1 of the current study (Kajino et al., 2019a). Even a single transport model with a single model domain predicted very different deposition fields and contributions from different deposition mechanisms (dry, fog, in-cloud, or below-cloud wet depositions) depending on the selection of meteorological fields. Due to the complex topography in the Fukushima area and the surrounding prefectures, the horizontal resolution is important for accurate simulations of plume transport, as indicated by a comparison of 5, 3, and 1-km resolution simulations (Sekiyama & Kajino, 2020). However, the effect of aerosol microphysical properties has not been fully investigated by numerical simulations.

Kaneyasu et al. (2012) showed that the size distributions of radio-Cs were very close to those of sulphate, which is water-soluble particles (WSPs) with submicron size ranges (0.1–1 μm in diameter) and concluded that sulphate was the potential carrier of radio-Cs. WSPs were assumed to be the carrier of radio-Cs for all previous simulations, except that of Adachi et al. (2013). Adachi et al. (2013) discovered Cs-glassy and spherical particles that were totally hydrophobic and larger than 1 μm, the environmental behaviors of which should be very different from those of WSPs. The particles were named Cs-bearing microparticles (CsMPs) and extensively studied in the subsequent literatures (e.g., Igarashi et al., 2019). Based on limited knowledge, Adachi et al. (2013) conducted a transport simulation of CsMPs for a limited period (March 15) and showed a significant difference in the deposition patterns. However, there was no knowledge on the abundance of CsMPs at that time, and only a few particles were found from an air sample.

After Adachi et al. (2013), successful isolations of CsMPs from various samples, such as soil (Furuki et al., 2017; Ikehara et al., 2018; Satou et al., 2016, 2018), plant leaves and agricultural materials (Kogure et al., 2016; Okumura et al., 2019a; Yamaguchi et al, 2016, 2018), masks (Higaki et al., 2017), and rivers (Miura et al., 2018), were performed. Extensive studies have been performed on the physical and chemical properties of CsMPs (Abe et al., 2014; Adachi et al., 2013; Kogure et al., 2016; Okumura et al., 2019b, 2019c; Satou et al., 2015, 2016, 2018; Yamaguchi et al., 2016); thus, knowledge has been accumulated (Igarashi et al., 2019). Based on the chemical compositions of CsMPs, locations of soil samples, and locations and timings of air samples, power plant units involved, formation mechanisms, emission events, and transport pathways were investigated (Hidaka, 2019; Igarashi et al., 2019; Ikehara et al., 2020; Onozaki et al., 2019; Satou et al, 2015, 2016, 2018). Recently, Ikehara et al. (2020) reported the activity fractions of CsMPs in the surface soil at 20 sites in the Fukushima prefecture, located 4.42–61.0 km from the F1NPP, which ranged from 1.63% to 80.2% of the total activity. As a result, we have observational evidence that the radioactivity of CsMPs was significant in the environment, and we can quantitatively compare those observational data with simulated CsMP deposition.

Based on the knowledge of CsMPs obtained so far, we conducted the first simulations for the dispersion and deposition of radio-Cs in March 2011 by taking the presence of CsMPs into account. Then we summarized

Table 1
Summary of Information for Type B and Type A Nonhygroscopic CsMPs

	Type B	Type A
Sample contained CsMPs	Soil (<10 km NNW of F1NPP)[a], Air (25 km N of F1NPP)[b]	Air (170 km SW of F1NPP)[c], Soil (20 km NW of F1NPP)[d], cloth on vegetable field[e]
Diameter found	70–400 μm[a], 1–5 μm[b]	1–10 μm[c,d], < 1 μm[e]
Hypothesized emission event	Unit 1, hydrogen explosion (March 12, 15:36 LT)	Unit 2, SRV openings (March 14, 21:30 and 23:25; March 15, 1:02 LT)[f] or Unit 3, core cooling water injection on March 15, 2:30 LT (Hidaka, 2019)[f]March 15, evening (Satou et al., 2015)[f]
Simulated duration of emission	March 12, 15:30–16:00 LT	[f]March 14, 21:00–22:00 LTMarch 14, 23:00–March 15, 0:00 LTMarch 15, 01:00–02:00 LT
Total emission amount	0.7 PBq	0.475 PBq[f]

[a]Satou et al. (2018). [b]Onozaki et al. (2019). [c]Adachi et al. (2013). [d]Satou et al. (2016, 2018). [e]Okumura et al. (2019a). [f]The emission event of type A CsMPs is still controversial, but the timings of the SRV openings of Unit 2 were in the simulation, because emission amount associated with the water injection event of Unit 3 is not currently available. Also, there could be additional source of type A CsMPs, March 15 evening, as suggested by Satou et al. (2015).

the environmental behaviors of CsMPs and their differences from the previous simulations, assuming 100% of submicron WSPs.

2. Materials and Methods

Many parts of the simulation methods used in this study are the same as those in our Part 1 paper (Kajino et al., 2019a). The common methods are roughly described herein, but the novel methods are extensively described in this section.

2.1. Meteorological Simulation

In Kajino et al. (2019a), an ensemble analysis of multiple meteorological models and modules was conducted with a 3-km grid resolution. The results showed that the chemical transport simulation that used the meteorological ensemble mean field (Met_EnsMean) was successful in terms of modeling cumulative precipitation, total ^{137}Cs deposition, and cumulative ^{137}Cs surface air concentrations. Thus, in this study, Met_EnsMean was selected as a reference meteorological field with which to conduct sensitivity tests of the microphysical properties of CsMPs using a chemical transport model.

Each meteorological simulation and the methods used to produce the Met_EnsMean are explained in Table 1 and Figure 1 of Kajino et al. (2019a). Two meteorological models were used: the Japan Meteorological Agency (JMA)'s non-hydrostatic model (NHM ver. 3.5; Saito et al., 2007) and the weather research and forecasting model (WRF ver. 3.5.1; Skamarock et al., 2008). Three types of simulations were conducted: NHM using JMA's meso-regional objective analysis (MANAL) as the boundary conditions, NHM using the local ensemble transform Kalman filter (LETKF; Kunii, 2013), and WRF driven by MANAL. Several WRF simulations with different cloud microphysics modules and different boundary layer turbulence schemes were also conducted to depict the variations in surface air concentration and deposition of ^{137}Cs depending on the physics modules and to produce the ensemble mean of the WRF simulations (WRF_EnsMean). Met_EnsMean was the ensemble mean of the NHM, NHM-LETKF, and WRF_EnsMean.

2.2. Transport Model

NHM-Chem (Kajino et al., 2019b) has been used for simulating the dispersion and deposition of radionuclides. NHM-Chem is a Eulerian chemical transport model (CTM) that can be offline-coupled or online-coupled with the NHM. The offline coupling mode was used for this study. Because the transport process is embedded as a subroutine of the NHM in the online coupling mode, the CTM is driven only by the NHM. On the other hand, the offline coupling mode is composed of a standalone CTM and the interface

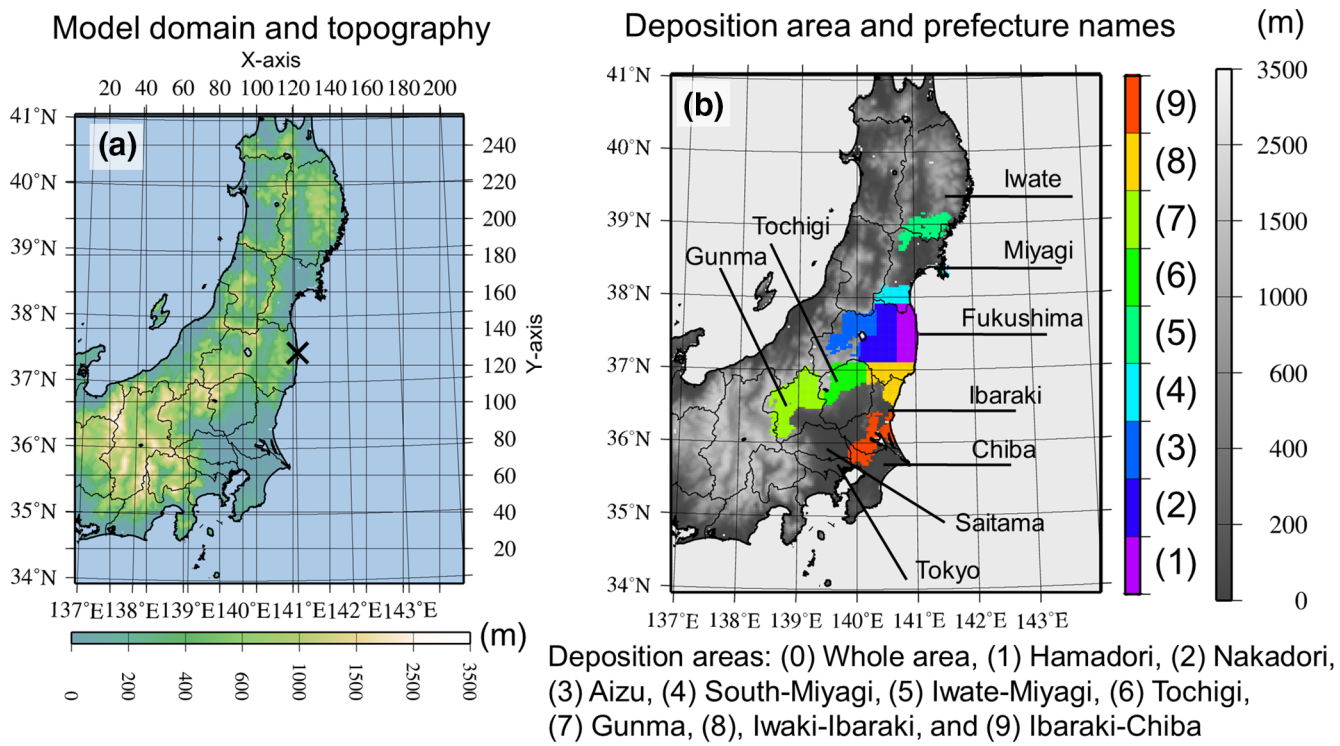

Figure 1. (a) Model domain and the topography of the region. The cross indicates the location of the F1NPP. (b) Deposition area defined in this study. (0) Whole area indicates the sum of areas (1) to (9).

processor, which converts the meteorological model output into the input for the CTM; thus, other meteorological models can be used to drive NHM-Chem by preparing interface processors for other meteorological fields, such as Met_EnsMean and those made by WRF.

NHM-Chem considers major tropospheric photochemical reactions and aerosol dynamic processes, but a simplified version for radionuclides was used in this study, as presented in Kajino et al. (2019a): no chemical reactions and the relevant aerosol processes, such as nucleation, condensation and coagulation, were considered, while changes in size distribution due to deposition were considered by using a triple-moment modal method, assuming log-normal size distributions. Changes in size distribution during transport can be ignored for submicron particles, as in Kajino et al. (2019a) and almost all the previous simulations, because their gravitational settling velocities are negligibly small. In contrast, the size distributions of CsMPs, the diameters of which are as large as 10–100 μm, should vary significantly during transport, as the larger particles are readily deposited on the surface within 10–100 km (e.g., as shown later in Figure 3). The predicted size distributions were applied for the calculations of the dry deposition, gravitational settling, and below-cloud scavenging processes. For in-cloud scavenging, the prescribed cloud condensation nuclei (CCN) activation fractions were applied as described later in Section 2.3.2. This is the only difference from Kajino et al. (2019a) in the elementary processes of the CTM: the prescribed "hygroscopicity" ($\kappa = 0.4$) was applied for the simulation of WSPs for the calculation of CCN activation in Kajino et al. (2019a).

2.3. Simulation Setup

2.3.1. Model Domain and Simulation Period

The model domain, which covers the eastern and northeastern parts of Japan (213 × 257 grid cells with a 3-km grid resolution using a Lambert conformal coordinate system) is presented in Figure 1a. There are 48 vertical layers, up to ~22 km above sea level (ASL), for the NHM and 27 layers, up to 100 hPa, for the WRF on a terrain-following coordinate system with vertically stretched grids (with more grids at lower levels to

resolve boundary layer dynamics and fewer grids in the free troposphere). Since the vertical grid structures of the NHM and WRF are different, as is the standalone CTM part of the offline NHM-Chem, the meteorological fields were vertically interpolated to the vertical layers of the CTM, which include 19 layers up to 10 km ASL. The output time interval of the NHM and WRF are 1 h, and thus the input/output time interval for the CTM is also 1 h. The horizontal grid of the CTM was the same as that of the meteorological models. The simulation period is from 00 Cooridated Universal Time (UTC) on March 11 to 00 UTC on April 1, with a spin-up period of 20 h; the onset of emission was 20 UTC on March 11.

A tagged simulation method was used in this study. Tagged tracers (^{137}Cs) were released every 30 min at a rate of 1 TBq h^{-1}. Each simulation stopped when the maximum concentration over the model domain was below a very small value (10^{-15} Bq m^{-3}). After all the simulations, the prescribed emission rate at each 30 min interval was multiplied by the corresponding tagged concentration and deposition fields, and all the tagged simulations were summed to derive the full simulation results. The tagged method is useful because the environmental behaviors of radionuclides should not be very nonlinear. However, note that due to numerical errors, the tagged results were different from those of the standard simulation: the results assuming WSPs for the whole period presented in this study were different from those of Met_EnsMean presented in Kajino et al. (2019a). The difference is also due to using different settings for the microphysical properties of the WSPs (see Section 2.3.3) and different formulations of CCN activation between Kajino et al. (2019a) and this study (see Section 2.2).

2.3.2. Emission Amount and Period for ^{137}Cs and CsMPs

The most commonly used estimation by the Japan Atomic Energy Agency (JAEA) (Katata et al., 2015) was used for the emission inventory of ^{137}Cs in the simulation. WSPs were assumed to be the radionuclide carrier particles in the same manner as in Kajino et al. (2019a), except for two periods, when two types of CsMPs were assumed to be emitted.

The current knowledge on the two types of CsMPs is summarized in Table 1. The readers can find very detailed information on CsMPs from the extensive review by Igarashi et al. (2019); this information is briefly described here. Type A CsMPs were first found by Adachi et al. (2013) in a sample from a high-volume air sampler filter in Tsukuba, ∼170 km southwest (SW) of the F1NPP. Type A CsMPs were also found by Satou et al. (2016) in the soil sampled ∼20 km northwest (NW) of the F1NPP. The diameters of the isolated type A CsMPs thus far range from 1 to 10 μm; these particles have spherical shapes and high specific radioactivity (Adachi et al., 2013; Igarashi et al., 2019; Satou et al., 2016). Additionally, type A CsMPs smaller than 0.5 μm in diameter were recently found (Okumura et al., 2019a). Type B CsMPs were first found by Satou et al. (2018) in soil samples in Fukushima, within 10 km north-northwest (NNW) of the F1NPP. The diameters of the isolated type B CsMPs so far range from 70 to 400 μm; these particles have irregular shapes and low specific radioactivity but high activity values, reaching beyond 1 kBq (Igarashi et al., 2019; Satou et al., 2018). Recently, type B CsMPs with a few micrometers in diameter (1–5 μm) were also found in an air sample at a station ∼25 km north of the F1NPP (Onozaki et al., 2019).

Satou et al. (2018) discussed that the emission of type B CsMPs is associated with the hydrogen explosion of Unit 1, which occurred on March 12, 15:36 local time (LT; UTC+9). This is because the isotopic activity ratios (^{134}Cs/^{137}Cs) of the type B CsMPs were similar to those of the estimated fuel composition of Unit 1 and because the dispersion of such large particles (∼100 μm in diameter) over significant distances (∼20 km away from the F1NPP) should require considerable energy, such as a hydrogen explosion. According to Katata et al. (2015), the simulated duration of the emission on March 12 lasted from 15:30 to 16:00 LT, and the total emission amount was 0.7 PBq (Table 1).

On the other hand, the timing of the emission of type A CsMPs is still controversial. The activity ratios of the type A CsMPs were significantly different from those of Unit 1, but it is difficult to identify the origin of the particles because the isotopic activity ratios of Units 2 and 3 were similar to each other (Igarashi et al., 2019; Satou et al., 2018). Judging from the air sample that contained type A CsMPs (sampled from March 14 at 21:00 to March 15 at 9:10 LT) and the tagged simulation results, Adachi et al. (2013) estimated that the air mass that contained type A CsMPs should have started in the F1NPP between March 14 at 17:00 to March 15 at 2:00 LT. According to Katata et al. (2015), during this period, three peak emission events occurred, and the safety relief valve (SRV) of Unit 2 opened at 21:00 and 23:00 LT on March 14 and at 1:00 LT on March 15.

In contrast, based on the engineering of the reactor, Hidaka (2019) argued that the formation of type A CsMPs in Unit 2 is unlikely. The author proposed that type A CsMPs were also formed due to the hydrogen explosion of Unit 3 at 11:01 LT on March 14. The particles were mostly dispersed toward the ocean during the time of formation, but part of them were deposited on the reactor building of Unit 3 and could have been resuspended and released into the environment due to a restart of the core cooling water injection at 2:30 LT on March 15. This argument is consistent with the result of the atmospheric simulation: the environmental dose rate measured in Tsukuba peaked twice (at 4:24 (0.5 μSv h^{-1}) and 9:12 (1.1 μSv h^{-1}) LT on March 15); the latter peak was associated with the water injection time according to the tagged simulation of Adachi et al. (2013). Nevertheless, we had to use the events of Unit 2 as the source for the type A CsMPs, which amounted to 0.475 PBq (Table 1), because the Katata et al. (2015)'s source term does not consider emissions of the Unit 3 during the time. There could be other emission events of type A CsMPs, such as on the evening of March 15, as suggested by Satou et al. (2015). However, the measurement of these particles was conducted using soil samples, so it is difficult to associate the samples with the emission events. Thus, the events on the evening of March 15 were not assessed in the current study as a CsMP type A emission source.

2.3.3. Microphysical Properties of ^{137}Cs and CsMPs

In Kajino et al. (2019a), the ^{137}Cs-bearing particles were assumed to be WSPs in all cases, and the microphysical properties of these particles were set as follows: the number-equivalent geometric mean dry diameter ($D_{g,n,\mathrm{dry}}$) was 102 nm, the geometric standard deviation (σ_g) was 1.6, the particle density (ρ_p) was 1.83×10^3 kg m^{-3} (assuming ammonium sulfate) and the hygroscopicity (κ) was 0.4 (to calculate hygroscopic growth and CCN activation). In Adachi et al. (2013), for simplicity, we excluded the in-cloud scavenging processes (CCN activation and subsequent cloud microphysical processes), as the CsMPs were water-insoluble and thus not activated as CCN. However, this is not true in all cases: even relatively large nonhygroscopic particles can be activated at higher supersaturations (e.g., Petters and Kreidenweis, 2007). To consider the activation of nonsoluble particles and to make the simulation simpler, the CCN activation fractions of the CsMPs were prescribed for the sensitivity simulations.

Tables 2 and 3 summarize the sensitivity tests for the microphysical properties of type B and type A CsMPs, respectively. The number-equivalent geometric mean diameters ($D_{g,n}$) at emission were set at logarithmic intervals from 0.1 to 100 μm for type B and 0.1 to 10 μm for type A. Note that $D_{g,n}$ in the environment = $D_{g,n,\mathrm{dry}}$ because CsMPs are nonhygroscopic. σ_g was set to unity (monodispersed) for the type B simulation to see the simple relationship between size and transportation/deposition. The weather pattern was simple, the wind was mostly southerly during the 30-min emission duration, and in reality, most of the type B CsMPs were deposited within 10 km of the F1NPP, as these CsMPs were large. On the other hand, type A CsMPs traveled a longer distance (more than 100 km) over complex terrain and/or within complex meteorological fields, so sensitivity tests were conducted for σ_g values ranging from monodispersal ($\sigma_g = 1.0$) to broad dispersal ($\sigma_g = 2.0$). Information on σ_g has not yet been yielded from field observations, but this is a key parameter for atmospheric simulations because larger particles are deposited more rapidly and substantial changes in size distribution during transport could occur for broadly dispersed particles larger than 1 μm in diameter. For example, when $D_{g,n} = 1$ μm, the mass-equivalent mean diameter is $D_{g,m} = 1$ μm for $\sigma_g = 1.0$ but $D_{g,m} = 4.2$ μm for $\sigma_g = 2.0$, according to the relationships between number-equivalent and mass-equivalent mean diameters as follows:

$$\ln D_{g,m} = \ln D_{g,n} + 3\left(\ln \sigma_g\right)^2. \quad (1)$$

Table 2
Sizes and Prescribed Activated Fractions of Type B CsMPs

Experiment name	B15	B14	B13	B12	B11	B10	B09	B08	B07	B06	B05	B04	B03	B02	B01	B00
$D_{g,n}$ (μm)[a]	100	63.1	39.8	25.1	15.8	10.	6.31	3.98	2.51	1.58	1.0	0.631	0.398	0.251	0.158	0.1
Fog[b]	1	1	1	1	1	1	0	0	0	0	0	0	0	0	0	0
Cloud[b]	1	1	1	1	1	1	1	1	1	0	0	0	0	0	0	0

[a]Number-equivalent geometric mean diameter at emission. [b]Derived using prescribed supersaturations (0.01% for fog and 0.1 for clouds); $\kappa = 0$.

The settling velocity is 17.6-fold larger for particles with $\sigma_g = 2.0$ than for particles with $\sigma_g = 1.0$ for same $D_{g,n}$. The prescribed activated fractions were calculated using prescribed supersaturations of 0.01% and 0.1% for fog and clouds, respectively. The activated fractions of fog were applied for ^{137}Cs at the bottom layer of the model domain, and those of clouds were applied above the bottom layer. This method comprises several uncertainties. (1) Changes in activated fractions during transport due to changes in size distributions cannot be considered. (2) Substantial electrical charges of the type A CsMPs significantly enhanced scavenging by cloud droplets (Dépée et al., 2019), but this effect was not considered. Electrical charges can reduce the surface tension of droplets so that the activated fraction can be enhanced (Holländer & Schumann, 1979). (3) Fog deposition over mountains could occur when clouds over the plains approach the mountain surface (Hososhima & Kaneyasu et al., 2015; Imamura et al., 2020; Sanada et al., 2018); therefore, it might be better to use the activated fraction for clouds.

As shown in Tables 2 and 3, we defined the experiment names as follows: For the type B case, B00-B15 represent simulations from 0.1 to 100 μm of $D_{g,n}$, respectively. For the type A case, A00 to A10 represent simulations from 0.1 to 10 μm of $D_{g,n}$. In addition, for the type A case, symbols from a to d are added to the end of the experiment names indicating the sensitivity of σ_g from 1.0 to 2.0, respectively. For example, B10-A05c means a sensitivity study with ($D_{g,n}$, σ_g) = (10 μm, 1.0) for type B CsMPs and ($D_{g,n}$, σ_g) = (1.0 μm, 1.6) for type A CsMPs.

For the WSPs, the $D_{g,n}$ and σ_g at emission were set as 0.5 μm and 1.6, respectively, with prescribed activation fractions of 1.0 for both fog and clouds. Note that $D_{g,n}$ in the environment = $D_{g,n,\mathrm{dry}}$ because hygroscopic growth was not considered in the simulation method. ρ_p was assumed to be 1.83×10^3 kg m^{-3} in all cases because the particle densities of the CsMPs were not available.

2.4. Observation Data and Deposition Areas

The radioactivity observation data sets used in Kajino et al. (2019a) were also used in this study: aircraft measurement data for cumulative depositions of ^{137}Cs were provided by NRA (2012) and Torii et al. (2012) and hourly surface air concentrations of ^{137}Cs were provided by Tsuruta et al. (2014) and Oura et al. (2015), except for the Tokai site (station d of Figure 11), for which data were obtained from Okura et al. (2012). Tsuruta et al. (2014) developed a method to retrieve hourly surface air concentrations of ^{137}Cs using the filter tapes for the suspended particle matter (SPM; 100% cut-off at 10 μm) monitoring. ^{137}Cs concentration data measured at 99 stations were released by Tsuruta et al. (2014) and Oura et al. (2015). For the Tokai site, the filter sampling was made only when the gamma dose rates were high with sampling intervals from 20 min to half a day (Okura et al., 2012). For the sake of comparison against the hourly simulation data, we produced hourly data from the raw data of time intervals less than 1 hour (20 and 45 min). Because NRA (2012) did not provide deposition amounts for the restricted flight zone of the F1NPP (an area 3 km

Table 3
Size Distributions and Prescribed Activated Fractions of Type a CsMPs

Experiment name	A10a-d[a]	A09	A08	A07	A06	A05	A04	A03	A02	A01	A00
$D_{g,n}$ (μm)[b]	10.	6.31	3.98	2.51	1.58	1.0	0.631	0.398	0.251	0.158	0.1
Fog ($\sigma_g = 1.0$)[c]	1	0	0	0	0	0	0	0	0	0	0
Fog ($\sigma_g = 1.3$)[c]	0.97	0.53	0.05	0	0	0	0	0	0	0	0
Fog ($\sigma_g = 1.6$)[c]	0.98	0.84	0.51	0.17	0.03	0	0	0	0	0	0
Fog ($\sigma_g = 2.0$)[c]	0.99	0.96	0.87	0.68	0.43	0.20	0.07	0.01	0	0	0
Cloud ($\sigma_g = 1.0$)[c]	1	1	1	1	0	0	0	0	0	0	0
Cloud ($\sigma_g = 1.3$)[c]	1	1	1	0.99	0.74	0.14	0	0	0	0	0
Cloud ($\sigma_g = 1.6$)[c]	1	1	1	0.99	0.91	0.64	0.27	0.05	0	0	0
Cloud ($\sigma_g = 2.0$)[c]	1	1	1	1	0.98	0.91	0.76	0.51	0.26	0.1	0.03

[a]a–d correspond to σ_g, namely, a, b, c, and d are experiments with σ_g = 1.0, 1.3, 1.6, and 2.0 respectively. Same for A00 to A09. [b]Number-equivalent geometric mean diameter at emission. [c]Derived using prescribed supersaturations (0.01% for fog and 0.1 for clouds); $\kappa = 0$.

in radius), in this study, radiation monitoring data, which totaled 45 TBq, collected using an unmanned helicopter and provided by Sanada et al. (2014) were used. Precipitation data were not used in the study because the simulated precipitation was already evaluated in Kajino et al. (2019a). The detection limits of observed surface air concentration of ^{137}Cs were ~0.1–0.6 Bq m^{-3} and 0.1–0.3 Bq m^{-3} for Tsuruta et al. (2014) and Oura et al. (2015), respectively. The detection limit of observed deposition was ~15 kBq m^{-2} (Torii et al., 2012).

The deposition areas used for the process analysis in both Kajino et al. (2019a) and this study are shown in Figure 1b. To focus on the areas in which CsMPs were deposited, we discussed only Hamadori (Area 1), a coastal area in Fukushima prefecture, which includes the F1NPP, Tochigi and Gunma (Area 6 and Area 7), where the mountains were contaminated mainly due to fog (or cloud) deposition, and Iwaki-Ibaraki and Ibaraki-Chiba (Area 8 and Area 9), which are south and downwind of the F1NPP for assessing type A particle transportation. Fog deposition partly contributed to deposition in Iwaki-Ibaraki (Kajino et al., 2019a; Sanada et al., 2018), but there was almost no fog contribution to Ibaraki-Chiba because the contaminated areas were located over the Kanto Plain (Figure 1a). The Kanto Plain, which includes Ibaraki, Chiba, Tochigi, Gunma, and Tokyo prefectures, is the most populated plain in Japan, as shown in Figure 1b.

The observed total amount of ^{137}Cs deposited over the entire land area of Japan (denoted as Area 0) was 2.59 PBq excluding the restricted flight zone and 2.64 PBq including it. The largest deposition (1.43 PBq) was observed in Area 1 (including deposition in the restricted zone). The observed depositions over Areas 6 and 7, and Areas 8 and 9 were 0.21 and 0.16 PBq, respectively.

3. Results

3.1. Type B

Surface weather charts for the periods during which emissions of type B and type A CsMPs occurred are presented in Figure 2, together with the timings of their possible emission sources. The hourly mean measured and simulated wind vectors at F1NPP are also presented. The wind speed and direction were measured on the premises of the F1NPP by a monitoring car, https://www.tepco.co.jp/nu/fukushima-np/f1/

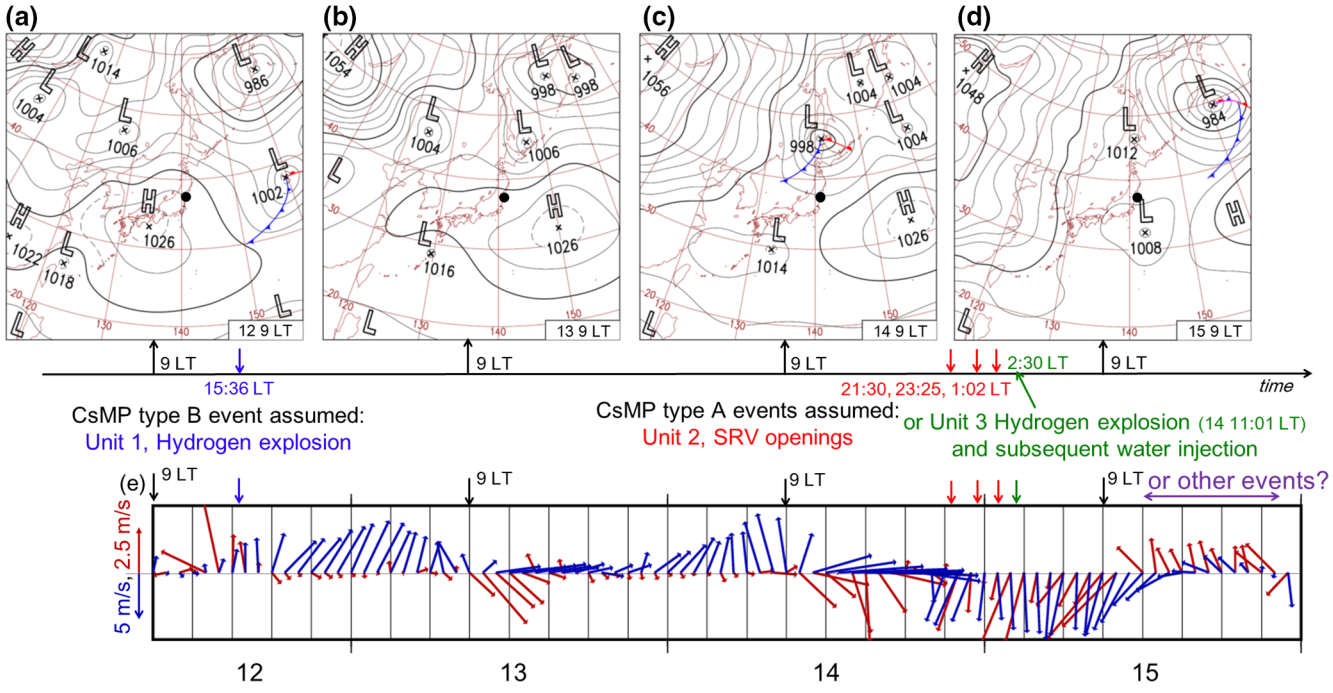

Figure 2. (a–d) Surface weather charts provided by the Japan Meteorological Agency for the assumed emission events of type B and type A CsMPs from March 12 to 15, 9 local time (LT) (0 UTC). (e) Observed (red) and simulated (blue) hourly wind vectors at the F1NPP.

indexold-j.html (last accessed: June 5, 2020). There are significant discrepancies in the wind field due to the differences in the measurement height (probably at 2 m) and simulation height (10 m) and the coarse resolution ($\Delta x = 3$ km) needed to resolve the wind field by the coast.

During the emission of type B CsMPs (from the hydrogen explosion of Unit 1), the southerly wind associated with a migrating anticyclone situated to the south of the F1NPP transported type B CsMPs northward and deposited them as shown in Figure 3. The wind directions of the measurement and simulation were similar, but the simulated wind direction was shifted slightly toward the east, in the direction of the ocean. Figure 3 shows the cumulative concentration and deposition of ^{137}Cs at different sizes of CsMPs (0.1, 1, 10, and 100 μm). The transport distances and deposition amounts are summarized in Figure 4. The simulated deposition amounts and the deposition processes that contributed to the model are summarized in Figure 5.

There were significant differences in both the concentration and deposition fields for the CsMPs with diameters ranging between 0.1 and 100 μm, as shown in Figure 3. Under the influences of the anticyclone, no precipitation or fog events occurred during the emission and transport of type B CsMPs in the afternoon of March 12; thus, only dry deposition contributed to the overall deposition (Figure 5). In Figure 3, the horizontal distributions of the cumulative surface air concentrations remain unchanged from a $D_{g,n}$ of 0.1 μm up to a $D_{g,n}$ of 10 μm because the gravitational settling velocities are low for this size range. On the other hand, the deposition amounts significantly increased from a $D_{g,n}$ of 10 μm due to the significant increase in dry deposition velocity because of the large inertia of the particles. Consequently, the regional impact of dry deposition (or the deposition amount over downwind areas) was largest at a $D_{g,n}$ of 10 μm (these particles were widely distributed in significant amounts). Certainly, the total deposition amount was largest at a $D_{g,n}$ of 100 μm, but the contaminated area was limited (to only near the emission source).

This trend is clearly shown in Figure 4. In Figure 4a, the transport distances (defined as Dist_{66}, the smallest radius of a circle around the F1NPP in which 66% of the total deposition occurred) below a $D_{g,n}$ of 10 μm were almost the same (>100 km), which indicates that dry deposition velocities were unsignificant, such that the meteorology determined the dispersion and deposition of the particles. On the other hand, when $D_{g,n}$ was larger than 10 μm, the gravitational settling velocities became significantly larger

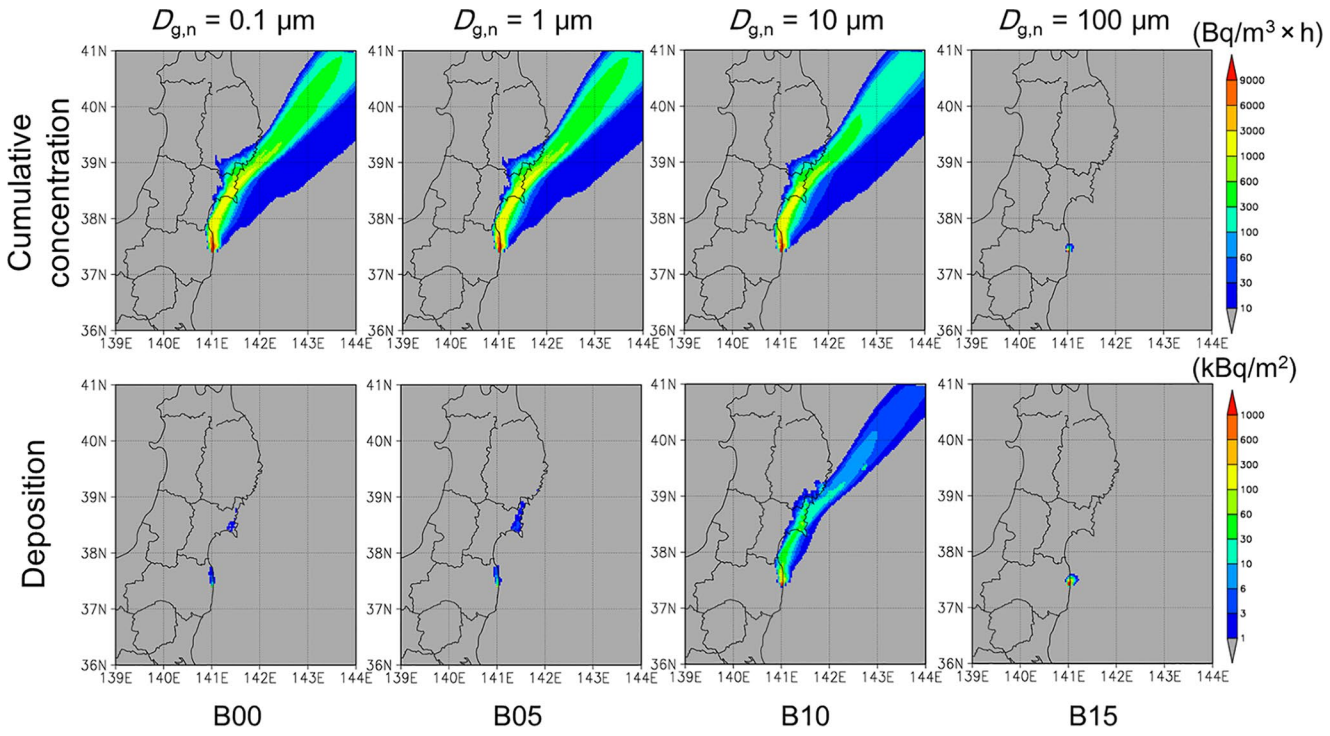

Figure 3. The simulated (upper panels) cumulative concentration and (lower panels) deposition of ^{137}Cs carried by type B CsMPs for different $D_{g,n}$ values (0.1, 1, 10, and 100 μm, from left to right). The experiment names are depicted in the bottom.

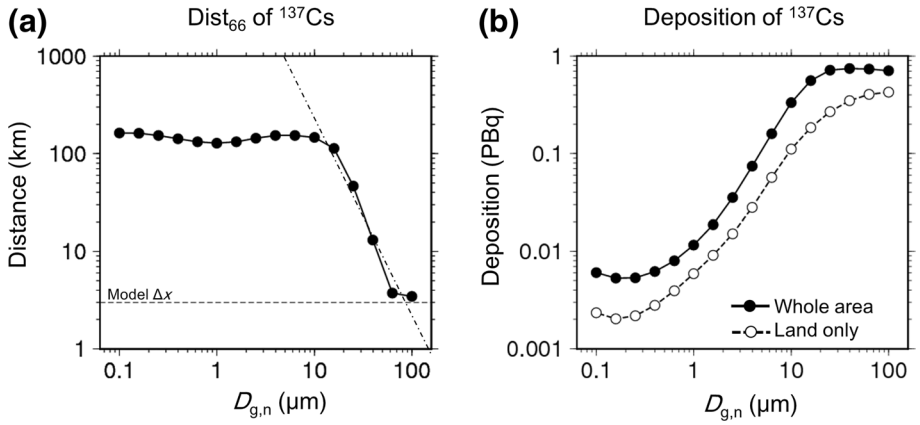

Figure 4. (a) The simulated transport distance ($Dist_{66}$: the smallest radius of a circle around the F1NPP in which 66% of the total deposition amount is included). The dashed line indicates the model grid resolution (Δx = 3 km), and the dashed dotted line is a slope inversely proportional to the square of $D_{g,n}$. (b) The total deposition amounts of ^{137}Cs carried by type B CsMPs at different $D_{g,n}$ values in the model domain over land (open circles and dashed line) and over the whole area (land and ocean; closed circles/solid line).

and affected the transport distances of the particles. For the size ranges, the decrease in $Dist_{66}$ was inversely proportional to the square of $D_{g,n}$ (dashed dotted line). Certainly, $Dist_{66}$ cannot be lower than the model Δx (= 3 km) because NHM-Chem is a Eulerian model. It cannot resolve the phenomena smaller than Δx. However, judging from the dashed dotted line (inversely proportional to square of diameter and thus inversely proportional to gravitational settling velocity), $Dist_{66}$ could be extrapolated to ~1 km at a $D_{g,n}$ of 100 μm.

While the transport distance changes with $D_{g,n}$ values from 10 to 100 μm, the deposition amounts started to increase for particles with $D_{g,n}$ values from 1 to 10 μm due to a significant increase in dry deposition velocity (Figure 4b). The total deposition amounts over the model domain were unchanged above 10 μm, but the contaminated areas significantly differed (Figures 3 and 4a). Figure 4b shows the simulated depositions over both the whole area (land and ocean) and land only. The aircraft observation data were collected only over the land, but the simulation caused depositions over both the land and ocean due to its crude Δx (the model grid including the F1NPP was covered partly with ocean (39%) and partly with land (61%) and deviations in the wind direction (the simulated wind direction was shifted slightly eastward compared to the observed wind direction). Based on observational studies (Chino et al., 2016; Satou et al., 2015), the contamination caused by type B CsMPs occurred mainly over land. Serious contamination occurred northwest of the F1NPP, as shown in Figure 9. Satou et al. (2015) and Chino et al. (2016) used isotopic activity ratios of ^{110m}Ag/^{137}Cs from soil samples and ^{134}Cs/^{137}Cs from an unmanned helicopter survey, respectively, and successfully identified the source reactor units. The ^{137}Cs deposition due to type B CsMPs occurred not in the center of the northwestern zone but in the vicinity of the zone and toward the north (i.e., in the NNW direction), ~15 km from the F1NPP.

In Kajino et al. (2019a), from an ensemble analysis of multiple meteorological models and physical modules, we concluded that the simulated total deposition amounts over land (1.23 PBq of Met_EnsMean), assuming WSPs as carriers of ^{137}Cs, significantly underestimated the aircraft observation (2.59 PBq) due to the underestimation of deposition rates of NHM-Chem. Among the deposition processes, we hypothesized that the below-cloud scavenging rate could be the main reason for underestimation because the value we used was based on theories that have been known to underestimate values derived by field experiments (e.g., Wang et al., 2010; Zhang et al., 2013). Figure 5 indicates another reason for the discrepancy between the simulated and observed total deposition. The difference between the aircraft observations (2.64 PBq, with additional deposition within 3 km of the F1NPP) and the current simulation, assuming 100% WSP carriers (1.19 PBq), was 1.45 PBq. Approximately half of this underestimation can be explained by the presence of type B CsMPs (0.7 PBq), if the emission estimated by Katata et al. (2015) during the hydrogen explosion of Unit 1 consisted solely of type B CsMPs and the diameters of all the particles were much larger than 10 μm

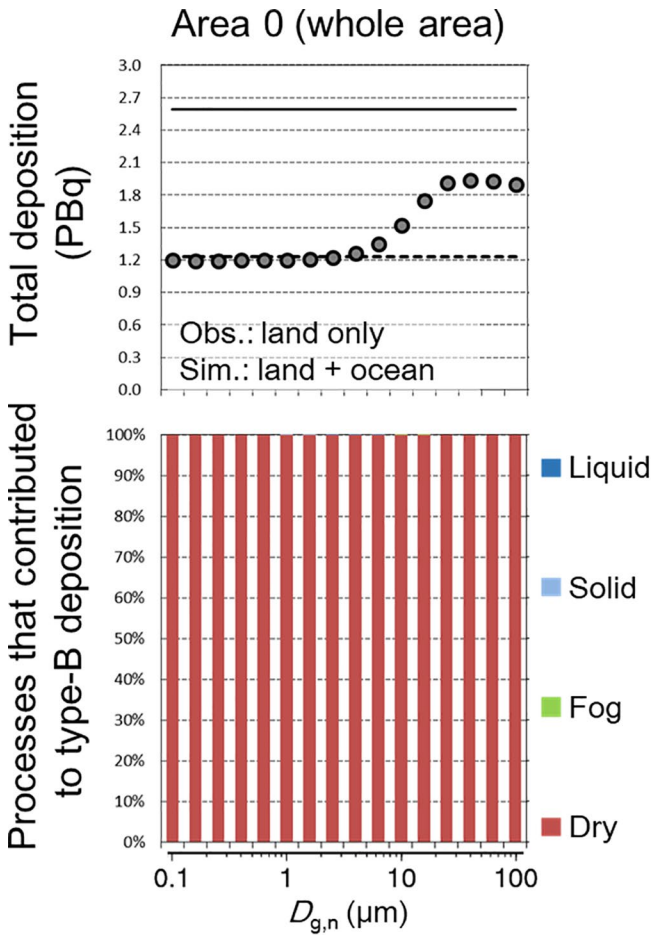

Figure 5. Upper panels: the observed (solid line) and simulated total depositions of ^{137}Cs for (circles) different sensitivity tests of type B CsMPs and (dashed line) 100% WSPs over the entire land area of Japan (denoted as Area 0), as defined in Figure 1. Note that the simulation includes deposition over both land and ocean. Lower panels: the simulated contributions of each deposition process to the deposition of ^{137}Cs by type B CsMPs: red, dry deposition; green, fog deposition; sky blue, wet deposition by solid precipitation; navy, wet deposition by liquid precipitation.

(as suggested by Satou et al., 2018 [70–400 μm]) so that they were readily deposited onto the ground surface within less than 100 km from the F1NPP. Onozaki et al. (2019) found type B CsMPs smaller than 10 μm in diameter from air samples collected at a station located 25 km north of the F1NPP. The relative contributions of radioactivity from type B CsMPs larger than 10 μm and smaller than 10 μm would have been a key factor controlling the surface air concentration and deposition of radio-Cs during the emission event. By considering the presence of type B CsMPs, the estimated emission amounts during the emission event could be significantly different from the value previously estimated by assuming WSP carrier aerosols (e.g., Katata et al., 2015), as presented in Section 3.4.

3.2. Type A

During the emission of type A CsMPs (SRV openings of Unit 2 or hydrogen explosion of Unit 3 and subsequent water injection), twin extratropical cyclones, often observed in the early and late stages of winter, were situated north and south of the Japanese archipelago and migrated eastward (Figure 2). Both the observed and simulated wind directions were northerly during the emission period, although there were some deviations between them. The simulated wind direction was more inland (toward the west) and more toward the ocean (toward the east) before and after 0:00 LT on March 15. Figure 6 shows the cumulative concentration and deposition of ^{137}Cs for CsMPs with different $D_{g,n}$ values (0.1, 1, and 10 μm) and different σ_g values (1.0 and 2.0). As shown in Figure 6, the anticyclonic circulation between the two cyclones moved the air mass containing the type A CsMPs to the Kanto Plain (Figure 6). The transport distances and deposition amounts are summarized in Figure 7.

In the type A simulation, σ_g was altered between 1.0 (monodispersed), 1.3 (narrowly dispersed), 1.6 (standard dispersal), and 2.0 (broadly dispersed). The type A CsMPs were transported over a long distance; therefore, substantial changes in the size distribution (D_g and σ_g) of the particles could occur during transport. This is also because, in addition to D_g, σ_g is also a key factor: atmospheric behaviors change substantially depending on σ_g even for the same D_g. For example, the ratios of the concentration of particles with a median diameter characterized by mass ($D_{g,m}$) to those of particles with a median diameter characterized by number ($D_{g,n}$) are 1, 1.2, 1.9, and 4.2 for σ_g values of 1.0, 1.3, 1.6, and 2.0, respectively (see Equation 1).

In Figure 6, the $D_{g,m}$ values are 0.1, 0.42, 1.0, 4.2, 10.0, and 42.2 μm. For the type A CsMPs, other deposition processes, such as fog deposition and wet deposition, occurred, as shown in Figure 8, while only dry deposition affected the type B CsMPs. However, features similar to those in Figure 3 are observed: no significant difference in the cumulative concentration of particles smaller than 1.0 μm (for $D_{g,m}$), gradually increasing deposition amounts and gradually decreasing cumulative concentrations of particles ranging between 1.0 and 10 μm (for $D_{g,m}$), and a significant decrease in the cumulative concentration of particles with $D_{g,m}$ greater than 10 μm. Figures 7a and 7b also show similar features. The Dist_{66} decreased in a manner inversely proportionally to the square of $D_{g,n}$ for σ_g of 2.0 and $D_{g,n}$ values larger than ~3 μm ($D_{g,m}$ = 12.2 μm) in Figure 7a. Adachi et al. (2013) found substantial amounts of type A CsMPs in the air samples in Tsukuba, 170 km from the F1NPP; therefore, we can safely conclude that $D_{g,m}$ could be much smaller than 42.2 μm ($D_{g,n}$ = 10 μm, σ_g = 2.0) (see the rightmost panels of Figures 6 and 7a). This finding is also supported by the fact that type A CsMPs with diameters much larger than 10 μm have not been found in any field experiments so far (Igarashi et al., 2019).

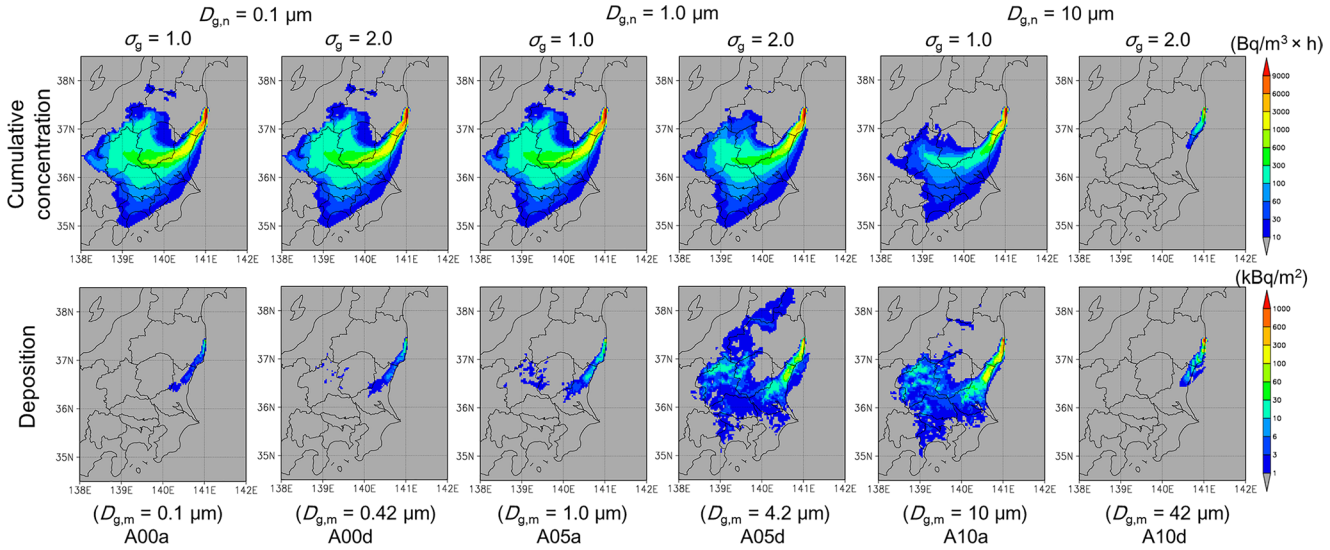

Figure 6. The information presented in this figure is the same as that in Figure 3, but for the type A CsMPs with different $D_{g,n}$ (0.1, 1, and 10 μm) and σ_g (1.0 and 2.0) values. The corresponding $D_{g,m}$ and experiment names are depicted in the bottom.

Figure 8 presents the total deposition amounts over the whole terrestrial area of Japan (Area 0) and regions affected by the deposition and transport of type A CsMPs (i.e., Areas 1, 6, 7, 8, and 9), together with the contributions of processes to the total deposition of type A CsMPs. In Area 1, the contribution of dry deposition to type A deposition was almost 100%. As the particle sizes increased, the total deposition amount approached the observed value, but it is unlikely as described before ($D_{g,m}$ could be much smaller than 42.2 μm). In Areas 6 and 7, the simulated deposition based on an assumption of 100% WSPs (dashed line) underestimated the observed deposition by ~50% but was larger than the results of any other sensitivity tests for the type A CsMPs. This is because the prescribed activated fractions of the type A CsMPs, with smaller diameters for clouds and fog, were either 0 or less than 1 (Table 3), whereas those for WSPs are assumed to be 1. As the sizes were larger for σ_g values of 1.0 and 2.0, the contributions of fog deposition and wet deposition were enhanced and peaked at 0.07 PBq in the areas. However, the total deposition decreases as the sizes increase further (i.e., $D_{g,n} > 2$ μm for $\sigma_g = 2.0$) because the type A CsMPs were deposited before reaching areas such as the Ibaraki and Saitama prefectures. The contributions of wet and fog depositions increased to 60% and 50%, respectively, at larger sizes. This is the major difference from the study by Adachi et al. (2013), in which the activated fractions of the CsMPs are assumed to be zero. Whereas the presence of type B CsMPs could partly explain the underestimation of simulated deposition, the presence of type

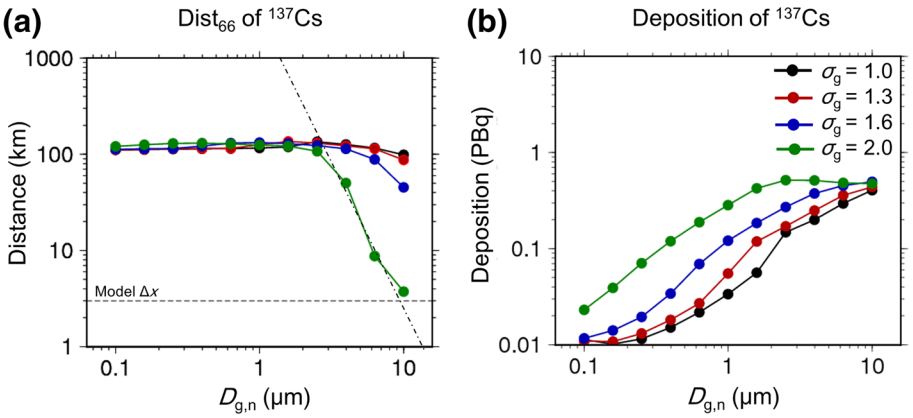

Figure 7. The information presented in this figure is the same as that in Figure 4, but for type A CsMPs at different σ_g values: 1.0 (black), 1.3 (red), 1.6 (blue), and 2.0 (green). Note that the simulated depositions over the whole area (land and ocean) (shown by the closed circles and solid lines) are presented in Figure 7b.

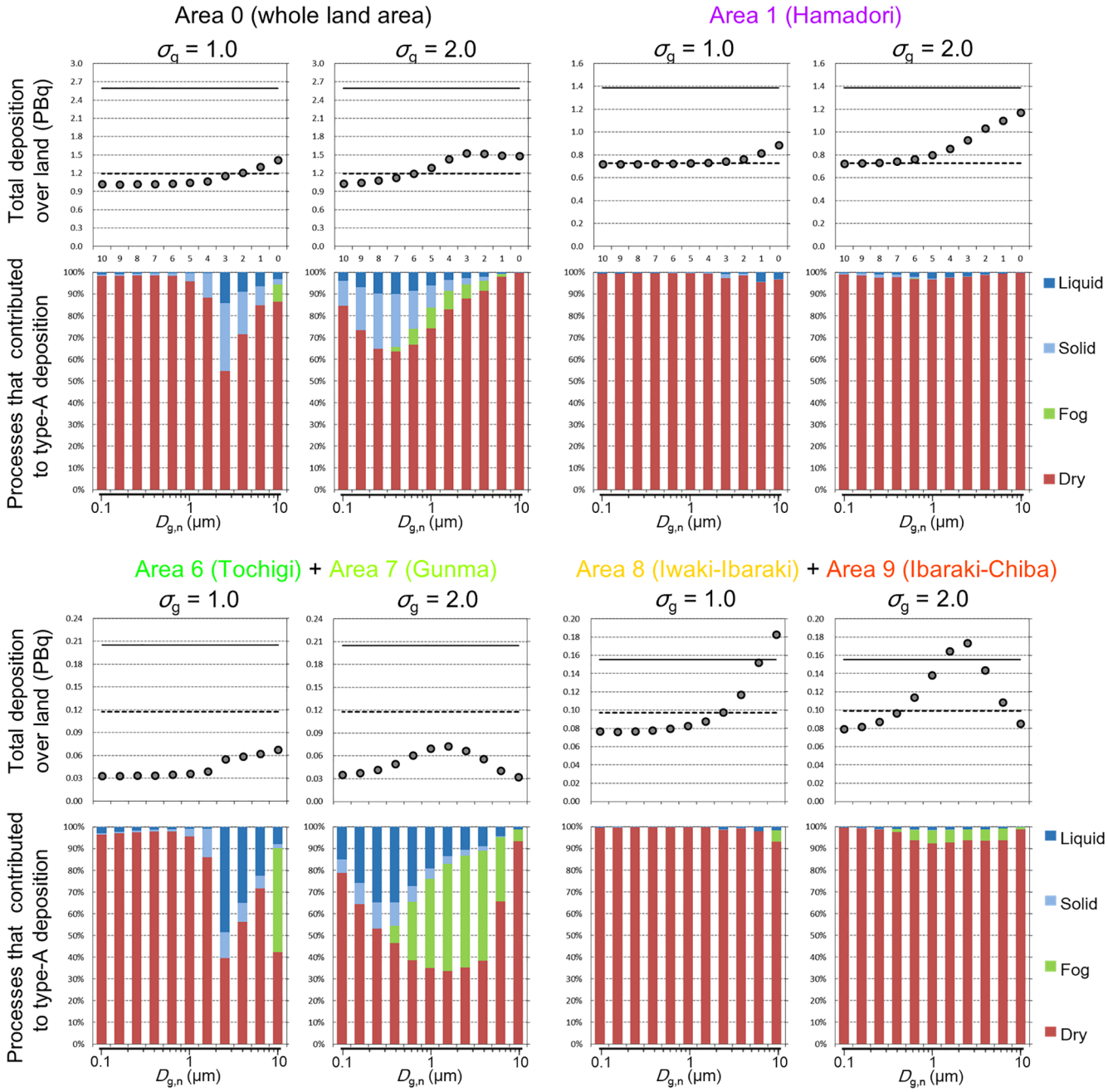

Figure 8. The information presented in this figure is the same as that in Figure 5, but for type A CsMPs at different σ_g values (1.0 and 2.0) over the whole land area (Area 0), Hamadori (Area 1), Tochigi and Gunma (Areas 6 and 7), and Iwaki-Ibaraki and Ibaraki-Chiba (Areas 8 and 9). Unlike Figure 5, the simulation results shown in this figure do not include depositions over the ocean, consistent with the observations.

A particles could not explain the underestimation of deposition in Areas 6 and 7. For Areas 8 and 9, the contribution of dry deposition was dominant, but the same patterns were observed: the deposition amounts increased as the sizes increased but started to decrease as the sizes grew even larger (i.e., $D_{g,n} > 3$ μm for $\sigma_g = 2.0$). Because Areas 8 and 9 were closer than Areas 6 and 7 to the F1NPP along with the transport pathway of type A CsMPs, the $D_{g,n}$ showing a deposition peak of $\sigma_g = 2.0$ for Areas 8 and 9, which was larger than that for Areas 6 and 7. The simulated peak depositions (0.18 PBq) exceeded the observed deposition (0.16 PBq). For Areas 8 and 9, the presence of type A CsMPs could explain the simulated underestimation of deposition. At smaller sizes, the total deposition in the sensitivity tests for type A CsMPs was smaller than

that for the WSPs. This is because type A CsMPs were deposited over the ocean off the coastline of Ibaraki prefecture by wet deposition. As presented in the upper panels of Figure 6, a part of the air mass containing type A CsMPs was transported over the ocean. Overall, for Area 0, the presence of type A CsMPs could not explain the underestimation of the simulated depositions. The contributions of dry deposition were the largest, and those of wet and fog depositions were up to 45% and 10%, respectively, depending on the size parameters.

The sizes of the type A CsMPs isolated from field experiments ranged from 0.1 to 10 μm (Adachi et al., 2013; Satou et al., 2016, 2018; Okumura et al., 2019a; Igarashi et al., 2019 and references therein). The sensitivity, especially focusing on the observational data, can be obtained from the simulation differences at $\sigma_g = 1.0$ (monodispersal), as shown in Figures 6–8; the environmental behaviors of the CsMPs with diameters of 0.1, 1, and 10 μm were drastically different. The horizontal distributions were also different (Figure 6). Among the total emissions assumed in the simulation (0.475 PBq), only 0.01–0.03 PBq was deposited over the model domain for particles with a size of 1 μm or smaller, while more than 10 times (0.4 PBq; more than 80% of the emission) that amount was deposited for particles with a size of 10 μm (Figure 7b). The deposition mechanisms could be drastically different, especially for Areas 6 and 7 (Figure 8): the contribution of dry deposition was almost 100% for particles with a size of 1 μm or smaller, whereas the contribution of fog deposition was the largest (50%) for particles with a size of 10 μm. For particles ranging in size between 0.1 and 10 μm, wet deposition also significantly contributed to the overall deposition and varied substantially up to 60%.

3.3. Horizontal Distributions of Cumulative Concentrations and Depositions

Figures 9 shows the horizontal distributions of the observed and simulated cumulative surface air concentrations (Bq m^{-3} h), while Figure 10 shows the horizontal distributions of the observed and simulated depositions (kBq m^{-2}). From left to right, the figures show the simulation results for the models using WSPs for the whole period, sensitivity simulation results showing the maximum areal total deposition (Max_depo; B13-A07 d), minimum areal total deposition (Min_depo; B01-A01a), maximum areal mean cumulative concentration (Max_conc; B11-A01a), and minimum areal mean cumulative concentration (Min_conc; B15-A10 d). We found that the results showing the best *R* in deposition was identical to Min_depo.

The correlation coefficients of the sensitivity simulations did not significantly differ for the cumulative concentrations and showed relatively high values (0.8), as found in Kajino et al. (2019a) (Figure 9). On the

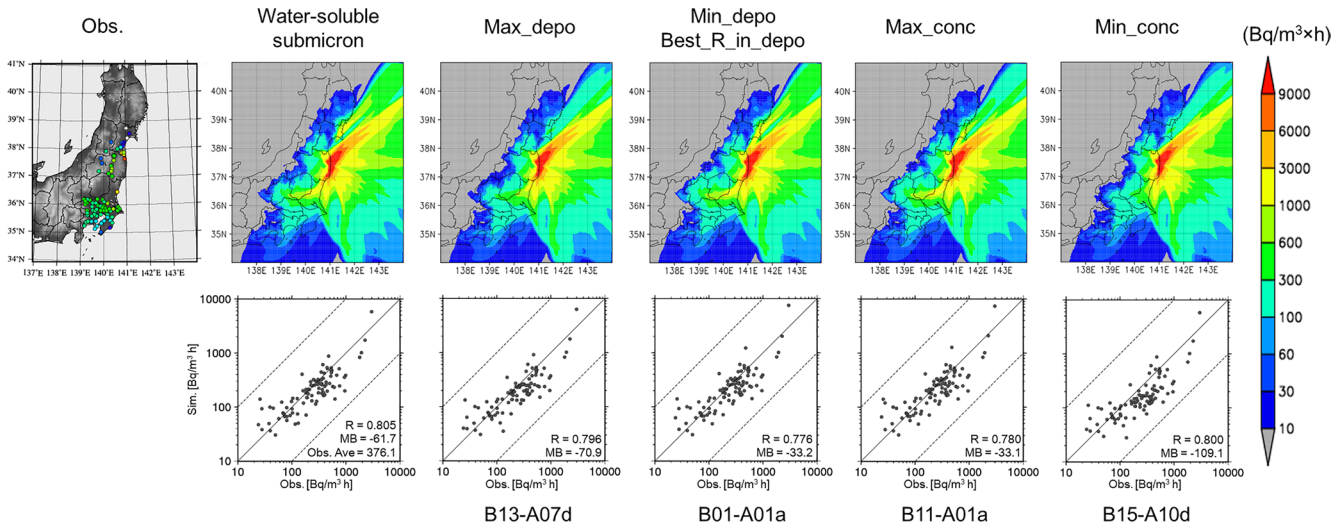

Figure 9. Horizontal distributions of the observed and simulated cumulative surface air concentrations of ^{137}Cs from 13 to 23 March and scattergrams between observations and the sensitivity simulations (from left to right, with only WSPs, maximum and minimum areal total depositions (Max_depo and Min_depo, respectively), and maximum and minimum areal mean cumulative concentrations (Min_conc and Min_conc, respectively). Note that best *R* in deposition was identical to Min_depo. The correlation coefficient (*R*), observed areal average (*Obs. Ave.*), and mean bias (*MB*) values are embedded in the panels. The observation data in each model grid cell were averaged and used for the comparison. The combinations of experiment names are embedded in the bottom.

other hand, *MB* varied substantially, from −33.1 to −109.1 Bq m^{-3} h, with an observed average of 376.1 Bq m^{-3} h. In terms of *MB*, the best performances were yielded from the simulations with low deposition rates (Min_depo, Max_conc), but the spatial *R* values were somewhat smaller than those in the other cases. Cases with relatively high *MB* values were somewhat unlikely because the observed CsMPs were much larger than these cases. However, these less likely smaller size cases (Min_depo) showed better *R* values for depositions (Figure 10). In the cases in which the performance of the *MB* was better for given depositions (Max_depo and Min_conc), the *R* values were much lower (0.3–0.4). These cases were also somewhat unlikely based on the observations (type B CsMPs might be reasonable, but type A CsMPs should not be so large). These contradictory statistical metrics indicate that the discrepancies between the observed and simulated depositions have not yet been resolved by considering the presence of type A and type B CsMPs. Further studies for the improvements of simulated depositions are indispensable.

3.4. Transport Events and CsMP Pathways

Figure 11 shows the time series of the observed and simulated surface air concentrations of ^{137}Cs at several stations in the Fukushima, Ibaraki, and Saitama prefectures over the transport pathways of type A CsMPs.

The pathway of type B CsMPs was not depicted in the figure, because the pathway was simple and no observed values were available during the period. It was not depicted also because most of ^{137}Cs from type B CsMPs might not be captured by the SPM filters as most of their sizes could be larger than the cut-off size of the SPM sampling (100% cut-off at 10 μm). For the type B CsMPs case, the comparison of simulated and observed deposition may be more useful, which was presented later in Section 3.5. The type B CsMPs were emitted in the afternoon of March 12 and arrived at a SPM station, located 25 km NNW of the F1NPP, after 1 h. The simulated concentration was enhanced for 3 h, from 16 to 19 LT. Onozaki et al. (2019) isolated CsMPs from air samples at the same station, but collected them later, from 20 to 21 LT and 0 to 1 LT on March 13. The emission of type B CsMPs could have lasted longer after the hydrogen explosion. The simulated 3-h cumulative concentration spanned more than a 4-fold difference, from 1,470 to 6,900 Bq m^{-3} h, depending on the particle sizes (0.1–100 μm), which could substantially affect the source term estimation, as discussed in Section 3.1. An estimated amount (0.7 PBq) was obtained from the simulation, assuming submicron carrier particles (Katata et al., 2015). If the typical sizes of type B CsMPs (70–400 μm) were considered, more emission would be required to explain the observed surface air concentration (or dose rate from cloud shine). On the other hand, the dose rate from ground shine should be enhanced due to fast settling velocities; therefore, the assumption of the relative fractions of cloud shine and ground shine should be modified. There were also type B CsMPs with diameters of 1–5 μm floating in the air (Onozaki

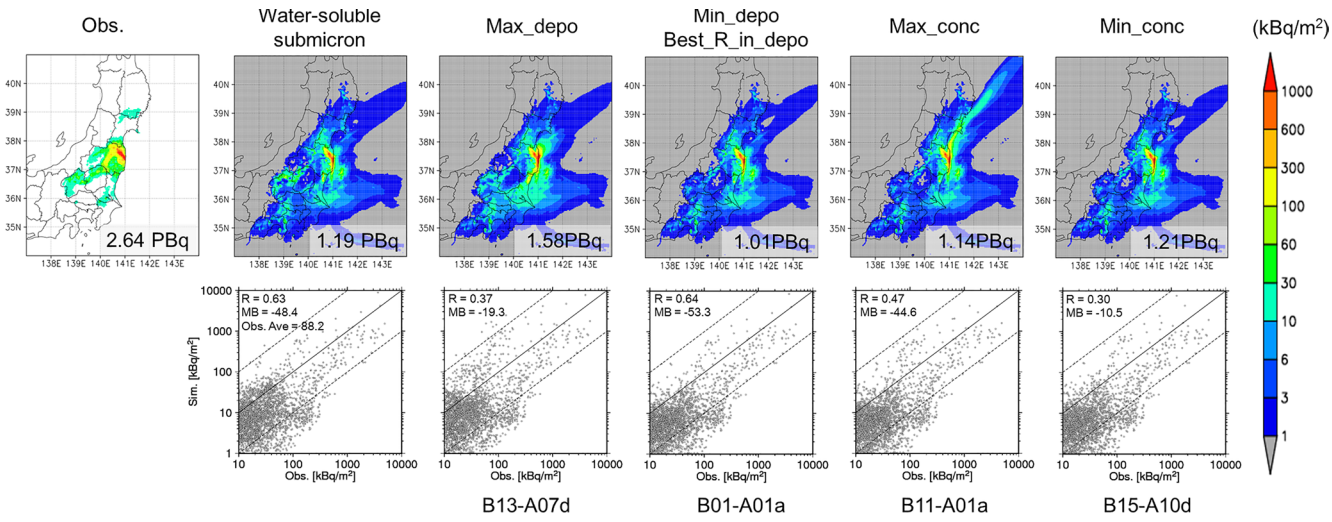

Figure 10. The information presented in this figure is the same as that in Figure 9, but for the observed and simulated cumulative deposition of ^{137}Cs. The areal total deposition amounts over land are also embedded in the upper panels.

et al., 2019). Thus, it is currently still not clear whether the estimated amount will be increased or decreased by considering the microphysical properties of type B CsMPs.

In the time series panels on the left in Figure 11, the red shaded areas indicate the range of simulated ^{137}Cs concentrations obtained from the size distribution sensitivity studies. The simulated type A particles were emitted during the night from March 14 to 15 and transported south and southwest over southern Fukushima, Ibaraki, Saitama, and Gunma prefectures due to anticyclonic circulation, which was identified as plume P2 (Nakajima et al., 2017; Tsuruta et al., 2014). Hereafter, note that the "observed event" was defined as a surface air concentration exceeding 1 Bq m^{-3} (well above the higher detection limit, i.e., 0.6 Bq m^{-3}) and the "simulated event" was defined as a surface air concentration larger than 0.5 Bq m^{-3} (half the criteria of observed event). The "simulated event affected by the presence of type A CsMP" (or simply "simulated type A event") was defined as a relative difference between the simulated maximum and minimum surface air concentration for the type A CsMPs sensitivity tests exceeded 10%. The emission timing of the type A CsMPs is still controversial, but both the observed and simulated surface air concentrations started to increase at 1 LT on March 15 at the earliest among the selected stations (i.e., station [d]). The observed event ended at 10 LT, while the simulated event lasted longer, up to 17 LT. The simulated event was affected by type A for the whole event. The observed 9-h (1–10 LT) cumulative concentration was 770 Bq m^{-3} h, whereas the simulated 16-h (1–17 LT) cumulative concentration, which was significantly underestimated, ranged from 16 to 202 Bq m^{-3} h for the ranges of $D_{g,n}$ = 0.1–10 μm and σ_g = 1.0–2.0. The underestimation was due probably to the discrepancy of simulated plume center, because the horizontal plume size was narrow. It was also due probably to the underestimation of emission. Still, however, the emission could be reasonable because the observed values were well within the simulated range in the further downwind locations (e.g., station [f]).

It must also be noted here that during the transport events of the type A CsMPs, substantial amounts of WSPs existed; as such, both the simulated and observed cumulative concentrations included both types of particles. The cumulative concentrations purely from type A CsMPs are shown in the upper panels of Figure 6 and the right panel of Figure 11. Thus, the discrepancies between the simulated and observed cumulative concentrations for the transport periods of the type A CsMPs were not associated solely with the uncertainty in the type A simulations. However, the difference between the simulated maximum and minimum concentrations was associated with the differences in the assumed size parameters for the type A CsMPs.

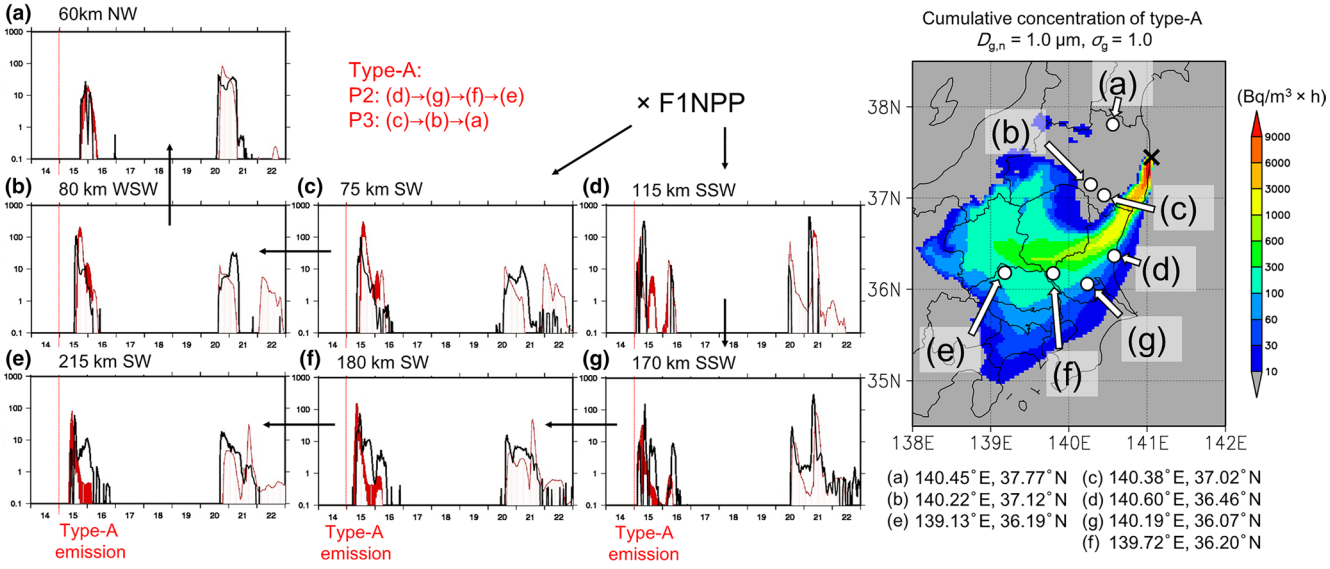

Figure 11. Left panels: time series of the observed (black) and simulated (red) surface air concentrations of ^{137}Cs (Bq m^{-3}) at monitoring stations (a) to (g) in Fukushima, Ibaraki, and Saitama prefectures over the transport pathways of type A CsMPs. The *x*-axis indicates the dates in LT. The red shaded areas indicate the range of simulated ^{137}Cs concentrations obtained from the sensitivity tests. The timing of assumed emissions of the type A CsMPs are shown by the red dashed lines in the panels. The rough sequences of plume arrivals at the stations for type A CsMPs along with the plumes P2 and P3 (Nakajima et al., 2017; Tsuruta et al., 2014) are indicated with arrows. Right panel: the locations of the monitoring stations are depicted over a map of the cumulative concentration of type A CsMPs for $D_{g,n}$ = 1.0 μm and σ_g = 1.0 (A05a). Latitude and longitude information of each station is also depicted.

Along with the plume P2 (stations d, g, f, and e), simulated type A CsMPs arrived at station (g) in Ibaraki 2 h after their arrival at station (d), at 3 LT on March 15, and remained for 8 h, up to 11 LT. The observed event started at 2 LT, 1 h earlier than the simulation, remained for 16 h. The observed 16-h (2–18 LT) cumulative concentration was 230 Bq m^{-3} h, whereas the simulations ranged from 5.9 to 94 Bq m^{-3} h. Next, the simulated type A CsMPs arrived at station (f) at 5 LT (7 LT based on the observations) and at station (e) at 8 LT (9 LT based on observations). The durations of observed event, simulated event, and simulated type A events at station (f) were 15, 12, and 10 h and those at station (e) were 19, 10, and 9 h, respectively. The observed cumulative concentrations at stations (f) and (e) were 250 and 180 Bq m^{-3} h, respectively, whereas the simulated cumulative concentrations were 25–400 and 5.8–160 Bq m^{-3} h, respectively. There were no observation data available for Gunma prefecture, but station (e) in Saitama prefecture is the closest to Gunma prefecture. The data suggest that type A CsMPs were next transported to Gunma prefecture.

The plume P3, identified by Tsuruta et al. (2014) and Nakajima et al. (2017) could also be affected by type A CsMPs. Along with P3, (stations c, b, and a), the simulated type A CsMPs arrived at station (c) in Fukushima at 11 LT on March 15, 3 h after the onset of observed event (8 LT). The durations of observed event, simulated event, and simulated type A events at station (c) were 15, 21, and 17 h, respectively. The observed cumulative concentration at station (c) was 240 Bq m^{-3} h, and the simulated concentration ranged from 187 to 1,036 Bq m^{-3} h. Next, simulated type A CsMPs arrived at station (b) at 14 LT, 2 h after the onset of observed event (12 LT). The durations of observed event, simulated event, and simulated type A events at station (b) were 13, 17, and 13 h, respectively. The observed cumulative concentration at station (b) was 280 Bq m^{-3} h, and the simulated cumulative concentration ranged from 141 to 740 Bq m^{-3} h. The simulated type A CsMPs arrived at stations (a) at 17 LT (same as the observation time). The durations of observed event, simulated event, and simulated type A events at station (a) were 10, 13, and 13 h, respectively. The observed cumulative concentrations at station (a) was 91 Bq m^{-3} h and the simulated cumulative concentrations at station (a) was 43–120 Bq m^{-3} h. Efforts to isolate CsMPs from samples along with pathway P3 are currently ongoing.

There may be a contradiction between the observed and simulated transport pathways of type A CsMPs, given the fact that relatively large type A CsMPs (up to 6.4 μm in diameter) were found in soil samples at 20 km NW of the F1NPP (Satou et al., 2015). For the assumed emission periods of the type A CsMPs, a northerly wind prevailed, causing most of the type A CsMPs to be transported first toward the south along with the plume P2 (Figure 2). Type A CsMPs were also transported along with the plume P3 traveling north back to Fukushima after traveling for a long distance (~100 km). It is slightly difficult to believe that such large type A CsMPs can travel that distance (certainly, "lucky" particles can travel long distances). There is a possibility that another emission of type A CsMPs occurred when the wind direction was southeasterly, from 12 to 22 LT (Figure 2), as proposed by Satou et al. (2015). During this time (on the evening of March 15), there was a significant enhancement in the estimated radio-Cs emissions (Katata et al., 2015). However, it is still difficult to estimate the timing of emission because the particles were not observed in the air sample but in the soil.

3.5. Activity Fractions of CsMPs to the Total Cumulative Depositions

The simulated activity fractions of the CsMPs to the total cumulative depositions for all the sensitivity tests are illustrated and compared against the observed values from the surface soil at 20 sites in Fukushima (Ikehara et al., 2020) in Figure 12. The simulated spatial distributions are shown in the top panels with the two combinations of sensitivity tests. The top-left panel shows that the fraction exceeded 90% in the grid cell including the F1NPP due to the large size of the type B CsMPs ($D_{g,n}$ = 100 μm), and the fraction ranged from 30% to 90% along with the plume P2 (stations d, g, f, and e; Figure 11) due to the large dry deposition velocity of the type A CsMPs ($D_{g,n}$ = 10 μm). Because the activated fraction of the size of the type A CsMPs in fog was one (Table 3), significant depositions of type A CsMPs occurred over the mountain forests in the Gunma prefecture due to fog (also see Figure 8). In the top-right panel, the activity fraction of the CsMPs in the F1NPP grid cell was lower than 5% due to the low gravitational settling velocities of type A and type B CsMPs. The activity fractions exceeded 90% over wide areas north and northeast of the F1NPP, as type B CsMPs ($D_{g,n}$ = 10 μm) could travel long distances and be deposited to a greater extent than type A CsMPs (Figure 3). The activity fractions of the type A CsMPs ($D_{g,n}$ = 1 μm), which are much smaller than the type B CsMPs ($D_{g,n}$ = 10 μm), ranged from 5% to 40% along the plume

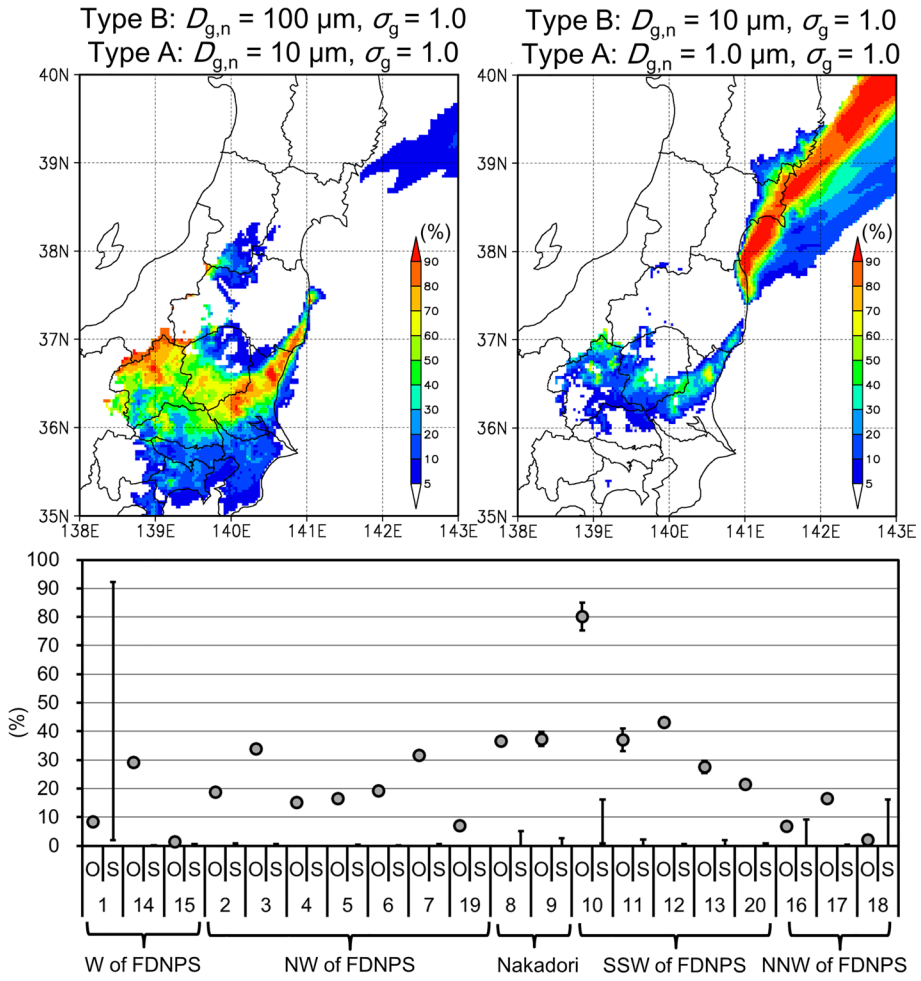

Figure 12. Top panels: simulated activity fractions of the CsMPs to the total cumulative depositions for the two sensitivity tests of the type B and type A CsMPs (left: B15-A10a, right: B10-A05a). The values are depicted where the simulated deposition exceeded 1 kBq m^{-2}. Bottom panel: The observed (O) activity fractions of CsMPs with measurement errors at the 20 sites in Fukushima based on a study conducted by Ikehara et al. (2020) and ranges of the simulated (S) maximum and minimum activity fractions of CsMPs for all the sensitivity tests.

P2 mainly due to the lower dry deposition velocity. The bottom panel of Figure 12 shows a comparison between the observations (with the measurement errors) and simulations (with the maximum and minimum values of the sensitivity tests). Note that all the stations were located in Fukushima prefecture, 4.42–61.0 km from the F1NPP. The station numbers were reordered based on geographical categories (W, NW, SSW, and NNW of the F1NPP and Nakadori valley) (Figure 1b), including stations (a) and (c) in Figure 11 and the simulated pathway of the type A CsMPs along with the plume P3. It is apparent that the simulated activity fractions of the CsMPs were substantially underestimated except at site #1 (W of the F1NPP) and sites NNW of the F1NPP (#16 and #18). Site #1 is located only 4.42 km from the F1NPP; therefore, its location was difficult to simulate using a 3-km model. In fact, the model grid cell in which site #1 was located was the same as the grid cell in which the F1NPP was located, so the large variation in the simulation (1.95%–92.2%) was simply due to the large variation in the settling velocity of the type B CsMPs (0.01–100 μm in diameter). Sites #16–18 were also located along the simulated pathway of the type B CsMPs. The relatively better performance of the simulated activity fractions at the north-northwestern sites indicated the successful simulations of emission, transport, and deposition of type B CsMPs. On the other hand, the simulated values affected by the presence of type A CsMPs were all underestimated. Among the south-southwestern sites, the location of the observed peak (#10) was the same as that for the simulation, but the values were much smaller (the observed peak was 80.2% and the simulated peak was

0.85%–16.2%), even though the emission during the events (0.475 PBq) was assumed to be 100% CsMPs. The simulated cumulative surface air concentrations were not very different from those observed along the pathways of the type A CsMPs (Figure 11), and there were two reasons for the large underestimation: there were more type A particle fractions in the source term of Katata et al. (2015) or the simulated deposition rates were underestimated. A similar assumption can be made for the Nakadori sites, along with the plume P3, on which the observed values were ∼40% and the simulated maximum was 5% at site #8. The simulated performance at the northwestern sites (#2–7 and #19) was the worst among the geographical categories, simply because the type A particle emissions that might have occurred during the evening of March 15 were not included in the simulation. The observed values ranged from 7.25% to 34.0%, whereas the simulated maximum value was 0.75% (#2). Further observational and simulation studies are required to constrain the source term estimation and size distribution of CsMPs, especially for type A CsMPs, to better understand the abundance and environmental behaviors of type A CsMPs.

4. Conclusions

The dispersion and deposition of radio-cesium (^{137}Cs) carried by two types (type A and type B) of water-insoluble Cs-bearing microparticles (CsMPs) released due to the Fukushima nuclear accident were simulated for the first time by using the multimodel meteorological ensemble mean field created in Part 1 of the current study (Kajino et al., 2019a). The results were compared against field observations of the surface air concentration and deposition. The results were also compared with the previous simulation, in which it was assumed that 100% of the carrier aerosols of ^{137}Cs were water-soluble particles (WSPs) with a submicron size range.

The presence of type B CsMPs (70–400 μm in soil (Satou et al., 2018) and 1–5 μm in air (Onozaki et al., 2019) arising from the hydrogen explosion of Unit 1 occurred on March 12, 15:36 LT; UTC+9; 0.7 PBq) could partly explain the simulated underestimation of the total deposition over land when assuming 100% WSPs. The observed deposition over land totaled 2.64 PBq, whereas the simulated deposition assuming submicron carriers was 1.19 PBq. The type B CsMPs were so large that almost 100% of the emission was deposited near the F1NPP. The deposition of type B CsMPs (0.7 PBq) accounts for ∼50% of the total underestimation (1.45 PBq). The relative magnitudes of the radioactivity of the type B CsMPs larger than 10 μm and smaller than 10 μm should be a key factor in the surface air concentration and deposition during the emission event. Considering the presence of type B CsMPs in the source term estimation (e.g., Katata et al., 2015) could alter the estimated amount of radio-Cs emitted by the Unit 1 hydrogen explosion.

The environmental behaviors of type A CsMPs of 0.1, 1, and 10 μm could be drastically different. The origin of type A CsMPs is still controversial (it could be Units 2 or 3), but these particles were emitted in the midnight between March 14 and 15 and transported southward over the Kanto Plain, the most populated plain in Japan, along with the plume P2 (Nakajima et al., 2017; Tsuruta et al., 2014) and also transported to Fukushima, along with the plume P3 (Nakajima et al., 2017; Tsuruta et al., 2014). The size of the particles ranged from 1 to 10 μm both in the air in Tsukuba, located in Kanto (Adachi et al., 2013), and in the soil in Fukushima (Satou et al., 2016); however, recently, type A CsMPs smaller than 1 μm were also found in Fukushima (Okumura et al., 2019a). Due to the differences in size distributions, the surface air concentration over Kanto varied substantially, by up to more than one order of magnitude. The major deposition mechanisms varied among dry, wet, and fog deposition depending on the size distribution of the particles. There might have been other emission events of type A CsMPs from Units 2 or 3 in the evening of March 15, followed by transport toward the northwest and deposition in the mountain region in Fukushima.

The simulated activity fractions of CsMPs to the total cumulative depositions were compared to those in the surface soil observed in Fukushima (Ikehara et al., 2020) for the first time. The observed activity fractions could have settled within the ranges of the simulated sensitivity tests for the locations under the influence of the type B CsMPs (near the F1NPP and NNW of the F1NPP). On the other hand, the simulation substantially underestimated the observed activity fractions for the locations along the transport pathways of the type A CsMPs (SSW of the F1NPP and Nakadori and NW of the F1NPP). There could be more fractions of type A CsMPs in the estimated source term than assumed in this study, and/or the simulated deposition rates might be underestimated.

Works on the isolation of CsMPs from hourly air filters at one hundred locations (Oura et al., 2015; Tsuruta et al., 2014) are currently ongoing (partly reported by Onozaki et al., 2019). Information on the relative magnitudes of radioactivity from CsMPs and WSPs is essential. These efforts will certainly promote the precise estimations of emission events, the timing and origins of emission events, and the amounts of radioactivity associated with CsMPs. This may help to improve the understanding of the formation mechanisms of CsMPs in reactors, together with the mechanisms of emission into the environment, which are still controversial.

The elementary process modeling of numerical simulations needs to be improved. The possible underestimation of deposition suggested in Part 1 (Kajino et al., 2019a) has not yet been resolved. An improvement in the below-cloud scavenging rate (Kajino et al., 2019a) and the implementation of the substantial electrical charges of type A CsMPs (Dépée et al., 2019) will be incorporated in the future. The self-electrical charge of type A CsMPs should enhance the rates of dry deposition and below-cloud scavenging, which may improve the significant underestimation of the deposition fraction from CsMPs SSW of the F1NPP and Nakadori. The charging effect should be assessed in the future steps of the current work.

Numerical simulations also need to be improved in terms of horizontal grid resolution. A new simulation with a finer grid resolution ($\Delta x = 1$ km; Sekiyama & Kajino, 2020) indicated that our $\Delta x = 3$ km simulation would be significantly improved in terms of the reproduction of wind fields along the coastline of Fukushima, which may lead to improvements in plume directions starting from the F1NPP (e.g., for type B CsMPs). Due to the complex topography in inland areas of Fukushima (with mountains and valleys), air masses transported inland will also be improved by fine-scale grid simulations (e.g., type A CsMPs in Nakadori along with plume P3 and type A CsMPs which might have been emitted in the evening of March 15 and transported to the northwest).

Data Availability Statement

The simulated and observed data used in all the figures are available at https://mri-2.mri-jma.go.jp/owncloud/s/pz8T2P2XfKJMi3X (last accessed: June 5, 2020). In terms of the raw observation data sets, the surface air activity concentration data are available in Appendix A of Oura et al. (2015), and the activity deposition data are available at https://emdb.jaea.go.jp/emdb/en/portals/b1010301/ (last accessed: June, 5 2020).

Acknowledgments
The authors are thankful for the useful comments of Drs Akihide Hidaka and Hiroaki Terada of JAEA on the possible formation mechanisms of type A CsMPs, Dr Yukihisa Sanada of JAEA for providing the unmanned helicopter measurement data within 3 km of the F1NPP, and Prof. Yoshinari Abe of Tokyo Denki University for providing information on CsMPs isolated from air samples. The authors are grateful for the support of Mr. Shoichi Akami of the University of Tsukuba for figure generation. This research was mainly supported by the Environmental Research and Technology Development Fund of the Environmental Restoration and Conservation Agency (ERCA) (JPMEERF20155001 and JPMEERF20181002) and by Grants-in-Aid for Scientific Research on Innovative Areas 24110002 and 24110003 of the Ministry of Education, Culture, Sports, Science and Technology (MEXT). It was partially supported by the Japanese Radioactivity Survey from the NRA, Japan, and the Japanese Society for the Promotion of Sciences (JSPS) (KAKENHI grant nos. JP15H02811, JP16KK0018, JP19H02649, and JP19H01155).

References

Abe, Y., Iizawa, Y., Terada, Y., Adachi, K., Igarashi, Y., & Nakai, I. (2014). Detection of uranium and chemical state analysis of individual radioactive microparticles emitted from the Fukushima nuclear accident using multiple synchrotron radiation X-ray analyses. *Analytical Chemistry*, *86*, 8521–8525. https://doi.org/10.1021/ac501998d

Adachi, K., Kajino, M., Zaizen, Y., & Igarashi, Y. (2013). Emission of spherical cesium-bearing particles from an early stage of the Fukushima nuclear accident. *Scientific Reports*, *3*, 2554. https://doi.org/10.1038/srep02554

Aoyama, M., Kajino, M., Tanaka, T. Y., Sekiyama, T. T., Tsumune, D., Tsunbono, T., et al. (2016). ^{134}Cs and ^{137}Cs in the North Pacific Ocean derived from the March 2011 TEPCO Fukushima Dai-ichi Nuclear Power Plant accident, Japan. Part two: Estimation of ^{134}Cs and ^{137}Cs inventories in the North Pacific Ocean. *Journal of Oceanography*, *72*, 67–76. https://doi.org/10.1007/s10872-015-0332-2

Chino, M., Nakayama, H., Nagai, H., Terada, H., Katata, G., & Yamazawa, H. (2011). Preliminary estimation of release amounts of ^{131}I and ^{137}Cs accidentally discharged from the Fukushima Daiichi nuclear power plant into the atmosphere. *Journal of Nuclear Science and Technology*, *48*, 1129–1134. https://doi.org/10.1080/18811248.2011.9711799

Chino, M., Terada, H., Nagai, H., Katata, G., Mikami, S., Torii, T., et al. (2016). Utilization of 134Cs/137Cs in the environment to identify the reactor units that caused atmospheric releases during the Fukushima Daiichi accident. *Scientific Reports*, *6*, 31376. https://doi.org/10.1038/srep31376

Dépée, A., Lamaitre, P., Gelain, T., Mathieu, A., Monier, M., & Flossmann, A. (2019). Theoretical study of aerosol particle electroscavenging by clouds. *Journal of Aerosol Science*, *135*, 1–20. https://doi.org/10.1016/j.jaerosci.2019.04.001

Draxler, R., Arnold, D., Chino, M., Galmarini, S., Hort, M., Jones, A., et al. (2015). World Meteorological Organization's model simulations of the radionuclide dispersion and deposition from the Fukushima Daiichi nuclear power plant accident. *Journal of Environmental Radioactivity*, *139*, 172–184.

Furuki, G., Imoto, J., Ochiai, A., Yamasaki, S., Nanba, K., Ohnuki, T., et al. (2017). Caesium-rich micro-particles: A window into the meltdown events at the Fukushima Daiichi Nuclear Power Plant. *Scientific Reports*, *7*, 42731. 10. https://doi.org/10.1038/srep42731

Hidaka, A. (2019). Formation mechanisms of insoluble Cs particles observed in Kanto district four days after Fukushima Daiichi NPP accident. *Journal of Nuclear Science and Technology*, *16*(9–10), 831–841. https://doi.org/10.1080/00223131.2019.1583611

Higaki, S., Kurihara, Y., Yoshida, H., Takahashi, Y., & Shinohara, N. (2017). Discovery of non-spherical heterogeneous radiocesium-bearing particles not derived from Unit 1 of the Fukushima Dai-ichi Nuclear Power Plant, in residences five years after the accident. *Journal of Environmental Radioactivity*, *177*, 65–70. https://doi.org/10.1016/j.jenvrad.2017.06.006

Hirao, S., Yamazawa, H., & Nagae, T. (2013). Estimation of release rate of iodine-131 and cesium-137 from the Fukushima Daiichi nuclear power plant. *Journal of Nuclear Science and Technology*, *50*, 139–147. https://doi.org/10.1080/00223131.2013.757454

Holländer, W., & Schumann, G. (1979). Droplet growth on hydrophobic and charged nuclei in expansion condensation nuclei counters. *Journal of Colloid and Interface Science*, *72*(1), 123–129. https://doi.org/10.1016/0021-9797(79)90188-7

Hososhima, M., & Kaneyasu, N. (2015). Altitude-dependent distribution of ambient gamma dose rates in a mountainous area of Japan caused by the Fukushima nuclear accident. *Environmental Science and Technology*, *49*, 3341–3348. https://doi.org/10.1021/es504838w

Igarashi, Y., Kajino, M., Zaizen, Y., Adachi, K., & Mikami, M. (2015), Atmospheric radioactivity over Tsukuba, Japan: A summary of three years of observations after the FDNPP accident. *Progress in Earth and Planetary Science*, *2*(44), 19. https://doi.org/10.1186/s40645-015-0066-1

Igarashi, Y., Kogure, T., Kurihara, Y., Miura, H., Okumura, T., Satou, Y., et al. (2019). A review of Cs-bearing microparticles in the environment emitted by the Fukushima Dai-ichi Nuclear Power Plant accident. *Journal of Environmental Radioactivity*, *205–206*, 101–118. https://doi.org/10.1016/j.jenvrad.2019.04.011

Ikehara, R., Morooka, K., Suetake, M., Komiya, T., Kurihara, E., Takehara, M., et al. (2020). Abundance and distribution of radioactive cesium-rich microparticles released from the Fukushima Daiichi Nuclear Power Plant into the environment. *Chemosphere*, *241*, 125019. 9 https://doi.org/10.1016/j.chemosphere.2019.125019

Ikehara, R., Suetake, M., Komiya, T., Furuki, G., Ochiai, A., Yamasaki, S., et al. (2018). Novel method of quantifying radioactive cesium-rich microparticles (CsMPs) in the environment from the Fukushima Daiichi nuclear power plant. *Environmental Science and Technology*, *52*, 6390–6398. https://doi.org/10.1021/acs.est.7b06693

Imamura, N., Katata, G., Kajino, M., Kobaayshi, M., Itoh, Y., & Akama, A. (2020). Fogwater deposition of radiocesium in the forested mountains of East Japan during the Fukushima Daiichi Nuclear Power Plant accident: A key process in regional radioactive contamination. *Atmospheric Environment*, *224*, 117339. 11 https://doi.org/10.1016/j.atmosenv.2020.117339

Kajino, M., Deushi, M., Sekiyama, T. T., Oshima, N., Yumimoto, K., Tanaka, T. Y., et al. (2019). NHM-Chem, the Japan meteorological agency's regional meteorology – Chemistry model: Model evaluations toward the consistent predictions of the chemical, physical, and optical properties of aerosols. *Journal of the Meteorological Society of Japan*, *97*(2), 337–374. https://doi.org/10.2151/jmsj.2019-020

Kajino, M., Sekiyama, T. T., Igarashi, Y., Katata, G., Sawada, M., Adachi, K., et al. (2019a). Deposition and dispersion of radio-cesium released due to the Fukushima nuclear accident: Sensitivity to meteorological models and physical modules. *Journal of Geophysical Research*, *124*(3), 1823–1845. https://doi.org/10.1029/2018JD028998

Kajino, M., Sekiyama, T. T., Mathieu, A., Korsakissok, I., Périllat, R., Quélo, D., et al. (2018). Lessons learned from atmospheric modeling studies after the Fukushima nuclear accident: Ensemble simulations, data assimilation, elemental process modeling, and inverse modeling. *Geochemical Journal*, *52*, 85–101. https://doi.org/10.2343/geochemj.2.0503

Kaneyasu, N., Ohashi, H., Suzuki, F., Okada, T., & Ikemori, F. (2012). Sulphate aerosol as a potential transport medium of radiocesium from the Fukushima nuclear accident. *Environmental Science and Technology*, *46*, 5720–5726.

Katata, G., Chino, M., Kobayashi, T., Terada, H., Ota, M., Nagai, H., et al. (2015). Detailed source term estimation of the atmospheric release for the Fukushima Daiichi Nuclear Power Station accident by coupling simulations of an atmospheric dispersion model with an improved deposition scheme and oceanic dispersion model. *Atmospheric Chemistry and Physics*, *15*, 1029–1070. https://doi.org/10.5194/acp-15-1029-2015

Kitayama, K., Morino, Y., Takigawa, M., Nakajima, T., Hayami, H., Nagai, H., et al. (2018). Atmospheric modeling of 137Cs plumes from the Fukushima Daiichi Nuclear Power Plant - Evaluation of the model intercomparison data of the science Council of Japan. *Journal of Geophysical Research*, *123*(14), 7047–7796. https://doi.org/10.1029/2017JD028230

Kogure, T., Yamaguchi, N., Sagawa, H., Mukai, H., Motai, S., Akiyama-Hasegawa, K., et al. (2016). Constituent elements and their distribution in the radioactive Cs-bearing silicate glass microparticles released from Fukushima nuclear plant. *Microscopy*, *65*(5), 451–459. https://doi.org/10.1093/jmicro/dfw030

Kristiansen, N. I., Stohl, A., Olivie, D. J. L., Croft, B., Sovde, O. A., Klein, H., et al. (2016). Evaluation of observed and modelled aerosol lifetimes using radioactive tracers of opportunity and an ensemble of 19 global models. *Atmospheric Chemistry and Physics*, *16*, 3525–3561. https://doi.org/10.5194/acp-16-3525-2016

Kunii, M. (2013). Mesoscale data assimilation for a local severe rainfall event with the NHM-LETKF system. *Weather and Forecasting*, *29*(5), 1093–1105. https://doi.org/10.1175/WAF-D-13-00032.1

Masson, O., Baeza, A., Bieringer, J., Brudecki, K., Bucci, S., Cappai, M., et al. (2011). Tracking of airborne radionuclides from the damaged Fukushima Dai-ichi nuclear reactors by European networks. *Environmental Science and Technology*, *45*, 7670–7677. https://doi.org/10.1021/es2017158

Masson, O., Ringer, W., Mala, H., Rulik, P., Dlugosz-Lisiecka, M., Eleftheriadis, K., et al. (2013). Size distributions of airborne radionuclides from the Fukushima nuclear accident at several places in Europe. *Environmental Science and Technology*, *47*, 10995–11003. https://doi.org/10.1021/es401973c

Mathieu, A., Kajino, M., Korsakissok, I., Périrat, R., Quélo, D., Quérel, A., et al. (2018). Fukushima Daiichi-derived radionuclides in the atmosphere, transport and deposition in Japan: A review. *Applied Geochemistry*, *91*, 122–139. https://doi.org/10.1016/j.apgeochem.2018.01.002

Miura, H., Kurihara, Y., Sakaguchi, A., Tanaka, K., Yamaguchi, N., Higaki, S., et al. (2018). Discovery of radiocesium-bearing microparticles in river water and their influence on the solid-water distribution coefficient (K_d) of radiocesium in the Kuchibuto River in Fukushima. *Geochemical Journal*, *52*(2), 145–154. https://doi.org/10.2343/geochemj.2.0517

Morino, Y., Ohara, T., & Nishizawa, M. (2011): Atmospheric behavior, deposition, and budget of radioactive materials from the Fukushima Daiichi nuclear power plant in March 2011, *Geophysical Research Letters*, *38*(7), L00G11. https://doi.org/10.1029/2011GL048689

Morino, Y., Ohara, T., Watanabe, S., Hayashi, S., & Nishizawa, M. (2013). Episode analysis of deposition of radiocesium from the Fukushima Daiichi nuclear power plant accident. *Environmental Science and Technology*, *47*, 2314–2322.

Nakajima, T., Misawa, S., Morino, Y., Tsuruta, H., Goto, D., Uchida, J., et al. (2017). Model depiction of the atmospheric flows of radioactive cesium emitted from the Fukushima Daiichi Nuclear Power Station accident. *Progress in Earth and Planetary Science*, *4*(2), 18. https://doi.org/10:1186/s40645-017-0117-x

Nuclear Regulation Authority (2012), Airborne monitoring results in each prefecture. Available at http://radioactivity.nsr.go.jp/en/list/203/list-1.html (last access: 12 February 2018).

Okumura, T., Yamaguchi, N., Dohi, T., Iijima, K., & Kogure, T. (2019b). Inner structure and inclusions in radiocesium-bearing microparticles emitted in the Fukushima Daiichi Nuclear Power Plant accident. *Microscopy*, *68*(3), 234–242. https://doi.org/10.1093/jmicro/dfz004

Okumura, T., Yamaguchi, N., Dohi, T., Iijima, K., & Kogure, T. (2019c). Dissolution behaviour of radiocaesium-bearing microparticles released from the Fukushima nuclear plant. *Scientific Reports*, *9*, 3520. https://doi.org/10.1038/s41598-019-40423-x

Okumura, T., Yamaguchi, N., & Kogure, T. (2019a). Finding radiocesium-bearing microparticles more minute than previously reported, emitted by the Fukushima nuclear accident. *Chemistry Letters*, *48*, 1336–1338. https://doi.org/10.1246/cl.190581

Okura, T., Oishi, T., Taki, M., Shibanuma, Y., Kikuchi, M., Akino, H., et al. (2012). *Emergency monitoring of environmental radiation and atmospheric radionuclides at nuclear science researhc institute, JAEA following the accident of Fukushima Daiichi nuclear power plant* (pp. 37). Japan Atomic Energy Agency Report JAEA-Date/Code 2012-010. https://doi.org/10.11484/jaea-data-code-2012-010

Onozaki, H., Abe, Y., Nakai, I., Adachi, K., Igarashi, Y., Oura, Y., et al. (2019). Investigation of physical and chemical characteristics of radioactive aerosols emitted from reactor unit 1 by Fukushima Daiichi Nuclear Power Plant Accident. *Bunseki Kagaku*, *68*(10), 757–768 (in Japanese).

Oura, Y., Ebihara, M., Tsuruta, H., Nakajima, T., Ohara, T., Ishimoto, M., et al. (2015). A database of hourly atmospheric concentration of radiocesium (^{134}Cs and ^{137}Cs) in suspended particulate matter collected in March 2011 at 99 air pollution monitoring stations in eastern Japan. *Journal of Nuclear and Radiochemical Sciences*, *15*(2), 15–26.

Petters, M. D., & Kreidenweis, S. M. (2007). A single parameter representation of hygroscopic growth and cloud condensation nucleus activity. *Atmospheric Chemistry and Physics*, *7*, 1961–1971. https://doi.org/10.5194/acp-7-1961-2007

Saito, K., Ishida, J., Aranami, K., Hara, T., Segawa, T., Narita, M., et al. (2007). Nonhydrostatic atmospheric models and operational development at JMA. *Journal of the Meteorological Society of Japan*, *85B*, 271–304. https://doi.org/10.2151/jmsj.85B.271

Sanada, Y., Katata, G., Kaneyasu, N., Nakanishi, C., Urabe, Y., & Nishizawa, Y. (2018). Altitudal characteristics of atmospheric deposition of aerosols in mountainous regions: Lessons from the Fukushima Daiichi Nuclear Power Station accident. *Science of the Total Environment*, *618*, 881–890. https://doi.org/10.1016/j.scitotenv.2017.08.246

Sanada, Y., Kondo, A., Sugita, T., Nishizawa, Y., Yuuki, Y., Ikeda, K., et al. (2014). Radiation monitogin using an unmanned helicopter in the evacuation zone around the Fukushima Daiichi nuclear power plant. *Exploration Geophysics*, *45*(1), 3–7. https://doi.org/10.1071/EG13004

Sato, Y., Sekiyama, T. T., Fang, S., Kajino, M., Quérel, A., Quélo, D., et al. (2020). A model intercomparison of atmospheric ^{137}Cs concentrations from the Fukushima Daiichi Nuclear Power Plant accident, phase III: Simulation with an identical source term and meteorological filed at 1-km resolution. *Atmospheric Environment X*, *7*, 100086. https://doi.org/10.1016/j.aeaoa.2020.100086

Sato, Y., Takigawa, M., Sekiyama, T. T., Kajino, M., Terada, H., Nagai, H., et al. (2018). Model intercomparison of atmospheric ^{137}Cs from the Fukushima Daiichi Nuclear Power Plant accident: Simulations based on identical input data. *Journal of Geophysical Research*, *123*, 11748–11765. https://doi.org/10.1029/2018JD029144

Satou, Y., Sueki, K., Sasa, K., Adachi, K., & Igarashi, Y. (2016). First successful isolation of radioactive particles from soil near the Fukushima Daiichi Nuclear Power Plant. *Anthropocene*, *14*, 71–76. https://doi.org/10.1016/j.ancene.2016.05.001

Satou, Y., Sueki, K., Sasa, K., Matsunaka, T., Shibayama, N., & Kinoshita, N. (2015). Classification using ^{110m}Ag/^{137}Cs ratio in high dose area at the northwestern from Fukushima Daiichi nuclear plant. *Houshakagaku*, *31*, 28–29 (in Japanese).

Satou, K., Sueki, Y., Sasa, K., Yoshikawa, H., Nakama, S., Minowa, H., Abe, Y., et al. (2018). Analysis of two forms of radioactive particles emitted during the early stages of the Fukushima Dai-ichi Nuclear Power Station accident. *Geochemical Journal*, *52*, 137–143. https://doi.org/10.2343/geochemj.2.0514

Saunier, O., Mathieu, A., Didier, D., Tombette, M., Quélo, D., Winiarek, V., et al. (2013). An inverse modeling method to assess the source term of the Fukushima Nuclear Power Plant accident using gamma dose rate observations. *Atmospheric Chemistry and Physics*, *13*, 11403–11421. https://doi.org/10.5194/acp-13-11403-2013

Saya, A., Yoshikane, T., Chang, E. C., Yoshimura, K., & Oki, T. (2018) Precipitation redistribution method for regional simulations of radioactive material transport during the Fukushima Daiichi Nuclear Power Plant accident. *Journal of Geophysical Research*, *123*, 10248–10259. https://doi.org/10.1029/2018JD028531

Science Coucil of Japan (2014), A review of the model comparison of transportation and deposition of radioactive materials released to the environment as a result of the Tokyo Electric Power Company's Fukushima Daiichi Nuclear Power Plant accident (36 pp) Available at http://www.scj.go.jp/ja/info/kohyo/pdf/kohyo-22-h140902-e1.pdf (last access: April 17, 2018).

Sekiyama, T. T., & Iwasaki, T. (2018). Mass flux analysis of ^{137}Cs plumes emitted from the Fukushima Daiichi nuclear power plant. *Tellus B: Chemical and Physical Meteorology*, *70*(1), 11. https://doi.org/10.1080/16000889.2018.1507390

Sekiyama, T. T., & Kajino, M. (2020). Reproducibility of surface wind and tracer transport simulations over complex terrain using 5-, 3-, and 1-km-grid models. *Journal of Applied Meteorology and Climatology*, *59*, 937–952. https://doi.org/10.1175/JAMC-D-19-0241.s1

Sekiyama, T. T., Kajino, M., & Kunii, M. (2017). The impact of surface wind data assimilation on the predictability of near-surface plume advection in the case of the Fukushima nuclear accident. *Journal of the Meteorological Society of Japan*, *95*(6), 447–454. https://doi.org/10.2151/jmsj.2017-025

Sekiyama, T. T., Kunii, M., Kajino, M., & Shimbori, T. (2015). Horizontal resolution dependence of atmospheric simulations of the Fukushima nuclear accident using 15-km, 3-km, and 500-m grid models. *Journal of the Meteorological Society of Japan*, *93*(1), 49–64. https://doi.org/10.2151/jmsj.2015-002

Skamarock, W. C., Klemp, J. B., Dudhia, J., Gill, D. O., Barker, D. M., Duda, M. G., et al. (2008). *A description of the advanced research WRF version 3. Technical Note, NCAR/TN-475+STR* (pp. 125). Boulder, CO: National Center for Atmospheric Research.

Stohl, A., Seibert, P., Wotawa, G., Arnold, D., Burkhart, J. F., Eckhardt, S., et al. (2012). Xenon-133 and caesium-137 releases into the atmosphere from the Fukushima Dai-ichi nuclear power plant: Determination of the source term, atmospheric dispersion, and deposition. *Atmospheric Chemistry and Physics*, *12*, 2313–2343. https://doi.org/10.5194/acp-12-2313-2012

Terada, H., Katata, G., Chino, M., & Nagai, H. (2012). Atmospheric discharge and dispersion of radionuclides during the Fukushima Daiichi Nuclear Power Plant accident, Part II: Verification of the source term and analysis of regional-scale atmospheric dispersion. *Journal of Environmental Radioactivity*, *112*, 141–154. https://doi.org/10.1016/j.jenvrad.2012.05.023

Terada, H., Nagai, H., Tsuduki, K., Furuno, A., Kadowaki, M., & Kakefuda, T. (2020). Refinement of source term and atmospheric dispersion simulations of radionuclides during the Fukushima Daiichi Nuclear Power Station accident. *Journal of Environmental Radioactivity*, *213*, 106104. 13 https://doi.org/10.1016/j.jenvrad.2019.106104

Torii, T., Sanada, Y., Sugita, T., Kondo, A., Shikaze, Y., Takahashi, M., et al. (2012). *Investigation of radionuclide distribution using aircraft for surrounding environmental survey from Fukushima Dai-ichi nuclear power plant* (pp. 182). Japan Atomic Energy Agency (in Japanese with English abstract).

Tsuruta, H., Moriguchi, Y., & Nakajima, T. (2019). Dynamics of atmospheric ^{131}I in radioactive plumes in eastern Japan immediately after the Fukushima accident by analysing published data. *Scientific Reports*, *9*, 13240. https://doi.org/10.1038/s41598-019-49379-4

Tsuruta, H., Oura, Y., Ebihara, M., Moriguchi, Y., Ohara, T., & Nakajima, T. (2017). Spatio-temporal distribution of atmospheric radiocesium in Eastern Japan just after the TEPCO Fukushima Daiichi Nuclear Power Plant Accident – Analysis of used filter-tapes of SPM monitors in air quality monitoring stations–. *Earozoru Kenkyu*, *32*(4), 244–254. https://doi.org/10.11203/jar.32.244

Tsuruta, H., Oura, Y., Ebihara, M., Moriguchi, Y., Ohara, T., & Nakajima, T. (2018). Time-series analysis of atmospheric radiocesium at two SPM monitoring sites near the Fukushima Daiichi Nuclear Power Plant just after the Fukushima accident on March 11, 2011. *Geochemical Journal*, *52*, 103–121. https://doi.org/10.2343/geochemj.2.0520

Tsuruta, H., Oura, Y., Ebihara, M., Ohara, T., & Nakajima, T. (2014). First retrieval of hourly atmospheric radionuclides just after the Fukushima accident by analyzing filter-tapes of operational air pollution monitoring stations. *Scientific Reports*, *4*, 6717. https://doi.org/10.1038/srep06717

Wang, X., Zhang, L., & Moran, M. D. (2010). Uncertainty assessment of current size-resolved parameterizations for below-cloud particle scavenging by rain. *Atmospheric Chemistry and Physics*, *10*, 5685–5705.

Wetherbee, G. A., Gay, D. A., Debey, T. M., Lehmann, C. M. B., & Nilles, M. A. (2012). Wet deposition of fission-product isotopes to North America from the Fukushima Dai-ichi incident, March 2011. *Environmental Science and Technology*, *46*(5), 2574–2582. https://doi.org/10.1021/es203217u

Winiarek, V., Bocquet, M., Duhanyan, N., Roustan, Y., Saunier, O., & Mathieu, A. (2014). Estimation of the caesium-137 source term from the Fukushima Daiichi nuclear power plant using a consistent joint assimilation of air concentration and deposition observations. *Atmospheric Environment*, *82*, 268–279.

Yamaguchi, N., Kogure, T., Mukai, H., Akiyama-Hasegawa, K., Mitome, M., Hara, T., et al. (2018). Structures of radioactive Cs-bearing microparticles in non-spherical forms collected in Fukushima. *Geochemical Journal*, *52*(2), 123–136. https://doi.org/10.2343/geochemj.2.0483

Yamaguchi, N., Mitome, M., Akiyama-Hasegawa, K., Asano, M., Adachi, K., et al. (2016). Internal structure of cesium-bearing radioactive microparticles released from Fukushima nuclear power plant. *Scientific Reports*, *6*, 20548. https://doi.org/10.1038/srep20548

Yumimoto, K., Morino, Y., Ohara, T., Oura, Y., Ebihara, M., Tsuruta, H., et al. (2016). Inverse modeling of the 137Cs source term of the Fukushima Dai-ichi Nuclear Power Plant accident constrained by a deposition map monitored by aircraft. *Journal of Environmental Radioactivity*, *164*, 1–12.

Zhang, L., Wang, X., Moran, M. D., & Feng, J. (2013). Review and uncertainty assessment of size-resolved scavenging coefficient formulations for below-cloud snow scavenging of atmospheric aerosols. *Atmospheric Chemistry and Physics*, *13*, 10005–10025.

https://doi.org/10.5194/acp-2021-687
Preprint. Discussion started: 20 September 2021

Atmospheric Chemistry and Physics Discussions

Reassessment of the radiocesium resuspension flux from contaminated ground surfaces in East Japan

Mizuo Kajino[1,2,3], Akira Watanabe[4,5], Masahide Ishizuka[6], Kazuyuki Kita[7], Yuji Zaizen[1], Takeshi Kinase[8,1], Rikuya Hirai[9,10], Kakeru Konnai[9], Akane Saya[1], Kazuki Iwaoka[11], Yoshitaka Shiroma[12], Hidenao Hasegawa[13], Naofumi Akata[2], Masahiro Hosoda[2], Shinji Tokonami[2], and Yasuhito Igarashi[14,7]

[1]Meteorological Research Institute (MRI), Japan Meteorological Agency (JMA), Tsukuba, Ibaraki 305–0052, Japan
[2]Institute of Radiation Emergency Medicine (IREM), Hirosaki University, Hirosaki, Aomori 036–8564, Japan
[3]Faculty of Life and Environmental Sciences, University of Tsukuba, Tsukuba, Ibaraki 305–8572, Japan
[4]Faculty of Symbiotic Systems Science, Fukushima University, Fukushima, Fukushima 960–1296, Japan
[5]Institute for Climate Change, Fukushima, Fukushima 960–0231, Japan
[6]Faculty of Engineering and Design, Kagawa University, Takamatsu, Kagawa 761–0396, Japan
[7]Graduate School of Science and Engineering, Ibaraki University, Mito, Ibaraki 310–8512, Japan
[8]Institute of Arctic Climate and Environmental Research (IACE), Japan Agency for Marine-Earth Science and Technology (JAMSTEC) Yokohama, Kanagawa 236–0001, Japan
[9]School of Life and Environmental Sciences, University of Tsukuba, Tsukuba, Ibaraki 305–8572, Japan
[10]Research Center for Advance Science and Technology (RCAST), University of Tokyo, Meguro, Tokyo 153–0041, Japan
[11]National Institute of Radiological Sciences, National Institues for Quantum and Radiological Science and Technology, Chiba, Chiba 263–8555, Japan
[12]Faculty of Education, University of the Ryukyus, Nishihara, Okinawa 903–0213, Japan
[13]Institute for Environmental Sciences, Rokkasho, Aomori 039–3212, Japan
[14]Institute for Integrated Radiation and Nuclear Science (KURNS), Kyoto University, Kumatori, Osaka 590–0494, Japan

Correspondence to: M. Kajino (kajino@mri-jma.go.jp)

https://doi.org/10.5194/acp-2021-687
Preprint. Discussion started: 20 September 2021

Atmospheric Chemistry and Physics Discussions

Abstract. Resuspension of ^{137}Cs from the contaminated ground surface to the atmosphere is essential for understanding the environmental behaviors of ^{137}Cs and estimating external and inhalation exposure of residents. Kajino et al. (2016) assessed the ^{137}Cs resuspension flux from bare soil and forest ecosystems in East Japan in 2013 using a numerical simulation constrained by surface air concentration measurements. However, the simulation was found to underestimate the observed deposition amounts by two orders of magnitude. The reason for this underestimation is that the simulation assumed that resuspended ^{137}Cs is carried by submicron aerosols, which have low deposition rates. Based on the observational indications that soil dust and bioaerosols are the major carriers of resuspended ^{137}Cs, a new simulation is performed with higher deposition rates constrained by both surface concentrations and deposition amounts. In the new estimation, the areal total annual resuspension of ^{137}Cs in 2013 is 25.7 TBq, which is equivalent to 0.96% of the initial deposition (2.68 PBq). Due to the rapid deposition rates, the annual redeposition amount is also large at 10.6 TBq, approximately 40% of the resuspended ^{137}Cs. The resuspension rate through the atmosphere (0.96% y^{-1}) seems slow, but it (2.6×10^{-5} d^{-1}) may not be negligibly small compared to the actual decreasing trend of the ambient gamma dose rate obtained in Fukushima Prefecture after the radioactive decay of ^{137}Cs plus ^{134}Cs in 2013 is subtracted ($1.0–7.9\times10^{-4}$ d^{-1}): Resuspension can account for 1–10% of the decreasing rate due to decontamination and natural decay through land surface processes. The current simulation underestimated the ^{137}Cs deposition in Fukushima city in winter by more than an order of magnitude, indicating the presence of additional resuspension sources. The site of Fukushima city is surrounded by major roads. Heavy traffic on wet and muddy roads after snow removal operations could generate superlarge (approximately 100 μm in diameter) road dust or road salt particles, which is not included in the model but might contribute to the observed ^{137}Cs at the site.

Keywords: Fukushima nuclear accident, resuspension of ^{137}Cs, submicron and supermicron aerosols, dust and forest aerosols, source-receptor analysis, seasonal budget.

https://doi.org/10.5194/acp-2021-687
Preprint. Discussion started: 20 September 2021

Atmospheric Chemistry and Physics Discussions

1 Introduction

More than ten years have passed since the Fukushima Daiichi Nuclear Power Plant (F1NPP) accident. Extensive studies have been performed thus far using field observations, laboratory experiments, and numerical simulations aiming at a full understanding of atmospheric dispersion and deposition of directly emitted radionuclides associated with the accident, which occurred in March 2011 (i.e., primary emission). It is difficult to cite all relevant papers here, so one can refer to review papers such as Mathieu et al. (2018), but a few remarkable studies are introduced here with some updates. Aircraft monitoring studies (NRA, 2012; Torii et al., 2012; 2013; Sanada et al., 2014) have provided the spatial distributions of radio-Cs and radio-I that were deposited to the ground surface in March 2011 over all of Japan. Tsuruta et al. (2014) and Oura et al. (2015) measured the hourly surface air activity concentrations of ^{137}Cs at 99 stations in East Japan. These two powerful spatiotemporal measurement datasets together with comprehensive emission scenarios provided by the Japan Atomic Energy Agency (e.g., Katata et al., 2015; Terada et al., 2020) enable us to identify transport and deposition events over the land surface in Japan (e.g., Tsuruta et al., 2014; Nakajima et al., 2017; Sekiyama and Iwasaki, 2018). These data were also useful to validate the numerical simulation results provided by various regional-scale atmospheric models (Draxler et al., 2015; Leadbetter et al., 2015; Kitayama et al., 2018; Sato et al., 2018; 2020; Kajino et al., 2019; Goto et al., 2020) and were applied for other advanced numerical techniques, such as inverse modeling (Yumimoto et al., 2016; Li et al., 2019), ensemble forecasting (Sekiyama et al., 2021), and data assimilation (Sekiyama and Kajino, 2020).

In addition to spatial observations, detailed measurements have been helpful to investigate the mechanisms of atmospheric deposition and emissions from reactors. Kaneyasu et al. (2012) used size distribution measurements of multiple chemical components obtained in April and May 2011 to indicate that submicron sulfate aerosols can be a major carrier of radio-Cs, and in fact, numerical simulations assuming hydrophilic submicron carrier aerosols have been successful (all models mentioned above made this assumption). On the other hand, Adachi et al. (2013) isolated hydrophobic supermicron Cs-bearing particles (referred to as Cs-bearing microparticles; CsMPs) from aerosol filters collected in March 2011; the atmospheric behaviors of these CsMPs could be quite different from those of hydrophilic submicron particles. Detailed analyses of CsMPs are helpful for understanding emission events and mechanisms (Igarashi et al., 2019a; Kajino et al., 2021) and deposition processes (Dépée et al., 2019). Vertical measurements obtained on mountains (Hososhima and Kaneyasu, 2014; Sanada et al., 2018) have revealed the importance of cloud deposition over mountainous forests in East Japan. Even though the cloud deposition process is not included in other models, its importance has been inferred from some numerical simulations (Katata et al., 2015; Kajino et al., 2019).

A great number of numerical studies have been conducted for primary emissions, but only one numerical study (Kajino et al., 2016, hereinafter K16) has been performed on the atmospheric dispersion and deposition of radionuclides that have been resuspended from contaminated ground surfaces (secondary emissions). For primary emissions, the emission point is known, and many emission events can be identified, whereas for secondary emissions, the emission mechanisms are

https://doi.org/10.5194/acp-2021-687
Preprint. Discussion started: 20 September 2021


Atmospheric Chemistry and Physics Discussions

unknown, and the ground surfaces (as emission sources) are highly heterogeneous. It is impossible to measure radio-Cs resuspension fluxes from every ground surface, but knowledge has been accumulated from long-term atmospheric measurements recorded at several locations. Ochiai et al. (2016) showed that the surface concentrations of ^{137}Cs were high in summer and low in winter in the contaminated forest area in the Abukuma Highlands. Ochiai et al. (2016) also showed that the temporal variations in fine-mode (< 1.1 μm in diameter) and coarse-mode (> 1.1 μm) ^{137}Cs behaved differently by season, indicating that the major emission sources could be different between winter and summer. Nakagawa et al. (2018) conducted size-resolved *n*-alkane and ^{137}Cs measurements in similar forest areas and concluded that among biogenic emission sources, epicuticular wax is less likely and bioaerosols such as pollen and fungal spores are more likely. Based on long-term measurements taken in the same forest area, Kinase et al. (2018) indicated the association of mineral dust in late spring and bioaerosols in summer and autumn. Kinase et al. (2018) also found that the contribution of the forest fires that occurred in March 2013 to the surface ^{137}Cs concentrations was negligibly small. Kinase et al. (2018) reported that the surface concentration of ^{137}Cs was positively correlated with the surface wind speed in winter but not in summer. Igarashi et al. (2019b) further investigated the possible sources of ^{137}Cs-rich bioaerosols in summer and suggested the substantial involvement of fungal spores. Atmospheric humidity plays a key role in the discharge of fungal spores, which is consistent with the findings of Kita et al. (2020), who stated that the surface concentration of ^{137}Cs in mountainous forests became higher in the presence of precipitation in summer. Cedar pollen particles could contain a considerable amount of ^{137}Cs in the forest areas of Abukuma Highlands, but they are emitted from late February to early May, not during summer (Igarashi et al., 2019b). In fact, number of pollen particles was 1/10 of number of bacteria (including spores) or less in summer (Kinase et al., 2018; Igarashi, 2021).

The numerical simulations conducted by K16 were consistent with the findings described above: the surface concentrations in the mountainous forest area are low in winter and high in summer, the contributions of mineral dust are high in winter, and those of bioaerosols are high in summer. However, Watanabe et al. (2021) found that the simulations of K16 underestimated the observed deposition amounts by approximately two orders of magnitude. The major reason for this large discrepancy in deposition is the incorrect assumption of the physical properties of resuspended ^{137}Cs by K16. K16 constrained the deposition efficiency of ^{137}Cs in their simulations to be consistent with the primary emission period (March 2011), which involved submicron carriers; however, based on the above-described measurements, the major carriers of ^{137}Cs should be much larger. In the current study, the deposition efficiency of ^{137}Cs in the simulation is constrained to be consistent with the measured concentration and deposition amounts in the resuspension period (i.e., 2013). The regional budgets of ^{137}Cs are thoroughly reassessed using more realistic model configurations, and the differences between the old and current estimates are clearly compared in this study.

https://doi.org/10.5194/acp-2021-687
Preprint. Discussion started: 20 September 2021

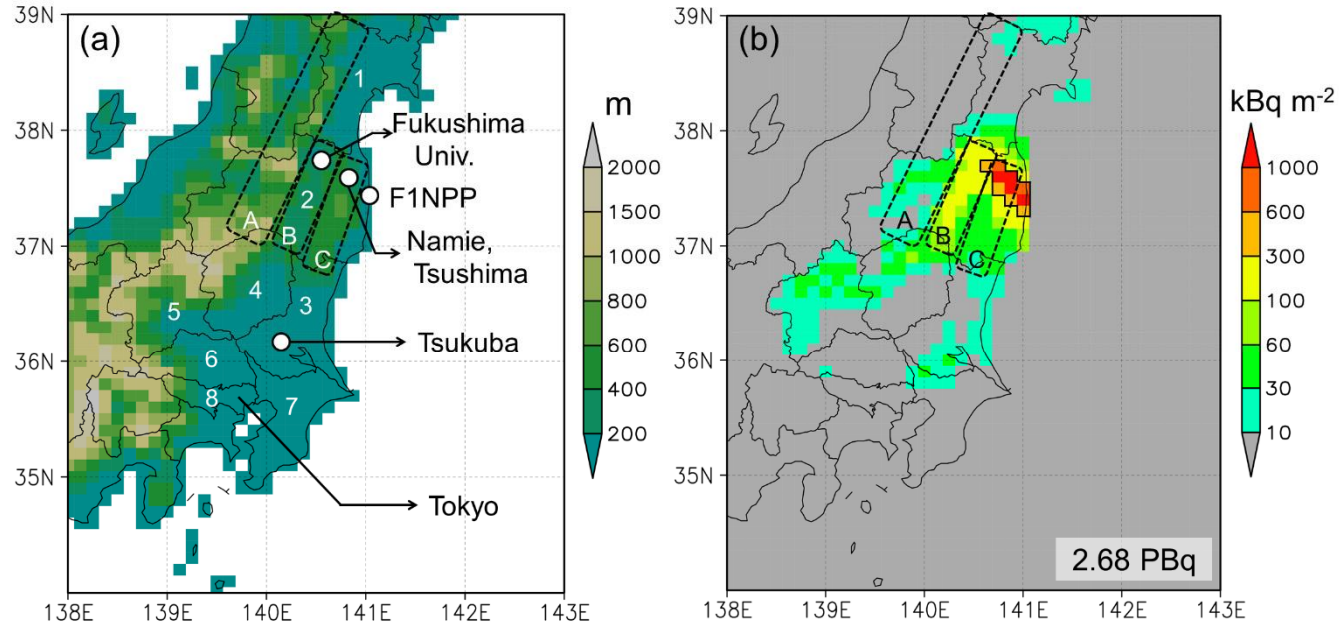

Name of prefectures: 1. Miyagi, 2. Fukushima, 3. Ibaraki, 4. Tochigi, 5. Gunma, 6. Saitama, 7. Chiba, 8. Tokyo
Geographical features: A. Ou Mountains, B. Nakadori Valley, C: Abukuma Highlands

Figure 1: (a) Model domain (Δ longitude = 0.125° and Δ latitude = 0.1°), terrestrial elevations, major locations, and names of prefectures and geographical features. (b) Initial deposition amounts of ^{137}Cs measured by aircraft (NRA, 2012) and used as boundary conditions for the simulation. The decay correction for the observation was made for March-May 2012, depending on the regions. The area surrounded by the black solid line is defined as the resuspension source area (> 300 kBq m^{-2}) in the source-receptor analysis presented in Sect. 3.5. The total areal amount is embedded at the bottom right of the panel.

2 Methods

2.1 Observation data

To constrain the deposition rates and resuspension fluxes used in the simulations, activity measurement data containing surface concentrations and deposition amounts at three observation sites, one in a contaminated forest (Namie, Tsushima), one in an urban/rural area near the contaminated forest (Fukushima), and one in a downwind location (Tsukuba), are used (Fig. 1).

The Namie (Tsuhima) site is approximately 30 km northwest of the F1NPP, is located in the difficult-to-return zone (DRZ; >50 mSv y^{-1}), and is surrounded by forests in the Abukuma Highlands. The center of Namie town is located near the coast of the Pacific Ocean, but the observation site is surrounded by mountainous forests. Thus, to avoid confusion, the site is denoted as Namie (Tsushima) throughout the manuscript. The initial deposition amount indicated by the airborne measurements was 2300 kBq m^{-2} (Fig. 1b), and decontamination work was not conducted in 2013. The locations at which the surface concentration measurements and deposition measurements are taken are different but are very close to each other (the

https://doi.org/10.5194/acp-2021-687
Preprint. Discussion started: 20 September 2021


Atmospheric Chemistry and Physics Discussions

direct distance is approximately 400 m). The concentration measurements are conducted in the schoolyard of a high school (140.768°E, 37.562°N) (Ishizuka et al., 2017; Kinase et al., 2018), and the deposition measurements are made by Fukushima Prefecture at Tsushima Screening Center (140.765°E, 37.561°N) (data available at https://www.pref.fukushima.lg.jp/site/portal/genan225.html, last accessed June 30, 2021). The sampling intervals of the concentration and deposition measurements at this site are 1–2 days and 1 month, respectively.

The Fukushima site is in Fukushima city, located approximately 60 km northwest of the F1NPP. The Fukushima site is located in the Fukushima Basin in the Nakadori Valley, surrounded by the Ou Mountains (the peaks of which are 1000 – 2000 m in elevation) to the west and the Abukuma Highlands (the peaks of which are mostly lower than 1000 m in elevation) to the east (Fig. 1). The concentration and deposition measurements are conducted at Fukushima University (140.45°E, 37.68°N) (Watanabe et al., 2021). Fukushima University is located on a small hill at the southern edge of the Fukushima Basin and is surrounded by major roads. The distances from Route 4 and national highway E4 to the university are shorter than 1 km. The land use type of the site is characterized as urban/rural. The initial deposition amount indicated by the airborne measurement was 190 kBq m^{-2} (Fig. 1b), one order of magnitude smaller than that at the Namie (Tsushima) site. Decontamination was conducted in 2013 in Fukushima city, and almost 90% of decontamination was completed for agricultural fields and public facilities by March 2014 (Watanabe et al., 2021). The achievement ratios of decontamination for other land use types are 50%, 9%, and 5% for residential areas, roads, and forests (only living areas; the removal of shrub and litter layers within 20 meters from the forest edges), respectively (Watanabe et al., 2021). The sampling intervals of the concentration and deposition measurements at this site are 3 days and 1 month, respectively.

The Tsukuba site is located in Tsukuba city, Ibaraki Prefecture, approximately 170 km southwest of the F1NPP. It is located in the eastern part of the Kanto Plain, the most populated area in Japan. The concentrations and deposition amounts are measured at the Meteorological Research Institute (140.13°E, 36.06°N) (Igarashi et al., 2015). The initial deposition amount was 21 kBq m^{-2} (Fig. 1b), one order of magnitude smaller than that at the Fukushima site and two orders of magnitude smaller than that at the Namie (Tsushima) site. Decontamination was not conducted in most of the areas around this site due to the low ambient gamma dose rates. The sampling intervals of the concentration and deposition measurements at this site are 1 week and 1 month, respectively.

The locations, geographical features, and airborne-measured initial deposition amounts of these sites are visualized using Google Earth in the Supplement 1.

2.2 Numerical simulations

The Lagrangian model (LM) developed by K16 was used in this study. Thus far, a cumulus convection parameterization of Emanuel and Zivkovic-Rothman (1999) has been implemented to the model. The model description and simulation setup used in this study are identical to those of K16, except the cumulus convection parameterization, but are briefly repeated in this

https://doi.org/10.5194/acp-2021-687
Preprint. Discussion started: 20 September 2021


Atmospheric Chemistry and Physics Discussions

section. The differences of simulations with and without the cumulus convection are presented later in Fig. 10 in Sect. 3.4. Errors between the original 1-D Eulerian model and the 1-D Lagrangian model developed and implemented to LM in the current study are summarized in Supplement 2. The LM considers the advection, turbulent diffusion, dry deposition, and wet deposition of atmospheric constituents. In the case of radionuclides, radioactive decay is also considered. As shown in Fig. 1a, the model domain covers the eastern part of Japan, from 138–140°E and from 34–39°N, with the same horizontal resolutions (Δx is approximately 11 km; Δ longitude = 0.125° and Δ latitude = 0.1°) as the meteorological analysis data, the Grid Point Value-Mesoscale Model (GPV-MSM) of the Japan Meteorological Agency (JMA). The GPV-MSM provides data on three hourly meteorological variables on the surface and at vertical layers from 1000 hPa to 100 hPa. No meteorological models are applied to simulate finer-scale phenomena or to obtain detailed meteorological variables such as turbulent diffusivities or hydrometeor concentrations. The fundamental variables such as the wind field, temperature, humidity, and geopotential height obtained from the meteorological analysis data are interpolated horizontally and temporally and applied to simulate the locations and masses (or radioactivities) of Lagrangian particles. The simulation period is from December 1, 2012, to January 1, 2013, and the analysis period is the full year of 2013, from January 1, 2013, to January 1, 2014.

2.2.1 Deposition schemes

The key parameters used in this study are introduced below using equations. The LM does not include comprehensive deposition schemes; deposition processes are simply parameterized. The wet scavenging rate Λ_{wet} (s^{-1}) is expressed as a function of the surface precipitation rate P (mm s^{-1}) as follows:

$$\Lambda_{\text{wet}} = \frac{3}{4}\frac{E_c(a_m,r_m)}{a_m}P, \quad (1)$$

where E_c is the collection efficiency of aerosols by the hydrometeor and a_m and r_m are the mean radii of the hydrometeor and aerosols, respectively. Empirically, a_m is characterized by P as $a_m = 0.35\ P^{0.25}$. E_c is a function of a_m and r_m, but, practically, a single constant value is used for each simulation. Eq. 1 is applied for all types of wet deposition. The differences among rain, snow, and graupel precipitation and the differences between in-cloud and below-cloud scavenging are not considered.

The dry scavenging rate Λ_{wet} (s^{-1}) is expressed as follows:

$$\Lambda_{\text{dry}} = \frac{2}{z_{srf}}\left(1-\frac{z}{z_{srf}}\right)v_d, \quad (2)$$

where z is the height of Lagrangian particles, z_{srf} is the surface layer height set as 100 m in this study, and v_d is the dry deposition velocity. v_d depends on aerosol sizes and surface conditions such as wind speed, roughness, and land use types, but a single

https://doi.org/10.5194/acp-2021-687
Preprint. Discussion started: 20 September 2021


Atmospheric Chemistry and Physics Discussions

constant value is applied in this study. We only consider the difference in v_d over the land and the ocean; v_d over the ocean is 0.1 times smaller than that over the land (K16).

Fog or cloud deposition plays a key role in the deposition of ^{137}Cs over the mountains in East Japan (Hososhima and Kaneyasu, 2015; Katata et al., 2015; Sanada et al., 2018; Kajino et al., 2019; Imamura et al., 2020) but is not considered in the study because the GPV-MSM product does not provide fog data (or cloud water in the bottom layers of the model grids).

In K16, we determined an E_c value of 0.04 and a v_d over land (simply referred to as v_d hereinafter) value of 0.1 cm s^{-1}, so the initial deposition amount of ^{137}Cs over land (2.53 PBq) simulated using the emission scenario of Katata et al. (2015) was closest to that observed (2.68 PBq, see Fig. 1b) among the various sensitivity simulations. However, the major carriers of ^{137}Cs during primary emissions (i.e., the direct emissions associated with the nuclear accident) are submicron particles (several 100 nm in diameter, e.g., Kaneyasu et al., 2012); thus, the optimized deposition parameters are the orders of these submicron particles. However, the major carriers of ^{137}Cs resuspended from the ground surface could be supermicron particles such as soil dust and bioaerosols (from 1–several 10 μm in diameter, e.g., Ishizuka et al., 2017; Kinase et al., 2018); thus, the deposition parameters should be much larger. In this study, E_c and v_d are significantly improved from those used in K16, as is extensively described later in Sect. 2.3.

2.2.2 Resuspension schemes

K16 considered three emission sources during the analysis period of 2013: resuspension from bare soil, resuspension from forest ecosystems, and additional emissions from the reactor buildings of the F1NPP. K16 simulated the contributions from these additional emissions as being two to three orders of magnitude smaller than the observed surface activity concentrations, and these contributions were thus neglected in this study. The emission flux of ^{137}Cs carried by dust aerosols from a bare soil surface, F_{dust} (Bq m^{-2} s^{-1}), is formulated by Ishizuka et al. (2017) as follows:

$$F_{\mathrm{dust}} = p_{20\mu\mathrm{m}} F_{\mathrm{M}} (1 - f_{\mathrm{forest}}) B_{5\mathrm{mm}}(t) C_{\mathrm{const}}, \quad (3)$$

where $p_{20\mu\mathrm{m}}$ is the surface area fraction of dust particles smaller than 20 μm in diameter against soil containing a maximum particle size of 2 mm and varies depending on the soil texture (1.3×10^{-8} for sand, 0.19 for loamy sand, 0.45 for sandy loam, and 0.80 for silt loam), F_{M} is the total dust mass flux (kg m^{-1} s^{-1}) as a function of the friction velocity, f_{forest} is the forest areal fraction, and $B_{5\mathrm{mm}}(t)$ is the specific radioactivity of the surface soil (from the surface to a depth of 5 mm; Bq kg^{-1}) as a function of time considering radioactive decay. Changes in the vertical profiles of ^{137}Cs due to land surface processes or decontamination are not considered in the study. The f_{forest} value is obtained from the Weather Research and Forecasting model version 3 database (WRFV3; Skamarock et al., 2018). Eq. 3 was developed based on measurements taken in a schoolyard, so it may not be applicable for every soil surface type. For simplicity, we introduce the constant correction factor C_{const} to adjust

https://doi.org/10.5194/acp-2021-687
Preprint. Discussion started: 20 September 2021


Atmospheric Chemistry and Physics Discussions

the simulated ^{137}Cs in dust aerosols to the observed value. C_{const} was set to five in K16. This adjustment factor differs in this study because a larger adjustment factor is required to sustain the observed surface concentration levels for faster deposition rates, as shown later in Sect. 2.3.

The resuspension flux of ^{137}Cs from forest ecosystems (regarded as forest aerosols), F_{forest} (Bq m^{-2} s^{-1}), is formulated by K16 as follows:

$$F_{\mathrm{forest}} = f_{\mathrm{forest}} f_{\mathrm{green}} r_{\mathrm{const}} B_{\mathrm{obs}} R_{\mathrm{decay}}(t), \quad (4)$$

where f_{green} is the monthly mean green area fraction, r_{const} is the constant resuspension coefficient (s^{-1}), B_{obs} is the observed initial deposition amount (Bq m^{-2}, Fig. 1b), and $R_{decay}(t)$ is the radioactive decay. f_{green} is obtained from the WRFV3 database and was originally derived from Advanced Very High Resolution Radiometer (AVHRR) normalized difference vegetation index (NDVI) data. r_{const} is the adjustment parameter and was set as 10^{-7} h^{-1} in K16 for adjustment to the observed surface concentrations in the forests in summer. Similar to the dust aerosol case, a larger adjustment factor is required due to the faster deposition rates to sustain the simulated surface concentrations close to the observed values, as is shown later in Sect. 2.3. Similar to the dust aerosol case, no ^{137}Cs migration within the local forest ecosystems due to land surface processes is considered in the formulation.

For both the dust and forest aerosol cases, only emissions from the grids in which the mean initial deposition amounts exceed 10 kBq m^{-2}, the detection limit of the airborne measurements, are considered (NRA, 2012). However, excluding regions in which the deposition amount is 9.9 kBq m^{-2}, for example, may not be appropriate. Thus, a sensitivity test is performed to additionally consider areas with deposition amounts of 1–10 kBq m^{-2} as emission sources, as is presented in Sect. 3.4.

Other sources, such as the unexpected releases associated with the debris removal operations at the F1NPP site that occurred in August 2013 (NRA, 2014; Steinhauser et al., 2015; K16), forest fires, and resuspension due to decontamination work, are not considered in the study. The debris removal operations caused a sporadic peak in the surface concentrations (60.4 mBq m^{-3} from 13:00 LT on August 14 to 13:00 LT on August 15 at Namie (Tsushima), Figs. 4a and 4b), but these elevated values may not affect the background (or steady state) concentrations for the full year, which are the target of this study. Forest fires may not be a major source of ^{137}Cs resuspension in Fuskuhima because the temporal variations in levoglucosan concentrations were not found to be associated with those of ^{137}Cs (Kinase et al., 2018). Resuspension due to decontamination work should be considered, but it was hard to estimate because the emission factor and the precise location and time of decontamination are unknown. It should be noted here that, as described in Sect. 2.1, decontamination was not performed around the Namie (Tsushima) or Tsukuba sites, and decontamination might have been performed around the Fukushima site in 2013.

https://doi.org/10.5194/acp-2021-687
Preprint. Discussion started: 20 September 2021

Atmospheric Chemistry and Physics Discussions

2.3 Constrained deposition parameters and emission flux adjustments based on field observation data

2.3.1 Constraint of modeled deposition parameters

Since K16 was published, several emission sources of resuspended ^{137}Cs have been indicated, such as soil dust (Ishizuka et al., 2017; Kinase et al., 2018) and bioaerosols (Kinase et al., 2018; Nakagawa et al., 2018; Igarashi et al., 2019b; Kita et al., 2020; Minami et al., 2020; Igarashi, 2021), but the relative contributions of these sources, the spatiotemporal variations in the associated emission fluxes, and their size distributions are still not well understood. Kita et al. (2020) indicated the associations of rain with fungal spore emissions, and Minami et al. (2020) estimated the emission flux of ^{137}Cs associated with bioaerosols; however, the emission flux has not yet been formulated as a function of meteorological or land surface variables. Therefore, the same formulations as those applied in K16 (Eqs. 3 and 4) are used in this study. It is also noted here that the same deposition rates are applied for both dust and forest aerosols, even though the size distributions of these two aerosol types should be different.

K16 had two major drawbacks: (1) K16 constrained the deposition parameters (i.e., E_c and v_d) by using the primary ^{137}Cs emission and initial ^{137}Cs deposition amounts measured in March 2011, and (2) K16 did not compare their simulation results against the deposition amounts. Recently, Watanabe et al. (2021) evaluated the performance of the K16 model using concentrations and deposition amounts measured at Fukushima sites and found that the seasonal variations in simulated concentrations were opposite to those observed and that the simulated deposition amounts were underestimated by one to two orders of magnitude. The reason for this underestimation of the deposition amounts is obvious; the typical deposition rates of major carrier aerosols (submicron aerosols) are much smaller than the resuspension rates (supermicron aerosols). For example, the dry deposition velocities of aerosols with diameters of approximately 10 μm are two to three orders of magnitude larger than those of aerosols with diameters of approximately 0.1–1 μm (e.g., Petroff and Zhang, 2010). The difference between these two size ranges for below-cloud scavenging due to rain is also two to three orders of magnitude (e.g., Wang et al., 2010). To constrain the deposition parameters suitable for ^{137}Cs resuspension, we performed a climatological deposition velocity analysis similar to that conducted by Watanabe et al. (2021).

Suppose there is a simple nonlinear relationship between the periodic mean deposition flux (D) (Bq m^{-2} s^{-1}, for example) and periodic mean surface concentration (C) (Bq m^{-3}):

$$D = aC^b, \quad (5)$$

where a represents the removal rate and b represents nonlinear features such as spatial and temporal variabilities. If b = 1, the unit of a is m/s, which is on the dimension of the deposition velocity. If long-term averaging is conducted, Eq. 5 may hold. Eq. 5 is reformulated as follows:

https://doi.org/10.5194/acp-2021-687
Preprint. Discussion started: 20 September 2021

Atmospheric Chemistry and Physics Discussions

$$log(D) = b\, log(C) + log(a). \quad (6)$$

A log-log scatter plot between the monthly mean surface concentrations and monthly cumulative depositions is shown in Fig. 2. The purple, orange, and green symbols indicate the observations, simulations by K16 (E_c = 0.04 and v_d = 0.1 cm s^{-1}) and simulations conducted in this study (E_c = 0.4 and v_d = 10 cm s^{-1}). This analysis is novel because emission flux adjustments (C_{const} in Eq. 3 and r_{const} in Eq. 4) do not change the slope of the regressions, so the deposition parameters can be adjusted independently from the emission flux adjustment. The intercept of the y-axis indicates the deposition velocity. Among the several sensitivity tests with the combinations of E_c = 0.04 and 0.4 and v_d = 0.1, 1, and 10 cm s^{-1}, the y-axis intercept of the simulation with E_c = 0.4 and v_d = 10 cm s^{-1} matched best with that of the observations.

The slope of the observed regression line, b, is 0.92, so the relationship between the concentrations and depositions of resuspended ^{137}Cs in East Japan is almost linear, but the relationship itself is not very solid (coefficient of determination (R^2) = 0.018). However, by excluding two exceptional data points, the observations obtained in January at Fukushima (maximum deposition) and August at Namie (Tsushima) (maximum concentration), the R^2 increases to 0.65, and b becomes 0.98 (not shown in the figure). In January at Fukushima, the measured deposition is extremely high compared to the surface concentration. Watanabe et al. (2021) hypothesized the existence of superlarge particles (~100 μm in diameter) whose gravitational deposition velocities are too fast (as fast as drizzle) to enter the high-volume air samplers used for the concentration measurements but are efficiently collected deposition samplers, as the traveling distance is approximately 1 km (e.g., Kajino et al., 2012; Kajino et al., 2021). January is the month with the highest snow cover in Fukushima city and the highest snow removal operations (using snowblowers and deicing agents), and heavy traffic on the major roads within 1 km of the Fukushima site produce substantial amounts of superlarge particles from wet and muddy road surfaces. The August data at Namie (Tsushima) are also exceptional because the surface concentrations are biased due to the sporadic peak associated with the debris removal operation in the F1NPP (K16). Because the aerosols associated with the debris removal operation traveled a sufficiently long distance (i.e., 30 km), the deposition velocity was not significantly large and did not affect the monthly mean deposition, although it did affect the monthly mean concentration. Therefore, the data obtained in August at Namie (Tsushima) are exceptional when compared to the trends shown by other datasets. The slopes of the simulated regression lines are b =1.17 for K16 (orange line) and b =1.16 for this study (green line). R^2 values of 0.71 and 0.97 were obtained by K16 and this study, respectively. The difference in the magnitude of R^2 can be explained by the differences in the deposition rates. Because the deposition rates obtained in this study are much faster than those applied by K16, the deposition amounts are more strongly associated with the concentrations in this study. In other words, this climatological deposition velocity analysis was successful (by excluding the two exceptional datapoints) because the sizes of the major carrier aerosols of resuspended ^{137}Cs in reality are sufficiently large (the observed deposition amounts are sufficiently associated with the observed concentrations). The regression slopes of the simulations (b ~ 1.2) are somewhat different from those observed (b ~ 0.9 or 1.0). Nevertheless, the regression line of this study crosses that of the observations at the middle points of the

https://doi.org/10.5194/acp-2021-687
Preprint. Discussion started: 20 September 2021

Atmospheric Chemistry and Physics Discussions

concentration and deposition ranges (approximately 0.1 mBq m^{-3} and 50 Bq m^{-2}, respectively). This indicates that the constrained deposition rates may be consistent with the average features of the environmental behaviors of resuspended ^{137}Cs in East Japan.

This analysis is conventional but has been found to be quite successful in constraining the deposition rates of resuspended ^{137}Cs in East Japan.

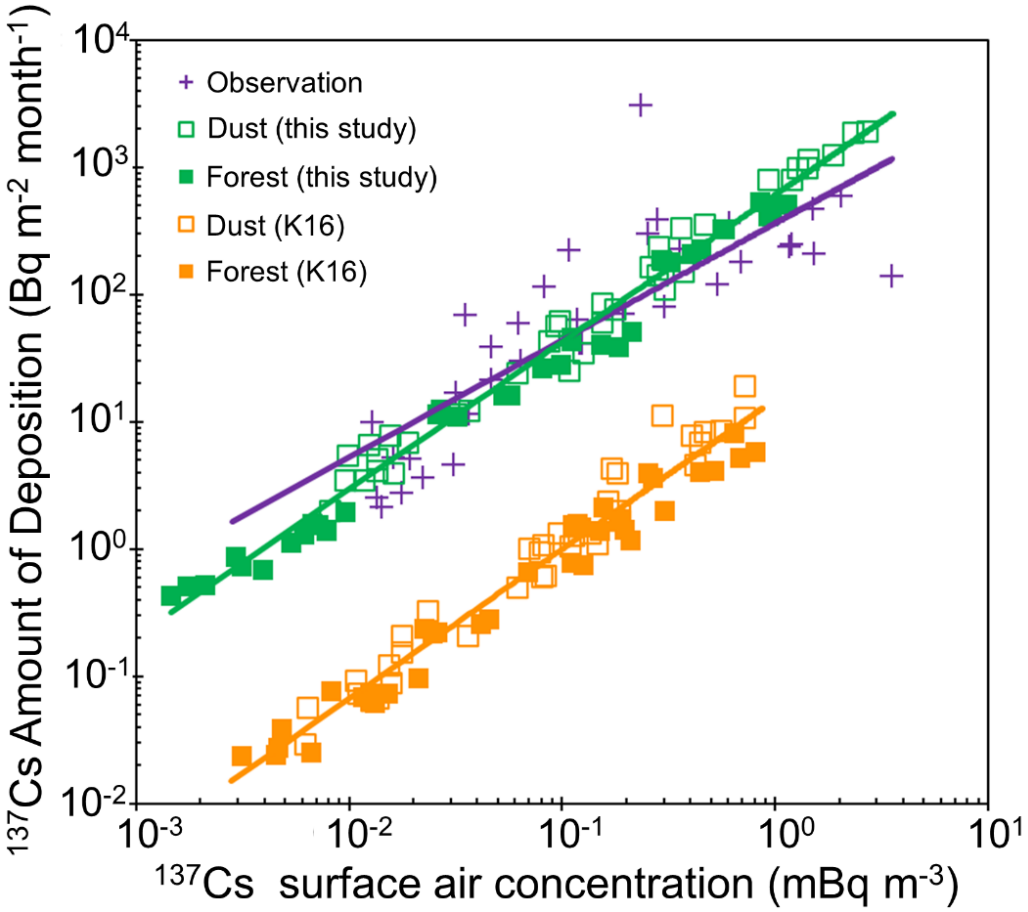

Figure 2: Scatter diagram of the depositions of ^{137}Cs over the monthly mean (purple crosses) observed surface concentrations at Namie (Tsushima), Fukushima, and Tsukuba in 2013 and those simulated by Kajino et al., 2016 (K16) (E_c and v_d are 0.04 and 0.1 cm s^{-1}, respectively) considering different emission sources: the open orange squares represent mineral dust particles from bare soil (dust aerosols), and the closed orange squares denote bioaerosols emitted from forest ecosystems (forest aerosols). The green open and closed squares are the same as the orange squares but are simulated by this study (E_c and v_d are 0.4 and 10 cm s^{-1}, respectively). The purple, orange, and green lines indicate the regression lines of the purple crosses, orange squares (open plus closed), and green squares (open plus closed), respectively.

https://doi.org/10.5194/acp-2021-687
Preprint. Discussion started: 20 September 2021


Atmospheric Chemistry and Physics Discussions

320 *2.3.2 Adjustment of emission fluxes*

In K16, the emission fluxes of ^{137}Cs associated with dust and forest aerosols were adjusted to match the surface concentrations at Namie (Tsushima). In K16, first, C_{const} in Eq. 3 was set to five so that the simulated dust ^{137}Cs concentrations matched the observations in winter, when the temporal variation in the observed ^{137}Cs concentration at Namie (Tsuhima) correlated well with that of the wind speed (Kinase et al., 2018) and when the vegetation activity was supposed to be low. The 325 adjusted dust ^{137}Cs concentrations could not reproduce the enhanced concentrations measured at Namie (Tsushima) in summer (Fig. 4a). Thus, r_{const} in Eq. 4 was set to 10^{-7} h^{-1} so that the simulated forest ^{137}Cs concentrations matched the observations in summer. The temporal variation of ^{137}Cs was not correlated with that of the wind speed in summer (Kinase et al., 2018).

Because the deposition rates are significantly increased in this study, we require much larger emission fluxes to sustain the simulated surface concentrations at the observed levels. The same adjustment procedure as that used in K16 could be 330 applied to the simulations in this study; however, for example, adjusting the values at Namie causes the values to be underestimated at Tsukuba, so it is hard to find a combination of C_{const} and r_{const} that is best for all aspects (i.e., concentrations and depositions of the three sites). Thus, for simplicity, we multiplied both fluxes used in K16 by 20 so that C_{const} was 100 and r_{const} was 2×10^{-6} h^{-1}. The discrepancies between the simulated and observed concentrations and depositions at the three sites are summarized later in Sect. 3.1.

335 **3 Results and discussion**

3.1 Seasonality and quantity of surface air concentrations and depositions

Figure 3 shows the observed and simulated (dust and forest) activity deposition amounts of ^{137}Cs at Namie (Tsushima), Fukushima, and Tsukuba for the submicron (K16) and supermicron (this study) cases. Statistical measures such as the correlation coefficient (*R*), simulation-to-observation median ratio (*Sim/Obs*), numerical fraction of data within a factor of two 340 (*FA2*), and numerical fraction of data within a factor of five (*FA5*) are embedded in the panels. Note that the simulated temporal variation lines show the dust and forest amounts separately, but the statistical measures are derived using the summation of the two aerosol sources. As discussed in the previous sections and presented in Fig. 2, the underestimation of simulations assuming submicron particles is remarkable, with simulated values approximately two orders of magnitude lower than the observations at all sites. On the other hand, the simulations assuming supermicron particles are significantly improved. Positive 345 correlations are found at Namie (Tsushima) and Tsukuba ($R \sim 0.6$–0.7), and the same order of median ratios are found at Fukushima and Tsukuba (*Sim/Obs* = 1.2–1.3, *FA5* = 0.9–1.0). In terms of the seasonal variations, the monthly trend (high in winter and spring and low in summer) at Tsukuba is explained well by the simulated dust aerosols. Due to the land use types around the site (over the plain), the ^{137}Cs of dust aerosols is larger than that of forest aerosols throughout the year. In summer, the contributions of forest aerosols are larger than those of dust aerosols at Namie (Tsushima) and Fukushima, which are

https://doi.org/10.5194/acp-2021-687
Preprint. Discussion started: 20 September 2021


Atmospheric Chemistry and Physics Discussions

surrounded by mountainous forest and close to the forest area, respectively. Despite the overestimation at Namie (Tsushima) (*Sim/Obs* = 4.8), the monthly trend is reproduced well by the model: both the observations and simulations show double peaks in winter and summer. Most likely, the same emission factors of mineral dust should not be applied to the whole area. Nevertheless, we regard this application as acceptable in the current study, as this study aims to grasp a rough outline of the atmospheric behaviors of resuspended ^{137}Cs. The monthly variations output by the simulations do not match those of the observations at Fukushima due to the exceptionally high deposition amounts observed in January. This is possibly due to the existence of superlarge particles, as described in Sect. 2.3.1. The snow coverage in Fukushima city is highest in January, but there are certain areas of snow coverage in December and February as well. However, the *R* value of deposition at Fukushima is not greatly improved if the winter datasets are excluded.

The initial ^{137}Cs depositions at the three sites are 2300, 190, and 21 kBq m^{-2}, and the differences are approximately on one order of magnitude. The orders of the monthly depositions in 2013 at the three sites are 0.1% of the initial deposition, at 10^2-10^3, approximately 10^2, and approximately 10^1 Bq m^{-2}, which are similar to the order differences obtained for the initial depositions. A value of 0.1% per month is 1% per year. K16 reported an annual resuspension ratio of 0.048% y^{-1}, but this simple order estimation readily shows that this value is excessively underestimated. As shown later in Fig. 8, the improved annual resuspension ratio is 0.96%, which is consistent with the deposition measurements at the three sites. From this estimation, one can assume that the observed deposition amounts at Fukushima in January (3100 Bq m^{-2}) are exceptionally high.

https://doi.org/10.5194/acp-2021-687
Preprint. Discussion started: 20 September 2021

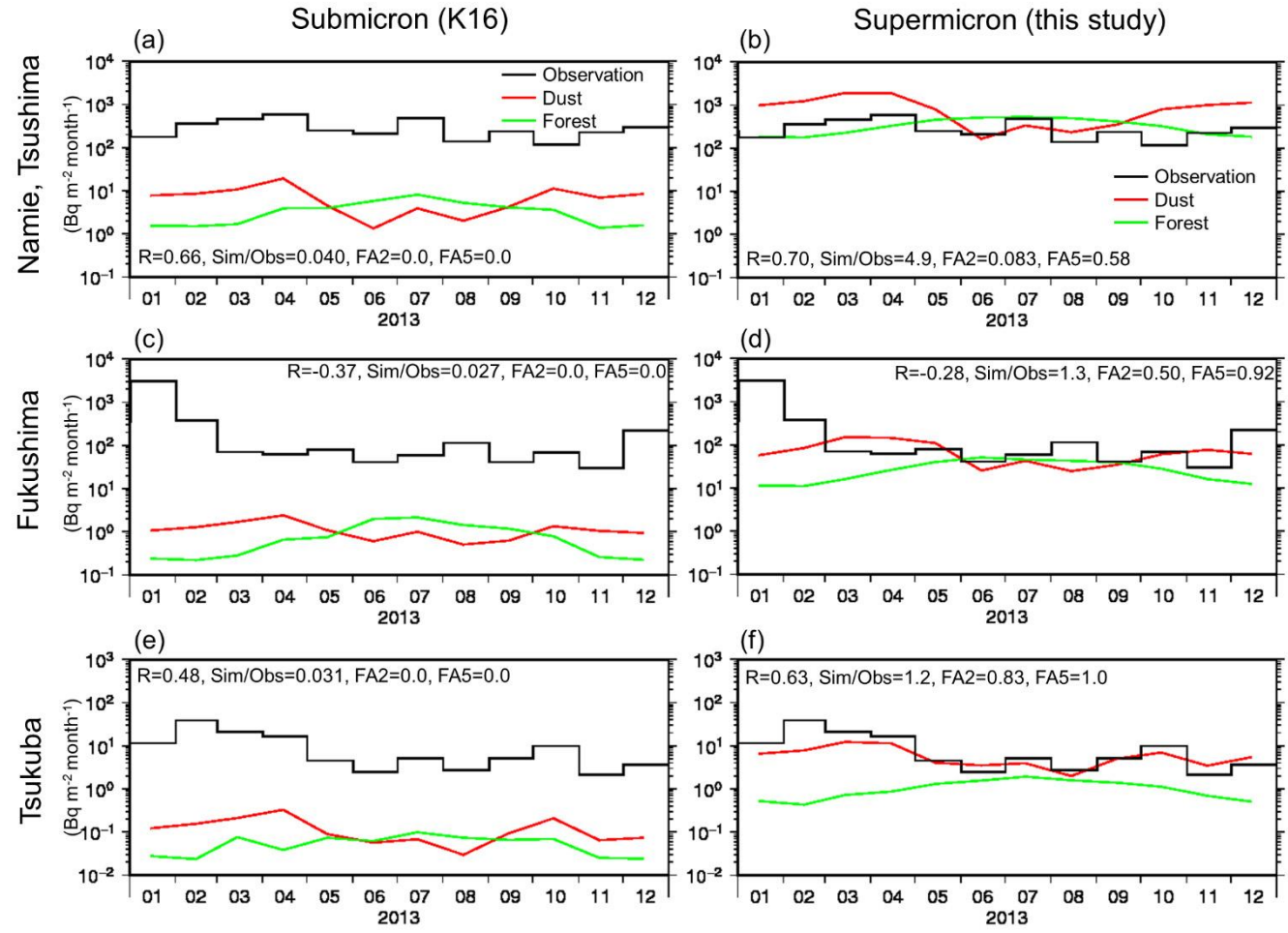

Figure 3: Monthly deposition amounts of (black) observed ^{137}Cs and simulated ^{137}Cs associated with (red) dust aerosols and (lime) forest aerosols at Namie (Tsushima), Fukushima, and Tsukuba (Bq m^{-2}). The simulation results assuming submicron particles (K16; E_c and v_d are 0.04 and 0.1 cm/s, respectively) and those assuming supermicron particles (this study; E_c and v_d are 0.4 and 10 cm/s, respectively) are shown on the left and right, respectively. The statistical measures, such as the correlation coefficient (*R*), simulation-to-observation median ratio (*Sim/Obs*), numerical fraction of data within a factor of two (*FA2*), and numerical fraction of data within a factor of five (*FA5*), between the observations and the simulations (dust plus forest) for each simulation result are embedded in each panel.

https://doi.org/10.5194/acp-2021-687
Preprint. Discussion started: 20 September 2021

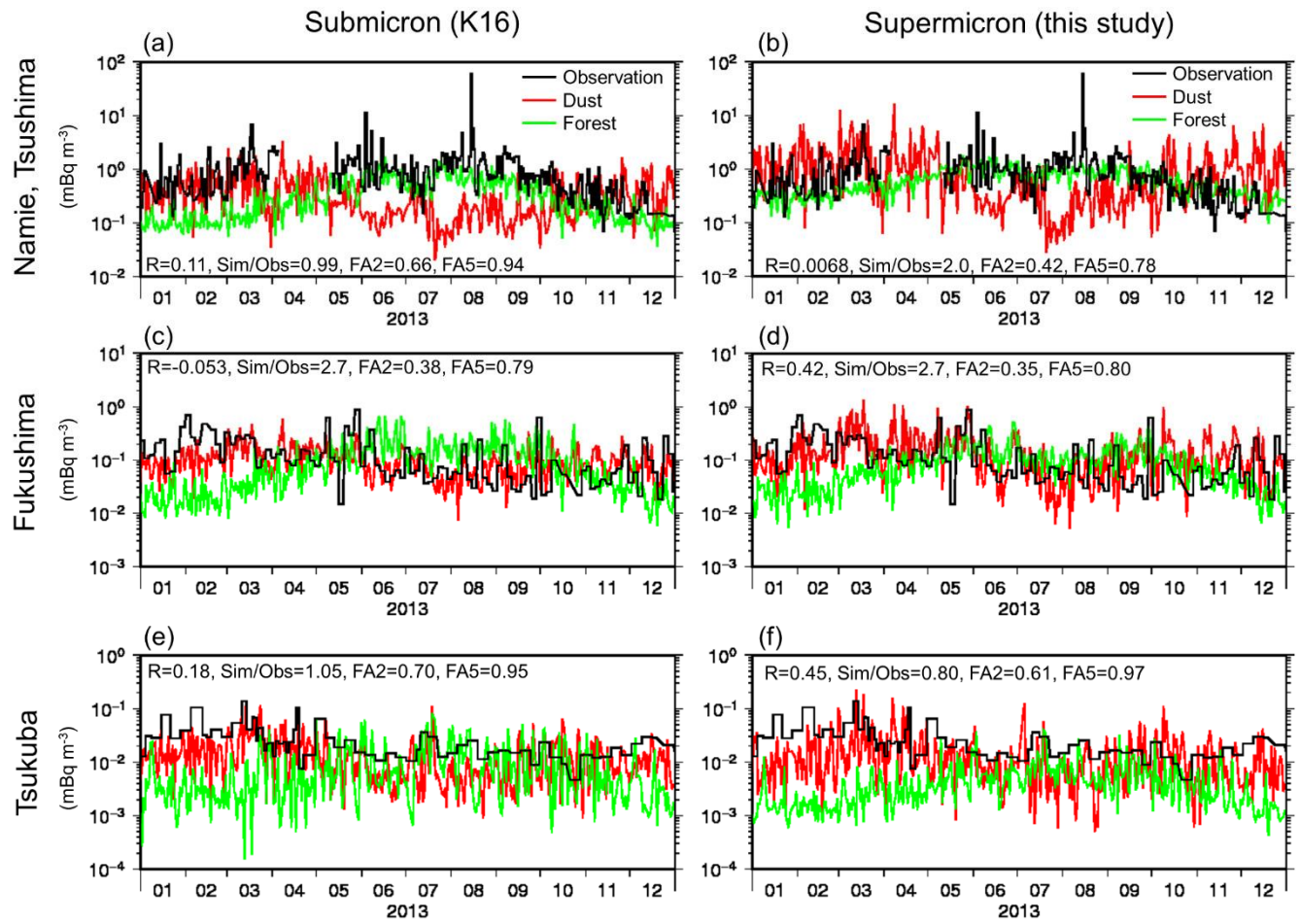

Figure 4: Same as Fig. 3 but for the surface activity concentrations of ^{137}Cs (mBq m^{-3}). The sampling intervals are used for the observations, but daily mean values are depicted for the simulations.

380

Figure 4 shows the observed and simulated (dust and forest) surface air activity concentrations of ^{137}Cs at the three sites for the submicron (K16) and supermicron (this study) cases. The statistical measures *R*, *Sim/Obs*, *FA2*, and *FA5* between the observations and simulations (dust plus forest) are also embedded in the panels. The lines are depicted using different temporal resolutions (sampling intervals for the observations and daily for the simulations), but the temporal resolutions are
385 unified to the sampling intervals to obtain the statistical measures. The measurements of the three sites are not directly comparable because their temporal resolutions are different (1 d for Namie (Tsushima), 2–3 d for Fukushima and 1 w for Tsukuba), but those of the two aerosol cases (submicron and supermicron) are comparable. Although *R* is low for the submicron

https://doi.org/10.5194/acp-2021-687
Preprint. Discussion started: 20 September 2021


Atmospheric Chemistry and Physics Discussions

case at Namie (Tsushima), good consistency *Sim/Obs* (0.99) and *FA5* (0.94) values are obtained because the emission factors C_{const} and r_{const} are adjusted to this case. However, the unrealistic assumption of aerosol sizes results in the opposite simulated seasonal trend at Fukushima: the simulations are high in summer due to forest aerosols. The Fukushima site is located downwind of the contaminated forest in the Abukuma Highlands in summer (Fig. S1), so the transport of ^{137}Cs from the forest area is dominant. However, as the particle sizes are larger and the traveling distances are shorter, the summer enhancement due to forest aerosols is less dominant (Fig. 4d). The observed surface concentrations are high at Fukushima in winter, and the observed short-term peaks correspond to the simulated dust aerosols, indicating that the emission of resuspended ^{137}Cs at Fukushima in winter is driven by wind. The *Sim/Obs*, *FA2*, and *FA5* values of submicrons and supermicrons at Fukushima are similar, but *R* is substantially improved. At Tsukuba, like the Fukushima site, the contribution of forest aerosols is less in the supermicron case than in the submicron case due to less transport from the forest area. The contribution of dust particles is dominant in winter, but the simulated dust aerosols are underestimated compared to the observations in winter. Nevertheless, *Sim/Obs* is not very low (0.80), and the *R* value obtained for supermicrons is improved from the submicron case (from 0.18 to 0.45).

The orders of the surface concentrations at the three sites are 10^{0}, 10^{-1}, and 10^{-2}-10^{-1} mBq m^{-3}. These order differences are similar to those of the initial depositions. One can assume that the resuspension and redeposition of ^{137}Cs occurs within a limited areal scale (e.g., several tens of km) and that long-range transport (i.e., hundreds to a thousand km) from the emission source is not very dominant.

In the following subsections (Sects. 3.2 and 3.3), the source-receptor relationship and annual resuspension ratios are discussed, but it should be noted that the numbers presented in these sections are associated with the discrepancies in the simulations described in the current section. Nevertheless, we can safely conclude here that the supermicron simulations are more (or maybe much more) consistent with the observations than the submicron simulations are.

https://doi.org/10.5194/acp-2021-687
Preprint. Discussion started: 20 September 2021

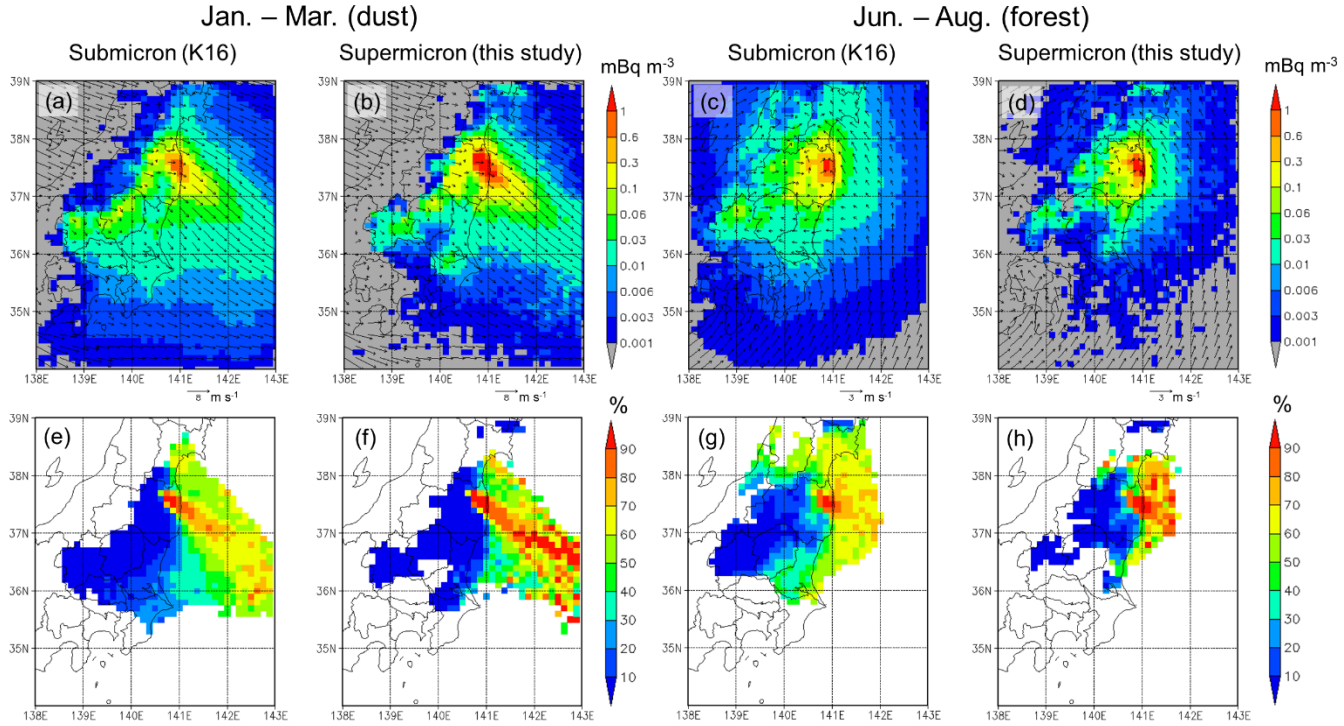

Figure 5: (top panels) Seasonal mean surface concentrations of (a,c) submicron (K16; E_c and v_d are 0.04 and 0.1 cm s^{-1}, respectively) and (b,d) supermicron (this study; E_c and v_d are 0.4 and 10 cm s^{-1}, respectively) ^{137}Cs associated with (a,b) dust aerosols in winter to early spring (January, February, and March) and (c,d) forest aerosols in summer (June, July, and August) (mBq m^{-3}). The seasonal mean surface wind vectors are also depicted in the panels. (bottom panels) Same as top panels but for the fractional contributions from the resuspension source area (defined as the initial depositions of ^{137}Cs exceeding 300 kBq m^{-2}, see Fig. 1b) to the surface concentrations (%).

3.2 Source-receptor relationship and its seasonality

Figure 5 shows the simulated seasonal mean concentrations and the horizontal distributions of the source-receptor relationship. The resuspension source area is defined as grids in which the grid-mean initial deposition exceeds 300 kBq m^{-2} (Fig. 1b). Thus, Namie (Tsushima) (2300 kBq m^{-2}) is located within the source area, but Fukushima (190 kBq m^{-2}) and Tsukuba (21 kBq m^{-2}) are outside the source area (or are regarded as being in downwind area). The source-receptor relationship maps (or source contribution maps) (Figs. 5e–5h) are derived using the seasonal mean concentrations from 300-kBq m^{-2} areas divided by those from whole areas (i.e., > 10 kBq m^{-2}). Because of the shorter atmospheric lifetime of supermicron ^{137}Cs-bearing particles, the concentration maps of the supermicron cases are patchy due to insufficient amounts of Lagrangian particles (Figs. 5b and 5d) compared to the submicron cases (Figs. 5a and 5c), especially in areas where the seasonal mean surface concentrations are below 0.01 mBq m^{-3}. There are substantial numerical errors in these areas, so the source contribution shades (Figs. 5e–5h)

https://doi.org/10.5194/acp-2021-687
Preprint. Discussion started: 20 September 2021


Atmospheric Chemistry and Physics Discussions

depict only areas in which the seasonal mean concentrations exceed 0.01 mBq m^{-3} (Figs. 5a–5d). We select two three-monthly means, covering January, February, and March for winter to early spring (or simply winter hereinafter) when the simulated dust aerosols are dominant and June, July, and August for summer when the simulated forest aerosols are dominant.

In winter, northwesterly monsoon winds prevail over Fukushima Prefecture (Figs. 5a and 5b). In particular, fall and gap winds from the Ou Mountains caused strong winds in the Nakadori Valley, which in turn cause high dust aerosol surface concentrations in these areas in winter. Even though the surface concentrations of supermicron particles over Fukushima Prefecture are larger than those of submicron particles (Fig. 5b), the supermicron concentrations over the downwind regions are smaller (e.g., concentrations > 0.01 mBq m^{-3} over Saitama (#6 in Fig. 1) for the submicron case but of < 0.01 mBg m^{-3} for the supermicron case) due to the shorter lifetime of supermicron particles. This feature is also significant for the source contribution maps (Figs. 5e and 5f). Due to the northwesterlies, most of the resuspended ^{137}Cs is transported toward the southeast over the ocean, the values are 40–90%, and the source contributions of the downwind regions over the land are lower than 10%, except the coastal regions in Ibaraki (#3 in Fig. 1) and Chiba (#7 in Fig. 1) Prefectures for the submicron case (20–30%) due to the longer lifetimes of these particles in air (Fig. 5e).

In summer, southerly winds prevail over East Japan due to the marginal flows of the Pacific High. The wind speeds are generally lower in summer than in winter (please see that the lengths of the arrows are different in Figs. 5a–5b and 5c–5d). The seasonal mean wind patterns are complex over land (Figs. 5c–5d), but the seasonal mean source contribution maps reflect the seasonal mean transport patterns from the source areas (Figs. 5g–5h). Even though the seasonal mean wind fields over the ocean close to land are directed toward the land, substantial proportions of ^{137}Cs in forest aerosols are transported toward the ocean in summer (the source contributions are > 60% for submicron and >70% for supermicron cases). Then, the ^{137}Cs transported toward the ocean are transported toward the land again to Ibaraki and Miyagi (#1 in Fig. 1) prefectures. The source contributions over Ibaraki and Miyagi are substantial for the submicron case (30–70%). For the supermicron case, the source contributions over Ibaraki and Miyagi exceeded 30% at a limited number of grids, but the mean concentrations were much lower (Fig. 5d) than those in the submicron case (Fig. 5c) over the prefectures. Due to the lower wind speeds in summer and the short lifetime of the supermicron particles, the horizontal spread of the mean concentrations (e.g., areas > 0.01 mBq m^{-3}) of supermicron forest aerosols in summer (Fig. 5d) is obviously smaller than that of any other case (Fig. 5a–5c).

https://doi.org/10.5194/acp-2021-687
Preprint. Discussion started: 20 September 2021

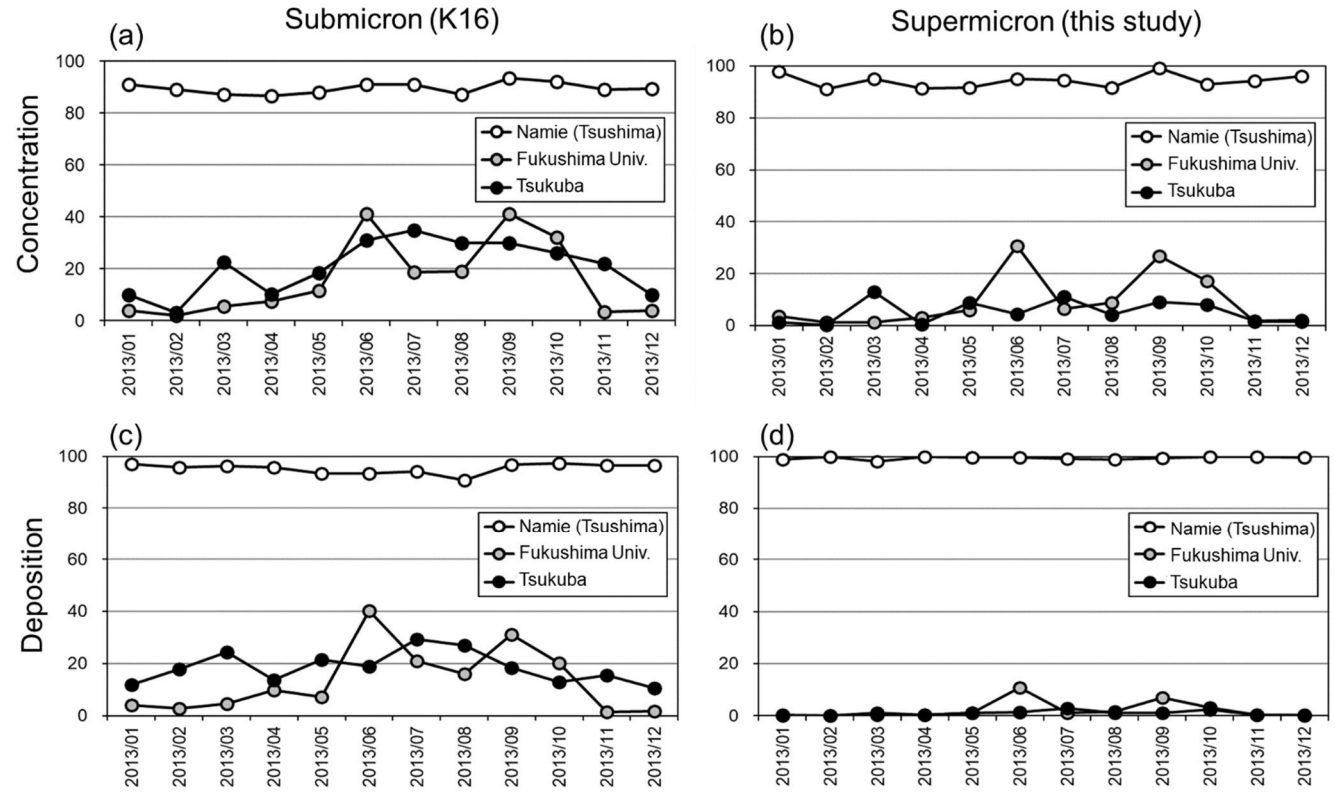

455 **Figure 6:** Monthly mean fractional contributions from the resuspension source area (defined as initial depositions of ^{137}Cs exceeding 300 kBq m^{-2}) to the (a,b) surface concentrations and (c,d) deposition amounts assuming (a,c) submicron (K16; E_c and v_d are 0.04 and 0.1 cm s^{-1}, respectively) and (b,d) supermicron (this study; E_c and v_d are 0.4 and 10 cm s^{-1}, respectively) sizes of ^{137}Cs-bearing particles at Namie (Tsushima), Fukushima, and Tsukuba.

460 Figure 6 shows the simulated monthly mean source contributions for the concentrations and depositions at the three sites and compares these contributions between the submicron and supermicron cases. At Namie (Tsushima), more than 90% of the surface concentrations originate from the source area. The annual mean values are 90% for the submicron case (Fig. 6a) and 94% for the supermicron case (Fig. 6b). It is natural that the source contributions are larger in the source area (Namie (Tsushima)) for the supermicron case, as the lifetime of these particles is shorter than that of submicron particles. As previously 465 discussed, the submicron source contributions at Fukushima are larger in summer and autumn (approximately 40% in June, September, and October and 20% in July and August) (Fig. 6a). The source contributions of supermicrons in summer and autumn are approximately 50% smaller than those of submicrons in July and August (10%) and are slightly smaller in June, September, and October (20–30%) (Fig. 6b). The annual mean concentration values at Fukushima are 16% for submicrons (Fig. 6a) and 9% for supermicrons (Fig. 6b). As observed in Figs. 4e–4f and Figs. 5e–5h, the source contributions of 470 submicrons and supermicrons at Tsukuba are remarkably different. The source contributions of submicrons are larger in

https://doi.org/10.5194/acp-2021-687
Preprint. Discussion started: 20 September 2021


Atmospheric Chemistry and Physics Discussions

summer and autumn at approximately 30%, with an annual mean value of 21% (Fig. 6a). On the other hand, those of supermicrons are smaller than 20% for all months, and the annual mean value is 5% (Fig. 6b).

In terms of deposition, the source contributions of submicrons (Fig. 6c) are similar to those for the concentrations (Fig. 6a), but the source contributions of supermicrons (Fig. 6d) are remarkably different. As presented later in Fig. 7, approximately 40% of supermicron emissions were deposited in the same grid. Thus, the local deposition contributions become much larger than the concentration contributions. Consequently, as shown in Fig. 6c, the annual mean source contributions are 95%, 13%, and 19% for Namie (Tsushima), Fukushima, and Tsukuba, respectively, which are equivalent to those of the concentrations (90%, 16%, and 21% in Fig. 6a), whereas in Fig. 6d, the annual mean source contributions of supermicron depositions are shown to be 99.5%, 2.2%, and 1.0% for Namie (Tsushima), Fukushima, and Tsukuba, respectively.

3.3 Annual total resuspension amounts

Figure 7 presents the simulated annual resuspension and redeposition amounts for the submicron and supermicron cases. The areal summation values are embedded in the panels. Figure 8 shows the annual resuspension ratio, which is the annual total resuspension amount divided by the initial deposition (Fig. 1b), and the annual redistribution amount, which is the deviation between the annual total redeposition amount and the resuspension amount. Negative redistribution values indicate a decrease in deposition due to resuspension, and positive values indicate an increase in deposition due to resuspension. The annual total amounts embedded in Figs. 8b and 8d (-1.06 TBq and -15.1 TBq) indicate the amount of ^{137}Cs transported outside the model domain.

As previously discussed, due to the faster deposition rates and thus larger emission fluxes necessary to sustain the surface concentrations at the observed levels, the annual resuspension and redeposition amounts are both larger for the supermicron case than for the submicron case (Figs. 7c–7d). In K16, the total areal resuspension amount was 1.28 TBq (Fig. 7a), equivalent to only 0.048% of the initial deposition (2.68 PBq), and the redeposition amount was approximately 20% of the resuspension amount. On the other hand, based on the new estimations, the annual resuspension amount (25.7 TBq) is approximately 20 times the previous estimate, and the redeposition amount is even larger (10.6 TBq), at 50 times the previous estimate (0.22 TBq).

The areal mean annual resuspension ratio obtained by K16 (Fig. 8a) was 0.048%, with high values above 0.1% in Nakadori Valley and the mountainous areas of Tochigi (#4 in Fig. 1) and Gunma (#5 in Fig. 1) Prefectures. The new estimate of the annual mean areal resuspension ratio is 0.96%, with high-value areas showing values of 1–3% (Fig. 8c). Iwagami et al. (2017) evaluated that the annual discharge rate from the local environment through rivers was 0.02–0.3% y^{-1}. The new estimate of the resuspension rate through air (0.96% y^{-1}) is much larger than the discharge rate through rivers but is still not very large (i.e., only 1% per year of surface contamination). We can conclude here that the ground surface ^{137}Cs stays or circulates within the local terrestrial ecosystems and is hardly discharged through the air or rivers.

https://doi.org/10.5194/acp-2021-687
Preprint. Discussion started: 20 September 2021


Atmospheric Chemistry and Physics Discussions

However, when these values are compared with the actual decreasing trends in the ambient gamma dose rate in Fukushima Prefecture, we can reach a different conclusion. The first-order decrease rate of the dose rate in Fukushima Prefecture ranged from 1.0 to 7.9×10^{-4} d^{-1} in 2013 after the radioactive decay of ^{137}Cs plus ^{134}Cs ($3.0–4.2\times10^{-4}$ d^{-1} in 2013) (K16) was subtracted. The previous and current resuspension rate estimates, 0.048% y^{-1} and 0.96% y^{-1}, are equivalent to 1.3×10^{-6} d^{-1} and 2.6×10^{-5} d^{-1}, respectively. K16 concluded that the impact of resuspension to the atmosphere was negligibly (two to three orders of magnitude) small in the gross decreasing rate of ground surface contamination, such as by land surface processes or decontamination. However, the difference between the current estimate (2.6×10^{-5} d^{-1}) and the decreasing trend without radioactive decay ($1.0–7.9\times10^{-4}$ d^{-1}) is only one to two orders of magnitude. The annual resuspension ratio in 2013 was only 0.96% of the initial deposition amount, but the amount of ^{137}Cs discharged due to resuspension through the air could contribute approximately 1–10% of the gross decreasing rate, which may not be negligibly small.

For the submicron case (Fig. 8b), the positive redistribution area (area enhanced deposition due to resuspension) is limited, and the amounts are up to 10 Bq m^{-2} per year. On the other hand, for the supermicron case (Fig. 8a), even though the transport distance is shorter than that for submicrons, the positive redistribution area for 1–10 Bq m^{-2} is much larger, and the maximum values are up to 100 Bq m^{-2} for the downwind regions close to the emission sources, especially over the ocean close to the land of Fukushima Prefecture. Nevertheless, these values are much smaller than those obtained for the initial deposition amounts (the lowest limit value is 10 kBq m^{-2}, which is two to three orders of magnitude larger than the annual enhanced deposition amounts of 10–100 Bq m^{-2}).

https://doi.org/10.5194/acp-2021-687
Preprint. Discussion started: 20 September 2021

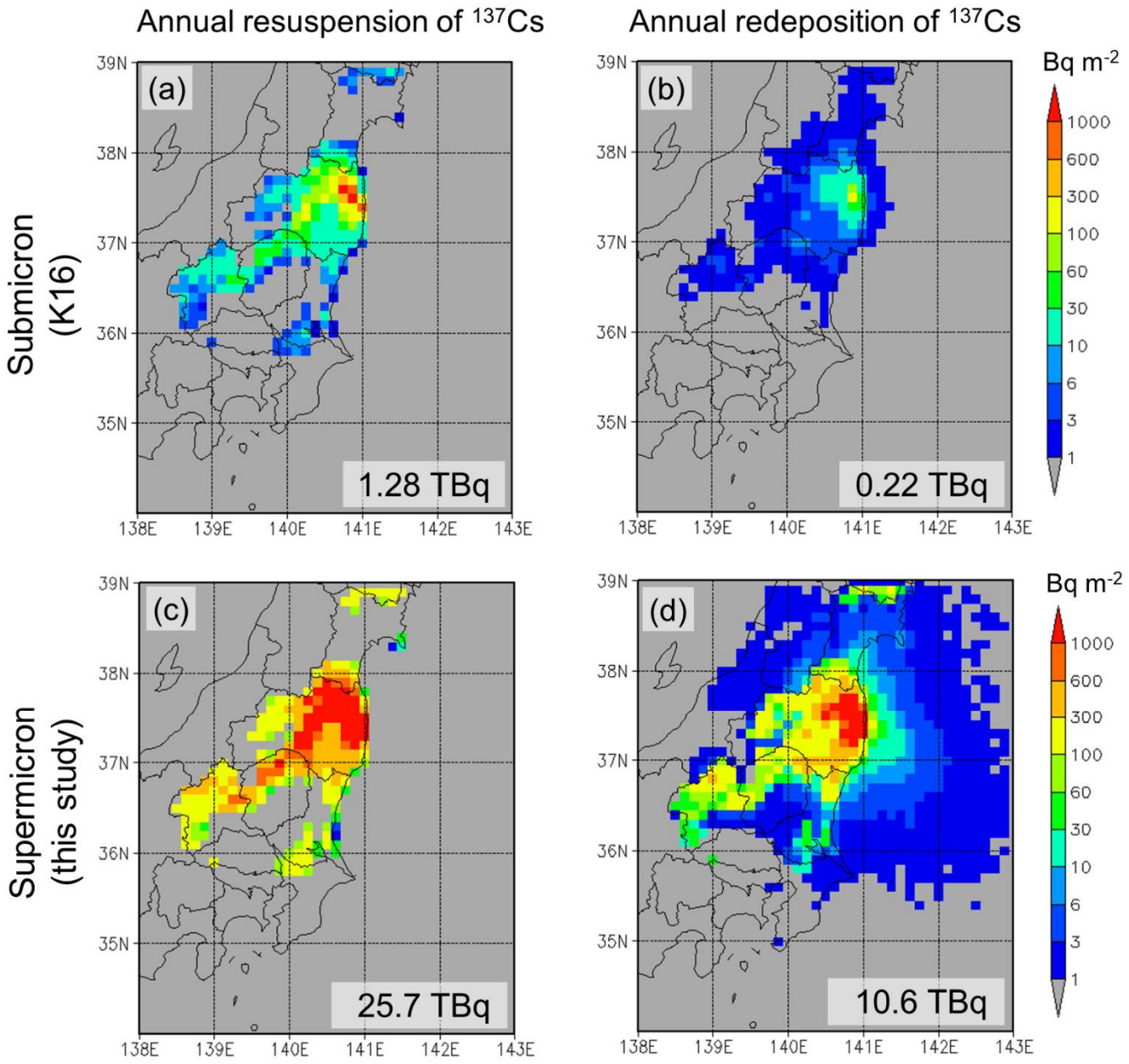

Figure 7: Horizontal distributions of (a,c) the annual total amounts of resuspended ^{137}Cs (Bq m^{-2}) and (b,d) redeposited amounts of resuspended ^{137}Cs (Bq m^{-2}) obtained from the simulations assuming (a,b) submicron (K16; E_c and v_d are 0.04 and 0.1 cm s^{-1}, respectively) and (c,d) supermicron (this study; E_c and v_d are 0.4 and 10 cm s^{-1}, respectively) sizes of ^{137}Cs-bearing particles. The areal total amounts are embedded at the bottom right of each panel.

https://doi.org/10.5194/acp-2021-687
Preprint. Discussion started: 20 September 2021

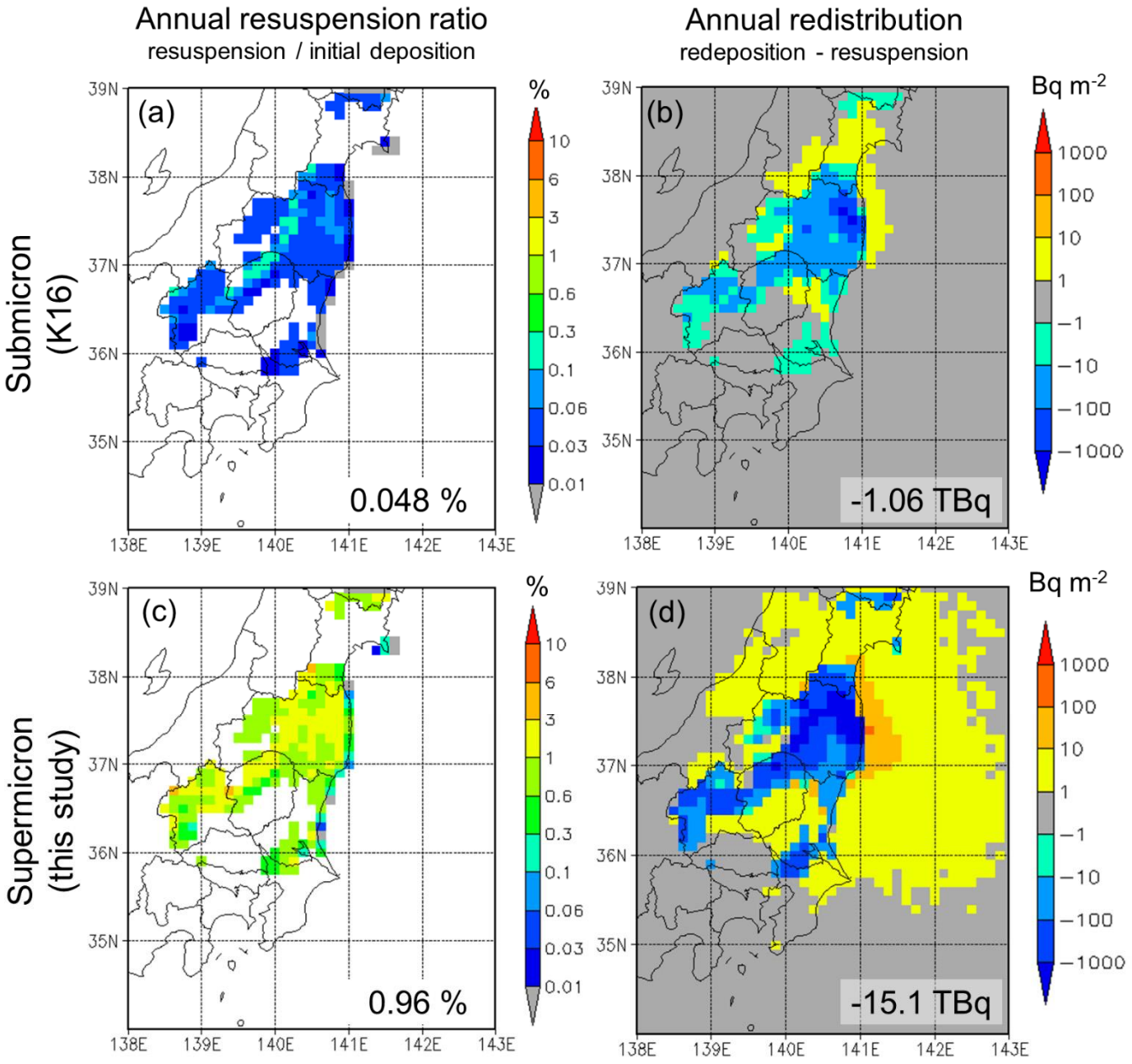

Figure 8: Horizontal distributions of (a,c) the annual total resuspension ratio (ratio of resuspension amounts to initial deposition amounts) of ^{137}Cs (%) and (b,d) the annual redistribution (redeposited minus resuspended amounts) of ^{137}Cs (Bq m^{-2}) obtained from simulations assuming (a,b) submicron (K16; E_c and v_d are 0.04 and 0.1 cm s^{-1}, respectively) and (c,d) supermicron (this study; E_c and v_d are 0.4 and 10 cm s^{-1}, respectively) sizes of ^{137}Cs-bearing particles. The areal total amounts ratios (a,c) and the areal total amounts (b,d) are embedded at the bottom right of the panels.

https://doi.org/10.5194/acp-2021-687
Preprint. Discussion started: 20 September 2021


Atmospheric Chemistry and Physics Discussions

3.4 Sensitivities

Several sensitivity tests are performed, as shown in the current section. Since the cumulus convection parameterization scheme is installed, a comparison is made between the simulations performed with (in the current study) and without (in K16) this scheme. The current study assumes that resuspension occurred from the grids in which the grid-mean initial deposition amount exceeded 10 kBq m^{-2}, the reliable limit of the aircraft measurement. On the other hand, it is inappropriate to exclude grids in which, for example, the deposition amount was 9.9 kBq m^{-2}, so additional sensitivity tests include resuspension from grids with 1–10 kBq m^{-2}. As was discussed in part in the previous sections, the snow cover effect is also tested. In summary, for each aerosol size case, we conduct four sensitivity tests: (1) No cumulus parameterization, denoted as [No. cuml.], (2) with cumulus parameterization [Cuml.], (3) [Cuml.] plus the inclusion of resuspension from 1–10-kBq m^{-2} grids [1–10kBg m^{-2}], and (4) [Cuml.] plus [1–10 kBq m^{-2}] plus the snow cover effect [Snow cover]. Thus, the submicron case of [No cuml.] was used in the study of K16, and the supermicron case of [Cuml.] is used as the simulation in this study. Note that the submicron simulations shown in the current study are [Cuml.]. While this parameterization is complicated, the differences between [Cuml.] and [No cuml.] are exceedingly small.

Figure 9 presents monthly mean snow cover data interpolated to the model grids. The original data are the MODerate resolution Imaging Spectroradiometer (MODIS) snow cover collection 6 level-3 data (MOD10CM, global, monthly, 0.05° resolution) (Riggs et al., 2016). In the presence of snow cover, the simulated dust emission is suppressed by the snow cover fraction (Eq. 3 is multiplied by one minus snow cover). No impact of snow cover on forest emissions is assumed in the simulation. December, January, and February are the months with the widest snow coverage in East Japan. In November, only small snow cover fractions are observed in the high-mountain areas (i.e., > 1000 m in Fig. 1a). In March, the snow cover in the low-elevation areas (i.e., < 1000 m in Fig. 1a and over all prefectures numbered in Fig. 1b except the western part (Ou Mountains) of Fukushima Prefecture) is mostly melted. The snow cover in the Nakadori valley, including at the Fukushima site, is highest in January. Some areas over the Kanto Plain are covered with snow in January. Extensive snow cover is also observed in the Abukuma Highlands, including in Namie (Tsushima), in February.

Figure 10 compares the statistical metrics *R*, *Sim/Obs*, *FA2*, and *FA5* of the concentrations (daily to weekly depending on the site) and monthly depositions for the eight sensitivity tests. As previously discussed, the statistical scores of the supermicron simulations are significantly greater than those of the submicron simulations, especially the *R* values of the concentrations at Fukushima and Tsukuba, the *R* value of deposition at Tsukuba, the *Sim/Obs* values at Fukushima and Tsukuba, and the *FA2* and *FA5* values of deposition at all sites. Including the cumulus parameterization was successful in the sense that it did not cause any significant deterioration in the statistical scores. The supermicron simulations indicate slight improvements due to cumulus convection, such as increased *R* values of the concentrations at Fukushima and Tsukuba, but the *FA2* values of the concentrations at Fukushima and Tsukuba are slightly decreased. The impact of including a 1–10-kBq m^{-2} area would

https://doi.org/10.5194/acp-2021-687
Preprint. Discussion started: 20 September 2021

Atmospheric Chemistry and Physics Discussions

565 be larger at Tsukuba, which is surrounded by less contaminated regions. The supermicron simulations indicate a slight improvement in the *R* value of the concentrations at Tsukuba, but the *R* value of the deposition at Tsukuba decreases.

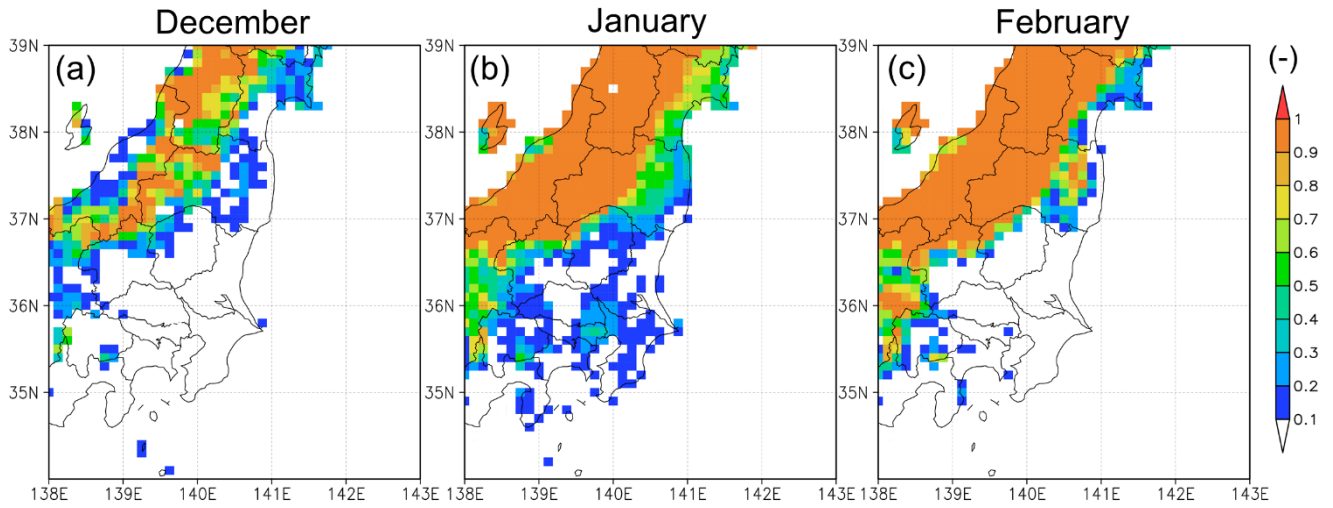

Figure 9: Monthly mean MODIS snow cover fractions interpolated to the model grids.

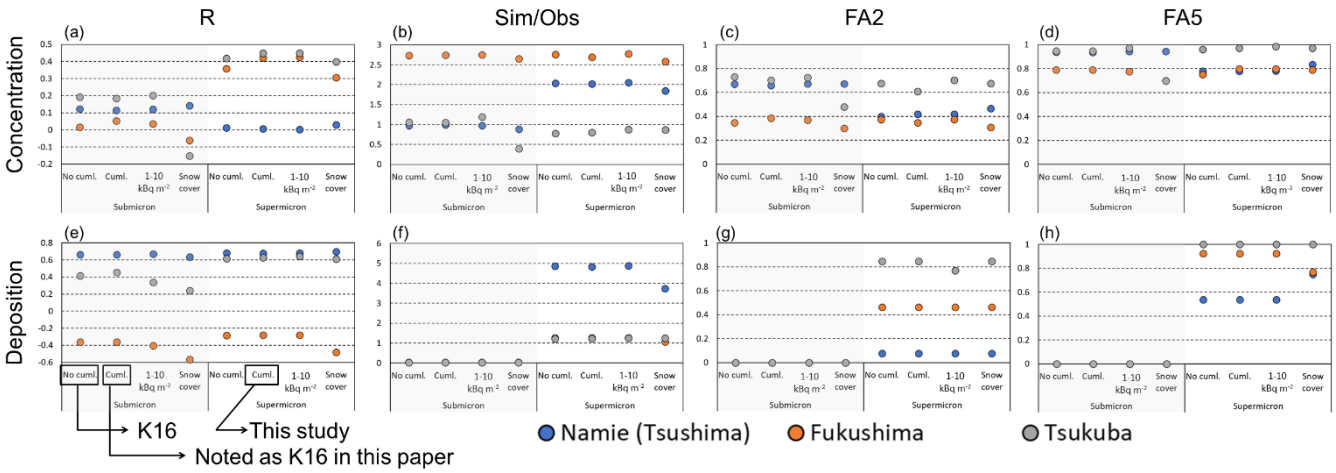

570 **Figure 10:** Summary of statistical measures between the observations and the simulations (dust plus forest) for various sensitivity tests, such as (from left to right) the correlation coefficient (*R*), simulation-to-observation median ratio (*Sim/Obs*), numerical fraction of data within a factor of two (*FA2*), and numerical fraction of data within a factor of five (*FA5*) for (top) the surface concentrations and (bottom) depositions at (blue) Namie (Tsushima), (orange) Fuklushima, and (gray) Tsukuba. The four sensitivity tests are conducted for both the submicron and supermicron cases and consider no cumulus convection
575 parameterization [No cuml.], the addition of the cumulus convection parameterization [Cuml.], cumulus convection plus emissions from grids in which the initial deposition amounts are 1 – 10 kBq m^{-2} [1–10 kBq m^{-2}], and cumulus convection plus emissions from the 1 – 10-kBq m^{-2} areas plus suppressed emissions in the presence of snow coverage [Snow cover]. Thus, "Submicron of [No cuml.]" is the simulation setting of K16, "Submicron of [Cuml.]" is the setting denoted as K16 in this paper, and "Supermicron of [Cuml.]" is the setting of this study.

https://doi.org/10.5194/acp-2021-687
Preprint. Discussion started: 20 September 2021

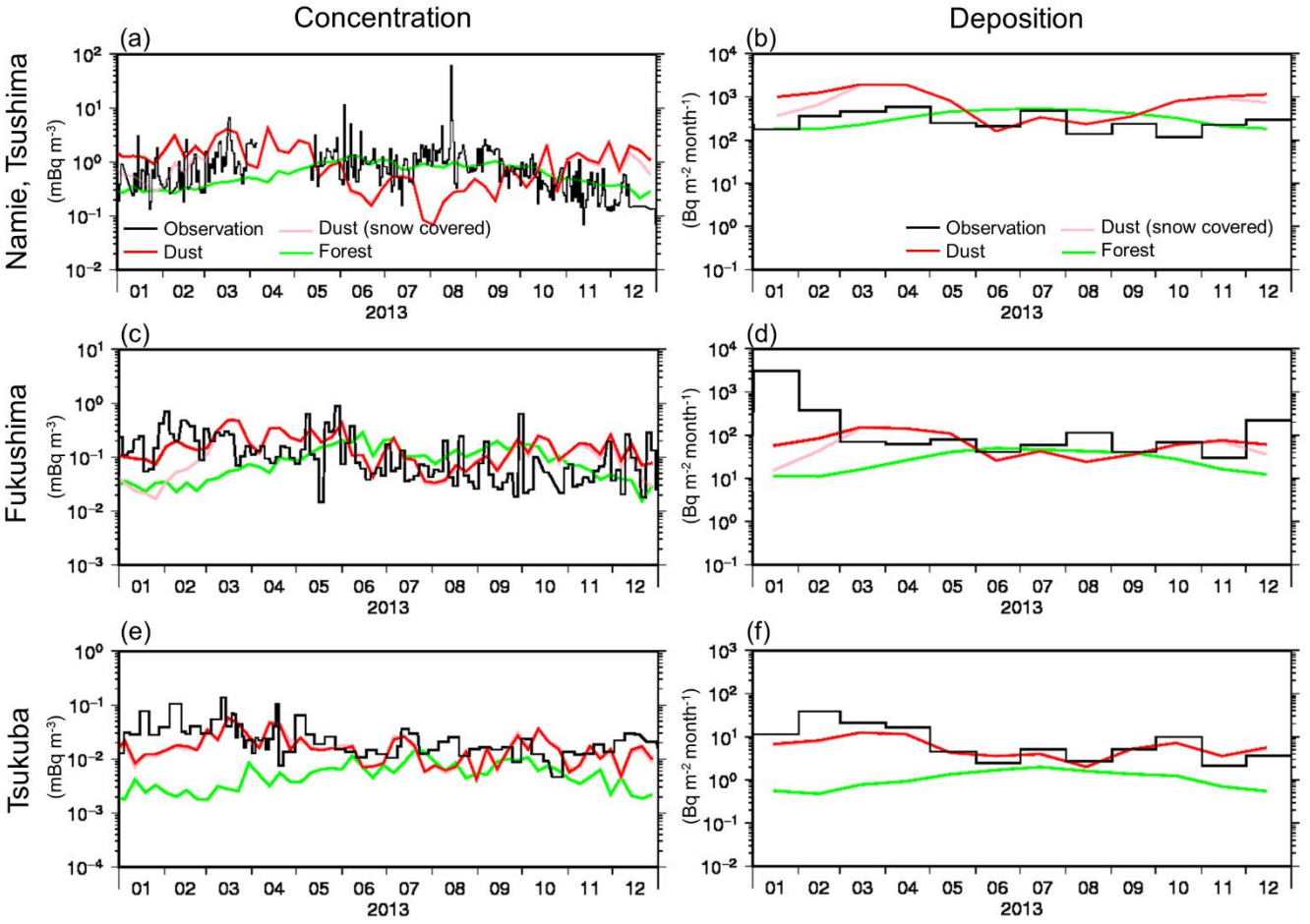

Figure 11: (Left) Temporal variations in the surface concentrations of (black) observed ^{137}Cs and simulated ^{137}Cs associated with (red) dust aerosols (denoted as [1–10 kBq m^{-2}] in Fig. 10), (pink) dust aerosols with emissions suppressed by surface snow coverage (denoted as [Snow cover] in Fig. 10), and (lime) forest aerosols (denoted as "1–10 kBq m^{-2}" in Fig. 10), assuming supermicron sizes of ^{137}Cs-bearing particles at (top to bottom) Namie (Tsushima), Fukushima, and Tsukuba (mBq m^{-3}). The sampling intervals are used for the observations, but weekly mean values are depicted for the simulations. (Right) Same as the left panels but for the monthly cumulative deposition amounts (Bq m^{-2}).

Among the sensitivity tests, implementation of the cumulus convection parameterization [Cuml.] and the inclusion of less-contaminated areas [1–10 kBq m^{-2}] do not cause any substantial differences in the performances of simulating the concentrations and depositions, but the difference induced by including the snow cover effect [Snow cover] is significant. The supermicron simulations indicate that including snow cover improves the performance at Namie (Tsushima) (indicated by the *Sim/Obs* and *FA5* values of the deposition) but deteriorates the performance at Fukushima (as indicated by the *R* value of the concentrations and the *FA5* value of the deposition). Fig. 11 compares the simulated dust between these two settings, [1–10 kBq m^{-2}] and [Snow cover], to analyze the concentrations and depositions of the supermicron case at the three sites. Apparently,

https://doi.org/10.5194/acp-2021-687
Preprint. Discussion started: 20 September 2021


Atmospheric Chemistry and Physics Discussions

[Snow cover] improves both the concentration and deposition simulations at Namie (Tsushima) in January, February, and December, but deteriorates both the concentration and deposition simulations at Fukushima. This result is consistent with the fact that no decontamination work occurred in the DRZ around Namie (Tsushima) in 2013, so snow cover suppressed resuspension from the bare soil. On the other hand, people lived in Fukushima city and the surrounding municipalities, so snow removal operations (deicing agents and snowblowers) are applied after each snowfall. In fact, substantial amounts of road salts are observed in road-side PM_{10} measurements in Nordic countries in winter (Denby et al., 2016), indicating the presence of road dust emissions after snow removal operations. In Fukushima city in 2013, most public facilities and agricultural fields were already decontaminated, but the achievement ratios of decontamination on roads and forests were lower than 10% (Watanabe et al., 2021). Thus, snowfall did not suppress the dust emissions around Fukushima city, which may be the reason why [Snow cover] deteriorated the model performance at the Fukushima site. In addition, as previously discussed, we hypothesize that the deposition amount in January 2013 at Fukushima was much higher than that at Namie due to the opposing impacts of snow cover on dust emissions over the two different locations: the suppression around the Namie site and the production of very large road dust particles around the Fukushima site.

4 Conclusions

The regional budget of resuspended ^{137}Cs originating from the Fukushima nuclear accident assessed by Kajino et al. (2016) (K16) for 2013 is reassessed in this study. K16 assumed resuspension aerosol sizes similar to those of primary emissions (the direct emissions from the F1NPP associated with the accident), which are submicron-sized. However, Watanabe et al. (2021) determined that the deposition amounts simulated by K16 were significantly underestimated. Based on recent cumulative knowledge, major resuspension aerosols could be supermicron-sized, such as soil dust (Ishizuka et al., 2017; Kinase et al., 2018) and bioaerosols (Kinase et al., 2018; Igarashi et al., 2019b; Kita et al., 2020; Minami et al., 2020; Igarashi, 2021). Lower possibilities of submicron particle involvement, such as that resulting from forest fires (Kinase et al., 2018) and epicuticular wax (Nakagawa et al., 2018), have been reported. Thus, the regional budget considering supermicron aerosols is significantly different from that considering submicron aerosols: faster supermicron deposition rates necessitated higher emission fluxes to sustain the simulated surface concentrations at the observed levels.

To evaluate the simulations, measured concentration and deposition data obtained at three stations, Namie (Tsushima), Fukushima, and Tsukuba, are used. In this study, the resuspension source area is defined as areas in which the initial deposition amounts exceed 300 kBq m^{-2}. The Namie (Tsushima) site (2300 kBq m^{-2}) is in the resuspension source area and is surrounded by mountainous forests in the Abukuma Highlands. The Fukushima site (190 kBq m^{-2}) is characterized as an urban/rural region located outside but nearby the source area. The Tsukuba site (21 kBq m^{-2}) is characterized as a downwind region. A source-receptor relationship analysis is performed, and resuspension ratios and redistribution amounts are derived. The effects of snow

https://doi.org/10.5194/acp-2021-687
Preprint. Discussion started: 20 September 2021

cover on resuspension and the contributions of resuspension to the actual decreasing trends in the ambient gamma dose rates are discussed.

The major findings in the context of contrasting the two different particle sizes are summarized as follows.

- Regarding the submicron particles, the surface concentrations of ^{137}Cs at Namie (Tsushima) in winter are quantitatively explained by multiplying the dust emission scheme of Ishizuka et al. (2017) by five, but these values are significantly underestimated in the summer. Additional forest emissions with a factor of 10^{-7} h^{-1} explain the enhancement of the observed ^{137}Cs surface concentrations in summer at Namie (Tsushima). However, this effect causes opposite seasonal variations at the Fukushima site: the simulated concentrations are high in summer, but the observations are low in summer. In addition, this factor causes deposition underestimations by two orders of magnitude at all sites, Namie (Tsushima), Fukushima, and Tsukuba. The annual mean source contributions for the concentrations are 90%, 16%, and 21%, and those for the depositions are 95%, 13%, and 20% for Namie (Tsushima), Fukushima, and Tsukuba, respectively. The total areal annual resuspension of ^{137}Cs is 1.28 TBq, which is equivalent to only 0.048% of the initial deposition in March 2011, i.e., 2.68 TBq. The decreasing trend of the observed gamma dose rate in Fukushima Prefecture was $1.0–7.9\times10^{-4}$ d^{-1} in 2013 after the radioactive decay of ^{134}Cs and ^{137}Cs was excluded. The decreasing trend is due to decontamination and natural decay, such as that occurring due to land surface processes. The resuspension rate through the atmosphere is 0.048% y^{-1} (1.3×10^{-6} d^{-1}), which is negligibly small compared to the decreasing trend. Together with the discharge rate through rivers estimated as 0.02–0.3% y^{-1} (Iwagami et al., 2017), K16 concluded that ground-surface ^{137}Cs stays or circulates within local terrestrial ecosystems and is hardly discharged through the atmosphere or rivers.

- Regarding the supermicron particles, by using the climatological deposition velocity analysis proposed by Watanabe et al. (2021), the dry and wet deposition parameters are successfully constrained by the concentrations and depositions measured at the three sites. The constrained dry and wet scavenging rates of supermicrons are 100 times and 10 times those of submicrons, respectively, resulting in the emission fluxes of both dust and forest aerosols to be enhanced twenty-fold. Compared to the submicron case, the source contributions of supermicrons are higher in the source areas and lower in the receptor regions. The annual mean source contributions for the concentrations are 94%, 9.1%, and 5.4%, and those for the depositions are 99.5%, 2.2%, and 1.0% at Namie (Tsushima), Fukushima, and Tsukuba, respectively. The areal total annual resuspension of ^{137}Cs is 25.7 TBq, which is equivalent to 0.96% of the initial deposition. Due to the rapid deposition rates, the annual redeposition amount is also large, at 10.6 TBq; thus, approximately 40% of emissions are redistributed over East Japan. However, the traveling distance should not be large because the source contributions of the depositions at Fukushima and Tsukuba are only 2.2% and 1.0%, respectively. The resuspension rate through the atmosphere is 0.96% y^{-1} (2.6×10^{-5} d^{-1}), which may not be negligibly small, as it can account for 1–10% of the decreasing rate due to decontamination and natural decay except radioactive decay ($1.0–7.9\times10^{-4}$ d^{-1}). The areas with positive redistribution

https://doi.org/10.5194/acp-2021-687
Preprint. Discussion started: 20 September 2021


Atmospheric Chemistry and Physics Discussions

amounts (enhanced deposition due to resuspension) of 1–10 Bq m^{-2} are much larger for the supermicron case than those for the submicron case, and the maximum values are up to 100 Bq m^{-2}, especially over the ocean close to the coast of Fukushima Prefecture.

From the current analysis, it is likely that snow cover in winter (January, February, and December) suppressed the dust emissions in the source areas around the Namie (Tsushima) site but did not suppress emissions around the Fukushima site. This is because Namie (Tsushima) is located in the DRZ and human activities in this region were very limited in 2013, whereas snow removal operations involving deicing agents and snow blowers were performed in Fukushima city and the surrounding municipalities at this time. In addition, heavy traffic on the major roads close to the Fukushima site (< 1 km) may produce substantial numbers of superlarge road dust (or road salt) particles (~100 μm, which can travel only 1 km) from wet and muddy surfaces, which may cause exceptionally large deposition amounts in Fukushima in January. The completion of decontamination in 2013 was lower than 10% for roads and forests in Fukushima city.

More than ten years have passed since the accident but the issues to be resolved in the future are still the same as those listed in K16. The current study represents an order estimation of the regional budget for only one year using a simple model and schemes. In addition to the utilized model and schemes, the current horizontal grid resolution is too coarse to reflect the heterogeneous distributions of various land use types. Soil dust and road dust emissions are relatively well-formulated, but bioaerosols are not. Substantial efforts have been made to understand the emission mechanisms and quantifications of bioaerosol emission fluxes (Igarashi et al., 2019b; Kita et al., 2020; Minami et al., 2020), but it is still difficult to establish a set of formulas that is applicable for various vegetation surfaces. Our hypothesis of the existence of superlarge particles is not proven at all. The decreasing trends in atmospheric ^{137}Cs differ between the periods before and after approximately 2015 (Watanabe et al., 2021), but the reason for this distinction is not clear. A long-term (i.e., 10-year) assessment using long-term measurements and numerical simulations is required. The quantification and formulation of size-resolved ^{137}Cs emission fluxes from various sources should directly connect to the comprehensive understanding of the regional budget of resuspended ^{137}Cs.

Data and code availability

The observation and simulation data used for the figures and source codes of the LM are available at https://mri-2.mri-jma.go.jp/owncloud/s/Cr6nS3iJXPTZLf7 (last access: 20 August 2021).

Author contribution

MK developed the numerical model with RH and performed the numerical simulations with MI and KI. AW conducted the measurements at Fukushima University, and KK and TK conducted the concentration measurements at Namie (Tsushima). YS, HH, NA, MH, and ST supported the Namie (Tsushima) measurements and data analysis of the deposition measurements.

https://doi.org/10.5194/acp-2021-687
Preprint. Discussion started: 20 September 2021


Atmospheric Chemistry and Physics Discussions

685 YZ, YI, and TK conducted the measurements at Tsukuba. KK and AS supported the data analysis and figure generation. MK designed the manuscript structure and completed the draft together with all authors.

Competing interests

The authors declare that they have no conflicts of interest.

Acknowledgments

690 This work was supported by Grants-in-Aid for Scientific Research (KAKENHI) with Grant Numbers JP19H01155 and JP16KK0018. This work was also supported by the Japanese Radioactivity Survey from the Nuclear Regulation Authority (NRA), Japan, the Environmental Research and Technology Development Fund (JPMEERF20215003) of the Environmental Restoration and Conservation Agency of Japan (ERCA), and Arctic Challenge for Sustainability II (ArCS II) with Grant Number JPMXD1420318865 from the Ministry of Education, Culture, Sports, Science, and Technology Japan (MEXT).

695

https://doi.org/10.5194/acp-2021-687
Preprint. Discussion started: 20 September 2021

Atmospheric Chemistry and Physics Discussions

References

Adachi, K., Kajino, M., Zaizen, Y. and Igarashi, Y.: Emission of spherical cesium-bearing particles from an early stage of the Fukushima nuclear accident, Sci. Rep., 3(Plume 1), 12–15, doi:10.1038/srep02554, 2013.

Denby, B. R., Ketzel, M., Ellermann, T., Stojiljkovic, A., Kupiainen, K., Niemi, J. V., Norman, M., Johansson, C., Gustafsson, M., Blomqvist, G., Janhäll, S. and Sundvor, I.: Road salt emissions: A comparison of measurements and modelling using the NORTRIP road dust emission model, Atmos. Environ., 141, 508–522, doi:10.1016/j.atmosenv.2016.07.027, 2016.

Dépée, A., Lemaitre, P., Gelain, T., Mathieu, A., Monier, M. and Flossmann, A.: Theoretical study of aerosol particle electroscavenging by clouds, J. Aerosol Sci., 135, 1–20, doi:10.1016/j.jaerosci.2019.04.001, 2019.

Draxler, R., Arnold, D., Chino, M., Galmarini, S., Hort, M., Jones, A., Leadbetter, S., Malo, A., Maurer, C., Rolph, G., Saito, K., Servranckx, R., Shimbori, T., Solazzo, E. and Wotawa, G.: World Meteorological Organization's model simulations of the radionuclide dispersion and deposition from the Fukushima Daiichi nuclear power plant accident, J. Environ. Radioact., 139, 172–184, doi:10.1016/j.jenvrad.2013.09.014, 2015.

Emanuel, K. A. and Živković-Rothman, M.: Development and evaluation of a convection scheme for use in climate models, J. Atmos. Sci., 56(11), 1766–1782, doi:10.1175/1520-0469(1999)056<1766:DAEOAC>2.0.CO;2, 1999.

Goto, D., Morino, Y., Ohara, T., Thomas Sekiyama, T., Uchida, J. and Nakajima, T.: Application of linear minimum variance estimation to the multi-model ensemble of atmospheric radioactive Cs-137 with observations, Atmos. Chem. Phys., 20(6), 3589–3607, doi:10.5194/acp-20-3589-2020, 2020.

Hososhima, M. and Kaneyasu, N.: Altitude-dependent distribution of ambient gamma dose rates in a mountainous area of japan caused by the fukushima nuclear accident, Environ. Sci. Technol., 49(6), 3341–3348, doi:10.1021/es504838w, 2015.

Igarashi, Y., Kajino, M., Zaizen, Y., Adachi, K. and Mikami, M.: Atmospheric radioactivity over Tsukuba, Japan: a summary of three years of observations after the FDNPP accident, Prog. Earth Planet. Sci., 2(1), doi:10.1186/s40645-015-0066-1, 2015.

Igarashi, Y., Kogure, T., Kurihara, Y., Miura, H., Okumura, T., Satou, Y., Takahashi, Y. and Yamaguchi, N.: A review of Cs-bearing microparticles in the environment emitted by the Fukushima Dai-ichi Nuclear Power Plant accident, J. Environ. Radioact., 205–206(April), 101–118, doi:10.1016/j.jenvrad.2019.04.011, 2019a.

Igarashi, Y., Kita, K., Maki, T., Kinase, T., Hayashi, N., Hosaka, K., Adachi, K., Kajino, M., Ishizuka, M., Sekiyama, T. T., Zaizen, Y., Takenaka, C., Ninomiya, K., Okochi, H. and Sorimachi, A.: Fungal spore involvement in the resuspension of radiocaesium in summer, Sci. Rep., 9(1), doi:10.1038/s41598-018-37698-x, 2019b.

Igarashi, Y.: Bioaerosols emission from forest ecosystem - Close look at fungal spore, Earozoru Kenkyu, 36(1), 5–18, doi:10.11203/jar.36.5, 2021.

Imamura, N., Katata, G., Kajino, M., Kobayashi, M., Itoh, Y. and Akama, A.: Fogwater deposition of radiocesium in the forested mountains of East Japan during the Fukushima Daiichi Nuclear Power Plant accident: A key process in regional radioactive contamination, Atmos. Environ., 224(February), 117339, doi:10.1016/j.atmosenv.2020.117339, 2020.

https://doi.org/10.5194/acp-2021-687
Preprint. Discussion started: 20 September 2021


Atmospheric Chemistry and Physics Discussions

Ishizuka, M., Mikami, M., Tanaka, T. Y., Igarashi, Y., Kita, K., Yamada, Y., Yoshida, N., Toyoda, S., Satou, Y., Kinase, T., Ninomiya, K. and Shinohara, A.: Use of a size-resolved 1-D resuspension scheme to evaluate resuspended radioactive material associated with mineral dust particles from the ground surface, J. Environ. Radioact., 166, 436–448, doi:10.1016/j.jenvrad.2015.12.023, 2017.

Iwagami, S., Onda, Y., Tsujimura, M. and Abe, Y.: Contribution of radioactive 137Cs discharge by suspended sediment, coarse organic matter, and dissolved fraction from a headwater catchment in Fukushima after the Fukushima Dai-ichi Nuclear Power Plant accident, J. Environ. Radioact., 166, 466–474, doi:10.1016/j.jenvrad.2016.07.025, 2017.

Kajino, M., Deushi, M., Maki, T., Oshima, N., Inomata, Y., Sato, K., Ohizumi, T. and Ueda, H.: Modeling wet deposition and concentration of inorganics over Northeast Asia with MRI-PM/c, Geosci. Model Dev., 5(6), doi:10.5194/gmd-5-1363-2012, 2012.

Kajino, M., Ishizuka, M., Igarashi, Y., Kita, K., Yoshikawa, C. and Inatsu, M.: Long-term assessment of airborne radiocesium after the Fukushima nuclear accident: Re-suspension from bare soil and forest ecosystems, Atmos. Chem. Phys., 16(20), doi:10.5194/acp-16-13149-2016, 2016.

Kajino, M., Sekiyama, T. T., Igarashi, Y., Katata, G., Sawada, M., Adachi, K., Zaizen, Y., Tsuruta, H. and Nakajima, T.: Deposition and Dispersion of Radio-Cesium Released Due to the Fukushima Nuclear Accident: Sensitivity to Meteorological Models and Physical Modules, J. Geophys. Res. Atmos., 124(3), 1823–1845, doi:10.1029/2018JD028998, 2019.

Kajino, M., Adachi, K., Igarashi, Y., Satou, Y., Sawada, M., Thomas Sekiyama, T., Zaizen, Y., Saya, A., Tsuruta, H. and Moriguchi, Y.: Deposition and Dispersion of Radio-Cesium Released due to the Fukushima Nuclear Accident: 2. Sensitivity to Aerosol Microphysical Properties of Cs-Bearing Microparticles (CsMPs), J. Geophys. Res. Atmos., 126(1), doi:10.1029/2020JD033460, 2021.

Kaneyasu, N., Ohashi, H., Suzuki, F., Okuda, T. and Ikemori, F.: Sulfate aerosol as a potential transport medium of radiocesium from the fukushima nuclear accident, Environ. Sci. Technol., 46(11), 5720–5726, doi:10.1021/es204667h, 2012.

Katata, G., Chino, M., Kobayashi, T., Terada, H., Ota, M., Nagai, H., Kajino, M., Draxler, R., Hort, M. C., Malo, A., Torii, T. and Sanada, Y.: Detailed source term estimation of the atmospheric release for the Fukushima Daiichi Nuclear Power Station accident by coupling simulations of an atmospheric dispersion model with an improved deposition scheme and oceanic dispersion model, Atmos. Chem. Phys., 15(2), doi:10.5194/acp-15-1029-2015, 2015.

Kinase, T., Kita, K., Igarashi, Y., Adachi, K., Ninomiya, K., Shinohara, A., Okochi, H., Ogata, H., Ishizuka, M., Toyoda, S., Yamada, K., Yoshida, N., Zaizen, Y., Mikami, M., Demizu, H. and Onda, Y.: The seasonal variations of atmospheric 134,137Cs activity and possible host particles for their resuspension in the contaminated areas of Tsushima and Yamakiya, Fukushima, Japan, Prog. Earth Planet. Sci., 5(1), doi:10.1186/s40645-018-0171-z, 2018.

Kita, K., Igarashi, Y., Kinase, T., Hayashi, N., Ishizuka, M., Adachi, K., Koitabashi, M., Sekiyama, T. T. and Onda, Y.: Rain-induced bioecological resuspension of radiocaesium in a polluted forest in Japan, Sci. Rep., 10(1), 1–15, doi:10.1038/s41598-020-72029-z, 2020.

https://doi.org/10.5194/acp-2021-687
Preprint. Discussion started: 20 September 2021


Atmospheric Chemistry and Physics Discussions

Kitayama, K., Morino, Y., Takigawa, M., Nakajima, T., Hayami, H., Nagai, H., Terada, H., Saito, K., Shimbori, T., Kajino, M., Sekiyama, T. T., Didier, D., Mathieu, A., Quélo, D., Ohara, T., Tsuruta, H., Oura, Y., Ebihara, M., Moriguchi, Y. and Shibata, T.: Atmospheric Modeling of ^{137}Cs Plumes From the Fukushima Daiichi Nuclear Power Plant—Evaluation of the Model Intercomparison Data of the Science Council of Japan, J. Geophys. Res. Atmos., 123(14), 7754–7770, doi:10.1029/2017JD028230, 2018.

Li, X., Sun, S., Hu, X., Huang, H., Li, H., Morino, Y., Wang, S., Yang, X., Shi, J. and Fang. S.: Source inversion of both long- and short-lived radionuclide releases from the Fukushima Daiichi nuclear accident using on-site gamma dose rates, J. Hazard. Mater., 379, 120770, doi:10.1016/j.jhazmat.2019.120770, 2019.

Leadbetter, S. J., Hort, M. C., Jones, A. R., Webster, H. N. and Draxler, R. R.: Sensitivity of the modelled deposition of Caesium-137 from the Fukushima Dai-ichi nuclear power plant to the wet deposition parameterisation in NAME, J. Environ. Radioact., 139, 200–211, doi:10.1016/j.jenvrad.2014.03.018, 2015.

Mathieu, A., Kajino, M., Korsakissok, I., Périllat, R., Quélo, D., Quérel, A., Saunier, O., Sekiyama, T. T., Igarashi, Y. and Didier, D.: Fukushima Daiichi–derived radionuclides in the atmosphere, transport and deposition in Japan: A review, Appl. Geochemistry, 91, doi:10.1016/j.apgeochem.2018.01.002, 2018.

Minami, K., Katata, G., Kita, K., Sorimachi, A., Hosaka, K. and Igarashi, Y.: Numerical Analyses of Transport Processes of Bioaerosol Released from a Temperate Deciduous Broad-Leaved Forest, Earozoru Kenkyu, 35(3), 208–218, doi:10.11203/jar.35.208, 2020.

Nakagawa, M., Yamada, K., Toyoda, S., Kita, K., Igarashi, Y., Komatsu, S., Yamada, K. and Yoshida, N.: Characterization of hydrocarbons in aerosols and investigation of biogenic sources as a carrier of radiocesium isotopes, Geochem. J., 52(2), 163–172, doi:10.2343/geochemj.2.0512, 2018.

Nakajima, T., Misawa, S., Morino, Y., Tsuruta, H., Goto, D., Uchida, J., Takemura, T., Ohara, T., Oura, Y., Ebihara, M. and Satoh, M.: Model depiction of the atmospheric flows of radioactive cesium emitted from the Fukushima Daiichi nuclear power station accident, Prog. Earth Planet. Sci., 4(1), doi:10.1186/s40645-017-0117-x, 2017.

NRA (Nuclear Regulation Authority): Airborne Monitoring Results in each prefecture, available from: http://radioactivity.nsr.go.jp/en/list/203/list-1.html (last access: 31 July 2021), 2012.

Ochiai, S., Hasegawa, H., Kakiuchi, H., Akata, N., Ueda, S., Tokonami, S. and Hisamatsu, S.: Temporal variation of post-accident atmospheric 137Cs in an evacuated area of Fukushima Prefecture: Size-dependent behaviors of 137Cs-bearing particles, J. Environ. Radioact., 165, 131–139, doi:10.1016/j.jenvrad.2016.09.014, 2016.

Oura, Y., Ebihara, M., Tsuruta, H., Nakajima, T., Ohara, T., Ishimoto, M., Sawahata, H., Katsumura, Y. and Nitta, W.: A Database of Hourly Atmospheric Concentrations of Radiocesium (^{134}Cs and ^{137}Cs) in Suspended Particulate Matter Collected in March 2011 at 99 Air Pollution Monitoring Stations in Eastern Japan, J. Nucl. Radiochem. Sci., 15(2), 2_1-2_12, doi:10.14494/jnrs.15.2_1, 2015.

Petroff, A. and Zhang, L.: Development and validation of a size-resolved particle dry deposition scheme for application in aerosol transport models, Geosci. Model Dev., 3(2), 753–769, doi:10.5194/gmd-3-753-2010, 2010.

https://doi.org/10.5194/acp-2021-687
Preprint. Discussion started: 20 September 2021


Atmospheric Chemistry and Physics Discussions

Riggs, G. A., Hall, D. and Román, M. O.: MODIS Snow Products Collection 6 User Guide, Earth Sci., 6 (August), 1–80 [online] Available from: https://modis-snow-ice.gsfc.nasa.gov/uploads/C6_MODIS_Snow_User_Guide.pdf (last access: 31 July 2021), 2016.

Sanada, Y., Kondo, A., Sugita, T., Nishizawa, Y., Yuuki, Y., Ikeda, K., Shoji, Y. and Torii, T.: Radiation monitoring using an unmanned helicopter in the evacuation zone around the Fukushima Daiichi nuclear power plant, Explor. Geophys., 45(1), 3–7, doi:10.1071/EG13004, 2014.

Sanada, Y., Katata, G., Kaneyasu, N., Nakanishi, C., Urabe, Y. and Nishizawa, Y.: Altitudinal characteristics of atmospheric deposition of aerosols in mountainous regions: Lessons from the Fukushima Daiichi Nuclear Power Station accident, Sci. Total Environ., 618, 881–890, doi:10.1016/j.scitotenv.2017.08.246, 2018.

Sato, Y., Takigawa, M., Sekiyama, T. T., Kajino, M., Terada, H., Nagai, H., Kondo, H., Uchida, J., Goto, D., Quélo, D., Mathieu, A., Quérel, A., Fang, S., Morino, Y., von Schoenberg, P., Grahn, H., Brännström, N., Hirao, S., Tsuruta, H., Yamazawa, H. and Nakajima, T.: Model Intercomparison of Atmospheric 137Cs From the Fukushima Daiichi Nuclear Power Plant Accident: Simulations Based on Identical Input Data, J. Geophys. Res. Atmos., 123(20), 11,748-11,765, doi:10.1029/2018JD029144, 2018.

Sato, Y., Sekiyama, T. T., Fang, S., Kajino, M., Quérel, A., Quélo, D., Kondo, H., Terada, H., Kadowaki, M., Takigawa, M., Morino, Y., Uchida, J., Goto, D. and Yamazawa, H.: A model intercomparison of atmospheric 137Cs concentrations from the Fukushima Daiichi Nuclear Power Plant accident, phase III: Simulation with an identical source term and meteorological field at 1-km resolution, Atmos. Environ. X, 7(August), doi:10.1016/j.aeaoa.2020.100086, 2020.

Sekiyama, T. T. and Iwasaki, T.: Mass flux analysis of 137Cs plumes emitted from the Fukushima Daiichi nuclear power plant, Tellus, Ser. B Chem. Phys. Meteorol., 70(1), 1–11, doi:10.1080/16000889.2018.1507390, 2018.

Sekiyama, T. T. and Kajino, M.: Reproducibility of surface wind and tracer transport simulations over complex terrain using 5-, 3-, and 1-km-grid models, J. Appl. Meteorol. Climatol., 59(5), 937–952, doi:10.1175/JAMC-D-19-0241.1, 2020.

Sekiyama, T. T., Kajino, M. and Kunii, M.: Ensemble dispersion simulation of a point-source radioactive aerosol using perturbed meteorological fields over eastern Japan, Atmosphere (Basel)., 12(6), doi:10.3390/atmos12060662, 2021.

Skamarock, W. C., Klemp, J. B., Dudhia, J. B., Gill, D. O., Barker, D. M., Duda, M. G., Huang, X.-Y., Wang, W. and Powers, J. G.: A description of the Advanced Research WRF Version 3, NCAR Technical Note TN-475+STR, Tech. Rep., 113, 2008.

Steinhauser, G., Niisoe, T., Harada, K. H., Shozugawa, K., Schneider, S., Synal, H. A., Walther, C., Christl, M., Nanba, K., Ishikawa, H. and Koizumi, A.: Post-Accident Sporadic Releases of Airborne Radionuclides from the Fukushima Daiichi Nuclear Power Plant Site, Environ. Sci. Technol., 49(24), 14028–14035, doi:10.1021/acs.est.5b03155, 2015.

Terada, H., Nagai, H., Tsuduki, K., Furuno, A., Kadowaki, M. and Kakefuda, T.: Refinement of source term and atmospheric dispersion simulations of radionuclides during the Fukushima Daiichi Nuclear Power Station accident, J. Environ. Radioact., 213(November 2019), 106104, doi:10.1016/j.jenvrad.2019.106104, 2020.

https://doi.org/10.5194/acp-2021-687
Preprint. Discussion started: 20 September 2021


Atmospheric Chemistry and Physics Discussions

Torii, T., Sanada, Y., Shikaze, Y., Takahashi, M., Ishida, M., Nishizawa, Y., Urabe, Y., Sugita, T. and Kondo, A.: Investigation of radionuclide distribution using aircraft for surrounding environmental survey from Fukushima Dai-ichi Nuclear Power Plant, 182 [online] Available from: https://inis.iaea.org/search/search.aspx?orig_q=RN:44087099 (last access: 2 August 2021), 2012.

Torii, T., Sugita, T., Okada, C. E., Reed, M. S. and Blumenthal, D. J.: Enhanced analysis methods to derive the spatial distribution of 131I deposition on the ground by airborne surveys at an early stage after the fukushima daiichi nuclear power plant accident, Health Phys., 105(2), 192–200, doi:10.1097/HP.0b013e318294444e, 2013.

Tsuruta, H., Oura, Y., Ebihara, M., Ohara, T. and Nakajima, T.: First retrieval of hourly atmospheric radionuclides just after the Fukushima accident by analyzing filter-tapes of operational air pollution monitoring stations, Sci. Rep., 4, 1–32, doi:10.1038/srep06717, 2014.

Wang, X., Zhang, L. and Moran, M. D.: Uncertainty assessment of current size-resolved parameterizations for below-cloud particle scavenging by rain, Atmos. Chem. Phys., 10(12), 5685–5705, doi:10.5194/acp-10-5685-2010, 2010.

Watanabe, A., Kajino, M., Ninomiya, K., Nagahashi, Y. and Shinohara, A.: Eight-year variations in atmospheric radiocesium in Fukushima City, Atmos. Chem. Phys. Discuss. [preprint], doi:10.5194/acp-2021-591, in review, 2021.

Yumimoto, K., Morino, Y., Ohara, T., Oura, Y., Ebihara, M., Tsuruta, H. and Nakajima, T.: Inverse modeling of the 137Cs source term of the Fukushima Dai-ichi Nuclear Power Plant accident constrained by a deposition map monitored by aircraft, J. Environ. Radioact., 164, 1–12, doi:10.1016/j.jenvrad.2016.06.018, 2016.

NOTES AND CORRESPONDENCE

Performance of a 250-m Grid Eulerian Dispersion Simulation Evaluated at Two Coastal Monitoring Stations in the Vicinity of the Fukushima Daiichi Nuclear Power Plant

Tsuyoshi Thomas SEKIYAMA

Meteorological Research Institute, Tsukuba, Japan

and

Mizuo KAJINO

Meteorological Research Institute, Tsukuba, Japan
Faculty of Life and Environmental Sciences, University of Tsukuba, Tsukuba, Japan

(Manuscript received 16 March 2021, in final form 22 April 2021)

Abstract

Using two horizontal resolutions (3 km and 250 m), this study examined the performance of Eulerian models in simulating dispersion fields at two coastal monitoring stations in the vicinity of a pollutant source (3.2 km and 17.5 km distant) under the situation of the Fukushima 2011 nuclear accident. A 250-m grid simulation was newly conducted for the examination and was able to reproduce the wind and concentration fields in detail over complex terrain. The 3-km grid model could not reproduce the details of the winds and plumes around the Fukushima Daiichi Nuclear Power Plant but occasionally yielded a higher performance with a lower undetected error rate compared with the 250-m grid model due to the large numerical diffusion of the former. A disadvantage of Eulerian dispersion models is expected to be the artificial numerical diffusion in the advection process near emission sources. The artificial numerical diffusion increases the false alarm ratio (number of strikeouts while swinging) but fortunately decreases the undetected error rate (number of strikeouts while looking). This characteristic is appropriate for environmental emergency response (EER) systems. Furthermore, the 250-m grid model result was improved by a plume augmentation (i.e., max pooling) process, which enlarged the plume widths and masked short time lags and small plume drifts. Plume augmentation was advantageous to the high-resolution model for improving statistical scores, which is beneficial for EER systems.

Keywords high resolution modeling; weather modeling; advection modeling; radioactive cesium-137; environmental emergency response

Citation Sekiyama, T. T., and M. Kajino, 2021; Performance of a 250-m grid Eulerian dispersion simulation evaluated at two coastal monitoring stations in the vicinity of the Fukushima Daiichi Nuclear Power Plant. *J. Meteor. Soc. Japan*, **99**, 1089–1098, doi:10.2151/jmsj.2021-052.

Corresponding author: Tsuyoshi Thomas Sekiyama, Meteorological Research Institute, 1-1 Nagamine, Tsukuba, Ibaraki 305-0052, Japan
E-mail: tsekiyam@mri-jma.go.jp
J-stage Advance Published Date: 10 May 2021

1. Introduction

The authors have previously investigated the dependence of dispersion model performance on the horizontal resolution using the data of the Fukushima 2011 nuclear accident (Sekiyama et al. 2015, 2017; Sato et al. 2018, 2020; Sekiyama and Kajino 2020). These studies have essentially found that when using 15-, 5-, 3-, and 1-km grid models, higher-resolution models yield better performance over complex Japanese terrain. Specifically, while the 3-km and 1-km grid models performed comparably over plain regions more than 100 km from the Fukushima Daiichi Nuclear Power Plant (FDNPP), the 1-km grid model was evidently superior to the 3-km grid model over mountainous regions approximately 50 km from the FDNPP. Unfortunately, the 15-km and 5-km grid models exhibited poorer performance compared with the 3-km and 1-km grid models.

The Cs-137 concentration data used for validation in these studies were retrieved by Tsuruta et al. (2014) and Oura et al. (2015) and recorded at approximately 100 monitoring stations. However, most of the stations are located more than 50 km from the FDNPP; among them, the nearest station is 26 km away. Consequently, these studies did not evaluate the model performance in the area immediately surrounding the FDNPP. In principle, Eulerian models, which were utilized in these studies, are generally not expected to be good at simulating plume dispersion in the vicinity of emission sources (cf. Rood 1987). However, it is not theoretically trivial to estimate the poor performance of a Eulerian model, especially when the horizontal resolution is almost comparable to the distance between a monitoring point and an emission source. Therefore, the model performance should be evaluated through observations at not only distant but also close ranges.

In this paper, the close-range performance of Eulerian dispersion simulations is evaluated using two horizontal resolutions, namely, 3 km and 250 m. The 3-km grid simulation is derived from Sekiyama and Kajino (2020), whereas the 250-m grid simulation is newly conducted for the evaluation. Fortunately, Tsuruta et al. (2018) released new Cs-137 concentration data retrieved at two monitoring stations in the vicinity of the FDNPP (3.2 km and 17.5 km distant). This new dataset allows the authors to evaluate the close-range dispersion model performance. The 250-m grid plume dispersion is categorized as a sub-kilometer-scale simulation, which is currently being examined by an increasing number of studies, mainly for complex terrain (e.g., Bao et al. 2018; Wiersema et al. 2020) and urban pollution (e.g., Lateb et al. 2016; Nakayama et al. 2016; Li et al. 2018; Hamer et al. 2020). The authors would like to contribute to the studies on high-resolution geophysical model by focusing on the rural and coastal locations near the FDNPP.

In addition, in the case of environmental emergency responses (EER; cf. World Meteorological Organization 2006), both the Eulerian and Lagrangian plume dispersion models would be required, especially in the areas very close to emission sources. Hence, we should understand beforehand what types of models, what model resolution, and what model configuration are needed for EER. The authors hope that this paper will provide insight into what model resolution and configuration are suitable for supporting EER.

2. Methodology

2.1 Models

The 3-km grid meteorological analysis was provided at an hourly resolution by Sekiyama et al. (2017) and Sekiyama and Kajino (2020). This simulation was performed using a 4-dimensional data assimilation system consisting of a nonhydrostatic regional weather prediction model (referred to as the NHM; cf. Saito et al. 2006, 2007), a local ensemble transform Kalman filter (LETKF; cf. Miyoshi and Aranami 2006; Kunii 2014), and Japan Meteorological Agency (JMA) operational observation datasets. The NHM was being operationally used by JMA at the time of the Fukushima nuclear accident (March 2011) for daily national weather forecasts with four-dimensional variational assimilation (cf. Honda et al. 2005). The analysis has 60 vertical layers from the surface to a 22-km elevation within the model domain over eastern Japan, as presented in Fig. 1a. The boundary conditions for the model domain were provided by the JMA operational global analysis system. The details of the model and data assimilation settings are described in Sekiyama et al. (2017) and Sekiyama and Kajino (2020). This meteorological analysis has been employed not only by the above studies referenced but also by Sato et al. (2018), Sekiyama and Iwasaki (2018), Iwasaki et al. (2019), Takagi et al. (2020), and Goto et al. (2020) for nuclear accident air pollution modeling.

The 250-m grid meteorological analysis was calculated by the NHM nested by the 1-km meteorological analysis within the model domain, as presented in Fig. 1b. The 1-km analysis was provided by Sekiyama and Kajino (2020), who implemented a one-way nested data assimilation scheme (Kunii 2014) nested by the 3-km meteorological analysis aforementioned. Note that the 3-km, 1-km, and 250-m grid analyses were

calculated using the same model and physical configurations, except for the model domains and horizontal resolution-dependent setups. All the resolution models implemented the improved Mellor–Yamada level 3 closure model (Nakanishi and Niino 2004, 2006) as a turbulence scheme. A cumulus parameterization was not utilized for any models in this study. The 250-m grid NHM calculation lasted 20 h for a 24-h simulation using 96 cores of Fujitsu FX100 with 840 × 980 grids. On the other hand, the 3-km grid NHM calculation lasted 4 h for a 24-h simulation using one core of Fujitsu FX100 with 215 × 259 grids.

Cs-137 plume dispersion was calculated by an offline Eulerian regional air quality model, which was driven by either the 3-km or 250-m grid meteorological analysis. This model was previously developed and evaluated by Kajino et al. (2012, 2016, 2018, 2019a, b) and Mathieu et al. (2018). The 3-km and 250-m grid meteorological analyses were input at 1-h (3-km grid) or 10-min (250-m grid) intervals into the offline air quality model, in which the dynamical time step was set to 24 s (3-km grid) or 2 s (250-m grid) using the time-interpolated meteorological analysis. The Cs-137 emission scenario was provided by Katata et al. (2015). In this model, Cs-137 was assumed to be mixed in sulfate-organic mixture aerosol particles, which were injected into a grid cell above the FDNPP at 20–150-m heights, following the time-varying emission scenario. The details of the model settings are described in Sekiyama et al. (2015, 2017) and Sekiyama and Kajino (2020). The 250-m grid offline model calculation lasted 12 h for a 24-h dispersion simulation using 112 cores of Intel Xeon (Haswell) with the same domain as the 250-m grid NHM. On the other hand, the 3-km grid offline model calculation lasted 0.5 h for a 24-h dispersion simulation using eight cores of Intel Xeon (Haswell) with the same domain as the 3-km grid NHM.

2.2 *Observations*

The observational Cs-137 concentrations were retrieved hourly from filter tapes installed in prefectural governments' suspended particulate matter (SPM) monitors, of which the theoretical detection limit was 0.1 Bq m^{-3} (Tsuruta et al. 2014, 2018). The two SPM monitoring stations, as reported by Tsuruta et al. (2018), were located at Futaba and Naraha in the vicinity of the FDNPP along the east coast of Fukushima Prefecture (Fig. 1c). The Futaba and Naraha monitoring stations were located 3.2-km northwest and 17.5-km south–southwest of the FDNPP, respectively. The plume arrivals were defined with a threshold of 1.5

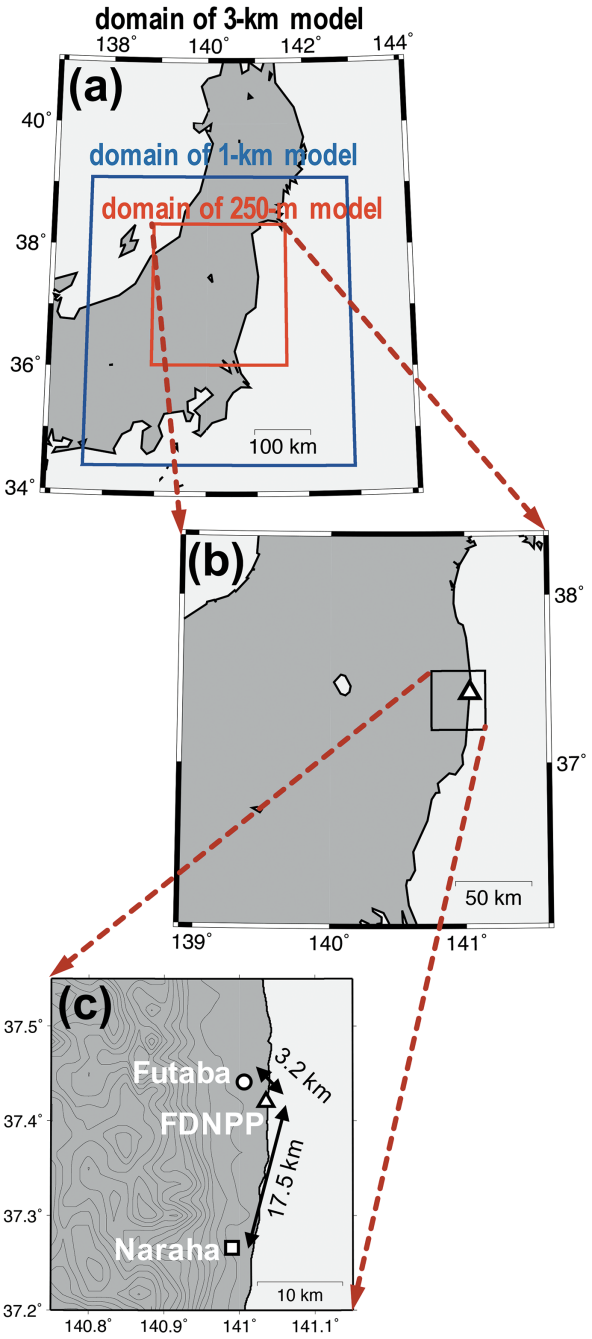

Fig. 1. Model domains of (a) the 3-km grid model and (b) the 250-m grid model. (c) Detailed locations of the Fukushima Daiichi Nuclear Power Plant (FDNPP), Futaba monitoring station, and Naraha monitoring station with 50-m interval elevation contours.

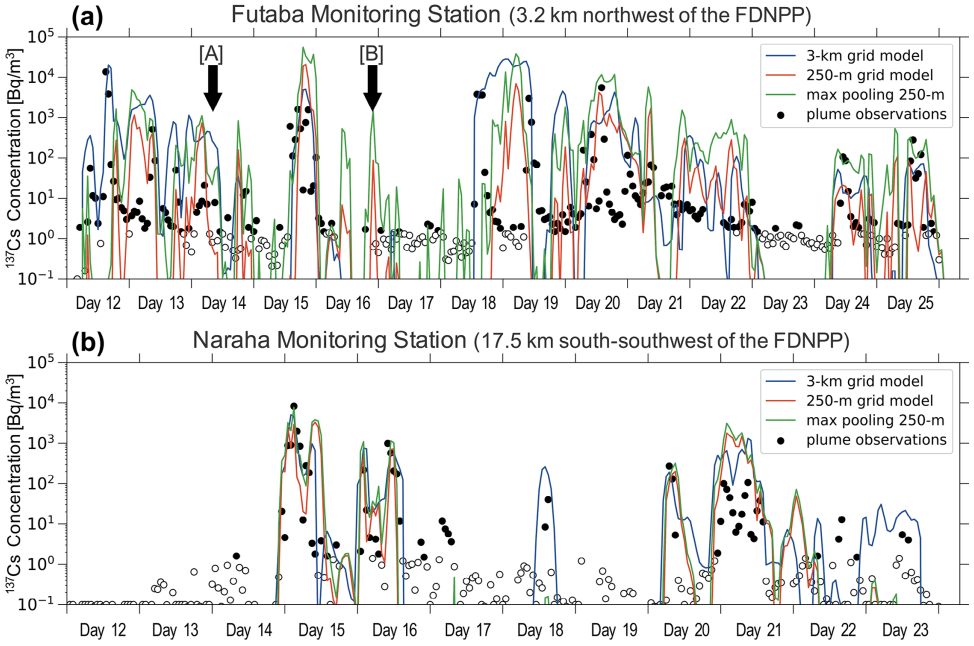

Fig. 2. Time series of the hourly averaged Cs-137 concentrations in March 2011 local time at the (a) Futaba monitoring station and (b) Naraha monitoring station. [A] and [B] indicate the snapshot times for Figs. 3a and 3b, respectively. Closed and open circles are observations defined as plumes (equal to or more than 1.5 Bq m^{-3}) and non-plumes (less than 1.5 Bq m^{-3}), respectively.

Bq m^{-3} using hourly averaged concentrations. The modeled concentrations were spatially linear-interpolated at each monitoring station. Sekiyama et al. (2017) and Sekiyama and Kajino (2020) utilized a threshold of 1.0 Bq m^{-3}; the reason why this study used a threshold of 1.5 Bq m^{-3} is described below.

The major leakage of radioactive substances caused by the Fukushima nuclear accident lasted for 2 or 3 weeks starting on March 12, 2011, the day after the great earthquake. Most of the plumes flowed offshore to the Pacific Ocean with the Siberian winter monsoon. Nakajima et al. (2017) reported that the time windows of onshore plumes were limited to less than 50 h in total. However, the plumes often reached both Futaba and Naraha, as reported by Tsuruta et al. (2018), as these stations are near the FDNPP along the Pacific Ocean coast. Tsuruta et al. (2018) reported that high Cs-137 concentrations were observed at Futaba intermittently at a local time (LT) between March 12 and March 25, 2011, and at Naraha intermittently (LT) between March 14 and March 23, 2011. The observed concentrations are presented in Fig. 2, where the closed (open) circles indicate the existence (nonexistence) of a plume defined by a threshold of 1.5 Bq m^{-3}.

The background concentration seems to be approximately 1 Bq m^{-3} at Futaba (Fig. 2a), which is probably due to equipment contamination and filter tape cross-contamination (cf. Tsuruta et al. 2014, 2018). The background concentration at Naraha is also higher than the detection limit (0.1 Bq m^{-3}) with a large deviation, in which the maximum values seem to exceed 1 Bq m^{-3} (Fig. 2b). This is also probably due to contamination and cross-contamination. Although turbulent diffusion may have partially influenced the background concentrations near the FDNPP, it is unnatural that the values did not fall below 1 Bq m^{-3}, even during time slots in which winds are strongly directed toward the ocean at the FDNPP. Therefore, the threshold of plume existence/nonexistence was defined as 1.5 Bq m^{-3} to avoid contamination errors at these two locations. The sensitivity of the statistical scores to the threshold value was small between 1.5 Bq m^{-3} and 3 Bq m^{-3}, although the scores evidently deteriorated with the threshold of 1 Bq m^{-3}.

In this study, the model performance was evaluated by the following statistical scores, namely, the proportion correct (PC), false alarm ratio (FAR), undetected error rate (UER), bias score (BS), and threat score (TS) (see Appendix). These statistics are based on

Table 1. Statistics (cf. Appendix) of each model at the Futaba monitoring station and the Naraha monitoring station.

		FO	XO	FX	XX	Proportion Correct	False Alarm Ratio	Undetected Error Rate	Bias Score	Threat Score
Futaba	3 km-grid model	140	48	41	122	0.75	0.23	0.26	0.96	0.61
	250 m-grid model	104	84	35	128	0.66	0.25	0.45	0.74	0.47
	Max pooling 250 m-grid model	139	49	67	96	0.67	0.33	0.26	1.10	0.55
Naraha	3 km-grid model	49	11	49	194	0.80	0.50	0.18	1.63	0.45
	250 m-grid model	41	19	23	220	0.86	0.36	0.32	1.07	0.49
	Max pooling 250 m-grid model	44	16	27	216	0.86	0.38	0.27	1.18	0.51

the occurrence of a binary event, in this study, the existence/nonexistence of a Cs-137 plume. Thus, a threshold was required to determine the plume arrival period. Plume arrivals can be detected by not only the concentration but also the radiation dose rate at each station. However, since the equipment for measuring the radiation dose rate is often seriously contaminated in the environment, especially after rainfall, concentration observations are favorable for detecting plumes with high temporal resolution (cf. Tsuruta et al. 2018). Unlike the observational plume arrivals, the modeled plume arrivals were easily detected without the influence of the threshold. This is because the plume edge concentration is increased by more than five orders of magnitude in the model simulations (cf. Iwasaki et al. 2019).

3. Results and discussion

3.1 Model simulations

Figure 2a presents the modeled concentrations at Futaba, which is located in the grid immediately next to the grid of the FDNPP in the 3-km grid model. The 3-km grid model (blue lines) and 250-m grid model (red lines) are often synchronized with each other. However, the concentration spikes in the 3-km grid model tend to be broader than those in the 250-m grid model. In other words, the plumes tend to stay for a longer time in the 3-km grid model than in the 250-m grid model upon their arrival. This tendency is expected as low-resolution Eulerian models experience large numerical diffusion near emission sources. Moreover, at Naraha (five times farther from the FDNPP than Futaba), the synchronization between the 3-km and 250-m grid models is less prominent, as presented in Fig. 2b. The plumes in the 3-km grid model evidently arrive more often at Futaba than at Naraha. This is mainly due to the large numerical diffusion of the 3-km grid model. Note that both models tend to overestimate the concentration at Futaba (nearer to the FDNPP), which is probably due to the model's dynamic errors rather than the emission scenario error, as the models are less likely to overestimate the concentration at Naraha.

Within the time windows presented in Figs. 2a and 2b, the statistical scores were calculated for Futaba and Naraha (Table 1). At Futaba, the PC is higher for the 3-km grid model as the UER (the number of strikeouts while looking, if using a baseball analogy) is much lower. In this case, since the FARs (the number of strikeouts while swinging, if using a baseball analogy) are similar between the 3-km and 250-m grid models, a lower UER results in a higher PC. The lower UER is due to the larger numerical diffusion of the 3-km grid model. Since the BS is smaller than 1 for the 250-m grid model, the horizontal diffusion in the models might be weaker than that in reality. This is because the model probably underestimates the frequency of high-concentration events when the BS is much smaller than 1.

In contrast, at Naraha, the 250-m grid model has a slightly higher PC than the 3-km grid model. In this case, the 3-km grid model has a much lower UER but a much higher FAR due to large numerical diffusion, as half of the alarms are false ("the boy who cried wolf" events). Consequently, the BS value is inflated, and the TS value deteriorates in the 3-km grid model. The combination of a high BS and a low TS leads to people adopting a normalcy bias, which is not appropriate for an EER model. Conversely, super high-resolution models generally tend to have a high UER due to the narrowness of plumes, which is also not appropriate for an EER model. Therefore, plume augmentation, or image processing for model results, might raise the statistical scores when using super high-resolution models. Such processing is described and evaluated in the next section.

3.2 Max pooling model

To augment the plume widths, a max pooling process was applied to the 250-m grid model result. At each grid point, an alternative value was sampled by taking the maximum value inside of a circle with a radius of 1.5 km from the grid point. This process is equivalent to the max-pooling layer of an artificial neural network with a 1-grid stride and a 12-grid pooling size. In the output distributions, the plumes were broadened to be comparable to the 3-km grid plumes. The time series of the concentrations and statistical scores for the max-pooling 250-m grid model are presented in Fig. 2 indicated by green lines and listed in Table 1, respectively.

As presented in Fig. 2a, compared with the original 250-m grid model, the plumes arrive more frequently at Futaba (nearer to the FDNPP) in the max-pooling model, and the concentration spikes are evidently broader and higher for the max-pooling model. Consequently, the BS value is improved, and the UER value is successfully decreased to the level of the 3-km grid model (see the rows for Futaba in Table 1). In the case of the original 250-m grid model, the BS value was much smaller than 1 as FO was small while (FO + XO) was large. Therefore, the improvement in the BS indicates the increase in FO, which results in the improvement in the TS. Although the improvement in the PC is small because of the deterioration in the FAR, the TS value is significantly improved from 0.47 to 0.55. In contrast, the difference between the original and max-pooling 250-m grid models is very small at Naraha, as presented in Fig. 2b. This is probably because Naraha is farther from the FDNPP than Futaba, and thus, the pooling size (1.5-km radius) is relatively small in comparison with the plume width or distance between the plumes and Naraha. Consequently, there is slight improvement in the PC and FAR (see the rows for Naraha in Table 1). However, since the UER value is slightly improved, the TS value increases from 0.49 to 0.51. Note that the TS is higher than 0.5 for the max-pooling 250-m grid model at both stations, which is relatively good in comparison with the operational scores of heavy rain (> 10 mm h^{-1}) weather forecasts (cf. Appendix).

The scores were improved by the max-pooling process, especially at Futaba (nearer to the FDNPP). These improvements are presented in Fig. 3 for two time slots, [A] and [B], indicated in Fig. 2a. At time [A], the 3-km grid model successfully simulates the observed high concentration, but the original 250-m grid model fails with a sharp drop in its concentration (see Fig. 2a). In this case, as presented in Fig. 3a, while the 3-km grid plume spreads over the monitoring station with large numerical diffusion, the original 250-m grid plume slightly misses covering the monitoring station. Since the difference between the 3-km and 250-m grid surface wind fields is small around the FDNPP, the plume coverage mainly depends on the magnitude of numerical diffusion. In contrast, the edge of the max-pooling 250-m grid plume successfully covers the monitoring station.

At time [B], while the 3-km grid model completely fails, the original 250-m grid model almost successfully simulates the observed high concentration (see Fig. 2a). However, since the observed concentration rapidly fluctuates, the original 250-m grid model regrettably fails with a very small time lag. In this case, as presented in Fig. 3b, the 3-km grid plume misses covering the monitoring station as the surface wind around the FDNPP continuously flows in one direction opposite to the monitoring station. However, in the 250-m grid model, the surface wind around the FDNPP is not homogeneous and instead follows the complicated terrain near the FDNPP. Consequently, while the prevailing wind is in the opposite direction to the monitoring station, the fluctuating edge of the plume sometimes covers the monitoring station. Even if the timing of plume intrusion at Futaba is slightly lagged in the original 250-m grid model, the augmented plume constantly covers Futaba in the max-pooling 250-m grid model, which provides a lower UER (but a higher FAR) and a better TS.

This study examined the concentration data from two monitoring stations located along the Pacific coast (not in a mountainous region) in the vicinity of the FDNPP (only 3.2 km and 17.5 km distant). The topographical difference was one of the reasons why the higher-resolution model did not perform overwhelmingly better than the lower-resolution model in this study. Previous studies (Sekiyama et al. 2015; Sekiyama and Kajino 2020) mainly focused on inland complex terrain. Although the 3-km grid model could not reproduce the details of the wind direction and plume dispersion near the FDNPP (e.g., at time [B]), the low-resolution model was superior to the original 250-m grid model at Futaba due to the large numerical diffusion therein. This empirical knowledge is not trivial for the construction of EER systems. In addition, a max-pooling (or plume augmentation) process is probably beneficial to high-resolution EER systems. However, the optimal pooling size (or plume augmentation width) depends on the situation. In this study, 4-grid (500-m radius) and 40-grid (5-km radius) pooling sizes were also tested (not shown), but the 12-

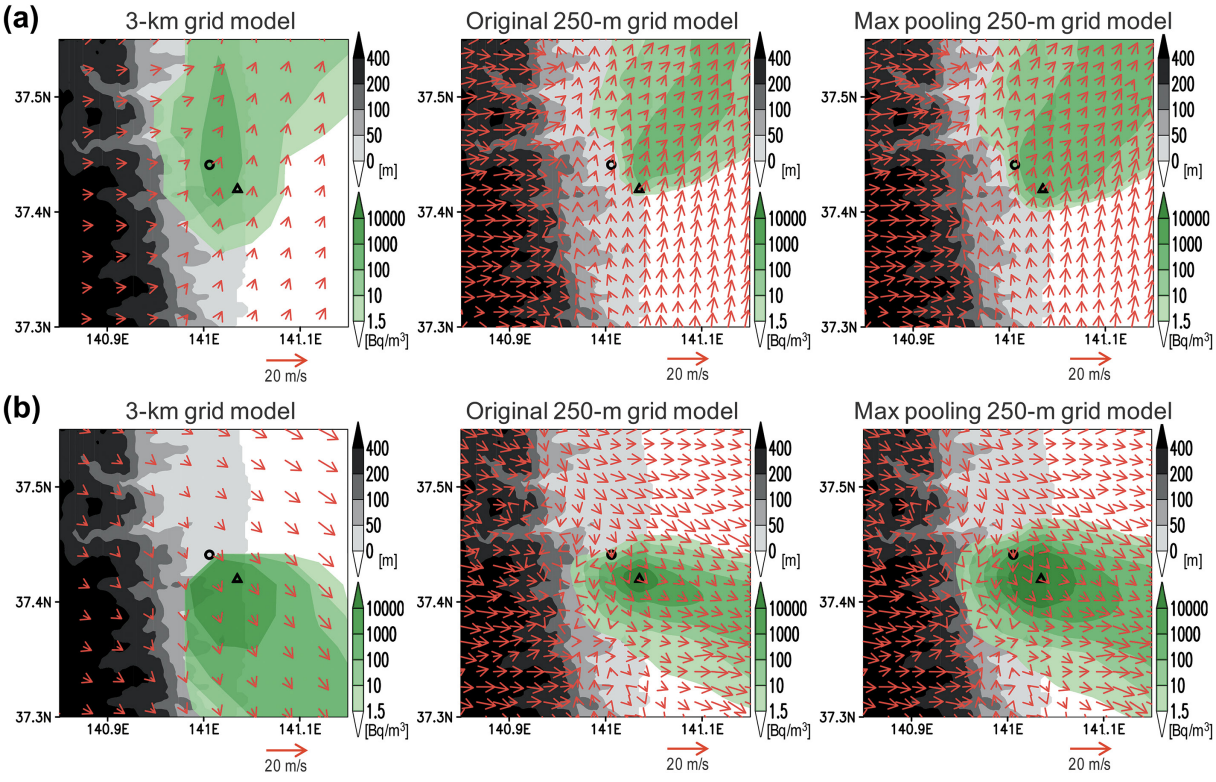

Fig. 3. Hourly averaged surface Cs-137 concentrations (green shading) and lowermost layer winds (red arrows) near Futaba and the FDNPP calculated using the models at (a) 0800–0900 local time on March 14, 2011, and (b) 2100–2200 local time on March 16, 2011. The 250-m grid winds are plotted every 6 grids (1.5 km). Gray shading indicates the elevation used in the 250-m grid models. The open triangle indicates the FDNPP. The open circle indicates the Futaba monitoring station.

grid (1.5-km radius) pooling size employed above was superior to the other options.

4. Conclusion

Generally, large numerical diffusion near an emission source is a disadvantage of Eulerian dispersion models, as increasing numerical diffusion increases the FAR (the number of strikeouts while swinging). Fortunately, this drawback, however, will decrease the UER (the number of strikeouts while looking). This characteristic is suitable for EER systems. We demonstrated that the performance of the 3-km grid model at Futaba (very close to the FDNPP) is better than that of the original 250-m grid model. On the one hand, it is scientifically important to determine the causes of plume errors on a case-by-case basis. On the other hand, it is technically troublesome that such a tiny plume location error can cause the pollutant concentration to not exceed a warning threshold. Therefore, it would be ideal for EER systems to use high-resolution models with augmented plumes, i.e., the max-pooling process. Note that high-resolution models are able to simulate the wind and dispersion fields affected by complex terrain in detail, as presented in Fig. 3b. In addition, plume augmentation effectively masks short time lags and small plume drifts in sub-kilometer-scale high-resolution models. Unfortunately, the computational burden is, however, theoretically $12 \times 12 \times 12 = 1728$ times different between the 3-km and 250-m grid models when compared in the same area according to the Courant–Friedrichs–Lewy (CFL) condition. Therefore, enhancing the model resolution to the sub-kilometer-scale is not cost-effective, considering the available computational resources as of 2021. The operationalization of sub-kilometer-scale dispersion models will be a future issue in the construction of EER systems.

Data availability statement

The 3-km and 250-m grid model data for both the meteorological and dispersion simulations are available upon request to the corresponding author. The authors obtained the Cs-137 observation data from Tsuruta et al. (2018) in text-file format upon request. The numerical model source codes used in this study are available under a collaborative framework between MRI and related institutes/universities.

Acknowledgments

This work was supported by the Environment Research and Technology Development Fund (1-1802) at the Environmental Restoration and Conservation Agency and by JSPS KAKENHI Grant Numbers JP17K00533, JP19H01155, and 21H03593.

Appendix

This appendix highlights the statistical indices referenced in this study. First, we define the following:

FO is the number of positive simulations and positive observations (correct hits),

XO is the number of negative simulations but positive observations (misses),

FX is the number of positive simulations but negative observations (false alarms), and

XX is the number of negative simulations and negative observations (correct rejections),

where positive simulations/observations indicate high Cs-137 concentrations (equal to or more than 1.5 Bq m^{-3}) in this study.

The proportion correct (PC) is the ratio of the number of correct events (hits and rejections) to the number of total events, defined by

$$\mathrm{PC} \equiv \frac{\mathrm{FO}+\mathrm{XX}}{\mathrm{FO}+\mathrm{XO}+\mathrm{FX}+\mathrm{XX}}, \quad (0 \le \mathrm{PC} \le 1).$$

A higher PC indicates higher model performance, especially when the number of positive observations is comparable to the number of negative observations.

The false alarm ratio (FAR) is the ratio of the number of false alarm events to the number of positive simulations, defined by

$$\mathrm{FAR} \equiv \frac{\mathrm{FX}}{\mathrm{FO}+\mathrm{FX}}, \quad (0 \le \mathrm{FAR} \le 1).$$

Cases with a high FAR are likened to "the boy who cried wolf" (or the number of strikeouts while swinging). Therefore, a lower FAR is better to prevent people from adopting a normalcy bias.

The undetected error rate (UER) is the ratio of the number of missed events to the number of positive observations, defined by

$$\mathrm{UER} \equiv \frac{\mathrm{XO}}{\mathrm{FO}+\mathrm{XO}}, \quad (0 \le \mathrm{UER} \le 1).$$

High-UER forecast models are apt to miss disasters (strikeout while looking), which is not desirable for an emergency management system.

The bias score (BS) is the ratio of the number of positive simulations to the number of positive observations, defined by

$$\mathrm{BS} \equiv \frac{\mathrm{FO}+\mathrm{FX}}{\mathrm{FO}+\mathrm{XO}}, \quad (0 \le \mathrm{BS}).$$

If the frequency of positive simulations is equal to that of positive observations, the BS is unity, which is the best score. The models with a high FAR (the models that "cry wolf") are more apt to yield a much higher BS than 1.

The threat score (TS) is the ratio of the number of correct hit events to the number of events other than correct rejections, defined by

$$\mathrm{TS} \equiv \frac{\mathrm{FO}}{\mathrm{FO}+\mathrm{FX}+\mathrm{XO}}, \quad (0 \le \mathrm{TS} \le 1).$$

The TS is often referred to as the critical success index (CSI). When the number of negative observations is increased, such as no rain or no tornado, XX (the number of correct rejections) tends to be large. In that case, the PC approaches unity and is less affected by the informative values, namely, FO, FX, and XO. In contrast, the TS excludes correct rejection events and thus is applicable to validation with a large number of negative observations. While the best value of the TS is 1, the TS rarely approaches the best value. For example, operational TS values vary between 0.1 and 0.5 for heavy rain (> 10 mm h^{-1}) forecasts in Japan with 0-h or 3-h lead times (Japan Meteorological Agency 2019).

References

Bao, J., F. K. Chow, and K. A. Lundquist, 2018: Large-eddy simulation over complex terrain using an improved immersed boundary method in the Weather Research and Forecasting Model. *Mon. Wea. Rev.*, **146**, 2781–2797.

Goto, D., Y. Morino, T. Ohara, T. T. Sekiyama, J. Uchida, and T. Nakajima, 2020: Application of linear minimum variance estimation to the multi-model ensemble of atmospheric radioactive Cs-137 with observations. *Atmos. Chem. Phys.*, **20**, 3589–3607.

Hamer, P. D., S.-E. Walker, G. Sousa-Santos, M. Vogt, D.

Vo-Thanh, S. Lopez-Aparicio, P. Schneider, M. O. P. Ramacher, and M. Karl, 2020: The urban dispersion model EPISODE v10.0 – Part 1: An Eulerian and subgrid-scale air quality model and its application in Nordic winter conditions. *Geosci. Model Dev.*, **13**, 4323–4353.

Honda, Y., M. Nishijima, K. Koizumi, Y. Ohta, K. Tamiya, T. Kawabata, and T. Tsuyuki, 2005: A pre-operational variational data assimilation system for a non-hydrostatic model at the Japan Meteorological Agency: Formulation and preliminary results. *Quart. J. Roy. Meteor. Soc.*, **131**, 3465–3475.

Iwasaki, T., T. T. Sekiyama, T. Nakajima, A. Watanabe, Y. Suzuki, H. Kondo, Y. Morino, H. Terada, H. Nagai, M. Takigawa, H. Yamazawa, D. Quélo, and A. Mathieu, 2019: Intercomparison of numerical atmospheric dispersion prediction models for emergency response to emissions of radionuclides with limited source information in the Fukushima Dai-ichi Nuclear Power Plant accident. *Atmos. Environ.*, **214**, 116830, doi: 10.1016/j.atmosenv.2019.116830.

Japan Meteorological Agency, 2019: *Outline of the operational numerical weather prediction at the Japan Meteorological Agency, March 2019. Appendix to WMO technical progress report on the global data-processing and forecasting system and numerical weather prediction*. Japan Meteorological Agency, 229 pp. [Available at https://www.jma.go.jp/jma/jma-eng/jma-center/ nwp/outline2019-nwp/index.htm.]

Kajino, M., Y. Inomata, K. Sato, H. Ueda, Z. Han, J. An, G. Katata, M. Deushi, T. Maki, N. Oshima, J. Kurokawa, T. Ohara, A. Takami, and S. Hatakeyama, 2012: Development of the RAQM2 aerosol chemical transport model and predictions of the Northeast Asian aerosol mass, size, chemistry, and mixing type. *Atmos. Chem. Phys.*, **12**, 11833–11856.

Kajino, M., M. Ishizuka, Y. Igarashi, K. Kita, C. Yoshikawa, and M. Inatsu, 2016: Long-term assessment of airborne radiocesium after the Fukushima nuclear accident: Re-suspension from bare soil and forest ecosystems. *Atmos. Chem. Phys.*, **16**, 13149–13172.

Kajino, M., T. T. Sekiyama, A. Mathieu, I. Korsakissok, R. Périllat, D. Quélo, A. Quérel, O. Saunier, K. Adachi, S. Girard, T. Maki, K. Yumimoto, D. Didier, O. Masson, and Y. Igarashi, 2018: Lessons learned from atmospheric modeling studies after the Fukushima nuclear accident: Ensemble simulations, data assimilation, elemental process modeling, and inverse modeling. *Geochem. J.*, **52**, 85–101.

Kajino, M., M. Deushi, T. T. Sekiyama, N. Oshima, K. Yumimoto, T. Tanaka, J. Ching, A. Hashimoto, T. Yamamoto, M. Ikegami, A. Kamada, M. Miyashita, Y. Inomata, S. Shima, A. Takami, A. Shimizu, S. Hatakeyama, Y. Sadanaga, H. Irie, K. Adachi, Y. Zaizen, Y. Igarashi, H. Ueda, T. Maki, and M. Mikami, 2019a: NHM-Chem, the Japan Meteorological Agency's regional meteorology-chemistry model: Model evaluations toward the consistent predictions of the chemical, physical, and optical properties of aerosols. *J. Meteor. Soc. Japan*, **97**, 337–374.

Kajino, M., T. T. Sekiyama, Y. Igarashi, G. Katata, M. Sawada, K. Adachi, Y. Zaizen, H. Tsuruta, and T. Nakajima, 2019b: Deposition and dispersion of radiocesium released due to the Fukushima nuclear accident: Sensitivity to meteorological models and physical modules. *J. Geophys. Res.: Atmos.*, **124**, 1823–1845.

Katata, G., M. Chino, T. Kobayashi, H. Terada, M. Ota, H. Nagai, M. Kajino, R. Draxler, M. C. Hort, A. Malo, T. Torii, and Y. Sanada, 2015: Detailed source term estimation of the atmospheric release for the Fukushima Daiichi Nuclear Power Station accident by coupling simulations of an atmospheric dispersion model with an improved deposition scheme and oceanic dispersion model. *Atmos. Chem. Phys.*, **15**, 1029–1070.

Kunii, M., 2014: Mesoscale data assimilation for a local severe rainfall event with the NHM–LETKF system. *Wea. Forecasting*, **29**, 1093–1105.

Lateb, M., R. N. Meroney, M. Yataghene, H. Fellouah, F. Saleh, and M. C. Boufadel, 2016: On the use of numerical modelling for near-field pollutant dispersion in urban environments – A review. *Environ. Pollut.*, **208**, 271–283.

Li, H., G. Cui, and Z. Zhang, 2018: A new scheme for the simulation of microscale flow and dispersion in urban areas by coupling large-eddy simulation with mesoscale models. *Bound.-Layer Meteor.*, **167**, 145–170.

Mathieu, A., M. Kajino, I. Korsakissok, R. Périllat, D. Quélo, A. Quérel, O. Saunier, T. T. Sekiyama, Y. Igarashi, and D. Didier, 2018: Fukushima Daiichi–derived radionuclides in the atmosphere, transport and deposition in Japan: A review. *Appl. Geochem.*, **91**, 122–139.

Miyoshi, T., and K. Aranami, 2006: Applying a four-dimensional local ensemble transform Kalman filter (4D-LETKF) to the JMA nonhydrostatic model (NHM). *SOLA*, **2**, 128–131.

Nakajima, T., S. Misawa, Y. Morino, H. Tsuruta, D. Goto, J. Uchida, T. Takemura, T. Ohara, Y. Oura, M. Ebihara, and M. Satoh, 2017: Model depiction of the atmospheric flows of radioactive cesium emitted from the Fukushima Daiichi Nuclear Power Station accident. *Prog. Earth Planet. Sci.*, **4**, 2, doi:10.1186/s40645-017-0117-x.

Nakanishi, M., and H. Niino, 2004: An improved Mellor–Yamada level-3 model with condensation physics: Its design and verification. *Bound.-Layer Meteor.*, **112**, 1–31.

Nakanishi, M., and H. Niino, 2006: An improved Mellor–Yamada level-3 model: Its numerical stability and application to a regional prediction of advection fog. *Bound.-Layer Meteor.*, **119**, 397–407.

Nakayama, H., T. Takemi, and H. Nagai, 2016: Devel-

opment of local-scale high-resolution atmospheric dispersion model using large-eddy simulation. Part 5: Detailed simulation of turbulent flows and plume dispersion in an actual urban area under real meteorological conditions. *J. Nucl. Sci. Tech.*, **53**, 887–908.

Oura, Y., M. Ebihara, H. Tsuruta, T. Nakajima, T. Ohara, M. Ishimoto, H. Sawahata, Y. Katsumura, and W. Nitta, 2015: A database of hourly atmospheric concentrations of radiocesium (^{134}Cs and ^{137}Cs) in suspended particulate matter collected in March 2011 at 99 air pollution monitoring stations in eastern Japan. *J. Nucl. Radiochem. Sci.*, **15**, 15–26.

Rood, R. B., 1987: Numerical advection algorithms and their role in atmospheric transport and chemistry models. *Rev. Geophys.*, **25**, 71–100.

Saito, K., T. Fujita, Y. Yamada, J. Ishida, Y. Kumagai, K. Aranami, S. Ohmori, R. Nagasawa, S. Kumagai, C. Muroi, T. Kato, H. Eito, and Y. Yamazaki, 2006: The operational JMA nonhydrostatic mesoscale model. *Mon. Wea. Rev.*, **134**, 1266–1298.

Saito, K., J. Ishida, K. Aranami, T. Hara, T. Segawa, M. Narita, and Y. Honda, 2007: Nonhydrostatic atmospheric models and operational development at JMA. *J. Meteor. Soc. Japan*, **85B**, 271–304.

Sato, Y., M. Takigawa, T. T. Sekiyama, M. Kajino, H. Terada, H. Nagai, H. Kondo, J. Uchida, D. Goto, D. Quélo, A. Mathieu, A. Quérel, S. Fang, Y. Morino, P. von Schoenberg, H. Grahn, N. Brännström, S. Hirao, H. Tsuruta, H. Yamazawa, and T. Nakajima, 2018: Model intercomparison of atmospheric ^{137}Cs from the Fukushima Daiichi Nuclear Power Plant accident: Simulations based on identical input data. *J. Geophys. Res.: Atmos.*, **123**, 11748–11765.

Sato, Y., T. T. Sekiyama, S. Fang, M. Kajino, A. Quérel, D. Quélo, H. Kondo, H. Terada, M. Kadowaki, M. Takigawa, Y. Morino, J. Uchida, D. Goto, and H. Yamazawa, 2020: A model intercomparison of atmospheric ^{137}Cs concentrations from the Fukushima Daiichi Nuclear Power Plant accident, phase III: Simulation with an identical source term and meteorological field at 1-km resolution. *Atmos. Environ.: X*, **7**, 100086, doi:10.1016/j.aeaoa.2020.100086.

Sekiyama, T. T., and T. Iwasaki, 2018: Mass flux analysis of ^{137}Cs plumes emitted from the Fukushima Daiichi nuclear power plant. *Tellus B*, **70**, 1–11.

Sekiyama, T. T., and M. Kajino, 2020: Reproducibility of surface wind and tracer transport simulations over complex terrain using 5-, 3-, and 1-km-grid models. *J. Appl. Meteor. Climatol.*, **59**, 937–952.

Sekiyama, T. T., M. Kunii, M. Kajino, and T. Shimbori, 2015: Horizontal resolution dependence of atmospheric simulations of the Fukushima nuclear accident using 15-km, 3-km, and 500-m grid models. *J. Meteor. Soc. Japan*, **93**, 49–64.

Sekiyama, T. T., M. Kunii, and M. Kajino, 2017: The impact of surface wind data assimilation on the predictability of near-surface plume advection in the case of the Fukushima nuclear accident. *J. Meteor. Soc. Japan*, **95**, 447–454.

Takagi, M., T. Ohara, D. Goto, Y. Morino, J. Uchida, T. T. Sekiyama, S. F. Nakayama, M. Ebihara, Y. Oura, T. Nakajima, H. Tsuruta, and Y. Moriguchi, 2020: Reassessment of early ^{131}I inhalation doses by the Fukushima nuclear accident based on atmospheric ^{137}Cs and ^{131}I/^{137}Cs observation data and multi-ensemble of atmospheric transport and deposition models. *J. Environ. Radioact.*, **218**, 106233, doi:10.1016/j.jenvrad.2020.106233.

Tsuruta, H., Y. Oura, M. Ebihara, T. Ohara, and T. Nakajima, 2014: First retrieval of hourly atmospheric radionuclides just after the Fukushima accident by analyzing filter-tapes of operational air pollution monitoring stations. *Sci. Rep.*, **4**, 6717, doi:10.1038/srep06717.

Tsuruta, H., Y. Oura, M. Ebihara, Y. Moriguchi, T. Ohara, and T. Nakajima, 2018: Time-series analysis of atmospheric radiocesium at two SPM monitoring sites near the Fukushima Daiichi Nuclear Power Plant just after the Fukushima accident on March 11, 2011. *Geochem. J.*, **52**, 103–121.

Wiersema, D. J., K. A. Lundquist, and F. K. Chow, 2020: Mesoscale to microscale simulations over complex terrain with the immersed boundary method in the Weather Research and Forecasting Model. *Mon. Wea. Rev.*, **148**, 577–595.

World Meteorological Organization, 2006: Environmental emergency response: WMO activities. *WMO Bull.*, **55**, 37–41.

atmosphere

MDPI

Article

Ensemble Dispersion Simulation of a Point-Source Radioactive Aerosol Using Perturbed Meteorological Fields over Eastern Japan

Tsuyoshi Thomas Sekiyama [1,*], Mizuo Kajino [1,2] and Masaru Kunii [3]

[1] Meteorological Research Institute, Tsukuba 3050052, Japan; kajino@mri-jma.go.jp
[2] Faculty of Life and Environmental Sciences, University of Tsukuba, Tsukuba 3058572, Japan
[3] Japan Meteorological Agency, Tokyo 1058431, Japan; mkunii@met.kishou.go.jp
* Correspondence: tsekiyam@mri-jma.go.jp

Abstract: We conducted single-model initial-perturbed ensemble simulations to quantify uncertainty in aerosol dispersion modeling, focusing on a point-source radioactive aerosol emitted from the Fukushima Daiichi Nuclear Power Plant (FDNPP) in March 2011. The ensembles of the meteorological variables were prepared using a data assimilation system that consisted of a non-hydrostatic weather-forecast model with a 3-km horizontal resolution and a four-dimensional local ensemble transform Kalman filter (4D-LETKF) with 20 ensemble members. The emission of radioactive aerosol was not perturbed. The weather and aerosol simulations were validated with in-situ measurements at Hitachi and Tokai, respectively, approximately 100 km south of the FDNPP. The ensemble simulations provided probabilistic information and multiple case scenarios for the radioactive aerosol plumes. Some of the ensemble members successfully reproduced the arrival time and intensity of the radioactive aerosol plumes, even when the deterministic simulation failed to reproduce them. We found that a small ensemble spread of wind speed produced large uncertainties in aerosol concentrations.

Keywords: probabilistic simulation; plume dispersion; data assimilation; ensemble spread; Fukushima nuclear accident; radioactive cesium

Citation: Sekiyama, T.T.; Kajino, M.; Kunii, M. Ensemble Dispersion Simulation of a Point-Source Radioactive Aerosol Using Perturbed Meteorological Fields over Eastern Japan. *Atmosphere* **2021**, *12*, 662. https://doi.org/10.3390/atmos12060662

Academic Editor: Chuen-Jinn Tsai

Received: 14 April 2021
Accepted: 19 May 2021
Published: 22 May 2021

1. Introduction

Ensemble simulation is a set of multiple numerical simulations that have slightly different initial conditions, boundary conditions, parameters, or models that are all geophysically plausible. Such a simulation enables the estimation of the predictability or reliability of the model simulation by providing a spread of ensemble forecasts. The simulation is most certain if the ensemble members are close to each other; otherwise, the ensemble provides a possible range of different events. Thus, probabilistic model information can be obtained from an ensemble simulation. Additionally, an ensemble simulation provides an ensemble average that is often more accurate than a deterministic single simulation because the model errors tend to be averaged out.

From a scientific viewpoint, the model predictability indicates not only the imperfection of simulation models but also the Lorenz's deterministic chaos of Earth systems. The error growth and propagation in the model simulation depend on the chaotic advection, diffusion, precipitation, thermodynamics, and chemistry, which all should be explored in detail. From a practical perspective, probabilistic model information complements deterministic model information, especially for atmospheric forecasts. Therefore, ensemble prediction systems (EPSs) have been developed worldwide by operational weather forecast centers. These systems have adopted initial-condition ensemble simulations that are suitable for error growth evaluation.

However, it is difficult to generate the ensemble perturbations of initial conditions because randomly chosen (Monte Carlo) perturbations are likely to fade away or fail to

grow through the simulations [1]. Therefore, more sophisticated perturbation methods are generally used for weather forecasts, e.g., the singular vector method or the ensemble Kalman filter method. The singular vector (SV) method was developed and implemented initially by the European Centre for Medium-range Weather Forecasting (ECMWF) [2]. This method inevitably requires the adjoint code of the forecast model. In contrast, the ensemble Kalman filter (EnKF) method, which is newer than the SV method, e.g., [3], does not require the adjoint code of the forecast model and hence has been used throughout this decade. In the EnKF method, the generation of initial perturbations is united with the data assimilation for building the initial conditions.

By contrast, atmospheric environmental EPSs have not been developed as extensively as weather EPSs, and hence the application of ensemble dispersion simulations (EDSs) has not been thoroughly explored. Most previous EDS studies were sensitivity tests validated by parameter/model ensembles, e.g., [4–8] that were relatively easily executable with a very small number of ensemble members, or they were Monte Carlo tests that were simply conducted with an offset modification of the initial/boundary conditions, e.g., [9–12]. Only a few EDS studies have been conducted with sophisticated initial perturbations, e.g., the ozone predictability experiments performed by Holt et al. [13] using an ensemble transform method, the CO_2 source/sink inversion experiments performed by Lauvaux et al. [14] using the SV method, the schematic dispersion experiments performed by Lattner and Cervone [15] using an ensemble particle filter method, and the global aerosol dispersion experiments performed by Haszpra et al. [16] using the ECMWF global ensemble forecasts.

Here, we have investigated the model uncertainty of a regional aerosol dispersion simulation with the meteorological initial perturbation generated by the EnKF. The knowledge of the dispersion model uncertainty will provide insight regarding what model configuration is suitable for scientific and operational model usage. Unfortunately, the dispersion model uncertainty has not been well explored with ensemble simulations because (1) it is difficult to prepare meteorological perturbations with sophisticated methods like the SV and EnKF methods and (2) even if ensemble simulations are performed, it is difficult to examine the probabilistic results in detail when tracer concentration observations and emission inventories are not sufficiently available.

Therefore, we introduced two original approaches to resolve these difficulties. (1) We generated the meteorological initial ensembles ourselves using an EnKF data assimilation system with an arbitrary model resolution and domain. (2) We examined the dispersion process of the radioactive aerosol tracer (Cs-137) stemming from a point source, i.e., the Fukushima Daiichi nuclear power plant (FDNPP). Point-source pollution data are ideal for the validation of dispersion models. Especially in the case of the FDNPP accident, the emission location is exactly identified, the emission time and strength can be estimated within a reasonable range to some extent, and the aerosol tracer concentration has been accurately observed using radiation measurements. The model uncertainty will be effectively investigated with these approaches. Meanwhile, the emission term was unperturbed and thus not investigated in this study.

2. Methodology

The EnKF is an approximate treatment of the Kalman filter for application to high-dimensional systems such as the atmosphere cf. [17,18]. The Kalman filter defines an analysis as an arithmetic weighted mean of forecasts and observations, imposing a minimum variance estimation of the analysis error on the weight optimization [19]. We simultaneously obtain data assimilation products (i.e., analysis) and perturbations (i.e., ensemble members) by repeating the EnKF procedure. The analysis is the mean of the ensemble members. The perturbations generated by the EnKF are qualitatively superior to a random perturbation because they reflect the model uncertainty distribution and are flow-dependent, similar to the SV method. Furthermore, Wang et al. [20] reported that when the ensemble size is small, the EnKF method has a statistical advantage because the other methods consistently generate symmetric positive–negative paired ensemble mem-

bers to keep the average value and thus cannot make statistical full use of the ensemble dimension. In contrast, the EnKF does not generate symmetric pairs but keeps the overall average. While the EnKF has several numerical implementation methods, the square root EnKF is implemented in this study. In the square root EnKF, each ensemble member retains its identity through the data assimilation cycle because its relative position in the state space among the ensemble members is invariant.

Prior to calculating the radioactive aerosol dispersion, we prepared the ensemble analysis and forecast of the meteorological variables to drive the dispersion model using an EnKF data assimilation system that was developed by Kunii [21]. This data assimilation system consists of the local ensemble transform Kalman filter (LETKF), i.e., one of the square root EnKF implementations [22], and the Japan Meteorological Agency's non-hydrostatic regional weather forecast model (JMA-NHM) [23,24]. The LETKF method has been applied to weather forecast modeling, e.g., [21,25–30] and tracer dispersion modeling, e.g., [31–41].

In this study, the model domain covered eastern Japan as shown in Figure 1 and its horizontal resolution was set to 3 km, which represented a typical grid scale for the regional simulations implemented for the FDNPP accident cf. [37,39]. The model settings, such as map projection, vertical coordinate, turbulence scheme, convective scheme, and terrain features, were the same as those of the 3-km grid simulation performed by Sekiyama et al. [37,39]. The domain consists of 215 $\times$ 259 horizontal grid points in the Lambert conformal projection and 60 vertical levels including 11 levels below 1 km above ground level. The terrain features were generated from the global digital elevation data with a horizontal grid spacing of 30 arc seconds (GTOPO30) provided from the U.S. Geological Survey. The turbulence scheme was based on the improved Mellor-Yamada level 3 closure model [42,43]. A cumulus parameterization was not used in this study.

The data assimilation system was initiated at 06:00 UTC on 10 March 2011 with 20 ensemble members and a 3-h time window. The assimilation settings, such as time slots (3 h), prognostic variables (three wind components, temperature, pressure, water vapor mixing ratio, and water/ice microphysics variables), inflation scheme (adaptively multiplicative factors at each grid point), and covariance localization ($1/e^{0.5}$ within 150 km in the horizontal and 0.2 natural-logarithmical p-coordinate in the vertical), were the same as those of the 3-km grid simulation performed by Sekiyama et al. [37,39]. We obtained the initial condition and the boundary conditions from the JMA operational global 15-km grid analysis.

We assimilated JMA's operational observation dataset, which was integrated and quality-controlled for the JMA mesoscale Non-hydrostatic-model four-dimensional Variational data Assimilation system (JNoVA) [44], similarly to Kunii [21] and Sekiyama et al. [37]. Additionally, we assimilated surface wind observations acquired by the Automated Meteorological Data Acquisition System (AMeDAS) similarly to Sekiyama et al. [39]. AMeDAS is a nationwide meteorological observation network managed by JMA. The data assimilation system generated 20 ensemble members every 3 h (hereafter called ensemble analysis members) and simultaneously calculated the mean value of the ensemble members as a deterministic analysis. The forecasts were calculated by the identical JMA-NHM using these 20 ensemble members and a deterministic analysis as the initial conditions. Hereafter, these forecasts are called ensemble forecast members and a deterministic forecast, respectively.

Using the meteorological analysis or forecast outputs, Eulerian dispersion simulations were conducted with the Regional Air Quality Model version 2 (RAQM2) [45–50]. All of the radioactive Cs-137 was contained in sulfate-organics-mixed aerosol particles when it was transported in the atmosphere. The details of the modeled aerosol physics are described in work of Kajino et al. [46] and Sekiyama et al. [37,39]. Note that the RAQM2 used in this study implements simplified aerosol dynamics compared with those of Kajino et al. [46] by assuming perpetual particle size distribution similarly to Sekiyama et al. [37,39]. The combination of the JMA-NHM, the LETKF, the JNoVA+AMeDAS ob-

servations, and the RAQM2 has been successfully used for the Fukushima radioactive pollution simulation [37,39–41,51–54].

We used the emission scenario of the radioactive Cs-137, which was released from the FDNPP, estimated by the Japan Atomic Energy Agency (JAEA) [55–57]. Cs-containing sulfate-organics-mixed aerosol particles [58] were injected at every time step into a grid cell above the FDNPP. The emission scenario has been revised by JAEA several times after 2012, e.g., [59]. However, the difference between the previous ones and the revised ones is not very large in comparison with the dispersion model uncertainty (i.e., ensemble spread) of Cs-137 concentrations in this study. Since we focus on the quantification of the dispersion model uncertainty, the revision of the Cs-137 emission scenario scarcely affects the results of the uncertainty evaluation in this study.

The data assimilation cycle and the dispersion simulations were performed continuously from 11 March to 1 April 2011. The "analysis" run contained 20 ensemble simulations and one deterministic simulation. Although the analysis is only provided every 3 h, the dispersion simulations require the meteorological variables at much smaller time intervals. Therefore, the meteorological variables were generated between the 3-h analysis points by the 3-h forecast runs using the identical JMA-NHM. The variables were stored at every 10 min of simulation time and inputted into the RAQM2, and the variables were linearly interpolated during each 10-min interval. Additionally, we performed a "forecast" run for 24 h in two specific periods (15 March and 21 March, see Section 3). Each forecast was started at 21:00 local time (JST) of the previous day using the "analysis" run as the initial condition. The "forecast" run also contained 20 ensemble simulations and one deterministic simulation.

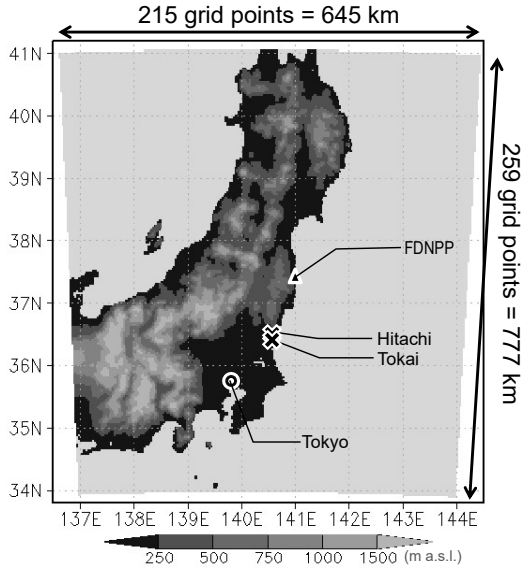

Figure 1. Model domain of the JMA-NHM and the RAQM2 used in this study, in which the model resolution is 3 km. The distance between the Fukushima Daiichi nuclear power plant (FDNPP) and Tokai is approximately 100 km.

3. Results and Discussion

Here, we focused on March 15 (Period 1) and 21 (Period 2), 2011 local time to investigate the radioactive plumes that were carried landward. Nakajima et al. [60] pointed out that the plume intrusion inland occurred twice on a large scale; i.e., 15 March and 20–21 March. The comparison of the radioactive aerosol concentration was performed at the model grid corresponding to the location of Tokai, where JAEA has been operationally monitoring radionuclide concentrations and clearly detected highly radioactive plumes on both 15 and 21 March, 2011 [61]. The JAEA Tokai facilities are located approximately 100 km south of the FDNPP (Figure 1). The meteorological components were compared

at the model grid corresponding to the location of Hitachi (Figure 1), where the nearest AMeDAS station (10 km north) to Tokai was located.

3.1. Period 1 (15 March 2011)

Figure 2a shows the time series of the meteorological ensemble analysis at the model surface layer (below 40 m) of the Hitachi AMeDAS station from 21:00 14 March to 21:00 15 March 2011 JST. The ensemble members are illustrated with the deterministic analysis, AMeDAS observations, and the JMA operational 5-km gridded analysis. The wind speed (u and v) ensemble had a small spread and was almost synchronized with the JMA operational analysis winds. The wind errors of the analysis members (i.e., the distance from filled circles to a bunch of black lines) were larger than the difference between the wind ensemble members (i.e., the spread width of a bunch of black lines). Figure 2b shows the forecast (initiated at 21:00 14 March 2011 JST) in which the wind ensemble had a large spread. However, the wind forecast spread was still smaller than the wind forecast error (i.e., the averaged distance from filled circles to a bunch of black lines).

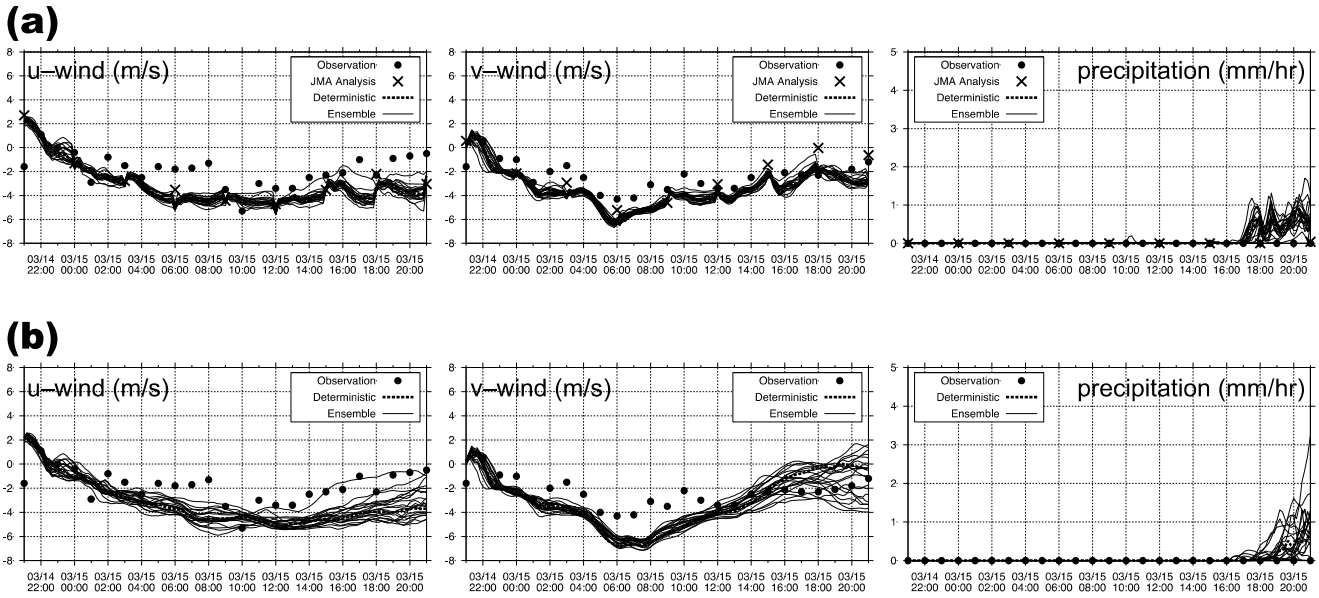

Figure 2. (**a**) Ensemble analysis members and a deterministic analysis member of east-west wind (u component), north-south wind (v component), and precipitation at the model surface layer (below 40 m) of the grid corresponding to Hitachi from 21:00 14 March to 21:00 15 March local time. (**b**) Same as (**a**) except for forecast members, which were initiated at 21:00 14 March local time. Circles indicate AMeDAS observations. Crosses indicate the JMA operational 5 km gridded analysis for the daily weather forecast.

The Cs-137 concentrations at the model surface layer (below 40 m) of the Tokai JAEA station are shown in Figure 3a with the JAEA observations from 21:00 14 March to 21:00 15 March 2011 JST. In contrast to the wind speed ensemble, the Cs-137 ensemble concentrations had a large spread. Some of the ensemble members successfully represented the real peak concentration but failed to represent the peak timing, appearing two hours early. The deterministic analysis underestimated the real concentration. In Figure 3b, the Cs-137 forecast members presented a larger ensemble spread for the concentration. Some of the Cs-137 forecast members presented large overestimations before and after the peak.

In this period, the radioactive aerosol plume projected from the FDNPP to the south, coastwise, and then swept across Tokai (Figure 4). The percentile distribution of the 20 ensemble members was narrow in the analysis (Figure 4a) but relatively broad in the forecast (Figure 4b), which was in agreement with the time series of the ensemble analysis/forecast concentrations at Tokai that are shown in Figure 3. The threshold (15 Bq/m^3) used here was defined as the half value of the air quality standard of Japan's radioisotope regulations.

The percentile distribution of aerosol concentrations can be usefully applied to probabilistic forecasts such as the chance-of-rain forecast. The probabilistic forecasts provide multiple scenarios for environmental pollution or disasters. Generally, the accuracy of the forecast decreases with time, and consequently the percentile distribution tends to diffuse with time. Figure 4 shows that the forecast percentile distributions were very similar to the analysis percentile distributions in the short forecasts (02:00 15 March and 06:00 15 March), indicating the high accuracy of the forecast. However, the distributions were less similar in the longer forecast (10:00 15 March), in which the forecast percentile distribution was diffused.

The ensemble analysis of the surface wind speed (u and v) exhibited a relatively small spread, which was usually less than 1 m/s even though the analysis errors (i.e., analysis minus observation) were generally 1 or 2 m/s. For example, the relative standard deviation (RSD) of the ensemble analysis for the specific 4 h during Period 1 (02:00–08:00 15 March) was 5% on average (Table 1). By contrast, the ensemble of the surface Cs-137 concentration had a large spread, in which some members occasionally presented almost zero concentrations, whereas others presented very high concentrations. The RSD of the Cs-137 concentration analysis for the same time periods was 93 % on average (Table 1). This result indicates that a small ensemble spread in meteorology produces a large ensemble spread for aerosol concentration. Thus, the uncertainty on the concentration is amplified in comparison with that on the wind field.

The ensemble forecast exhibited the same behavior as the analysis. The ensemble spread was relatively small in the meteorological simulation and very large in the dispersion simulation. The forecast RSD of the wind speed for the same time periods mentioned above (02:00–08:00 15 March) was 7% on average (Table 1). In contrast, the forecast RSD of the Cs-137 concentration was 82% (Table 1). A comparison of the analysis and forecast RSDs indicates that the errors of the dispersion models are not linearly correlated with the errors of the meteorological models.

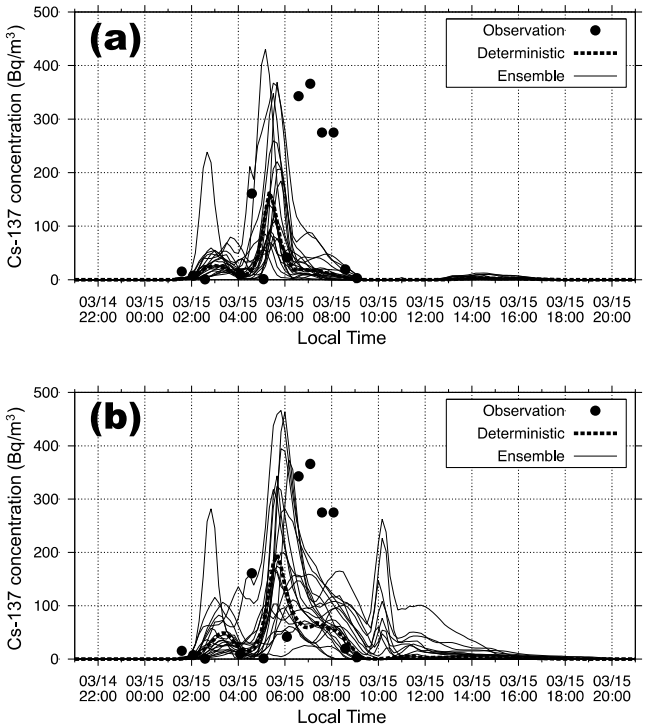

Figure 3. (**a**) Ensemble analysis members and a deterministic analysis member of Cs-137 concentration at the model surface layer (below 40 m) of the grid corresponding to Tokai from 21:00 14 March to 21:00 15 March local time. (**b**) Same as (**a**) except for forecast members, which were initiated at 21:00 14 March local time. Circles indicate the measurements at Tokai.

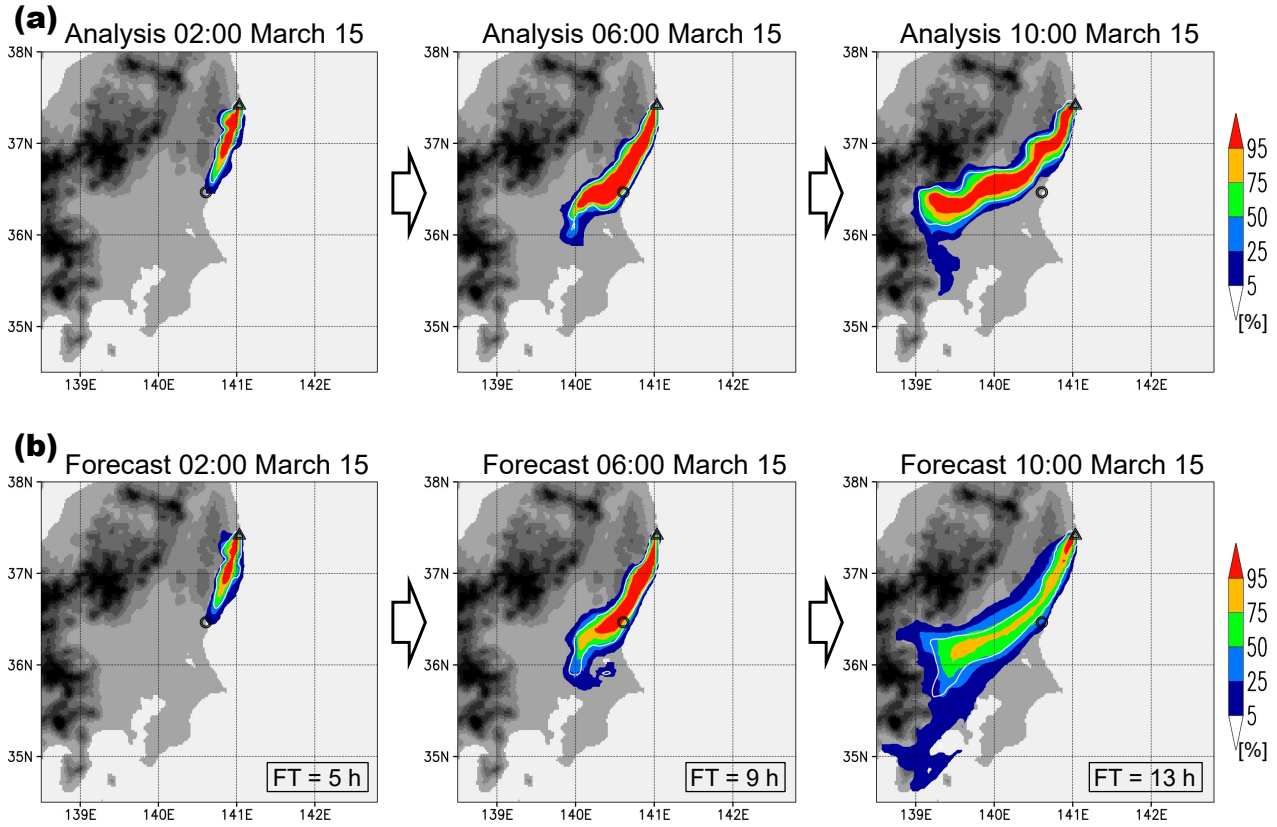

Figure 4. (**a**) Percentile distributions of the 20 ensemble analysis members, where the surface Cs-137 concentration is higher than the threshold (15 Bq/m^3). White contour lines indicate the 15 Bq/m^3 concentration of the deterministic analysis member. The open triangle and circle illustrate the locations of the FDNPP and Tokai, respectively. The local time of the snapshots was 2:00, 6:00, and 10:00 on 15 March, respectively. (**b**) Same as (**a**) except for the forecast, which was initiated at 21:00 14 March local time. The forecast duration was 5, 9, and 13 h, respectively.

Table 1. Relative Standard Deviations (RSD) [a] of the 20-member Ensembles.

	2:00–8:00 15 March		4:00–10:00 21 March	
	Analysis	**Forecast**	**Analysis**	**Forecast**
Wind speed	5%	7%	10%	23%
Cs-137 concentration	93%	82%	77%	235%

[a] RSD was calculated for the specified 4 h during Period 1 or Period 2 at Hitachi (wind speed) or Tokai (Cs-137 concentration).

3.2. Period 2 (21 March 2011)

In comparison with Period 1, the ensemble spreads tended to be larger in Period 2. Figure 5 shows time series of the meteorological ensembles at the Hitachi AMeDAS station similar to those in Figure 2 but for the time period from 21:00 20 March to 21:00 21 March, 2011 JST. Note that it was raining or snowing on this day in a wide area of eastern Japan. As seen in Figure 5b, the ensemble forecast (initiated at 21:00 20 March 2011 JST) presented chaotic motions of the wind speed (u and v). Furthermore, the ensemble spread of the precipitation forecast was extremely large.

The time series of the Cs-137 concentrations at the Tokai JAEA station are shown in Figure 6 similar to those in Figure 3, except that they are in the time period from 21:00 20 March to 21:00 21 March 2011 JST. The ensemble spreads were very large, similar to those in Period 1. As shown in Figure 6a, the deterministic analysis failed to represent the peak timing with a two-hour delay. However, some of the ensemble analysis members successfully represented the real peak timing and concentration. In contrast to the deterministic analysis, the deterministic forecast completely failed to represent the plume arrival

(Figure 6b). Many of the ensemble forecast members behaved similarly to the deterministic forecast. This failure was caused by the wet deposition (below-cloud scavenging) that occurred before the plume arrived at Tokai in the forecast simulations.

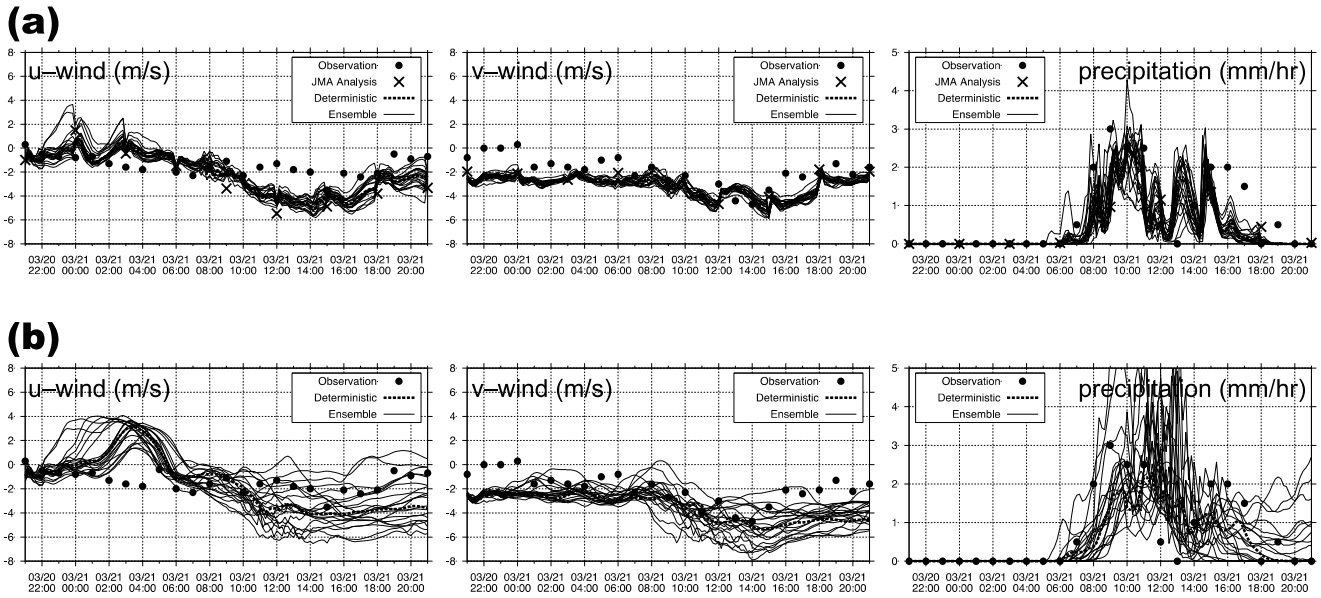

Figure 5. Same as Figure 2 but for the time period from 21:00 20 March to 21:00 21 March local time. The forecasts were initiated at 21:00 20 March local time.

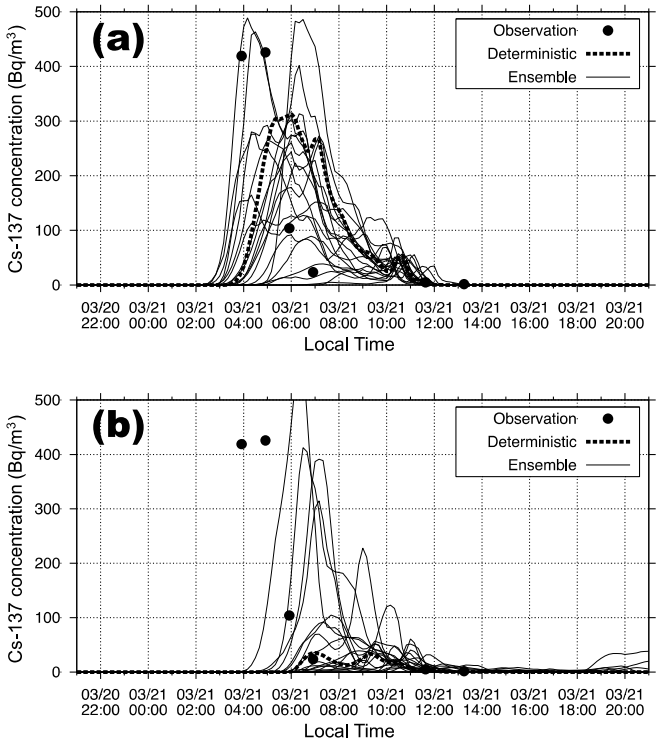

Figure 6. Same as Figure 3 but for the time period from 21:00 March 20 to 21:00 21 March local time. The forecasts were initiated at 21:00 20 March local time.

In Period 2, the RSD of the wind speed analysis for the specified 4 h (04:00–10:00 21 March) was 10% on average (Table 1). However, the RSD of the Cs-137 concentration analysis for the same time periods was 77% on average (Table 1). These scores also indicate that the uncertainty on the concentration is amplified as shown in Period 1. This

finding implies that if we deterministically pursue an accurate dispersion, it is necessary to unrealistically increase the accuracy of the meteorological simulation. As expected, the percentile distributions of the Cs-137 concentration (Figure 7) tended to be broader than those in Period 1 in both the analysis and forecast before raining (approximately 08:00 JST). The percentile distributions rapidly shrank after the rain because the radioactive aerosols were deposited through precipitation. In the forecast, the precipitation area or timing was slightly shifted from the actual values, and consequently, the distribution of wet deposition was inadequately distorted.

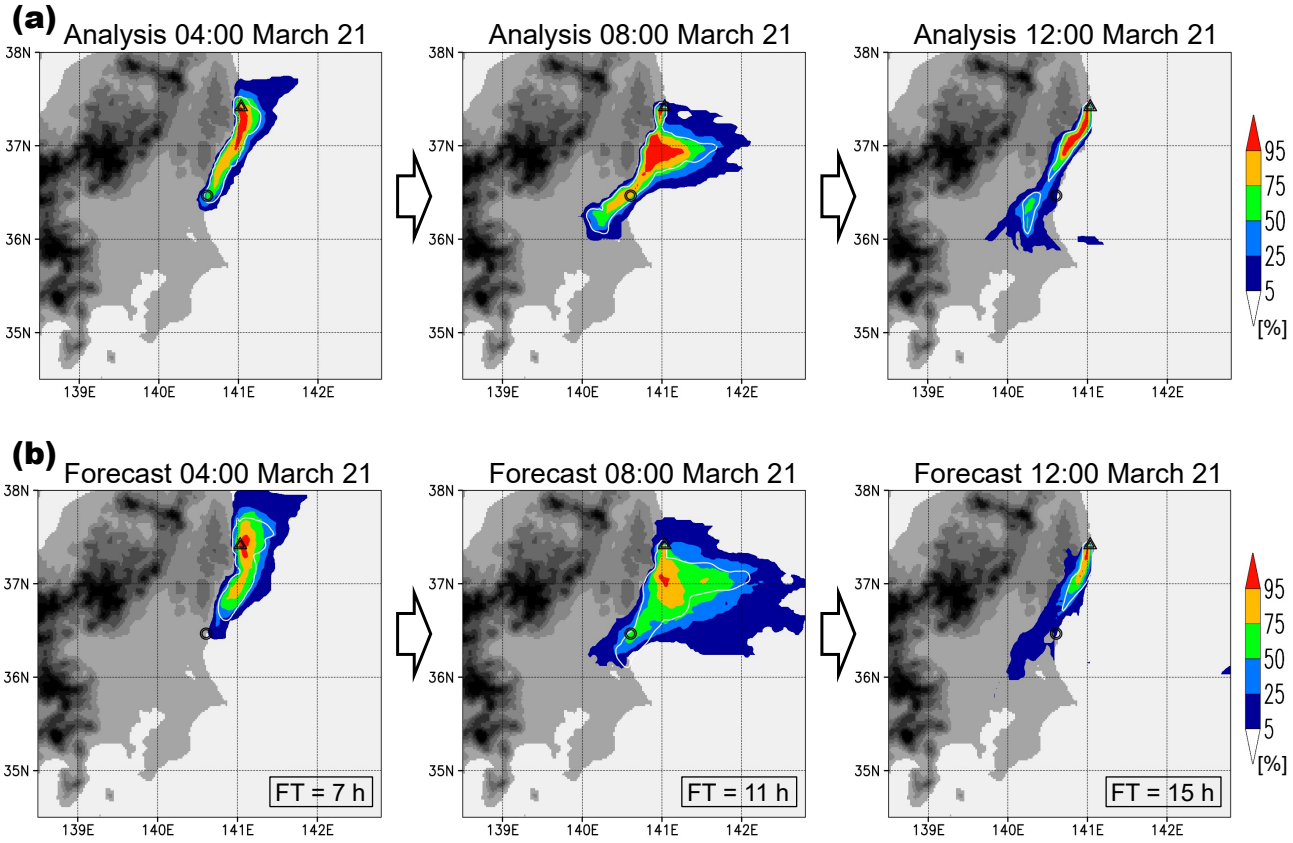

Figure 7. Same as Figure 4 but for 21 March. The local time of the snapshots was 4:00, 8:00, and 12:00 on 21 March, respectively. In the lower panels, the forecast duration was 7, 11, and 15 h, respectively.

The forecast RSD of the wind speed for the same time periods was 23% on average and that of the Cs-137 concentration was 235% (Table 1). The extremely large forecast errors of the Cs-137 concentration were caused by the forecast errors of the precipitation (not only the strength but also the timing). Specifically, the deterministic forecast almost completely failed to reproduce the Cs-137 plume arriving at Tokai (Figure 6b). In comparison with the extreme error of the Cs-137 concentration, the precipitation error was moderate as shown in the right panel of Figure 5b.

On this day, light precipitation was widespread over Japan (Figure 8a; derived from the JMA Radar/rain-gauge Analyzed Precipitation data [62]) and reasonably reproduced by the deterministic analysis (Figure 8b). The deterministic forecast (Figure 8c) produced a different distribution from the observed values (Figure 8a) and the analyzed values (Figure 8b). This difference caused the Cs-137 concentration to have a high error, indicating that the error of the dispersion models is not only amplified in comparison with the error of the wind speed but also crucially magnified by the error of the precipitation because of the high sensitivity of aerosol deposition on precipitation. However, even so, some of the ensemble members were successful in reproducing the high concentration at Tokai. This is the advantage of ensemble simulations.

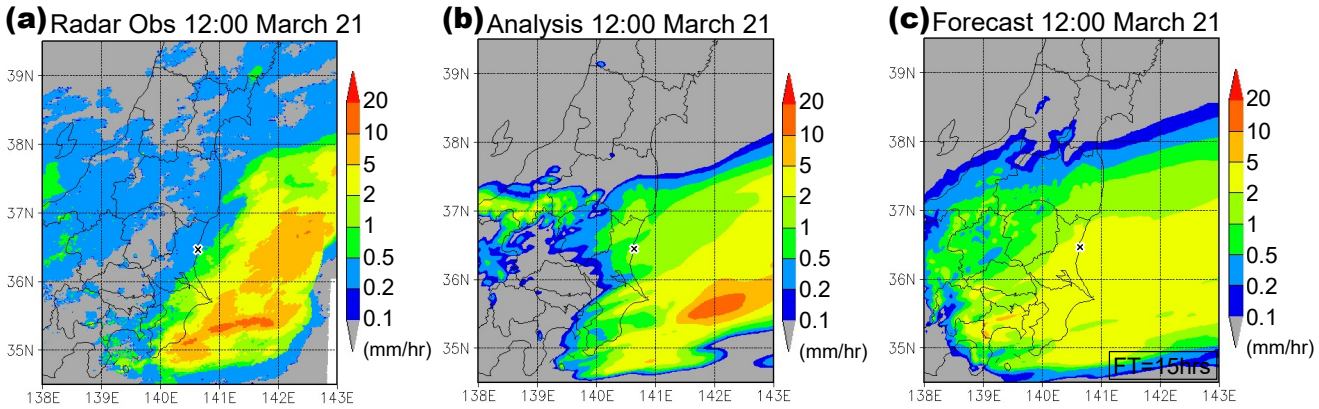

Figure 8. Precipitation (mm/hr) from 11:00 to 12:00 21 March local time derived from (**a**) the JMA operational radar/rain-gauge analyzed observations, (**b**) the deterministic analysis, (**c**) and the deterministic 15-h forecast. The cross mark illustrates the location of Tokai.

4. Conclusions

We conducted ensemble simulations for the dispersion of a point-source aerosol using perturbed meteorological fields. The ensemble simulations provided probabilistic information and multiple case scenarios for the aerosol dispersion. We found that a small ensemble spread of wind speed resulted in a large uncertainty in aerosol concentrations, i.e., the uncertainty on the aerosol dispersion was amplified in comparison with that on the wind simulation. This finding implies that a high accuracy of dispersion modeling requires much higher accuracy of meteorological modeling, thus representing a limitation of deterministic dispersion simulations for analyzing/predicting the location and intensity of aerosol plumes. Therefore, the probabilistic information of ensemble simulations exhibits great potential for aerosol analysis and prediction.

The deterministic simulation did not provide the best analysis/prediction in this study. However, some of the ensemble members successfully reproduced the arrival time and intensity of the aerosol plumes. With only a deterministic simulation, it is not possible to account for another event. Regrettably, in the field of atmospheric chemistry modeling, too much emphasis has been placed on deterministic simulations uncritically. The usefulness of ensemble simulations should be recognized to a greater extent.

The errors in the aerosol simulation were not only cumulative with the errors in wind speed simulation but also crucially magnified by the errors in the precipitation simulation because of the dependence of aerosol deposition on precipitation. Although the single-model initial-perturbed ensemble simulation as used in this study is a powerful tool to explore probabilistic analysis/prediction, the limitations of the single-model simulation should also be considered because the single-model simulation implements only a single module for the precipitation.

Author Contributions: Conceptualization, T.T.S.; Methodology, T.T.S., M.K. (Mizuo Kajino), and M.K. (Masaru Kunii); Software, M.K. (Mizuo Kajino) and M.K. (Masaru Kunii); Validation, T.T.S.; Formal Analysis, T.T.S.; Investigation, T.T.S.; Data Curation, T.T.S. and M.K. (Mizuo Kajino); Writing—Original Draft Preparation, T.T.S.; Writing—Review & Editing, T.T.S.; Visualization, T.T.S.; Funding Acquisition, T.T.S. and M.K. (Mizuo Kajino). All authors have read and agreed to the published version of the manuscript.

Funding: This work was supported by the Environment Research and Technology Development Fund (1-1802) at the Environmental Restoration and Conservation Agency and by JSPS KAKENHI Grant Numbers 24340115, 17K00533, 19H01155, and 21H03593.

Institutional Review Board Statement: Not applicable.

Informed Consent Statement: Not applicable.

Data Availability Statement: We thank M. Chino of JAEA for providing Cs-137 emission inventory data from their published papers [55–57]. We thank JAEA for providing their Cs-137 observation data from their published technical note [61]. The JMA data are available freely at their website or can be purchased via the Japan Meteorological Business Support Center. The numerical model source codes used in this study are available under a collaborative framework between MRI and related institutes/universities. The ensemble analysis and forecast data generated in this study is available on request to the corresponding author.

Acknowledgments: We greatly acknowledge K. Saito of JMA and T. Iwasaki of Tohoku University for their help and encouragement. We deeply thank S. Koizumi for his technical support.

Conflicts of Interest: The authors declare no conflict of interest.

References

1. Hoffman, R.N.; Kalnay, E. Lagged average forecasting, an alternative to Monte Carlo forecasting. *Tellus A* **1983**, *35*, 100–118. [CrossRef]
2. Molteni, F.; Buizza, R.; Palmer, T.N.; Petroliagis, T. The new ECMWF ensemble prediction system: Methodology and validation. *Q. J. R. Meteorol. Soc.* **1996**, *122*, 73–119. [CrossRef]
3. Houtekamer, P.L.; Mitchell, H.L.; Deng, X. Model Error Representation in an Operational Ensemble Kalman Filter. *Mon. Weather Rev.* **2009**, *137*, 2126–2143. [CrossRef]
4. Galmarini, S.; Bianconi, R.; Klug, W.; Mikkelsen, T.; Addis, R.; Andronopoulos, S.; Astrup, P.; Baklanov, A.; Bartniki, J.; Bartzis, J.C.; et al. Ensemble dispersion forecasting, Part 1: Concept, Approach and indicators. *Atmos. Environ.* **2004**, *38*, 4607–4617. [CrossRef]
5. Monache, L.D.; Deng, X.; Zhou, Y.; Stull, R. Ozone ensemble forecasts: 1. A new ensemble design. *J. Geophys. Res.* **2006**, *111*, D05307.
6. Hegarty, J.; Draxler, R.R.; Stein, A.F.; Brioude, J.; Mountain, M.; Eluszkiewicz, J.; Nehrkorn, T.; Ngan, F.; Andrews, A. Evaluation of Lagrangian Particle Dispersion Models with Measurements from Controlled Tracer Releases. *J. Appl. Meteorol. Clim.* **2013**, *52*, 2623–2637. [CrossRef]
7. Angevine, W.M.; Brioude, J.; McKeen, S.; Holloway, J.S. Uncertainty in Lagrangian pollutant transport simulations due to meteorological uncertainty from a mesoscale WRF ensemble. *Geosci. Model Dev.* **2014**, *7*, 2817–2829. [CrossRef]
8. Draxler, R.; Arnold, D.; Chino, M.; Galmarini, S.; Hort, M.; Jones, A.; Leadbetter, S.; Malo, A.; Maurer, C.; Rolph, G.; et al. World Meteorological Organization's model simulations of the radionuclide dispersion and deposition from the Fukushima Daiichi nuclear power plant accident. *J. Environ. Radioact.* **2015**, *139*, 172–184. [CrossRef] [PubMed]
9. Dabberdt, W.F.; Miller, E. Uncertainty, ensembles and air quality dispersion modeling: Applications and challenges. *Atmos. Environ.* **2000**, *34*, 4667–4673. [CrossRef]
10. Hanna, S.R.; Lu, Z.; Frey, H.C.; Wheeler, N.; Vukovich, J.; Arunachalam, S.; Femau, M.; Hansen, D.A. Uncertainties in predicted ozone concentrations due to input uncertainties for the UAM-V photochemical grid model applied to the July 1995 OTAG domain. *Atmos. Environ.* **2001**, *35*, 891–903. [CrossRef]
11. Draxler, R.R. Evaluation of an Ensemble Dispersion Calculation. *J. Appl. Meteorol.* **2003**, *42*, 308–317. [CrossRef]
12. Zhang, F.; Bei, N.; Nielsen-Gammon, J.W.; Li, G.; Zhang, R.; Stuart, A.; Aksoy, A. Impacts of meteorological uncertainties on ozone pollution predictability estimated through meteorological and photochemical ensemble forecasts. *J. Geophys. Res.* **2007**, *112*, D04304. [CrossRef]
13. Holt, T.; Pullen, J.; Bishop, C.H. Urban and ocean ensembles for improved meteorological and dispersion modelling of the coastal zone. *Tellus A* **2009**, *61*, 232–249. [CrossRef]
14. Lauvaux, T.; Pannekoucke, O.; Sarrat, C.; Chevallier, F.; Ciais, P.; Noilhan, J.; Rayner, P.J. Structure of the transport uncertainty in mesoscale inversions of CO_2 sources and sinks using ensemble model simulations. *Biogeosciences* **2009**, *6*, 1089–1102. [CrossRef]
15. Lattner, A.D.; Cervone, G. Ensemble modeling of transport and dispersion simulations guided by machine learning hypotheses generation. *Comput. Geosci.* **2012**, *48*, 267–279. [CrossRef]
16. Haszpra, T.; Lagzi, I.; Tél, T. Dispersion of aerosol particles in the free atmosphere using ensemble forecasts. *Nonlinear Process. Geophys.* **2013**, *20*, 759–770. [CrossRef]
17. Evensen, G. The Ensemble Kalman Filter: Theoretical formulation and practical implementation. *Ocean Dyn.* **2003**, *53*, 343–367. [CrossRef]
18. Kalnay, E. *Atmospheric Modeling, Data Assimilation and Predictability*; Cambridge University Press: Cambridge, UK, 2003.
19. Kalman, R.E. A New Approach to Linear Filtering and Prediction Problems. *Trans. ASME J. Basic Eng.* **1960**, *82D*, 35–45. [CrossRef]
20. Wang, X.; Bishop, C.H.; Julier, S.J. Which Is Better, an Ensemble of Positive–Negative Pairs or a Centered Spherical Simplex Ensemble? *Mon. Weather Rev.* **2004**, *132*, 1590–1605. [CrossRef]
21. Kunii, M. Mesoscale Data Assimilation for a Local Severe Rainfall Event with the NHM–LETKF System. *Weather Forecast.* **2014**, *29*, 1093–1105. [CrossRef]

22. Hunt, B.R.; Kostelich, E.J.; Szunyogh, I. Efficient data assimilation for spatiotemporal chaos: A local ensemble transform Kalman filter. *Phys. D* **2007**, *230*, 112–126. [CrossRef]
23. Saito, K.; Fujita, T.; Yamada, Y.; Ishida, J.; Kumagai, Y.; Aranami, K.; Ohmori, S.; Nagasawa, R.; Kumagai, S.; Muroi, C.; et al. The operational JMA nonhydrostatic mesoscale model. *Mon. Weather Rev.* **2006**, *134*, 1266–1298. [CrossRef]
24. Saito, K.; Ishida, J.; Aranami, K.; Hara, T.; Segawa, T.; Narita, M.; Honda, Y. Nonhydrostatic atmospheric models operational development at JMA. *J. Meteorol. Soc. Jpn.* **2007**, *85B*, 271–304. [CrossRef]
25. Miyoshi, T.; Aranami, K. Applying a four-dimensional local ensemble transform Kalman filter (4D-LETKF) to the JMA nonhydrostatic model (NHM). *SOLA* **2006**, *2*, 128–131. [CrossRef]
26. Miyoshi, T.; Yamane, S. Local ensemble transform Kalman filtering with an AGCM at a T159/L48 resolution. *Mon. Weather Rev.* **2007**, *135*, 3841–3861. [CrossRef]
27. Miyoshi, T. The Gaussian approach to adaptive covariance inflation and its implementation with the local ensemble transform Kalman filter. *Mon. Weather Rev.* **2011**, *139*, 1519–1535. [CrossRef]
28. Miyoshi, T.; Kunii, M. The local ensemble transform Kalman filter with the Weather Research and Forecast Model: Experiments with real observations. *Pure Appl. Geophys.* **2012**, *169*, 321–333. [CrossRef]
29. Kunii, M.; Miyoshi, T.; Kalnay, E. Estimating the impact of real observations in regional numerical weather prediction using an ensemble Kalman filter. *Mon. Weather Rev.* **2012**, *140*, 1975–1987. [CrossRef]
30. Kunii, M.; Miyoshi, T. Including uncertainties of sea surface temperature in an ensemble Kalman filter: A case study of Typhoon Sinlaku (2008). *Weather Forecast.* **2012**, *27*, 1586–1597. [CrossRef]
31. Miyazaki, K.; Eskes, H.J.; Sudo, K.; Takigawa, M.; van Weele, M.; Boersma, K.F. Simultaneous assimilation of satellite NO2, O3, CO, and HNO3 data for the analysis of tropospheric chemical composition and emissions. *Atmos. Chem. Phys.* **2012**, *12*, 9545–9579. [CrossRef]
32. Nakamura, T.; Akiyoshi, H.; Deushi, M.; Miyazaki, K.; Kobayashi, C.; Shibata, K.; Iwasaki, T. A multimodel comparison of stratospheric ozone data assimilation based on an ensemble Kalman filter approach. *J. Geophys. Res. Atmos.* **2013**, *118*, 3848–3868. [CrossRef]
33. Yumimoto, K.; Murakami, H.; Tanaka, T.Y.; Sekiyama, T.T.; Ogi, A.; Maki, T. Forecasting of Asian Dust Storm during 10-13 May in 2011 with an Ensemble-based Data Assimilation System. *Particuology* **2016**, *28*, 121–130. [CrossRef]
34. Sekiyama, T.T.; Tanaka, T.Y.; Shimizu, A.; Miyoshi, T. Data assimilation of CALIPSO aerosol observations. *Atmos. Chem. Phys.* **2010**, *10*, 39–49. [CrossRef]
35. Sekiyama, T.T.; Deushi, M.; Miyoshi, T. Operation-oriented ensemble data assimilation of total column ozone. *SOLA* **2011**, *7*, 41–44. [CrossRef]
36. Sekiyama, T.T.; Tanaka, T.Y.; Maki, T.; Mikami, M. The effects of snow cover and soil moisture on Asian dust: II. Emission estimation by lidar data assimilation. *SOLA* **2011**, *7A*, 40–43. [CrossRef]
37. Sekiyama, T.T.; Kunii, M.; Kajino, M.; Shimbori, T. Horizontal Resolution Dependence of Atmospheric Simulations of the Fukushima Nuclear Accident Using 15-km, 3-km, and 500-m Grid Models. *J. Meteorol. Soc. Jpn* **2015**, *93*, 45–60. [CrossRef]
38. Sekiyama, T.T.; Yumimoto, K.; Tanaka, T.Y.; Nagao, T.; Kikuchi, M.; Murakami, H. Data Assimilation of Himawari-8 Aerosol Observations: Asian Dust Forecast in June 2015. *SOLA* **2016**, *12*, 86–90. [CrossRef]
39. Sekiyama, T.T.; Kajino, M.; Kunii, M. The Impact of Surface Wind Data Assimilation on the Predictability of Near-Surface Plume Advection in the Case of the Fukushima Nuclear Accident. *J. Meteorol. Soc. Jpn* **2017**, *95*, 447–454. [CrossRef]
40. Sekiyama, T.T.; Iwasaki, T. Mass flux analysis of 137Cs plumes emitted from the Fukushima Daiichi Nuclear Power Plant. *Tellus B* **2018**, *70*, 1–11. [CrossRef]
41. Sekiyama, T.T.; Kajino, M. Reproducibility of Surface Wind and Tracer Transport Simulations over Complex Terrain Using 5-, 3-, and 1-km-Grid Models. *J. Appl. Meteor. Climatol.* **2020**, *59*, 937–952. [CrossRef]
42. Nakanishi, M.; Niino, H. An improved Mellor-Yamada level 3 model with condensation physics: Its design and verification. *Bound. Layer Meteorol.* **2004**, *112*, 1–31. [CrossRef]
43. Nakanishi, M.; Niino, H. An improved Mellor-Yamada level-3 model: Its numerical stability and application to a regional prediction of advection fog. *Bound. Layer Meteorol.* **2006**, *119*, 397–407. [CrossRef]
44. Honda, Y.; Nishijima, M.; Koizumi, K.; Ohta, Y.; Tamiya, K.; Kawabata, T.; Tsuyuki, T. A pre-operational variational data assimilation system for a non-hydrostatic model at the Japan Meteorological Agency: Formulation and preliminary results. *Q. J. R. Meteorol. Soc.* **2005**, *131*, 3465–3475. [CrossRef]
45. Adachi, K.; Kajino, M.; Zaizen, Y.; Igarashi, Y. Emission of spherical cesium-bearing particles from an early stage of the Fukushima nuclear accident. *Sci. Rep.* **2013**, *3*, 2554. [CrossRef]
46. Kajino, M.; Inomata, Y.; Sato, K.; Ueda, H.; Han, Z.; An, J.; Katata, G.; Deushi, M.; Maki, T.; Oshima, N.; et al. Development of the RAQM2 aerosol chemical transport model and predictions of the Northeast Asian aerosol mass, size, chemistry, and mixing type. *Atmos. Chem. Phys.* **2012**, *12*, 11833–11856. [CrossRef]
47. Kajino, M.; Sekiyama, T.T.; Mathieu, A.; Irène, K.; Périllat, R.; Quélo, D.; Quérel, A.; Saunier, O.; Adachi, K.; Girard, S.; et al. Lessons learned from atmospheric modeling studies after the Fukushima nuclear accident: Ensemble simulations, data assimilation, elemental process modeling, and inverse modeling. *Geochem. J.* **2018**, *52*, 85–101. [CrossRef]

48. Kajino, M.; Deushi, M.; Sekiyama, T.T.; Oshima, N.; Yumimoto, K.; Tanaka, T.; Ching, J.; Hashimoto, A.; Yamamoto, Y.; Ikegami, M.; et al. NHM-Chem, the Japan Meteorological Agency's Regional Meteorology-Chemistry Model: Model Evaluations toward the Consistent Predictions of the Chemical, Physical, and Optical Properties of Aerosols. *J. Meteorolo. Soc. Jpn* **2019**, *97*, 337–374. [CrossRef]
49. Kajino, M.; Sekiyama, T.T.; Igarashi, Y.; Katata, G.; Sawada, M.; Adachi, K.; Zaizen, Y.; Tsuruta, H.; Nakajima, T. Deposition and dispersion of radio-cesium released due to the Fukushima nuclear accident: Sensitivity to meteorological models and physical modules. *J. Geophys. Res.* **2019**, *124*, 1823–1845. [CrossRef]
50. Kajino, M.; Adachi, K.; Igarashi, Y.; Satou, Y.; Sawada, M.; Sekiyama, T.T.; Zaizen, Y.; Saya, A.; Tsuruta, H.; Moriguchi, Y. Deposition and Dispersion of Radio-Cesium Released Due to the Fukushima Nuclear Accident: 2. Sensitivity to Aerosol Microphysical Properties of Cs-bearing microparticles (CsMPs). *J. Geophys. Res.* **2021**, *126*, e2020JD033460. [CrossRef]
51. Sato, Y.; Takigawa, M.; Sekiyama, T.T.; Kajino, M.; Terada, H.; Nagai, H.; Kondo, H.; Uchida, J.; Goto, D.; Quélo, D.; et al. Model intercomparison of atmospheric 137Cs from the Fukushima Daiichi Nuclear Power Plant accident: Simulations based on identical input data. *J. Geophys. Res.* **2018**, *123*, 11748–11765. [CrossRef]
52. Sato, Y.; Sekiyama, T.T.; Fang, S.; Kajino, M.; Quérel, A.; Quélo, D.; Kondo, H.; Terada, H.; Kadowaki, M.; Takigawa, M.; et al. A model intercomparison of atmospheric 137Cs concentrations from the Fukushima Daiichi Nuclear Power Plant accident, Phase III: Simulation with an identical source term and meteorological field at 1-km resolution. *Atmos. Environ. X* **2020**, *7*, 100086. [CrossRef]
53. Kitayama, K.; Morino, Y.; Takigawa, M.; Nakajima, T.; Hayami, H.; Nagai, H.; Terada, H.; Saito, K.; Shimbori, T.; Kajino, M.; et al. Atmospheric modeling of 137Cs plumes from the Fukushima Daiichi Nuclear Power Plant—Evaluation of the model intercomparison data of the Science Council of Japan. *J. Geophys. Res.* **2018**, *123*, 7754–7770.
54. Iwasaki, T.; Sekiyama, T.T.; Nakajima, T.; Watanabe, A.; Suzuki, Y.; Kondo, H.; Morino, Y.; Terada, H.; Nagai, H.; Takigawa, M.; et al. Intercomparison of numerical atmospheric dispersion prediction models for emergency response to emissions of radionuclides with limited source information in the Fukushima Dai-ichi Nuclear Power Plant accident. *Atmos. Environ.* **2019**, *214*, 116830. [CrossRef]
55. Chino, M.; Nakayama, H.; Nagai, H.; Terada, H.; Katata, G.; Yamazawa, H. Preliminary estimation of release amounts of 131I and 137Cs accidentally discharged from the Fukushima Daiichi Nuclear Power Plant into the atmosphere. *J. Nucl. Sci. Technol.* **2011**, *48*, 1129–1134. [CrossRef]
56. Katata, G.; Ota, M.; Terada, H.; Chino, M.; Nagai, H. Atmospheric discharge and dispersion of radionuclides during the Fukushima Dai-ichi Nuclear Power Plant accident. Part I: Source term estimation and local-scale atmospheric dispersion in early phase of the accident. *J. Environ. Radioact.* **2012**, *109*, 103–113. [CrossRef]
57. Terada, H.; Katata, G.; Chino, M.; Nagai, H. Atmospheric discharge and dispersion of radionuclides during the Fukushima Dai-ichi Nuclear Power Plant accident. Part II: Verification of the source term and analysis of regional-scale atmospheric dispersion. *J. Environ. Radioact.* **2012**, *112*, 141–154. [CrossRef] [PubMed]
58. Kaneyasu, N.; Ohashi, H.; Suzuki, F.; Okuda, T.; Ikemori, F. Sulfate Aerosol as a Potential Transport Medium of Radiocesium from the Fukushima Nuclear Accident. *Environ. Sci. Technol.* **2012**, *46*, 5720–5726. [CrossRef]
59. Katata, G.; Chino, M.; Kobayashi, T.; Terada, H.; Ota, M.; Nagai, H.; Kajino, M.; Draxler, R.; Hort, M.C.; Malo, A.; et al. Detailed source term estimation of the atmospheric release for the Fukushima Daiichi Nuclear Power Station accident by coupling simulations of an atmospheric dispersion model with an improved deposition scheme and oceanic dispersion model. *Atmos. Chem. Phys.* **2015**, *15*, 1029–1070. [CrossRef]
60. Nakajima, T.; Misawa, S.; Morino, Y.; Tsuruta, H.; Goto, D.; Uchida, J.; Takemura, T.; Ohara, T.; Oura, Y.; Ebihara, M.; et al. Model depiction of the atmospheric flows of radioactive cesium emitted from the Fukushima Daiichi Nuclear Power Station accident. *Prog. Earth Planet. Sci.* **2017**, *4*, 2. [CrossRef]
61. Ohkura, T.; Oishi, T.; Taki, M.; Shibanuma, Y.; Kikuchi, M.; Akino, H.; Kikuta, Y.; Kawasaki, M.; Saegusa, J.; Tsutsumi, M.; et al. *Emergency Monitoring of Environmental Radiation and Atmospheric Radionuclides at Nuclear Science Research Institute, JAEA following the Accident of Fukushima Daiichi Nuclear Power Plant, JAEA-Data/Code 2012-010*; Japan Atomic Energy Agency: Tokai, Japan, 2012.
62. Makihara, Y.; Uekiyo, N.; Tabata, A.; Abe, Y. Accuracy of Radar-AMeDAS Precipitation. *IEICE Trans. Commun.* **1996**, *79*, 751–762.

https://doi.org/10.5194/acp-2021-591
Preprint. Discussion started: 30 July 2021

Atmospheric Chemistry and Physics Discussions

Eight-year variations in atmospheric radiocesium in Fukushima city

Akira Watanabe[1,2], Mizuo Kajino[3,4,5], Kazuhiko Ninomiya[6,7], Yoshitaka Nagahashi[1], and Atsushi Shinohara[6]

[1]Faculty of Symbiotic Systems Science, Fukushima University, Fukushima, Fukushima 960-1296, Japan
[2]Institute for Climate Change, Fukushima, Fukushima 960-0231, Japan
[3]Meteorological Research Institute (MRI), Japan Meteorological Agency (JMA), Tsukuba, Ibaraki 305-0052, Japan
[4]Faculty of Life and Environmental Sciences, University of Tsukuba, Tsukuba, Ibaraki 305-8572, Japan
[5]Institute of Radiation Emergency Medicine (IREM), Hirosaki, Aomori 036-8564, Japan
[6]Graduate School of Science, Osaka University, Toyonaka, Osaka 560-0043, Japan
[7]Intitute for Radiation Sciences, Osaka University, Toyonaka, Osaka 560-0043, Japan

Correspondence to: A. Watanabe (watamay1948@yahoo.co.jp), M. Kajino (kajino@mri-jma.go.jp), and K. Ninomiya (ninomiya@rirc.osaka-u.ac.jp)

https://doi.org/10.5194/acp-2021-591
Preprint. Discussion started: 30 July 2021

Atmospheric Chemistry and Physics Discussions

Abstract. After the Fukushima nuclear accident, atmospheric ^{134}Cs and ^{137}Cs measurements were taken in Fukushima city for eight years, from March 2011 to March 2019. The surface air concentrations and deposition of radio-Cs were high in winter and low in summer; these trends are the opposite of those observed in a contaminated forest area. The half-lives of ^{137}Cs in the concentrations and deposition before 2015 (275 d and 1.11 y) were significantly shorter than those after 2015 (756 d and 4.69 y). The dissolved fractions of precipitation were larger than the particulate fractions before 2015, but the particulate fractions were larger after 2016. The half-lives of ^{137}Cs in the concentrations and deposition were shorter before 2015, probably because the dissolved radio-Cs was discharged from the local terrestrial ecosystems more rapidly than the particulate radio-Cs. X-ray fluorescence analysis suggested that biotite may have played a key role in the environmental behavior of particulate forms of radio-Cs after 2014. However, the causal relationship between the seasonal variations in particle size distributions and the possible sources of particles is not yet fully understood. The current study also proposes a method of evaluating the consistency of a numerical model for radio-Cs resuspension and suggests that improvements to the model are necessary.

Keywords: Fukushima nuclear accident, long-term observation, radiocesium, atmospheric radioactivity, precipitation radioactivity

https://doi.org/10.5194/acp-2021-591
Preprint. Discussion started: 30 July 2021

Atmospheric Chemistry and Physics Discussions

1 Introduction

We conducted eight-year measurements of atmospheric ^{134}Cs and ^{137}Cs in Fukushima city after the Fukushima Daiichi Nuclear Power Plant (FDNPP) accident that occurred in March 2011 to understand the time variations in and emission sources of ^{134}Cs and ^{137}Cs and to propose effective ways to reduce atmospheric radioactivity. Among the various radionuclides released to the environment, radio-Cs is particularly important due to its abundance in terrestrial ecosystems (the impacts of other nuclides were negligibly small 100 days after the accident; Yoshimura et al., 2020), long half-lives (2.06 y for ^{134}Cs and 30.17 y for ^{137}Cs), and bioaccumulation (accumulation in muscle tissues, with biological half-lives of 30-150 d; WHO, 2011). Radio-Cs forms aerosols in the air and is therefore efficiently deposited onto the ground surface via precipitation in addition to via dry deposition. Approximately 30 % of the radio-Cs released in March 2011 was deposited onto the ground surface in Japan (the aircraft-measured deposition on the ground was 2.7 PBq for ^{137}Cs; NRA, 2012, and the most updated estimate of ^{137}Cs emissions by the Japan Atomic Energy Agency is 10 PBq; Terada et al., 2020). (The activity of ^{134}Cs in the environment was equivalent to that of ^{137}Cs in March 2011). Once radio-Cs is deposited onto the ground surface, it circulates within local terrestrial ecosystems, so the discharge from the local environment to downstream or downwind regions may not be substantial (0.02 - 0.3 % y^{-1} to river; Iwagami et al., 2017, approximately 1 % y^{-1} to atmosphere[1]). Thus, long-term monitoring of atmospheric radio-Cs at even one station may allow us to understand the mechanisms of its circulation in the local terrestrial ecosystems, to estimate the external and inhalation exposure risks to the local residents, to propose efficient ways to reduce health risks to the residents, and to assess the effectiveness of decontamination efforts.

To date, a great number of studies have focused on the circulation of radio-Cs in terrestrial ecosystems (Onda et al., 2020). In terms of the long-term monitoring of atmospheric radio-Cs with a focus on resuspension from the ground surface to the atmosphere, several papers have been published. Based on atmospheric measurements taken in the contaminated forest area of the Abukuma Highlands (30 km northwest of the FDNPP) from October 2012 to December 2014, Ochiai et al. (2016) reported that the surface activity concentrations of ^{137}Cs were higher in summer and lower in winter and that the time variations of the fine-mode (< 1.1 μm in diameter using an impactor) and coarse mode (> 1.1 μm) behaved differently. The coarse-mode fractions were larger in summer, and the fine-mode fractions were larger in winter. Kinase et al. (2018) conducted surface concentration measurements at four locations in the forest area of the Abukuma Highlands from July 2011 to March 2014 and found that the concentrations of ^{134}Cs and ^{137}Cs were lower in winter and early spring and higher from late spring to autumn. Their size-resolved measurements with a six-stage cascade impactor showed that the backup filter (< 0.39 μm) activity concentrations were high in winter, consistent with Ochiai et al. (2016). However, Kinase et al. (2018) found through scanning electron microscopy (SEM) that there were significant amounts of soil dust particles in the backup filter; these particles were larger but bounced off the upper impactor stages. Therefore, they concluded that the sizes of radioactive particles were not

[1] The annual resuspension rate to the atmosphere was estimated as 0.047 % y^{-1} by Kajino et al. (2016). However, the current study found that the resuspension rate was likely substantially underestimated (see Sect. 3.5 and Fig. 9). A value of approximately 1 % y^{-1} was obtained from improved simulations, but that manuscript is still in preparation.

https://doi.org/10.5194/acp-2021-591
Preprint. Discussion started: 30 July 2021


Atmospheric Chemistry and Physics Discussions

small but were actually large (coarse-mode particles). In late spring, the surface concentrations were positively correlated with the wind speed, so they concluded that the wind-blown soil particles carried radio-Cs in this season. In the summer and autumn, the concentrations were positively correlated with temperature but negatively correlated with wind speed, so they concluded that the resuspension mechanisms were different in the winter and summer. The SEM analysis revealed that there were more abundant bioaerosols in summer than in winter. Based on simulations, Kaijno et al. (2016) indicated that the summer peaks in surface concentrations in the Abukuma Highlands could be accounted for by the bioaerosol emissions from forest ecosystems, even though the emission mechanism remains unknown. Igarashi et al. (2019a) further investigated the mechanisms of bioaerosol emissions in forests in summer by using fluorescent optical microscopic observation and high-throughput DNA sequencing techniques. They suggested that the fungal spores that accumulate radio-Cs may be significantly involved in resuspension in the forest in summer. Kita et al. (2020) suggested that rain induced the emission of radio-Cs associated with fungal spores in the forest in summer. Minami et al. (2020) combined aerosol flux measurements and a multilayer atmosphere-soil-vegetation model and estimated that the bioaerosol emission flux was on the order of 10^{-2} μg m^{-2} s^{-1}, which could account for the surface concentrations of ^{137}Cs in the forests in summer (Kajino et al., 2016; Kinase et al., 2018; Igarashi et al., 2019a). Kinase et al. (2018) also showed that there was no enhancement in the ^{137}Cs concentration associated with forest fire events in the region. The surface concentration of ^{137}Cs was not correlated with that of levoglucosan, which is often used as a marker of biomass burning. These results are distinct from those from Chernobyl, where wildfire plays a key role in the migration of radio-Cs associated with the event (Ager et al., 2019; Igarashi et al., 2020). The contributions of additional ^{137}Cs emissions from the nuclear reactor buildings of FDNPP to the surface concentrations in Japan were negligibly small compared to the resuspensions from the ground surface (Kajino et al., 2016). On the other hand, unintentional emissions in the premises of FDNPP such as debris removal operations contributed to some observed sporadic peaks (Steinhouse et al., 2015; Kajino et al., 2016), although the impacts of such events might be small in terms of long-term averages and trends.

The current study is distinct from other studies, as it includes long-term comprehensive measurements (time-resolved and size-resolved measurements of surface air activity concentrations together with measurements of dissolved and particulate forms of activity in precipitation) at an urban/rural location in the Fukushima Basin in the vicinity of contaminated forests in the Abukuma Highlands. The field observation and the simulation methods are described in Sect. 2. Sect. 3 presents the results for the surface concentrations (Sect. 3.1), deposition amounts (Sect. 3.2), size distribution (Sect. 3.3), chemical compositions (Sect. 3.4), comparison with simulations (Sect. 3.5), and comparison with measurements taken outside Fukushima Prefecture (Sect. 3.6). The seasonal variations and possible emission sources are discussed in Sect. 4.1, the impacts of decontamination and natural variations on the differences in trends before and after approximately 2015 are discussed in Sect. 4.2, the reasons for the substantial deposition amount in January in Fukushima city are discussed in Sect. 4.3, and major findings and future issues are summarized in Sect. 5. The observation data used in the study are provided as a Microsoft Excel file in the Supplement.

https://doi.org/10.5194/acp-2021-591
Preprint. Discussion started: 30 July 2021

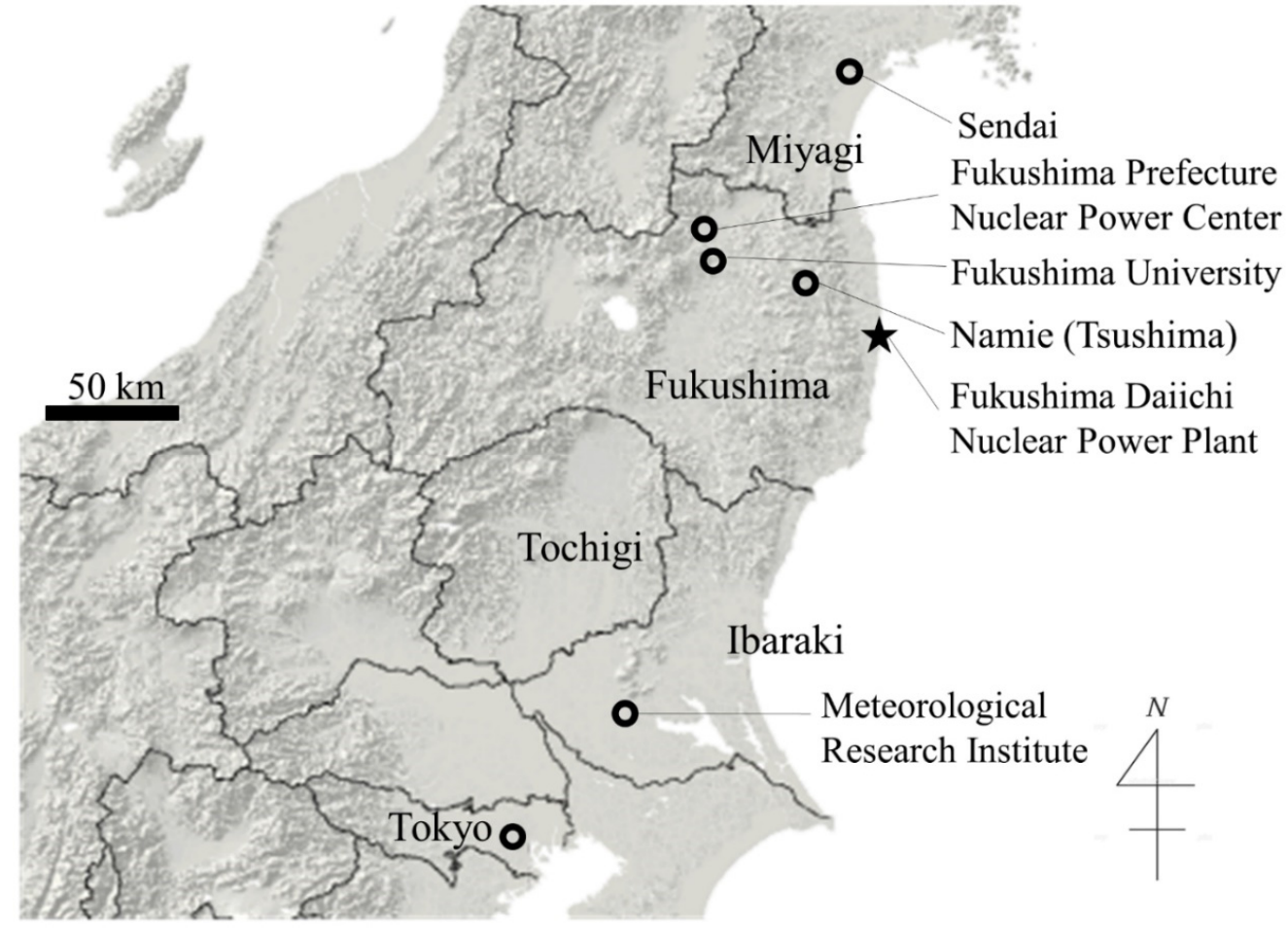

Figure 1: Map of Fukushima Prefecture and the surrounding prefectures. The locations mentioned in this study and terrestrial elevations are depicted in the map.

2 Methods

2.1 Sampling site

The observation site, Fukushima University, is located in Fukushima city, located in the northernmost basin (Fukushima basin) in the Nakadori Valley, surrounded by the Ou mountains to the west and the Abukuma Highlands to the east (Fig. 1). The distance of the observation site from the FDNPP is approximately 60 km. The Nakadori Valley was formed by the Abukuma River, which starts in the mountains in Fukushima Prefecture near the border of Tochigi Prefecture and flows northeast through the central parts of Fukushima city to the Pacific Ocean in Miyagi Prefecture. The major radioactive plumes arrived twice in Fukushima city, on March 15 and 20 (plume #3 and #8, as identified by Nakajima et al. (2017), respectively). These plumes were transported over the Abukuma Highlands (where the peaks are mostly lower than 1,000 m) but were blocked by the

https://doi.org/10.5194/acp-2021-591
Preprint. Discussion started: 30 July 2021


Atmospheric Chemistry and Physics Discussions

higher Ou Mountains (peaks are 1,000 - 2,000 m) and thus transported along the Nakadori Valley (Nakajima et al., 2017). The land surface of Fukushima city was contaminated mainly on the afternoon of March 15 with plume #3. The air dose rate in Fukushima city started to increase at 17:00 local time (LT), associated with the weak rain that started at 13:00 LT, and peaked at 19:30 LT at a value of 24.0 μSv h^{-1}.

2.2 Surface air concentrations

2.2.1 High-volume air sampler, cascade impactor, and radioactivity measurement

The air samples were collected using high-volume air samplers (Kimoto electric Co., Ltd., Model-120SL) placed on the roof of the building at Fukushima University (37.68°N, 140.45°E) at a height of 25 m from ground level. In this study, we carried out two types of air sampling: time-resolved observations and aerosol size-resolved observations. In the former case, aerosol samples were collected on a quartz fiber filter (Tisch Environmental, Inc., TE-QMA-100). The air suction rate of the sampler was 700 L min^{-1}. The typical duration of each sample collection was 24 hours, from May 8 to September 2, 2011. Then, we switched to 72 hours of collection until December 27, 2017; after that, 1 week of continuous collection was performed until March 28, 2019. For the latter observations, a cascade impactor system (Shibata Scientific Technology Ltd., HV-RW) was placed into a high-volume air sampler. The air suction rate was 566 L min^{-1}. The aerosols were collected separately by diameter on six quartz filters (Kimoto, TE-236). The range of particle sizes in this system was 0.39-0.69, 0.69-1.3, 1.3-2.1, 2.1-4.2, 4.2-10.2, and >10.2 μm. (Note that the sizes in the manuscript indicate the 50 % cutoff aerodynamic diameters.) Fine particles with a size of <0.39 μm were captured on a backup filter (Kimoto, TE-230-QZ). The typical sample collection time for the size-resolved observations was three weeks. In types of both observations, activated carbon fiber filters (Toyobo Co., Ltd., KF-1700F 84 mmφ) were also placed at the exit of the high-volume air samplers to collect gas-state aerosols.

The collected aerosol samples were sealed into polyethylene bags at Fukushima University. After being shaped into definite shapes, the gamma rays from the samples were measured by high-purity germanium detectors (coaxial with 15, 35 and 40 % relative efficiencies, SEIKO EG&G, ORTEC and coaxial with 40 and 60 % relative efficiencies, CANBERRA) connected to a multichannel analyzer system (MCA7600, SEIKO EG&G) at the Radioisotope Research Center, Osaka University. The radioactivities of ^{134}Cs and ^{137}Cs were identified at gamma-ray intensities of 605 keV and 662 keV, respectively. The detection efficiencies of the respective detectors for each gamma ray were determined from the same-shape filter samples from standard ^{134}Cs and ^{137}Cs solutions obtained from the Japan Radioisotope Association. The typical measurement time of each sample was 1-3 days. Under these conditions, the detection limits of ^{134}Cs and ^{137}Cs were approximately 5×10^{-3} Bq. The errors in the measured values are derived from the systematic error of geometrical configuration and the standard sample itself in addition to statistical error. All radioactivities determined by our measurements were corrected at mid sampling times.

https://doi.org/10.5194/acp-2021-591
Preprint. Discussion started: 30 July 2021


Atmospheric Chemistry and Physics Discussions

The radioactivities of both ^{134}Cs and ^{137}Cs were identified for most filter samples. The deviation in concentration between ^{134}Cs and ^{137}Cs became larger over time due to the relatively short half-life of ^{134}Cs. According to the radioactive decay correction performed in March 2011, the activity ratios of $^{134}Cs/^{137}Cs$ were approximately 1. These ratios are consistent with those in other reports related to FDNPP accident, so we concluded that the detected radiocesium originated from FDNPP accident. During the measurement period, no radioactivity from ^{134}Cs and ^{137}Cs was detected from the carbon filters; that is, the component of gaseous radioactive cesium was negligibly small.

2.2.2 Impactor/cyclone system

Since the filters for the high-volume air samples were quartz fiber filters, they could not be used for elemental analysis with X-ray fluorescence spectrometry (XRF). For the XRF analysis, we used an impactor/cyclone system (Tokyo Dylec Corp., no-number special order, 1100 L min^{-1}) in which the aerosols were separated by size into < 2.5 μm and > 2.5 μm using an impactor; those < 2.5 μm and >0.1 μm were sampled in glass bottles (As One corp., 2-4999-07) using a 0.1 μm cyclone with sampling intervals of one month from September 2014 to January 2018. Aerosols larger than 2.5 μm were collected on quartz fiber filters in the system. Aerosol samples in glass bottles (0.1 – 2.5 μm) were defined as fine-mode PM (PM_f), and those on quartz fiber filters (> 2.5 μm) were defined as coarse-mode PM (PM_c). The radioactivities of ^{134}Cs and ^{137}Cs in the samples were also measured in the same manner.

2.2.3 Possible artifacts of impactor measurements

Size separation by an impactor is associated with the artifacts caused by bouncing effects. In fact, in cascade impactor measurements, Kinase et al. (2018) observed abundant coarse-mode particles such as mineral dust and bioaerosol particles in the backup filters due to bouncing effects. In the impactor/cyclone system, the glass fiber filters used as an impaction surface were immersed in silicone oil to prevent particles from bouncing (Okuda et al., 2015). In this study, silicone oil was not used for the cascade impactor but was used in the impactor/cyclone system. However, the long-duration measurements (such as the monthlong measurements) could be associated with the larger particles that rebounded at the impactor and were collected in glass bottles (Okuda et al., 2015).

2.3 Deposition (dry plus wet deposition, dissolved and particulate fractions)

The total deposition (dry plus wet deposition or fallout) samples were collected with a precipitation sampler (Miyamoto Riken Ind. Co., Ltd., RS-20) with a funnel diameter of 20 cm. Since a heating device was not installed on the sampler, any snow in the funnel was manually melted in a water bath in winter. The accumulated snow in the funnel never reached the top of the funnel during the whole observation period. A filtration device was installed in the sampler using membrane filters (Advantec, 4-880-03) with a pore size of 0.45 μm. The radioactivities of ^{134}Cs and ^{137}Cs in the filtered water stored in the polyethylene bottle and those on the filters were both measured by high-purity germanium detectors at Osaka University and were defined

https://doi.org/10.5194/acp-2021-591
Preprint. Discussion started: 30 July 2021


Atmospheric Chemistry and Physics Discussions

as the dissolved and particulate fractions of the deposition, respectively. It should be noted here that this separation does not perfectly differentiate water-soluble and insoluble radio-Cs. The clogging of the pores of the membrane filter can occur during filtration. The measured total (dissolved plus particulate) deposition amounts were compared with those measured by the official method at the Fukushima Prefecture Nuclear Power Center (Fig. 1), which is located 6.5 km north-northwest of Fukushima University. Our method was found to be consistent with their official method: the correlation coefficient R was 0.81, with a slope of 1.158 (the values from Fukushima University were larger by 16 %). Differences in locations and sampling intervals (daily at the Fukushima Prefecture Nuclear Power Center; monthly at Fukushima University) could also have contributed to the differences in the measured values at the two sites.

2.4 X-ray fluorescence analysis (aerosols, deposition, and river sediments)

X-ray fluorescence (XRF) analysis was carried out by using a RIX1000 (Rigaku Corp.) at Fukushima University. The measurement setup recommended by the manufacturer was used for the XRF. The major and trace element contents were analyzed by the fundamental parameter method and calibration curve method, respectively (Takase and Nagahashi, 2007). Measurements were conducted for PM_f (see Sect. 2.2.2), the particulate fractions of precipitation (see Sect. 2.3), and the river sediments. River sediments were collected at 15 sites upstream and downstream of Fukushima city in the Abukuma River and its tributaries in 2010. Samples were taken from the gravel layer of the lower terrace at 5 sites, from alluvial fan deposits at 1 site, and from current riverbed sediments at 9 sites. The dried sediment samples were sieved and divided into two grain size groups: particles smaller than 180 μm (defined as fine sediment particles) and particles 180 μm - 2 mm (coarse sediment particles).

2.5 Numerical simulation and validation data

Kajino et al. (2016) used a Lagrangian model (LM) to simulate the atmospheric dispersion and deposition of ^{137}Cs resuspended from bare soil and forest ecosystems from January to December 2013. Since the resuspension fluxes and size distributions were unknown, they adjusted the flux from bare soil (forest ecosystems) so that the simulated surface concentrations matched those measured in Namie (Tsushima) (Namie High School Tsushima Campus, 37.56°N, 140.77°E, 30 km northwest of the FDNPP) (Fig. 1) in the winter (summer) of 2013, and they adjusted the dry and wet deposition parameters (reflecting the size distributions and hygroscopicity) so that the simulated total (dry plus wet) deposition over land in March 2011 matched those measured by the aircraft measurements (NRA, 2012). Thus, note that the size distribution of the simulation was assumed to have submicron size ranges that were consistent with those of the primary emissions (the direct emissions associated with the FDNPP accident in March 2011) but that may not be applicable for resuspension events; the carrier aerosols are presumed to be soil dust or bioaerosols, which are usually larger than the submicron size range. Kajino et al. (2016) concluded that their simulations are likely reliable because the simulated differences between the surface concentrations in the contaminated area (or emission source area) (i.e., Tsushima) and those in the downwind area (Meteorological Research Institute (MRI), Tsukuba

https://doi.org/10.5194/acp-2021-591
Preprint. Discussion started: 30 July 2021


Atmospheric Chemistry and Physics Discussions

city, 36.06°N, 140.13°E, 170 km southwest of the FDNPP) (Fig. 1) were consistent with the observed differences at the two locations.

However, Kajino et al. (2016) used only surface concentration measurements to validate the simulations. The current study also used concentration and deposition measurements from Fukushima University for model validation. The previous study compared only the two locations in the contaminated forest areas and in the downwind urban/rural regions; the current study includes an additional location in the urban/rural region near the contaminated forest of the Abukuma Highlands (60 km northwest of the FDNPP).

3 Results

3.1 Surface air concentrations

Figure 2 shows the time variations in the atmospheric radioactivity concentrations of ^{137}Cs from May 2011 to March 2019. Just after the accident, the ^{137}Cs concentrations were higher than 0.01 Bq/m^3, and the maximum concentration of 0.0169 Bq/m^3 was detected on May 23, 2011. The concentration quickly decreased to a level of 10^{-4} Bq/m^3, and the minimum concentration of 4.05×10^{-6} Bq/m^3 was obtained on December 5, 2018. By taking the annual averaged value, the decreasing tendency in the atmospheric concentration could be expressed as $Y = 0.0418X^{-0.476}$, where Y indicates the annual mean ^{137}Cs concentration and X means the number of years elapsed. The coefficient of determination, R^2, is 0.993. This demonstrates that the surface concentration decreased exponentially and halved in approximately 4 years; thus, the decrease rate was higher than the rate of radioactive decay of ^{137}Cs.

It is remarkable that the decreasing trends in the earlier stage and the later stage were different. The regression lines of the raw data time intervals for the whole period (red; May 2011 - March 2019), the earlier stage (blue; May 2011 - December 2014), and the later stage (green; January 2015 - March 2019) are shown in Fig. 2, with the half-life (T_h) in days and the decrease rate (R_d) in % y^{-1}. The decreasing trend (T_h = 275 d, R_d = 92.0 % y^{-1}) of the earlier stage is approximately three times faster than that of the later stage (T_h = 756 d, R_d = 33.5 % y^{-1}). It is shown later in Fig. 3 in Sect. 3.2 and discussed in Sect. 4.2, but this could be related to the relative abundance of particulate and dissolved fractions of radio-Cs in the environment. The dissolved fractions of radio-Cs may discharge faster than the particulate fractions from contaminated environments, such as soils and plants. The relative abundance of the dissolved fractions was larger in the earlier stage than in the later stage such that the decreasing trend in the surface air concentration was faster than that in the later stage. In addition to the natural variability, decontamination work, which was completed by March 2018 in Fukushima city and the surrounding municipalities, may also have contributed to the difference in the decrease rates; this possibility is also discussed in Sect. 4.2.

https://doi.org/10.5194/acp-2021-591
Preprint. Discussion started: 30 July 2021

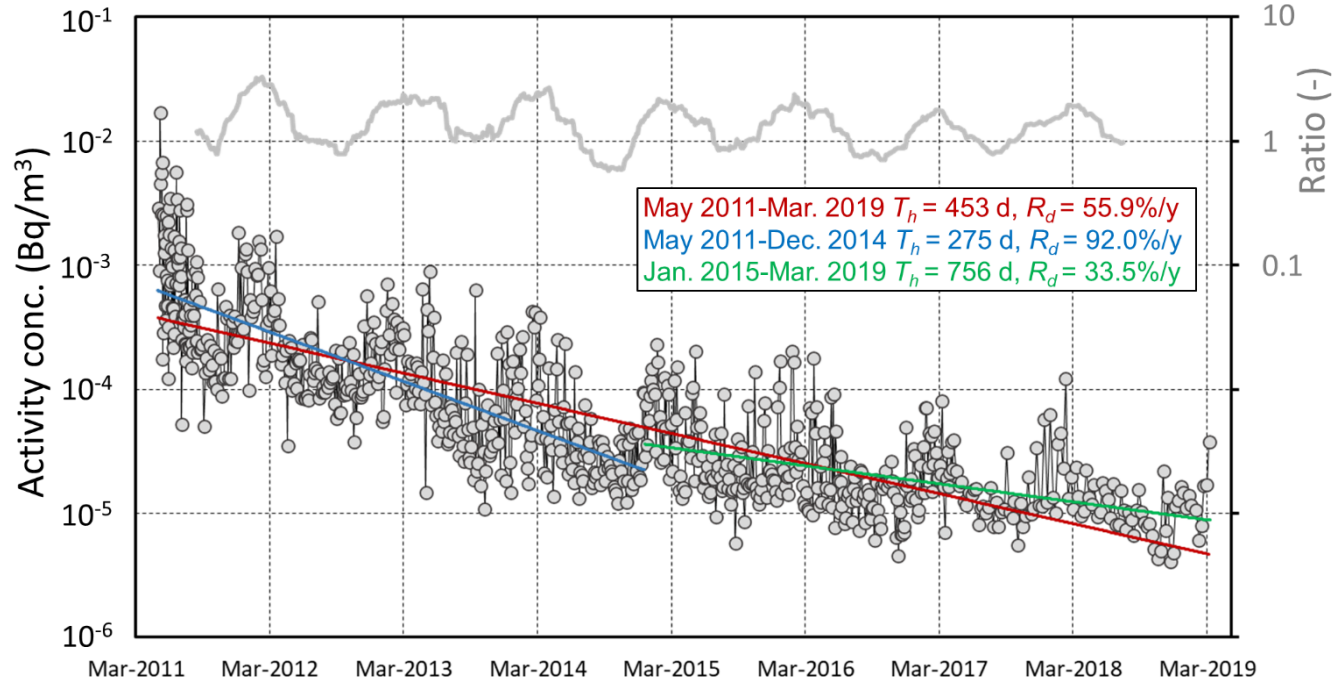

Figure 2: Time series of surface air activity concentrations of ^{137}Cs on the left axis. The red, blue, and green lines indicate the regression lines of the whole period, before 2015, and after 2015, respectively. The half-lives (T_h) and decay rates (R_d) are also depicted. The gray line indicates the ratio of the running mean of 20 data points (an approximately monthly cycle) to the running mean of 160 data points (an approximately annual cycle) on the right axis to show its seasonal variation.

It is also interesting that our data show different seasonal variations from those measured in Tsushima by Ochiai et al. (2016) and Kinase et al. (2018). The levels in their studies were high in summer and low in winter, but as depicted in the gray line in Fig. 2, the concentration rose starting in October, with maxima in the spring season around March and minima in the summer. The maxima in the spring are approximately one order of magnitude larger than the minima in the summer. The measurements of their studies were conducted in high-dose areas in the mountain forest (approximately 400 m above sea level (a.s.l.)), and the high-volume samplers were set near the ground surface. In contrast, the current air sampling was conducted in a relatively low-dose area (10 times lower than that in Tsushima) located in an urban/rural region on a hill (approximately 200 m a.s.l.) at the southern end of the Fukushima Basin. The heights of the samples were 25 m from the ground surface. Such geographical and altitude differences could have caused these differences.

https://doi.org/10.5194/acp-2021-591
Preprint. Discussion started: 30 July 2021


Atmospheric Chemistry and Physics Discussions

3.2 Deposition amounts

Figure 3 shows the monthly cumulative deposition of ^{137}Cs from March 2011 to March 2019. The monthly deposition amount peaked in March 2011 as 202200 Bq m^{-2}, decreased to 1 % of the initial amount after one year, and decreased to an order of 1 Bq m^{-2} after eight years. It also showed seasonal variation and was high from winter to spring. Nevertheless, the current level is from two to three orders of magnitude larger than that before the Fukushima nuclear accident. The monthly trend is expressed as $Y = 48232X^{-1.944}$, where Y indicates the monthly cumulative ^{137}Cs deposition and X means the number of months elapsed. R^2 is 0.697.

The decrease rates of deposition (T_h = 1.11 – 4.69 y) were generally slower than those of the surface concentrations (T_h = 275 - 756 d). It is hard to identify the reason for this phenomenon. A perfect simulation could answer this question, but high uncertainties in atmospheric deposition modeling and land surface modeling inhibit a perfect understanding of these long-term circulations of radio-Cs in the environment. It is safe to presume here that the decreasing trends in deposition and surface concentrations are different because the contributions of major emission sources to deposition and surface concentrations are different. If the dominant source of the surface concentration is near (far from) the observation site and that for of deposition is far from (near) the site, the faster decrease rate in concentration is due to the faster (slower) reduction rate in the nearby sources of emissions than in the far sources.

There is also a distinct difference in the decreasing trends before and after 2015. In addition to the effect of decontamination work, as previously discussed in Sect. 3.1, the relative abundances of the dissolved and particulate fractions of ^{137}Cs could be a part of the reason. The particulate fraction made up 72.6 % of the deposition of March 2011, which is presumed to be largely influenced by primary emissions. Here, it is interesting to note that most primary radio-Cs emissions are thought to be composed of water-soluble submicron aerosol particles (e.g., Kaneyasu et al., 2012 and almost all numerical simulations afterwards, such as Sato et al., 2020), while water-insoluble Cs-bearing microparticles (CsMP; Adachi et al., 2013, Igarashi et al., 2019b) may contribute somewhat to primary emissions (Ikehara et al., 2020, Kajino et al., 2021). If the primary radio-Cs in aerosols were 100 % in water-soluble forms, the particulate fraction should have made up 0% of the precipitation in March 2011 (although, some of the water-soluble Cs could have converted to a water-insoluble form through adsorption to soil particles accumulated on the membrane filter during filtration). After April 2011, as the contributions of resuspension were thought to be dominant, the dissolved fractions became larger. The ratio varied, but the dissolved fractions were generally higher before 2016, and the particulate fractions became dominant after 2016. There seemed to be a regime change in the physicochemical properties of radio-Cs circulating in the environment in the area in approximately 2015 and 2016, which could have changed the decreasing trends of both the surface concentrations and deposition before and after 2015. This result is consistent with the finding of Manaka et al. (2016), who reported that the exchangeable proportions of radio-Cs rapidly decreased in forest soils from two to four years after the accident, i.e., from 2013 - 2015.

https://doi.org/10.5194/acp-2021-591
Preprint. Discussion started: 30 July 2021

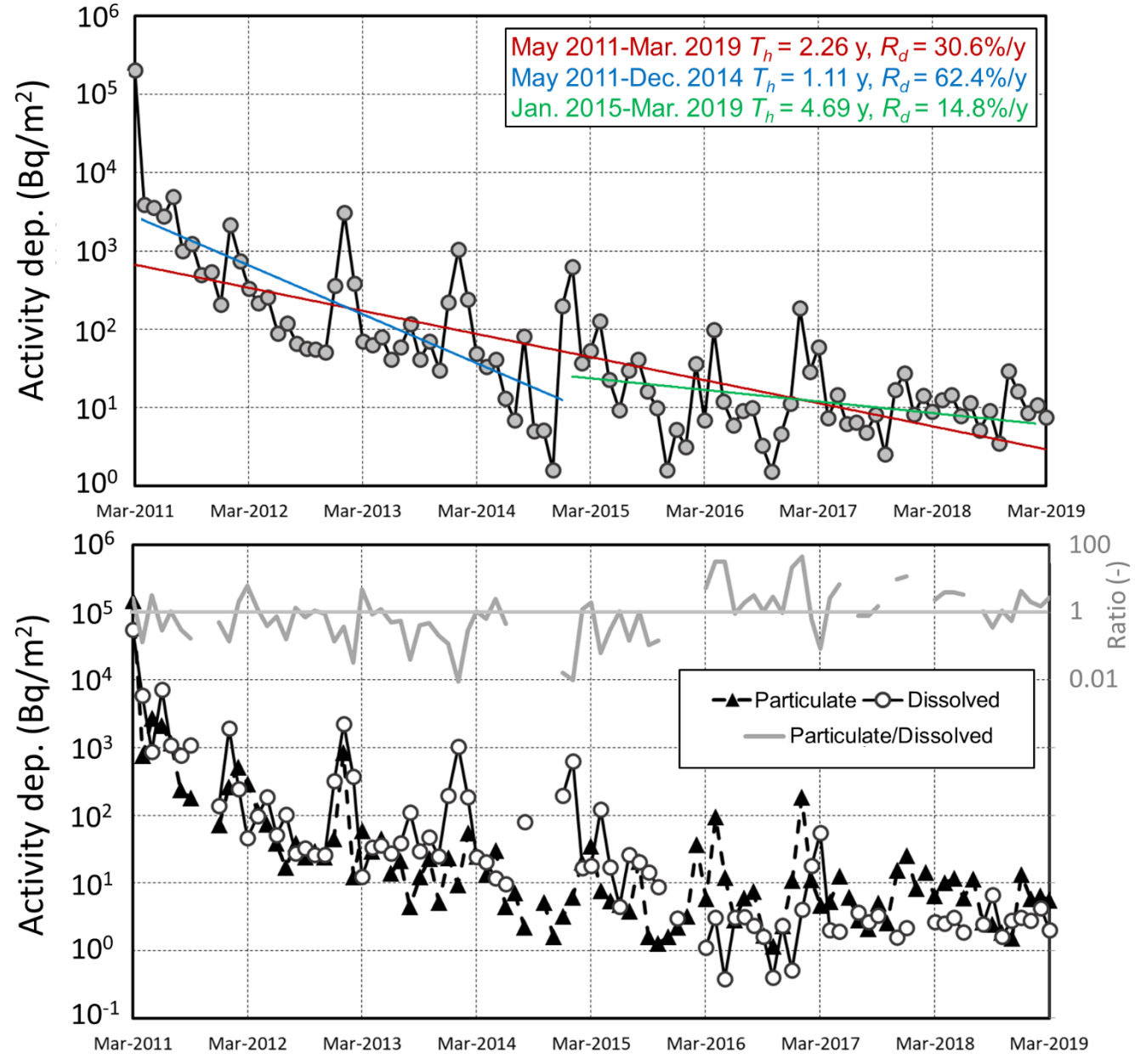

Figure 3: (Top) Time series of ^{137}Cs activity deposition. The red, blue, and green lines indicate the regression lines of the whole period, before 2015, and after 2015, respectively. The half-lives (Th) and decay rates (Rd) are also depicted. (Bottom) Time series of particulate and dissolved forms of ^{137}Cs deposition on the left axis and the ratio of particulate to dissolved ^{137}Cs on the right axis.

https://doi.org/10.5194/acp-2021-591
Preprint. Discussion started: 30 July 2021


Atmospheric Chemistry and Physics Discussions

The seasonal variations in particulate and dissolved ^{137}Cs were slightly different from each other and different from those of the surface concentration. The surface concentration peaked in March in almost all years, and the total deposition peaked in January. The peaks of the total deposition in January coincided with those of the dissolved ^{137}Cs before 2016, but the peaks of the dissolved ^{137}Cs became unclear afterwards. The peaks of particulate ^{137}Cs occurred in March before 2016, which coincided with those of the surface concentrations. After 2016, there were no clear seasonal variations in particulate ^{137}Cs. There are clear and different seasonal variations in the surface concentration and deposition. However, at the current stage, we have no knowledge of or numerical tools to reveal the hidden mechanisms underlying these variations.

3.3 Size distributions

Figure 4 shows the time series of the seasonal mean atmospheric radioactivity concentrations of ^{137}Cs obtained from the cascade impactor measurements. The sampling interval for the cascade impactor measurements was three weeks. The seasonal means included a sampling period if any part of the sampling period was included in the season. For example, the raw data from the sampling period from February to March contributed to the averages of both DJF (December, January, and February, i.e., winter) and MAM (March, April, and May, i.e., spring). The seasonal mean total (all sizes) concentrations of cascade impactor measurements during the sampling period agreed well with those of the time-resolved observations (Fig. 2), with R^2 = 0.93. The same seasonal variation discussed for the time-resolved observations (Sect. 3.1) was also observed; the atmospheric ^{137}Cs concentration was relatively high in DJF and MAM compared to that in JJA (June, July, and August, i.e., summer) and SON (September, October, and November, i.e., autumn).

The most dominant size range in activity was the backup filter (< 0.39 μm, or rebounded particles such as soil dust and bioaerosols; Kinase et al., 2018), and its seasonal variation agreed well with that of the total particle concentration (high in DJF and MAM). On the other hand, the second largest contribution was made by the size range of 4.2-10.2 μm, which showed the opposite seasonal variation and was relatively high in JJA and SON. The seasonal variations in the largest particle fraction, larger than 10.2 μm, are interesting. The trend appears to be synchronized with that of the backup filter particles (high in DJF and MAM), but the opposite trend was observed in 2016 and 2017 (high in JJA). The contributions of other fractions, i.e., 0.49-4.2 μm, were small in the measured period. Even though the contributions were small, the seasonal trend of 0.39-0.69 μm was similar to that of the backup filter particles, but that of 1.3-2.1 μm was similar to that of 4.2-10.2 μm. The current measurement indicates that the dominant particles and their sizes may be distinct depending on the season. The decrease rates of each size were different before and after approximately 2015, as discussed in Sects. 3.1 and 3.2, but the size distribution of the surface activity did not change substantially before and after approximately 2015.

https://doi.org/10.5194/acp-2021-591
Preprint. Discussion started: 30 July 2021

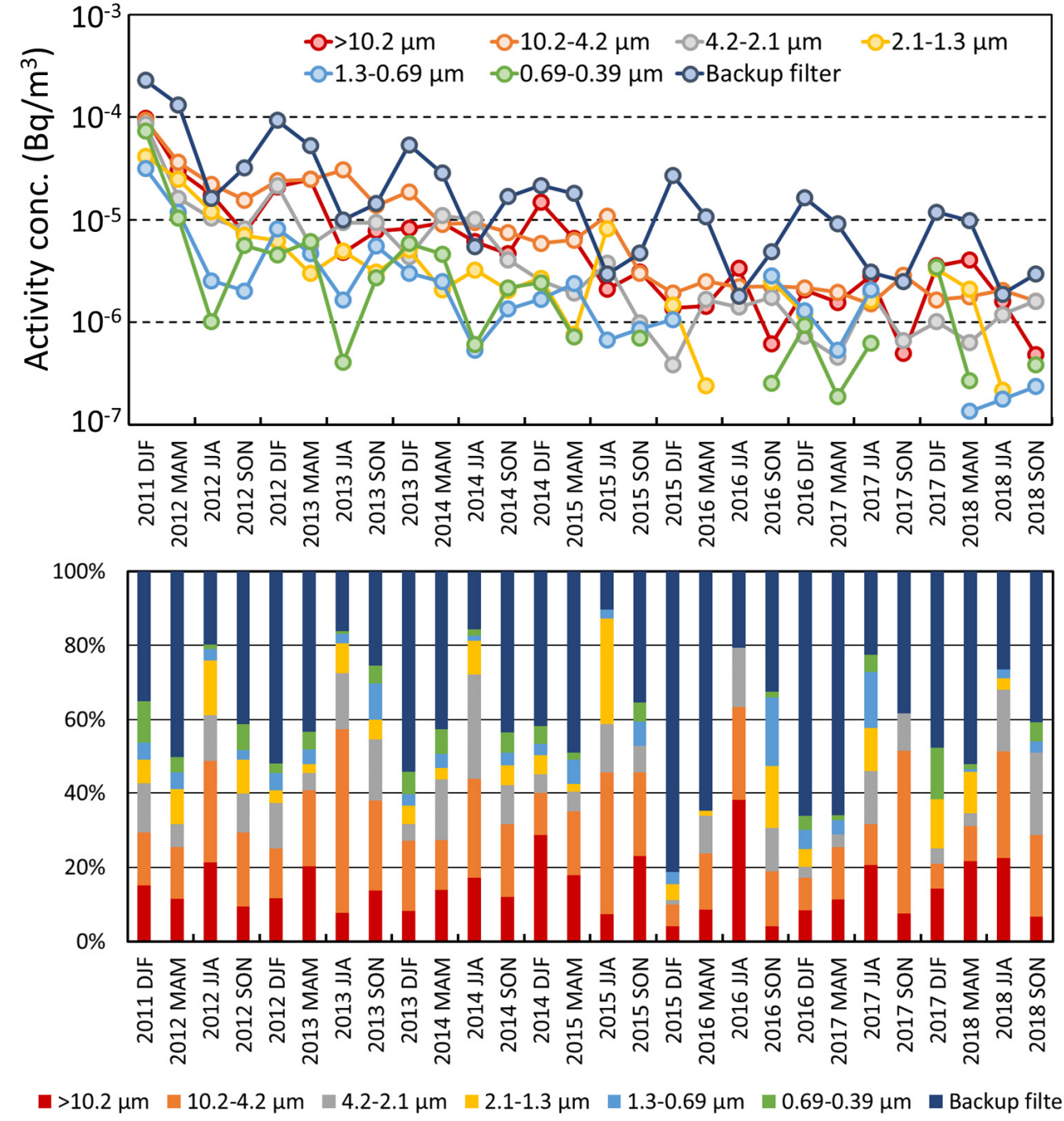

Figure 4: (Top) Time series of seasonal mean size-resolved surface activity concentrations of ^{137}Cs and (bottom) their relative fractions.

https://doi.org/10.5194/acp-2021-591
Preprint. Discussion started: 30 July 2021

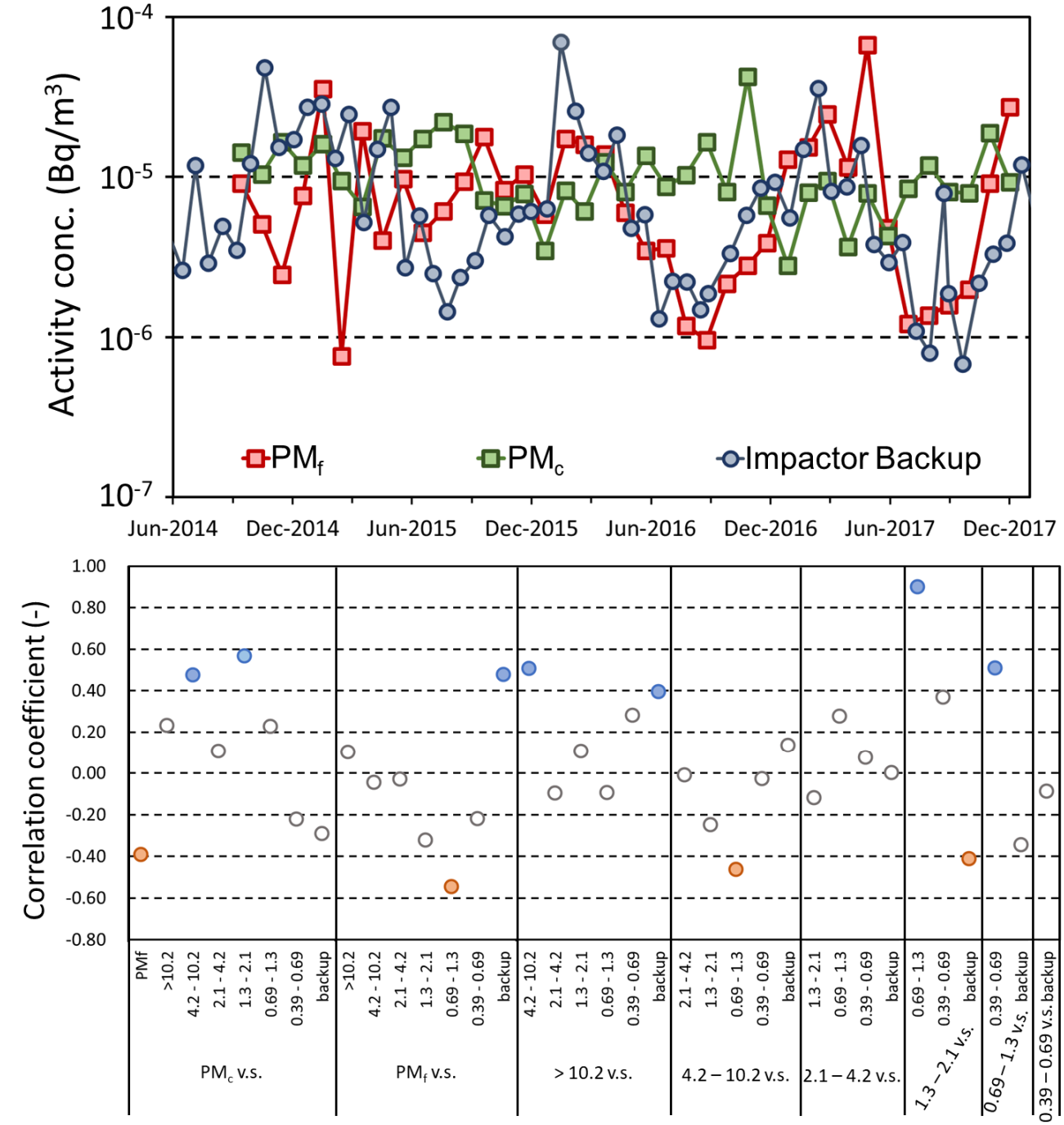

Figure 5: (Top) Time series of surface activity concentrations of ^{137}Cs in PM_f (0.1-2.5 μm) and PM_c (>2.5 μm) collected by the impactor/cyclone system and those of the backup filter of the cascade impactor. (Bottom) Correlation coefficients of temporal variations among seasonal mean ^{137}Cs activity concentrations of different sizes measured by the impactor/cyclone and the cascade impactor. Correlation coefficients higher than approximately 0.4 and lower than approximately -0.4 are colored blue and orange, respectively.

https://doi.org/10.5194/acp-2021-591
Preprint. Discussion started: 30 July 2021


Atmospheric Chemistry and Physics Discussions

Cascade impactor sampling is associated with the bouncing effect, whereas filters for the impactor/cyclone system were immersed in silicone oil to prevent the bouncing effect. Thus, compared the cascade impactor and the impactor/cyclone measurement data, as shown in Fig. 5. The top panel of Fig. 5 shows the data with the same measurement time intervals (three weeks for the cascade impactor data and one month for the impactor/cyclone data). The surface activity concentrations of ^{137}Cs in the backup filters were well correlated with those of PM_f. No remarkable seasonality was observed in PM_c, but some enhancements were observed in JJA in 2015 and SON in 2016.

The bottom panel of Fig. 5 shows the correlation coefficients among the seasonal mean size-resolved data from the cascade impactor and impactor/cyclone measurements. If we assume that the bouncing effect on the impactor/cyclone measurements was negligible, the cascade impactor data and the impactor/cyclone data were consistent. There was a positive correlation between PM_f and the backup filter data. There were also positive correlations between PM_c and the 1.3-2.1 μm and 4.2-10.2 μm data. There was a negative correlation between PM_c and PM_f. We can assume that fine-mode particles are the dominant carriers of ^{137}Cs in winter and spring and that coarse-mode particles are the dominant carriers of ^{137}Cs in summer and autumn. However, there was also a contradiction in the data. There were low or negative correlation coefficients between the backup filter data and the cascade impactor data at smaller size ranges, such as 0.39-0.69, 0.69-1.3, and 1.3-2.1 μm, but the backup filter data were positively correlated with the impactor data for > 10.2 μm. It appears that bouncing effect occurred; particles larger than 10.2 μm bounced in the latter stages and were captured in the backup filter. However, as previously discussed, the behaviors of the >10.2 μm-particle data were not consistent in time, i.e., they were generally high in DJF and MAM and were high in JJA in 2016 and 2017 (Fig. 4). Kinase et al. (2018) and Igarashi et al. (2019a) considered that the dominant carriers of resuspended ^{137}Cs were coarse-mode particles such as soil dust and bioaerosols. Ochiai et al. (2016) conducted two-stage impactor sampling and measured the surface activity concentrations of ^{134}Cs and ^{137}Cs above and below 1.1 μm from 2012 to 2014. They showed that the contributions of coarse-mode particles (> 1.1 μm) were dominant, with maxima in summer. The contributions of the fine-mode particles (< 1.1 μm) were much smaller, and no significant seasonal variations were found. All of their measurement sites were surrounded by contaminated forests in the Abukuma Highlands (Tsushima and the nearby sites), so the sampling sites were different from those in our study. Such larger particles may have contributed to the backup filter data in the current measurements; however, based on the fact that the backup filter data were positively correlated with PM_f and not with PM_c, fine-mode particles (< 2.5 μm) should also play a key role in determining the surface air concentrations in Fukushima city.

On the other hand, if we assume that the bouncing effect is also significant in the impactor/cyclone system due to the long sampling duration, as suggested by Okuda et al. (2015), the positive correlation between the backup filter particles and PM_f was simply due to the bouncing effects of the larger particles in both systems.

https://doi.org/10.5194/acp-2021-591
Preprint. Discussion started: 30 July 2021


Atmospheric Chemistry and Physics Discussions

Even though the emission sources of the dominant particles collected by the size-resolved measurements could not be identified in this study, the possible aerosol sources that would explain the differences in size and seasonality of the two locations are discussed later, in Sect. 4.1.

3.4 Chemical characterizations of particles in the air, rainfall, and river sediments

Figure 6 shows the relative abundance of the XRF-measured atomic number concentrations of elements in the PM_f monthly sample from September 2014 to January 2018. Among the 15 detected species, PM_f was mainly composed of SiO_2, Al_2O_3, and SO_3. The fractions of SiO_2 show clear seasonal variations and were higher around May. The seasonal variations in Al_2O_3 and SO_3 are the opposite of that of SiO_2. A positive temporal correlation was obtained between the ^{137}Cs in PM_f and SiO_2 (R = 0.30). Negative correlations were obtained for Al_2O_3 and SO_3, with correlation coefficients of -0.36 and -0.35, respectively. Note that these results do not prove that the SiO_2-bearing aerosols are the carriers of resuspended ^{137}Cs, but we can safely conclude that the origins of SiO_2 and ^{137}Cs may be close to each other (i.e., that both come from the same source or the same area/direction).

Figure 7 shows comparisons of the relative abundance of the periodic mean XRF measured atomic number concentrations in different samples, fine sediment particles, coarse sediment particles, PM_f, and particulate fractions of precipitation. The PM_f and precipitation data over the same period, from October 2014 and December 2012, were averaged. The sediment samples were collected in 2010. The 10 species that were common to all samples are shown in Fig. 7. The correlation coefficients for the compositions among samples are above 0.9, showing that the samples have similar origins. The features of the PM_f composition were distinct from the others. PM_f included SO_3 (17.8 %) and Cl (2.65 %), while the others did not.

Weathered biotite is abundant in the soil in Fukushima and absorbs radio-Cs efficiently (Kogure et al., 2019). The compositional correlation coefficients between the weathered biotite (Takase, 2020) and the four samples were high, at 0.73 to 0.87. However, when the two major components SiO_2 and Al_2O_3 were excluded, the compositional correlation coefficients changed significantly. The eight compositional correlation coefficients between the fine and coarse sediment particles were 0.98, but those between the sediments and PM_f were 0.01 and 0.19 for the fine and coarse sediment particles, respectively. The eight compositional correlation coefficients for the particulate fractions of precipitation were moderate, at 0.36, 0.44, and 0.45 for fine sediment particles, coarse sediment particles, and PM_f, respectively. The eight compositional correlation coefficients for weathered biotite were 0.76, 0.71, 0.50, and -0.14 for fine sediment particles, coarse sediment particles, particulate fractions of precipitation, and PM_f, respectively.

https://doi.org/10.5194/acp-2021-591
Preprint. Discussion started: 30 July 2021

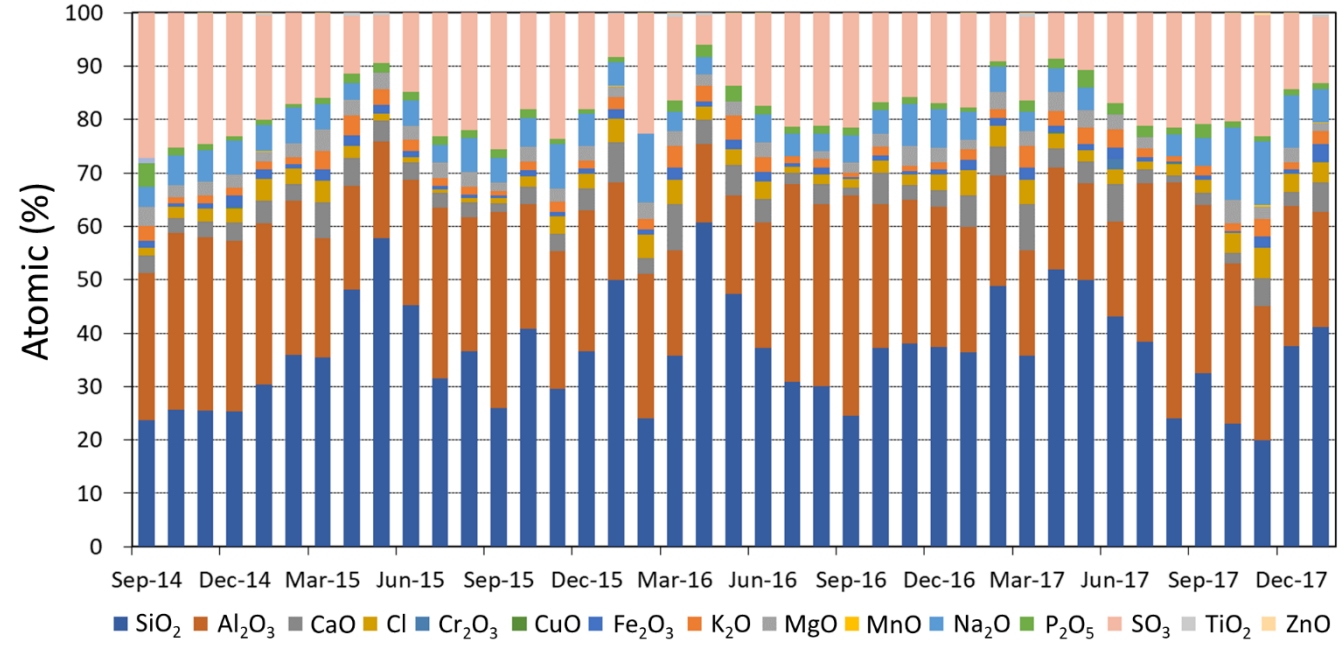

Figure 6: Temporal variations in the chemical composition of PM_f as measured by XRF.

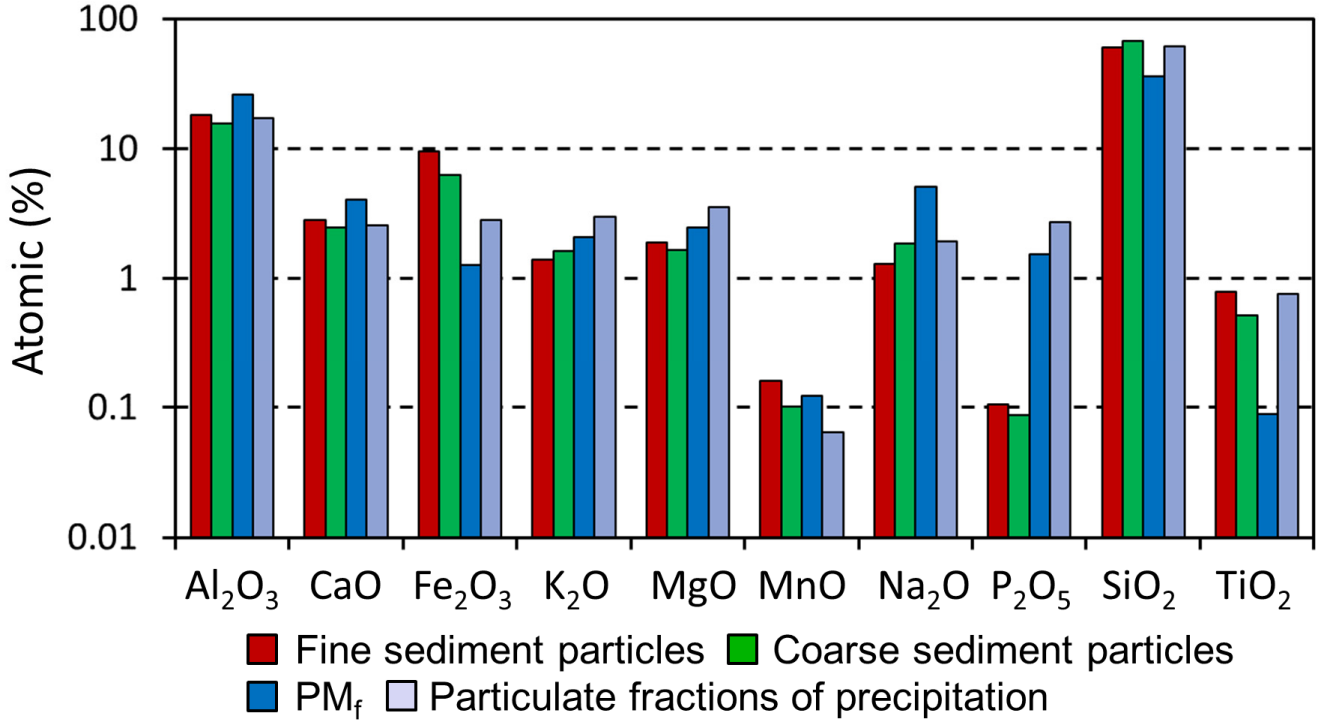

Figure 7: Periodic mean chemical compositions of fine particles and coarse particles in sediments, PM_f, and the precipitation filter (the particulate fraction of precipitation) measured by XRF.

https://doi.org/10.5194/acp-2021-591
Preprint. Discussion started: 30 July 2021

Atmospheric Chemistry and Physics Discussions

The findings from the current section are summarized as follows. The mean compositions of both fine and coarse sediment particles are similar to those of biotite, which absorbs radio-Cs efficiently. The similar composition feature was observed for the particulate fractions of precipitation. The composition of PM_f was slightly different from those of the other samples, but the ^{137}Cs concentrations in PM_f become larger when the relative fractions of SiO_2, the major component of biotite, increased. Thus, biotite may have played a key role in the environmental behavior of radio-Cs in Fukushima city since September 2014. However, the major carriers of radio-Cs before September 2014 and those in the dissolved fractions in precipitation are still unknown.

3.5 Comparison with the simulation results and climatological deposition velocity analysis

In Fig. 8, the surface concentrations of ^{137}Cs in 2013 simulated by Kajino et al. (2016) are compared with the time-resolved observation data (Fig. 2). Kajino et al. (2016) included ^{137}Cs resuspended from bare soil, ^{137}Cs resuspended from forest ecosystems, and additional ^{137}Cs emissions from the FDNPP. The additional ^{137}Cs emissions were negligibly small, the concentrations of which in East Japan were two to three orders of magnitude smaller than those from the two sources. Therefore, they are not depicted in the figure. The simulation was successful in explaining the magnitude and seasonal variations in surface concentrations at Tsushima and the MRI, but the simulation at Fukushima city disagreed with the observations. The simulation showed an enhancement of ^{137}Cs from forests in the summer, but that was not detected in the observations. The observed magnitude and seasonal trends are rather similar to those simulated for ^{137}Cs from soil dust.

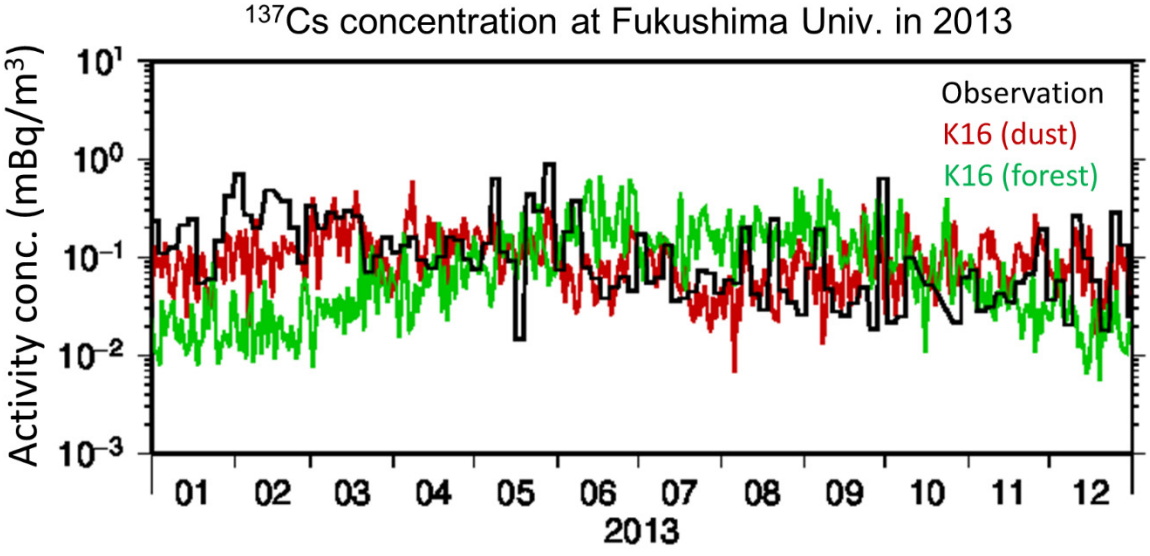

Figure 8: Time series of (black) measured surface activity concentrations of ^{137}Cs and those simulated (by Kajino et al., 2016; K16) considering different emission sources, (red) mineral dust from bare soil and (green) aerosols emitted from forest ecosystems.

https://doi.org/10.5194/acp-2021-591
Preprint. Discussion started: 30 July 2021

Atmospheric Chemistry and Physics Discussions

Kajino et al. (2016) used only the observed surface concentrations to estimate the regional budget of resuspended ^{137}Cs in the air, but we used the observed deposition to evaluate the model, as shown in Fig. 9. Suppose there is a simple nonlinear relationship between the deposition (D) and surface concentration (C):

$$D = aC^b, \quad (1)$$

where a represents a removal rate and b represents nonlinearity, such as spatial and temporal variabilities. If one can take a long-term average of D and C, Eq. (1) may hold. Eq. (1) is reformulated as

$$log(D) = b\ log(C) + log(a). \quad (2)$$

The log-log scatter plot between the monthly mean surface concentrations and monthly cumulative deposition of observed (purple) and simulated (orange) ^{137}Cs are depicted in the left panel of Fig. 9. The coefficient of determination of the observation was 0.678, with a risk factor for < 0.1 %. Eq. (1) holds for the monthly mean resuspended ^{137}Cs at Fukushima University. As seen in Eq. (2), the intercept of the Y-axis indicates the removal rate a. log(a) is dimensionless, but if b is close to one, the unit of a can be m s^{-1}. From Fig. 9, b of observation is close to one. Therefore, the ratios of the monthly deposition amounts to the monthly mean surface concentrations are referred to as the climatological deposition velocity (m s^{-1}). Time series of the climatological deposition velocity are presented in the right panel of Fig. 9.

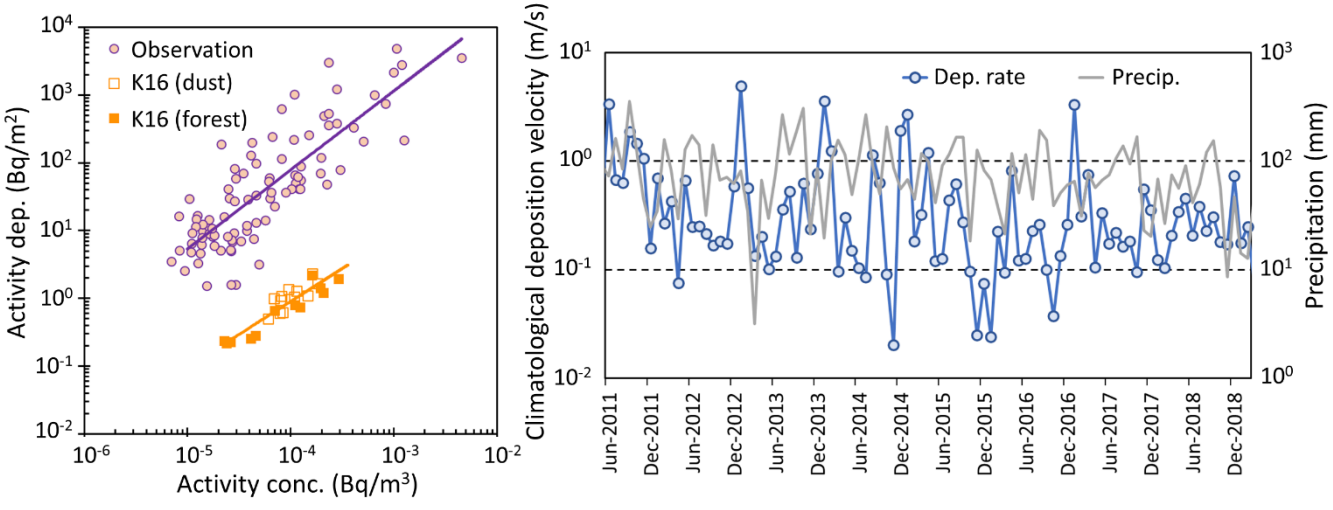

Figure 9: (Left) Scatter diagram of (purple circles) observed surface concentrations and deposition of ^{137}Cs and those simulated (by Kajino et al., 2016; K16) considering different emission sources, (orange open squares) mineral dust from bare soil and (orange close squares) aerosols emitted from forest ecosystems. The purple and orange lines indicate the regression lines of the observed data and the simulated (both dust and forest) data. (Right) Time series of (blue) climatological deposition velocity on the left axis and (gray) precipitation amounts on the right axis.

https://doi.org/10.5194/acp-2021-591
Preprint. Discussion started: 30 July 2021

Atmospheric Chemistry and Physics Discussions

The left panel of Fig. 9 clearly shows that the removal rate (a) used in Kajino et al. (2016) can be underestimated by one to two orders of magnitude. The deposition velocities used in Kajino et al. (2016) were estimated from the observation of ^{137}Cs in March 2011, which was supposed to be mainly composed of submicron water-soluble particles. However, the current study and the series of previous studies regarding resuspended ^{137}Cs indicated that the host particles of ^{137}Cs could be substantially larger (e.g., soil and bioaerosols). This may be the reason for the overestimation of simulated ^{137}Cs from forests in the summer in Fukushima city. If the deposition velocities of the model increased by one to two orders of magnitude, the transport of ^{137}Cs from the contaminated forest to Fukushima city in summer may decrease such that the simulated surface concentration in Fukushima city agrees with the observation. Certainly, their simulated regional budget needs to be reassessed using the realistic deposition velocities indicated in the current study.

The observed climatological deposition velocity varied by more than one order of magnitude over time. There are two main deposition mechanisms: dry deposition and wet deposition. Wet deposition is associated with precipitation. The variations in the climatological deposition rate seem to agree with the observed precipitation, but almost no correlation was observed ($R \sim 0.10$). The mean climatological deposition velocity was 5.3×10^{-1} m s^{-1}, and the peak values occurred in January. The maximum value was 4.9 m s^{-1} in January 2013, when the monthly precipitation was not very high (81.2 mm). Possible reasons for these peaks in January are discussed later, in Sect. 4.3. The typical order of the dry deposition velocity of supermicron (1–10 μm in diameter) particles is approximately 10^{-3}–10^{-2} m s^{-1} (e.g., Petroff and Zhang, 2010), which is substantially lower than the values in our climatological deposition velocity analysis. Certainly, the magnitudes of the instant deposition velocity and our climatological deposition velocity are not directly comparable, but it seems that wet deposition plays an important role in the removal of resuspended ^{137}Cs-bearing atmospheric aerosols.

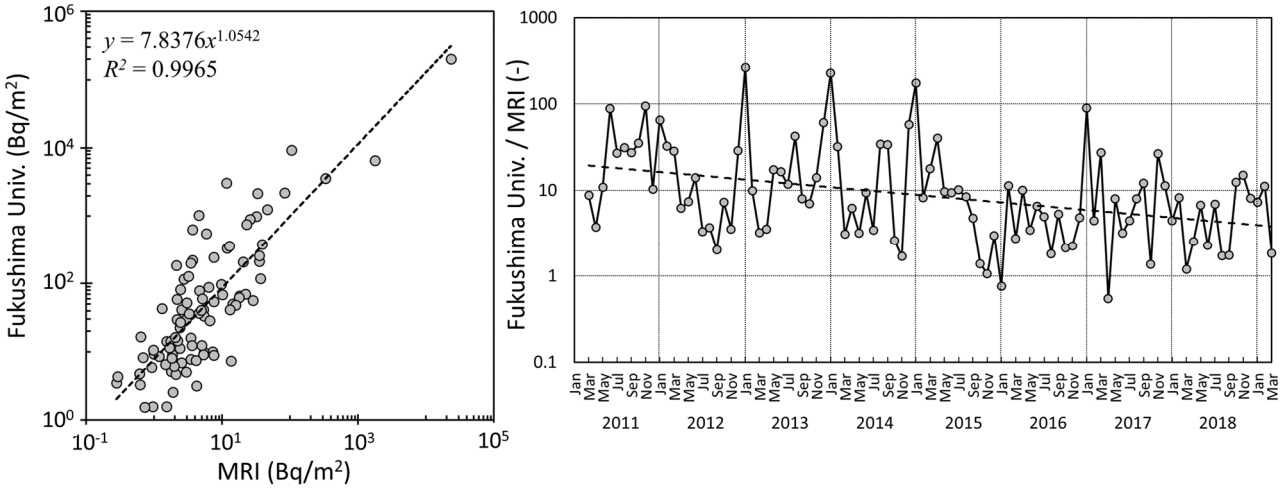

Figure 10: (Left) Scatter diagram of the observed surface deposition of ^{137}Cs at Fukushima University and the MRI from March 2011 to March 2019, with a regression line. (Right) Time series of the ratio of deposition at Fukushima University to deposition at the MRI, with a regression line.

https://doi.org/10.5194/acp-2021-591
Preprint. Discussion started: 30 July 2021


Atmospheric Chemistry and Physics Discussions

3.6 Comparison of deposition amounts at Fukushima University and the MRI

Figure 10 compares the deposition amounts of ^{137}Cs at Fukushima University (60 km northwest of the FDNPP) and the MRI (170 km southwest of the FDNPP) from March 2011 to March 2019. The deposition data at the MRI are available from Environmental Radioactivity and Radiation in Japan (https://www.kankyo-hoshano.go.jp/data/database/, last accessed: June 14, 2021). There was a significant positive correlation between the deposition amounts of ^{137}Cs at the two sites. The slope of the regression indicates that the ratio of deposition at Fukushima University to that at the MRI did not change significantly from the initial ratio during the eight years, which is approximately 8-9 times (202200 Bq m^{-2} at Fukushima University and 23100 Bq m^{-2} at the MRI). This indicates that deposition was influenced by emissions from nearby sources and was not substantially influenced by long-range transport at either site. The right panel of Fig. 10 indicates that the deposition ratios at the two sites were approximately 10, with a variation of more than one order of magnitude and peaks in winter (especially January) that decreased slightly over time. The right panel of Fig. 9 shows that the January peak is a feature of Fukushima city and was not observed at the MRI. The possible reasons for the January peak in Fukushima City are discussed later, in Sect. 4.3. The slight decreasing trend was probably due to decontamination, which was ongoing in Fukushima during the period until 2018, as shown later in Table 1. Certainly, natural variations could also have contributed to the decreasing trend.

4 Discussion

Even eight years after the FDNPP accident, the surface air activity concentration of ^{137}Cs had not fallen to the level before the accident, which was at an order of magnitude of 10^{-6} Bq m^{-3}. In difficult-to-return zones, the surface concentrations sometimes still exceed 10^{-2} Bq m^{-3}. Based on long-term measurements, this study tries to understand the characteristics of radio-Cs in the air and its deposition and to reveal its origins in order to identify effective ways to reduce radioactivity in contaminated terrestrial ecosystems.

4.1 Seasonal variation and possible sources

The current study clearly shows that the surface concentrations of ^{137}Cs are high from winter to spring, with peaks in March and lows from summer to autumn, in the urban/rural area of Fukushima city (60 km northwest of the FDNPP). It also shows that the deposition amounts of ^{137}Cs are high in the winter, especially in January, and low from summer to autumn. This seasonal trend is the opposite of that observed in a forested area in the Abukuma Highlands (Tsushima, 30 km northwest of the FDNPP), which was high in the summer (Ochiai et al., 2016; Kinase et al., 2017). From winter to spring, northwesterly winds prevail over the region associated with migrating disturbances, while southeasterly winds prevail over the region associated with the Pacific high. The three simulated monthly mean surface wind fields for January to March and June to August are shown in Kajino et al. (2016).

https://doi.org/10.5194/acp-2021-591
Preprint. Discussion started: 30 July 2021


Atmospheric Chemistry and Physics Discussions

In summer, Fukushima city is downwind of Tsushima. The surface concentrations of ^{137}Cs at Tsushima are approximately ten times greater than those at Fukushima city, and Fukushima city is downwind of Tsushima, but there is no enhancement of ^{137}Cs in summer. The traveling distances of carrier aerosols depend on their aerodynamic diameters. The distance between the two sites is approximately 30 km. The traveling distances of aerosols below < 10 μm are not very different and are larger than 100 km because their gravitational deposition velocities are negligibly small. On the other hand, the traveling distances rapidly decrease proportionally to a square of the diameter above 10 μm, and the traveling distance of an aerosol with a diameter of 100 μm is an order of 1 km (Kajino et al., 2021). Aerosols below < 10 μm can travel longer distances, but their dry deposition amounts increase significantly from 1 μm to 10 μm (Kajino et al., 2021). Igarashi et al. (2019a) reported that the major proportions of bioaerosols in forests in summer are smaller than 5 μm in diameter and can travel a fairly long distance. Pollen is much larger than 10 μm, but pollen emission is limited in summer (Igarashi et al., 2019a). Consequently, there was a significant enhancement in surface concentrations in the forests in summer but no enhancement in the downwind urban/rural areas, probably because the carrier aerosols were efficiently deposited onto the ground surface before significant amounts of atmospheric ^{137}Cs reached the downwind areas. Consistent with our findings presented in Fig. 5, ^{137}Cs in PM_c was more abundant than that in PM_f and the backup filter particles in summer. To obtain a quantitative understanding of the regional cycle of atmospheric ^{137}Cs in the northern part of Fukushima Prefecture, accurate simulations are required in the future.

In winter and spring, the surface concentrations of ^{137}Cs are probably enhanced due to the local emissions from the nearby sources because the location of the sampling site is upwind of the Abukuma Highlands and the ground surface in the upwind areas of the sampling site in the season (northwest directions) is less contaminated than the site. In winter and spring, ^{137}Cs in the backup filter particles and PM_f are pronounced in Fukushima city. These characteristics are somewhat different from those reported in previous studies. Miyamoto et al. (2014) measured the size distributions of radio-Cs with a cascade impactor for two periods, from March 17 to April 1 and May 9 to 13, 2011, at a site 120 km southwest of the FDNPP. They showed that the peak size ranges were 1.2 - 2.1 μm and 0.65 - 1.1 μm in the former and latter periods, respectively. Doi et al. (2013) reported that the peak diameters of the ^{137}Cs concentration from April 4 to 11 were 1.0 μm and 1.5 μm at Tsukuba, 170 km southwest of the FDNPP. Kaneyasu et al. (2017) measured the size distributions of ^{137}Cs and other chemical components six times at Tsukuba from April to September 2011. The peak diameter ranges were 0.49 - 0.7 μm in the earlier stages (before June 9), but the contributions of coarse-mode particles (> 1 μm) increased after June 9, and the second modes appeared in the ranges of 3.5 - 5.2 μm and 7.8 - 11 μm in July and September, respectively. Judging from their measured mass size distributions of Ca, which is assumed to originate from mineral soil, Kaneyasu et al. (2017) concluded that soil particles could be the major carrier of resuspended radio-Cs in Tsukuba. Our XRF analysis indicated that radio-Cs is carried mainly by soil particles in Fukushima city, but the size distributions are greater in PM_f (<2.5 μm) and in the backup filter particles. If radio-Cs is carried by soil particles, it is natural to presume that the fractions of radio-Cs in PM_c would be large (e.g., Fig. 3 of Kaneyasu et al., 2012 or Fig. 4 of Kaneyasu et al., 2017). One could argue that the bounced coarse mode soil particles are observed in the backup filters, but in fact, the seasonal mean Cs concentrations in the backup filter are positively correlated with PM_f and

https://doi.org/10.5194/acp-2021-591
Preprint. Discussion started: 30 July 2021


Atmospheric Chemistry and Physics Discussions

negatively correlated with PM_c (Fig. 5). One could further argue that bounced large particles are also collected in PM_f despite the special procedures employed to prevent rebound in the impactor/cyclone system.

There are four possible explanations for these results: (1) If the bouncing effect did not occur in either system, the major sources of radio-Cs in Fukushima city are probably related to combustion (a mass peak below 0.39 μm means that the number peak is approximately 100 nm). If the bouncing effect occurred only in the cascade impactor, (2) if the origin of radio-Cs is soil particles, the size distributions of soil particles in Fukushima city are smaller, or radio-Cs in the soil exists more within finer particles; (3) if the origin of radio-Cs is soil particles, the coarse-mode fraction deposits to the ground surface faster than the fine-mode fraction, such that the proportion of Cs in PM_f is larger in Fukushima city. (4) The bouncing effect occurs in both systems, and the origin of radio-Cs is coarse-mode soil particles. (1) is less likely because there is little chance of the artificial combustion of contaminated biomass. In fact, there were no temporal correlations between the ^{137}Cs and levoglucosan (a biomass burning marker) surface air concentrations at Tsushima during the forest fire event in the Abukuma Highlands that occurred in March 2013 (Kinase et al., 2018). (3) is also less likely because long-range transport (at least 100 km) is required for the major proportions of coarse-mode particles to deposit to the ground surface, whereas Fukushima city is characterized as the emission source region in that season. In terms of (2), the latter sentence, "radio-Cs in the soil exists more with finer particles", contradicts Kaneyasu et al. (2017), suggesting that the radio-Cs is uniformly distributed on the surface of soil particles. (4) is possible, but rebound is prevented in the impactor/cyclone system, and there is also no evidence that rebound occurred in the impactor/cyclone system (certainly, there is also no evidence that rebound did not occur). Further experiments are required to determine whether (2) or (4) is more likely and whether some sources are missing. As Kaneyasu et al. (2012) and (2017) reported, comparing the size distributions of ^{137}Cs with those of other chemical components in Fukushima city would be an effective way to investigate the origin of resuspended radio-Cs from winter to spring. Alternatively, a $PM_{2.5}$ cyclone or virtual impactor could be used to separate the fine-mode and coarse-mode particles, that can completely exclude the bouncing effect.

4.2 Differences in trends before and after approximately 2015 (natural variation and decontamination)

As described in Sects. 3.1 and 3.2, distinct decrease rates were observed before and after approximately 2015 in both the surface concentrations and the deposition. There may be two main reasons for this: natural variation and decontamination. The natural variation (the dissolved fractions of precipitation or the exchangeable proportions of forest soils discharging faster than other forms from the local ecosystems (Manaka et al., 2016)) was previously described, and the effect of decontamination is presented in some detail here.

https://doi.org/10.5194/acp-2021-591
Preprint. Discussion started: 30 July 2021

Atmospheric Chemistry and Physics Discussions

Table 1: Decontamination achievement ratios in Fukushima City and the surrounding municipalities (Nihonmatsu City, Kawamata Town[a], Date City, and Koori Town)

	March 2014	March 2015	March 2016	March 2017	March 2018
Fukushima City					
Residential area (Number of houses)	50.2 %	62.3 %	100.0 %	100.0 %	100.0 %
Public facility (Number of facilities)	89.3 %	92.3 %	97.5 %	100.0 %	100.0 %
Road (km)	9.1 %	16.1 %	39.6 %	50.2 %	100.0 %
Agricultural field (ha)	94.0 %	94.4 %	95.2 %	96.0 %	100.0 %
Forest (living area)[b] (ha)	5.0 %	6.3 %	37.3 %	80.8 %	100.0 %
The surrounding municipalities					
Residential area (Number of houses)	87.2 %	97.4 %	99.6 %	100.0 %	100.0 %
Public facility (Number of facilities)	34.3 %	55.3 %	80.2 %	94.9 %	100.0 %
Road (km)	48.7 %	56.8 %	67.5 %	82.0 %	100.0 %
Agricultural field (ha)	99.0 %	99.0 %	99.6 %	100.0 %	100.0 %
Forest (living area)[b] (ha)	23.9 %	36.7 %	64.1 %	88.6 %	100.0 %

[a]Only the western part of Kawamata town. The decontamination of areas with an annual cumulative dose exceeding 20 mmSv was assigned to the central government, and that in areas with a dose below 20 mmSv was assigned to municipal governments. The decontamination of the eastern part of Kawamata town was conducted by the central government.

[b]Removal of the litter layer in forests within 20 meters of the forest edge.

Table 1 summarizes the achievement ratios of the scheduled decontamination of different land use types in Fukushima city and the surrounding municipalities (available at https://www.pref.fukushima.lg.jp/site/portal/progress.html, last accessed: June 14, 2021). The municipalities are in the northern part of Fukushima Prefecture, which comprises 55 % forest area, 15 % farmland area, 6 % residential area, and 23 % other areas (https://www.pref.fukushima.lg.jp/uploaded/attachment/42042.pdf, last accessed: June 14, 2021). More than 94 % decontamination was achieved for the farmland area by March 2014. For the residential and public facility areas, some parts were decontaminated by March 2014, but some others were not fully decontaminated until March 2018. For the road and forest areas, decontamination was not completed in most areas by March 2014, but extensive decontamination was conducted from 2014 to 2018. Note that only a part of the forest (20 m from the forest edges) was decontaminated, which accounts for approximately 1 % of the whole forest area of the northern part of Fukushima Prefecture. Additionally, only the litter layer of the forest was removed, and the soil layer remained.

Suppose that if contamination occurred independently of the land use type, approximately 30 % (farmland + half of residential and other) of northern Fukushima was decontaminated by 2014, and an additional 15 % (half of residential and other) was continuously decontaminated by 2018. The difference between the decrease rate from May 2011 to December 2014 (93.1 % y^{-1}) and that after (30.7 %y^{-1}) was higher than the decontamination rate (30 - 45 % per three to seven years). If the

https://doi.org/10.5194/acp-2021-591
Preprint. Discussion started: 30 July 2021


Atmospheric Chemistry and Physics Discussions

surface concentration at Fukushima University was affected mainly by the emissions from nearby sources (i.e., within the northern part of Fukushima Prefecture), decontamination would not be the sole reason for the change in the decrease rates before approximately 2015 and after. Natural variation (i.e., regime changes in the chemical forms of radio-Cs) would likely occur during that period. As previously discussed, biotite may have played a key role in the environmental behaviors of radio-Cs in Fukushima city after approximately 2015, but the current study could not identify the key aerosol particles that carried dissolved (or exchangeable) radio-Cs and were abundant in Fukushima city before approximately 2015.

4.3 Substantial deposition amounts in January in Fukushima city

The climatological deposition velocities (or the ratios of the deposition rate to the mean surface concentration) in Fukushima City were remarkably high in January 2013, 2014, 2015, and 2017 (Fig. 9). They were approximately one order of magnitude larger than those in the other months. The ratio of the deposition in Fukushima and to that at the MRI was approximately 10 on average, but those in January of those years exceeded 100 (Fig. 10). On the other hand, no peaks were observed in January of 2012, 2016, or 2018.

There are two possible explanations for these results: vertical distribution and the existence of superlarge particles. In terms of the former, the substantial proportions of ^{137}Cs in the upper air may have caused lower surface concentrations but higher deposition due to the wet removal of ^{137}Cs aloft. However, due to the northwesterly winter monsoon, the upper air over Fukushima city is also upwind of the Abukuma Highlands; thus, this possibility is less likely. In terms of the latter, superlarge particles (~100 μm or larger in diameter), have settling velocities that are too high (as high as those of drizzle droplets) to enter the high-volume air sampler but that allow them to settle efficiently in a deposition sampler. A similar feature has been observed in the relationship of the deposition and surface concentration of sodium at observation sites near coastal areas (e.g., particles denoted as large sea salt particles (LSPs) in Kajino et al., 2012). The travel distance of such large particles is approximately 1 km (e.g., Kajino et al., 2021), and Fukushima University is surrounded by major roads, such as Route 4 and National Highway E4, within 1 km. January is the month when the highest snow depth occurs in the Fukushima Basin, and the road surface may be wet and muddy due to snow removal work using deicing agents and daytime snow melt on pavements; therefore, road dust emissions from busy transportation activities may be enhanced. The muddy surface conditions may produce even larger road dust particles. Although there is no evidence of the existence of such superlarge particles, they may be a possible reason for the substantial deposition amounts in January in Fukushima city. In fact, substantial amounts of road salt from deicing agents could contribute to roadside PM_{10} samples in winter (Denby et al., 2016), indicating that there could be emissions of particles even larger than 10 μm in diameter. In addition to the direct deposition of ^{137}Cs to the rain sampler at Fukushima University, the immediate resuspension of deposited ^{137}Cs associated with road dust or road salt from nearby roads around the university could contribute additional deposition to the rain sampler. Unfortunately, analyses of the surface meteorological observational data for Fukushima City from the JMA, such as temperature, precipitation, snow cover, and wind

https://doi.org/10.5194/acp-2021-591
Preprint. Discussion started: 30 July 2021


Atmospheric Chemistry and Physics Discussions

speed data, did not reveal the differentiating features between the years with (2013, 2014, 2015, and 2017) and without (2012, 2016, and 2018) high deposition peaks.

5 Conclusions

Eight-year measurements of atmospheric ^{134}Cs and ^{137}Cs conducted at Fukushima University from March 2011 to March 2019 are summarized in this study. A high-volume sampler, a cascade impactor, and an impactor/cyclone system were used to collect aerosol samples, and the activity concentrations of radio-Cs were detected by high-purity germanium detectors. A precipitation sampler was used to collect deposition samples, and the dissolved and particulate fractions of radio-Cs in the samples were measured. X-ray fluorescence (XRF) analysis was carried out to measure the elemental contents of the aerosol and precipitation samples. The concentration and deposition data measured at Fukushima University were compared with numerical simulation results.

The major findings are itemized as follows:

(1) The observed surface concentrations and deposition at Fukushima University (an urban/rural area of Fukushima city, 60 km northwest of the FDNPP) were high in winter and low in summer; these seasonal trends are the opposite of those observed in a contaminated forest area (Ochiai et al., 2016; Kinase et al., 2018) (30 km northwest of the FDNPP, in the Abukuma Highlands). Resuspension due to bioaerosol emissions (Kinase et al., 2018; Igarashi et al., 2019a) may be substantial in forests but may not be in urban/rural areas. The half-life (T_h) and decrease rate (R_d) for the eight years were 456 d and 55.6 % y^{-1} for the concentrations and 2.35 y and 29.5 % y^{-1} for the deposition, respectively.

(2) The decreasing trends changed in approximately 2015 and were associated with changes in the dissolved/particulate fractions of ^{137}Cs in precipitation. The T_h and R_d for concentrations before 2015 were 272 d and 93.1 % y^{-1}, whereas they were 825 d and 30.7 % y^{-1} after 2015. The T_h and R_d for deposition before 2015 were 1.10 y and 63.2 % y^{-1}, whereas they were 5.39 y and 12.9 % y^{-1} after 2015. The dissolved fractions were higher before 2015, whereas the particulate fractions were higher after 2016. This may have been because the dissolved proportion of radio-Cs discharged faster than its particulate forms from the local terrestrial ecosystems. This is consistent with the findings of Manaka et al. (2016). Decontamination likely also contributed to the difference because the decontamination of some land use types, such as agricultural fields, was completed before 2014, and 100 % of the planned decontamination was completed by March 2018. The contribution of decontamination was estimated in this study to be 30 - 45 % for the three to seven years, which is significantly smaller than the differences in the R_d of the concentrations (93.1 % y^{-1} before 2015 and 30.7 % y^{-1} after 2015). Therefore, decontamination may play a partial role in explaining the differences in T_h and R_d before and after 2015, but changes in the chemical forms of radio-Cs likely play a major role.

https://doi.org/10.5194/acp-2021-591
Preprint. Discussion started: 30 July 2021


Atmospheric Chemistry and Physics Discussions

(3) The size-resolved measurements showed that the dominant size range in activity in the cascade impactor data was the backup filter (<0.39 μm in diameter, or particles rebounded from larger stages), followed by the 4.2-10.2 μm and >10.2 μm sizes. The backup filter particles were abundant in winter. The seasonal mean ^{137}Cs concentrations in the backup filter of the cascade impactor were positively correlated with those in the fine-mode aerosols collected by the impactor/cyclone system (PM_f) and negatively correlated with those in the coarse-mode aerosols (PM_c). PM_c was high in summer. The impactor/cyclone system prevented the bouncing effect, but bouncing may still have occurred during long-duration samplings. The XRF analysis showed that biotite may have played a key role in the environmental circulation of particulate forms of resuspended radio-Cs in Fukushima city after September 2014.

(4) The deposition amounts of ^{137}Cs in January were remarkably high compared to the surface concentrations of ^{137}Cs and the deposition amounts of ^{137}Cs at the MRI. Although we have no observational evidence, we hypothesize that the existence of superlarge particles (~100 μm or larger, with a distance of ~ 1 km or less) associated with snow removal operations on major roads near Fukushima University may be one of the reasons for the remarkable high deposition amounts in January.

Certain issues remained unresolved, and topics for future study are summarized as follows:

(1) The Abukuma Highlands are upwind of Fukushima city in summer. The enhancement of ^{137}Cs in PM_c in summer is consistent with the fact that most bioaerosols exist in coarse mode. However, if radiocesium is carried mainly by biotite (i.e., soil particles) in winter, there should be an enhancement of ^{137}Cs in PM_c because major proportions of soil particles exist in coarse mode (e.g., Kaneyasu et al., 2017). On the other hand, sources of Cs-bearing fine-mode particles such as combustion emissions may be less likely. Thus, the main carrier of radio-Cs may be biotite in winter, but this is still not fully confirmed. XRF measurements were conducted for PM_f from September 2014 to January 2018, when the particulate proportions were dominant in the precipitation. Thus, the carrier aerosols of dissolved radio-Cs in Fukushima city are still unknown. As Kaneyasu et al. (2012) and (2017) reported, comparisons of the size distributions of ^{137}Cs with those of other chemical components in Fukushima city would be an effective way to investigate the origin of resuspended radio-Cs from winter to spring. Alternatively, a $PM_{2.5}$ cyclone or virtual impactor could be applied to separate the fine-mode and coarse-mode particles, which can completely exclude the bouncing effect.

(2) The simulation used in this study was made to be consistent with the surface concentrations in a contaminated forest (Tsushima) and those in a downwind area (the MRI, 170 km southwest of the FDNPP). However, the current study found that the simulated seasonal variation in Fukushima city was totally opposite to the observations. The current study indicated that the deposition velocities applied in the simulation were significantly underestimated. Numerical simulation is a powerful tool for quantitative assessment, but the current simulation requires further improvement. The reasons for the seasonal variations in concentrations and deposition in the different locations need to be investigated with an improved model.

https://doi.org/10.5194/acp-2021-591
Preprint. Discussion started: 30 July 2021

Atmospheric Chemistry and Physics Discussions

Data availability

The observation data used in the study are provided as a Microsoft Excel file in the supplement.

Author contribution

AW conducted the long-term measurements together with KN and AS. YN performed the XRF analysis, and MK performed the numerical simulation. AW, MK, and KN designed the manuscript structure and completed the draft together with all authors.

Competing interests

The authors declare that they have no conflicts of interest.

Acknowledgments

This work was supported by Grants-in-Aid for Scientific Research (KAKENHI), grant numbers JP16H01777 and JP24110009. This work was also supported by the Sumitomo Foundation's Environmental Studies Grant and partly supported by the Environment Research and Technology Development Fund (JPMEERF20215003) of the Environmental Restoration and Conservation Agency of Japan. The authors thank Dr. Teruyuki NAKAJIMA of the National Institute for Environmental Studies and Dr. Haruo TSURUTA of the Remote Sensing Technology Center for proving and installing a high-volume sampler and Prof. Naohiro YOSHIDA of Tokyo Institute of Technology for the installation of an impactor observation system. The authors thank Dr. Shogo TOGO of the Isotope Research Center of the University of Tokyo for the radioactivity measurements of the initial samples and Dr. Yoshiaki YAMAGUCHI, Dr. Zijian ZHANG, Dr. Makoto INAGAKI, Mr. Shunsuke KAKITANI, Mr. Kazuya FUJIHARA and Mr. Nobufumi FUJITA of Osaka University for their support with the radioactivity measurements of the air samples. The authors also thank Mr. Kakeru KONNAI of the University of Tsukuba for data visualization, Dr. Akane SAYA of the MRI for a useful discussion of aerosol deposition processes, and Prof. Tomoaki OKUDA of Keio University for a useful discussion of the possible artifacts in the impactor measurements.

https://doi.org/10.5194/acp-2021-591
Preprint. Discussion started: 30 July 2021


Atmospheric Chemistry and Physics Discussions

References

Adachi, K., Kajino, M., Zaizen, Y. and Igarashi, Y.: Emission of spherical cesium-bearing particles from an early stage of the Fukushima nuclear accident, Sci. Rep., 3(Plume 1), 12–15, doi:10.1038/srep02554, 2013.

Ager, A. A., Lasko, R., Myroniuk, V., Zibtsev, S., Day, M. A., Usenia, U., Bogomolov, V., Kovalets, I. and Evers, C. R.: The wildfire problem in areas contaminated by the Chernobyl disaster, Sci. Total Environ., 696(August), 133954, doi:10.1016/j.scitotenv.2019.133954, 2019.

Denby, B. R., Ketzel, M., Ellermann, T., Stojiljkovic, A., Kupiainen, K., Niemi, J. V., Norman, M., Johansson, C., Gustafsson, M., Blomqvist, G., Janhäll, S. and Sundvor, I.: Road salt emissions: A comparison of measurements and modelling using the NORTRIP road dust emission model, Atmos. Environ., 141, 508–522, doi:10.1016/j.atmosenv.2016.07.027, 2016.

Igarashi, Y., Kita, K., Maki, T., Kinase, T., Hayashi, N., Hosaka, K., Adachi, K., Kajino, M., Ishizuka, M., Sekiyama, T. T., Zaizen, Y., Takenaka, C., Ninomiya, K., Okochi, H. and Sorimachi, A.: Fungal spore involvement in the resuspension of radiocaesium in summer, Sci. Rep., 9(1), doi:10.1038/s41598-018-37698-x, 2019a.

Igarashi, Y., Kogure, T., Kurihara, Y., Miura, H., Okumura, T., Satou, Y., Takahashi, Y. and Yamaguchi, N.: A review of Cs-bearing microparticles in the environment emitted by the Fukushima Dai-ichi Nuclear Power Plant accident, J. Environ. Radioact., 205–206(April), 101–118, doi:10.1016/j.jenvrad.2019.04.011, 2019b.

Igarashi, Y., Onda, Y., Wakiyama, Y., Konoplev, A., Zheleznyak, M., Lisovyi, H., Laptev, G., Damiyanovich, V., Samoilov, D., Nanba, K. and Kirieiev, S.: Impact of wildfire on 137Cs and 90Sr wash-off in heavily contaminated forests in the Chernobyl exclusion zone, Environ. Pollut., 259, 113764, doi:10.1016/j.envpol.2019.113764, 2020.

Ikehara, R., Morooka, K., Suetake, M., Komiya, T., Kurihara, E., Takehara, M., Takami, R., Kino, C., Horie, K., Takehara, M., Yamasaki, S., Ohnuki, T., Law, G. T. W., Bower, W., Grambow, B., Ewing, R. C. and Utsunomiya, S.: Abundance and distribution of radioactive cesium-rich microparticles released from the Fukushima Daiichi Nuclear Power Plant into the environment, Chemosphere, 241, 125019, doi:10.1016/j.chemosphere.2019.125019, 2020.

Iwagami, S., Onda, Y., Tsujimura, M. and Abe, Y.: Contribution of radioactive 137Cs discharge by suspended sediment, coarse organic matter, and dissolved fraction from a headwater catchment in Fukushima after the Fukushima Dai-ichi Nuclear Power Plant accident, J. Environ. Radioact., 166, 466–474, doi:10.1016/j.jenvrad.2016.07.025, 2017.

Kajino, M., Deushi, M., Maki, T., Oshima, N., Inomata, Y., Sato, K., Ohizumi, T. and Ueda, H.: Modeling wet deposition and concentration of inorganics over Northeast Asia with MRI-PM/c, Geosci. Model Dev., 5(6), doi:10.5194/gmd-5-1363-2012, 2012.

Kajino, M., Ishizuka, M., Igarashi, Y., Kita, K., Yoshikawa, C. and Inatsu, M.: Long-term assessment of airborne radiocesium after the Fukushima nuclear accident: Re-suspension from bare soil and forest ecosystems, Atmos. Chem. Phys., 16(20), doi:10.5194/acp-16-13149-2016, 2016.

Kajino, M., Sekiyama, T. T., Igarashi, Y., Katata, G., Sawada, M., Adachi, K., Zaizen, Y., Tsuruta, H. and Nakajima, T.: Deposition and Dispersion of Radio-Cesium Released Due to the Fukushima Nuclear Accident: Sensitivity to

https://doi.org/10.5194/acp-2021-591
Preprint. Discussion started: 30 July 2021


Atmospheric Chemistry and Physics Discussions

Meteorological Models and Physical Modules, J. Geophys. Res. Atmos., 124(3), 1823–1845, doi:10.1029/2018JD028998, 2019.

Kajino, M., Adachi, K., Igarashi, Y., Satou, Y., Sawada, M., Thomas Sekiyama, T., Zaizen, Y., Saya, A., Tsuruta, H. and Moriguchi, Y.: Deposition and Dispersion of Radio-Cesium Released due to the Fukushima Nuclear Accident: 2. Sensitivity to Aerosol Microphysical Properties of Cs-Bearing Microparticles (CsMPs), J. Geophys. Res. Atmos., 126(1), doi:10.1029/2020JD033460, 2021.

Kaneyasu, N., Ohashi, H., Suzuki, F., Okuda, T. and Ikemori, F.: Sulfate aerosol as a potential transport medium of radiocesium from the fukushima nuclear accident, Environ. Sci. Technol., 46(11), 5720–5726, doi:10.1021/es204667h, 2012.

Kinase, T., Kita, K., Igarashi, Y., Adachi, K., Ninomiya, K., Shinohara, A., Okochi, H., Ogata, H., Ishizuka, M., Toyoda, S., Yamada, K., Yoshida, N., Zaizen, Y., Mikami, M., Demizu, H. and Onda, Y.: The seasonal variations of atmospheric 134,137Cs activity and possible host particles for their resuspension in the contaminated areas of Tsushima and Yamakiya, Fukushima, Japan, Prog. Earth Planet. Sci., 5(1), doi:10.1186/s40645-018-0171-z, 2018.

Kinase, T., Adachi, K., Sekiyama, T. T., Kajino, M., Zaizen, Y. and Igarashi, Y.: Temporal variations of 90Sr and 137Cs in atmospheric depositions after the Fukushima Daiichi Nuclear Power Plant accident with long-term observations, Sci. Rep., 10(1), 1–8, doi:10.1038/s41598-020-78312-3, 2020.

Kita, K., Igarashi, Y., Kinase, T., Hayashi, N., Ishizuka, M., Adachi, K., Koitabashi, M., Sekiyama, T. T. and Onda, Y.: Rain-induced bioecological resuspension of radiocaesium in a polluted forest in Japan, Sci. Rep., 10(1), 1–15, doi:10.1038/s41598-020-72029-z, 2020.

Kogure, T., Mukai, H., and Kikuchi, R.: Weathered biotite: A key material of radioactive contamination in Fukushima, *in Agricultural Implications of the Fukushima Nuclear Accident (III): After 7 years*, eds. Nakanishi, T. M., O'Brien, M., and Tanoi, K., Springer Open, Singapore, ISBN978-981-13-3218-0, doi:10.1007/978-981-13-3218-0, 2019.

Manaka, T., Imamura, N., Kaneko, S., Miura, S., Furusawa, H. and Kanasashi, T.: Six-year trends in exchangeable radiocesium in Fukushima forest soils, J. Environ. Radioact., 203(October 2018), 84–92, doi:10.1016/j.jenvrad.2019.02.014, 2019.

Nakajima, T., Misawa, S., Morino, Y., Tsuruta, H., Goto, D., Uchida, J., Takemura, T., Ohara, T., Oura, Y., Ebihara, M. and Satoh, M.: Model depiction of the atmospheric flows of radioactive cesium emitted from the Fukushima Daiichi nuclear power station accident, Prog. Earth Planet. Sci., 4(1), doi:10.1186/s40645-017-0117-x, 2017.

Ochiai, S., Hasegawa, H., Kakiuchi, H., Akata, N., Ueda, S., Tokonami, S. and Hisamatsu, S.: Temporal variation of post-accident atmospheric 137Cs in an evacuated area of Fukushima Prefecture: Size-dependent behaviors of 137Cs-bearing particles, J. Environ. Radioact., 165, 131–139, doi:10.1016/j.jenvrad.2016.09.014, 2016.

Okuda, T., Isobe, R., Nagai, Y., Okahisa, S., Funato, K., and Inoue, K.: Development of a high-volume PM2.5 particle sample using impactor and cyclone techniques, Aerosol Air Qaul. Res., 15, 759–767, doi:10.4209/aaqr.2014.09.0194, 2015.

Onda, Y., Taniguchi, K., Yoshimura, K., Kato, H., Takahashi, J., Wakiyama, Y., Coppin, F. and Smith, H.: Radionuclides from the Fukushima Daiichi Nuclear Power Plant in terrestrial systems, Nat. Rev. Earth Environ., 1(12), 644–660, doi:10.1038/s43017-020-0099-x, 2020.

https://doi.org/10.5194/acp-2021-591
Preprint. Discussion started: 30 July 2021


Atmospheric Chemistry and Physics Discussions

Petroff, A. and Zhang, L.: Development and validation of a size-resolved particle dry deposition scheme for application in aerosol transport models, Geosci. Model Dev., 3, 753-769, doi:10.5194/gmd-3-753-2010, 2010.

Sato, Y., Sekiyama, T. T., Fang, S., Kajino, M., Quérel, A., Quélo, D., Kondo, H., Terada, H., Kadowaki, M., Takigawa, M., Morino, Y., Uchida, J., Goto, D. and Yamazawa, H.: A model intercomparison of atmospheric 137Cs concentrations from the Fukushima Daiichi Nuclear Power Plant accident, phase III: Simulation with an identical source term and meteorological field at 1-km resolution, Atmos. Environ. X, 7(August), doi:10.1016/j.aeaoa.2020.100086, 2020.

Steinhauser, G., Niisoe, T., Harada, K. H., Shozugawa, K., Schneider, S., Synal, H. A., Walther, C., Christl, M., Nanba, K., Ishikawa, H. and Koizumi, A.: Post-Accident Sporadic Releases of Airborne Radionuclides from the Fukushima Daiichi Nuclear Power Plant Site, Environ. Sci. Technol., 49(24), 14028–14035, doi:10.1021/acs.est.5b03155, 2015.

Takase, T. and Nagahashi, Y.: Determination of major and trace elements in rock samples by X-ray fluorescence spectrometry -Comparison with a glass bands and a powder pellets method-, Journal of the Center for Regional Affairs Fukushima University, 19(2), 32-47, 2007. (In Japanese)

Takase, T.: Study of the existence form of radioactive cesium – In the case of fine particles collected from the suburbs of FDNPP, Grant-in-Aid for Scientific Research Result Reports (grant number 17K00545), 9 pp., 2020. Available at https://kaken.nii.ac.jp/ja/file/KAKENHI-PROJECT-17K00545/17K00545seika.pdf (last accessed: June 23, 2021)

Terada, H., Nagai, H., Tsuduki, K., Furuno, A., Kadowaki, M. and Kakefuda, T.: Refinement of source term and atmospheric dispersion simulations of radionuclides during the Fukushima Daiichi Nuclear Power Station accident, J. Environ. Radioact., 213(November 2019), 106104, doi:10.1016/j.jenvrad.2019.106104, 2020.

WHO (World Health Organization): *IARC Monographs on the Evaluation of Carcinogenic Risks to Humans, Ionizing Radiation, Part 2: Some Internally Deposited Radionuclides*, Vol. 78, IARC Press, 617 pp., 2001.

Yoshimura, K., Saegusa, J. and Sanada, Y.: Initial decrease in the ambient dose equivalent rate after the Fukushima accident and its difference from Chernobyl, Sci. Rep., 10(1), 1–9, doi:10.1038/s41598-020-60847-0, 2020.

scientific reports

Check for updates

OPEN

Temporal variations of ^{90}Sr and ^{137}Cs in atmospheric depositions after the Fukushima Daiichi Nuclear Power Plant accident with long-term observations

Takeshi Kinase[1]✉, Kouji Adachi[1], Tsuyoshi Thomas Sekiyama[1], Mizuo Kajino[1], Yuji Zaizen[1] & Yasuhito Igarashi[2,3]

We have measured artificial radionuclides, such as ^{90}Sr and ^{137}Cs, in atmospheric depositions since 1957 in Japan. We observed the variations in ^{90}Sr and ^{137}Cs, which were emitted from atmospheric nuclear tests and nuclear power plant accidents, due to their diffusion, deposition, and resuspension. In March 2011, the Fukushima Daiichi Nuclear Power Plant accident occurred in Japan, and significant increases in ^{90}Sr and ^{137}Cs were detected at our main site in Tsukuba, Ibaraki. Our continual observations revealed that the ^{137}Cs monthly deposition rate in 2018 declined to ~ 1/8100 of the peak level, but it remained more than ~ 400 times higher than that before the accident. Chemical analysis suggested that dust particles were the major carriers of ^{90}Sr and ^{137}Cs during the resuspension period at our main site. Presently, the effective half-life for ^{137}Cs deposition due to radioactive decay and other environmental factors is 4.7 years. The estimation suggests that approximately 42 years from 2011 are required to reduce the atmospheric ^{137}Cs deposition to a state similar to that before the accident. The current ^{90}Sr deposition, on the other hand, shows the preaccident seasonal variation, and it has returned to the same radioactive level as that before the accident.

Atmospheric nuclear tests and nuclear power plant accidents have released artificial radionuclides into the atmosphere, land surface, and ocean. No artificial radionuclides occurred in the environment before 1945, and human activities have led to increases in environmental radioactivity levels. Thus, the monitoring of artificial radionuclides has been a global assignment[1,2]. We have continuously monitored artificial radionuclides in atmospheric depositions for more than 63 years in the Kanto areas around Tokyo, Japan. Our long-term observations clarified the historical variations in artificial radionuclides in atmospheric depositions as a result of nuclear tests and their atmospheric transport and circulation from the 1950s to the 1970s[3–8]. For example, after the Partial Test Ban Treaty (PTBT) in 1963, atmospheric radionuclide deposition from the stratosphere, called global fallout, started to decline. However, the decline of the deposition rate was slowed because China and France continued nuclear tests until 1980. After the last nuclear test in 1980, the decrease rate increased until ~ 1990 (Fig. 1). In 1986, the Chernobyl accident caused a temporary increase in radionuclide deposition[9–11]. From ~ 1990 until March 2011, the decrease of the deposition rate was slowed again because of the change in radionuclide deposition processes, i.e., resuspension of artificial radionuclides hosted by local and remote dust particles[12–15]. These long-term observations of atmospheric deposition have demonstrated that the radionuclide changes in the environment depend on both global and local phenomena. The radionuclides in atmospheric deposition continued to decrease even after the cessation of their direct emissions.

In March 2011, an earthquake with a magnitude of 9.0 occurred and the subsequent tsunami severely damaged the Fukushima Daiichi Nuclear Power Plant (FDNPP). The accident resulted in enormous emissions of

[1]Meteorological Research Institute, 1-1 Nagamine, Tsukuba, Ibaraki 305-0052, Japan. [2]Institute for Integrated Radiation and Nuclear Science, Kyoto University (KURNS), 2, Asashiro-Nishi, Kumatori, Sennan, Osaka 590-0494, Japan. [3]Ibaraki University, 2-1-1, Bunkyo, Mito, Ibaraki 310-8512, Japan. ✉email: tkinase@mri-jma.go.jp

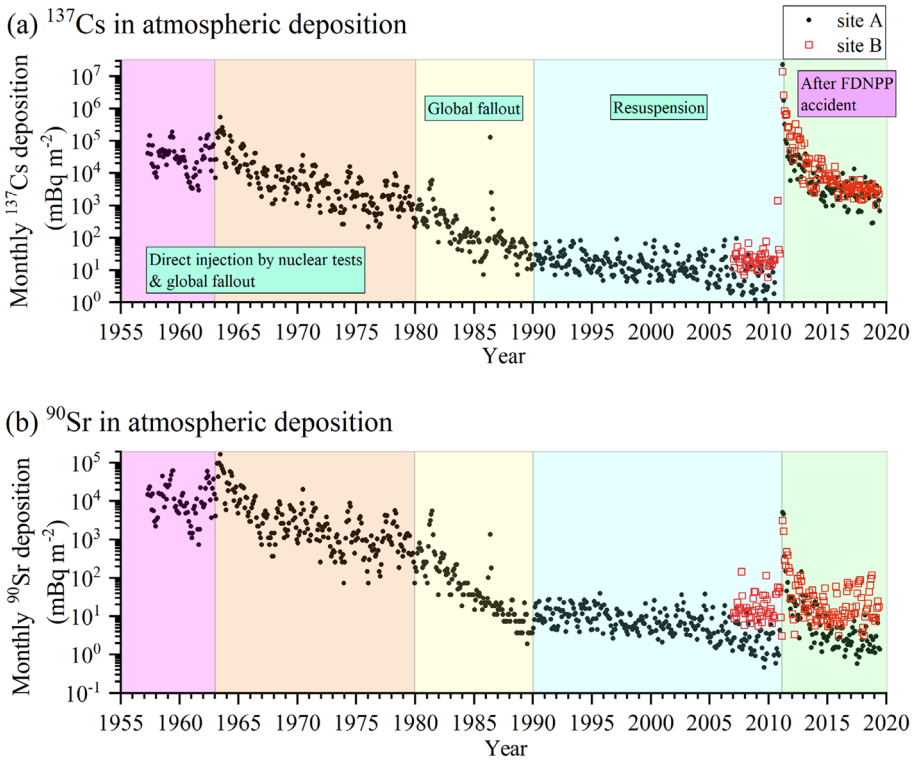

Figure 1. Historical observation of the activity of (**b**) ^{90}Sr and (**a**) ^{137}Cs in atmospheric depositions (mBq m^{-2}) and the change from 1957 to 2019 at site A (closed black circles) and that after 2007 at site B (open red squares).

artificial radionuclides including ^{90}Sr, ^{134}Cs, and ^{137}Cs (radiocesium) into the atmosphere and ocean[16–21]. Studies have estimated the amount of radioactive materials released from the accident[16,19,22] and their geographic distributions[23–25]. Other studies showed the chemical and physical properties of the carriers of radionuclides, such as glassy particles[26,27] and sulfate[28], and estimated the resuspension processes of ^{137}Cs in the atmosphere[29–36] through dust suspensions[32–34] or emissions of bioaerosols[34–36].

The radionuclides released into the environment eventually decline due to radioactive decay and other environmental processes. The rate of radioactive decay is inversely proportional to the respective physical half-life, which is 28.9, 2.1, and 30.2 years for ^{90}Sr, ^{134}Cs, and ^{137}Cs, respectively[37,38]. However, the rate of decline due to environmental removal processes is complex and depends on the weather, environment, and physical and chemical properties of radionuclides. It is crucial to understand the time scale of environmental decay to predict the fate of radioactive materials from accidents and to evaluate their long-term influences on the environment and human health. Hence, this study aims (1) to show our long-term observation results, (2) to estimate the current resuspension carriers of radionuclides, and (3) to evaluate their environmental decay period. To achieve this goal, we measured the radioactivities of ^{90}Sr, ^{134}Cs, and ^{137}Cs and stable elements and isotopes (Na, Mg, Al, K, Ca, Ti, Mn, Fe, Ni, Cu, Zn, Sr, Ba, ^{9}Be, ^{133}Cs, ^{232}Th, and ^{238}U) of monthly atmospheric deposition samples collected at two sites in different environments: suburban site A and mountain site B (Supplementary Fig. S1).

Results and discussion

Changes in radioactivity in atmospheric depositions after the accident. In March 2011, ^{134}Cs was detected with the same activity as that of ^{137}Cs. As ^{134}Cs had not been detected before the accident except during the emission period resulting from the Chernobyl accident in 1986[11,40,41], the observed ^{134}Cs/^{137}Cs ratio verified that the only source of ^{134}Cs and ^{137}Cs was the FDNPP (Supplementary Fig. S2). Our atmospheric aerosol samples indicated that at least three plumes resulting from the FDNPP accident passed across site A (Supplementary Fig. S3). When these plumes arrived at site A, the activities of ^{90}Sr and ^{137}Cs in atmospheric deposition increased to 2.7×10^3 and 3.2×10^6 times, respectively, higher than those before the accident (between July 2009 and June 2010) (Fig. 1). The ^{137}Cs/^{90}Sr activity ratio calculated from our observational results in March 2011 was 4.5×10^3. This large difference in the rate of increase between ^{90}Sr and ^{137}Cs reflects the discrepancy between their emission rates, i.e., the total amounts of ^{90}Sr and ^{137}Cs released were estimated as 0.02 PBq[39] and 14.5 PBq[23], respectively. These estimations indicated that the ^{90}Sr emission level was much lower than that of ^{137}Cs. The monthly ^{137}Cs deposition peak due to the FDNPP accident (2.31×10^4 Bq m^{-2}) was much higher than those resulting from nuclear weapon tests (548 Bq m^{-2}; June 1963) and the Chernobyl accident (131 Bq m^{-2}; May 1986) (Fig. 1a). On the other hand, the ^{90}Sr activity due to the FDNPP accident (5.2 Bq m^{-2}) was lower than that due to the nuclear tests in the 1960s (170 Bq m^{-2}; June 1963) (Fig. 1b). For comparison, the average ^{137}Cs values in atmospheric depositions before the FDNPP accident (between July 2009 and June 2010) were 7.0 (1.2–22.5) mBq m^{-2} at site A and 25.0 (6.1–76.4) mBq m^{-2} at site B, while those for ^{90}Sr amounted to 1.9 (ranging from not detectable

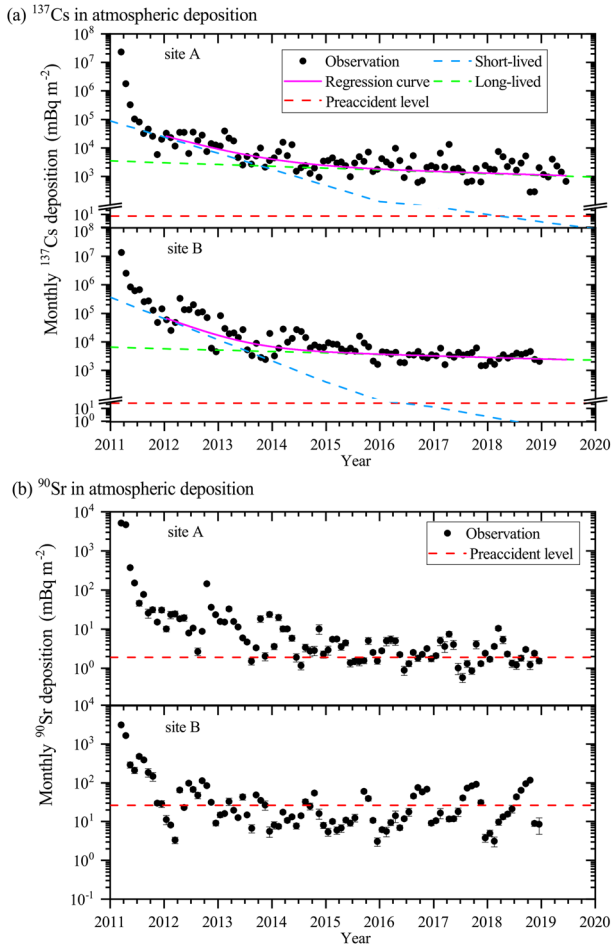

Figure 2. Activity of ^{90}Sr and ^{137}Cs in atmospheric depositions after the FDNPP accident from 2011 to 2018. (**a**) Cesium-137 in atmospheric depositions. (**b**) Strontium-90 in atmospheric depositions. The black points indicate the observational results. In panel (a), the pink lines indicate the regression curves. The green and blue curves indicate the exponential curves obtained via multiple exponential fitting. The red lines indicate the preaccident levels (the average monthly deposition between June 2009 and July 2010).

(N.D.)–6.0) mBq m^{-2} at site A and 26.0 (6.5–116.8) mBq m^{-2} at site B. The possible causes of the higher depositions rates at site B than those at site A are the differences in altitude (site A: 40 m; site B: ~ 1390 m) and local environmental effects (site A: open area; site B: surrounded by forestland).

The activity of ^{90}Sr and ^{137}Cs in atmospheric depositions and that of ^{137}Cs in aerosol samples rapidly decreased after the first surge in March 2011 (Fig. 2 and Supplementary Fig. S3). The decrease rate of radioactivity in atmospheric depositions at site A was due to the change in radionuclide emission, transport, and deposition processes[29]. We classify the period after the FDNPP accident into three phases. The first phase is dominated by direct emissions (March 2011), the second phase is dominated by tropospheric circulation and removal (from April to December 2011), and the third phase is dominated by resuspension (after January 2012). In the first phase, the direct discharge/emission of radioactive materials during the FDNPP accident and meteorological conditions governed the radionuclide concentration in the environment[29,42–44]. In the second phase, tropospheric transport of the radioactive materials remaining in the atmosphere after the FDNPP accident and their removal processes dominated atmospheric depositions[17,29]. The third phase (after January 2012) mainly depended on the resuspension of radioactive materials[29–31,33–36]. For comparison, the corresponding decrease rates (first, second, and third phases) resulting from the Chernobyl accident were shorter than those resulting from the FDNPP accident (for more discussion details, please refer to Supplementary Fig. S4 and the text). More discussions regarding the first and second phases were also presented in previous studies[29,34], and hence the scope of the present study is restricted to the third phase.

The latest average monthly ^{137}Cs atmospheric depositions in 2018 at sites A and B reached ~ 1/8100 (2.9 Bq m^{-2}) and ~ 1/4500 (3.0 Bq m^{-2}), respectively, with regard to the peak levels after the accident. But these levels were still ~ 400 and ~ 130 times, respectively, higher than those before the accident (Figs. 1a and 2a, respectively). On the other hand, the ^{90}Sr depositions in 2018 amounted to 3.0 (1.2–10.5) mBq m^{-2} and 33.8 (3.1–117) mBq m^{-2} at sites A and B, respectively (Figs. 1b and 2b, respectively). These ^{90}Sr deposition levels were almost at the same level as the preaccident deposition levels, and we concluded that the ^{90}Sr deposition levels at our observation sites had returned to the preaccident levels in at least 2015 (Fig. 2b).

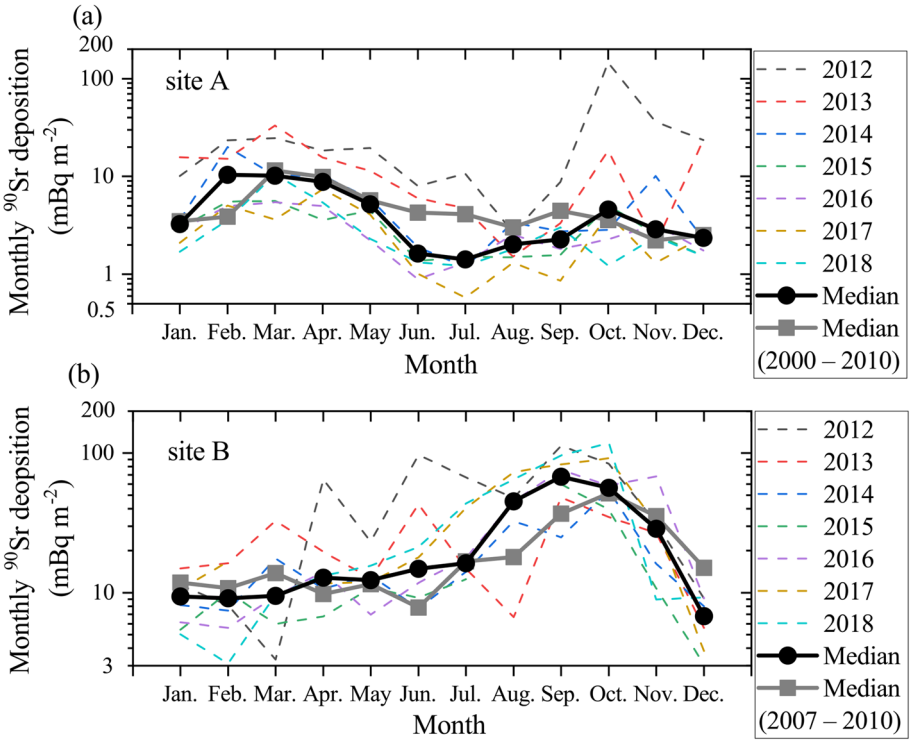

Figure 3. Seasonal changes in ^{90}Sr deposition from 2012 to 2018 at (**a**) site A and (**b**) site B. The black curves indicate the median values in each month after the FDNPP accident (from 2012 to 2018). The gray curves indicate those before the accident (from 2000 to 2010 at site A and from 2007 to 2010 at site B).

Before the FDNPP accident, the ^{90}Sr and ^{137}Cs activity in atmospheric deposition showed seasonal variations (Fig. 3 and Supplementary Figs. S5 and S6). The ^{137}Cs deposition value peaks in spring (April) at site A. On the other hand, it peaks twice in May and September at site B (Supplementary Figs. S4 and S5). Similarly, ^{90}Sr deposition reaches peak values during the spring season (March and April) at site A and during the fall season (September and October) at site B (Fig. 3). Studies have suggested that the ^{90}Sr and ^{137}Cs deposition peaks during the spring season at site A are caused by local and long-range transported dust particles[14,15,34,45,46].

After the FDNPP accident, direct emissions and their tropospheric removal processes governed the ^{90}Sr and ^{137}Cs activity in atmospheric depositions at sites A and B, and seasonal variations were not apparent in the first and second phases (Fig. 2). After 2012 (in the third phase), although the mean ^{137}Cs deposition value at site A had slightly increased in spring (peaking in April), no seasonal variations in ^{137}Cs at either site were observed (Fig. 2 and Supplementary Figs. S5 and S6). After 2014, in contrast, the seasonal variations in the ^{90}Sr radioactivity in atmospheric deposition at both sites showed similar trends to those before the accident (Figs. 2 and 3).

Possible carriers of ^{90}Sr and ^{137}Cs at sites A and B. The radionuclides in the atmosphere are generally carried by aerosol particles (host particles) emitted through, for example, geochemical and biological cycles. The correlations between dust components (e.g., Al and Fe) and radionuclides (^{90}Sr and ^{137}Cs) within the collected samples before the accident suggest that mineral dust particles are the dominant carriers of these radionuclides at site A (Fig. 4a). Previous studies have also demonstrated that the sources of these radionuclides are mainly resuspension of contaminated dust originating from long-range transport (large-scale phenomenon) and neighboring areas (local-scale phenomenon)[14,15,33,34,45,46]. After the accident, chemical analysis results indicate that dust particles are the dominant carriers of ^{90}Sr and ^{137}Cs at site A, except from 2012 to 2014 for ^{90}Sr when the contributions from the accident were high (Fig. 2).

The correlations between the dust components and radionuclides after the accident at site B were poor (Fig. 4b). However, the ^{90}Sr activity showed correlations with inorganic salts such as Mg, K, and Ca at site B. Scanning electron microscopy (SEM) observation exhibited the presence of inorganic salt particles including KCl, NaCl, and $CaSO_4$ in dried deposition samples (Supplementary Fig. S7). Although these salt particles had possibly crystallized during the preparation of the atmospheric deposition samples, it is probable that ^{90}Sr coexists with these components in the environment as they are abundantly present in the samples. Studies have indicated that the biological cycle may be a source of these inorganic elements in forests[47–49], i.e., the Mg, K, and Ca concentrations in throughfall depositions increase in forests due to foliar leaching. As Sr exhibits a similar geochemical behavior to that of Ca, the occurrence of Sr could be synchronous to that of Ca in the neighboring forest.

Before the accident, the ^{137}Cs activity at site B showed positive correlations with major mineral dust components such as Mg, Mn, Ca, K, Fe, and Al (Fig. 4), suggesting that dust particles were the dominant host particles

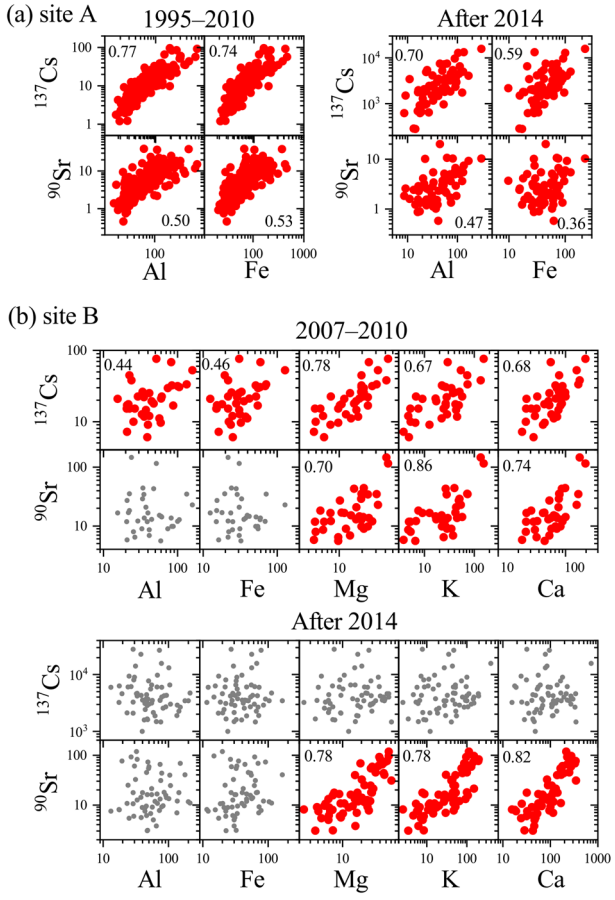

Figure 4. Correlations between radionuclides and stable elements at sites (**a**) A and (**b**) B. The units for ^{90}Sr and ^{137}Cs are mBq m^{-2}, and those for the stable elements are mg m^{-2}. The red points reveal that the correlations are significant ($p < 0.05$) based on the correlation coefficient values. The gray points show that the correlations are not significant ($p \geq 0.05$).

for ^{137}Cs. However, no significant correlation was detected between mineral dust and the ^{137}Cs activity after 2014. Previous studies have suggested that bioaerosols contribute to the resuspension of ^{137}Cs at forest sites in the contaminated area within the evacuation zone in Fukushima Prefecture[35,36]. Thus, it is possible that bioaerosols carry ^{137}Cs at site B. The differences between the possible carriers may cause the observed differences in the activity ratios of sites B and A ($R_{B/A}$) for ^{90}Sr and ^{137}Cs deposition after the accident (Supplementary Fig. S7).

Estimation of the environmental decrease in ^{137}Cs. With the use of regression curve fitting of the activity of ^{137}Cs in atmospheric deposition, we estimated its effective half-life due to radioactive decay and environmental removal processes (Fig. 2). We adopted a single-exponential function before the accident from January 1990 to July 2010 and a multiple exponential function after the accident (2012–2018; the resuspension phase). The detailed method of the calculation is described in the Supplementary Information.

The effective half-lives of the short- and long-lived components (t_1 and t_2, respectively) of the ^{137}Cs deposition were 195 days and 4.7 years, respectively, at site A, and those at site B were 148 days and 5.9 years, respectively. Interchange of the predominant short- and long-lived components occurred during the period between September and December 2013 (Fig. 2). Our estimation of the effective half-life of the long-lived component at site A is longer than the estimation by the previous study (~ 1.1 years)[29] possibly because our estimation 1) excluded the direct emission period and 2) extended observation data by the end of 2018. The effective half-life of the long-lived component of ^{137}Cs at site A after the FDNPP accident is shorter than that before the accident (8.5 years). There are two possible reasons for the difference between the effective half-lives before and after the accident. First, the dominant resuspension processes are different before and after the accident. Second, the elapsed time after contaminations is different between the pre and postaccident periods, i.e., more than 30 years had passed for the analysis period before the accident since the last atmospheric nuclear test, on the other hand, only 8 years had passed since the significant pollution after the FDNPP accident.

The above estimated effective half-lives imply that, based on the atmospheric ^{137}Cs deposition level, ~ 42 and ~ 48 years will be required from the year of the accident to reach the preaccident level at sites A and B, respectively. These estimates contain uncertainties due to the short observation period compared to the effective half-life before the FDNPP accident (8.5 years). A better understanding of the carriers, resuspension processes,

and environmental circulation conditions of radionuclides is needed to confirm the above estimates. The radionuclide decreasing trend may change in the future if resuspension process, biological recycling, and their carriers changed. Finally, our observations only pertain to atmospheric deposition and provide limited features of the environmental radionuclide cycle. The contamination in other fields, such as surface soils, forests, and oceans, will exhibit different effective half-lives. Nevertheless, our continuous observations of the radionuclides in atmospheric deposition before and after the accident enable the evaluation of the atmospheric phases and the changes in various processes to regain the environmental conditions before the nuclear power plant accident.

Material and methods

We collected monthly atmospheric deposition samples at two sites: a suburban site in the Kanto Plain (site A; 36.1°N, 140.1° E) and a mountain site in the northwestern corner of the Kanto Plain (site B, 36.5°N, 138.9° E) (Supplementary Fig. S1). Site A is the main observation base and was established in 1980 at the Meteorological Research Institute (MRI), Tsukuba, Japan. From 1957 to 1980, the main observation site was located in Koenji, Tokyo, which was shifted to the current base due to the move of the MRI in 1980[50]. Sampling trays were placed on the rooftop of one-story (1980–2011) and six-story buildings (2011–) on the MRI campus. Site B was established in 2007 at the top of the Mt. Haruna (1390 m above sea level), Gunma, Japan. Sites A and B are 170 and 250 km away, respectively, from the FDNPP.

Atmospheric deposition samples, which include both rain (wet deposition) and dry deposition, were collected using the above plastic trays with a total open area of 1–4 m^2, depending on the sampling period. The samples were sieved through a 106 μm mesh. The deposition samples were dried using rotary evaporators (Eyela NE-12, Tokyo Rikakikai Ltd., Japan) and evaporating dishes followed by weight measurements. After March 2011, we collected aerosol samples using high-volume air samplers (HV-1000F, Shibata Scientific Technology Ltd., Japan) on quartz fiber filters (QR100, Advantech Ltd., USA) at a flow rate of 700 L per minute to observe the atmospheric radioactivity concentration.

The activity of radiocesium was measured by Ge semiconductor detectors (of the coaxial type from ORTEC EG&G and Eurisys) coupled with a computed spectrometric analyzer (Oxford-Tennelec Multiport or Seiko EG&G 92x) using a maximum live time of 10^6 s after the FDNPP accident. After the radiocesium measurement, ^{90}Sr was radiochemically separated, purified, and solidified as Sr-carbonate precipitates. After leaving the sample for several weeks in order to achieve ^{90}Sr and ^{90}Y radioequilibrium, the β-activity was measured with an alpha/beta counting system (Tennelec LB5100, Mirion Technologies, USA) using a maximum live time of 10^3 min. The detection limits were 1.55 and 39.6 mBq m^{-2} for ^{90}Sr and ^{137}Cs, respectively, in the deposition samples, which were, obtained by multiplying each counting error measured in 2018 by three. Details on the sample preparation and measurement methods have been described in a previous study[51].

The stable elements (Na, Mg, Al, K, Ca, Ti, Mn, Fe, Ni, Cu, Zn, Sr, and Ba) and isotopes (^{9}Be, ^{133}Cs, ^{232}Th, and ^{238}U) were measured by inductively coupled plasma atomic emission spectrometry (CIROS-120, Rigaku Corp., Japan, or Vista-PRO, Varian Inc., USA) and inductively coupled plasma mass spectrometry (Agilent7500c or Agilent8000, Agilent, Ltd., USA), respectively, based on aliquots of the samples (3.6% in mass) during the acid decomposition processes. The detection limit and quantification values were estimated as three and ten times the standard deviation of ten measurements of 10 ppb standards. An SEM (SU-3500, Hitachi High Technologies Co., Japan) with an energy-dispersive X-ray spectrometer (EDX; E-max 50 mm, Horiba Ltd., Japan) was adopted for chemical and physical analysis of the dried deposition samples.

Received: 17 June 2020; Accepted: 18 November 2020
Published online: 10 December 2020

References

1. United Nations Scientific Committee on the Effects of Atomic Radiation (UNSCEAR). UNSCEAR 2000 Report to the General Assembly, with Scientific Annexes. *UNSCEAR*. https://www.unscear.org/docs/publications/2000/UNSCEAR_2000_Report_Vol.I.pdf (2000).
2. United Nations Scientific Committee on the Effects of Atomic Radiation (UNSCEAR). UNSCEAR 2013 Report to the General Assembly, with Scientific Annexes, Volume2 Scientific Annex B. *UNSCEAR*. https://www.unscear.org/docs/publications/2013/UNSCEAR_2013_Report_Vol.II.pdf (2013)
3. Hirose, K., Sugimura, Y. & Katsuragi, Y. ^{90}Sr and $^{239+240}$Pu in the surface air in Japan: their concentrations and size distributions. *Pap. Meteorol. Geophys.* **37**(4), 255–269. https://doi.org/10.2467/mripapers.37.255 (1986).
4. Katsuragi, Y. A study of ^{90}Sr fallout in Japan. *Pap. Meteorol. Geophys.* **33**(4), 277–291. https://doi.org/10.2467/mripapers.33.277 (1983).
5. Katsuragi, Y. & Michio, A. Seasonal variation of Sr-90 fallout in Japan through the end of 1983. *Pap. Meteorol. Geophys.* **37**(1), 15–36. https://doi.org/10.2467/mripapers.37.15 (1986).
6. Miyake, Y. The artificial radioactivity in rain water observed in Japan, from Autumn 1954 to Spring 1955. *Pap. Meteorol. Geophys.* **5**(2), 53–62. https://doi.org/10.2467/mripapers1950.6.1_26 (1955).
7. Miyake, Y., Saruhashi, K., Katsuragi, Y., Kanazawa, T. & Tsunogai, S. Deposition of Sr-90 and Cs-137 in Tokyo through the end of July 1963. *Pap. Meteorol. Geophys.* **14**, 58–65 (1963).
8. Miyake, Y., Katsuragi, Y. & Sugimura, Y. A study on Plutonium fallout. *J. Geophys. Res.* **75**(12), 2329–2330. https://doi.org/10.1029/JC075i012p02329 (1970).
9. Aoyama, M., Hirose, K., Suzuki, Y., Inoue, H. & Sugimura, Y. High level radioactive nuclides in Japan in May. *Nature* **321**, 819–820. https://doi.org/10.1038/321819a0 (1986).
10. Aoyama, M., Hirose, K. & Sugimura, Y. Deposition of gamma-emitting nuclides in Japan after the reactor-IV accident at Chernobyl. *J. Radioanal. Nucl. Chem.* **116**, 291–306. https://doi.org/10.1007/BF02035773 (1987).
11. Hirose, K., Takatani, S. & Michio, A. Wet deposition of radionuclides derived from the Chernobyl accident. *J. Atmos. Chem.* **17**, 61–71. https://doi.org/10.1007/BF00699114 (1993).

12. Igarashi, Y., Otsuji-Hatori, M. & Hirose, K. Recent deposition of ^{90}Sr and ^{137}Cs observed in Tsukuba. *J. Environ. Radioact.* **31**(2), 157–169. https://doi.org/10.1016/0265-931X(96)88491-8 (1996).
13. Igarashi, Y., Aoyama, M., Miyao, T., Hirose, K. & Tomita, M. Anomalous ^{90}Sr deposition during the fall, 1995 at MRI, Tsukuba Japan. *J. Radioanal. Nucl. Chem.* **239**(3), 539–542. https://doi.org/10.1007/bf02349065 (1999).
14. Igarashi, Y. *et al.* Resuspension: decadal monitoring time series of the anthropogenic radioactivity deposition in Japan. *J. Radiat. Res.* **44**, 319–328. https://doi.org/10.1269/jrr.44.319 (2003).
15. Igarashi, Y. *et al.* Possible change in Asian dust source suggested by atmospheric anthropogenic radionuclides during the 2000s. *Atmos. Environ.* **43**, 2971–2980. https://doi.org/10.1016/j.atmosenv.2009.02.018 (2009).
16. Chino, M. *et al.* Preliminary estimation of release amounts of ^{131}I and ^{137}Cs accidentally discharged from the Fukushima Daiichi Nuclear Power Plant into the atmosphere. *J. Nucl. Sci. Technol.* **48**(7), 1129–1134. https://doi.org/10.1080/18811248.2011.9711799 (2011).
17. Hirose, K. Fukushima Daiichi Nuclear Plant accident: Atmospheric and oceanic impacts over the five years. *J. Environ. Radioact.* **157**, 113–130. https://doi.org/10.1016/j.jenvrad.2016.01.011 (2016).
18. Masson, O. *et al.* Variation in airborne ^{134}Cs, ^{137}Cs, particulate ^{131}I and ^{7}Be maximum activities at high-altitude European locations after the arrival of Fukushima-labeled air masses. *J. Environ. Radioact.* **162–163**, 14–22. https://doi.org/10.1016/j.jenvrad.2016.05.004 (2016).
19. Steinhauser, G. *et al.* Post-accident sporadic release of airborne radionuclides from the Fukushima Daiichi Nuclear Power Plant Site. *Environ. Sci. Technol.* **49**, 14038–14035. https://doi.org/10.1021/acs.est.5b03155 (2015).
20. Buesseler, K., Michio, A. & Fukasawa, M. Impacts of the Fukushima Nuclear Power Plants on marine radioactivity. *Environ. Sci. Technol.* **45**, 9931–9935. https://doi.org/10.1021/es202816c (2011).
21. Aoyama, M. *et al.* 134Cs and 137Cs in the North Pacific Ocean derived from the March 2011 TEPCO Fukushima Daiichi Nuclear Power Plant accident, Japan. Part two: estimation of 134Cs and 137Cs inventories in the North Pacific Ocean. *J. Oceanogr.* **72**, 67–76. https://doi.org/10.1007/s10872-015-0332-2 (2016).
22. Katata, G., Ota, M., Terada, H., Chino, M. & Nagai, H. Atmospheric discharge and dispersion of radionuclides during the Fukushima Daiichi Nuclear Power Plant accident Part I: source term estimation and local-scale atmospheric dispersion in early phase of the accident. *J. Environ. Radioact.* **109**, 103–113. https://doi.org/10.1016/j.jenvrad.2012.02.006 (2012).
23. Katata, G. *et al.* Detailed source term estimation of the atmospheric release for the Fukushima Daiichi Nuclear Power Station accident by coupling simulations of an atmospheric dispersion model with an improved deposition scheme and oceanic dispersion model**15**, 1029–1070. Atmos. Chem. Phys. https://doi.org/10.5194/acp-15-1029-2015 (2015).
24. Kajino, M. *et al.* Deposition and dispersion of radio-cesium released due to the Fukushima Daiichi Nuclear Accident: sensitivity to meteorological models and physical modules. *J. Geophys. Res-Atmos.* **124**, 1823–1845. https://doi.org/10.1029/2018JD028998 (2019).
25. Saito, K. *et al.* Detailed deposition density maps constructed by large-scale soil sampling for gamma-ray emitting radioactive nuclides from the Fukushima Dai-ichi Nuclear Power Plant accident. *J. Environ. Radioact.* **139**, 308–319. https://doi.org/10.1016/j.jenvrad.2014.02.014 (2015).
26. Adachi, K., Kajino, M., Zaizen, Y. & Igarashi, Y. Emission of spherical cesium-bearing particles from an early stage of the Fukushima nuclear accident. *Sci. Rep.* **3**, 2554. https://doi.org/10.1038/srep02554 (2013).
27. Satou, Y. *et al.* Analysis of two forms of radioactive particles emitted during the early stages of the Fukushima Dai-ichi Nuclear Power Station accident. *Geochem. J.* **52**, 137–143. https://doi.org/10.2343/geochemj.2.0514 (2018).
28. Kaneyasu, N., Ohashi, H., Suzuki, F., Okuda, T. & Ikemori, F. Sulfate aerosol as a potential transport medium of radiocesium from the Fukushima nuclear accident. *Environ. Sci. Technol.* **46**(11), 5720–5726. https://doi.org/10.1021/es204667h (2012).
29. Igarashi, Y., Kajino, M., Zaizen, Y., Adachi, K. & Miakami, M. Atmospheric radioactivity over Tsukuba, Japan: a summary of three years of observations after the FDNPP accident. *Prog. Earth Planet. Sci.* **2**, 44. https://doi.org/10.1186/s40645-015-0066-1 (2015).
30. Kitayama, K., Ohse, K., Shima, N., Kawatsu, K. & Ysukada, H. Regression model analysis of the decreasing trend of cesium-137 concentration in the atmosphere since the Fukushima accident. *J. Environ. Radioact.* **164**, 151–157. https://doi.org/10.1016/j.jenvrad.2016.07.015 (2016).
31. Ochiai, S. *et al.* Temporal variation of post-accident atmospheric ^{137}Cs in an evacuated area of Fukushima Prefecture: Size-dependent behaviors of ^{137}Cs-bearing particles. *J. Environ. Radioact.* **165**, 131–139. https://doi.org/10.1016/j.jenvrad.2016.09.014 (2016).
32. Zaunbrecher, L. K., Cygan, R. T. & Elliott, W. C. Molecular models of cesium and rubidium adsorption on weathered micaceous minerals. *J. Phys. Chem.* **119**, 5691–5700. https://doi.org/10.1021/jp512824k (2015).
33. Ishizuka, M. *et al.* Use of a size-resolved 1-D resuspension scheme to evaluate resuspended radioactive material associated with mineral dust particles from the ground surface. *J. Environ. Radioact.* **166**, 436–448. https://doi.org/10.1016/j.jenvrad.2015.12.023 (2017).
34. Kajino, M. *et al.* Long-term assessment of airborne radiocesium after the Fukushima nuclear accident: re-suspension from bare soil and forest ecosystems**16**, 13149–13172. Atmos. Chem. Phys. https://doi.org/10.5194/acp-16-13149-2016 (2016).
35. Igarashi, Y. *et al.* Fungal spore involvement in the resuspension of radiocaesium in summer. *Sci. Rep.* **9**, 1954. https://doi.org/10.1038/s41598-018-37698-x (2019).
36. Kinase, K. *et al.* The seasonal variations of atmospheric ^{134,137}Cs activity and possible host particles for their resuspension in the contaminated areas of Tsushima and Yamakiya, Fukushima Japan. *Prog. Earth Planet. Sci.* **5**, 12. https://doi.org/10.1186/s40645-018-0171-z (2018).
37. Unterweger, M. P. Half-life measurements at the National Institute of Standards and Technology. *Appl. Radiat. Isotopes.* **56**, 125–130. https://doi.org/10.1016/S0969-8043(01)00177-4 (2002).
38. MacMahon, D., Pearce, A. & Harris, P. Convergence of techniques for the evaluation of discrepant data. *Appl. Radiat. Isotopes.* **60**(2–4), 275–281. https://doi.org/10.1016/j.apradiso.2003.11.028 (2004).
39. Steinhauser, G., Brandl, A. & Johnson, T. E. Comparison of the Chernobyl and Fukushima nuclear accidents: a review of the environmental impacts. *Sci. Total Environ.* **470–471**, 800–817. https://doi.org/10.1016/j.scitotenv.2013.10.029 (2014).
40. Aoyama, M. Evidence of stratospheric fallout of caesium isotopes from the Chernobyl accident. *Geophys. Res. Lett.* **15**(4), 327–330. https://doi.org/10.1029/GL015i004p00327 (1988).
41. Aoyama, M., Hirose, K. & Sugimura, Y. The temporal variation of stratospheric fallout derived from the Chernobyl accident. *J. Environ. Radioact.* **13**(2), 103–115. https://doi.org/10.1016/0265-931X(91)90053-I (1991).
42. Sekiyama, T. T., Kunii, M., Kajino, M. & Shimbori, T. Horizontal Resolution Dependence of Atmospheric Simulations of the Fukushima Nuclear Accident Using 15-km, 3-km, and 500-m Grid Models. *J. Meteorol. Soc. JPN.* **93**(1), 49–64. https://doi.org/10.2151/jmsj.2015-002 (2015).
43. Sekiyama, T. T. & Kajino, M. Reproducibility of surface wind and tracer transport simulations over complex terrain using 5-, 3-, and 1-km grid models. *J. Appl. Meteorol. Climatol.* **59**(5), 937–952. https://doi.org/10.1175/JAMC-D-19-0241.1 (2020).
44. Tsuruta, H., Oura, Y., Ebihara, M., Ohara, T. & Nakajima, T. First retrieval of hourly atmospheric radionuclides just after the Fukushima accident by analyzing filter-tapes of operational air pollution monitoring stations. *Sci. Rep.* **4**, 6717. https://doi.org/10.1038/srep06717 (2014).

45. Igarashi, Y., Aoyama, M., Hirose, K., Povenic, P. & Yabuki, S. What anthropogenic radionuclides (^{90}Sr and ^{137}Cs) in atmospheric deposition, surface soils and aeolian dusts suggest for dust transport over Japan. *Water Air Soil Pollut.* **5**, 51–69. https://doi.org/10.1007/s11267-005-0726-z (2005).
46. Igarashi, Y., Fujiwara, H. & Jugder, D. Change of the Asian dust source region deduced from the composition of anthropogenic radionuclides in surface soil in Mongolia**11**, 7069–7080. Atmos. Chem. Phys. https://doi.org/10.5194/acp-11-7069-2011 (2011).
47. Houle, D., Quimet, R., Paquin, R. & Laflamme, J.-G. Interactions of atmospheric deposition with a mixed hardwood and a coniferous forest canopy at the Lake Clair Watershed (Duchesnay, Quebec). *Can. J. For. Res.* **29**, 1944–1957. https://doi.org/10.1139/x99-212 (1999).
48. Su, L., Zhao, C., Xu, W. & Xie, Z. Hydrochemical fluxes in bulk precipitation, throughfall, and stemflow in a mixed evergreen and deciduous broadleaved forest. *Forest* **10**, 507. https://doi.org/10.3390/f10060507 (2019).
49. Uehara, Y. *et al.* Atmospheric deposition and interactions with Pinus pumila regal canopy on Mount Tateyama in the northern Japanese Alps. *Arct. Alp. Res.* **47**(2), 389–399. https://doi.org/10.1657/AAAR0013-126 (2015).
50. Katsuragi, Y., Hirose, K. & Sugimura, Y. A study of Plutonium fallout in Japan. *Pap. Meteorol. Geophys.* **33**(2), 85–93. https://doi.org/10.2467/mripapers.33.85 (1982).
51. Otsuji-Hatori, M., Igarashi, Y. & Hirose, K. Preparation of a reference fallout material for activity measurements. *J. Environ. Radioact.* **3**(2), 143–155. https://doi.org/10.1016/0265-931X(95)00048-F (1996).

Acknowledgements

The authors thank Kenzo Hama, Keiko Kamioka and Minami Ide-Tanimoto (ATOX Co. Ltd.) for the samplings and measurements and Kayo Yanagida, Kyoko Kaneba and Joseph Ching (MRI) for sampling atmospheric deposition at site A. This study was financially supported by the former Ministry of Education, Culture, Sports, Science and Technology and the current Nuclear Regulation Authority (Japanese Radioactivity Survey) and the Environmental Restoration and Conservation agency (Grant Number: 1-1801).

Author contributions

T.K., Y.I. and Y.Z. collected samples. T.K. and M.K. analyzed the data. Y.I., T.S., M.K., and Y.Z. managed the project. T.K. and K.A. wrote this paper, and all authors contributed to discussions.

Competing interests

The authors declare no competing interests.

Additional information

Supplementary information is available for this paper at https://doi.org/10.1038/s41598-020-78312-3.

Correspondence and requests for materials should be addressed to T.K.

Reprints and permissions information is available at www.nature.com/reprints.

Publisher's note Springer Nature remains neutral with regard to jurisdictional claims in published maps and institutional affiliations.

SCIENTIFIC REPORTS
nature research

Check for updates

OPEN

Rain-induced bioecological resuspension of radiocaesium in a polluted forest in Japan

Kazuyuki Kita[1]✉, Yasuhito Igarashi[1,2,7]✉, Takeshi Kinase[3,8], Naho Hayashi[1], Masahide Ishizuka[4], Kouji Adachi[3], Motoo Koitabashi[5], Tsuyoshi Thomas Sekiyama[3] & Yuichi Onda[6]

It is the conventional understanding that rain removes aerosols from the atmosphere. However, the question of whether rain plays a role in releasing aerosols to the atmosphere has recently been posed by several researchers. In the present study, we show additional evidence for rain-induced aerosol emissions in a forest environment: the occurrence of radiocaesium-bearing aerosols in a Japanese forest due to rain. We carried out general radioactive aerosol observations in a typical mountainous village area within the exclusion zone in Fukushima Prefecture to determine the impacts and major drivers of the resuspension of radiocaesium originating from the nuclear accident in March 2011. We also conducted sampling according to the weather (with and without rain conditions) in a forest to clarify the sources of atmospheric radiocaesium in the polluted forest. We found that rain induces an increase in radiocaesium in the air in forests. With further investigations, we confirmed that the fungal spore sources of resuspended radiocaesium seemed to differ between rainy weather and nonrainy weather. Larger fungal particles (possibly macroconidia) are emitted during rainy conditions than during nonrainy weather, suggesting that splash generation by rain droplets is the major mechanism of the suspension of radiocaesium-bearing mould-like fungi. The present findings indicate that radiocaesium could be used as a tracer in such research fields as forest ecology, meteorology, climatology, public health and agriculture, in which fungal spores have significance.

We found a novel rain-related mechanism of bioecological resuspension of radiocaesium in a contaminated area in Japan. The research background is described below. It is widely known that atmospheric aerosols are removed by rain (wet removal, including in-cloud and below-cloud scavenging). However, in recent atmospheric studies, several examples of atmospheric aerosol releases supposedly related to rain have been reported[1–8]. The existence of odours known as petricor[9] and geosmin[10], which occur with the start of rain or with light rain, has been acknowledged for a long time, but their formation mechanism was revealed very recently[3,7,8]. In these cases, the suspension flux from the surface overwhelms the deposition flux of the aerosols in question in the near-surface air layer. The underlying mechanisms include (1) microbubbles bursting inside raindrops upon contact with the Earth's dried porous surface[3,7], (2) active fungal spore dispersion due to high humidity (e.g., ref.[2,4]), and (3) aerosol bursts caused by the splashing of raindrops (e.g. ref.[11]). Details of these phenomena are given in the Discussion section. Through such mechanisms, soil organics, fungal spores, bacteria and their fragments/contents

[1]Graduate School of Science and Engineering, Ibaraki University, 2-1-1 Bunkyo, Mito, Ibaraki 310-8512, Japan. [2]Institute for Integrated Radiation and Nuclear Science, Kyoto University, 2 Asashiro-Nishi, Kumatori, Sennan, Osaka 590-0494, Japan. [3]Meteorological Research Institute, 1-1 Nagamine, Tsukuba, Ibaraki 305-0052, Japan. [4]Faculty of Engineering and Design, Kagawa University, 2217-20 Hayashi-cho, Takamatsu, Kagawa 761-0396, Japan. [5]Forage Crop Protection Group, Division of Livestock Feeding and Management, Central Region Agricultural Research Center, National Agriculture and Food Research Organization, 768 Senbonmatsu, Nasushiobara, Tochigi 329-2793, Japan. [6]Center for Research in Isotopes and Environmental Dynamics, University of Tsukuba, 1-1-1 Tennodai, Tsukuba, Ibaraki 305-8577, Japan. [7]Present address: Institute for Integrated Radiation and Nuclear Science, Kyoto University and College of Science, Ibaraki University, Formerly at Center for Research in Isotopes and Environmental Dynamics, University of Tsukuba, Tsukuba, Japan. [8]Present address: Meteorological Research Institute and Formerly at College of Science, Ibaraki University, Ibaraki, Japan. ✉email: kazuyuki.kita.iu@vc.ibaraki.ac.jp; igarashi.yasuhito.4e@kyoto-u.ac.jp

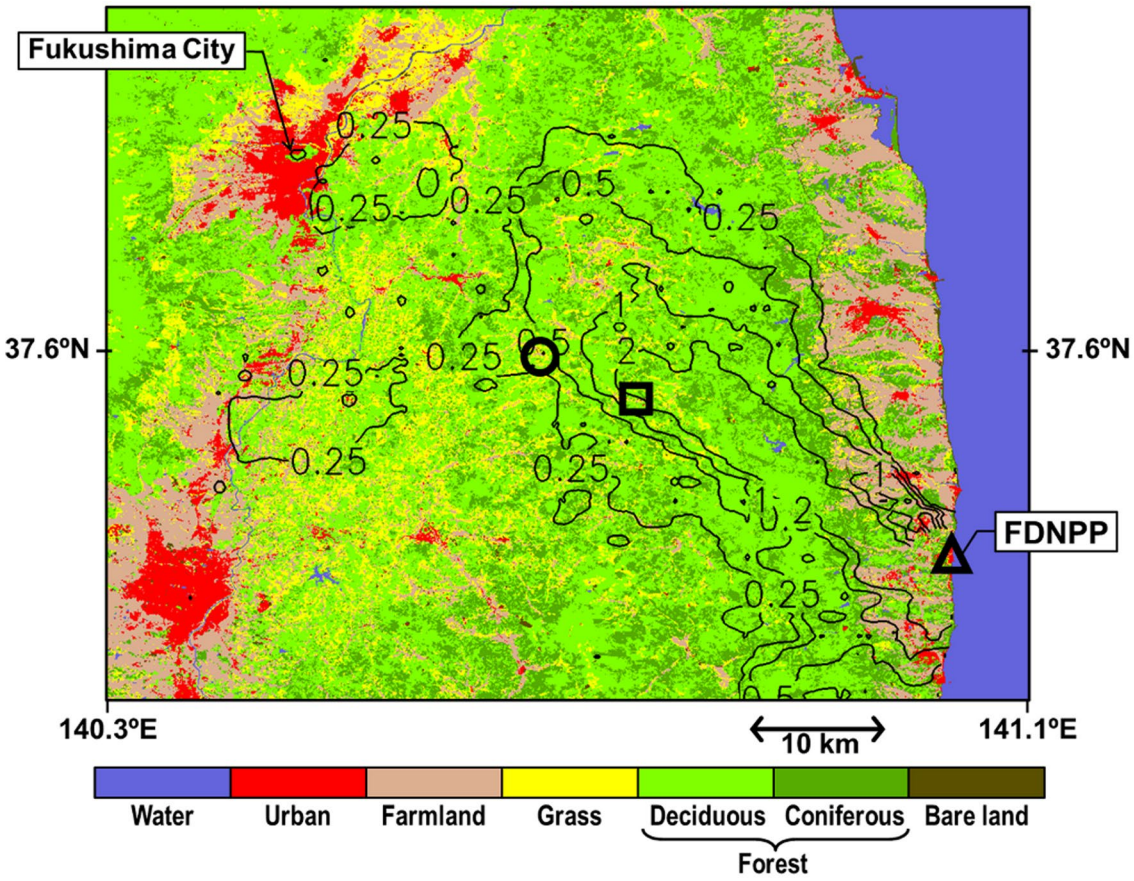

Figure 1. Observation site locations along with a land-cover map of the eastern part of Fukushima Prefecture before the F1NPP accident. Triangle, FDNPP (F1NPP); circle, Kawamata site; square, Namie site. The map was created by commands in GDAL version3.0.4 (open source under an X/MIT style Open Source License) and Microsoft PowerPoint 2018 for Mac and by using data from the High-Resolution Land Use and Land Cover map published by the Japan Aerospace Exploration Agency Earth Observation Research Center ALOS/ALOS-2 Science Project and the Earth Observation Priority Research: Ecosystem Research Group. The contour line shows the deposition density of ^{137}Cs originating from the F1NPP accident (MBq m^{-2}) at the end of May 2012[68]. Permission to use the data was granted. Deciduous forest is a mixture of various broadleaved trees, excluding evergreens. Coniferous forest excludes deciduous needleleaved trees, which are rare in the region.

(possibly formed during the rupture process[12]) can be liberated into the air. Radiocaesium (belonging to the same chemical family as potassium) can be involved in active bioecological circulation processes and can return to the atmosphere with bioaerosol release[13,14], which is likely to be partially induced by rain.

We carried out atmospheric observations of radiocaesium (^{134}Cs and ^{137}Cs) initially originating from the Fukushima Dai-ichi Nuclear Power Plant (F1NPP or FDNPP) accident in March 2011[15] to determine its concentrations, the processes involved in its aerosolization and the corresponding carrier[13,14,16]. Although the initial primary emission surge from the F1NPP site by the accident decreased circa the fall of 2011[17,18], radiocaesium has been detected continuously in the atmosphere since 2011. The source of these continuous atmospheric radiocaesium levels is considered to be resuspension (i.e., secondary emissions from polluted surfaces[19]); notably, the measured radiocaesium concentrations in the range of 10^{-1} to 10^{-5} Bq m^{-3} (Supplementary Information Figure S1) have not reached a level with certain health impacts (see Annex in Igarashi et al.[13]). In a typical mountainous village area in Fukushima (see Fig. 1 and Supplementary Photographs 1 and 2), we attempted to identify the key resuspension processes and carriers of radiocaesium in the atmosphere[13,14,20]. A Chernobyl study[21] described radioactive particle resuspension processes, such as wind uplift of the dust from contaminated surfaces, human activity and forest fires (e.g., ref.[22,23]). The Japanese summer is characterized by high rainfall and humid air, which may be unfavourable for both fugitive dust and general aerosol suspension due to wind uplift and forest fires. Furthermore, there is no evidence that photochemical reactions produce a burst of radiocaesium-bearing aerosols. We assume no emission/liberation of volatile organic Cs compounds under environmental temperatures (if any salt forms) from biota, as Cs is an alkaline metal. Our previous conclusion is that in cold seasons, a typical major driver of resuspension is the uplift of contaminated soil dust by gusts[16,20], while in warm seasons, the major factors are bioaerosols, including contaminated fungal spores[13,14] and cedar pollen[24]. Suspension of contaminated pollen was reported 6 years in Germany after the Chernobyl nuclear power plant accident[25]. Deposited radiocaesium was absorbed and strongly fixed by soil minerals, and a limited portion was taken up by vegetation. The time lapse from the accident suggests that the radiocaesium in pollen was

Sampling site	Conditions	Sample number (n)	Total* sampling span (yyyy/mm/dd)	^{134}Cs activity conc. in air** (Bq m^{-3})	^{137}Cs activity conc. in air** (Bq m^{-3})
Namie (deciduous forest)	With rain	6	2014/06/06–2014/07/18	$4.79\ (3.47–6.27)\times10^{-4}$	$1.21\ (0.87–1.67)\times10^{-3}$
	Without rain	6	2014/06/06–2014/07/18	$0.19\ (0.10–0.26)\times10^{-4}$	$0.50\ (0.28–0.70)\times10^{-3}$
Kawamata (coniferous forest)	With rain	7	2014/06/06–2014/08/01	$0.76\ (0.38–1.18)\times10^{-4}$	$2.04\ (1.10–3.68)\times10^{-4}$
	Without rain	7	2014/06/06–2014/08/01	$0.52\ (0.39–0.84)\times10^{-4}$	$1.48\ (1.17–2.34)\times10^{-4}$

Table 1. Summary of radiocaesium average concentrations in the air of the mountainous village area in the contaminated restricted zone of Fukushima Prefecture for samples with and without rain in the summer of 2014. *Real sampling durations were dependent on the rain sensor response, and several samples were collected during the span. **Minimum and maximum data are shown in parentheses.

related to water-soluble radiocaesium in the upper soil layer. Fungi are also a well-known bio-concentrator of radiocaesium (e.g., Ref.[26–28]). We refer to these biologically/ecologically mediated atmospheric phenomena as bioecological resuspension of radiocaesium.

The radiocaesium concentration in the atmosphere over the polluted mountainous village area investigated in this study is several times higher in summer than in winter[13,14]. Carbon with a biological origin in filter samples had a good correlation with radiocaesium concentrations, and there were sometimes close to 1 million bioaerosols per m^3 in summer[13]. In addition, based on a combination of optical and electron microscopy, state-of-the-art DNA analysis, and radiological measurement, it was confirmed that fungal spores, one of the major components of bioaerosols[29,30], were possibly the major host bioaerosol of radiocaesium (e.g., Ref.[31]) during summer[13]. A 3-D transport model study also revealed the significance of the secondary emission of radiocaesium from the forest during summer[20]. The seasonal trend of enhanced radiocaesium concentrations in summer has not changed significantly up to the present (Supplementary Figure S1). Here, we conducted specially designed sampling in a forest area in Fukushima Prefecture according to the weather, with the goal of determining the detailed radiocaesium emission mechanisms during the warm season. Our findings described below confirm that the polluted forest is the radiocaesium resuspension source[13,14,20] and provide details on the rain-induced emission mechanism of radiocaesium-bearing aerosols during the Japanese wet summer. It is shown that rain may induce bursts of radiocaesium-bearing aerosols (coarse bioaerosols mostly of macroconidia) inside both deciduous forests and coniferous forests.

Results

In 2014 and 2016 in Fukushima Prefecture, the amount of rain was higher than usual in the rainy season (from late spring to early summer), with a few to several hundred mm of rain in each month (see Supplementary Figures S2 and S3, respectively). At the end of June 2014, a temperate cyclone (on June 29, not a typhoon) developed and brought heavy rain to northern and northeastern Japan. Additionally, in August 2016, three typhoons (Chanthu, Minduleand and Lionrock on August 16–17, 22–23 and 29–30, respectively) brought large volumes of precipitation. We conducted atmospheric sampling under both rainy and nonrainy conditions at two heavily contaminated forest sites, the Namie site and the Kawamata site (Fig. 1 and Supplementary Photographs 1 and 2), which are dominated by deciduous trees and coniferous trees, respectively. The data for 2014 are presented in Table 1 and Fig. 2. More details of the high-volume aerosol (HV) sampling results are given in Supplementary Table S1. On average, the sampling time lengths of the nonrainy periods in 2014 were approximately 2.6 times longer than those of the rainy periods in both the deciduous and coniferous forests. We found that the concentrations of ^{137}Cs in the deciduous forest atmosphere with rain (average 1.21×10^{-3} ($\pm2.61\times10^{-4}$) Bq m^{-3}) were 2.42 times higher than those without rain (average 5.00×10^{-4} ($\pm1.89\times10^{-4}$) Bq m^{-3}) (Fig. 2a) on average. This difference was significant, with a p value of 0.0082 for a significance level of 1% using the paired t-test. Furthermore, this trend occurred in every consecutive sampling period. In the coniferous forests, this trend was observed in half of the sampling cases (Fig. 2b); on average, the ^{137}Cs concentration during the rainy period was 1.37 times higher than that during the nonrainy period. The average difference was only significant with a p value of 0.25, giving a significance level of 25%; thus, this difference was not as clear as that in the other case. The weighted average of the radiocaesium concentration, as shown below, was also applied to the results for the deciduous forest to determine whether the difference was robust.

$$\sum_i (R_i \times F_i / F_{total})$$

where R_i is the individual ^{137}Cs concentration, F_i is the individual sampled air volume and F_{total} represents the total sampled air volume. The ^{137}Cs concentration was higher during the rainy period (1.11×10^{-3} ($\pm1.00\times10^{-4}$) Bq m^{-3}) than during the nonrainy period (4.68×10^{-4} ($\pm2.61\times10^{-5}$) Bq m^{-3}), indicating that the difference was robust.

Considering that, among bioaerosols, fungal spores are major ^{137}Cs carriers in Fukushima forest areas[13,14], the different results for deciduous and coniferous forests could be caused by differences in the fungal populations or fungal phyla between the two types of forests[32]. Deciduous forests may be richer in fungal activity than coniferous forests[33]. Previous authors studied litter decomposition in coniferous and deciduous forests using the litter bag method. Their results suggested that the decomposition of litter is faster in deciduous forests than in coniferous

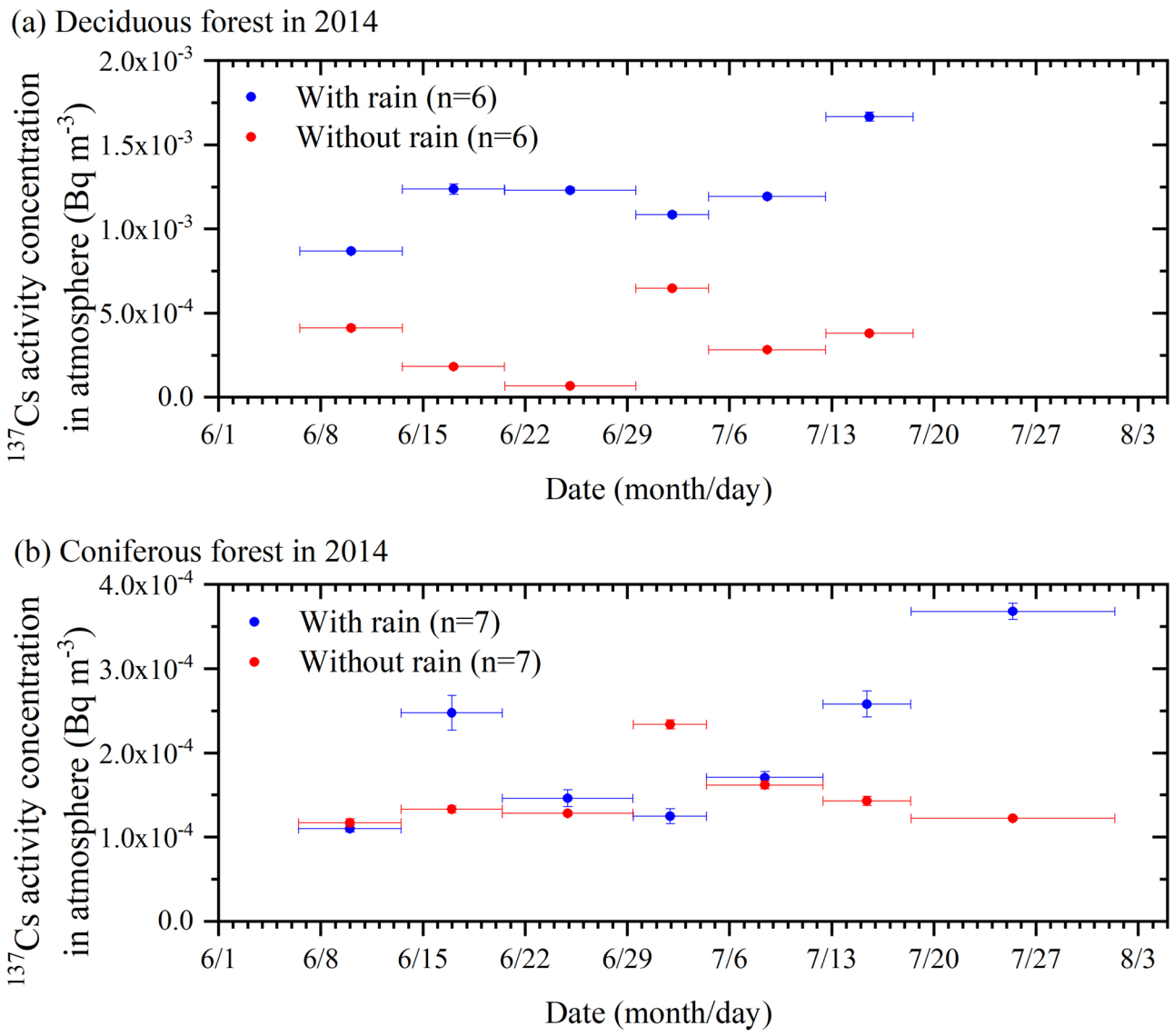

Figure 2. Atmospheric ^{137}Cs concentration inside the contaminated forest in Fukushima Prefecture, Japan, during the summer of 2014. Rainy/nonrainy sampling was carried out from June 6 to August 2, 2014. The sampling period was shorter in the deciduous forest than in the coniferous forest. Samples collected during rain periods are shown in blue, whereas those collected during periods without rain are shown in red. Horizontal error bars indicate the whole duration of the sampling, while the vertical bars exhibit errors in the activity measurement. The top (**a**) and bottom (**b**) panels show the data from the Namie deciduous (n = 6) and Kawamata coniferous (n = 7) forests, respectively. In the deciduous forest (**a**), the ^{137}Cs concentrations are always higher during the rainy period than during the nonrainy period. On the other hand, in the coniferous forest (**b**), the ^{137}Cs concentrations tended to be higher during the rainy period than during the nonrainy period, except in two observation spans of June 6–13 and June 29–July 4. Caesium-137 data and sampling details are summarized in Supplementary Table S1.

forests (*Castanopsis eyrei*) and that the species richness of fungi in deciduous forests (*Pinus massoniana*) is greater than that from coniferous forests, as indicated by the Shannon–Weaver diversity index[33].

To determine the relationship between fungal particles in the air and the ^{137}Cs activity concentration, we performed coloured fungal spore counting (Supplementary Figures S4 to S7) at the Namie site during the warm season in 2016; the results are shown in Fig. 3 (detailed information is given in Supplementary Table S2). Some of the data for nonrainy periods published (n = 6) in Igarashi et al.[13] were re-evaluated using the present spore counting method. The data set (total n = 14) is a composite of those obtained at a forest site (F) and at a bare ground site (G; school ground) near the forest (Supplementary Photograph 1). Regression curves were obtained by assuming that ^{137}Cs was carried only by fungal spores in order that the curves pass through the origin. Although there is uncertainty in the spore counts (see "Discussion" section), when the curves pass through the origin, fitted curves are evident, which suggests that the spore count has significance. The obtained linear relationship between the activity concentration of ^{137}Cs (Y) and the fungal spore number concentration (X) in a unit volume of air during

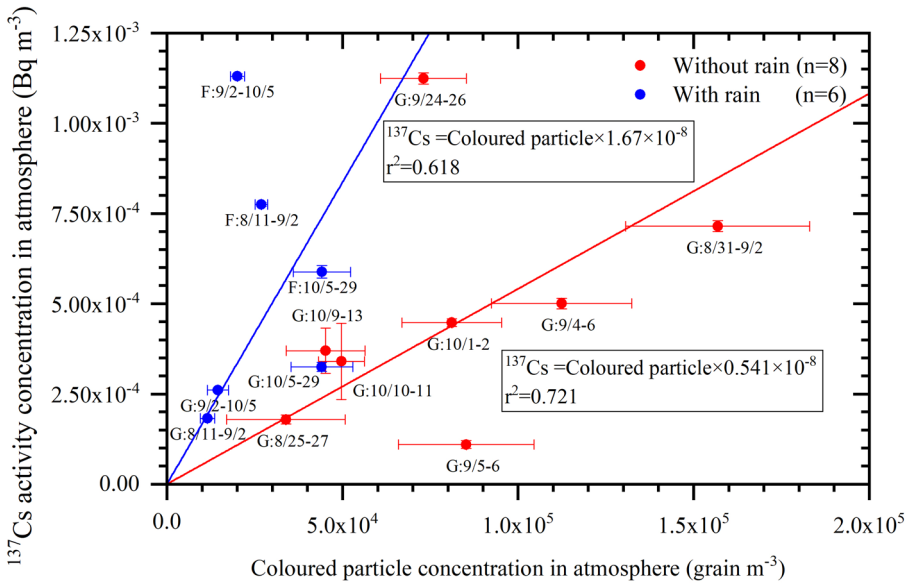

Figure 3. Relationship between the coloured fungal particle number concentration and ^{137}Cs activity concentration in the air at the Namie site (inside the forest (F) and the bare ground (G)) during the warm season in 2016. Sampling data are expressed as mm/dd (e.g., m_1/d_1-m_2/d_2). Six of the present plotted data for the nonrainy period that had been published in Igarashi et al.[13] were re-evaluated using the present spore counting method (see the text and Supplementary materials). The collection duration for nonrainy samples was 24 h in the daytime or nighttime (G:8/31–9/2, G:9/4–6 and G:9/24–26) of the dates shown next to each data point. For instance, daytime data of G:10/1–2 indicate that the sampling was performed from 6:00 to 18:00 on October 1 and October 2 for a total of 24 h. On the other hand, the collection duration for rainy samples encompassed several weeks due to the small percentage of the whole sampling period represented by rain. Here, regression curves were obtained by assuming that ^{137}Cs was carried only by fungal spores; thus, the curves should pass the origin. Caesium-137 data and sampling details are summarized in Supplementary Table S2.

the nonrainy period is expressed as $Y = 0.541 \times 10^{-8} \times X$. The slope of the regression curve gives the ^{137}Cs content in a single fungal spore, confirming the previous hypothesis that fungal spores carry radiocaesium[13]. On the other hand, the data for rainy periods exhibit the relationship of $Y = 1.67 \times 10^{-8} \times X$. Notably, the slope is approximately 3 times larger during the rainy period than during the nonrainy period.

This finding indicates two possibilities: (1) during the rainy period, spores with a relatively high Cs concentration are dominant or (2) the spores suspended during the rainy period have larger volumes than those suspended during the nonrainy period, although the Cs concentrations of the spores are similar during both periods. Figure 4 shows a comparison of typical optical microscopic photographs of HV filter samples collected during rainy and nonrainy periods at the bare ground site. Notably, the rainy and nonrainy collection durations differed significantly (the duration was approximately 7 times longer during rainy conditions; see the explanation of Fig. 4), resulting in differences in the particle number concentrations in the filter samples. However, Fig. 4 shows that long and coarse elliptical particles (some exceeding 20 μm), which may be macroconidia (based on size and morphology, see the Methods section), were significant components of the rainy samples.

To address the abovementioned hypothesis, we investigated whether there were changes in the size distribution of bioaerosol particles between rainy and nonrainy periods. Figure 5a shows the average size distribution of bioaerosols (projection area) for periods with and without rain, while Fig. 5b presents the normalized distribution (Supplementary Figure S8 presents the individual data). One pixel represents approximately 0.008 μm^2 (Supplementary Figure S5 for reference). In Fig. 5a,b, the bin width W is set as follows:

$$W = \log_{10}(\mathrm{Area(i)}) - \log_{10}(\mathrm{Area(i-1)}) = 0.05$$

where Area(i) and Area(i−1) express the ith and (i−1)th bins' highest edges, respectively. Therefore, the summation of the normalized size distribution of dN/dlogArea is $dN/(W)/\sum N$, yielding 10 instead of unity (Fig. 5b). Figure 5a indicates that the average total number of fungal spores suspended in rainy periods was significantly less than that in nonrainy periods (with a ratio of 0.34). However, Fig. 5b shows that the portion of particles larger than approximately 15 μm^2 was higher in rainy periods than in nonrainy periods (1.75 times; proportion in nonrainy periods: 0.19, proportion in rainy periods: 0.3) and that more particles finer than approximately 3 μm^2 were suspended in nonrainy periods than in rainy periods (1.24 times; proportion in nonrainy periods: 0.57, proportion in rainy periods: 0.46). Considering the results shown in Figs. 4, 5, 6, different types of bioaerosols (undoubtedly fungal spores) are emitted under rainy conditions than under fine weather conditions. The larger fungal spores released during rainy weather are macroconidia (often with multiple septa) according to the literature[34–37] and based on size and morphology. Although we need more evidence to support these results (see the Discussion section), the coarse elliptical particles resemble the conidia of graminicolous fungi,

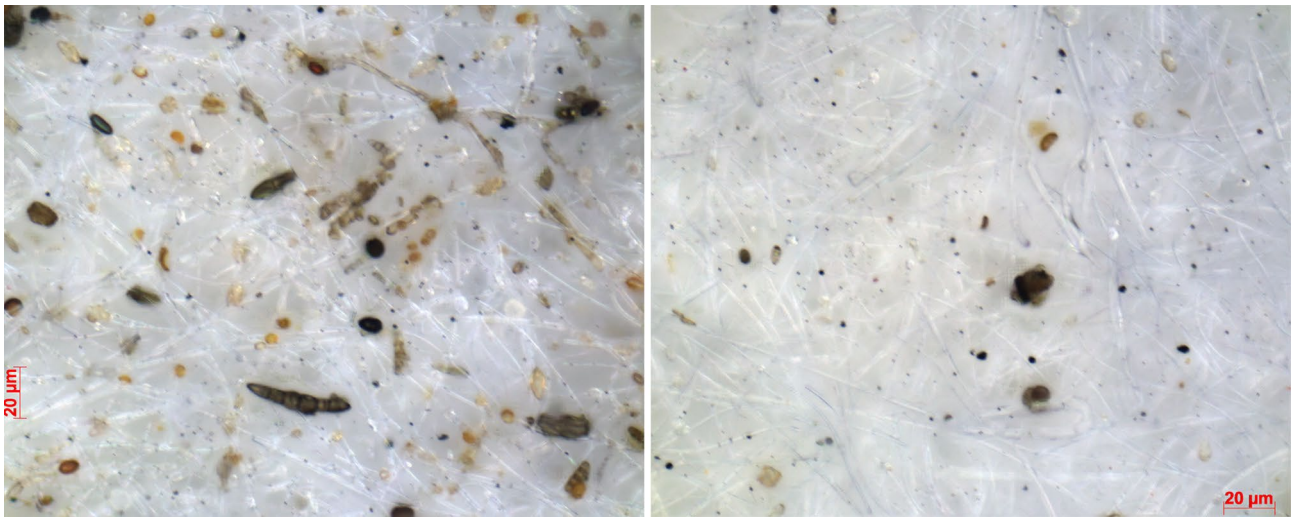

Figure 4. Comparison of typical optical microscopy photographs of HV filter samples (left: collected during the rainy period of September 2 to October 5, 2016, total volume of 9,094 m^3; right: collected during the nonrainy period of September 5 to September 6, 2016, total volume of 1,296 m^3). Samples from the rainy period display many coarse club- and oval-shaped particles, with some hypha-like materials. These are considered macroconidia. A portion of the particles exhibit sizes greater than 20 μm (red bar). On the other hand, the sample from the fine period displays many small dot-like particles of a few μm or smaller in size. Note that no size cut-off was applied during the sampling. The total pixel size of the photograph was originally $2,728 \times 2,198 = 5,996,144$.

such as Bipolaris, Exserohilum and Drechslera, as described in the abovementioned NARO encyclopaedia[34]. Photographs of fungal particles appearing in Fig. 6 validate our conclusion; beyond a 15 μm^2 projection size range, macroconidia are evident.

Conclusions

Compared to nonrainy conditions, rain induces the release of approximately twice as much radiocaesium-bearing coarse bioaerosols (especially with a projection size of > 15 μm^2) into the atmosphere in a polluted temperate forest range in Japan, although the total number concentration of bioaerosols is reduced to approximately one-third under rainy conditions. Macroconidia particles (e.g., ref.[34]) may represent the coarse bioaerosol particles based on the analysis of size and morphology (see Fig. 6 and the Discussion section, too). Therefore, one of the mechanisms behind the summer maxima in radiocaesium over the polluted forest[13,14,20] was revealed to be rain splash (e.g., ref.[11,38–40]). As Fukushima forests are ordinary temperate forests, the finding has many implications for forest ecology, meteorology, climate, public health, agriculture, and other fields (see the Discussion section) in which fungal spores play significant roles. However, there are limitations to the present study; we investigated the increase in bioaerosols on the basis of only radiocaesium and coloured spores, while other bioaerosol components such as organics[41,42] were not studied in detail. In future research, sampling and measurements with increased temporal resolution (e.g., hourly) using a real-time monitoring tool, for instance, UV-APS or WIBS (e.g., ref.[43]), should be applied, and a more detailed analysis of other bioaerosol components is needed. To understand the full range of rain-induced bioaerosol emission phenomena in forest areas, we need more observational research.

Discussion

Considering the projection sizes of the coloured fungal spores shown in Supplementary Figure S5, we determined the typical volume ratio of fungal spores suspended in the air for periods with and without rain. For example, in nonrainy periods, characteristic fungal spores exhibited a spherical size of 1,400 pixels (area size: approximately 11 μm^2). Using the circle area equation of πr^2, r is approximately 1.9 μm. In contrast, the typical size for spores during rainy periods was larger than 4,600 pixels (approximately 38 μm^2, as displayed in Supplementary Figure S5). We found that the aspect ratios of these particles were 1–1.8 and 2.6–3.4 for typical nonrainy and rainy periods, respectively. We calculated the average single-particle volumes by considering the rotating body of each particle with a rotation axis along the minimum particle diameter. The single-particle volumes were 4.28×10^6 μm^3 and 11.5×10^6 μm^3 for typical nonrainy and rainy periods, respectively. The ratio between the volumes of rainy and nonrainy periods was 2.69. This number is close to the ratio between the slopes during periods with and without rain for the activity concentration of ^{137}Cs (Y) and the coloured fungal spore number concentration (X) in the air (Fig. 3), i.e., $1.67/0.541 \simeq 3.1$. Each slope represented the relationship between ^{137}Cs air concentration (Y), the coloured fungal spore number concentration (X), the ^{137}Cs volume concentration (C) and the typical fungal spore volume (V) during the rainy and nonrainy periods as follows:

$$Y = C \times V \times X.$$

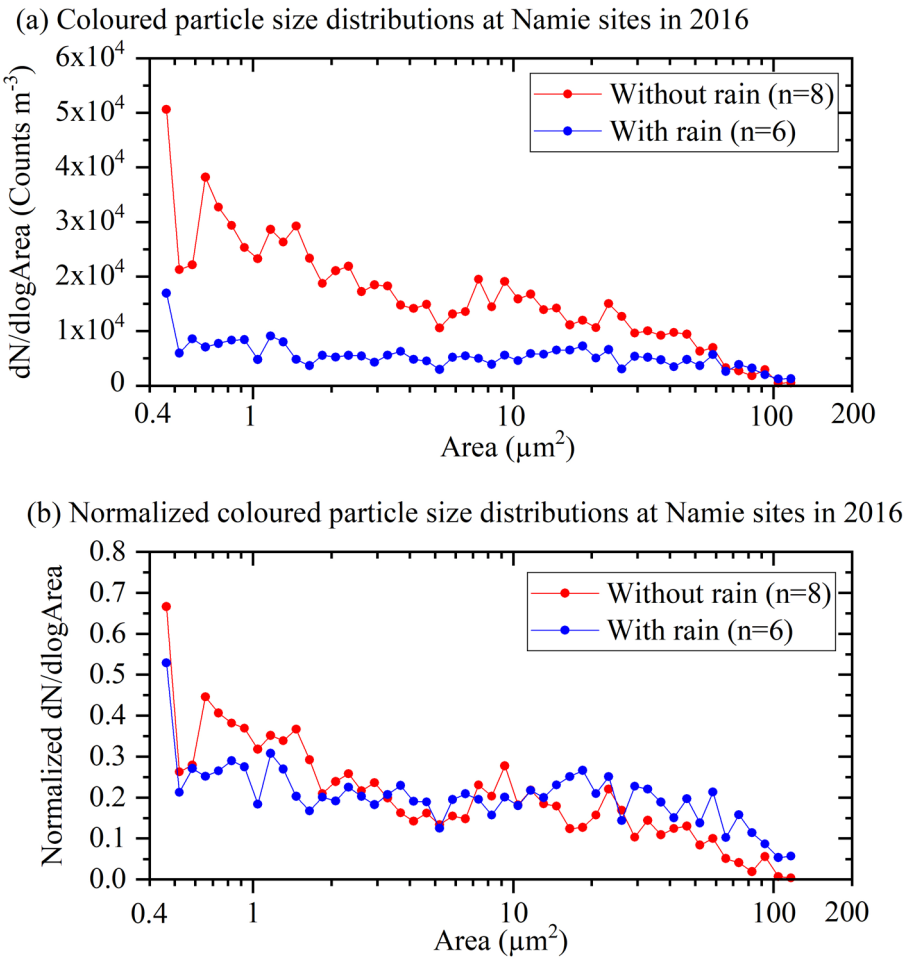

Figure 5. (**a**) Averaged (number concentrations per unit air volume (Y)) and (**b**) normalized (dividing by the sum of the total number (Y)) size distributions of fungal particles collected on the HV filters (n = 6 and 8 for rain and nonrain, respectively) obtained in 2016 using image analysis. In total, 4,672 and 3,764 particles were counted for nonrainy and rainy samples, respectively. The bin size of the horizontal axis (X; dlog Area) is 0.05 on the scale of the base 10 logarithm. Analysed optical microscopic images were taken from the same filter samples as those shown in Fig. 2. The size of each fungal particle is expressed in terms of the projected area. One pixel corresponds to approximately 0.008 μm^2. Particles beyond the size of approximately 120 μm^2 (more than 15,000 pixels) were cut-off to avoid overlapping images of particles. The scale of the typical bioaerosol sizes is the projection area shown in Supplementary Fig. 3. (**a**,**b**), respectively, reveal that the total number concentrations of coloured fungal spores decreased during rainy periods compared to during nonrainy periods (0.34) and that the portion of large spores (larger than approximately 15 μm^2) increased from 0.19 (nonrainy period) to 0.31 (rainy period), an increase of 1.75 times.

Therefore, we assumed the simplest case, in which only spherical spores were suspended in nonrainy periods, only spheroid (prolate) spores were suspended in rainy periods, and C remained the same. In this case, the slope ratio represents the ratio between the fungal particle volumes of the rainy and nonrainy periods. The above-mentioned approximate calculation could indicate that the assumptions are close to reality. The results in Fig. 5a show a decreasing number of fungal spores suspended in the air (the total number concentrations were lower during rainy periods than during nonrainy periods; 0.34), while Fig. 5b suggests that larger fungal spores are suspended in the air during rainy periods than during nonrainy periods (the proportion of large spores > 15 μm^2 was higher; 1.75). We concluded, as indicated in Fig. 6, that the conidia types of fungal spore, which are larger in size but have a similar Cs concentration as typical fungal spores, become predominant in the air when it rains in Fukushima forests. Therefore, in this study, we provide evidence that increases in bioaerosol concentrations occur due to rain in Japanese forest areas. Notably, this rain-induced bioaerosol phenomenon was once thought to occur only in specific forests, such as tropical rain forests[44], boreal forests[5] and semidry forests[2], and has never been considered in Japan, as the country is located in the temperate climate zone.

There are three possible major mechanisms for aerosol emissions due to rain:

(1) When a raindrop touches the bare, dry surface of the Earth containing many apertures (porous in nature), the raindrop does not penetrate the earth immediately, and for a short time, the raindrop retains its shape

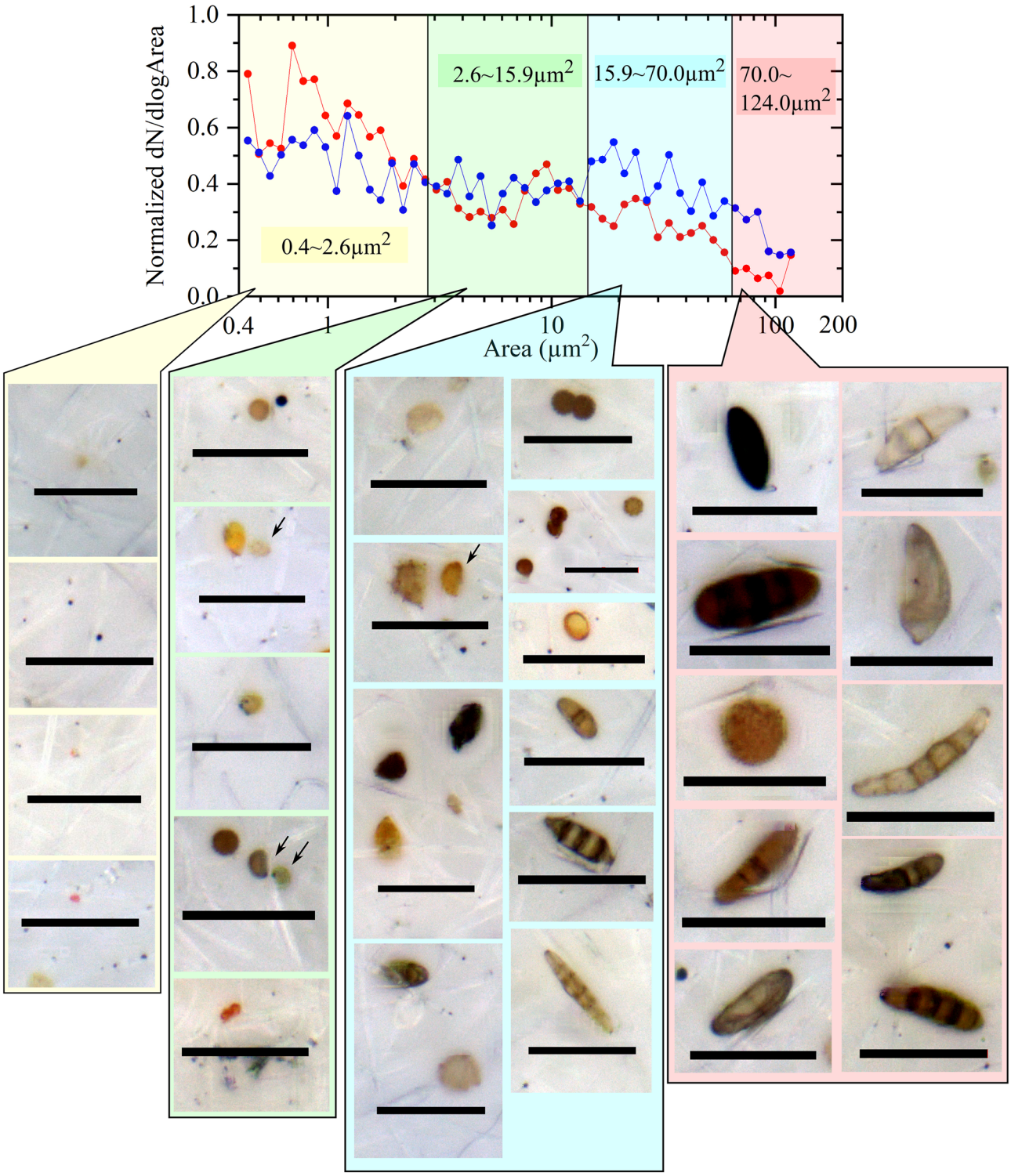

Figure 6. Typical examples of fungal spore particles on the HV filter samples taken at the Namie site during the 2016 summer, which are plotted along 4 projection size bins based on experimental/convenient classification. The size distribution plot is from Fig. 5b. Arrows indicate the particles concerned, and the bar length is 20 μm. Fungal spore particles are sorted according to the projection area. Beyond the 15 μm² range, macroconidia were dominant, as shown in this figure.

as a small water mass. Air bubbles are generated inside this water mass from the Earth's surface and then rise. When the tiny air bubbles rupture at the rain drop surface, very tiny droplets are ejected and result in aerosol generation[3,7]. Additionally, microbubbles burst inside a raindrop touching the Earth's surface.

The emitted aerosols can transfer material that was within/on the Earth's surface into the atmosphere; for example, this transfer explains why the smell of soil occurs during rain[3,7]. However, dry bare surfaces are scarce in the forest areas of Fukushima Prefecture, so this mechanism is not applicable in the present case.

(2) Fungi disperse spores using rain and high humidity[45–48]. Active spore dispersion could be a possible major process of bioaerosol releases in response to rain. The phyla Basidiomycota and Ascomycota in the kingdom Fungi are classified according to their different spore dispersion systems. They utilize atmospheric water in a highly dedicated structure and emit spores into the air; then, the spores become entrained due to turbulence over the Earth's surface. This is a plausible process that provides fungal spores (especially basidiospores) to the atmosphere. In our present observation, however, we could not see this effect clearly; the total number spore concentration decreased to approximately one-third during rain, as depicted in Figs. 3 and 5.

(3) It has been known for a long time (for instance, ref.[49,50]) that phytopathogens (e.g., rust fungi, which belong to Ascomycota) proliferate by rain splash[35,36,38,40]. Recently, high-speed video imaging technology has been applied, and the associated physical mechanisms have been studied[11,39,51]. Pathogen-bearing tiny droplets are dispersed by rain drop impacts on vegetation leaves. A more recent study[51] revealed that rain drop impacts induce the formation of small air vortexes, effectively liberating dry spores from leaves into the air. These studies have revealed the role of splashing in the spread of fungal pathogenic spores (mostly mould and anamorphic Ascomycota). Moreover, rain drop impacts deliver mechanical force onto the surface materials covering the leaves, branches and trunk of trees, etc., thereby liberating any surficial materials[11,39]. In addition, canopy interception losses of rainfall[52] may play a role in the hydrological and biogeochemical cycles in forested areas[11,39,40,53], in which a quantity of rainwater is intercepted by the forest canopy and thus does not reach the forest floor (throughfall). This interception varies between 15 and 45% in coniferous forests[54]. Possible mechanisms are described in the literature (e.g., ref.[53,55,56]). One explanation could be that water splashes evaporate[39], which thus could leave aerosols. We hypothesize that rain splash evaporation might add more ^{137}Cs to the atmosphere. Related to this, it would be interesting to know from which vertical region of the forest the emissions mostly occur: canopy or ground. The maximum height of the canopy of the Fukushima forest is 20–25 m. However, currently, we do not have the detailed data on the height distributions of bioaerosols necessary to form a conclusion. This will be a future task to be addressed. We consider litter to be important, as described later, so emissions could mainly occur from the ground.

As concluded above, rain can induce emissions of larger fungal spores (macroconidia, often with multiple septa) carrying radiocaesium. Igarashi et al.[13] reported that the spores and debris suspended during summer over the Fukushima typical mountainous village areas belonged to the phyla Ascomycota and Basidiomycota. They also noted that "rainwater samples exhibited larger proportions of Ascomycota, represented by the orders Capnodiales, Pleosporales, Dothidiales, Helotiales, Diaporthales, Hypocreales, and Xylariales, than did air samples". Their findings naturally suggest that rain splash also contains spore (conidia) of these orders. Furthermore, this assumption leads to the hypothesis that conidia particles may arise from mould species covering not only living trees but also contaminated litter. Litter should be covered with more mould than the living leaves of trees. This hypothesis is the most plausible for cases in which rain drops impact contaminated forest areas.

To confirm the conidia and ascospore hypothesis, we isolated and incubated fungal strains (Supplementary Figure S9) and used DNA analysis to identify the fungi. As shown in Table 2, 45 strains of fungi (4 of which were unidentified) were isolated from the four HV filter samples collected during rain in the summer of 2016 (data from the samples are shown in Fig. 3). Six strains, including *Trametes versicolor*, were derived from Basidiomycota, while the other 39 strains (87% of isolated strains) were identified as filamentous fungi derived from Ascomycota (see Table 2). These experimental results indicated that ascospores are more dominant than basidiospores in the typical mountainous village area in Fukushima during rain. In other words, the fungal spore sources in rainy weather seem to be different from those during fine weather (though the atmosphere has high humidity).

However, we do not have clear evidence that mould (Ascomycota) in general bioconcentrates radiocaesium, which mushroom fungi (mostly Basidiomycota) are known to do[26–28]. Another major uncertainty of the present study is related to the use of optical microscopy for fungal spore counting. In the present case, we counted only coloured spores (on the order of 10^4 to 10^5 grains per m^3), although we tried to count faintly coloured spores as often as possible. As mentioned in the Methods section, the spore counting method itself involves errors of approximately 10%. However, the present spore counting method gives an average that is approximately 3 times higher than the average of the previous counting method of Igarashi et al.[13]. As described in a previous report[13], "the total fungal spore number concentration, including both coloured and colourless ones, might be about one order of magnitude larger" (10^5 to 10^6 grains per m^3), as shown in Fig. 3 in the report[13]. Optical microscopy with fluorescent staining may miss dark-coloured spores, while coloured spore counting disregards transparent spores. Presently, fungal spore counting is methodology dependent, which is clearly a major source of uncertainties and limitations. However, these uncertainties and limitations do not subtract from the conclusions that fungal spores are carriers of radiocaesium and that rain induces the emission of bioaerosols. Certainly, more quantitative evaluations are necessary, and therefore, the application of sequential automated bioaerosol counting, such as UV-APS[57] or WIBS[58], to reveal if any correlation exists among bioaerosol counts, radiocaesium and weather parameters is another attractive challenge.

We add that the number of pollen particles suspended in the air was not significant during summer, as reported in ref.[13,14]. Pollen particles can contain a considerable amount of ^{137}Cs[24]; if significant numbers of these particles had been mixed with the other bioaerosols, the concentration of ^{137}Cs would have increased. As explained in Igarashi et al.[13], the major bioaerosols serving as radiocaesium carriers in summer are fungal spores,

Sample collection	Isolated and identified fungi (order level)	
Forest site in Namie during Aug. 11 to Sep. 2	*Cladosporium sphaerospermum*	Ascomycota
	Penicillium sp.	Ascomycota
	Bjerkandera adusta	Basidiomycota
	Talaromyces sp.	Ascomycota
	Thanatephorus cucumeris	Basidiomycota
	Cephalotheca sulfurea	Ascomycota
	Acremonium sp.	Ascomycota
	Daedalea dickinsii	Basidiomycota
Forest site in Namie during Sep. 2 to Oct. 5	*Toxicocladosporium irritans*	Ascomycota
	Pseudocercosporella fraxini	Ascomycota
	Toxicocladosporium irritans	Ascomycota
	Thanatephorus cucumeris	Basidiomycota
	Tilletiopsis sp.	Basidiomycota
	Other	
Bare ground site in Namie during Aug. 11 to Sep. 2	*Penicillium* sp.	Ascomycota
	Cladosporium sp.	Ascomycota
	Trametes versicolor	Basidiomycota
	Cladosporium sp.	Ascomycota
	Oidiodendron sp.	Ascomycota
	Fibulomyces mutabilis	Basidiomycota
Bare ground site in Namie during Sep. 2 to Oct. 5	*Fusicolla* sp.	Ascomycota
	Toxicocladosporium irritans	Ascomycota
	Pestalotiopsis microspore	Ascomycota
	Fusicolla sp.	Ascomycota
	Arthrinium phaeospermum	Ascomycota
	Xylomelasma sp.	Ascomycota
	Pestalotiopsis microspora	Ascomycota
	Talaromyces purpureogenus	Ascomycota
	Xylomelasma sp.	Ascomycota
	Fusarium merismoides	Ascomycota
	Valsaria insitiva	Ascomycota
	Sordariomycetidae sp.	Ascomycota
	Pestalotiopsis neglecta	Ascomycota
	Pestalotiopsis microspora	Ascomycota
	Pestalotiopsis microspora	Ascomycota
	Hypoxylon sp.	Ascomycota
	Arthrinium phaeospermum	Ascomycota
	Penicillium sp.	Ascomycota
	Xylariaceae sp.	Ascomycota
	Hypoxylon sp.	Ascomycota
	Xylomelasma sp.	Ascomycota
	Sordariales sp.	Ascomycota
	Others	

Table 2. Summary of isolated and identified fungi from the HV filter samples collected during the rainy period in the summer of 2016 at the Namie site. The identified fungi are attributed to the phyla Ascomycota or Basidiomycota. The 4 unidentified strains are expressed as other/others.

not pollen. Kinase et al.[14] manually counted the relative numbers of "pollen" and "bacteria" (note that the latter included "spores"), representing typical bioaerosols in the warm season, using scanning electron microscopy (SEM) images and concluded that the "pollen" concentration was indeed smaller than 1/10 of the "bacteria" concentration.

Thus, one of the possible mechanisms of radiocaesium resuspension from the polluted forest environment during the wet and warm periods was revealed in this study. In other words, radiocaesium can be used as a tracer to reveal unknown processes related to bioaerosol emissions from forest environments. Although the atmospheric radiocaesium activity concentration is decreasing (Supplementary Figure S1), radiocaesium can be measured more easily and precisely than bioaerosols, as described here. We estimated the apparent half-life of ^{137}Cs in air at the Namie site, and we found that at least 19 years will be necessary until the ^{137}Cs concentration decreases

below the limit of detection. Radiocaesium will certainly disappear in the future in the study region, and the current radiocaesium concentration level (10^{-3} to 10^{-5} Bqm^{-3}) in air can indeed help us to clarify the radiocaesium resuspension process, in which bioaerosols are certainly involved. However, to model rain-induced bioaerosol emissions, further research is necessary. In addition, we disregarded the possibility of bacterial suspension into the air by rain splash[59], although bacteria might also carry radiocaesium. Thus, to further reveal the radiocaesium cycle within the contaminated forest environment, we need to conduct additional research. In particular, we need more sophisticated definitions and measurement methodologies not only for bioaerosol counting but also emission/deposition flux observations.

No previous studies have reported the resuspension of radiocaesium by bioaerosols, namely, fungal spores, during summer in a forest, except for studies in which the present authors were involved[13,14,20]. We searched for any prior similar bioaerosol/primary biological aerosol particle (PBAP) study in Japan, but no studies have addressed rain and its relevance to the PBAP number concentration. Furthermore, even though a study on secondary organic aerosol (SOA) generation from isoprene and terpene derived from vegetation was carried out[60–62], primary material outflow from forest ecosystems has received almost no attention. Because two-thirds of the country is covered by forest, we strongly feel that there is a need for a full-scale study on bioaerosol and/or organic matter emissions in response to rain in Japan, and the results may be applicable for all temperate mixed forests worldwide. Additionally, the emitted fungal spores released during rain are primarily mould spores, so an allergy pandemic (e.g., ref.[63]) and agricultural pathogen epidemic (e.g., ref.[11,38,39,51]) in the rainy season might occur.

It has been discussed whether fungal spores can influence the weather or climate (e.g., ref.[64]), which is also an underlying motivation of the present research. We are collecting fungal fruits and obtaining spores not only from Fukushima but also from Tsukuba, Ibaraki and are trying to analyse their ice nuclei (IN) activity. Although the results are very preliminary, an example of a basidiospore is presented in Supplementary Figure S10. The ice nucleation onset was − 18 °C for the present case. Atmospheric IN in a pine forest (Colorado, United States) were measured in the summer of 2011[2,4,64], and the results revealed that bioaerosol and IN concentrations increased during and after rain events. These studies also found that typical IN were basidiospores[4,64], although the bioaerosols released due to rain/high humidity varied. Huffman et al.[2] thus noted the possibility that ascospore are also potential IN. The rain-induced spore species were different from the ones in the current study, a possible result of differences in the ecosystems or the effects of the particle size cut-off of the sampling methods. We applied no size cut-off in the HV filter sampling, which might have resulted in the observation of coarser bioaerosols in this study than in other studies. Very recently, in 2019, Iwata et al.[65] published a study stating that rain enhances the IN number (working > − 22 °C) in the air and that some of the IN seemed to be fungal spores based on observations on the coast of the Sea of Japan. They applied an impactor with a 50% cut-off diameter of 1.1 μm for sample collection[65]; thus, they might have observed different types of bioaerosols than we did. However, the report is agreement that fungal spores, compared to other IN materials, function at high temperatures of a few degrees below 0 °C to − 15 °C (e.g., ref.[66]). Fungal spores might also work as especially large cloud condensation nuclei (CCN), referred to as a giant CCN (GCCN)[46]. GCCN can form large droplets within a shorter period of time than small CCN, thereby removing water from the air column efficiently and contributing to enhanced precipitation strength. Macroconidia have a larger size than other PBAPs and might thus work more efficiently as GCCN than other PBAPs. However, we need to confirm these hypotheses in the future.

Methods

We have used two forest sites in a mountainous village area in the range of the evacuated zone (the administrative border is not shown) in Fukushima Prefecture: one is in Namie town and the other is in Kawamata town, as depicted in Fig. 1. This figure was created by using data from the High-Resolution Land Use and Land Cover map (JAXA EORC[67]), and the ^{137}Cs contour line was drawn based on the data of Torii et al.[68] The sampling points are also described in detail elsewhere[13,14,16,20]. The environment of the sampling sites is displayed in Supplementary Photographs 1 and 2 for reference. The Namie site is located approximately 30 km northwest of the F1NPP, and deciduous trees are dominant, although some red pine trees are present. This site is on a small hill, and the school athletic grounds (bare soil originally, though gradually covered by glasses with a few small pine trees) was within a few tens of metres. Decontamination work was later carried out within a range of 1 km (see ref.[14]), although most of the forest remained contaminated. The Kawamata site is approximately 6 km northwest of the Namie site, and the level of radioactive contamination is lower than that of the Namie site because the contamination by the radioactive plumes in 2011 was relatively lower. This site was an artificial conifer plantation (cedar forest) on a small hill. The contamination level of ^{134}Cs and ^{137}Cs was at approximately a few MBq m^{-2} at both sites in 2012, as evidenced by the contour in Fig. 1.

High-volume aerosol samplers (HV; Sibata HV 1000F and R, Tokyo, Japan) were employed to collect the resuspended ^{137}Cs with carrier aerosols (see Supplementary Photographs). No size cut-off was used for the sampling. One of the two HV samplers was automated to work for an hour after a sensor (Climatec, Tokyo, Japan) detected rain, while the other HV worked when the HV sampler for rain was not in operation. The automatic switch equipment was composed of a rain sensor (CPR-PPS-03), a logger (C-CR800-4 M), a 2-channel relay control driver (C-CPC-2), an alternating current (AC) relay, a power supply, a lightning arrester (C-PT10), USB-RS232C conversion cables, etc. When the sensor detected rain drops larger than 0.5 mmϕ, HV sampling started, which continued for one hour. Therefore, we could compare ^{137}Cs concentrations between periods with and without rain. The filters were made of silica fibre (Advantech QR100 or Pal flex 2,500 QAT-UP; 203 mm × 254 mm), which were treated in a furnace at 400 °C before use. The sampling was performed approximately 1.5 m above the ground from June 6 to August 1, 2014 (see Table 1 and Supplementary Table S1) at the Kawamata (rainy plus nonrainy samples, n = 14) and Namie (same as above, n = 12) sites (Supplementary Photographs 1 and 2). In the summer of 2016, a sampling campaign was conducted (same as above, n = 14) only at Namie from August 11 to

October 29 (see Supplementary Table S2). After sampling, the filters were wrapped by aluminium foil and then packed in a plastic sealing bag at the site and taken back to the laboratory. At the laboratory, they were kept at room temperature mostly with desiccation in a sealed plastic case, and a portion of approximately 2% of the filter area was punched out as circles (usually 8 pieces in total 16%) and used for the bioaerosol (fungal spore) counting (2 pieces kept at room temp.) and future chemical analysis (6 pieces kept in a refrigerator). Some of the latter punched-out samples were subjected to DNA analysis. The rest of the HV filters (84%) were subjected to radioactivity measurements.

The activity of ^{137}Cs in the HV filter samples was obtained by γ-ray spectrometry with an intrinsic germanium semiconductor detector (coaxial type from Ortec EG&G, Eurisys or Canberra, all from Tokyo, Japan) coupled with a computed multichannel analyser (Oxford-Tennelec Multiport or Seiko EG&G MCA7600, both from Tokyo, Japan). The detection limits of the measurement of ^{134}Cs and ^{137}Cs at the Meteorological Research Institute (MRI) were approximately 9 and 10 mBq per sample, respectively, for approximately 10^5 s. The temporal change in ^{137}Cs air concentrations derived from the F1NPP accident at the Namie site is shown in Supplementary Figure S1.

The fungal spore counts were performed using optical microscopy (OM). The OM instrument was an Axio Imager M2m (Carl Zeiss, Tokyo, Japan), and photographs were captured at 50 times magnification in reflection mode. A portion of the HV filter samples was placed directly on a slide glass and subjected to OM observation. The OM photograph was taken by a CCD camera (6 M pixels, Zeiss Axiocam 506 colour) equipped with self-adjustment functions for white balance and exposure time. Five sections of the OM photograph that minimized overlap and maximized the number of spore images were chosen, avoiding lumpy surfaces and pollen. To count coloured fungal spores digitally to the best extent possible, we defined a coloured particle as a particle darker than the filter fibre or as a particle with a different colour than the filter fibre. For these reasons, the original photograph was digitized by adjusting (a) contrast and brightness and (b) chroma saturation, and then coloured particles were selected. During the image retouching process with the free software ImageJ[69], the "Brightness/Contrast" and "Color Threshold" functions were used. The "Brightness" and "Contrast" setting were adjusted during the "Brightness/Contrast" process, and "Saturation" on the "Colour Threshold" palette was adjusted to obtain clear and distinct images. The obtained images were converted into binary images, and low levels of noise were removed using the median filter for two pixels. Two binary images were combined, and a final binary image (edge detected) of coloured fungal spores was obtained. In this procedure, the overlapped image was manually separated into single particles. Additionally, the particle hang on the frame was removed. The "Analyse particle" command was finally applied, and this automated counting procedure provided statistics on the coloured fungal spores. An example of the image analysis procedure is given in Supplementary Figure S4. For spore detection, the minimum spore size was set to approximately 0.4 μm^2 (50 pixels), and the maximum spore size was set to approximately 124 μm^2 (15,000 pixels). This corresponds to an equivalent diameter range of 0.73–12.6 μm. A typical size analysis of the coloured bioaerosol is shown in Supplementary Figure S5. The current counting method resulted in more coloured fungal spore counts than the previous method of Igarashi et al.[13]. The differences in the particle counts are shown in Supplementary Figure S6. In the figure, the present counting method yielded 1.8 times more coloured spores than the previous method[13], while on average, approximately 3 times more particles were identified. The present method identified a higher number of faintly coloured and small fungal spores. This is a methodological limitation, which should be solved in future studies.

Figure 5 was thus created based on the counting mentioned above. For the data plot, 584 ± 284 (n = 8; 1 s.d.) and 627 ± 316 (n = 6) particles on average were counted for nonrainy and rainy samples collected in 2016, respectively. Converting these values into totals yields 4,672 and 3,764 particles for nonrainy and rainy samples, respectively, which seem statistically significant. Additionally, the error in the spore counting was estimated on the basis of 3 factors: (1) the reproducibility of the counting and (2) and (3) the size measurement. (1) The same optical photograph (sample number NHVR-281029 Photo#6) was analysed 10 times for total spore counts, and the resulting average and standard deviation were 89.9 ± 11.1 fungal particles (relative error = 12.3%), so the fungal spore counting involves an error of approximately 10%. (2) A given scale printed on the photograph (20 μm) was measured 10 times and the average and standard deviation were obtained (average = 220.1 ± 0.43 pixels (relative error = 0.19%)). (3) Three coarse particles were measured for size 10 times (see also Supplementary Figure S7). Two spores with lengths of 13.7 and 17.4 μm yielded areas of 5,515 ± 218 pixels (relative error = 3.9%) and 9,581 ± 230 pixels (relative error = 2.4%), respectively. The largest spore was out of the current measurement range, which certainly represents a limitation of the present counting method. In total, simple summation of the errors in scale measurement and replication yields an error of less than 10%, so fungal spore counting is expected to involve an error of approximately 10%. The data reveal the current limitations of the methodology employed.

The samples subjected to DNA analysis were collected by HV filtering during rain in August and September 2016 in the deciduous forest and over bare ground (Namie). A piece of the quartz fibre filter was subjected to culturing on threefold diluted Gellan gum powder (2%, wt/vol) (plant tissue grade; Wako, Osaka, Japan) at 28 °C for a week, and a single colony was picked for further incubation. Supplementary Figure S9 displays examples of the incubated samples, indicating that they were well-isolated single species. Genomic DNA was extracted from the individual incubated samples according to the method described by Lee and Taylor[70]. Polymerase chain reaction (PCR) was performed as described by White et al.[71] using primers for internal transcribed spacers (ITSs; ITS1 and ITS4) with *Taq* DNA polymerase (Takara Bio Inc., Kusatsu, Shiga, Japan). The PCR products were purified and then sequenced using an Applied Biosystems 3730xl DNA Analyzer (Applied Biosystems, Foster City, CA, USA). Sequencing reactions were performed employing ABI PRISM Big Dye Terminator, v 3.1 (Applied Biosystems) using the primer ITS1. Sequence data of the ITS regions were downloaded from the DNA Data Bank of Japan and the European Molecular Biology Laboratory/genomic data bank (DDBJ/EMBL/GenBank) databases, and the Basic Local Alignment Search Tool (BLAST) was utilized to search for regions of similarity between biological sequences.

Meteorological conditions can influence bioaerosol species, some of which carry ^{137}Cs, and the number concentrations of bioaerosols. Therefore, precipitation data in 2014 (Supplementary Figure S2) were obtained from the AMeDAS (Automated Meteorological Data Acquisition System) Japan Meteorological Agency weather station at Tsushima (37°33.6′ N, 140°45.2′ E, altitude 400 m), which is approximately 6.2 and 1.2 km from the Kawamata and Namie sites, respectively. Additionally, we obtained data from an automated weather station (AWS) at the Namie bare ground site in 2016; these data are summarized in Supplementary Figure S3. The main types of measurements of the AWS are as follows: precipitation (Takeda Keiki Kougyou, TKF-1), wind speed (three-cup anemometer, R. M. Young, Model 3,102, and sonic anemometer, R. M. Young, Model 81,000), air temperature, and humidity (Vaisala Corp., HMP155D), with data recorded by a data logger (Campbell Scientific Inc., CR1000-4 M). Details are also given elsewhere[13,14,16].

Data availability

The data that support the findings of this study are available upon request. Please contact the corresponding authors.

Received: 6 December 2019; Accepted: 7 August 2020
Published online: 18 September 2020

References

1. Heo, K. J., Kim, H. B. & Lee, B. U. Concentration of environmental fungal and bacterial bioaerosols during the monsoon season. *J. Aerosol. Sci.* **77**, 31–37. https://doi.org/10.1016/j.jaerosci.2014.07.001 (2014).
2. Huffman, J. A. *et al.* High concentrations of biological aerosol particles and ice nuclei during and after rain. *Atmos. Chem. Phys.* **13**, 6151–6164. https://doi.org/10.5194/acp-13-6151-2013 (2013).
3. Joung, Y. S. & Buie, C. R. Aerosol generation by raindrop impact on soil. *Nat. Commun.* **6**, 6083. https://doi.org/10.1038/ncomms7083 (2015).
4. Prenni, A. J. *et al.* The impact of rain on ice nuclei populations at a forested site in Colorado. *Geophys. Res. Lett.* **40**, 227–231. https://doi.org/10.1029/2012gl053953 (2013).
5. Schumacher, C. J. *et al.* Seasonal cycles of fluorescent biological aerosol particles in boreal and semi-arid forests of Finland and Colorado. *Atmos. Chem. Phys.* **13**, 11987–12001. https://doi.org/10.5194/acp-13-11987-2013 (2013).
6. Yue, S. *et al.* Springtime precipitation effects on the abundance of fluorescent biological aerosol particles and HULIS in Beijing. *Sci. Rep.* **6**, 29618. https://doi.org/10.1038/srep29618 (2016).
7. Joung, Y. S., Ge, Z. & Buie, C. R. Bioaerosol generation by raindrops on soil. *Nat. Commun.* **8**, 14668. https://doi.org/10.1038/ncomms14668 (2017).
8. Wang, B. *et al.* Airborne soil organic particles generated by precipitation. *Nat. Geosci.* **9**, 433–437. https://doi.org/10.1038/ngeo2705 (2016).
9. Bear, I. J. & Thomas, R. G. Nature of argillaceous odour. *Nature* **201**, 993–1000. https://doi.org/10.1038/201993a0 (1964).
10. Gerber, N. N. Geosmin an earthy-smelling substance isolated from actinomycetes. *Biotechnol. Bioeng.* **9**, 321–330. https://doi.org/10.1002/bit.260090305 (1967).
11. Gilet, T. & Bourouiba, L. Rain-induced ejection of pathogens from leaves: revisiting the hypothesis of splash-on-film using high-speed visualization. *Integr. Comp. Biol.* **54**, 974–984. https://doi.org/10.1093/icb/icu116 (2014).
12. China, S. *et al.* Rupturing of biological spores as a source of secondary particles in Amazonia. *Environ. Sci. Technol.* **50**, 12179–12186. https://doi.org/10.1021/acs.est.6b02896 (2016).
13. Igarashi, Y. *et al.* Fungal spore involvement in the resuspension of radiocaesium in summer. *Sci. Rep.* **9**, 1954. https://doi.org/10.1038/s41598-018-37698-x (2019).
14. Kinase, T. *et al.* The seasonal variations of atmospheric ^{134,137}Cs activity and possible host particles for their resuspension in the contaminated areas of Tsushima and Yamakiya, Fukushima, Japan. *Progr. Earth Planet. Sci.* **5**, 12. https://doi.org/10.1186/s40645-018-0171-z (2018).
15. Holt, M., Campbell, R. J. & Nikitin, M. B. *Fukushima Nuclear Disaster*. (Library of Congress, Congressional Research Service, 2012)
16. Ishizuka, M. *et al.* Use of a size-resolved 1-D resuspension scheme to evaluate resuspended radioactive material associated with mineral dust particles from the ground surface. *J. Environ. Radioact.* **166**, 436–448. https://doi.org/10.1016/j.jenvrad.2015.12.023 (2017).
17. Igarashi, Y., Kajino, M., Zaizen, Y., Adachi, K. & Mikami, M. Atmospheric radioactivity over Tsukuba, Japan: A summary of three years of observations after the FDNPP accident. *Progr. Earth Planet. Sci.* **2**, 44. https://doi.org/10.1186/s40645-015-0066-1 (2015).
18. Hirose, K. Temporal variation of monthly ^{137}Cs deposition observed in Japan: Effects of the Fukushima Daiichi nuclear power plant accident. *Appl. Radiat. Isot.* **81**, 325–329. https://doi.org/10.1016/j.apradiso.2013.03.076 (2013).
19. Igarashi, Y. Anthropogenic radioactivity in aerosol—a review focusing on studies during the 2000s. *Jpn. J. Health Phys.* **44**, 313–323. https://doi.org/10.5453/jhps.44.313 (2009).
20. Kajino, M. *et al.* Long-term assessment of airborne radiocesium after the Fukushima nuclear accident: Re-suspension from bare soil and forest ecosystems. *Atmos. Chem. Phys.* **16**, 13149–13172. https://doi.org/10.5194/acp-16-13149-2016 (2016).
21. Garger, E. K., Kuzmenko, Y. I., Sickinger, S. & Tschiersch, J. Prediction of the ^{137}Cs activity concentration in the atmospheric surface layer of the Chernobyl exclusion zone. *J. Environ. Radioact.* **110**, 53–58. https://doi.org/10.1016/j.jenvrad.2012.01.017 (2012).
22. Evangeliou, N. *et al.* Resuspension and atmospheric transport of radionuclides due to wildfires near the chernobyl nuclear power plant in 2015: An impact assessment. *Sci. Rep.* **6**, 26062. https://doi.org/10.1038/srep26062 (2016).
23. Yoschenko, V. I. *et al.* Resuspension and redistribution of radionuclides during grassland and forest fires in the Chernobyl exclusion zone: Part I. Fire experiments. *J. Environ. Radioact.* **86**, 143–163. https://doi.org/10.1016/j.jenvrad.2005.08.003 (2006).
24. Kinase, S., Kimura, M. & Hato, S. in *International Symposium on Environmental monitoring and dose estimation of residents after accident of TEPCO's Fukushima Daiichi Nuclear Power Stations.*
25. Bunzl, K., Hotzl, H. & Winkler, R. Spruce pollen as a source of increased radiocesium concentrations in air. *Naturwissenschaften* **80**, 173–174. https://doi.org/10.1007/bf01226376 (1993).
26. Teherani, D. K. Accumulation of ^{103}Ru, ^{137}Cs and ^{134}Cs in fruitbodies of various mushrooms from Austria after the chernobyl incident. *J. Radioanal. Nucl. Chem.* **117**, 69–74. https://doi.org/10.1007/BF02165314 (1987).
27. Yoshida, S. & Muramatsu, Y. Concentrations of radiocesium and potassium in Japanese mushrooms. *Environ. Sci.* **7**, 63–70. https://doi.org/10.11353/sesj1988.7.63 (1994).
28. Duff, M. C. & Ramsey, M. L. Accumulation of radiocesium by mushrooms in the environment: A literature review. *J. Environ. Radioact.* **99**, 912–932. https://doi.org/10.1016/j.jenvrad.2007.11.017 (2008).

29. Sesartić, A. & Dallafior, T. N. Global fungal spore emissions, review and synthesis of literature data. *Biogeosciences (Online)* **8**, 1181–1192. https://doi.org/10.5194/bg-8-1181-2011 (2011).
30. Fröhlich-Nowoisky, J. *et al.* Bioaerosols in the earth system: Climate, health, and ecosystem interactions. *Atmos. Res.* **182**, 346–376. https://doi.org/10.1016/j.atmosres.2016.07.018 (2016).
31. Yamaguchi, T. *et al.* Autoradiography of the fruiting body and spore print of wood-cultivated shiitake mushroom (Lentinula Edodes) from a restricted habitation area. *Mushroom Sci. Biotechnol.* **23**, 125–129 (2015).
32. Urbanová, M., Šnajdr, J. & Baldrian, P. Composition of fungal and bacterial communities in forest litter and soil is largely determined by dominant trees. *Soil Biol. Biochem.* **84**, 53–64. https://doi.org/10.1016/j.soilbio.2015.02.011 (2015).
33. Zhang, P. *et al.* Effect of litter quality on its decomposition in broadleaf and coniferous forest. *Eur. J. Soil Biol.* **44**, 392–399. https://doi.org/10.1016/j.ejsobi.2008.04.005 (2008).
34. *NARO. National Agriculture and Food Research Organization, llustrated Encyclopedia of Forage Crop Disease*, <https://www.naro.affrc.go.jp/org/nilgs/diseases/detitle.html>
35. Almaguer, M., Aira, M. J., Rodriguez-Rajo, F. J., Fernandez-Gonzalez, M. & Rojas-Flores, T. I. Thirty-four identifiable airborne fungal spores in Havana, Cuba. *Ann. Agric. Environ. Med.* **22**, 215–220. https://doi.org/10.5604/12321966.1152068 (2015).
36. Kumar, A. & Attri, A. K. Characterization of fungal spores in ambient particulate matter: A study from the Himalayan region. *Atmos. Environ.* **142**, 182–193. https://doi.org/10.1016/j.atmosenv.2016.07.049 (2016).
37. Guarín, F. A., Abril, M. A. Q., Alvarez, A. & Fonnegra, R. Atmospheric pollen and spore content in the urban area of the city of Medellin, Colombia. *Hoehnea* **42**, 9–19 (2015).
38. Fitt, B. D. L., Mccartney, H. A. & Walklate, P. J. The role of rain in dispersal of pathogen inoculum. *Annu. Rev. Phytopathol.* **27**, 241–270. https://doi.org/10.1146/annurev.py.27.090189.001325 (1989).
39. Gilet, T. & Bourouiba, L. Fluid fragmentation shapes rain-induced foliar disease transmission. *J. R. Soc. Interface* **12**, 20141092. https://doi.org/10.1098/rsif.2014.1092 (2015).
40. Gregory, P. H., Guthrie, E. J. & Bunce, M. E. Experiments on splash dispersal of fungus spores. *J. Gen. Microbiol.* **20**, 328–354. https://doi.org/10.1099/00221287-20-2-328 (1959).
41. Bauer, H. *et al.* Arabitol and mannitol as tracers for the quantification of airborne fungal spores. *Atmos. Environ.* **42**, 588–593. https://doi.org/10.1016/j.atmosenv.2007.10.013 (2008).
42. Lau, A. P. S., Lee, A. K. Y., Chan, C. K. & Fang, M. Ergosterol as a biomarker for the quantification of the fungal biomass in atmospheric aerosols. *Atmos. Environ.* **40**, 249–259. https://doi.org/10.1016/j.atmosenv.2005.09.048 (2006).
43. Pöhlker, C., Huffman, J. A. & Pöschl, U. Autofluorescence of atmospheric bioaerosols—fluorescent biomolecules and potential interferences. *Atmos. Meas. Tech.* **5**, 37–71. https://doi.org/10.5194/amt-5-37-2012 (2012).
44. Pöschl, U. *et al.* Rainforest aerosols as biogenic nuclei of clouds and precipitation in the Amazon. *Science* **329**, 1513–1516. https://doi.org/10.1126/science.1191056 (2010).
45. Elbert, W., Taylor, P. E., Andreae, M. O. & Poschl, U. Contribution of fungi to primary biogenic aerosols in the atmosphere: Wet and dry discharged spores, carbohydrates, and inorganic ions. *Atmos. Chem. Phys.* **7**, 4569–4588. https://doi.org/10.5194/acp-7-4569-2007 (2007).
46. Hassett, M. O., Fischer, M. W. & Money, N. P. Mushrooms as rainmakers: How spores act as nuclei for raindrops. *PLoS ONE* **10**, e0140407. https://doi.org/10.1371/journal.pone.0140407 (2015).
47. Pringle, A., Patek, S. N., Fischer, M., Stolze, J. & Money, N. P. The captured launch of a ballistospore. *Mycologia* **97**, 866–871. https://doi.org/10.3852/mycologia.97.4.866 (2005).
48. Turner, J. C. R. & Webster, J. Mass and momentum transfer on the small scale: how do mushrooms shed their spores?. *Chem. Eng. Sci.* **46**, 1145–1149. https://doi.org/10.1016/0009-2509(91)85107-9 (1991).
49. Hirst, J. M. & Stedman, O. J. Dry liberation of fungus spores by raindrops. *J. Gen. Microbiol.* **33**, 335–344. https://doi.org/10.1099/00221287-33-2-335 (1963).
50. Huber, L., Madden, L. V. & Fitt, B. D. L. in *The Epidemiology of Plant Diseases* (ed D. Gareth Jones) Ch. Chapter 17, 348–370 (Springer Netherlands, Berlin, 1998).
51. Kim, S., Park, H., Gruszewski, H. A., Schmale, D. G. 3rd. & Jung, S. Vortex-induced dispersal of a plant pathogen by raindrop impact. *Proc. Natl. Acad. Sci. U.S.A.* **116**, 4917–4922. https://doi.org/10.1073/pnas.1820318116 (2019).
52. Levia, D. F., Hudson, S. A., Llorens, P. & Nanko, K. Throughfall drop size distributions: A review and prospectus for future research. *Wiley Interdiscip. Rev.-Water* **4**, e1225. https://doi.org/10.1002/wat2.1225 (2017).
53. Iida, S. I. *et al.* Intrastorm scale rainfall interception dynamics in a mature coniferous forest stand. *J. Hydrol.* **548**, 770–783. https://doi.org/10.1016/j.jhydrol.2017.03.009 (2017).
54. Sun, X. C., Onda, Y., Kato, H., Gomi, T. & Liu, X. Y. Estimation of throughfall with changing stand structures for Japanese cypress and cedar plantations. *For. Ecol. Manag.* **402**, 145–156. https://doi.org/10.1016/j.foreco.2017.07.036 (2017).
55. Murakami, S. A proposal for a new forest canopy interception mechanism: Splash droplet evaporation. *J. Hydrol.* **319**, 72–82. https://doi.org/10.1016/j.jhydrol.2005.07.002 (2006).
56. Murakami, S. Canopy interception and the effect of forest on rainfall increase. *Water Sci.* **56**, 82–99. https://doi.org/10.20820/suirikagaku.56.1_82 (2012).
57. Huffman, J. A., Treutlein, B. & Pöschl, U. Fluorescent biological aerosol particle concentrations and size distributions measured with an Ultraviolet Aerodynamic Particle Sizer (UV-APS) in Central Europe. *Atmos. Chem. Phys.* **10**, 3215–3233. https://doi.org/10.5194/acp-10-3215-2010 (2010).
58. Savage, N. J. *et al.* Systematic characterization and fluorescence threshold strategies for the wideband integrated bioaerosol sensor (WIBS) using size-resolved biological and interfering particles. *Atmos. Meas. Tech.* **10**, 4279–4302. https://doi.org/10.5194/amt-10-4279-2017 (2017).
59. Butterworth, J. & Mccartney, H. A. The dispersal of bacteria from leaf surfaces by water splash. *J. Appl. Bacteriol.* **71**, 484–496. https://doi.org/10.1111/j.1365-2672.1991.tb03822.x (1991).
60. Chatani, S., Matsunaga, S. N. & Nakatsuka, S. Estimate of biogenic VOC emissions in Japan and their effects on photochemical formation of ambient ozone and secondary organic aerosol. *Atmos. Environ.* **120**, 38–50. https://doi.org/10.1016/j.atmosenv.2015.08.086 (2015).
61. Han, Y. M., Iwamoto, Y., Nakayama, T., Kawamura, K. & Mochida, M. Formation and evolution of biogenic secondary organic aerosol over a forest site in Japan. *J. Geophys. Res.-Atmos.* **119**, 259–273. https://doi.org/10.1002/2013jd020390 (2014).
62. Miyazaki, Y. *et al.* Evidence of formation of submicrometer water-soluble organic aerosols at a deciduous forest site in northern Japan in summer. *J. Geophys. Res.-Atmos.* https://doi.org/10.1029/2012jd018250 (2012).
63. Pringle, A. Asthma and the diversity of fungal spores in air. *PLoS Pathog.* **9**, e1003371. https://doi.org/10.1371/journal.ppat.1003371 (2013).
64. Tobo, Y. *et al.* Biological aerosol particles as a key determinant of ice nuclei populations in a forest ecosystem. *J. Geophys. Res.-Atmos.* **118**, 10100–10110. https://doi.org/10.1002/jgrd.50801 (2013).
65. Iwata, A. *et al.* Release of highly active ice nucleating biological particles associated with rain. *Atmosphere* https://doi.org/10.3390/atmos10100605 (2019).
66. Murray, B. J., O'Sullivan, D., Atkinson, J. D. & Webb, M. E. Ice nucleation by particles immersed in supercooled cloud droplets. *Chem. Soc. Rev.* **41**, 6519–6554. https://doi.org/10.1039/c2cs35200a (2012).
67. Homepage of High-Resolution Land Use and Land Cover Map Products. https://www.eorc.jaxa.jp/ALOS/en/lulc/lulc_index.htm.

68. Torii, T. *et al.* Investigation of radionuclide distribution using aircraft for surrounding environmental survey from Fukushima Dai-ichi Nuclear Power Plant. *JAEA-Technology--2012–036*, 192 (2012).
69. Schneider, C. A., Rasband, W. S. & Eliceiri, K. W. NIH image to ImageJ: 25 years of image analysis. *Nat. Methods* **9**, 671–675. https://doi.org/10.1038/nmeth.2089 (2012).
70. Lee, S. B. & Taylor, J. W. In *PCR Protocols* (eds Innis, M. A. *et al.*) 282–287 (Academic Press, New York, 1990).
71. White, T. J., Bruns, T., Lee, S. & Taylor, J. In *PCR Protocols* (eds Innis, M. A. *et al.*) 315–322 (Academic Press, New York, 1990).

Acknowledgements

We thank Ms. K. Inukai, Ms. K. Kamioka, Mr. T. Kimura and Mr. K. Hama (Atox Co. Ltd.) for assistance with the activity measurements and Ms. K. Yanagida (Meteorological Research Institute; MRI) for logistics. We are appreciative to Ms. M. Kitamura (Institute for Integrated Radiation and Nuclear Science, Kyoto University) for editing the manuscript and redrawing the figures. We acknowledge Drs. Y. Zaizen and M. Kajino (MRI) for scientific discussions. We thank Dr. K. Ninomiya and Prof. Shinohara (Osaka University) for providing radiocaesium activity data for some HV samples. We acknowledge Mr. T. Kanari (Green Blue Co. Ltd.) for sustaining the sample exchange and the members and students of the College of Science and College of Engineering, Ibaraki University, for the maintenance and special installation of tools in the field and data collection. Ms. A. Hashimoto (Ibaraki University) is acknowledged for her help in data management. We acknowledge Dr. K. Hosaka (National Science Museum) for fungal fruit hunting in the Tsukuba Botanical Garden. A preliminary experiment on the IN activity of fungal spores was carried out by Mr. K. Sasaki, Ibaraki University. The scientific discussion with Dr. K. Hosaka and Prof. T. Maki, Kanazawa University (currently at Kindai University), facilitated our work. We also express our thanks to the local governments of Kawamata town and Namie town and to the Fukushima prefectural government, which kindly provided our monitoring opportunities. A weather-dependent switch for HV sampling was manufactured by Climatec, Japan, who helped with many observations in Fukushima Prefecture, to which the authors' thanks are due. We especially thank Mr. Hisanori Tanaka of Climatec. This work was supported financially by Grants-in-Aid for Scientific Research on Innovative Areas to the A01–2 research team of the "Interdisciplinary Study on Environmental Transfer of Radionuclides from the Fukushima Daiichi NPP Accident (ISET-R)" (grant numbers 24110003; PI: Prof. Yuichi Onda, University of Tsukuba, one of the present authors) and by the Ministry of Education, Culture, Sports, Science and Japanese Radioactivity Survey by Technology and Nuclear Regulation Authority, Japan, at the MRI. This research was also funded by Grants-in-Aid for Scientific Research (A) (No. 17H01478), (B) (Nos. 17H01873 and 18H03385) and (C) (No. 26340049).

Author contributions

K.K. and Y.I. made equal contributions to this work. They supervised the present project and planned the observations and data analysis. Y.O. suggested an original idea for observations during rain and possible significance of rain splash as a mechanism. K.K., T.K., and N.H. performed observations at the study site and carried out the experimental analysis. K.K. showed his leadership in the rain observation campaign, without which this study would not been completed. M.I. contributed meteorological observations. Y.I., K.K., and T.K. carried out radioactivity measurements. K.A. performed optical/electron microscopy analyses with T.K. and N.H. M.K. carried out the isolation and identification of fungal species. T.T.S. depicted the sampling location map. Y.I., T.K., K.K., N.H. and M.K. wrote the manuscript, and all authors contributed ideas for the paper and reviewed the manuscript.

Competing interests

The authors declare no competing financial interests.

Additional information

Supplementary information is available for this paper at https://doi.org/10.1038/s41598-020-72029-z.

Correspondence and requests for materials should be addressed to K.K. or Y.I.

Reprints and permissions information is available at www.nature.com/reprints.

Publisher's note Springer Nature remains neutral with regard to jurisdictional claims in published maps and institutional affiliations.

Reproducibility of Surface Wind and Tracer Transport Simulations over Complex Terrain Using 5-, 3-, and 1-km-Grid Models

TSUYOSHI THOMAS SEKIYAMA

Meteorological Research Institute, Tsukuba, Japan

MIZUO KAJINO

Meteorological Research Institute, and Faculty of Life and Environmental Sciences, University of Tsukuba, Tsukuba, Japan

(Manuscript received 1 October 2019, in final form 23 March 2020)

ABSTRACT

The reproducibility of surface wind and tracer transport simulations from high-resolution weather and transport models was studied over complex terrain in wintertime in Japan. The horizontal grid spacing was varied (5-, 3-, and 1-km grids), and radioactive cesium (Cs-137) from the Fukushima nuclear power plant was used as a tracer. Fukushima has complex terrain, such as mountains and valleys. The model results were validated by observations collected from the national networks of the automated meteorological data acquisition system and the hourly air pollution sampling system. The reproducibility depended on the model resolution, topographic complexity, and synoptic weather conditions. Higher model resolution led to higher reproducibility of surface winds, especially in mountainous areas when the Siberian winter monsoon was disturbed. In contrast, the model improvement was negligible or nonexistent over plain/coastal areas when the synoptic field was steady. The statistical scores of the tracer transport simulations often deteriorated as a result of small errors in the plume locations. However, the higher-resolution models advantageously performed better transport simulations in the mountainous areas because of the lower numerical diffusion and higher reproducibility of the mass flux. The reproducibility of the tracer distribution in the valley of the Fukushima mountainous region was dramatically improved with increasing model resolution. In the range of mesoscale model resolutions (commonly 1–10 km), it was concluded that a higher-resolution model is definitely recommended for tracer transport simulations over mountainous terrain.

1. Introduction

The time scale of atmospheric tracer transport simulations ranges from seconds to decades. The spatial scale also ranges from microscale to global. Global or synoptic-scale tracer simulations often assume that the tracer species are well mixed or continuously distributed in the atmosphere. The assumption is justified in treating carbon dioxide, ozone, or water vapor, which are universally present with widespread sources and sinks. However, the assumption often fails when the time scale is short (e.g., minutes or hours), the spatial scale is limited (e.g., mesoscale or less), and the background concentration is extremely low (e.g., point source pollution). In that case, the tracer distributions are not continuous, and their plumes have sharply outlined edges with concentration jumps of more than several orders of magnitude.

Modeling these sharp-edged plumes in the troposphere is crucial for urban pollution predictions or environmental emergency responses (World Meteorological Organization 2006). However, model performance of sharp-edged plumes is lower than that of continuous distributions because small errors in the plume location lead to large uncertainties in the concentration variations. Generally, the plume location is strongly influenced by the accuracy of wind fields (Angevine et al. 2014; Sekiyama et al. 2017), in which the acceptable range of wind velocity errors is narrower than usually expected. Especially in the planetary boundary layer (PBL), the wind field becomes complicated over complex

Supplemental information related to this paper is available at the Journals Online website: https://doi.org/10.1175/JAMC-D-19-0241.s1.

Corresponding author: Tsuyoshi Thomas Sekiyama, tsekiyam@mri-jma.go.jp

DOI: 10.1175/JAMC-D-19-0241.1

terrain, which impairs the reproducibility of surface wind and plume transport simulations (Srinivas et al. 2016). Consequently, the topographic model resolution has a large impact on the accuracy of plume transport simulations over complex terrain (Sekiyama et al. 2015). Therefore, plume transport simulations are more challenging than continuous transport simulations.

Meanwhile, the model validation of PBL wind and plume simulations is not straightforward because it requires widespread and frequent observations over complex terrain, including rural or mountainous areas, for both wind velocity and tracer concentration. Therefore, the reproducibility of PBL wind and plume simulations over complex terrain has not been investigated in detail. Although some previous studies addressed the model resolution dependence of tracer transport simulations, such as inert gases, nitrogen oxides, sulfur dioxide, carbon dioxide, and ozone, using high-resolution models (e.g., Nachamkin et al. 2007; Tie et al. 2010; Pillai et al. 2011; Cécé et al. 2016; Dingwell et al. 2016; Feng et al. 2016; Tang et al. 2019), they validated the tracer distributions at only a few selected observatories over complex terrain. They did not conduct plume verifications that required many concentration/wind observations. Although Sugiyama et al. (2012), Katata et al. (2012a,b), and Sekiyama et al. (2015) performed high-resolution simulations for radionuclide plumes over complex terrain, they did not validate the plume concentrations and motions focusing on model resolution.

Sekiyama et al. (2015) conducted plume simulations of radioactive cesium (Cs-137) emitted by the Fukushima Daiichi Nuclear Power Plant (FDNPP) accident after the 2011 Tohoku great earthquake in Japan. The Japanese archipelago consists of steep mountains, narrow plains/basins, and small peninsulas/islands; that is, the terrain is highly complex (Fig. 1). In particular, Fukushima is one of the mountainous regions in Japan, and the FDNPP is located on the coastline of the Pacific Ocean and only a few kilometers from mountains as high as 1000 m. Fukushima also has 2000-m mountain peaks and a narrow basin between the 2000-m mountain peaks and the 1000-m mountains behind the FDNPP. In contrast, Tokyo, more than 200 km south-southwest of Fukushima, is located in the largest plain in Japan. Nevertheless, the largest Japanese plain, or the Kanto Plain, is only 100–150 km in diameter and is surrounded by 1000–2000-m mountains. The Cs-137 that originated from Fukushima is an ideal tracer over the complex terrain (cf. Bieringer et al. 2013); therefore, Sekiyama et al. (2015) proceeded with their tracer model experiments. However, Sekiyama et al. (2015) could not obtain enough Cs-137 concentration data to validate the plume simulations. Therefore, they validated only 1-month

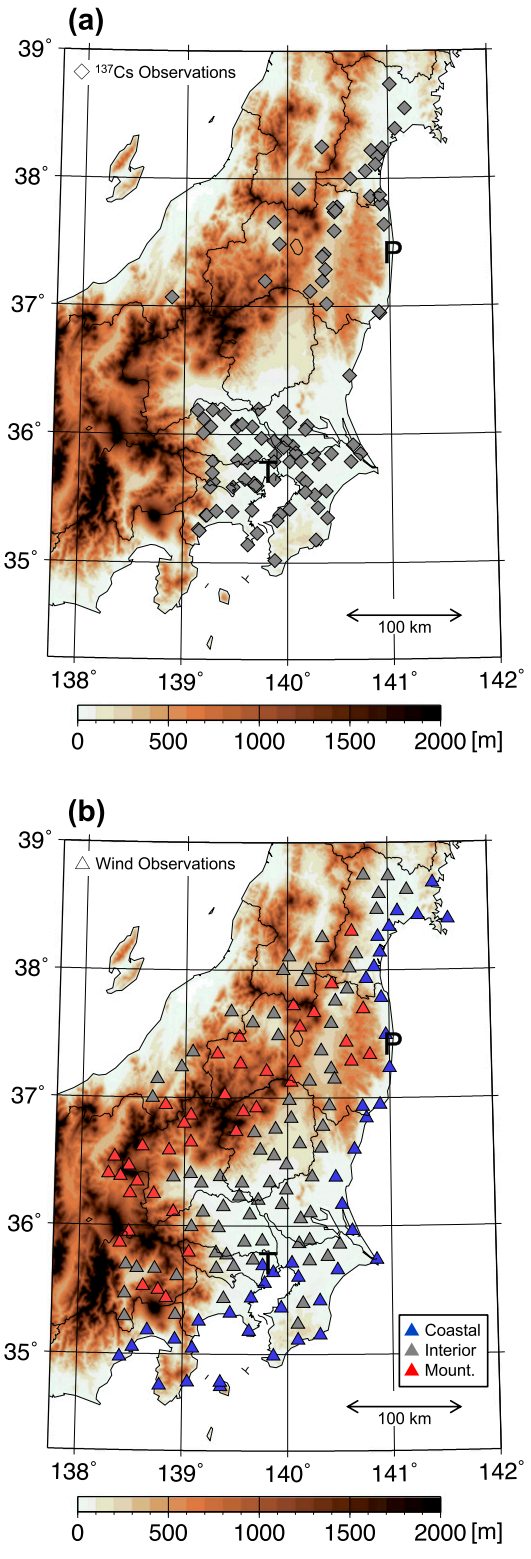

FIG. 1. Observation stations used in this study for (a) surface Cs-137 concentrations provided by the SPM sampling network and (b) surface winds provided by the AMeDAS network. Capital letters P and T indicate the locations of the Fukushima Daiichi Nuclear Power Plant and Tokyo City, respectively. Brown shades indicate the elevations. Blue, gray, and red triangles represent coastal, interior, and mountainous stations, respectively.

accumulated deposition distributions without wind comparison.

Since then, the Cs-137 concentrations at more than 100 monitoring stations have been retrieved hourly by Tsuruta et al. (2014), Oura et al. (2015), and Tsuruta et al. (2018). These authors analyzed filter tapes for ambient suspended particulate matter (SPM) sampling in and near Fukushima and Tokyo. In addition, high-quality meteorological variables are universally measured in Japan by the Japanese government even immediately after the Tohoku great earthquake and during the FDNPP accident (cf. Sekiyama et al. 2017). These widespread and frequent observations for both surface winds and Cs-137 concentrations are used in this study to overcome the difficulty with plume transport model validation over complex terrain. This study must be the first attempt to investigate the reproducibility of both surface winds and plume concentrations over complex terrain and its dependence on the model resolution using high-resolution (5, 3, and 1 km) meteorological analyses and models. The details of the observational data are described in section 2a. Then, the meteorological analyses used for the tracer transport simulations are explained in section 2b. The transport model descriptions are also presented in section 2b. The results and discussion are presented in section 3, and the conclusions are given in section 4.

2. Data and models

a. Observational data

1) Surface Cs-137 observations

Tsuruta et al. (2014) developed a method to retrieve hourly averaged surface Cs-137 concentrations using SPM sampling filter tapes with a theoretical detection limit of 0.1 $\mathrm{Bq\,m^{-3}}$. The SPM sampling network is nationwide and deployed by national and local governments. Some of the local governments provided the SPM sampling filter tapes for researchers to retrieve the Cs-137 concentrations during the FDNPP accident. Tsuruta et al. (2014) and Oura et al. (2015) released Cs-137 concentration data for 99 SPM sampling stations in eastern Japan. The air intakes are usually installed at a height of several meters at each sampling station. In addition, the Japan Atomic Energy Agency (JAEA) was operationally measuring hourly Cs-137 concentrations on the premises of their Tokai facilities (36.46°N, 140.60°E) located between Tokyo and Fukushima (Ohkura et al. 2012). These locations are illustrated in Fig. 1a for both the SPM sampling stations and Tokai facilities. As illustrated in Fig. 1a, the sampling stations are mainly distributed around the FDNPP (P in the figure) and Tokyo (T in the figure). While the terrain surrounding the FDNPP is complex with mountains, valleys, and basins, the terrain surrounding Tokyo is relatively flat (the Kanto Plain). These Cs-137 observations are used for model validation when the value is larger than the practical detection limit (approximately 1.0 $\mathrm{Bq\,m^{-3}}$).

2) Surface wind observations

To acquire widespread and frequent surface wind observations for model validation, we used a dataset from the automated meteorological data acquisition system (AMeDAS) managed by the Japan Meteorological Agency (JMA) of the Japanese government. The AMeDAS is a land surface observation network that comprises more than 1000 stations throughout Japan with an average interval of 10–20 km. Anemometers are usually installed at a height of 10 m at each AMeDAS station (hereinafter, we call the 10-m-height winds U_{10} or V_{10}). Although a few of the AMeDAS stations stopped working immediately after the earthquake, almost every station was operational even during the FDNPP accident. In this study, hourly AMeDAS data (5-min averages on the hour) were used. To restrict the wind field validation to the area with Cs-137 observations, the AMeDAS data in this study were limited within southern Tohoku (around the FDNPP), the Kanto Plain (around Tokyo), and the mountainous vicinity of these areas, as shown in Fig. 1b.

In general, AMeDAS stations are located in populated areas, that is, coasts, plains, and basins. However, fortunately, some of the stations are installed in mountainous locations. Thus, in this study, we categorized the AMeDAS stations into three location types, as shown in Fig. 1b: coastal, interior, and mountainous stations, which have approximately 40, 80, and 40 stations, respectively. The mountainous stations were selected only if they are surrounded on all four sides by steep terrain and located more than 350 m above sea level (MSL). Some stations were classified as interior locations since they are between steep slopes that shape valleys. We calculate the statistics classifying wind observation locations into these three categories (mountainous, interior, and coastal winds) and present them in the following sections.

b. Meteorological analyses and models

1) Meteorological analyses

Prior to the tracer transport simulation, we prepared meteorological analyses with three different horizontal resolutions (5-, 3-, and 1-km grids) to drive a tracer

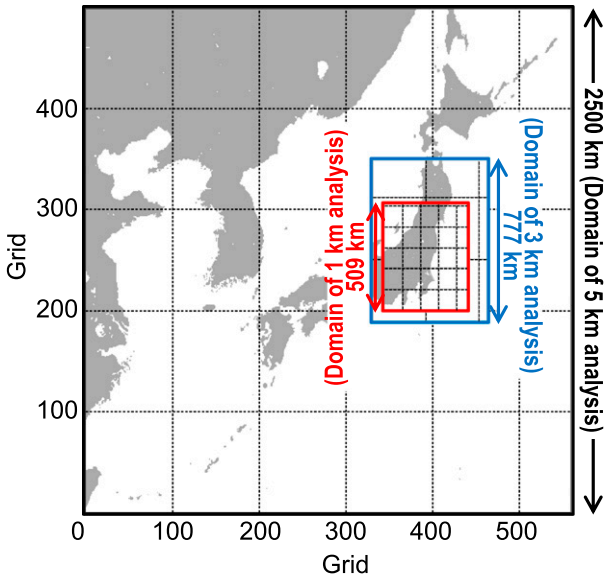

FIG. 2. Domains for the 5-, 3-, and 1-km meteorological analyses. Grid lines are drawn every 100 grids for not only the 5-km analysis but also the 3- and 1-km analyses.

transport model. The 5-km-grid analysis was made from the operational mesoscale gridpoint value (hereinafter, meso GPV) dataset that is produced by the JMA and distributed to the public as a part of weather information. The 3-km-grid analysis was performed by Sekiyama et al. (2017). The 1-km-grid analysis was uniquely performed for this study. All of these analyses were calculated by the same weather forecast model using the unified observations.

The 5-km operational meso GPVs are calculated by the JMA nonhydrostatic-model four-dimensional variational data assimilation (JNoVA) system (Honda et al. 2005), whose domain covers East Asia (Fig. 2). The JNoVA system consists of the JMA nonhydrostatic regional weather forecast model (JMA-NHM; Saito et al. 2006, 2007) and a four-dimensional variational (4DVar) data assimilation module. The lateral boundary conditions are obtained from the JMA operational global analysis with an approximately 20-km horizontal resolution (World Meteorological Organization 2011). The JNoVA system assimilates meteorological observations quality controlled by the JMA; these data include land surface pressure, sea surface winds, and observations from radiosondes, pilot balloons, wind profilers, aircrafts, ships, buoys, radars, and satellites. Although the 5-km operational meso GPV dataset has been archived with a 3-h time interval, the tracer transport simulation requires meteorological analysis stored at higher time resolution. Therefore, we conducted a 5-km-grid JMA-NHM run every 3 h with the same model parameters as the operational JNoVA settings using the 3-hourly 5-km operational meso GPVs as the initial and boundary conditions to obtain new hourly meteorological variables.

The 3-km-grid analysis was provided by another data assimilation system (Kunii 2014), which consists of the JMA-NHM and the four-dimensional local ensemble transform Kalman filter (4D-LETKF; cf. Miyoshi and Aranami 2006). Hereinafter, we call this system NHM-LETKF. This data assimilation system has been applied to Fukushima nuclear pollutant simulations (Sekiyama et al. 2015, 2017; Sekiyama and Iwasaki 2018; Iwasaki et al. 2019). Sekiyama et al. (2017) calculated the 3-km-grid analysis using the same JMA-NHM configurations as the 5-km-grid analysis or the operational meso GPVs except for the model resolution and the convective parameterization (not activated for the 3-km-grid JMA-NHM). The model domain covered only eastern Japan, of which lateral boundary conditions were obtained from the JMA operational global analysis same as the operational meso GPVs (Fig. 2). Sekiyama et al. (2017) assimilated the JNoVA observations except for radar precipitation and satellite radiance (but included satellite-observed wind velocities). Additionally, AMeDAS surface wind observations were assimilated for the 3-km-grid analysis.

The 1-km-grid analysis was calculated by the NHM-LETKF with the same observations and configurations as the 3-km-grid analysis (Sekiyama et al. 2017), except for the model domain and resolution. The lateral boundary conditions and perturbations were obtained from the outputs of the 3-km-grid analysis (Sekiyama et al. 2017), which implemented a one-way nested data assimilation scheme (Kunii 2014). In the same way as the 3-km-grid analysis (Sekiyama et al. 2017), the LETKF was driven by 20 ensemble members with a covariance localization of 50 km in the horizontal dimension, 0.1 natural-logarithm-pressure coordinate in the vertical dimension, and 3 h in the time dimension, employing an adaptive inflation scheme (Miyoshi 2011; Miyoshi and Kunii 2012). The model domain consisted of 461 × 509 horizontal grid points on the Lambert conformal projection and 60 vertical levels up to approximately 22 km in the terrain-following hybrid vertical coordinates, which included 11 levels below 1 km above ground level (the lowermost level is at 20 m above the ground), the same as the 5- and 3-km-grid analyses.

Terrain features in the model domains of the 5-, 3-, and 1-km-grid JMA-NHMs were generated from global elevation data with a horizontal grid spacing of 30 arc s (GTOPO30) from the U.S. Geological Survey (https://doi.org/10.5066/F7DF6PQS), which is approximately 700 m in the east–west direction and 900 m in the south–north direction. The terrains were numerically smoothed in the models of all resolutions to satisfy the

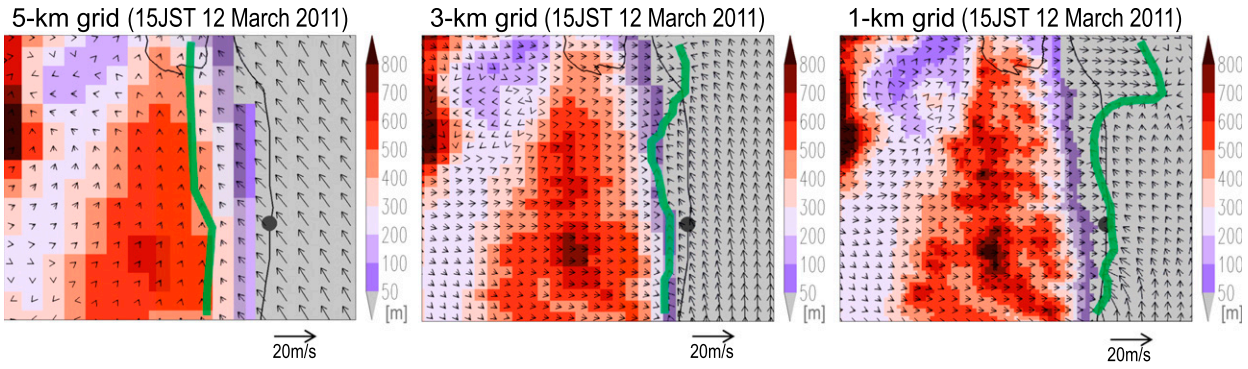

FIG. 3. Fukushima topography depicted by the 5-, 3-, and 1-km grid resolutions. The filled black circle is the location of the FDNPP. Arrows and green lines indicate the surface (10-m height) wind vectors of the analyses and their convergence zones, respectively, at 1500 Japanese standard time (JST) 12 Mar 2011. The arrows for the 1-km-grid wind field are shown at every third grid point (=3-km spacing). Thin black lines depict the coastline and a prefectural borderline.

maximum slope of 150‰ (≈ 8.6°). This smoothing procedure was done to avoid numerical instability due to steep slopes. Fukushima's complex topography is depicted by the 5-, 3-, and 1-km-grid analyses in Fig. 3. Fine structures of small valleys and ridges are well reproduced by the 1-km-grid analysis, while the 5-km-grid analysis fails to detect them and barely reproduces the rough shapes of mountains and basins.

As described above, the 3-km-grid analysis (Sekiyama et al. 2017) and 1-km-grid analysis are perfectly consistent using completely the same model (JMA-NHM), data assimilation scheme (LETKF), observation dataset, and configurations except for the model resolution setup. Note that the 5-km-grid analysis is calculated by a different data assimilation scheme (4DVar) assimilating a slightly different observation dataset, although the same forecast model is used. However, previous studies have confirmed that the 4DVar and the LETKF generally provide comparable performances as meteorological data assimilation schemes (cf. Kalnay et al. 2007). Furthermore, all three of these analyses are confirmed to reproduce very close structures of synoptic-scale disturbances because they share the same global analysis as lateral boundary conditions. The lack of satellite radiance data assimilation does not have a large impact on the 3- and 1-km-grid wind fields, probably due to their small domain sizes. In addition, we find that the 3-km analysis often shows intermediate behavior between the 5- and 1-km analyses in the lower troposphere. For example, the location of the surface wind convergence zone undergoes a gradual transition from west to east with increasing resolution in the case of Fig. 3.

2) OFFLINE TRANSPORT MODEL

The tracer (Cs-137) transport simulations were performed by an offline Eulerian regional air quality model, which was driven by the 5-, 3-, and 1-km-grid meteorological analyses mentioned above. The offline Eulerian regional air quality model was originally developed by Kajino et al. (2012, 2019a) for nonradioactive aerosol simulations and has subsequently been used for Fukushima nuclear pollutant simulations by Adachi et al. (2013), Sekiyama et al. (2015, 2017), Kajino et al. (2016, 2018, 2019b), Inomata et al. (2018), Kitayama et al. (2018), Mathieu et al. (2018), Sato et al. (2018), Sekiyama and Iwasaki (2018), and Iwasaki et al. (2019).

In this model, the radionuclide Cs-137 was assumed to be well mixed with sulfate aerosol particles when it was transported in the atmosphere. The aerosol particle size was assumed to be log-normally distributed with a number equivalent geometric mean dry diameter = 0.5 μm, a geometric standard deviation = 1.6, a particle density = 1.83 g cm^{-3}, and a hygroscopicity = 0.4 assuming a sulfate-organic mixture. Compared with Kajino et al. (2012), simplified aerosol dynamics was implemented by assuming a constant particle size distribution, in which nucleation, condensation, and coagulation were not considered. However, the model still simulated the important nature of the aerosol dynamics, such as dry deposition and in-cloud/below-cloud scavenging (i.e., wet deposition) processes, based on the prescribed size distribution as described in Sekiyama et al. (2015).

The meteorological analysis was taken into the offline Eulerian model every 1 h and linearly interpolated to suitable time intervals (30, 24, and 8 s for the 5-, 3-, and 1-km-grid models, respectively). The vertical model coordinate was converted from 60 layers in the NHM-LETKF analyses (expanded from the surface to approximately 22 km) to 20 layers (expanded from the surface to approximately 10 km) to reduce the computational burden of calculations within the stratosphere.

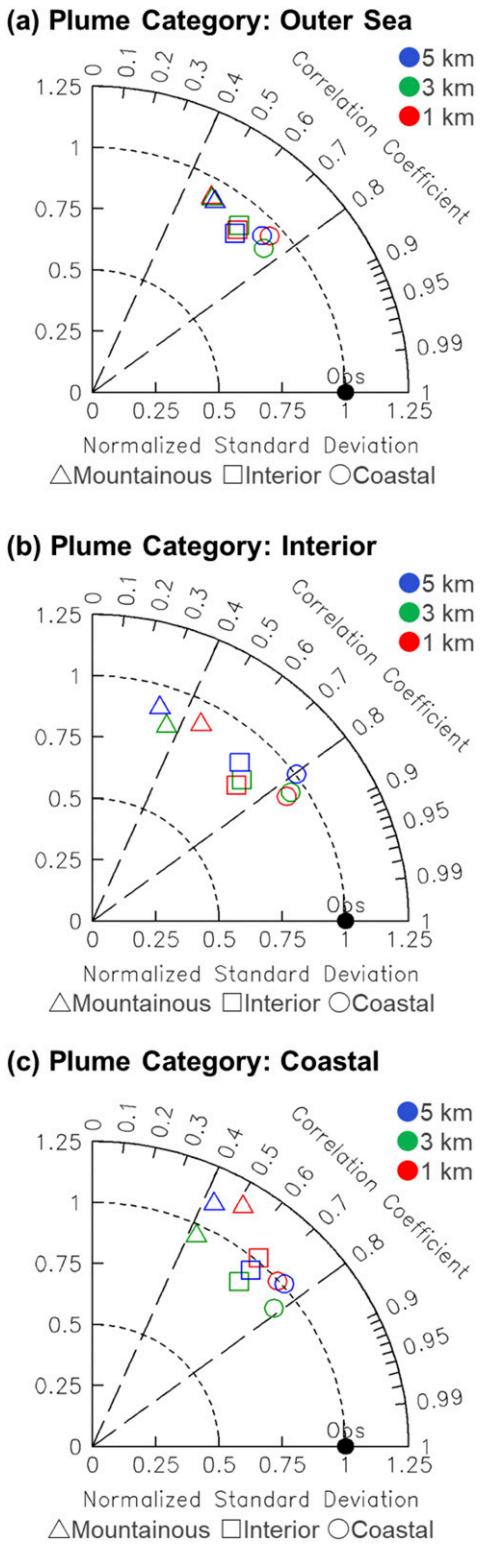

FIG. 4. Taylor diagrams for a comparison of surface wind analyses with AMeDAS observations categorized as (a) outer-sea plume periods, (b) interior plume periods, and (c) coastal plume periods. Open triangles, squares, and circles indicate mountainous, interior, and coastal locations, respectively, for the surface wind observations. Blue, green, and red colors indicate 5-, 3-, and 1-km-grid analyses, respectively. Black filled circles indicate observations.

The vertical resolution in the PBL was mostly unchanged. The 5- and 3-km-grid simulations shared the same model domain equivalent to that of the 3-km-grid meteorological analysis. The 1-km-grid simulation covered a smaller domain equivalent to the 1-km-grid meteorological analysis, as shown in Fig. 2. The Cs-137 emission scenario was provided by Katata et al. (2015), which was based on a source term estimation method (cf. Bieringer et al. 2013, 2017). Aerosol particles with Cs-137 were injected into a grid cell above the FDNPP at heights of 20–150 m above ground level based on a time-varying emission scenario, which was the same for all simulations. Each tracer transport simulation was performed from 11 to 31 March 2011.

In addition, a test simulation was performed to separate the effects of atmospheric resolution and topographic resolution. The additional simulation was run by the 1-km-grid-spacing model in the same way as the 1-km-grid simulation but driven by the 5-km-grid meteorological analysis as used in the 5-km-grid simulation. The 5-km-grid meteorological analysis was interpolated at 1-km intervals in the additional simulation, in which the numerical resolution was finer, but the terrain elevation and land use remained coarse. The additional simulation result was used for discrimination between the benefits of a highly resolved atmosphere and a highly resolved terrain. Hereinafter, the additional simulation is called the "5-to-1-km-grid" run.

3. Results and discussion

a. Plume classification

Major leakage of radioactive substances by the Fukushima nuclear accident lasted for three weeks from the day after the great earthquake (Hatamura et al. 2012). Most of the radioactive plumes during the three weeks flowed offshore (eastward) to the Pacific Ocean with the Siberian winter monsoon. The time windows of onshore (westward) plumes were limited to less than 50 h in total during the three weeks (Nakajima et al. 2017). Tsuruta et al. (2014) classified the onshore Cs-137 propagations into nine plumes (P1–P9) based on the time, location, and direction detected by their SPM sampling filter-tape observations. Sekiyama and Iwasaki (2018) clearly illustrated these nine plumes, as shown in the online supplemental material, using time- and column-integrated mass flux analysis. The plume numbers (P1–P9) in this study are unchanged from Tsuruta et al. (2014).

We categorize these nine plumes into three groups: outer-sea plumes (P1, P5, and P6), interior plumes (P2, P3, and P8), and coastal plumes (P4, P7, and P9), as shown in the online supplemental material. The

outer-sea plumes were detected only at a few SPM sampling stations along the coastline very close to the FDNPP. Therefore, the prevailing wind direction during the periods of the outer-sea plumes was westerly, which appears to be the typical Siberian winter monsoon with the Siberian high and the Aleutian low, as indicated in weather charts. The areas of Fukushima and Tokyo were under the stable condition of high pressure systems during these periods. In contrast, cyclones were moving through the area of Fukushima and Tokyo during the periods of the interior and coastal plumes. During the interior plume periods, cyclones were centered on Fukushima or Tokyo and completely disturbed the Siberian winter monsoon over the area. This information means that the radioactive plumes never intruded inland unless low pressure disturbances passed over Japan in wintertime. The statistics of the surface wind and Cs-137 concentration are determined using these three categories (outer-sea, interior, and coastal plumes) in the following sections.

b. *Surface winds*

Figure 4 shows Taylor diagrams (Taylor 2001) for a comparison of the surface wind analyses to the AMeDAS 10-m wind observations. The analyses are snapshots on the hour, while the observations are 5-min averages on the hour. The zonal winds (U_{10}) and meridional winds (V_{10}) were collectively processed to calculate the Pearson correlation coefficients and standard deviations because the same tendencies were consistently maintained for the U_{10}/V_{10} combined and separate statistics. The wind analyses at 0000, 0300, 0600, 0900, 1200, 1500, 1800, and 2100 UTC are the initial fields, but those at other hours are the forecast fields because the analyses were calculated with a 3-h assimilation time window. Meanwhile, the AMeDAS 10-m wind observations were used for the assimilation of the 3- and 1-km-grid analyses. Although the influence of the AMeDAS wind data assimilation on the analyses is minute (Sekiyama et al. 2017), the Taylor diagrams were drawn by a comparison of 1-h forecast fields, that is, the analyses at 0100, 0400, 0700, 1000, 1300, 1600, 1900, and 2200 UTC, to avoid a direct comparison of the initial fields with the assimilated observations.

Taylor diagrams indicate how observations and model results compare in terms of their correlation, root-mean-square error (RMSE), and standard deviations. Pattern similarities between the observed (y_i) and modeled (x_i) fields can be quantified by the Pearson correlation coefficient r. Amplitude similarities can be quantified by their standard deviations σ_x and σ_y. Now define the centered RMSE (CRMSE):

$$\mathrm{CRMSE} = \left\{ \frac{1}{N} \sum_{i=1}^{N} [(x_i - X) - (y_i - Y)]^2 \right\}^{1/2},$$

where X (or Y) indicates the sample mean of x_i (or y_i) and N is the number of samples. The CRMSE indicates the model errors and tends to zero when the patterns and amplitudes of the two fields are very similar. Taylor (2001) indicated that these quantities (r, σ_x, σ_y, and CRMSE) are related by

$$(\mathrm{CRMSE})^2 = \sigma_x^2 + \sigma_y^2 - 2\sigma_x\sigma_y r.$$

In Taylor diagrams, the standard deviations σ_x and σ_y are represented by the radial distances from the origin. The mark of observation data is always located on the x axis with the value of σ_y since the autocorrelation coefficient is 1 at all times. The Pearson correlation coefficient r between observations and model results is shown by the azimuthal position. Then, the distance between the observation mark and the model result mark shows the value of the CRMSE because of the law of cosines when the azimuth is represented by $\cos^{-1} r$. Taylor diagrams are often drawn with normalized standard deviations (NSD), in which σ_x, σ_y, and CRMSE are normalized to the standard deviation of observations σ_y (as shown in Fig. 4). This normalization allows multiple data plots with different locations and/or time periods. Nevertheless, the distance between the observation ($r = 1$; NSD = 1) and the model result indicates the relative model error.

Figure 4 illustrates that the model errors in surface winds, or the distances from the observation ($r = 1$; NSD = 1), are always in the order of "mountainous location > interior location > coastal location" for any model resolution (5-, 3-, and 1-km grids) or plume category (Figs. 4a–c). The spread of the CRMSEs is much smaller for the outer-sea plume periods (Fig. 4a) than for the interior/coastal plume periods (Figs. 4b,c). This result indicates that the topographic dependence of the model performance is small when the atmosphere is stable under high pressure systems with the prevailing Siberian winter monsoon. Interestingly, the accuracy of winds at coastal stations (indicated by open circles) is lower for Siberian winter monsoon conditions (Fig. 4a) than for cyclonic conditions (Fig. 4b), while the accuracy of winds at mountain stations (indicated by open triangles) demonstrates the opposite behavior.

In terms of the model-resolution dependence, the differences are completely negligible among the 5-, 3-, and 1-km-grid models even for mountainous locations when the Siberian winter monsoon prevails under high pressure systems (Fig. 4a). This finding is contrary to common expectations that a higher resolution leads to a

better performance. However, the 1-km grid resolution demonstrates the best performance among the three model resolutions during the interior plume periods (Fig. 4b), in which the Siberian winter monsoon over Japan is completely disturbed by cyclones. The model errors are consistently in the order of "5-km grid > 3-km grid > 1-km grid" for any location (mountainous, interior, and coastal areas) as expected. Although the 1-km grid resolution is constantly superior to the 5- and 3-km grid resolutions during the interior plume periods, the difference is particularly large for mountainous locations. This result is reasonable given that the complexity of the terrain features is remarkable in mountainous areas. The complexity results in a large discrepancy in modeled terrains between different resolutions. The different terrains yield different dynamics (=wind fields) in the models. On the other hand, the superiority of the 1-km grid resolution is not very noticeable during the coastal plume periods (Fig. 4c). Although the 1-km-grid model performs better than the others in the mountainous and interior locations (indicated by open triangles and squares, respectively), the 3-km-grid model is superior in the coastal location (indicated by open circles). Note that the improvement of the plume transport performance is significant even when the surface wind performance improves only slightly (Nachamkin et al. 2007; Sekiyama et al. 2017) because the transport error is accumulated along the route. Therefore, we expect the 1-km-grid model to produce superior transport simulations in the next section.

c. *Cs-137 plumes*

Figure 5 shows a Taylor diagram for a comparison of the modeled Cs-137 concentrations to the SPM sampling filter-tape observations. The outer-sea plumes are excluded from the statistics since only a few observations were obtained over land during the outer-sea plume periods. Station locations are not classified as in the comparison of the surface wind validation because 1) the number of Cs-137 observation stations is fewer than that of the AMeDAS, 2) only a few "mountainous" stations observed Cs-137, and 3) almost no concentration record is available in the interior areas during the coastal plume periods. The comparison is performed by using time-integrated concentrations at each station to avoid a deterioration of statistical scores caused by small differences in plume arrival times. The time integral intervals are 6 h since all interior plumes (plumes 2, 3, and 8) and coastal plumes (plumes 4, 7, and 9) lasted for 6 h by definition, as indicated by Tsuruta et al. (2014), Oura et al. (2015), Nakajima et al. (2017), and Sekiyama and Iwasaki (2018) (also see the online supplemental material).

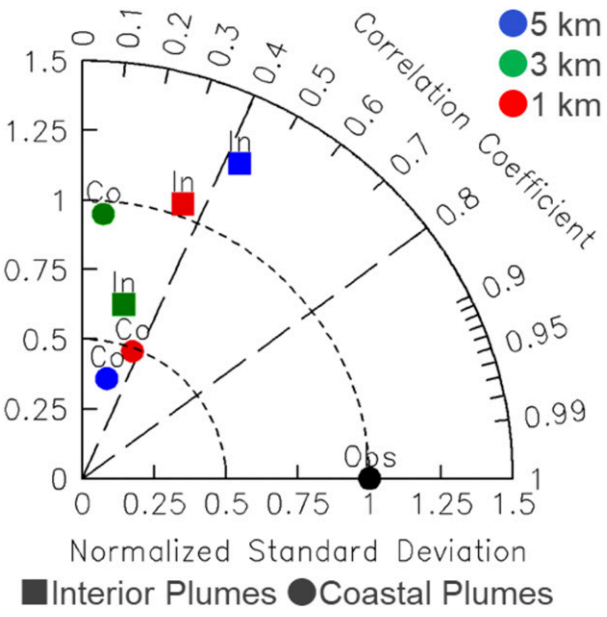

FIG. 5. Taylor diagram for a comparison of Cs-137 transport model results with SPM sampling filter-tape observations. Colored filled squares and circles indicate statistics during interior and coastal plume periods, respectively. Blue, green, and red colors indicate 5-, 3-, and 1-km-grid model results, respectively. A black filled circle indicates observations.

Certainly, the 1-km grid resolution (indicated by red marks in Fig. 5) demonstrates a good performance among the three model resolutions during both the interior and coastal plume periods. However, the correlations are evidently weak for all resolutions and plume periods. In addition, the model performance is unexpectedly in the order of "3-km grid < 5-km grid < 1-km grid" for both categories. The normalized standard deviations range more widely (0.35–1.25) than those of the surface wind analyses (0.8–1.2). This contrast is partly caused by the wet deposition of aerosols, which leads to large discrepancies in the aerosol concentration when the precipitation location and timing are differently simulated. The precipitation and foggy areas are not exactly identical among the three resolution models, which leads to large discrepancies in the deposition location. The authors have previously performed some Fukushima simulations with and without deposition processes (Sato et al. 2018; Iwasaki et al. 2019). The impact of wet deposition on the simulations appeared large in the northern part of the Kanto Plain probably because of drizzle or fog on 15 March 2011 over the Kanto Plain. However, unfortunately, no observations for Cs-137 were obtained in the northern part of the Kanto Plain (Fig. 1a) because the local governments had disposed of the SPM sampling filter tapes. In addition, rainy areas (especially on 21 March 2011) were mainly

located in the ocean or coastal regions, where the model resolution effect is quite small. Therefore, the impact of wet deposition on the statistics cannot be evaluated adequately in this study. Perhaps, transport error accumulation is also the cause of the contrast because transport errors are accumulated along the route with wind errors (Nachamkin et al. 2007; Sekiyama et al. 2017). The 5-to-1-km-grid simulation statistics were nearly identical to those of the 5-km-grid simulation (not shown), which implies that the impact of topographic resolution on plume simulation is much larger than that of atmospheric resolution.

Scatter diagrams are exhibited in Fig. 6 for the comparison between Cs-137 observations and model results to clarify the situation of the interior plume statistics shown by the abovementioned Taylor diagram. The plot is partly magnified (from the right panels to the left panels in Fig. 6) since most of the samples range within 100 h Bq m^{-3}. The distributions for both the 3- and 1-km-grid models are clearly split into two clusters, while the 5-km-grid model evidently results in a widely scattered distribution, that is, a weak correlation. In Fig. 6b, cluster (p) indicates good performance by the 3-km-grid model with a high correlation and a moderate slope angle. This cluster extends to a higher-concentration area, as shown by (p′). However, cluster (q) is almost parallel to the x axis with a weak correlation, in which the modeled concentrations scarcely fluctuate even when high concentrations are detected at each station in actuality. The combination of clusters (p) and (q) results in the underestimation (i.e., NSD < 1) of the 3-km-grid model for the interior plumes shown in Fig. 5. Likewise, cluster (r) for the 1-km-grid model also shows a high correlation (Fig. 6c), although it overestimates the concentrations. This cluster smoothly extends to a higher-concentration area, as shown by (r′). Cluster (r′) seems better than cluster (p′) in terms of the correlation. Meanwhile, cluster (s) underestimates with a gradual slope. The combination of clusters (r) and (s) results in a plausibly good amplitude (NSD ≈ 1), as shown in Fig. 5. The problem is that these split distributions for the 3- and 1-km-grid models make their overall correlations extremely lower even if each cluster is not widespread. Clusters (q) and (s) are formed by plumes that are slightly shifted from their real locations (as shown later), which is hardly avoidable in simulations of sharply edged plumes.

In contrast, in the case of the coastal plumes (Fig. 7), the differences are very small among the 5-, 3-, and 1-km-grid models, although the 1-km-grid model performs slightly better. The data points are almost evenly scattered, and no cluster is formed except for ones on the x axis. The reason for no plots on the y axis is that the observations have a detection limit. The transport models have only small dependence on the model resolution for the coastal plumes since the coastal winds originally differ just slightly between the model resolutions at all times, as shown in Fig. 4 (indicated by open circles). Both the plume locations and Cs-137 observations are mostly located in the coastal areas for this plume category. Therefore, most of the plots are not sampled from complex terrain in Fig. 7. Although the coastal winds show a good performance ($r = 0.7 \sim 0.9$, NSD ≈ 1), the transport simulations perform much worse due to small errors in the plume locations and precipitation areas. Small errors in the plume locations lead to deterioration of the correlation. Small errors in the precipitation lead to deterioration of the amplitude similarity.

Figures 8–10 illustrate the geographical distributions of the interior plumes over the Fukushima mountainous region, which is a typical example of a complex terrain, to detail the cluster formation described above in the scatter diagrams. At first glance, the plume shape of the 1-km-grid simulation appears sharper than those of the 5- and 3-km resolutions. The plume edges of the 5- and 3-km-grid simulations are blurred and broadened due to the strong numerical diffusion (or discretization error). The plume shape of the 5-to-1-km-grid simulation is very similar to that of the 5-km-grid simulation, but the plume edge diffusion is smaller in the 5-to-1-km-grid simulation. This indicates that the benefit of a highly resolved terrain is much larger than that of a highly resolved atmosphere. Moreover, the 5-km-grid plumes not only are numerically broadened but also are not blocked by the mountain range, or the Ou Mountains, and do not follow the shapes of valleys. Plume 8 (Fig. 8) of the 1-km-grid simulation coincides fairly well with observations, whereas that of the 5-km-grid simulation completely fails to move south along the central Fukushima Valley that is located between the mountain range (1000–2000 m MSL) and the Abukuma Highlands (500–1000 m MSL). These results indicate that the mountain range is not well reproduced in the 5-km-grid model. In the case of plume 8, the mass flux (shown by arrowheads) is evidently directed southward along the central Fukushima Valley in the 1-km-grid simulation, directed incorrectly northward in the 5-km and 5-to-1-km-grid simulations, and directed moderately southward in the 3-km-grid simulation. The mass flux along the valley strongly depends on the topographic resolution because the mountains/highlands seriously lower down using low-resolution terrains.

In contrast, in the case of plume 3 (Fig. 9), the high-concentration tail of the plume is successfully blocked by the mountains and does not intrude into the central

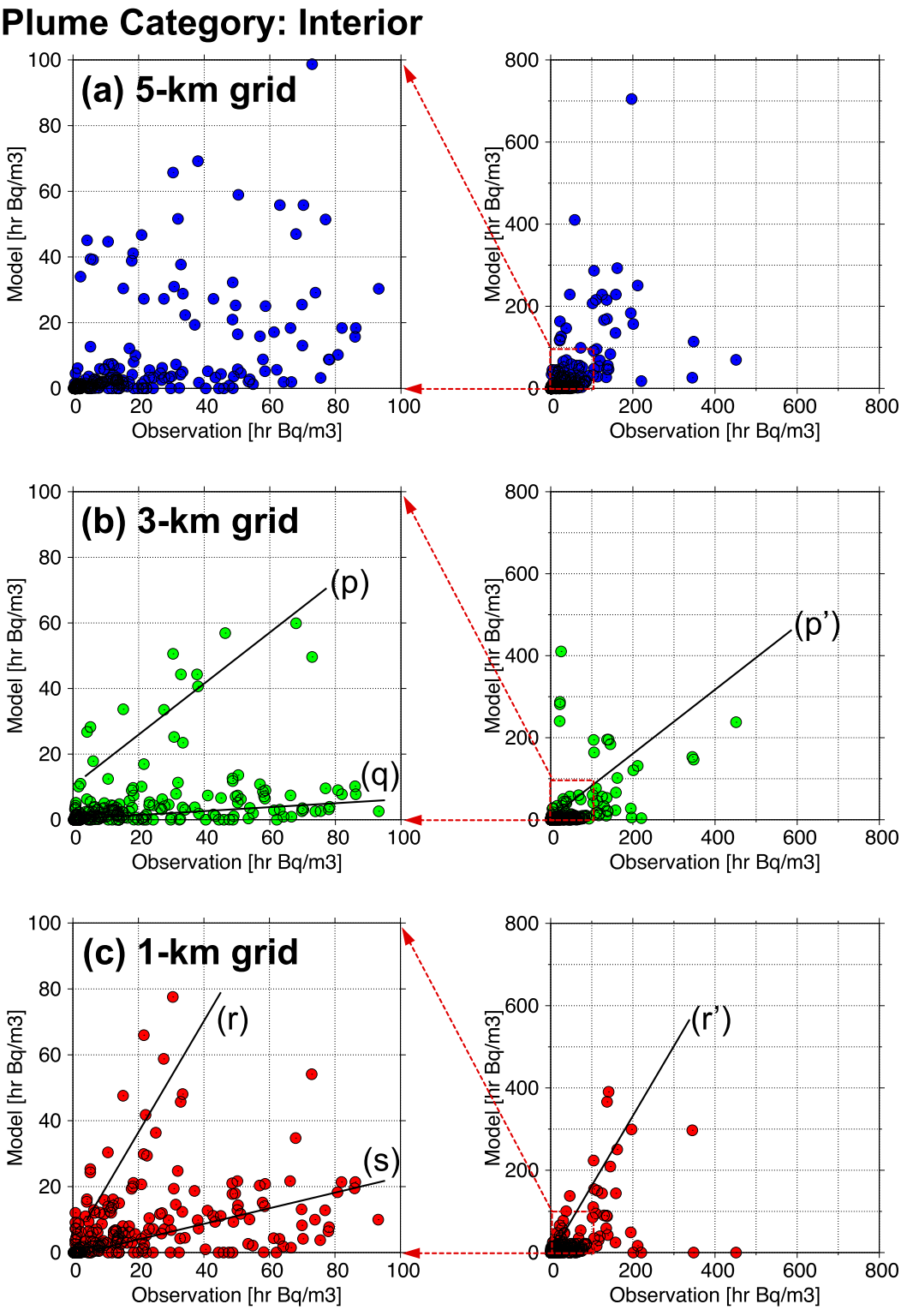

FIG. 6. Scatter diagrams for a comparison between Cs-137 observations and transport model results at each station for the interior plume category for the (a) 5-, (b) 3-, and (c) 1-km-grid models. The concentrations are 6-hourly time-integrated at each station. (left) Magnified views of a portion (range: 0–100 h Bq m^{-3}) of the (right) full plots (range: 0–800 h Bq m^{-3}). The symbols p, p′, q, r, r′, or s indicate each cluster of data points. The black lines with these symbols approximately indicate cluster locations and slopes, which are not regression lines.

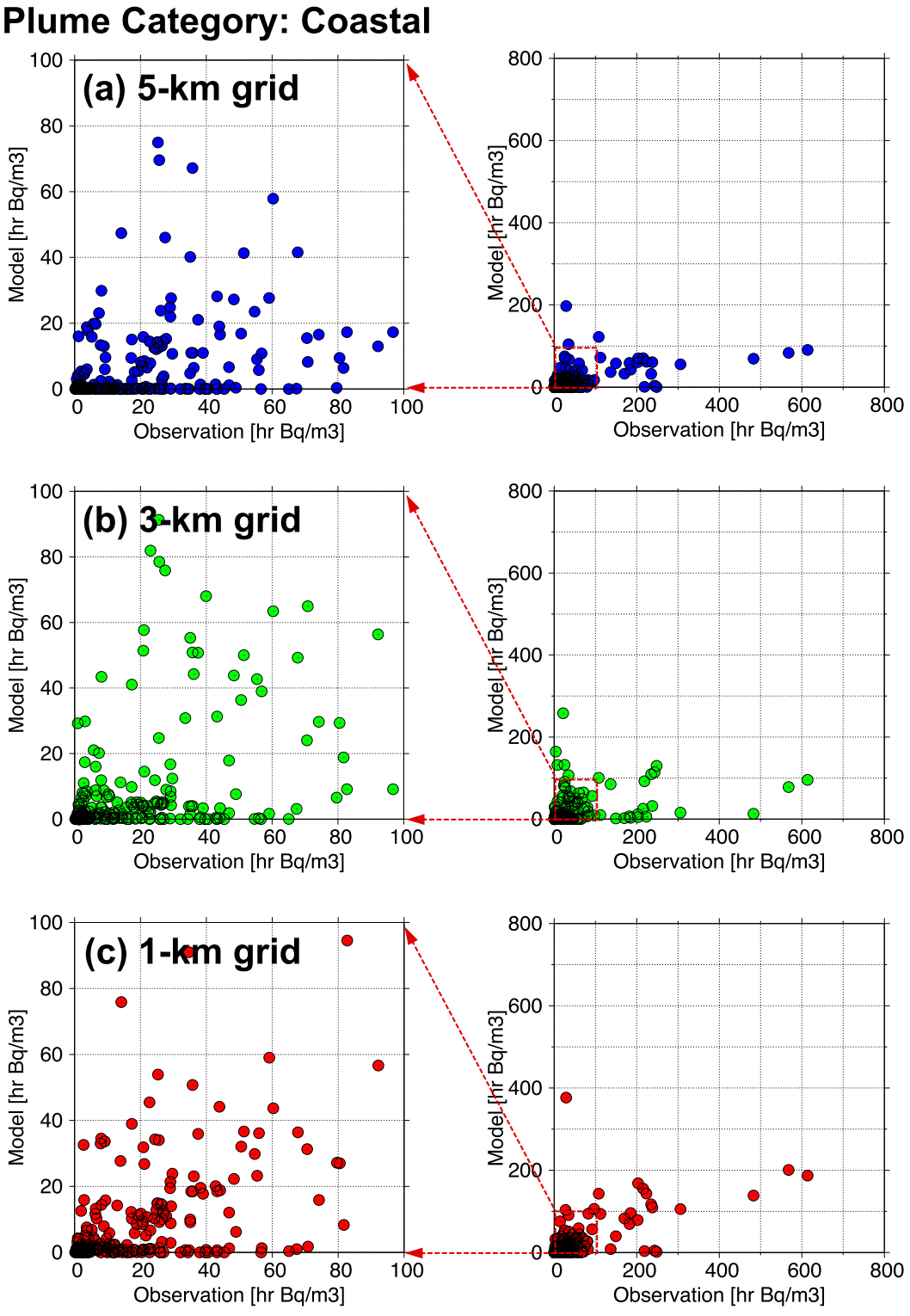

FIG. 7. As in Fig. 6, but for the coastal plume category.

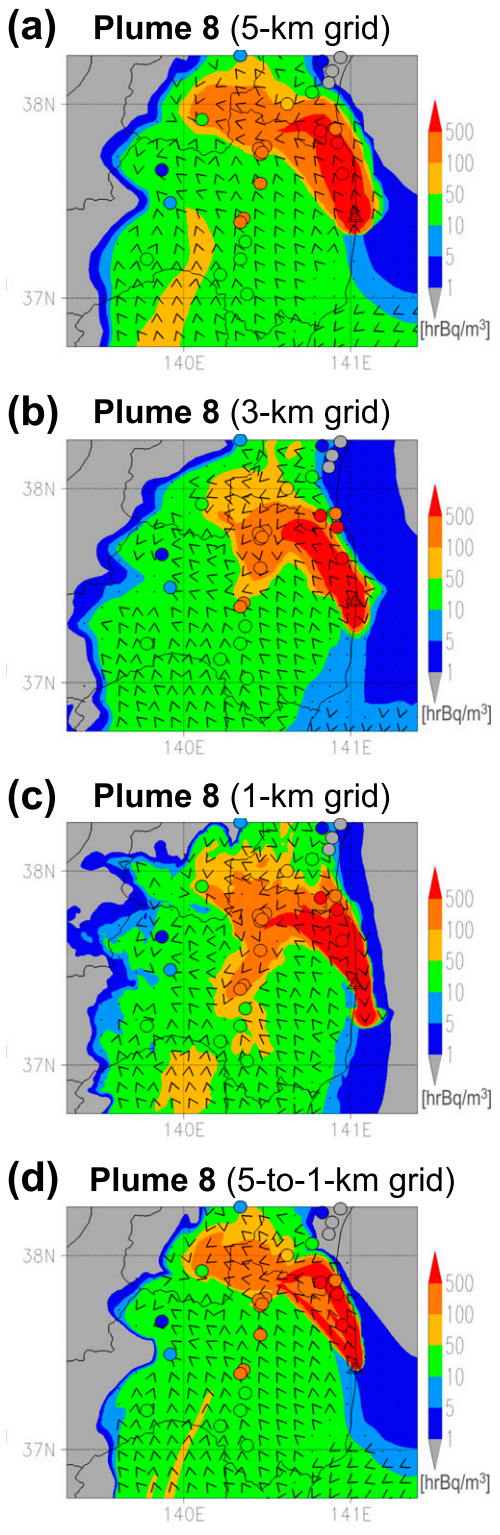

FIG. 8. Geographical distributions of the 6-h time-integrated surface Cs-137 concentration over the Fukushima region for the time period of plume 8. Shaded colors indicate the (a) 5-, (b) 3-, (c) 1-, and (d) 5-to-1-km-grid model results. Color circles indicate SPM sampling filter-tape observations. Arrowheads indicate the direction of the 6-h time-integrated mass flux (Sekiyama and Iwasaki 2018) at the ground surface in the models. The open triangle is the location of the FDNPP.

Fukushima Valley in the 1-km-grid simulation. However, the tails intrude broadly into the valley in the 5- and 3-km-grid simulations in contradiction to the observation results. This discrepancy is probably caused by the modeled height of the Abukuma Highlands that is properly reproduced by the 1-km-grid terrain but failed by the 5- and 3-km-grid terrains. The FDNPP is located at a narrow coastal area between the Abukuma Highlands and the Pacific Ocean. Therefore, the reproducibility of the Abukuma Highlands is crucial for the plume simulation. Meanwhile, the wide diffusion at the plume edges sometimes avoids large concentration errors. For example, in the case of plume 2 (Fig. 10), only the 1-km-grid simulation fails to reproduce the high-concentration observations in the central Fukushima Valley. This error results in cluster formation adjacent to the x axis, such as cluster (s). Numerical diffusion (or discretization error) improves the plume correlation in some situations. For example, plume 2 is broadened and extended to the central Fukushima Valley passing over the Abukuma Highlands in the 5- and 3-km-grid simulations. This is also caused by the lower altitude of the Abukuma Highlands in the lower-resolution simulations. Although the real plume distribution is unknown here, a large discrepancy is avoided because of this numerical diffusion, which probably results in good scores for the 5-km-grid simulation in Fig. 5. In both cases of plumes 2 and 3, the plume distributions of the 5-to-1-km-grid simulation are close to those of the 5-km-grid simulation because of the same terrain resolution. However, striped patterns often appear only in the 5-to-1-km-grid plumes, especially near the emission source. This is probably caused by spacing imbalance between wind fields and a transport resolution or by small diffusion of the 5-to-1-km-grid simulation relative to the 5-km-grid simulation.

In contrast with the Fukushima region, no large differences in the plume distribution among the three model resolutions (5-, 3-, and 1-km grids) are observed in the Kanto Plain or the Tokyo region (not shown). Unfortunately, these modeled plumes are slightly shifted from the actual distributions; therefore, the samples from the Kanto Plain compose cluster (q) or (s) close to the x axis in the scatter diagrams. Similar to the interior plumes arriving in the Kanto Plain, the coastal plumes do not show any noticeable differences among the three model resolutions since most of the coastal plumes are observed only in the Kanto Plain far from mountainous regions. We maintained the

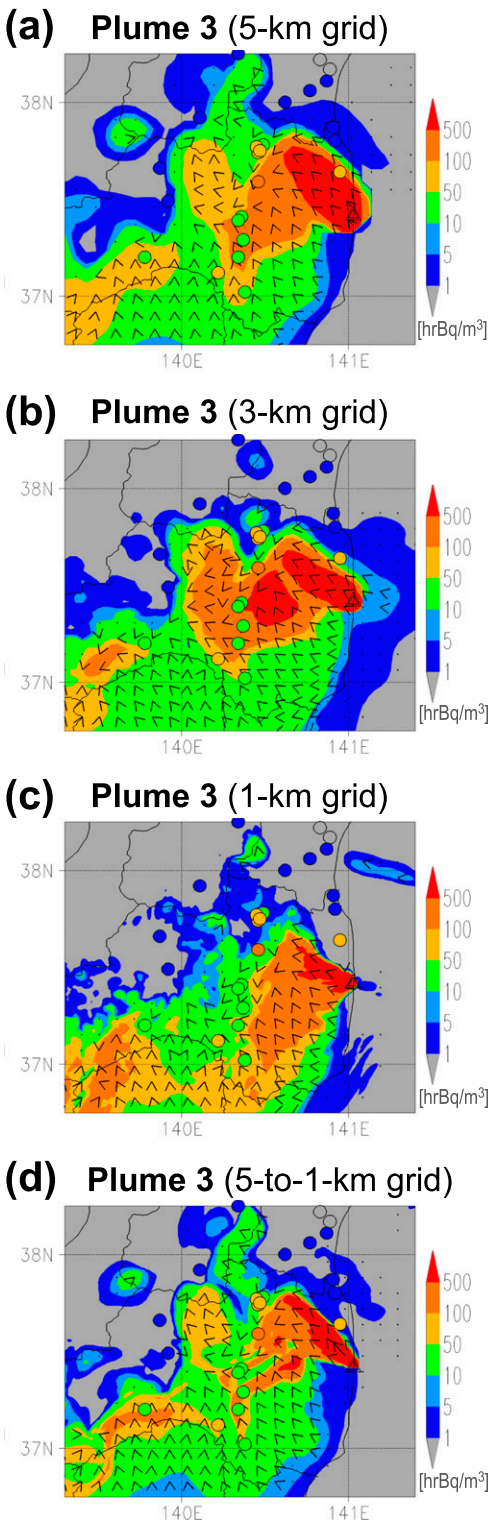

FIG. 9. As in Fig. 8, but for plume 3.

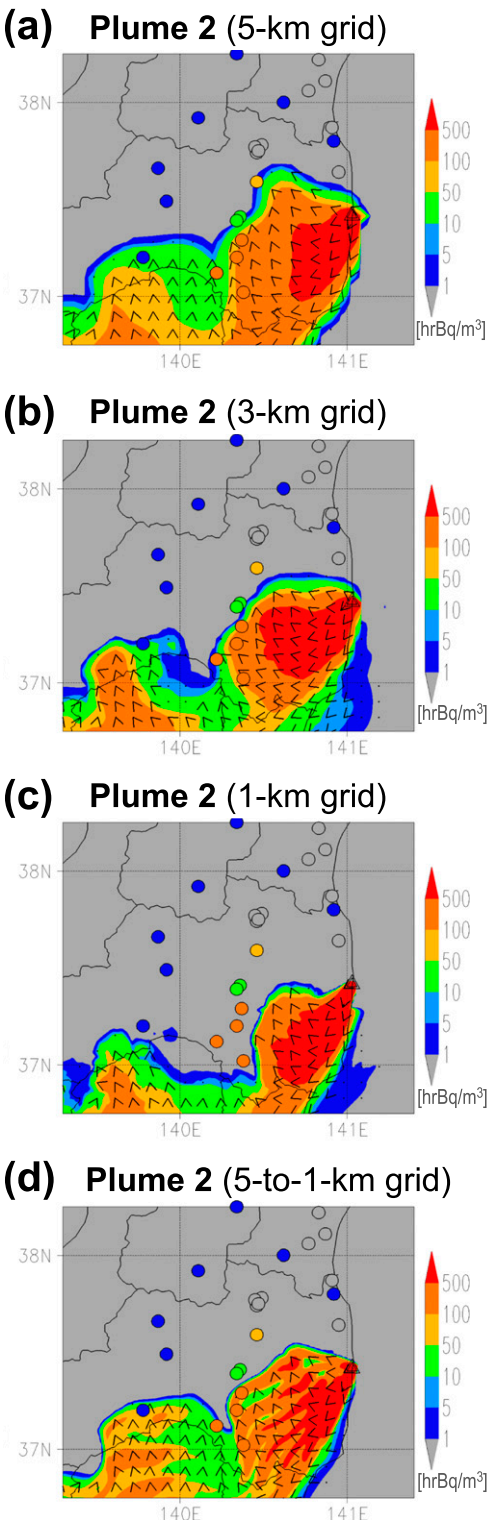

FIG. 10. As in Fig. 8, but for plume 2.

same vertical resolution and physics schemes for all the 5-, 3-, and 1-km-grid models in this study. The nuclear accident occurred in the cold winter season, when the PBL is relatively stable. In addition, vertical plume distribution strongly depends on modeled physics schemes for vertical diffusion, not the meteorological analysis (Iwasaki et al. 2019). Therefore, we could not find any noticeable differences in the boundary layer depth, static stability, and vertical plume distribution among the three model resolutions.

4. Conclusions

The surface wind and plume transport simulations in this study revealed that the model performance depends on the horizontal resolution, topographic complexity, and synoptic weather conditions. Higher model resolution surely led to higher reproducibility of surface winds in mountainous areas only when the synoptic weather conditions were disturbed. No resolution dependence was observed when the synoptic field was steady at least in the areas and periods we investigated in this study. Only a small dependence on the model resolution appeared in the coastal and plain areas. The concentration correlations tended to deteriorate due to small errors in the plume locations. However, the higher-resolution models could advantageously perform better transport simulations in the Fukushima mountainous region because of the lower numerical diffusion and higher accuracy of the mass flux. The model performance of the plume distribution in the valley of the Fukushima mountainous region was dramatically improved in the order of the model resolution (1, 3, and 5 km). The improvement was caused by the benefit of a highly resolved terrain, not a highly resolved atmosphere. The spatial representabilities of the observations for the surface winds and tracer concentrations are probably less than $1 \times 1\,\mathrm{km}^2$ over complex terrain under disturbed synoptic conditions and more than $5 \times 5\,\mathrm{km}^2$ otherwise. Mesoscale numerical weather prediction models are operated worldwide with horizontal resolutions of 1–10 km as of 2019 (World Meteorological Organization 2017). In this range of mesoscale model resolution, we conclude that a higher-resolution model is definitely recommended for tracer transport simulations over complex terrain.

Acknowledgments. This work was supported by the Environment Research and Technology Development Fund (1-1802) at the Environmental Restoration and Conservation Agency and by JSPS KAKENHI Grants JP17K00533, JP16H02946, and JP19H01155.

Data availability statement: The 3- and 1-km-grid data for both the meteorological and concentration analyses are available upon request to the corresponding author (T. T. Sekiyama 2017, 2019, unpublished data). The 5-km-grid data for the concentration analysis are also available upon request to T. T. Sekiyama (2019, unpublished data). The 5-km-grid data for the meteorological analysis and the 20-km-grid data for the global analysis are provided operationally by the Japan Meteorological Agency via the Japan Meteorological Business Support Center (2019, updated daily, unpublished data), which are free for research purpose. The surface wind data can be obtained from the website of the Japan Meteorological Agency (2019, updated daily, unpublished data, http://www.jma.go.jp/jma/indexe.html, accessed 23 March 2020). The Cs-137 concentration data were obtained from Tsuruta et al. (2014, unpublished data) and Oura et al. (2015, unpublished data) in text-file format upon request. Only the Cs-137 concentration data at Tokai (Ohkura et al. 2012) are downloadable in PDF format (https://jopss.jaea.go.jp/pdfdata/JAEA-Data-Code-2012-010.pdf, accessed 23 March 2020).

REFERENCES

Adachi, K., M. Kajino, Y. Zaizen, and Y. Igarashi, 2013: Emission of spherical cesium-bearing particles from an early stage of the Fukushima nuclear accident. *Sci. Rep.*, **3**, 2554, https://doi.org/10.1038/srep02554.

Angevine, W. M., J. Brioude, S. McKeen, and J. S. Holloway, 2014: Uncertainty in Lagrangian pollutant transport simulations due to meteorological uncertainty from a mesoscale WRF ensemble. *Geosci. Model Dev.*, **7**, 2817–2829, https://doi.org/10.5194/gmd-7-2817-2014.

Bieringer, P. E., S. Hanna, G. Young, B. Kosovic, J. Hannan, and R. Ohba, 2013: Methods for estimating the atmospheric radiation release from the Fukushima Dai-ichi nuclear power plant. *Bull. Amer. Meteor. Soc.*, **94**, ES1–ES4, https://doi.org/10.1175/BAMS-D-12-00090.1.

——, G. S. Young, L. M. Rodriguez, A. J. Annunzio, F. Vandenberghe, and S. E. Haupt, 2017: Paradigms and commonalities in atmospheric source term estimation methods. *Atmos. Environ.*, **156**, 102–112, https://doi.org/10.1016/j.atmosenv.2017.02.011.

Cécé, R. D., D. Bernard, J. Brioude, and N. Zahibo, 2016: Microscale anthropogenic pollution modelling in a small tropical island during weak trade winds. Lagrangian particle dispersion simulations using real nested LES meteorological fields. *Atmos. Environ.*, **139**, 98–112, https://doi.org/10.1016/j.atmosenv.2016.05.028.

Dingwell, A., A. Rutgersson, B. Claremar, S. Arellano, M. M. Yalire, and B. Galle, 2016: Seasonal and diurnal patterns in the dispersion of SO_2 from Mt. Nyiragongo. *Atmos. Environ.*, **132**, 19–29, https://doi.org/10.1016/j.atmosenv.2016.02.030.

Feng, S., and Coauthors, 2016: Los Angeles megacity: A high-resolution land–atmosphere modelling system for urban CO_2 emissions. *Atmos. Chem. Phys.*, **16**, 9019–9045, https://doi.org/10.5194/acp-16-9019-2016.

Hatamura, Y., and Coauthors, 2012: Final report. Investigation Committee on the Accident at the Fukushima Nuclear Power Stations of Tokyo Electric Power Company Rep., 454 pp., https://www.cas.go.jp/jp/seisaku/icanps/eng/final-report.html.

Honda, Y., M. Nishijima, K. Koizumi, Y. Ohta, K. Tamiya, T. Kawabata, and T. Tsuyuki, 2005: A pre-operational variational data assimilation system for a non-hydrostatic model at the Japan Meteorological Agency: Formulation and preliminary results. *Quart. J. Roy. Meteor. Soc.*, **131**, 3465–3475, https://doi.org/10.1256/qj.05.132.

Inomata, Y., and Coauthors, 2018: Estimate of Fukushima-derived radiocaesium in the North Pacific Ocean in summer 2012. *J. Radioanal. Nucl. Chem.*, **318**, 1587–1596, https://doi.org/10.1007/s10967-018-6249-7.

Iwasaki, T., and Coauthors, 2019: Intercomparison of numerical atmospheric dispersion prediction models for emergency response to emissions of radionuclides with limited source information in the Fukushima Dai-ichi Nuclear Power Plant accident. *Atmos. Environ.*, **214**, 116830, https://doi.org/10.1016/j.atmosenv.2019.116830.

Kajino, M., and Coauthors, 2012: Development of the RAQM2 aerosol chemical transport model and predictions of the northeast Asian aerosol mass, size, chemistry, and mixing type. *Atmos. Chem. Phys.*, **12**, 11 833–11 856, https://doi.org/10.5194/acp-12-11833-2012.

——, M. Ishizuka, Y. Igarashi, K. Kita, C. Yoshikawa, and M. Inatsu, 2016: Long-term assessment of airborne radiocesium after the Fukushima nuclear accident: Re-suspension from bare soil and forest ecosystems. *Atmos. Chem. Phys.*, **16**, 13 149–13 172, https://doi.org/10.5194/acp-16-13149-2016.

——, and Coauthors, 2018: Lessons learned from atmospheric modeling studies after the Fukushima nuclear accident: Ensemble simulations, data assimilation, elemental process modeling, and inverse modeling. *Geochem. J.*, **52**, 85–101, https://doi.org/10.2343/geochemj.2.0503.

——, and Coauthors, 2019a: NHM-chem, the Japan Meteorological Agency's regional meteorology-chemistry model: Model evaluations toward the consistent predictions of the chemical, physical, and optical properties of aerosols. *J. Meteor. Soc. Japan*, **97**, 337–374, https://doi.org/10.2151/jmsj.2019-020.

——, and Coauthors, 2019b: Deposition and dispersion of radiocesium released due to the Fukushima nuclear accident: Sensitivity to meteorological models and physical modules. *J. Geophys. Res. Atmos.*, **124**, 1823–1845, https://doi.org/10.1029/2018JD028998.

Kalnay, E., H. Li, T. Miyoshi, S.-C. Yang, and J. Ballabrera-Poy, 2007: 4-D-Var or ensemble Kalman filter? *Tellus*, **59A**, 758–773, https://doi.org/10.1111/j.1600-0870.2007.00261.x.

Katata, G., M. Ota, H. Terada, M. Chino, and H. Nagai, 2012a: Atmospheric discharge and dispersion of radionuclides during the Fukushima Dai-ichi Nuclear Power Plant accident. Part I: Source term estimation and local-scale atmospheric dispersion in early phase of the accident. *J. Environ. Radioact.*, **109**, 103–113, https://doi.org/10.1016/j.jenvrad.2012.02.006.

——, H. Terada, H. Nagai, and M. Chino, 2012b: Numerical reconstruction of high dose rate zones due to the Fukushima Dai-ichi Nuclear Power Plant accident. *J. Environ. Radioact.*, **111**, 2–12, https://doi.org/10.1016/j.jenvrad.2011.09.011.

——, and Coauthors, 2015: Detailed source term estimation of the atmospheric release for the Fukushima Daiichi Nuclear Power Station accident by coupling simulations of an atmospheric dispersion model with an improved deposition scheme and oceanic dispersion model. *Atmos. Chem. Phys.*, **15**, 1029–1070, https://doi.org/10.5194/acp-15-1029-2015.

Kitayama, K., and Coauthors, 2018: Atmospheric modeling of ^{137}Cs plumes from the Fukushima Daiichi Nuclear Power Plant—Evaluation of the model intercomparison data of the science council of Japan. *J. Geophys. Res. Atmos.*, **123**, 7754–7770, https://doi.org/10.1029/2017JD028230.

Kunii, M., 2014: Mesoscale data assimilation for a local severe rainfall event with the NHM–LETKF system. *Wea. Forecasting*, **29**, 1093–1105, https://doi.org/10.1175/WAF-D-13-00032.1.

Mathieu, A., and Coauthors, 2018: Fukushima Daiichi–derived radionuclides in the atmosphere, transport and deposition in Japan: A review. *Appl. Geochem.*, **91**, 122–139, https://doi.org/10.1016/j.apgeochem.2018.01.002.

Miyoshi, T., 2011: The Gaussian approach to adaptive covariance inflation and its implementation with the local ensemble transform Kalman filter. *Mon. Wea. Rev.*, **139**, 1519–1535, https://doi.org/10.1175/2010MWR3570.1.

——, and K. Aranami, 2006: Applying a four-dimensional local ensemble transform Kalman filter (4D-LETKF) to the JMA nonhydrostatic model (NHM). *SOLA*, **2**, 128–131, https://doi.org/10.2151/sola.2006-033.

——, and M. Kunii, 2012: The local ensemble transform Kalman filter with the Weather Research and Forecasting model: Experiments with real observations. *Pure Appl. Geophys.*, **169**, 321–333, https://doi.org/10.1007/s00024-011-0373-4.

Nachamkin, J. E., J. Cook, M. Frost, D. Martinez, and G. Sprung, 2007: Evaluation of dispersion forecasts driven by atmospheric model output at coarse and fine resolution. *J. Appl. Meteor. Climatol.*, **46**, 1967–1980, https://doi.org/10.1175/2007JAMC1570.1.

Nakajima, T., and Coauthors, 2017: Model depiction of the atmospheric flows of radioactive cesium emitted from the Fukushima Daiichi Nuclear Power Station accident. *Prog. Earth Planet. Sci.*, **4**, 2, https://doi.org/10.1186/s40645-017-0117-x.

Ohkura, T., and Coauthors, 2012: Emergency monitoring of environmental radiation and atmospheric radionuclides at Nuclear Science Research Institute, JAEA following the accident of Fukushima Daiichi Nuclear Power Plant. Japan Atomic Energy Agency Rep. JAEA-Date/Code 2012-010, 37 pp., https://doi.org/10.11484/jaea-data-code-2012-010.

Oura, Y., and Coauthors, 2015: A database of hourly atmospheric concentrations of radiocesium (^{134}Cs and ^{137}Cs) in suspended particulate matter collected in March 2011 at 99 air pollution monitoring stations in eastern Japan. *J. Nucl. Radiochem. Sci.*, **15**, 2_1–2_12, https://doi.org/10.14494/jnrs.15.2_1.

Pillai, D., and Coauthors, 2011: High-resolution simulations of atmospheric CO_2 over complex terrain—Representing the Ochsenkopf Mountain tall tower. *Atmos. Chem. Phys.*, **11**, 7445–7464, https://doi.org/10.5194/acp-11-7445-2011.

Saito, K., and Coauthors, 2006: The operational JMA nonhydrostatic mesoscale model. *Mon. Wea. Rev.*, **134**, 1266–1298, https://doi.org/10.1175/MWR3120.1.

——, J. Ishida, K. Aranami, T. Hara, T. Segawa, M. Narita, and Y. Honda, 2007: Nonhydrostatic atmospheric models operational development at JMA. *J. Meteor. Soc. Japan*, **85B**, 271–304, https://doi.org/10.2151/jmsj.85B.271.

Sato, Y., and Coauthors, 2018: Model intercomparison of atmospheric ^{137}Cs from the Fukushima Daiichi Nuclear Power Plant accident: Simulations based on identical input data. *J. Geophys. Res. Atmos.*, **123**, 11 748–11 765, https://doi.org/10.1029/2018JD029144.

Sekiyama, T. T., and T. Iwasaki, 2018: Mass flux analysis of ^{137}Cs plumes emitted from the Fukushima Daiichi Nuclear Power Plant. *Tellus*, **70B**, 1–11, https://doi.org/10.1080/16000889.2018.1507390.

——, M. Kunii, M. Kajino, and T. Shimbori, 2015: Horizontal resolution dependence of atmospheric simulations of the Fukushima nuclear accident using 15-km, 3-km, and 500-m

grid models. *J. Meteor. Soc. Japan*, **93**, 49–64, https://doi.org/10.2151/jmsj.2015-002.

——, M. Kajino, and M. Kunii, 2017: The impact of surface wind data assimilation on the predictability of near-surface plume advection in the case of the Fukushima nuclear accident. *J. Meteor. Soc. Japan*, **95**, 447–454, https://doi.org/10.2151/jmsj.2017-025.

Srinivas, C. V., K. B. R. R. Hari Prasad, C. V. Naidu, R. Baskaran, and B. Venkatraman, 2016: Sensitivity analysis of atmospheric dispersion simulations by FLEXPART to the WRF-simulated meteorological predictions in a coastal environment. *Pure Appl. Geophys.*, **173**, 675–700, https://doi.org/10.1007/s00024-015-1104-z.

Sugiyama, G., J. Nasstrom, B. Pobanz, K. Foster, M. Simpson, P. Vogt, F. Aluzzi, and S. Homann, 2012: Atmospheric dispersion modeling: Challenges of the Fukushima Daiichi response. *Health Phys.*, **102**, 493–508, https://doi.org/10.1097/HP.0b013e31824c7bc9.

Tang, Z., J. Cai, Q. Li, and J. Zhao, 2019: The regional scale atmospheric dispersion of radionuclide ^{131}I: A simulation method based on WRF-Chem model. *Radiat. Phys. Chem.*, **156**, 81–93, https://doi.org/10.1016/j.radphyschem.2018.10.029.

Taylor, K. E., 2001: Summarizing multiple aspects of model performance in a single diagram. *J. Geophys. Res.*, **106**, 7183–7192, https://doi.org/10.1029/2000JD900719.

Tie, X., G. Brasseur, and Z. Ying, 2010: Impact of model resolution on chemical ozone formation in Mexico City: Application of the WRF-Chem model. *Atmos. Chem. Phys.*, **10**, 8983–8995, https://doi.org/10.5194/acp-10-8983-2010.

Tsuruta, H., Y. Oura, M. Ebihara, T. Ohara, and T. Nakajima, 2014: First retrieval of hourly atmospheric radionuclides just after the Fukushima accident by analyzing filter-tapes of operational air pollution monitoring stations. *Sci. Rep.*, **4**, 6717, https://doi.org/10.1038/srep06717.

——, ——, ——, Y. Moriguchi, T. Ohara, and T. Nakajima, 2018: Time-series analysis of atmospheric radiocesium at two SPM monitoring sites near the Fukushima Daiichi Nuclear Power Plant just after the Fukushima accident on March 11, 2011. *Geochem. J.*, **52**, 103–121, https://doi.org/10.2343/geochemj.2.0520.

World Meteorological Organization, 2006: Environmental emergency response: WMO activities. *WMO Bull.*, **55**, 37–41.

——, 2011: WMO Technical Progress Report on the Global Data Processing and Forecasting System and Numerical Weather Prediction Research 2011. Accessed 1 September 2019, https://www.wmo.int/pages/prog/www/DPFS/ProgressReports/2012/2011_GDPFS-NWP.html.

——, 2017: WMO Technical Progress Report on the Global Data Processing and Forecasting System and Numerical Weather Prediction Research 2017. Accessed 1 September 2019, https://www.wmo.int/pages/prog/www/DPFS/GDPFS-ProgressReports.html.

SCIENTIFIC REPORTS

OPEN

Fungal spore involvement in the resuspension of radiocaesium in summer

Received: 18 January 2018
Accepted: 10 December 2018
Published online: 13 February 2019

Yasuhito Igarashi[1,2,3,11], Kazuyuki Kita[2], Teruya Maki[4], Takeshi Kinase[1,2,12], Naho Hayashi[2], Kentaro Hosaka[5], Kouji Adachi[1], Mizuo Kajino[1], Masahide Ishizuka[6], Tsuyoshi Thomas Sekiyama[1], Yuji Zaizen[1], Chisato Takenaka[7], Kazuhiko Ninomiya[8], Hiroshi Okochi[9] & Atsuyuki Sorimachi[10]

We observed the atmospheric resuspension of radiocaesium, derived from the Fukushima Dai-ichi Nuclear Power Plant accident, at Namie, a heavily contaminated area of Fukushima, since 2012. During the survey periods from 2012 to 2015, the activity concentrations of radiocaesium in air ranged from approximately 10^{-5} to 10^{-2} Bq per m^3 and were higher in the warm season than in the cold season. Electron microscopy showed that the particles collected on filters in summer were predominantly of biological origin (bioaerosols), with which the observed radiocaesium activity concentration varied. We conducted an additional aerosol analysis based on fluorescent optical microscopic observation and high-throughput DNA sequencing technique to identify bioaerosols at Namie in 2015 summer. The concentrations of bioaerosols fluctuated the order of 10^6 particles per m^3, and the phyla Basidiomycota and Ascomycota (true Fungi) accounted for approximately two-thirds of the bioaerosols. Moreover, the fungal spore concentration in air was positively correlated with the radiocaesium concentration at Namie in summer 2016. The bioaerosol emissions from Japanese mixed forests in the temperate zone predominately included fungal cells, which are known to accumulate radiocaesium, and should be considered an important scientific issue that must be addressed.

Several years have passed since the March 2011 accident at the Fukushima Dai-ichi Nuclear Power Plant (FDNPP) operated by Tokyo Electric Power Company. Approximately 71% of Fukushima Prefecture is covered by forest (see Supplementary Fig. S1), and 44% of the forested area was contaminated with at least 10–30 kBq m^{-2} of ^{137}Cs (corresponding to 1 mSv y^{-1} of excess exposure) by the accident[1]. The forest contamination by the FDNPP accident was most serious to the northwest[2,3]. This heavily contaminated (>0.5 MBq m^{-2} of ^{137}Cs) forest area consists of 428 km^2 (approximately 3% of the total area of Fukushima Prefecture; ca. 14,000 km^2)[3]. Since the accident, the radiological contamination of the forested area by ^{134}Cs and ^{137}Cs (radiocaesium) has decreased mainly due to radioactive decay, and not by erosion or other environmental mechanisms[2]. Therefore, the forest ecosystem is a large radiocaesium reservoir[1,3] and a potential secondary source of atmospheric radiocaesium[4]. The Chernobyl

[1]Meteorological Research Institute, 1-1 Nagamine, Tsukuba, Ibaraki, 305-0052, Japan. [2]Graduate School of Science and Engineering, Ibaraki University, 2-1-1 Bunkyo, Mito, Ibaraki, 310-8512, Japan. [3]Center for Research in Isotopes and Environmental Dynamics, University of Tsukuba, 1-1-1 Tennodai, Tsukuba, Ibaraki, 305-8577, Japan. [4]Institute of Science and Engineering, Kanazawa University, Kakumamachi, Kanazawa, Ishikawa, 920-1192, Japan. [5]Department of Botany, National Museum of Nature and Science, 4-1-1 Amakubo, Tsukuba, Ibaraki, 305-0005, Japan. [6]Faculty of Engineering and Design, Kagawa University, 2217-20 Hayashi-cho, Takamatsu, Kagawa, 761-0396, Japan. [7]Graduate School of Bioagricultural Sciences, Nagoya University, Furo-cho, Nagoya, 464-8601, Japan. [8]Graduate School of Science, Osaka University, 1-1, Machikaneyama, Toyonaka, Osaka, 560-0043, Japan. [9]Research Institute for Science and Engineering, Waseda University, 3-4-1 Okubo, Shinjuku, Tokyo, 169-8555, Japan. [10]Fukushima Medical University, 1 Hikariga-oka, Fukushima, 960-1295, Japan. [11]Present address: Center for Research in Isotopes and Environmental Dynamics, University of Tsukuba and Graduate School of Science and Engineering, Ibaraki University, and formerly at Meteorological Research Institute, Ibaraki, Japan. [12]Present address: Meteorological Research Institute and formerly at College of Science, Ibaraki University, Ibaraki, Japan. Correspondence and requests for materials should be addressed to Y.I. (email: yasuhito.igarashi.sci50@vc.ibaraki.ac.jp) or K.K. (email: kazuyuki.kita.iu@vc.ibaraki.ac.jp)

study[5] listed three mechanisms of secondary radioactive aerosol emissions (resuspension); (1) wind-blown suspension, (2) suspension due to human activities involving the contaminated fugitive dust; and (3) forest fires. Although resuspension sometimes refers only to (1), herein, we use the term in a more comprehensive sense. Notably, the Fukushima contamination exhibits bioecological resuspension from the contaminated forest, a new type of resuspension.

We measured radiocaesium resuspension[6] in the atmosphere at Kawamata and Namie, Fukushima Prefecture, after the accident[7,8]. In this area, which is 30 to 35 km northwest of the FDNPP and surrounded by heavily contaminated forest, as defined above, the effects of the primary emission of radiocaesium from the FDNPP likely ceased in fall 2011[9,10]; then, from 2012–2015, the radiocaesium activity concentration in the air slowly decreased, although seasonal fluctuations were observed, with increases during the warm season and decreases during the cold season (Supplementary Fig. S2). At Namie, the average summer concentration (June–August 2013–2014) was approximately 6 times the average winter concentration (December–February 2013–2014). This seasonal pattern is the opposite that observed in urban areas[8–11], but emission inventory calculations with an aerosol transport model have shown that direct/delayed primary emissions from the FDNPP cannot explain the seasonal fluctuations in 2013[4]. Monthly radiocaesium activity concentrations (September 2012 to December 2014) at a site in Namie close to that used in this study were previously reported[12]. The study showed summer maxima for both the ^{137}Cs concentration and the coarse particulate fraction (>1.1 μm) that support our radiocaesium record. However, the study attributed the seasonal trends to changes in the prevailing local wind direction and the distribution of surface contamination.

Optical microscopic observations suggested that the radiocaesium host particles in summer were fugitive dust (numerous coarse particles); their presence was initially attributed to the fact that no aerosol size cutoff was applied during high-volume (HV) aerosol sampling, but the radiocaesium host particles were subsequently shown to be of biological origin[8] (also see Supplementary Fig. S3). Biological origin particles, which include microorganisms, pollen, animal debris, and plant debris, are defined as bioaerosols. The bioaerosol concentrations and the ^{137}Cs activity concentration determined by the filter samples from Kawamata and Namie were both high in the warm season and low in the cold season, and these results suggested that bioaerosols may play an important role in radiocaesium resuspension during the warm season[8]. The previous work also suggested[8] a correlation between the ^{137}Cs concentration and air temperature from August to September. A 3D aerosol transport model with soil dust resuspension[7] and forest ecosystem emission schemes was employed to analyse the source and budget of radiocaesium in the air and showed that the resuspension of contaminated dust from the bare soil could not explain the summertime atmospheric radiocaesium level[4].

In this study, we examined the bioecological resuspension of radiocaesium and the composition of the bioaerosols that serve as host particles at Namie in August and September 2015. Fungi are known to accumulate radiocaesium, which they incorporate as analogue of potassium[13,14], and a very high radiocaesium concentration (629 Bq g^{-1} dry weight) was reported in fungal spores[15]. Therefore, we hypothesized that contaminated fungal spores may primarily account for the increased resuspension of radiocaesium during the summer. Here, we present novel data on the bioaerosols and the radiocaesium contamination of fungal spores and examine the associated relationships.

Results

At Namie, the activity level of ^{137}Cs in the air (based on HV aerosol sampling from 19 August to 25 September 2015) varied from approximately 100 to 600 μBq m^{-3}, and this variation was coincident with that of the carbon content based on scanning electron microscopy coupled with energy-dispersive X-ray spectrometry (SEM-EDS) (Fig. 1). Due to the absence of heavy industrial and urban activities near the observation site, we inferred from this correlation that organic particles (bioaerosols) carry radiocaesium originating from the FDNPP accident.

We observed aerosol particles in bioaerosol samples collected during the sampling days using a fluorescent optical microscope observation with 4,6-diamidino-2-phenylindole (DAPI) staining. The fluorescent aerosol (FA) could be classified according to their fluorescence colour and morphology (Fig. 2). In general, the most abundant FAs were yellow particles (diameter <5 μm; indicating fungal cells/debris), blue particles (microbial particles), and particles identified as sporangia or ascospores. In particular, numerous particles with multiple septa, which are most likely fungal spores of the phylum Ascomycota, were observed. Only small amounts of white FA (<5 μm in size) and black aerosols, identified as mineral particles and black carbon, respectively, were observed. The total concentrations of FAs ranged from 1.7×10^5 to 7.9×10^5 particles m^{-3} (Fig. 3). Fewer yellow particles were observed in September than in August (Figs 3 and 4), possibly because of a seasonal change in the bioaerosol source or rainy weather on the sampling days in September (Supplementary Fig. S4 and Table S1). The total FA concentration differed little between forest and adjacent bare soil observation sites. The bioaerosol concentration ranged from 2 to 8×10^5 particles m^{-3}, of which 30 to 65% were of fungal origin.

High-throughput DNA sequencing analysis (Fig. 4 and Supplementary Tables S3 and S4) revealed that the sequences of the phylum Basidiomycota accounted for more than 80% in the total sequences of all aerosol samples, regardless of the land cover (forest or bare soil) at the observation site. In August, the members of the order Polyporales in Basidiomycota composed dominant communities in the forest, whereas Russulales sequences was dominantly detected in September. At the bare soil location, the members of the orders Agaricales, Boletales, Russulales, and Hymenochaetales in Basidiomycota were dominant in August. In September, rainwater samples exhibited larger proportions of Ascomycota, represented by the orders Capnodiales, Pleosporales, Dothidiales, Helotiales, Diaporthales, Hypocreales, and Xylariales, than did air samples. Ascomycota is the most species-rich phylum of Kingdom Fungi, and it includes numerous taxa with a prominent anamorphic (mould) stage during their life cycle[16]. Therefore, these results suggest that moulds were abundant in the observed environment.

We compared the number of coloured fungal spores (colourless spores were not counted) countable by optical microscopy (without DAPI staining) and the ^{137}Cs activity in aerosol samples collected by an HV sampler

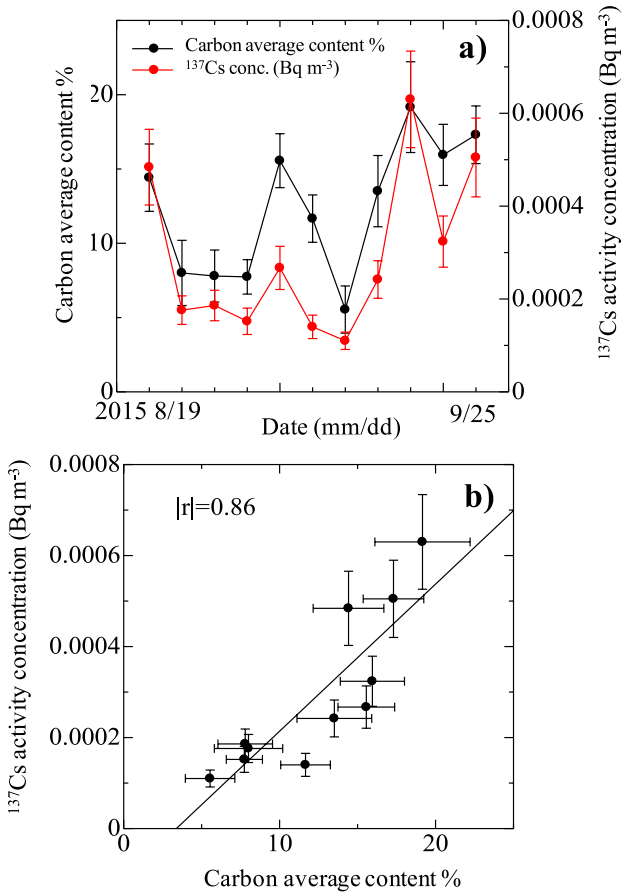

Figure 1. (**a**) Time series and (**b**) scatter plot of ^{137}Cs activity concentrations and the average carbon content (area-averaged relative percentage) in August and September 2015. Carbon data were obtained by scanning electron microscopy coupled with energy-dispersive X-ray spectroscopy. Error bars indicate the measurement error (1σ). The good correlation between the two parameters suggests that organic particles (bioaerosols) are carriers of radiocaesium.

at Namie in summer 2016 (Fig. 5). Sampling was conducted over 24 hours of daytime or nighttime (see the explanation of Fig. 5). Weather information on the 2016 sampling days is given in Supplementary Fig. S5 and Table S2. Although the data show considerable scatter, the correlation is relatively good in Fig. 5. The spore number concentration reached 5×10^4 m^{-3}, and the average ^{137}Cs activity per fungal spore (grain), which is the slope of the correlation curve, was approximately 1.7×10^{-8} Bq/grain; this value is near the median of the estimated range (2.8×10^{-9} to 2.6×10^{-7}) (Supplementary Information and Tables S5–S7). Some uncertainty (one order of difference) was associated with the spore number counting, as colourless spores were neglected (see the following discussion). Despite the uncertainty, the estimated and observed ^{137}Cs activities in a single fungal spore were generally in good agreeance, which suggested that fungal spores are likely a significant atmospheric source of radiocaesium derived from the FDNPP accident, especially in late summer in the heavily contaminated forest area.

The monthly distribution of fungal specimens (fruiting bodies) collected from 2012–2015 at the Tsukuba Botanical Garden (36.10°N, 140.11°E, approximately 170 km southwest of FDNPP; area of ~140,000 m^2; Fig. 6) supports our data on the fungal spore content of aerosols. The largest number of specimens was collected in July (all years), and the second largest number was collected in October (2012 and 2013) September (2014), and June (2015). In each year, the number of fruiting bodies collected was high from June–October, although fewer were collected in August. Additionally, relatively few fruiting bodies were collected from winter to early spring (December to March).

Discussion

Recently, it was reported that in a temperate forest in Wakayama, Japan, approximately 3.5° latitude south of Namie in August 2010, fungal spores accounted for 45% of organic carbon aerosol at nighttime and 22% in the daytime, whereas biogenic volatile organic compound oxidation products accounted for 15% of organic carbon at nighttime and 19% during the daytime[17]. The results support our inference that in the forest at Namie, fungal spores rather than other bioaerosols are the major source of radiocaesium in the air in summer. The taxonomic composition varied even over the short observation period (Fig. 4), perhaps reflecting the seasonality of the fungal groups or the occurrence of rain. However, some members of Basidiomycota and Ascomycota would be the major carriers of radiocaesium at Namie.

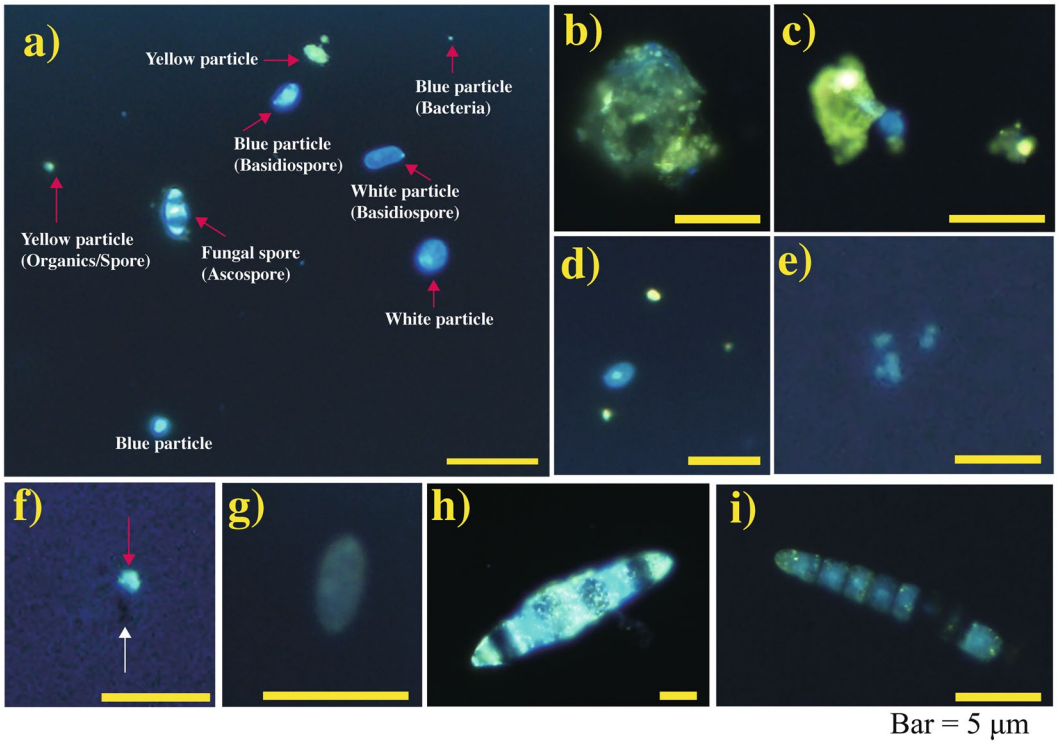

Figure 2. Fluorescent micrographs of DAPI-stained particles (indicated by red arrows) in the bioaerosol samples collected at Namie site in August and September 2015 (**a**). The aggregated particles observed as yellow particles (**b**,**c**), yellow and blue particles (**d**), blue particles (**e**), black (indicated by the white arrow) and white (indicated by the red arrow) particles (**f**), white particles (**g**) and spores form particles that are likely ascospores (**h**,**i**). The bars indicate a length of 10 μm. The assignment results were used to construct Fig. 3. In the photo, white and yellow particles may not exhibit the colours seen by the naked eye on the microscopic screen.

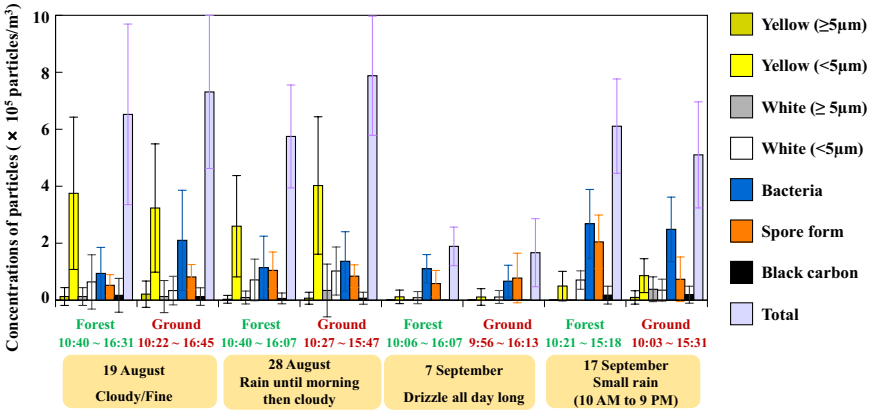

Figure 3. Number concentrations of DAPI-stained particles observed in the air samples collected from the forested and bare soil areas at Namie on 19 and 28 August and 7 and 17 September 2015, and the weather conditions on each sampling day. Particles have been classified by their colour and morphology: yellow particles ≥5 μm, organic aggregates; yellow particles <5 μm, organic particles/fungal spores; white particles ≥5 μm, mineral particles; white particles <5 μm, microbial particles; bacteria particles, bacteria; and black carbon particles, soot (so-called black carbon). Spore forms (orange bars), likely ascospores, were identified by morphology (see Fig. 2h,i).

A single sample of shiitake mushroom (*Lentinula edodes*) spores obtained in the northwestern evacuation area in 2014 was contaminated with 122 Bq g^{-1} dry weight of ^{134}Cs and 629 Bq g^{-1} dry weight of ^{137}Cs[15]. These concentrations are 1.9–9.0 and 2.5–10.9 times, respectively, higher than those in the fruiting bodies, suggesting radiocaesium bioaccumulation in fungal spores. It is probable that other fungi in the heavily contaminated area have similar radiocaesium activity levels in their spores.

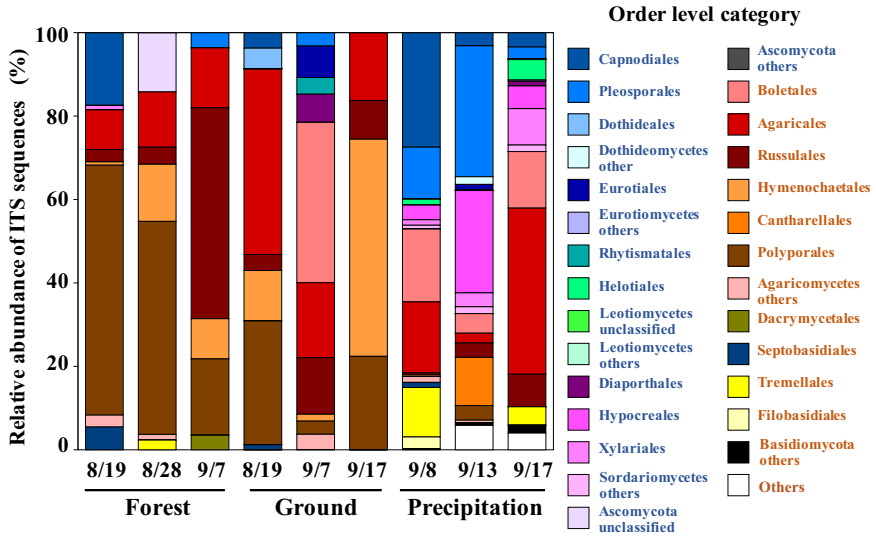

Figure 4. Results of the metagenomic analysis showing the relative abundance of identified fungal taxa in the samples collected at the forested and bare soil sites in Namie and contained in rain water collected at the site during summer 2015. Ascomycota are indicated in blue font, Basidiomycota in red font. Sampling dates are expressed as mm/dd. The compositional differences among sampling dates may reflect seasonal and weather differences.

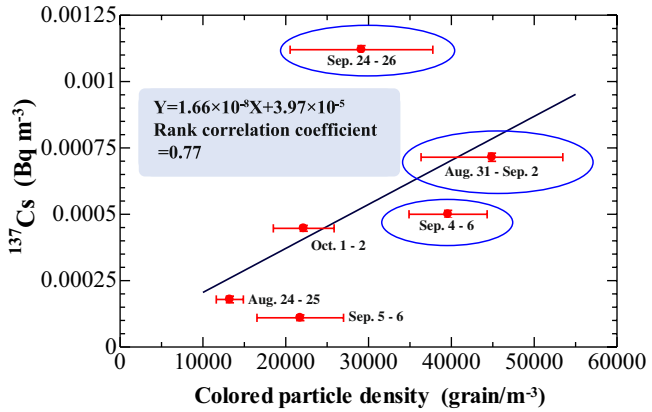

Figure 5. The relationship between the concentration of coloured fungal spores (countable without DAPI staining by optical microscopy) and the ^{137}Cs activity in air at the Namie site in summer 2016. The sampling duration was 24 hours of daytime or nighttime (circled data; e.g., daytime data from Aug. 24–25 indicates that sampling was performed from 6:00 to 18:00 on August 24 and 25, a total of 24 hours). Despite the large scatter, the spore number and ^{137}Cs concentration exhibited a positive correlation (rank correlation; significant at 8% based on a t-test). The slope of the fitted curve (1.66×10^{-8} Bq/grain) corresponds to the lower range of estimated values (see Supplementary Tables S5–S7).

These data and various other assumptions were used for the estimation that, on average, the ^{137}Cs activity per fungal spore (Supplementary Tables S5–S7) ranges from 2.8×10^{-9} to 2.6×10^{-7} Bq/grain (see Methods and Supplementary Information). We should also note that the ^{137}Cs concentration frequency distribution in fungi is very long tailed[14]. Using the ^{137}Cs activity in shiitake mushroom spores (629 Bq g^{-1} dry)[15], the weight of a single basidiospore (spore produced by Basidiomycota; 33 pg) and the weight of a single ascospore (spore produced by Ascomycota; 65 pg) reported in the literature[18], we estimated ^{137}Cs activity values of 2×10^{-7} and 4×10^{-7} Bq/spore, respectively. Considering the decrease in the ^{137}Cs air concentration in each year (Supplementary Fig. S2), similarly, the ^{137}Cs activity in a single spore would become lower annually. In our data, the slope of the relationship between the number of coloured fungal spores and the ^{137}Cs concentration (Fig. 5), approximately 1.7×10^{-8} Bq/grain, is one order of magnitude lower than the abovementioned value, although it remains in the estimated range (Supplementary Tables S5–S7). The total fungal spore concentration, including both coloured and colourless spores, might be approximately one order of magnitude larger based on the data shown in Fig. 3. We have no reason to assume that coloured and colourless fungal spores have different mechanisms of emission, and they should move through the air in a similar manner and to similar extents. In this case, the ^{137}Cs activity in a spore (the slope of Fig. 5) might be on the order of 10^{-9} Bq/grain as a mixture of coloured and colourless spores, which

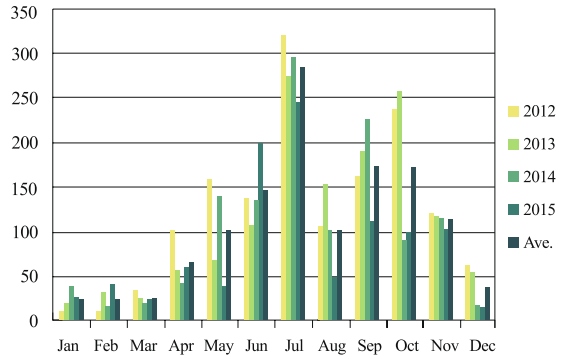

Figure 6. Monthly distribution of fungal specimens (both Basidiomycota and Ascomycota) collected at the Tsukuba Botanical Garden (Tsukuba, Japan) from 2012–2015 and the average values.

is also within the estimated range. These results strongly support fungal spore involvement in the resuspension of radiocaesium in the forested area at Namie during summer (bioecological resuspension).

Using a 3D aerosol transport model, the radiocaesium resuspension flux at Namie in summer 2013 was estimated[4] to be approximately 22 mBq m^{-2} h^{-1}. Spores with a radiocaesium content of 2.8×10^{-9} to 2.6×10^{-7} Bq/grain must be released from the forest at a rate of 2.2×10^{1} to 2.4×10^{3} grains m^{-2} s^{-1} to produce this ^{137}Cs flux. These values are similar to or an order of magnitude larger than the maximum spore emission rate from the forest (387 grains m^{-2} s^{-1}; Table 2 of ref.[19]). These findings suggest that fungal spores in Japan potentially have extensive environmental impacts, though internal radiation exposure via radiocaesium inhalation should be negligible (see the Appendix in the Supplementary Information).

The high-throughput DNA sequencing analysis showed that not only macroscopic fruiting bodies (i.e., mushrooms, mostly Basidiomycota) but also moulds (mostly Ascomycota), especially during precipitation periods, could provide major sources of bioaerosols (Fig. 4). Many species of Ascomycota are known to be plant pathogens or endophytes (fungi living inside plant tissues), and hyphae and spores on the tissue surfaces may concentrate radiocaesium and emit it into the air when the spores are launched. In the rain samples collected in September, Ascomycota accounted for as much as approximately 65% of the fungal groups, suggesting that the emission mechanism may be weather dependent (dry or wet).

It has been reported that the fungal spore count in air is high in summer and low in winter at several places around the world[20,21]. A review[22] also noted seasonal differences in the atmospheric fungal aerosol concentration. These findings are consistent with our results from the Tsukuba Botanical Garden (Fig. 6) for a temperate forest in Japan. We did not calculate the biomass of mushroom fruiting bodies because only the number of specimens, each with a varying number of fruiting bodies, was recorded. Although the number of specimens can only indirectly indicate the mushroom biomass, these data are nonetheless consistent with the findings based on independent observations, such as the high-throughput DNA sequencing analysis targeting gDNA extracted directly from forest bioaerosol samples (Fig. 4) and the fluorescence microscopic observation of aerosol particles (Fig. 2). These seasonal cycles were demonstrated using the global model[23].

Although no intensive fungal survey has been conducted in Namie area, and no intensive metagenomic analyses have been conducted in the Tsukuba Botanical Garden, both areas share similar climatic pattern and vegetation type (dominated by Quercus serrata and Q. acutissima of Fagaceae family). It is therefore mycologically unrealistic to assume that fungal flora between Namie and Tsukuba are dramatically different. Species composition between two areas may slightly differ, but we can empirically assume that family- and genus-level compositions, and seasonal patterns of fruiting, between Namie and Tsukuba are almost identical. Several pieces of direct and indirect evidence support this assumption. For example, all major orders of mushrooms detected by metagenomic analyses in Namie area (depicted in Fig. 4) have been reported from the Tsukuba Botanical Garden. In addition, all mushroom species, though sampling effort is limited, collected as the form of fruit bodies from Namie area during the 2017–2018 season (ca. 40 specimens) have been identified as genera and/or species that are also present in the Tsukuba Botanical Garden. Also, fluorescence microscopic observation indicated the airborne fungal spores and bacterial cells of Namie are similar to those in Tsukuba Botanical Garden site (Supplementary Fig. S6). Supplementary Fig. S7 also demonstrate similarities of bioaerosols over Namie and Tsukuba during summer rainy period. Besides, literature reports match our findings and suggest that radiocaesium activity associated with the movement of fungal spores is high in summer and low in winter. In addition, the high humidity and rainy conditions of the Japanese summer may favour the emission of fungal spores into the air[24–28].

In addition to fungal spores, one possible source of radiocaesium in the air is contaminated cedar pollen. At Namie, radiocaesium activity concentrations up to approximately 253 Bq g^{-1} dry weight were observed in cedar pollen from November 2011 to January 2012[29–31], but by 2015, they had decreased to no more than 25.4 Bq g^{-1}. Therefore, in recent years, cedar pollen has likely played a limited role in radiocaesium resuspension. Furthermore, in Japan, cedar pollen is emitted from late February to early May[32]; therefore, it would not have been a source of the radiocaesium at Namie in summer.

Considering other possible secondary bioecological sources of radiocaesium in the forest environment, radiocaesium contamination in pollen and bee honey was reported in Munich, Germany, following the Chernobyl accident (surface ^{137}Cs contamination, 17.4 kBq m^{-2} in early May 1986)[33]. The highest ^{137}Cs concentration in

pollen (>1 Bq g^{-1}) was recorded in May 1986, but this level rapidly decreased to approximately 0.2 Bq g^{-1} by July 1986. By considering the surface contamination level of 1.5 MBq m^{-2} at Namie[12] and assuming that the pollen contamination would be proportional to the surface contamination level, a pollen contamination level of up to 20 Bq g^{-1} can be estimated. In northern Italy during the early 2000s, the ^{137}Cs effective half life in honey was 1.25 years on average[34]. If the half life in pollen is similar to that in honey, then after 4 years, the concentration would be reduced to 1/10 of the original level. Therefore, the level of radiocaesium contamination in pollen in the heavily contaminated areas of Fukushima Prefecture would have been approximately 2 Bq g^{-1}. In addition, we detected no appreciable pollen, such as during the counting of bioaerosol fluorescent particles, because the sampling season (August and September) did not coincide with the flower bloom season. A previous work[8] counted relative numbers of bioaerosols in air ("pollen" and "bacteria" categories, the latter including "spores") in the warm season using scanning electron microscopy (SEM), and the results indicated that the "pollen" concentration was 1/10 of the "bacteria" concentration or less (Figure 12 in ref.[8]). Nevertheless, the pollen contribution to radiocaesium resuspension should still be considered because of the large size of pollen grains (≥30 μm[20]). Thus, even a small number of pollen grains might carry a detectable amount of radiocaesium.

Although no heavy radiocaesium contamination of pollen other than cedar has been reported in Japan, the suspension of pollen lasts until June, except for pollen from gramineous plants (Poaceae), ragweed, wormwood, and Japanese hop emitted from August to October based on an allergy study[35]. Furthermore, a significant amount of pollen was not found in the present DAPI-stained FA analysis or direct optical microscope observations (see Supplementary Information). Radiocaesium transfer in forest and aquatic ecosystems was examined in Fukushima Prefecture, and ^{137}Cs accumulation was found to occur in the following order: litter > detritivores > fungi > predators > plants > herbivores[36]. This result suggests that any plants in the forest can accumulate radiocaesium as fungi. Previous work suggested that contaminated pollen grains may have contributed to an increase in the radiocaesium concentration in the air at Namie in May and June 2015[8]. During this early summer peak period, the radiocaesium concentration correlated with wind speed, which suggests a wind-blown source, such as pollen or fungal spores. In the future, year-round changes in the bioaerosol composition at Namie should be examined. In addition to mushrooms and moulds, lichens (mostly Ascomycota), algae, mosses, and bryophytes also produce microscopic spores, and lichens[37] and mosses[38] are known to amass radiocaesium. Other spore-producing organisms may also be candidate sources of bioecological radiocaesium resuspension. Furthermore, bacteria can accumulate radiocaesium[39,40]. Currently, we cannot exclude these other possible bioecological sources of radiocaesium resuspension.

Primary bioaerosols, including fungal spores, suspended in the atmospheric environment can have impacts on air quality[19,22,41], agriculture[25], and human health[42,43]. In addition, bioaerosols often act[44–48] as ice-forming nuclei (IN) and cloud condensation nuclei (CCN). Thus, bioaerosols can have an appreciable effect on climate[22,41,48]. Previous reports of high fungal spore fluxes (1,000 or more spores m^{-2} s^{-1}) have been limited to tropical and subtropical rainforest regions[22], but the present findings suggest that even temperate-zone forests, such as those found in eastern Japan, can provide large sources of fungal spores and other bioaerosols. Our results are supported by those of a different study[49], which demonstrated that the diversity of some groups of fungi (e.g., ectomycorrhizal mushrooms) in temperate and boreal areas equals or even exceeds those in tropical regions. The bioaerosols emission inventory in temperate forests should be investigated worldwide, as should the bioaerosol activity as IN and CCN in different regions. Furthermore, radiocaesium, as a useful chemical tracer, resuspension studies should also focus on the origins of other organic aerosols, such as humic-like substances and water-soluble organic compounds possibly sourced from primary bioaerosols.

Methods

Atmospheric radiocaesium observations have been conducted in the contaminated area of Fukushima Prefecture since July 2011 (Supplementary Fig. S1). All sites are within 45 km to the northwest of the FDNPP and are inside the Planned Evacuation Area of 2011. Samples were collected using an HV aerosol sampler. The sampling locations and observations are described elsewhere in detail[4,7,8]. The activities of radiocaesium were measured at the Meteorological Research Institute (MRI) and at Osaka University by γ-ray spectrometry, following a procedure described elsewhere[8]. The morphology and elemental composition of aerosols collected on the filters were examined using SEM coupled with an energy-dispersive X-ray spectrometer (EDS), as well as a digital optical microscope (OM) with a data analyser.

Bioaerosols were sampled on sterilized polycarbonate filters at Namie from August—September 2015. Bioaerosols suspended in a few rain water samples were also collected on the filter by extracting a few tens of ml of the water by syringe. Bioaerosols on the filters were washed off with 1.5 mL of sterilized ultra-pure water containing 0.9% (w/v) of NaCl and shaken, and the solution samples were pelleted via centrifugation at 20,000 G. Genomic deoxyribonucleic acid (gDNA) was extracted using the combination of a phenol-chloroform extraction and the cell degradation by lysozyme, protease and sodium lauryl sulphate (SDS)[50]. Fragments of the internal transcribed spacer (ITS) region (approximately 400 base pairs; bps) were amplified from the extracted gDNA by polymerase chain reaction (PCR) using universal fungal primers ITS1-F -KYO1 (5′- Seq A - CTH GGT CAT TTA GAG GAA STA A -3′) and ITS2- KYO2 (5′- Seq B - TTY RCT RCG TTC TTC ATC -3′)[51] for the ITS region. The first PCR fragments were amplified again using the second PCR primers, which targeted the additional sequences of the first PCR primers and included 8 tag nucleotides, such as Seq A and Seq B, designed for sample identification barcoding. Thermal cycling conditions were employed from a previous investigation[50]. PCR amplicons were used for high-throughput sequencing with a MiSeq Genome Sequencer (Illumina, CA, USA). The paired-end sequences with a read length of 461 bp were grouped based on the tag sequences of each sample. In the PCR analysis steps, negative controls (no template and template from unused filters) contained no fragments of ITS amplicons exhibiting the absence of contamination during the process. After the forward and reverse paired-end reads in the raw sequencing database were merged, the irregularly merged reads (lengths outside the 200–500 bp

range or exceeding 6 photopolymers) and the error sequences with low Q-scores were removed. The remaining sequences were clustered into phylotypes using QIIME (Quantitative Insights Into Microbial Ecology; ver. 1.8.0) software with a minimum coverage of 99% and a minimum identity of 97%. The fungal compositions of the phylotypes were analysed using the Basic Local Alignment Search Tool (BLAST) to compare their sequences with references from the DNA Data Bank of Japan. Supplementary Tables S3 and S4 give numbers of ITS sequences classified into phylum and order, respectively. All sequences have been deposited in the DDBJ database (accession number of the submission is DRA007277).

We estimated the radiocaesium activity of a single fungal spore at Namie by assuming that the radiocaesium activity in fungi is proportional to the level of surface contamination. Potassium-40 concentration in fungi is often measured with the ^{137}Cs activity, K content in fungi and ^{40}K activity in the unit mass of K are known, and this approach could be employed to estimate the ^{137}Cs content in a single fungal spore (Supplementary Tables S5–S7). In the calculation, we applied no decay correction for ^{137}Cs due to its small effect on the estimation results. In the first and second approaches, fungal spores were assumed to be droplet and wooden particles, as shown in Supplementary Tables S5 and S6. The third approach (Supplementary Table S7) directly used the transfer factor in a forest. The estimates obtained by the three approaches overlap (approach 1, 8.1×10^{-9} to 7.8×10^{-8} Bq/grain; approach 2, 2.8×10^{-9} to 1.5×10^{-7} Bq/grain; and approach 3, 3.3×10^{-9} to 2.6×10^{-7} Bq/grain), which suggests that they are plausible and that the ^{137}Cs content in a single fungal spore at Namie ranges from 10^{-9} to 10^{-7} Bq. The range of estimates mostly results from (1) the size (volume) difference of the basidiospore and ascospore fungal spores and (2) the difference in the ^{137}Cs/^{40}K activity ratios of fungi based on the level of surface contamination.

Monthly fungal fruiting body abundance levels were retrieved from a mushroom survey project at the Tsukuba Botanical Garden (Tsukuba, Ibaraki, Japan). The survey was conducted every week from 2012–2015. Fruiting bodies of both Basidiomycota and Ascomycota of visible size were surveyed and collected weekly from forested areas of the garden by 3 to 30 investigators. Here, a specimen is defined as one or more fruiting bodies of the same species growing in the same vegetation type (section) in the garden. On the same day, multiple specimens of the same species could be collected if they were found in different section of the garden. The total number of mushroom specimens collected each month, regardless of species, was counted, and the monthly average from 2012–2015 was calculated.

The Supplementary Information gives additional details of the above methods.

References

1. Yoshihara, T. *et al.* Changes in radiocesium contamination from Fukushima in foliar parts of 10 common tree species in Japan between 2011 and 2013. *J. Environ. Radioact.* **138**, 220-226 (2014).
2. Saito, K. *et al.* Radiological conditions in the environment around the Fukushima Daiichi Nuclear Power Plant site. *Global Environ. Res.* **20**, 15–22 (2016).
3. Hashimoto, S., Ugawa, S., Nanko, K. & Shichi, K. The total amounts of radioactively contaminated materials in forests in Fukushima, Japan. *Sci. Rep.* **2**, 416 (2012).
4. Kajino, M. *et al.* Long-term assessment of airborne radiocesium after the Fukushima nuclear accident: re-suspension from bare soil and forest ecosystems. *Atmos. Chem. Phys.* **16**, 13149–13172 (2016).
5. Garger, E. K., Kuzmenko, Y. I., Sickinger, S. & Tschiersch, J. Prediction of the ^{137}Cs activity concentration in the atmospheric surface layer of the Chernobyl exclusion zone. *J. Environ. Radioact.* **110**, 53–58 (2012).
6. Igarashi, Y. Anthropogenic radioactivity in aerosol. *Japanese Journal of Health Physics* **44**, 313–323 (2009).
7. Ishizuka, M. *et al.* Use of a size-resolved 1-D resuspension scheme to evaluate resuspended radioactive material associated with mineral dust particles from the ground surface. *J. Environ. Radioact.* **166**, Part 3, 436–448 (2017).
8. Kinase, T. *et al.* The seasonal variations of atmospheric ^{134,137}Cs activity and possible host particles for their resuspension in the contaminated areas of Tsushima and Yamakiya, Fukushima, Japan. *Progress in Earth and Planetary Science* **5**, 12 (2018).
9. Igarashi, Y., Kajino, M., Zaizen, Y., Adachi, K. & Mikami, M. Atmospheric radioactivity over Tsukuba, Japan: a summary of three years of observations after the FDNPP accident. *Progress in Earth and Planetary Science* **2**, 44 (2015).
10. Hirose, K. Temporal variation of monthly ^{137}Cs deposition observed in Japan: effects of the Fukushima Daiichi nuclear power plant accident. *Appl. Radiat. Isot.* **81**, 325–329 (2013).
11. Akimoto, K. Annual and weekly cycles of radioactivity concentration observed in Fukushima City. *Health Phys.* **108**, 32–38 (2015).
12. Ochiai, S. *et al.* Temporal variation of post-accident atmospheric ^{137}Cs in an evacuated area of Fukushima Prefecture: size-dependent behaviors of ^{137}Cs-bearing particles. *J. Environ. Radioact.* **165**, 131–139 (2016).
13. Duff, M. C. & Ramsey, M. L. Accumulation of radiocesium by mushrooms in the environment: a literature review. *J. Environ. Radioact.* **99**, 912–932 (2008).
14. Yoshida, S. & Muramatsu, Y. Concentrations of radiocesium and potassium in Japanese mushrooms. *Environ. Sci.* **7**, 63–70 (1994).
15. Yamaguchi, T. *et al.* Autoradiography of the fruiting body and spore print of wood-cultivated shiitake mushroom (Lentinula edodes) from a restricted habitation area. *Mushroom Science and Biotechnology* **23**, 125–129 (2015).
16. Blackwell, M. The fungi: 1, 2, 3 … 5.1 million species? *Am. J. Bot.* **98**, 426–438 (2011).
17. Zhu, C., Kawamura, K., Fukuda, Y., Mochida, M. & Iwamoto, Y. Fungal spores overwhelm biogenic organic aerosols in a midlatitudinal forest. *Atmos. Chem. Phys.* **16**, 7497–7506 (2016).
18. Elbert, W., Taylor, P. E., Andreae, M. O. & Pöschl, U. Contribution of fungi to primary biogenic aerosols in the atmosphere: wet and dry discharged spores, carbohydrates, and inorganic ions. *Atmos. Chem. Phys.* **7**, 4569–4588 (2007).
19. Sesartic, A. & Dallafior, T. N. Global fungal spore emissions, review and synthesis of literature data. *Biogeosciences* **8**, 1181–1192 (2011).
20. Winiwarter, W., Bauer, H., Caseiro, A. & Puxbaum, H. Quantifying emissions of primary biological aerosol particle mass in Europe. *Atmos. Environ.* **43**, 1403–1409 (2009).
21. Ho, H.-M. *et al.* Characteristics and determinants of ambient fungal spores in Hualien, Taiwan. *Atmos. Environ.* **39**, 5839–5850 (2005).
22. Fröhlich-Nowoisky, J. *et al.* Bioaerosols in the Earth system: climate, health, and ecosystem interactions. *Atmos. Res.* **182**, 346–376 (2016).
23. Heald, C. L. & Spracklen, D. V. Atmospheric budget of primary biological aerosol particles from fungal spores. *Geophys. Res. Lett.* **36**, L09806 (2009).
24. Fitt, B. D. L., McCartney, H. A. & Walklate, P. J. The role of rain in dispersal of pathogen inoculum. *Annu. Rev. Phytopathol.* **27**, 241–270 (1989).

25. Gilet, T. & Bourouiba, L. Rain-induced ejection of pathogens from leaves: revisiting the hypothesis of splash-on-film using high-speed visualization. *Integr. Comp. Biol.* **54**, 974–984 (2014).
26. Hassett, M. O., Fischer, M. W. F. & Money, N. P. Mushrooms as rainmakers: how spores act as nuclei for raindrops. *PLoS One* **10**, e0140407 (2015).
27. Huffman, J. A. *et al*. High concentrations of biological aerosol particles and ice nuclei during and after rain. *Atmos. Chem. Phys.* **13**, 6151–6164 (2013).
28. Wright, T. P., Hader, J. D., McMeeking, G. R. & Petters, M. D. High relative humidity as a trigger for widespread release of ice nuclei. *Aerosol Sci. Technol.* **48**, i-v (2014).
29. Heisei 26 nendo Sugi Obana ni Fukumareru Houshasei Sesiumu Noudo no Chousa Kekka ni tsuite (About FY H26 investigation results on radiocaesium concentrations contained in cedar pollen) (in Japanese) *Forestry Agency*, *Japan* (*FAJ*), http://www.rinya.maff.go.jp/j/press/kaihatu/pdf/150130-01.pdf (2015).
30. Kanasashi, T., Sugiura, Y., Takenaka, C., Hijii, N. & Umemura, M. Radiocesium distribution in sugi (Cryptomeria japonica) in Eastern Japan: translocation from needles to pollen. *J. Environ. Radioact.* **139**, 398–406 (2015).
31. Kinase, S., Kimura, M. & Hato, S. Internal dosimetry for continuous chronic intake of caesium-137 in cedar pollen after the Fukushima Daiichi nuclear power plant accident. International Symposium on Environmental monitoring and dose estimation of residents after accident of TEPCO's Fukushima Daiichi Nuclear Power Stations (2012).
32. Yamada, T., Saito, H. & Fujieda, S. Present state of Japanese cedar pollinosis: the national affliction. *J. Allergy Clin. Immunol.* **133**, 632–639 e635 (2014).
33. Bunzl, K., Kracke, W. & Vorwohl, G. Transfer of Chernobyl-derived ^{134}Cs, ^{137}Cs, ^{131}I and ^{103}Ru from flowers to honey and pollen. *J. Environ. Radioact.* **6**, 261–269 (1988).
34. Panatto, D., Gasparini, R., Lai, P., Rovatti, P. & Gallelli, G. Long-term decline of ^{137}Cs concentration in honey in the second decade after the Chernobyl accident. *Sci. Total Environ.* **382**, 147–152 (2007).
35. Fujisaki, Y. & Fujisaki, S. A 30 year (1972-2002) airborne pollen record and pollinosis in Niigata City, Japan. *Japanese Journal of Palynology* **49**, 59–70 (2003).
36. Murakami, M. *et al*. Biological proliferation of cesium-137 through the detrital food chain in a forest ecosystem in Japan. *Sci. Rep.* **4**, 3599 (2014).
37. Ohmura, Y. *et al*. ^{137}Cs concentrations in foliose lichens within Tsukuba-city as a reflection of radioactive fallout from the Fukushima Dai-ichi Nuclear Power Plant accident. *J. Environ. Radioact.* **141**, 38–43 (2015).
38. Iurian, A., Hofmann, W., Lettner, H., Türk, R. & Cosma, C. Long term study of Cs-137 concentrations in lichens and mosses. *Environ. Phys.* **56**, 983–992 (2011).
39. Tomioka, N., Uchiyama, H. & Yagi, O. Cesium accumulation and growth characteristics of Rhodococcus erythropolis CS98 and Rhodococcus sp. Strain CS402. *Appl. Environ. Microbiol.* **60**, 2227–2231 (1994).
40. Zhang, P. *et al*. Characterization of cesium uptake mediated by a potassium transport system of bacteria in a soil conditioner. *Biol. Pharm. Bull.* **37**, 604–607 (2014).
41. Després, V. *et al*. Primary biological aerosol particles in the atmosphere: a review. *Tellus B Chem. Phys. Meteorol.* **64**, 15598 (2012).
42. Baxi, S. N., Portnoy, J. M., Larenas-Linnemann, D. & Phipatanakul, W. & Environmental Allergens Workgroup. Exposure and health effects of fungi on humans. *J. Allergy Clin. Immunol. Pract.* **4**, 396–404 (2016).
43. Pringle, A. Asthma and the diversity of fungal spores in air. *PLoS Pathog.* **9**, e1003371 (2013).
44. DeMott, P. & Prenni, A. New directions: need for defining the numbers and sources of biological aerosols acting as ice nuclei. *Atmos. Environ.* **44**, 1944–1945 (2010).
45. Murray, B. J., O'Sullivan, D., Atkinson, J. D. & Webb, M. E. Ice nucleation by particles immersed in supercooled cloud droplets. *Chem. Soc. Rev.* **41**, 6519–6554 (2012).
46. Szyrmer, W. & Zawadzki, I. Biogenic and anthropogenic sources of ice-forming nuclei: a review. *Bull. Am. Meteorol. Soc.* **78**, 209–228 (1997).
47. Christner, B. C., Morris, C. E., Foreman, C. M., Cai, R. & Sands, D. C. Ubiquity of biological ice nucleators in snowfall. *Science* **319**, 1214–1214 (2008).
48. Tobo, Y. *et al*. Biological aerosol particles as a key determinant of ice nuclei populations in a forest ecosystem. *J. Geophys. Res. Atmos.* **118**, 10100–10110 (2013).
49. Tedersoo, L. *et al*. Global diversity and geography of soil fungi. *Science* **346**, 1256688 (2014).
50. Maki, T. *et al*. Variations in airborne bacterial communities at high altitudes over the Noto Peninsula (Japan) in response to Asian dust events. *Atmos. Chem. Phys.* **17**, 11877–11897 (2017).
51. Toju, H., Tanabe, A. S., Yamamoto, S., & Sato, H. High-coverage ITS primers for the DNA-based identification of ascomycetes and basidiomycetes in environmental samples. PloS one, e40863. (2012).

Acknowledgements

We thank Ms. K. Inukai, Ms. K. Kamioka and Mr. T. Kimura (Atox Co. Ltd.) for assistance with the activity measurements; Ms. K. Yanagida (Meteorological Research Institute; MRI) for logistics help; and Ms. Y. Kamiya (MRI) for help with the manuscript editing. We also acknowledge Mr. T. Kanari (Green Blue Co. Ltd.) for maintaining the measurement sites and Mr. H. Demizu and other members and students of the College of Science and College of Engineering, Ibaraki University, for the maintenance of the tools, special installations in the field and data collection. We also express our thanks to the local governments of Kawamata and Namie and to the Fukushima prefectural government, who kindly provided the monitoring opportunity. Y.I. is grateful to Dr. K. Tagami, National Institute of Radiological Sciences, for discussion of the transfer factor in forests. Ms. M. Nara helped finishing the figure to fulfil the QC requirement. This work was financially supported by Grants-in-Aid for Scientific Research in Innovative Areas granted to the A01–2, A03–6 and A04–8 research teams of the "Interdisciplinary Study on Environmental Transfer of Radionuclides from the Fukushima Dai-ichi NPP Accident (ISET-R)" (grant numbers 24110003, 24110007, and 24110009, respectively; PI: Professor Yuichi Onda, University of Tsukuba) and by the Ministry of Education, Culture, Sports, Science and Japanese Radioactivity Survey by Technology and Nuclear Regulation Authority, Japan at the MRI. This research was also funded by Grants-in-Aid for Scientific Research (A) (No. 17H01478), (B) (No. 24340115, 26304003 and 17H01873) and (C) (No. 17K00533 and 26340049). We would like to give our special thanks to the ISET-R PI, Prof. Onda, and his staff.

Author Contributions

Y.I. and K.K. supervised the project and planned the observations and data analysis. K.K., T.M., T.K., N.H. and M.I. performed observations at the site and conducted the experimental analysis. T.M. was in charge of the bioaerosol sampling and analysis. K.H. conducted mushroom survey at Tsukuba Bitanical Garden and analyze fruit body production data. M.I. contributed meteorological observations. Y.I., Y.Z., K.K., T.K. and K.N. collected radioactivity measurements. K.A. performed electron microscopic analysis with T.K. and N.H. M.K. and M.I. performed the aerosol transport modelling and provided the data. T.T.S. drew the land use map. C.T., H.O. and A.S. helped with the data analysis from the viewpoint of forest ecology, organics in the air, and aerosol fluxes, respectively. C.T. also estimated the ^{137}Cs burden of a fungal spore. A.S. helped with the radiation dose estimation. Y.I., T.M., K.H. and K.K. wrote the manuscript, and all authors contributed ideas for the paper and reviewed the manuscript.

Additional Information

Supplementary information accompanies this paper at https://doi.org/10.1038/s41598-018-37698-x.

Competing Interests: The authors declare no competing interests.

Publisher's note: Springer Nature remains neutral with regard to jurisdictional claims in published maps and institutional affiliations.

Atmospheric Environment 214 (2019) 116830

Contents lists available at ScienceDirect

Atmospheric Environment

journal homepage: www.elsevier.com/locate/atmosenv

Intercomparison of numerical atmospheric dispersion prediction models for emergency response to emissions of radionuclides with limited source information in the Fukushima Dai-ichi nuclear power plant accident

Toshiki Iwasaki[a], Tsuyoshi Thomas Sekiyama[b,*], Teruyuki Nakajima[c], Akira Watanabe[d], Yasushi Suzuki[e], Hiroaki Kondo[e,f], Yu Morino[g], Hiroaki Terada[h], Haruyasu Nagai[h], Masayuki Takigawa[i], Hiromi Yamazawa[j], Denis Quélo[k], Anne Mathieu[k]

[a] Graduate School of Science, Tohoku University, Aoba-ku, Sendai, 980-8578, Japan
[b] Meteorological Research Institute, Tsukuba, 305-0052, Japan
[c] Earth Observation Research Center, Japan Aerospace Exploration Agency, Tsukuba, 305-8505, Japan
[d] Faculty of Symbiotic Systems Science, Fukushima University, Fukushima, 960-1296, Japan
[e] Japan Weather Association, Toshima-ku, Tokyo, 170-6055, Japan
[f] Environmental Management Research Institute, National Institute of Advanced Industrial Science and Technology, Tsukuba, 305-8569, Japan
[g] National Institute for Environmental Studies, Tsukuba, 305-8506, Japan
[h] Japan Atomic Energy Agency, Tokai, Ibaraki, 319-1195, Japan
[i] Japan Agency for Marine-Earth Science and Technology, Kanazawa-ku, Yokohama, 236-0001, Japan
[j] Graduate School of Engineering, Nagoya University, Chikusa-ku, Nagoya, 464-8603, Japan
[k] Institute for Radiological Protection and Nuclear Safety, 92262, Fontenay-aux-Roses Cedex, France

GRAPHICAL ABSTRACT

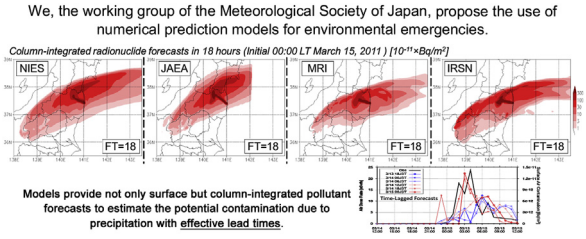

ARTICLE INFO

Keywords:
Environmental emergency response
Numerical atmospheric dispersion prediction
Model intercomparison
Fukushima nuclear accident

ABSTRACT

The utilization of numerical atmospheric dispersion prediction (NDP) models for assisting the emergency response to emission of radionuclides has been recommended by a working group of the Meteorological Society of Japan. This paper verifies the feasibility of the recommendation through NDP model intercomparison with limited emission source information for the case of the Fukushima Dai-ichi Nuclear Power Plant accident caused by the Great East Japan Earthquake in 2011. According to the recommendation of the working group, the NDP models are run under the assumption of a constant rate of emission during the whole forecast period. This is the worst-case scenario when limited source information is available. Generally, no information is provided on the temporal variability and strength of the emissions, while the source location is known. Surface air radionuclide forecasts are utilized for providing warnings of the risk of inhaling radioactive substances suspended in the low-level atmosphere, whereas column-integrated radionuclide forecasts are utilized for estimating the potential maximum wet deposition of radioactive materials on the ground due to precipitation. The NDP model short-range forecasts were validated with observational data for three locations, at the times when the most serious

* Corresponding author.
E-mail address: tsekiyam@mri-jma.go.jp (T.T. Sekiyama).

https://doi.org/10.1016/j.atmosenv.2019.116830
Received 26 December 2018; Received in revised form 9 July 2019; Accepted 11 July 2019
Available online 12 July 2019

contamination events occurred at each of the three monitoring stations. The NDP models successfully predicted the risk of surface air contamination and/or ground surface contamination caused by wet deposition in these cases. Particularly, the NDP model forecasts allow us to disseminate warnings at effective lead times before exposure to radiation. The different NDP models gradually deviate their forecasts as the lead time progresses. The deviations may indicate the magnitude of forecast errors. Thus, the use of multi-model forecasts is of greater benefit than the single model forecasts, because forecast error information is suggested.

1. Introduction

1.1. Discontinuation of the use of NDP model forecasts for aiding emergency response

The Fukushima Dai-Ichi Nuclear Power Plant (FDNPP) was damaged during the Great East Japan Earthquake and subsequent tsunami on 11th March 2011, and released a huge amount of radionuclides to the atmosphere through explosions, ventilations and leaks from a broken reactor pressure vessel (Chino et al., 2011). The released radionuclides were transferred by the wind and deposited on the ground. The wet deposition seriously contaminated land, forests, houses and water, even at locations outside the urgent protective action planning zone (UPZ) of 30 km from the emission source (MEXT, 2011). On that occasion, however, the public was not provided with sufficient information on the contamination to properly mitigate their exposure to radiation.

The World Meteorological Organization (2006) has recommended the use of computer-based atmospheric dispersion simulations for environmental emergency response activities, including nuclear accidents. A numerical atmospheric dispersion prediction (NDP) model of radioactive substances, named the System for Prediction of Environmental Emergency Dose Information (SPEEDI), was developed by the Japan Atomic Energy Research Institute as a government-commissioned project for environmental emergencies caused by the release of radioactive substances (Imai et al., 1985). In the FDNPP accident, however, forecasts by SPEEDI were not utilized for the mitigation of radiation exposure. The reason for this was that the time series of radionuclide emission intensity could not be obtained. Information on the emission intensities would normally have been provided to SPEEDI by the Emergency Response Support System (ERSS). At that time, the ERSS did not work, since its power supply was broken by the earthquake (Hatamura et al., 2011, 2012). As a result, evacuation orders were issued only by considering the distance from the emission source. In 2014, three years after the accident, the Nuclear Regulation Authority of Japan (NRA) decided to discontinue the use of SPEEDI for environmental emergencies, because of uncertainties both in the temporal variation of the emission intensity and in the weather forecasts (NRA, 2014). The Meteorological Society of Japan (MSJ) disagreed with the decision by the NRA and issued a proposal on the use of NPD model forecasts of radioactive substances accidentally released from nuclear power related facilities, based on the recommendations of a report by a working group of the MSJ (2015).

1.2. Recommendation on utilization of NDP model forecasts

The working group of the MSJ recommended the following approach to utilize NDP models in environmental emergencies for the mitigation of radiation exposure. Basically, NDP model forecasts should be provided to avoid the risk of “failure to notice” rather than to avoid that of “false alarm” by considering the worst-case scenario, because the accidental release of radioactive substances causes a risk of serious radiation exposure to many people. NPD model forecasts for the worst-case scenario can help us choose a safer time and place of evacuation and greatly reduce exposure to radiation.

Generally, it is hard to obtain the time series of emission intensity just after an accident. If these data are not available, NDP models should be run assuming a constant emission rate during an environmental emergency (cf. World Meteorological Organization, 2010) with limited source information. Note that this assumption corresponds to the worst-case scenario, since breaks in the emission tend to reduce the size of the area at risk of contamination. If evacuation orders are issued under the assumption of a constant rate of emission, then the affected people are expected to be safe under any emission scenario. Of course, if a reliable emission scenario is available in real time, it should be used for the NPD model forecasts.

We briefly explain the NDP model products to be disseminated to the public. One of the most serious forms of radiation exposure is the direct inhalation of radioactive substances suspended in the low-level atmosphere. To mitigate the inhalation of suspended substances, we should utilize a geographical map of radioactive substance density in the low-level atmosphere (hereafter called the surface air contamination). When surface air contamination is expected, we can mitigate the radiation exposure by advising people to stay indoors.

Another exposure process arises through the deposition of radioactive substances resulting in internal exposure through the intake of contaminated water/food and the external exposure to radiation from the environment. Precipitation deposits almost all substances below rainmaking clouds on the ground. Sometimes the ground surface is heavily contaminated, even though the radioactive substance density is small in the surface atmosphere. NDP models can directly forecast the amount of wet deposition using the output variables of precipitation and radiative substance density. However, we do not recommend the utilization of model-derived wet deposition, since it has the risk of failing to issue a warning when the model fails to forecast precipitation. In brief, wet deposition forecasts cannot be used to predict the worst-case scenario. Instead, we recommend the use of the column-integrated amount of radioactive substances to estimate the maximum wet deposition (hereafter called the column-integrated contamination). We note that there is a possibility that the precipitation is contaminated at locations where NDP forecasts indicate high column-integrated contamination. Unless it rains at these locations, the warning associated with serious wet deposition may be withdrawn. If it does rain at these locations, we can effectively survey the contamination area by limiting only to locations where the actual precipitation coincides with high column-integrated contamination. In fact, the wet deposition can result in serious contamination over a much greater area than the UPZ of 30 km away from the emission source. We can quickly estimate the range of the contaminated area with the help of the NDP forecasts.

NDP model forecasts contain uncertainty arising from imperfections in the atmospheric initial conditions and NDP models. When utilizing the model forecasts, both for the surface air contamination and column-integrated contamination, we ought to assume the contaminated area and period to be larger and longer than in the NDP model forecasts by considering the uncertainty of the forecasts. In addition, the model uncertainty could be estimated or reduced by multi-model forecasts. In this study, we perform multi-model prediction experiments to clarify the advantages of the model prediction for environmental emergencies when the emission source information is limited.

2. Experiments

2.1. NDP model forecast intercomparison

We conduct an intercomparison of the NDP models to validate the NDP model performance with the observation data for the FDNPP accident, and to confirm the suitability of the recommendations by the MSJ working group. In this experiment, the reliability of NDP models is assessed on the basis of the forecast consistency among models. Multi-model ensemble approaches are used to provide information on the forecast reliability for tropical cyclone track forecasts (Goerss, 2000). Information on the forecast reliability is useful for decision-making regarding evacuation during extreme events. Here, we consider the effectiveness of multi-model ensemble forecasts of NPD models.

After the Chernobyl nuclear accident in 1986, many types of NDP models have been developed to forecast the atmospheric dispersion of radioactive substances during environmental emergencies (e.g., Ehrhardt, 1997; Brandt et al., 2002; Hoe et al., 2009). After the FDNPP accident, many model intercomparison experiments have been conducted (e.g., Draxler et al., 2015; Kristiansen et al., 2016; Kitayama et al., 2018; Sato et al., 2018). However, they were all reanalysis model studies. To the best knowledge of the authors, there is no study dealing with forecast (or hindcast) model intercomparions for the FDNPP accident. Our intercomparison experiment was focused on short-range forecasts (from several hours to several days), during which the serious contamination occurred. In the FDNPP accident, radionuclides were spread over several hundred kilometers from the source over the course of about 2 days. Thus, we compared NDP models, which have domains of about 800 km × 800 km around the source position and a horizontal resolution of about 3 km. Passive tracers were released from the lowermost layer at FDNPP at a constant rate of 1 Bq/h. We need only relative concentration values when the outer edge of radioactive plumes has to be detected. This is because the background concentration of anthropogenic nuclear products is almost zero. The plume edge has a jump of concentration values by 10^{10}–10^{20} times in model simulations even though the constant emission rate is a unit amount (1 Bq/h). It is exactly the reason why WMO recommends assuming an emission rate of 1 Bq/h (World Meteorological Organization, 2010). The definition of plume outer edges is $10^{-13} \times \mathrm{Bq/m^3}$ or $10^{-11} \times \mathrm{Bq/m^2}$ in this study because this definition makes a jump of concentration between the inside and outside of plumes larger than ten digits to detect the edge line of potential contaminated areas.

The forecast period was 30 h, because lateral boundary conditions for NDP models could be taken from the stored JMA's operational mesoscale forecasts that extend to up to 33 h. The forecast products to be compared were the geographical distributions of the surface air contamination and the column-integrated amount. For the worst-case scenario, no dry/wet deposition was included in the NDP models, so that the maximum potential contamination was provided by the forecasts. While the output time interval of the NDP models is generally variable, we used hourly outputs for the model validation.

In this study, four NDP models participated in the short-range forecast experiment for radioactive substances. These models were developed by the National Institute for Environmental Studies (NIES) of Japan, the Japan Atomic Energy Agency (JAEA), the Meteorological Research Institute (MRI) of Japan, and the French Institute for Radiological Protection and Nuclear Safety (IRSN). The model domains were set to cover eastern Japan with an approximately 3-km horizontal resolution. The dynamical frameworks of the NIES and JAEA models were based on the weather research and forecast model (WRF) version 3 (Skamarock et al., 2008), and the initial and lateral boundary conditions were obtained from the Japan Meteorological Agency (JMA) operational mesoscale analysis and forecast, respectively. The dispersion calculation of the NIES model was performed by the Community Multiscale Air Quality (CMAQ) Eulerian model version 4.6 (Byun and Schere, 2006) as described in detail in Morino et al. (2013) and Nakajima et al. (2017). The JAEA dispersion calculation module was a Lagrangian model, and was included in the Worldwide version of the System for the Prediction of Environmental Emergency Dose Information (WSPEEDI) used for planning the response to environmental emergencies (Terada and Chino, 2008; Katata et al., 2015).

Both the MRI and IRSN models adopted a Eulerian scheme for material transport and shared the same meteorological forecasts that were prepared by MRI using the JMA non-hydrostatic weather forecast model and local ensemble transform Kalman filter (JMANHM-LETKF) data assimilation system (Kunii, 2014; Sekiyama et al., 2015, 2017) with JMA's operational meteorological observations, including the near-surface wind velocities. The JMANHM-LETKF data assimilation system was implemented with a 3-km horizontal resolution, where the lateral boundary conditions were obtained from the JMA operational global deterministic and ensemble forecasts. The NDP configuration details of the MRI model were described in Sekiyama et al. (2017) and Kajino et al. (2018), in which the model performance was quantitatively examined. The JMANHM-LETKF meteorological field was also used to drive the offline NDP model of IRSN. The dispersion calculation for the IRSN model was detailed in Mathieu et al. (2012, 2018), Saunier et al. (2013), Groëll et al. (2014), and Quérel et al. (2015). For Eulerian NPD models (NIES, MRI, and IRSN models), the time series of contamination at each monitoring station was extracted by the linear interpolation of the nearest grid cells. For a Lagrangian NPD model (JAEA model), the gridded output was calculated from the particle density and then the time series was extracted by the linear interpolation of the nearest grid cells.

2.2. Monitoring data for validation

Three cases were chosen to assess the performance of NDP model forecasts. Fig. 1 shows the time series of the air dose rate and precipitation intensity at the Iwaki and Fukushima monitoring stations (Working group of MSJ, 2015) for validating the model forecasts. At Iwaki station, the most serious event occurred in the early morning on 15th March. The air dose rate suddenly increased to more than 20 μSv/h in the early morning, and then rapidly decreased to less than 2 μSv/h around noon. The high level of radiation mostly came from a radioactive plume in the low-level atmosphere (cloud shine). It did not come from deposited substances on the ground (ground shine), because no precipitation was observed at Iwaki.

At the Fukushima monitoring station, the most serious event occurred in the evening on the 15th of March. Around 1700 JST, the air dose rate rapidly rose to about 20 μSv/h at the same time of precipitation was observed as shown in Fig. 1. Since the air dose rate did not rapidly return to the normal value, the radiation is considered to come from substances deposited on the ground (ground shine). If it had not rained, the radioactive substances would not have contaminated the ground so much. The large amount of wet deposition resulted from the spatiotemporal overlap of the precipitation with the column-integrated contamination. After the 16th of March, the radiation gradually decreased in accordance with the volatilization and decay of iodine's isotope, ^{131}I, whose half-life is about 8 days, and partly due to soil infiltration of radioactive metal ions.

Kashiwa City in the Kanto area was also contaminated as shown in Fig. 2 (Working group of MSJ, 2015). At the Kashiwa Campus of the University of Tokyo, the air dose rate increased between the evening of the 20th and the morning of the 21st of March, and remained constant afterwards. Precipitation was observed from 0800 JST on the 21st at the nearest Automated Meteorological Data Acquisition System (AMeDAS) observation station at Abiko. It is likely that precipitation deposited radioactive substances on the ground at that time.

Detailed observations exist for the above-mentioned contamination events at the Iwaki, Fukushima and Kashiwa stations, and thus these events were selected as the targets of the model intercomparison experiment. The locations of these stations are illustrated in Fig. 3. The

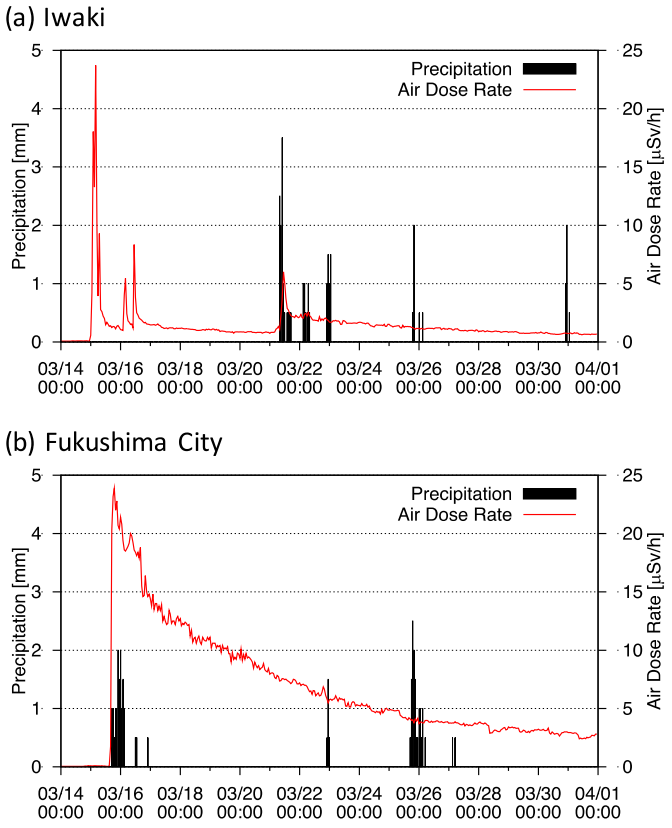

Fig. 1. Time series of the hourly air dose rate (red line, μSv/h) and precipitation (black bars) at monitoring stations in Iwaki City (140.88 °E, 37.05 °N, upper panel) and in Fukushima City (140.47 °E, 37.76 °N, lower panel), hourly from March 14 to 31, 2011, respectively. Precipitation was observed at the Onahama AMeDAS station, which is about 12 km southeast of the Iwaki station, and at the Fukushima Local Meteorological Observatory, which is about 1 km from the Fukushima monitoring station. This figure was reproduced from an earlier study (Working group on "Radioactive substances accidentally released from nuclear power related facilities", Meteorological Society of Japan, 2015) for validation of model results. (For interpretation of the references to color in this figure legend, the reader is referred to the Web version of this article.)

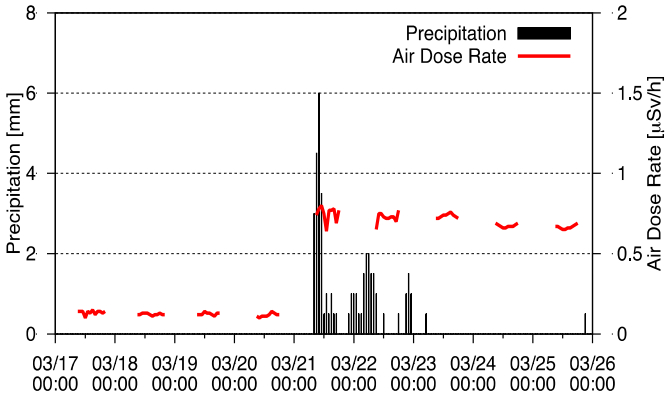

Fig. 2. Time series of the hourly air dose rate (red lines, μSv/h) at the University of Tokyo Kashiwa Campus and precipitation (black bars, mm/h) at Abiko AMeDAS station, which is about 8 km from the monitoring station, from 0000 JST 17th to 0000 JST 26th, March. The air dose rate was observed with a NaI(TI) scintillation detector at a height of 1 m. Observations were only made in the day time. This figure was reproduced from an earlier study (Working group, Meteorological Society of Japan, 2015) for validation of model results. (For interpretation of the references to color in this figure legend, the reader is referred to the Web version of this article.)

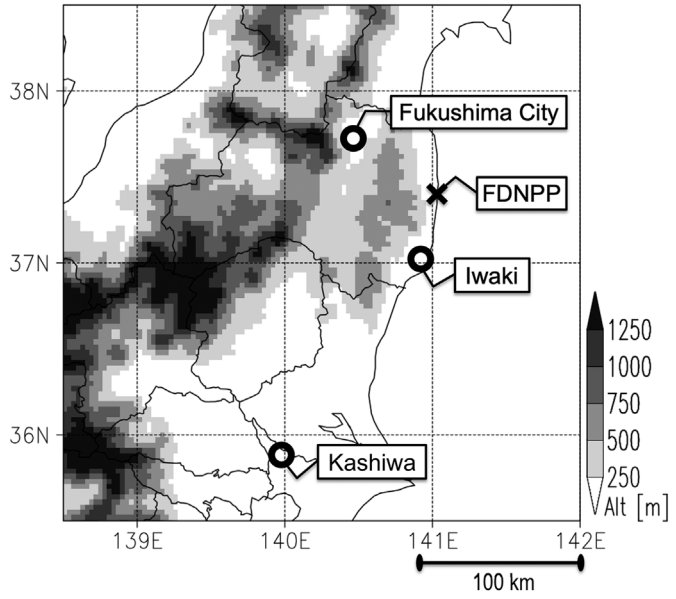

Fig. 3. Locations of the Fukushima Dai-ichi Nuclear Power Plant (FDNPP), and the Fukushima, Iwaki, and Kashiwa monitoring stations. Gray shading indicates the ground elevation at intervals of 250 m.

Iwaki station is located about 40 km SSW from the emission source at FDNPP, the Fukushima station is located about 60 km NW, and the Kashiwa station is at about 200 km SSW. In addition, we were able to acquire the ground surface concentration data of radioactive cesium (Oura et al., 2015) in Kashiwa City very close to the Kashiwa station.

3. Results and discussion

3.1. NDP model forecasts for surface air contamination at Iwaki and Kashiwa

At first, the NDP model intercomparison was conducted with a focus on the maximum air dose rate observed at the Iwaki monitoring station. The NDP models were initialized at 0000 JST on March 15th, where radioactive substances were assumed to be emitted at a constant rate from the same initial time, 0000 JST. As mentioned above, the high level of radiation observed at Iwaki is considered to come from the plume suspended in the low level atmosphere (cloud shine). Therefore, the forecasts of the surface air contamination are validated with the observations at Iwaki. As shown in Fig. 4, all four models forecast a dense plume moving SSW which extended over Iwaki at a forecast time of 6 h (FT = 6). After that, the surface wind gradually turned clockwise and the plume moved away from Iwaki. At a forecast time of 30 h (FT = 30), the models again forecast a low-level plume moving southward and air contamination around the Iwaki station. These forecasts are consistent with the monitoring results of a large peak in the air dose rate in the early morning of the 15th of March, and a moderate peak in the early morning of the 16th (see Fig. 1), although NDP models have larger differences in the geographical distributions at a forecast time of 30 h than at a forecast time of 6 h. Fig. 5 shows the vertical east-west cross section of the radioactive substance density along a line of the latitude of Iwaki (37.05° N). The vertical extension of radioactive substances is somewhat different among the models, which may reflect the magnitude of the vertical diffusion. Nevertheless, the density forecasts all show a maximum in the lowermost layer.

Time series of the NDP forecasts consistently indicate the maximum contamination occurred at the Iwaki station in the early morning of the 15th, as illustrated in Fig. 6a. Strictly speaking, the forecast time of the radioactive substances was about 2 h later than the observed time. One of the reasons for this may be that the initialization time of the

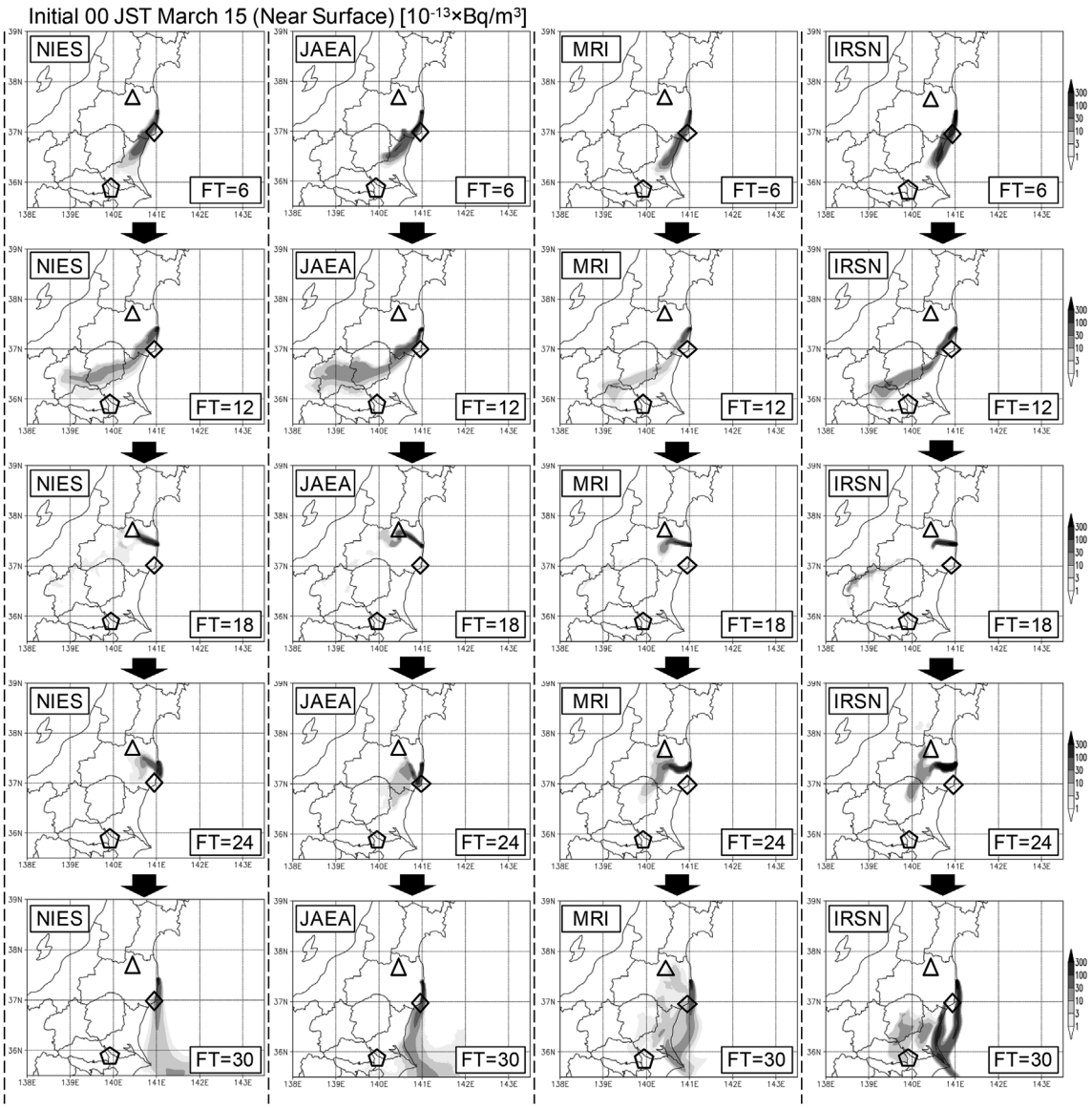

Fig. 4. Geographical distributions of the surface air contamination forecasts (concentration of radioactive substances in the lowermost layer; 10^{-13} × Bq/m^3) from the model initialization time of 0000 JST on 15th of March at forecast times of 6, 12, 18, 24 and 30 h, by the NDP models of the NIES, JAEA, MRI and IRSN. A constant emission rate of 1 Bq/h at FDNPP is assumed in the forecasts. The triangle, diamond, and pentagon indicate the locations of Fukushima City, Iwaki, and Kashiwa, respectively.

emissions in NDP models of 0000 JST was later than the actual emission time of the substances which arrived at the Iwaki station. In this case, the forecast times of 3–6 h are too short for us to take preventive action. An additional experiment was conducted to increase the lead time up to 24 h using the MRI model (Fig. 6b). Although the forecasts contained more uncertainty, depending on the initial time they predicted the air contamination within an error of 2 h over Iwaki on the morning of the 15th of March. As shown in Fig. 6a, the maximum surface air contamination differed between models, and the forecast spread ($\approx 1.5 \times 10^{-11}$Bq/m^3) was more than 50 percent of the ensemble

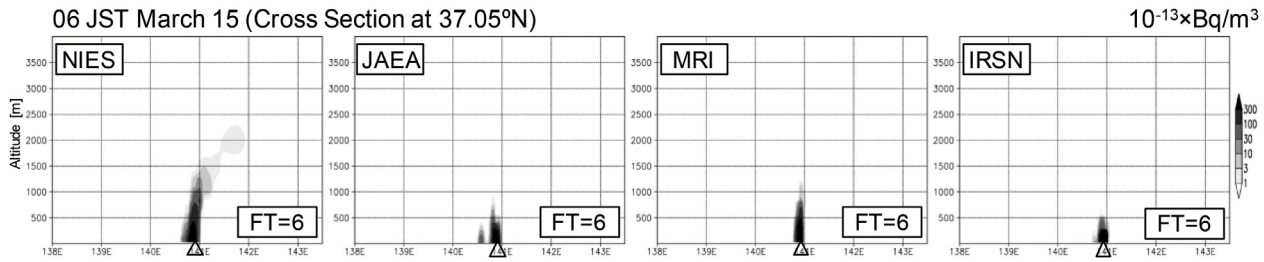

Fig. 5. East-west and vertical cross sections of the 6-h forecasts of the air contamination along a line of the latitude of Iwaki (37.05° N) from the initialization time of 0000 JST on 15th March by the four models (unit; 10^{-13} × Bq/m^3). A constant emission rate of 1 Bq/h at FDNPP is assumed in the forecasts. Open triangles indicate the longitude of Iwaki (140.9° E).

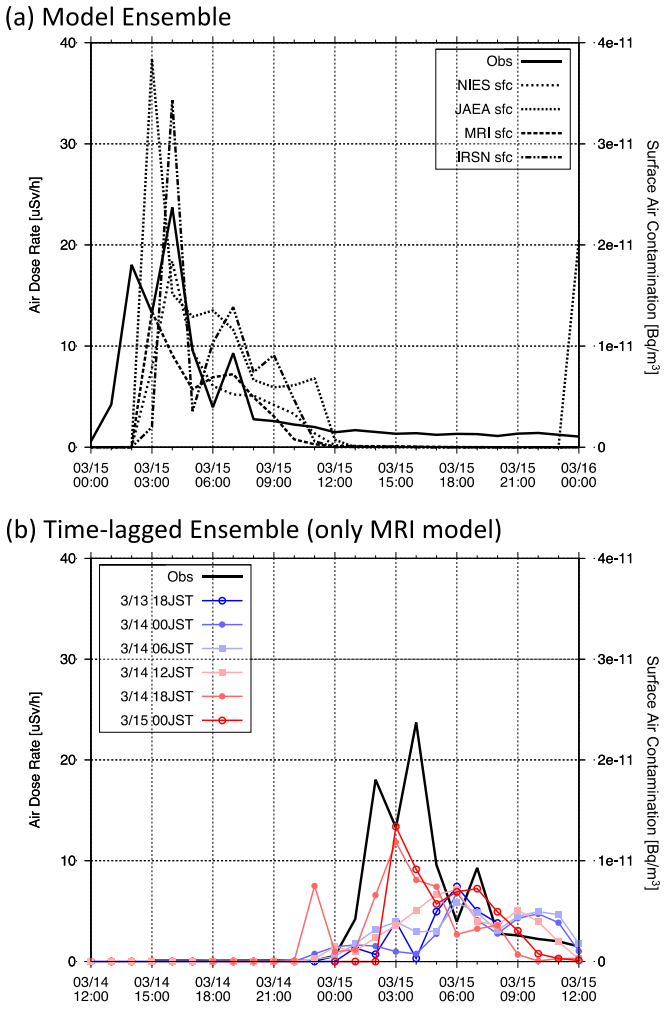

Fig. 6. Time series of the surface air contamination forecasts (units; Bq/m^3) together with the observations of air dose rate (unit; μSv/h) at the Iwaki station. The upper panel (a) shows forecasts from the initialization time of 0000 JST on 15th March by the NDP models at NIES, JAEA, MRI and IRSN, and the lower panel (b) shows the lagged forecasts by the MRI model. The lines for each forecast and observation are indicated in the legend. A constant emission rate of 1 Bq/h at FDNPP is assumed in the forecasts.

mean value ($\approx 2.5 \times 10^{-11}$Bq/m^3), suggesting a fair amount of uncertainty in the forecasts. In the time series of the surface air contamination, relatively greater values indicate the periods when there is a high risk of inhalation of dangerous levels of radiation with a valuable lead time.

The radioactive plume shown in Figs. 5 and 6 flowed southward and arrived at Kashiwa about 7 h later (Fig. 7). The forecast time of the radioactive substances in Kashiwa was about 2 h earlier than the observed time as shown in Fig. 7a. This case involves a longer forecast lead time and a farther distance from the emission source than the case of Iwaki. Therefore, the time-lagged ensemble (Fig. 7b) indicates larger errors of the plume arrival time when the forecast initial time is earlier than 0000 JST on 15th March. Generally speaking, the uncertainty in plume advection simulations is accumulated along the pathway of the plume; i.e., small differences in the wind velocity along the pathway may cause large differences in the plume location (Sekiyama et al., 2017). Therefore, especially when the forecast initial time is earlier and the lead time is longer, we ought to prepare for the slightly longer time window and broader area of air contamination than the model forecasts.

For these events, NDP models indicate the possibility that the surface air would be contaminated with radioactive substances at Iwaki and Kashiwa on the mornings of the 15th and 16th, as a worst-case scenario. If people were informed of the possible risk of the surface air contamination on the mornings of the 15th and 16th, they could remain indoors until the contaminated surface air had passed. In other words, the models indicated that the health risk from surface air contamination would be smaller in other time periods, because the models assumed a continuous rate of emission after initialization without any emission breaks.

3.2. NDP model forecasts for wet deposition at Fukushima City

Next, NDP model forecasts are validated with the observations at the Fukushima monitoring station. As mentioned above, precipitation caused a large amount of wet deposition at about 1700 JST on the 15th of March, and thereafter radionuclides deposited on the ground continued to emit radiation.

In the worst-case scenario for wet deposition, the precipitation deposits all of the column-integrated radioactive substances on the ground. Here, we examine whether NDP model forecasts of the column-integrated contamination correctly predicted the possibility of wet deposition on the ground. Fig. 8 shows NDP model forecasts of the column-integrated amount of radioactive substances initialized at 0000 JST on March 15. Note that these are the same forecasts as shown previously. The spatial pattern of the vertically integrated amount shown in Fig. 8 is significantly different from that of the surface air contamination shown in Fig. 4, reflecting the vertical wind shear. At 1800 JST (FT = 18), the area of the contaminated column shown in Fig. 8 is much greater than the area of contaminated surface air shown in Fig. 4. According to a detailed tracer flux analysis (Sekiyama and Iwasaki, 2018), radioactive substances emitted from FDNPP passed over Fukushima City around 1800 JST through two routes. The first route was that of the substances emitted early in the morning, which went southward, turned clockwise and then moved northeastward. These substances gradually rose while moving northeastward, and reached a height of about 3000 m. They were dispersed horizontally under the strong wind shear. The second route was that of the substances emitted in the afternoon, which went northwestward directly to Fukushima City. Large differences in the distribution of potential

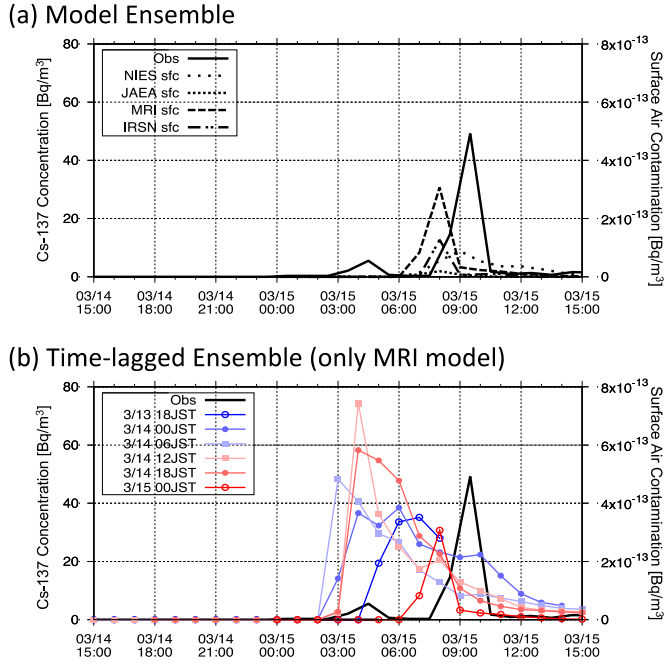

Fig. 7. Same as Fig. 6, but at the Kashiwa station; the observation is ground surface Cs-137 concentration (Oura et al., 2015), not air dose rate.

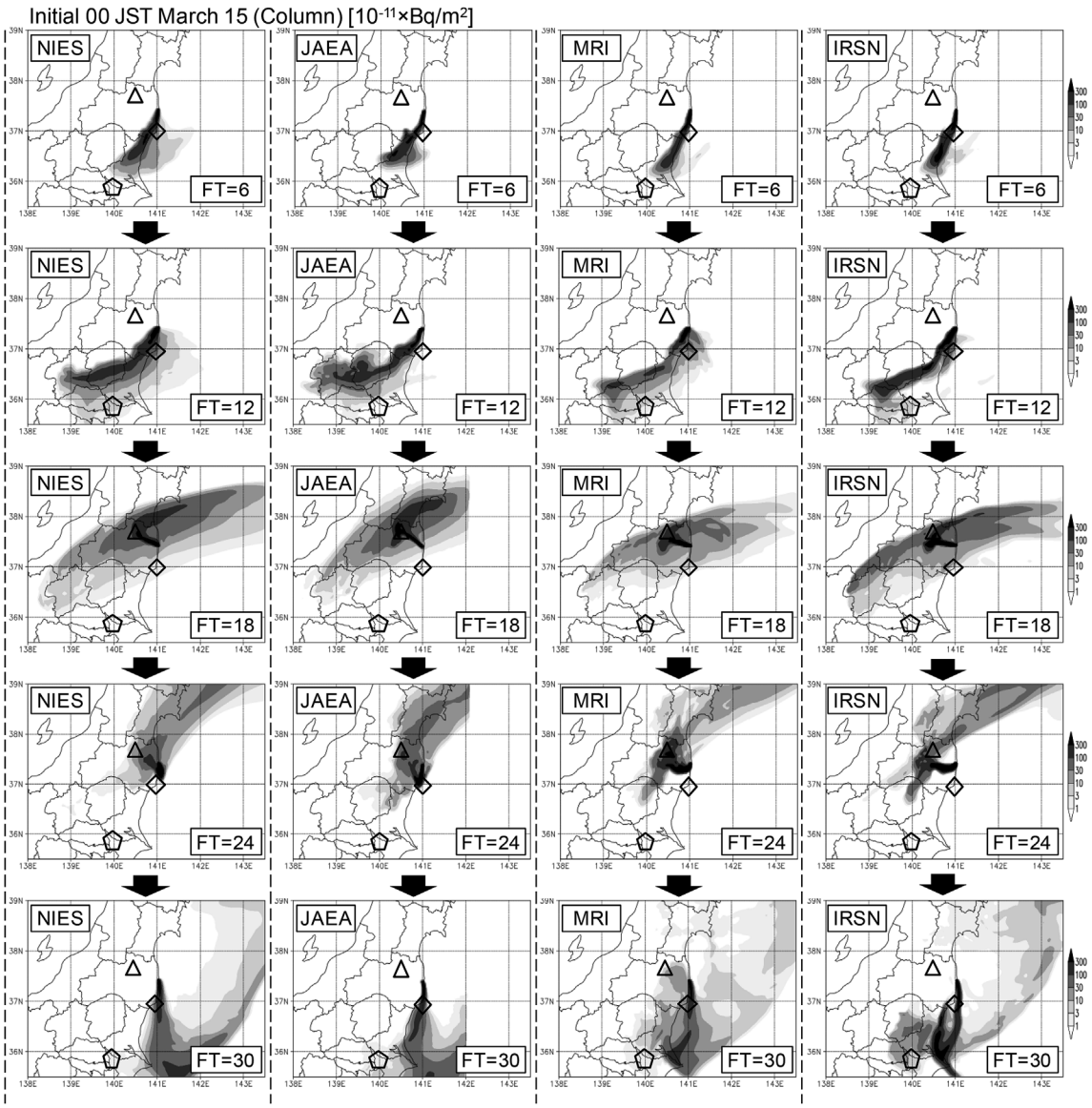

Fig. 8. Same as Fig. 4 but for the column-integrated contamination forecasts (10^{-11} × Bq/m^2).

contamination among the four NDP models were not found in Fig. 8 as far as the short-range (30-h) forecasts are concerned. Stacked bar charts in Fig. 9b shows the similarity degree of the potential contamination area among the four NDP models depicted in Fig. 8. If the stacked bar charts are exclusively colored with "1-Model Only" then the potential contamination areas are completely non-overlapped among the four NDP models. In contrast, stacked bar charts with a 100% proportion of "4-Model Ovlp" indicates the perfect match of the four NDP models. Fig. 9b illustrates a large similarity (but a moderate difference) among the four NDP models with a small portion of "1-Model Only" areas. The forecast similarity in Fig. 9b (related to Fig. 8) is higher than that in Fig. 9a (related to Fig. 4) because the distribution of contamination in Fig. 8 is column-integrated, which is apt to mask the difference in vertical diffusion between models, while that in Fig. 4 illustrates only the surface layer.

Fig. 10 is the vertical cross section of the substance density along a line of the latitude of Fukushima City (37.76° N). The contaminated air extended up to an altitude of about 3000 m. The upper portions of the contaminated air were emitted in the early morning, and widely dispersed by the wind shear. The lower portions of relatively dense radioactive substances were mainly emitted in the afternoon. The NDP models forecasted the low-level air contamination to be lower at Fukushima City than that at Iwaki, under the assumption of a constant emission rate. The risk of internal exposure by inhalation at Fukushima City might be much less than that at Iwaki 12 h earlier. On the other hand, the large column-integrated amount indicated the risk of wet deposition around Fukushima City in the evening. Indeed, as shown in Fig. 1, the precipitation caused the wet deposition and the ground contamination at the Fukushima station. Fig. 11 shows that the precipitation started around 1400 JST (FT = 14) and the surface contamination mainly occurred at about 1700 JST (FT = 17). The NDP models forecasted that the radioactive plume would be widely spread over Fukushima City at about 1800 JST (FT = 18). Note that previous studies have indicated that the reproducibility of the northwestward wind from the nuclear power plant to Fukushima City is not good in the afternoon 15th of March (e.g., Morino et al., 2013; Sekiyama et al., 2015; Nakajima et al., 2017), attributable to the orographic model resolution or boundary conditions. This type of meteorological uncertainty cannot be completely removed by the ensemble forecast or proper use of NDP models. Nonetheless, in Fig. 11, one ensemble member (JAEA model) was able to predict the contamination arrival time more accurately than other members. This indicates the benefit of

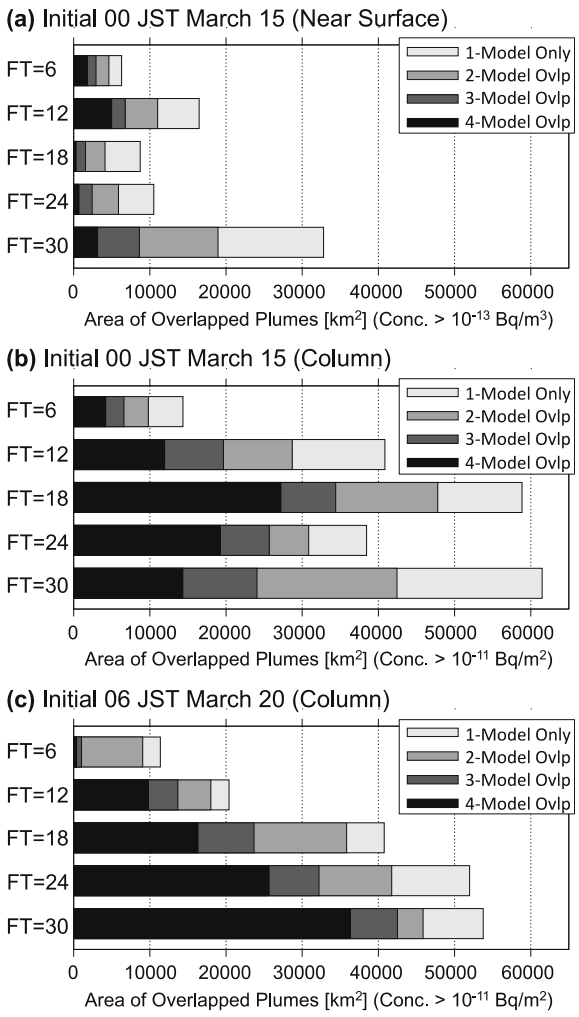

Fig. 9. Overlapped and distinct plume areas (km^2) between the four NDP models at forecast times (FT) of 6, 12, 18, 24, and 30 h within the latitude 35.5° N – 39.0° N and longitude 138.0° E − 142.0° E. In the legend, 4-Model Ovlp, 3-Model Ovlp, 2-Model Ovlp, and 1-Model Only indicate the area where all the four NDP model plumes are overlapped, the total area where three out of the four NDP model plumes are overlapped, the total area where two out of the four NDP model plumes are overlapped, and the total area where only one plume exists (= non-overlapped with any others), respectively. (a) Statistics related to Fig. 4 with the plume edge definition of $10^{-13} \times Bq/m^3$, (b) related to Fig. 8 with the plume edge definition of $10^{-11} \times Bq/m^2$, and (c) related to Fig. 12 with the plume edge definition of $10^{-11} \times Bq/m^2$.

the model ensemble forecast.

If the column-integrated contamination forecasts had been available, we could have prepared for contaminated precipitation in the region of high column-integrated contamination. If it rains in the region where a large column-integrated amount is forecasted, residents can be warned not to use rainwater to avoid internal exposure, and check the contamination of the rainwater. If it does not rain, we can withdraw the wet deposition warning.

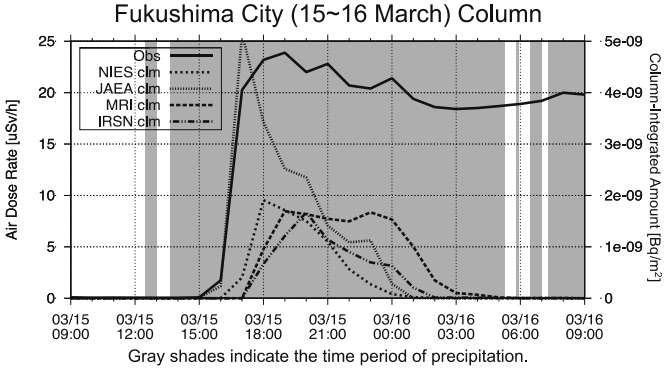

Fig. 11. Time series of the column-integrated contamination amount forecasts (unit; Bq/m^2) together with the observations of air dose rate (unit; μSv/h) at the Fukushima station. A constant emission rate of 1 Bq/h at FDNPP is assumed in the forecasts.

3.3. NDP model forecasts for wet deposition at Kashiwa

Although Kashiwa is located about 200 km SSW of FDNPP, significant contamination on the ground was recorded due to the wet deposition around 0800 JST on the 21st of March as shown in Fig. 2. All of the NDP model forecasts indicated that the tongue of the radiative plume passed over Kashiwa at this time as shown in Fig. 12. The forecasted arrival times of the plume by the NIES and JAEA models were a little earlier than those by the MRI and IRSN models. This is probably because these NDP forecasts are coupled with different mesoscale numerical weather prediction (NWP) models. The former two models implemented the WRF model, whereas the MRI implemented the JMA non-hydrostatic weather forecast model (JMANHM). The IRSN model was an off-line transport model, and was driven by the same meteorological parameters from the JMANHM. Nonetheless, there are no large differences in the distribution of contamination among models as shown in Fig. 9c which indicates a higher similarity than in Fig. 9b.

Similar to Fukushima City, if the above forecasts had been available, people in Kashiwa would have been able to prepare for the contaminated precipitation. We should survey the ground contamination due to wet deposition only when precipitation occurs in the forecasted regions of high column-integrated contamination. It is not necessary to survey the ground contamination in the non-precipitation area. Thus, we can quickly determine which areas are at risk of ground contamination by considering only the areas both experiencing precipitation and predicting column-integrated contamination.

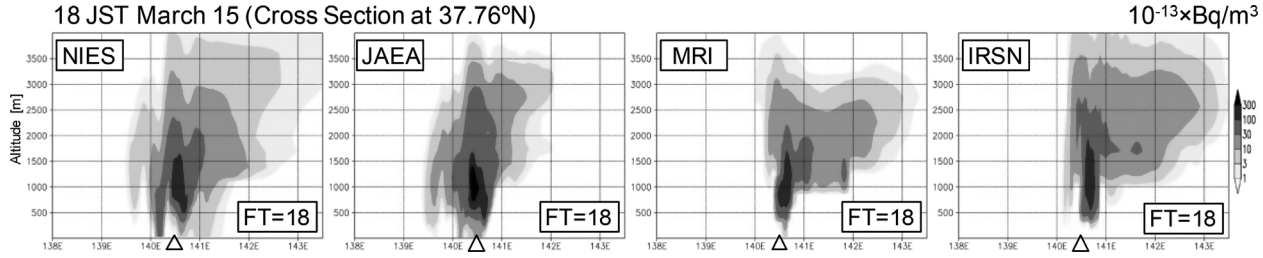

Fig. 10. Same as Fig. 5 but for the 18-h forecast along a line of the latitude of Fukushima City (37.76° N). Open triangles indicate the longitude of Fukushima City (140.5° E).

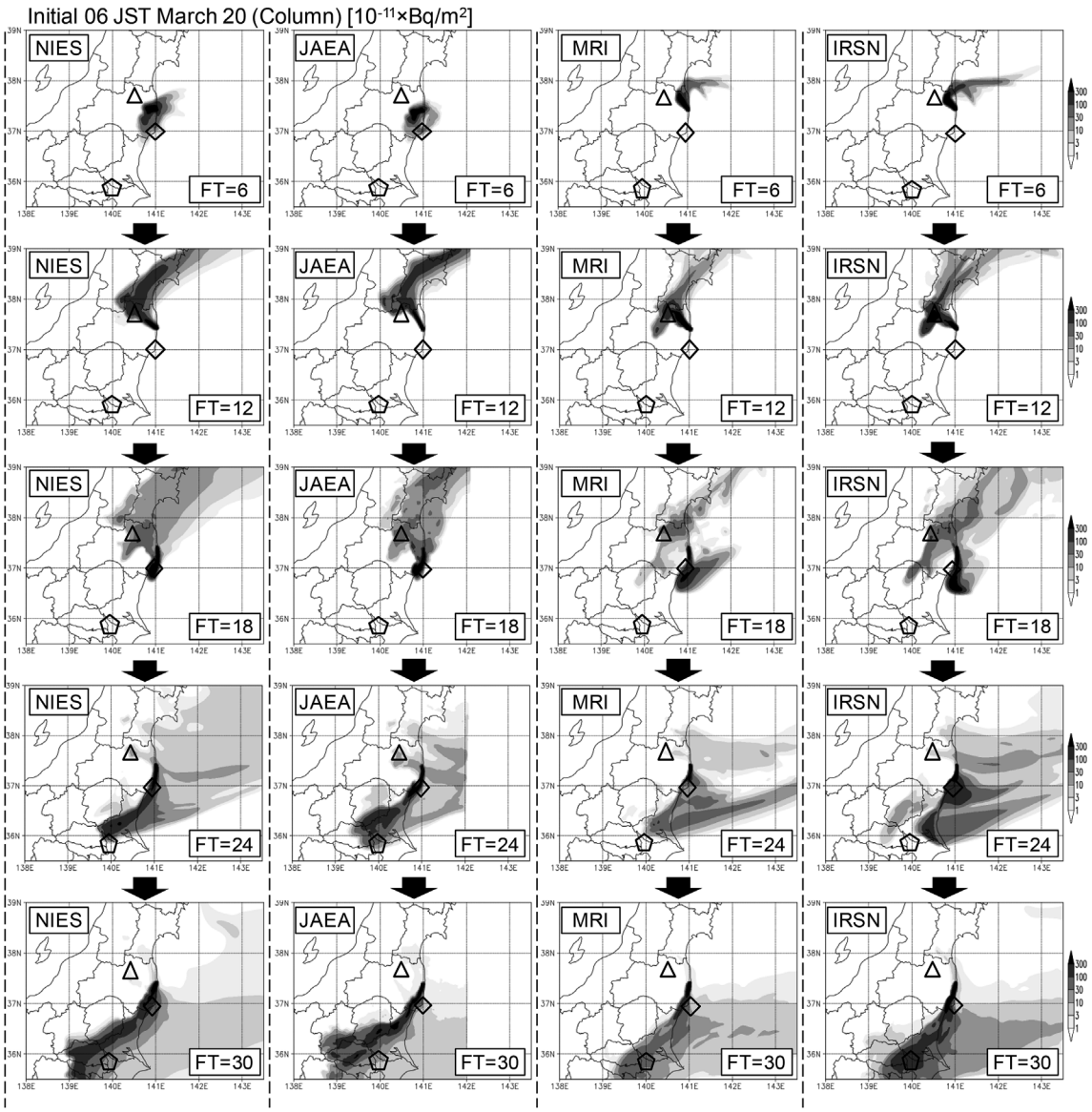

Fig. 12. Same as Fig. 8 but for the initialization time of 0600 JST on 20th March.

4. Conclusions

4.1. How to utilize NDP models for environmental emergencies

All four NDP models succeeded in forecasting the three-dimensional distribution on short time scales for the three locations considered here. The NDP models have the potential to provide useful information to the public on the surface air contamination and column-integrated contamination even if the emission inventory information is not available. The surface air contamination forecasts can be utilized for mitigating the inhalation of radioactive substances, and the column-integrated contamination forecasts for mitigating the radiation exposure associated with the wet deposition. Note that the column-integrated contamination is the worst-case scenario for wet-deposition. As with all natural hazard forecasts, the greatest benefit of using forecasts is the increased lead time at which warnings can be provided, giving more time to prepare.

Accurate observational data are also valuable for preparing preventive measures against nuclear disasters. Emergency systems based only on observations, however, may not be able to provide timely information. Also, the use of observations only incurs the risk of unobserved contamination because of coarse spatial distributions when there are insufficient stations available. For example, precipitation can significantly contaminate the ground surface even far away from the emission source, where it is difficult to deploy observatories enough to depict the whole contaminated area. Emergency systems should be established to effectively survey the contamination due to wet deposition on the ground over wide areas. The utilization of the NDP models helps us to reduce the radiation exposure by considering the match of the predicted plume with the observed precipitation. For determining preventive actions, we should use information from both the observations and forecasts (World Meteorological Organization, 2006).

4.2. Recommendation

The reason why the NRA discontinued the use of NDP model forecasts for environmental emergencies was that both the time-dependent emission scenarios and weather forecasts contain considerable uncertainties. According to them, model forecasts can hardly be used quantitatively, for example, compared with the threshold density values, to issue evacuation orders. Thus, we recommend using model forecasts for qualitative indications of the worst-case scenario, which

can help us choose a safer time and place of evacuation and greatly reduce exposure to radiation. The assumption of emission rate constancy provides the worst-case scenario when limited source information is available. Under the constant emission scenario, it does not matter what absolute values of emission are used in NDP models because the hazardous plumes can be discriminated with a huge gap of concentration in the model simulations.

On the other hand, NDP model forecasts also have uncertainties arising from the forecasts of dynamic and thermodynamic fields. If these meteorological fields are inaccurate, then the location of safe areas may not be safe even though the NDP model forecasts suggest it is. The differences in the vertical diffusion schemes between models result in differences in the vertical distributions of the contamination and subsequently the horizontal distributions. The intercomparison experiment, however, did not find large differences in the distribution of contamination among models, as far as the short-range (30-h) forecasts are concerned. The consistency among different model forecasts indicated that short-range forecasts were reliable enough to detect qualitatively hazardous areas. However, as mentioned above, we ought to consider the risk of contamination to be slightly broader and longer than forecasted, considering the uncertainty in the meteorological fields.

Finally, we recommend the use of various ensemble techniques to improve the reliability of the NDP forecasts, for example, the time-lagged ensemble method (cf. Figs. 6b and 7b), in which outputs from different initialization times provide us with reliable forecasts and the approximate magnitude of forecast errors. The multi-model ensemble also should be utilized to illustrate the forecast uncertainties and provide the extended hazardous time and areas as shown in this study. Nowadays, many operational NWP centers provide ensemble weather forecasts using perturbed initial conditions, whose products can also be used for the initial and lateral boundary conditions of NDP models (cf., Kajino et al., 2018). The NDP model intercomparison experiment strongly indicated the effectiveness of multi-model ensemble techniques in this study. We hope that the multi-model ensemble techniques will be used not only for the reanalysis of the nuclear accident (e.g., Draxler et al., 2015; Kristiansen et al., 2016; Kitayama et al., 2018; Sato et al., 2018) but also for a forecast (or hindcast) purpose. The uncertainty of numerical weather forecasts still remains especially for ground surface wind because the wind in the planetary boundary layer (PBL) strongly depends on the orographic reproducibility in the model. Therefore, we sincerely expect the model resolution of operational weather forecasts to be heightened to reduce the uncertainties of the PBL wind and NPD forecasts.

Declaration of competing interest

The authors declare that they have no known competing financial interests or personal relationships that could have appeared to influence the work reported in this paper.

Acknowledgements

We acknowledge the committee members of the working group on “Radioactive substances accidentally released from nuclear power related facilities” for their cooperation in drafting the MSJ's proposal and their encouragement throughout this study. We are also indebted to Dr. Tetsuji Yamada for valuable comments on this manuscript. This work was supported by activity of the Core Research Cluster of Disaster Science in Tohoku University. This work was supported by the Environment Research and Technology Development Fund (5-1501 and 1-1802) at the Environmental Restoration and Conservation Agency and partly by JSPS KAKENHI Grant Number JP17K00533. The model data used in this paper are available upon request to the corresponding author.

References

Brandt, J., Christensen, J.H., Frohn, L.M., 2002. Modelling transport and deposition of caesium and iodine from the Chernobyl accident using the DREAM model. Atmos. Chem. Phys. 2, 397–417. https://doi.org/10.5194/acp-2-397-2002.

Byun, D., Schere, K.L., 2006. Review of the governing equations, computational algorithms, and other components of the models-3 community Multiscale Air quality (CMAQ) modeling system. Appl. Mech. Rev. 59, 51–77. https://doi.org/10.1115/1.2128636.

Chino, M., Nakayama, H., Nagai, H., Terada, H., Katata, G., Yamazawa, H., 2011. Preliminary estimation of release amounts of 131I and 137Cs accidentally discharged from the Fukushima daiichi nuclear power plant into the atmosphere. J. Nucl. Sci. Technol. 48, 1129–1134. https://doi.org/10.1080/18811248.2011.9711799.

Draxler, R., Arnold, D., Chino, M., Galmarini, S., Hort, M., Jones, A., Leadbetter, S., Malo, A., Maurer, C., Rolph, G., Saito, K., Servranckx, R., Shimbori, T., Solazzo, E., Wotawa, G., 2015. World meteorological organization's model simulations of the radionuclide dispersion and deposition from the Fukushima daiichi nuclear power plant accident. J. Environ. Radioact. 139, 172–184. https://doi.org/10.1016/j.jenvrad.2013.09.014.

Ehrhardt, J., 1997. The RODOS system: decision support for off-site emergency management in Europe. Radiat. Prot. Dosim. 73, 35–40. https://doi.org/10.1093/oxfordjournals.rpd.a032160.

Goerss, J.S., 2000. Tropical cyclone track forecasts using an ensemble of dynamical models. Mon. Weather Rev. 128, 1187–1193. https://doi.org/10.1175/1520-0493(2000)128<1187:TCTFUA>2.0.CO;2.

Groëll, J., Quélo, D., Mathieu, A., 2014. Sensitivity analysis of the modelled deposition of 137Cs on the Japanese land following the Fukushima accident. Int. J. Environ. Pollut. 55, 67–75. https://doi.org/10.1504/IJEP.2014.065906.

Hatamura, Y., Oike, K., Kakinuma, S., Takasu, Y., Takano, T., Tanaka, Y., Hayashi, Y., Furukawa, M., Yanagida, K., Yoshioka, H., Abe, S., Fuchigami, M., 2011. *Interim Report*, Investigation Committee on the Accident at the Fukushima Nuclear Power. Stations of Tokyo Electric Power Company, Cabinet Secretariat, Japan, pp. 236.

Hatamura, Y., Oike, K., Kakinuma, S., Takasu, Y., Takano, T., Tanaka, Y., Hayashi, Y., Furukawa, M., Yanagida, K., Yoshioka, H., Abe, S., Fuchigami, M., 2012. *Final Report*, Investigation Committee on the Accident at the Fukushima Nuclear Power Stations of Tokyo Electric Power Company. Cabinet Secretariat, Japan, pp. 454.

Hoe, S., McGinnity, P., Charnock, T., Gering, F., Schou Jacobsen, L.H., Havskov Sørensen, J., Andersson, K.G., Astrup, P., 2009. ARGOS Decision Support System for Emergency Management. Argentine Radiation Protection Society (last access on: http://orbit.dtu.dk/files/3924948/Hoe_paper.pdf, Accessed date: 18 October 2018.

Imai, K., Chino, M., Ishikawa, H., Kai, M., Asai, K., Homma, T., Hidaka, A., Nakamura, Y., Iijima, T., Moriuchi, S., 1985. SPEEDI: a Computer Code System for the Real-Time Prediction of Radiation Dose to the Public Due to an Accidental Release. JAERI–1297, Japan Atomic Energy Research Institute, Japan, pp. 93.

Kajino, M., Sekiyama, T.T., Mathieu, A., Korsakissok, I., Perillat, R., Quelo, D., Querel, A., Saunier, O., Adachi, K., Girard, S., Maki, T., Yumimoto, K., Didier, D., Masson, O., Igarashi, Y., 2018. Lessons learned from atmospheric modeling studies after the Fukushima nuclear accident: ensemble simulations, data assimilation, elemental process modeling, and inverse modeling. Geochem. J. 52, 85–101. https://doi.org/10.2343/geochemj.2.0503.

Katata, G., Chino, M., Kobayashi, T., Terada, H., Ota, M., Nagai, H., Kajino, M., Draxler, R., Hort, M.C., Malo, A., Torii, T., Sanada, Y., 2015. Detailed source term estimation of the atmospheric release for the Fukushima Daiichi Nuclear Power Station accident by coupling simulations of an atmospheric dispersion model with an improved deposition scheme and oceanic dispersion model. Atmos. Chem. Phys. 15, 1029–1070. https://doi.org/10.5194/acp-15-1029-2015.

Kitayama, K., Morino, Y., Takigawa, M., Nakajima, T., Hayami, H., Nagai, H., Terada, H., Saito, K., Shimbori, T., Kajino, M., Sekiyama, T.T., Didier, D., Mathieu, A., Quélo, D., Ohara, T., Tsuruta, H., Oura, Y., Ebihara, M., Moriguchi, Y., Shibata, T., 2018. Atmospheric modeling of 137Cs plumes from the Fukushima daiichi nuclear power plant – evaluation of the model intercomparison data of the science council of Japan. J. Geophys. Res. 123, 7754–7770. https://doi.org/10.1029/2017JD028230.

Kristiansen, N.I., Stohl, A., Olivié, D.J.L., Croft, B., Søvde, O.A., Klein, H., Christoudias, T., Kunkel, D., Leadbetter, S.J., Lee, Y.H., Zhang, K., Tsigaridis, K., Bergman, T., Evangeliou, N., Wang, H., Ma, P.-L., Easter, R.C., Rasch, P.J., Liu, X., Pitari, G., Di Genova, G., Zhao, S.Y., Balkanski, Y., Bauer, S.E., Faluvegi, G.S., Kokkola, H., Martin, R.V., Pierce, J.R., Schulz, M., Shindell, D., Tost, H., Zhang, H., 2016. Evaluation of observed and modelled aerosol lifetimes using radioactive tracers of opportunity and an ensemble of 19 global models. Atmos. Chem. Phys. 16, 3525–3561. https://doi.org/10.5194/acp-16-3525-2016.

Kunii, M., 2014. Mesoscale data assimilation for a local severe rainfall event with the NHM–LETKF system. Weather Forecast. 29, 1093–1105. https://doi.org/10.1175/WAF-D-13-00032.1.

Mathieu, A., Korsakissok, I., Quélo, D., Groëll, J., Tombette, M., Didier, D., Quentric, E., Saunier, O., Benoit, J.-P., Isnard, O., 2012. Atmospheric dispersion and deposition of radionuclides from the Fukushima daiichi nuclear power plant accident. Elements 8, 195–200. https://doi.org/10.2113/gselements.8.3.195.

Mathieu, A., Kajino, M., Korsakissok, I., Périllat, R., Quélo, D., Quérel, A., Saunier, O., Sekiyama, T.T., Igarashi, Y., Didier, D., 2018. Fukushima Daiichi–derived radionuclides in the atmosphere, transport and deposition in Japan: a review. Appl. Geochem. 91, 122–139. https://doi.org/10.1016/j.apgeochem.2018.01.002.

Meteorological Society of Japan, 2015. The proposal on strengthening of analysis and prediction system for radioactive substances accidentally released from nuclear power related facilities. Tenki 62, 111–112.

MEXT, 2011. On the Airborne Monitoring Results by MEXT and US-DOE. (last access: 18 October, 2018), in Japanese. http://radioactivity.nsr.go.jp/ja/contents/4000/3710/

24/1305820_20110506.pdf.
Morino, Y., Ohara, T., Watanabe, M., Hayashi, S., Nishizawa, M., 2013. Episode analysis of deposition of radiocesium from the Fukushima daiichi nuclear power plant accident. Environ. Sci. Technol. 47, 2314–2322. https://doi.org/10.1021/es304620x.
Nakajima, T., Misawa, S., Morino, Y., Tsuruta, H., Goto, D., Uchida, J., Takemura, T., Ohara, T., Oura, Y., Ebihara, M., Satoh, M., 2017. Model depiction of the atmospheric flows of radioactive cesium emitted from the Fukushima Daiichi Nuclear Power Station accident. Prog. Earth. Planet. Sci. 4, 2. https://doi.org/10.1186/s40645-017-0117-x.
Nuclear Regulation Authority, 2014. Utilization of System for Prediction of Environmental Emergency Dose Information (SPEEDI). (last access: 18 October, 2018), in Japanese. https://www.nsr.go.jp/data/000027740.pdf.
Oura, Y., Ebihara, M., Tsuruta, H., Nakajima, T., Ohara, T., Ishimoto, M., Sawahata, H., Katsumura, Y., Nitta, W., 2015. A database of hourly atmospheric concentrations of radiocesium (134Cs and 137Cs) in suspended particulate matter collected in March 2011 at 99 air pollution monitoring stations in eastern Japan. J. Nucl. Radiochem. Sci. 15, 15–26. https://doi.org/10.14494/jnrs.15.2_1.
Quérel, A., Roustan, Y., Quélo, D., Benoit, J.-P., 2015. Hints to discriminate the choice of wet-deposition models applied to an accidental radioactive release. Int. J. Environ. Pollut. 58, 268–279. https://doi.org/10.1504/IJEP.2015.077457.
Sato, Y., Takigawa, M., Sekiyama, T.T., Kajino, M., Terada, H., Nagai, H., Kondo, H., Uchida, J., Goto, D., Quélo, D., Mathieu, A., Quérel, A., Fang, S., Morino, Y., von Schoenberg, P., Grahn, H., Brännström, N., Hirao, S., Tsuruta, H., Yamazawa, H., Nakajima, T., 2018. Model intercomparison of atmospheric 137Cs from the Fukushima Daiichi Nuclear Power Plant accident: simulations based on identical input data. J. Geophys. Res. 123 (11), 765. https://doi.org/10.1029/2018JD029144. 748–11.
Saunier, O., Mathieu, A., Didier, D., Tombette, M., Quélo, D., Winiarek, V., Bocquet, M., 2013. An inverse modeling method to assess the source term of the Fukushima Nuclear Power Plant accident using gamma dose rate observations. Atmos. Chem. Phys. 13, 11403–11421. https://doi.org/10.5194/acp-13-11403-2013.
Sekiyama, T.T., Kunii, M., Kajino, M., Shimbori, T., 2015. Horizontal resolution dependence of atmospheric simulations of the Fukushima nuclear accident using 15-km, 3-km, and 500-m grid models. J. Meteor. Soc. Japan 93, 49–64. https://doi.org/10.2151/jmsj.2015-002.
Sekiyama, T.T., Kajino, M., Kunii, M., 2017. The impact of surface wind data assimilation on the predictability of near-surface plume advection in the case of the Fukushima nuclear accident. J. Meteor. Soc. Japan 95, 447–454. https://doi.org/10.2151/jmsj.2017-025.
Sekiyama, T.T., Iwasaki, T., 2018. Mass flux analysis of Cs-137 plumes emitted from the Fukushima daiichi nuclear power plant. Tellus B 70 (1), 1–11. https://doi.org/10.1080/16000889.2018.1507390.
Skamarock, W.C., Klemp, J.B., Dudhia, J., Gill, D.O., Barker, D.M., Duda, M.G., Huang, X.Y., Wang, W., Powers, J.G., 2008. A Description of the Advanced Research WRF Version 3. Tech. Note, NCAR/TN.475+STR. National Center for Atmospheric Research, Boulder, pp. 135. https://doi.org/10.5065/D68S4MVH.
Terada, H., Chino, M., 2008. Development of an atmospheric dispersion model for accidental discharge of radionuclides with the function of simultaneous prediction for multiple domains and its evaluation by application to the Chernobyl nuclear accident. J. Nucl. Sci. Technol. 45, 920–931. https://doi.org/10.3327/jnst.45.920.
Working group on "Radioactive substances accidentally released from nuclear power related facilities", Meteorological Society of Japan. In: Report on utilization of numerical transport model for the atmospheric dispersion of radioactive substances. Tenki. 62. pp. 113–123 (in Japanese).
World Meteorological Organization, 2006. Environmental emergency response: WMO activities. World Meteorol. Organ. Bull. 55 (1), 37–41.
World Meteorological Organization, 2010. Documentation on RSMC Support for Environmental Emergency Response. (targeted for meteorologists at National Meteorological Services), WMO Technical Document No. 778. http://www.wmo.int/pages/prog/www/DPFSERA/td778.html, Accessed date: 18 October 2018 (last access:.

JGR Atmospheres

RESEARCH ARTICLE
10.1029/2018JD028998

Deposition and Dispersion of Radio-Cesium Released Due to the Fukushima Nuclear Accident: Sensitivity to Meteorological Models and Physical Modules

Mizuo Kajino[1,2], Tsuyoshi Thomas Sekiyama[1], Yasuhito Igarashi[1,3,4], Genki Katata[5], Morihiro Sawada[6], Kouji Adachi[1], Yuji Zaizen[1], Haruo Tsuruta[7], and Teruyuki Nakajima[8]

[1]Meteorological Research Institute, Japan Meteorological Agency, Tsukuba, Japan, [2]Faculty of Life and Environmental Sciences, University of Tsukuba, Tsukuba, Japan, [3]Institute for Integrated Radiation and Nuclear Science, Kyoto University, Kumatori, Japan, [4]College of Science, Ibaraki University, Mito, Japan, [5]Institute for Global Change Adaptation Science, Ibaraki University, Mito, Japan, [6]Graduate School of Life and Environmental Sciences, University of Tsukuba, Tsukuba, Japan, [7]Remote Sensing Technology Center of Japan, Tokyo, Japan, [8]Earth Observation Research Center, Japan Aerospace Exploration Agency, Tsukuba, Japan

Key Points:
- Sensitivity to meteorological models was assessed for the first time for the Fukushima nuclear accident study
- Modeled deposition rates were underestimated, while precipitation values and source term were reasonable
- In-cloud scavenging was the most dominant mechanism for radio-Cs deposition, followed by dry and fog depositions

Correspondence to:
M. Kajino,
kajino@mri-jma.go.jp

Citation:
Kajino, M., Sekiyama, T. T., Igarashi, Y., Katata, G., Sawada, M., Adachi, K., et al. (2019). Deposition and dispersion of radio-cesium released due to the Fukushima nuclear accident: Sensitivity to meteorological models and physical modules. *Journal of Geophysical Research: Atmospheres*, *124*, 1823–1845. https://doi.org/10.1029/2018JD028998

Received 18 MAY 2018
Accepted 10 JAN 2019
Accepted article online 15 JAN 2019
Published online 2 FEB 2019

Author Contributions:
Conceptualization: Mizuo Kajino, Tsuyoshi Thomas Sekiyama, Yasuhito Igarashi, Genki Katata
Data curation: Mizuo Kajino, Kouji Adachi, Yuji Zaizen, Haruo Tsuruta
Formal analysis: Mizuo Kajino
Funding acquisition: Yasuhito Igarashi, Teruyuki Nakajima
Investigation: Mizuo Kajino
Methodology: Mizuo Kajino, Tsuyoshi Thomas Sekiyama, Genki Katata
Resources: Mizuo Kajino, Kouji Adachi, Yuji Zaizen, Haruo Tsuruta
Supervision: Mizuo Kajino, Yasuhito Igarashi, Genki Katata, Kouji Adachi, Yuji Zaizen, Haruo Tsuruta, Teruyuki Nakajima
Validation: Mizuo Kajino
Visualization: Mizuo Kajino, Morihiro Sawada
Writing - original draft: Mizuo Kajino

Abstract To assess the uncertainty of meteorological simulations in the transport and deposition of radio-Cs release associated with the Fukushima Daiichi Nuclear Power Station accident in Japan, a multiple meteorological model and module ensemble analysis with a single chemical transport model (CTM) was conducted. Although several multimodel ensemble studies have previously been performed, the current type (i.e., one CTM with several meteorological fields) was applied for the first time and represents a useful way to evaluate the uncertainty of each component of CTM. The current analysis concluded that the underestimation of the deposition efficiency of CTM was the reason for the underestimation of simulated radio-Cs deposition, whereas the simulated dispersion and precipitation and estimated source term were all reasonable: all of the simulations underestimated the deposition amount, whereas some underestimated but others overestimated the simulated precipitation and radio-Cs concentrations. The CTM simulation performed using the meteorological ensemble mean field was successful in reducing variance, and they gave reasonable results. The simulated deposition using the meteorological ensemble was better than others because the ensemble mean enlarged the light precipitation areas and because the land contamination was mainly caused by light precipitation. The current ensemble study indicated that in-cloud scavenging was the most dominant mechanism of radio-Cs deposition, followed by dry deposition and fog deposition over the entire land area. In some deposition regions, fog deposition was dominant, exceeding 80%, depending on the simulations. The simulated concentrations and depositions varied by more than twofold, depending on the selection of the meteorological field.

1. Introduction

The Fukushima Daiichi Nuclear Power Station (FDNPS) accident released fission products to the environment in March 2011 and contaminated land ecosystems through the air. The aircraft-measured deposition of ^{137}Cs over the land was approximately 3 PBq (NRA [Nuclear Regulation Authority], 2012; Torii et al., 2012), excluding the area within 3 km of FDNPS because no measurements were available from this area (no-fly zone). Due to the huge amount of land deposition, together with the longer half lives of ^{137}Cs (30.1 years) and ^{134}Cs (2.07 years), there still remain habitation-restricted zones in Fukushima prefecture. In addition, once deposited to the land, radio-Cs only circulates within local land ecosystems, and its migration out of the local ecosystem has been found to be not very rapid: The resuspension rate from the land to the atmosphere was lower than 0.1% per year during the year 2013 (Kajino et al., 2016), and the discharge rate from the land to the river was 0.73–3.7% per year from August 2012 to September 2013 (Iwagami et al., 2016). Therefore, a better understanding of the dispersion and deposition mechanisms of primary-emitted radio-Cs is critically needed.

Thanks to the substantial efforts to reveal the atmospheric behavior and budget of radio-Cs by using field observations and numerical models, knowledge has been accumulated (Kajino, Sekiyama, et al., 2018; Mathieu et al., 2018). The major isotopes of radio-Cs emitted to the air were ^{134}Cs and ^{137}Cs, with almost equal activity. The total primary deposition (3 PBq) amounted to 20% of the estimated released amount,

15 PBq (Katata et al., 2015); thus, most of the ^{137}Cs was transported and deposited outside Japanese territory. Transport events of ^{137}Cs toward land in Japan occurred several times in March 2011 (Nakajima et al., 2017; Tsuruta et al., 2014), which were associated with some proportions of immediate resuspension from the ground (Igarashi et al., 2015). Wet deposition processes played key roles in ground surface contamination in Japan (e.g., Morino et al., 2013; Quérel et al., 2015). This occurred because the sizes of the major proportions of Cs-bearing particles were as small as 1 μm or less in aerodynamic diameter (Doi et al., 2013; Kaneyasu et al., 2012; Masson et al., 2013); thus, the dry deposition velocity of radio-Cs was not very large.

Nevertheless, there is a relatively large uncertainty in the source term estimation of ^{137}Cs (10–50 PBq; Mathieu et al., 2018). The atmospheric behavior of radio-Cs is much simpler compared to that of radio-I: Radio-Cs exists only in the aerosol phase in the air, whereas radio-I exists in the aerosol phase, as inorganic gas, and as organic gas. However, the contributions of deposition processes have varied between models (e.g., SCJ [Science Coucil of Japan], 2014). To quantify the uncertainty in the atmospheric budget estimation and to identify the source of the uncertainty, several multimodel intercomparison studies (Draxler et al., 2015; Kitayama et al., 2018; Kristiansen et al., 2016; SCJ, 2014) and sensitivity analyses of model parameters (sometimes referred to as intracomparisons; Girard et al., 2014, 2016; Groëll et al., 2014; Leadbetter et al., 2015; Morino et al., 2013; Quérel et al., 2015) have been conducted. Each method has its pros and cons. The intercomparison of different source terms, meteorological fields, and transport models (Kitayama et al., 2018; SCJ, 2014) can quantify the overall uncertainty in the system but cannot quantify the uncertainty of each component. In contrast, the intercomparison of different transport models with a common configuration (such as the common source term, Draxler et al., 2015; Kristiansen et al., 2016) can quantify the uncertainty of each component but cannot quantify the overall uncertainty. A model intercomparison study can quantify the magnitude of the uncertainty but cannot adequately identify the reason for the uncertainty. On the other hand, an intracomparison study can identify the reason for an uncertainty but only for a single model case, even though the results could vary substantially depending on models. Consequently, the accumulation of knowledge using several combinations of model intercomparison and intracomparison studies is important.

Thus far, one kind of combination of model comparison (or sensitivity analysis) studies has been missing: a single transport model applied to multiple meteorological fields. Sekiyama et al. (2015) performed an ensemble dispersion simulation using a square root Kalman filter to assess the uncertainties in meteorological simulations. Their method can quantify the uncertainty in the initial and boundary conditions of meteorological fields, but it cannot quantify the uncertainty in the simulation of each meteorological process, such as cloud microphysics, solar and terrestrial radiation, boundary layer turbulence, and surface fluxes. The purpose of the present study is to quantify the differences in the simulated concentration and deposition of ^{137}Cs due to the selection of meteorological simulations and to identify the reason for the discrepancies between simulations and observations. Also investigated are the contributions of each process to ^{137}Cs deposition, such as dry deposition, in-cloud scavenging, below-cloud scavenging, and fog deposition over different regions and between different meteorological simulations.

2. Materials and Methods

2.1. Transport Model

The regional-scale Eulerian transport model NHM-Chem (Kajino, Deushi, et al., 2018; Kajino et al., 2019) has been used for simulations of the transport and deposition of radionuclides. NHM-Chem is a chemical transport model (CTM) coupled with a meteorological model, that is, the Japan Meteorological Agency's (JMA) Nonhydrostatic Model (NHM; Saito et al., 2007). The CTM part of NHM-Chem solves for tropospheric photochemical reactions and aerosol dynamics processes, but a simplified version was built and applied for this study. A previous version of the CTM part was called the Regional Air Quality Model 2 (RAQM2; Kajino et al., 2012), and its simplified version (Adachi et al., 2013) was also applied to previous studies of the atmospheric simulations of the radionuclides released in association with the FDNPS accident (Adachi et al., 2013; Sekiyama et al., 2015, 2017).

Since the model applied to this study was modified for the transport of radionuclides, it is briefly described here, with a focus on its differences from the models of Kajino, Deushi, et al. (2018) and Adachi et al. (2013). This model considers nine tracers, that is, gas-phase ^{131}I, aerosol-phase ^{131}I, ^{132}Te, ^{137}Cs, ^{134}Cs, and ^{133}Xe, and the three moments (number, surface area, and volume concentrations) of aerosols, which carry the

radionuclides released from FDNPS. Thus, all nuclides are assumed to be carried by the same type of aerosols, and the carrier aerosols are assumed to have no interaction with other environmental aerosols or condensable gases. Here note that an aerosol "type" is the same as an aerosol category of Kajino, Deushi, et al. (2018), which has some size distribution but has a uniform chemical composition, density, and shape. (Diesel exhaust, brake wearing, sea-salt, mineral dust, or pollen is an example of a "type," defined). As the chemical compositions are not explicitly treated in the current model, a prescribed hygroscopicity was applied to the type of carrier aerosols to calculate its hygroscopic growth and cloud condensation nuclei (CCN) activation. A log-normal size distribution was assumed for the population of carrier aerosols. Because three log-normal parameters are used to identify the size distribution, that is, the number, geometric mean diameter, and geometric standard deviation, the three log-normal parameters can be fixed by the simulated three moments. The algorithms of advection, turbulent diffusion, dry deposition, fog deposition, gravitational settling, in-cloud and below-cloud scavenging processes were the same as those used by Kajino, Deushi, et al. (2018). Photochemical reactions and thus aerosol microphysical processes, such as new particle formation, condensation/evaporation, and coagulation, were not considered in the simulation, but changes in the size distributions during transport due to deposition processes were considered in the simulation. (Changes in the size distributions during transport were not considered in Adachi et al., 2013.) The ice nuclei activation was not considered in this study, as it is not the major process in terms of the removal of aerosol mass, and the CCN activation was substantially simplified. The CCN activation fraction was prescribed as unity, as indicated by Kaneyasu et al. (2012): Sulfate is a carrier of radio-Cs. The unit activation fraction was assumed for all cloud types, including fog and stratiform and convective clouds. Although there existed other types of Cs-bearing particles, found and named as Cs-ball by Adachi et al. (2013), which are totally different in size and hygroscopicity (super micron and nonhygroscopic) than sulfate particles (submicron and hygroscopic), the Cs-ball was not considered in the current simulation, following almost all previous simulation studies, except those of Adachi et al. (2013) and Kajino, Sekiyama, et al. (2018). The impact of Cs-ball on dispersion and deposition will be presented and quantitatively discussed in our next paper. Two options are available for the below-cloud scavenging processes in NHM-Chem, namely, the conventional method and size-resolved method (Kajino, Deushi, et al., 2018). The latter was used for the current simulation, as it is time consuming but considers other processes, such as thermophoresis, diffusiophoresis, and electrostatic forces, which the conventional method does not take into account.

The offline-coupled NHM-Chem was used for this study. An offline model comprises an interface connecting the meteorology model part and the CTM part, which is converting the meteorological model output into the CTM input. An advantage of offline coupling is that various meteorological simulation results can be used for the input of CTM, only by preparing the interfaces between them. On the other hand, hard coding is needed to embed the CTM program into the meteorological model for online coupling.

2.2. Meteorological Simulations and Ensembles

As listed in Table 1, transport simulations using combinations of several meteorological models and simulation settings were compared in this study. Figure 1 shows the purpose of the comparison of meteorological simulations and the method used to produce the ensemble mean of the meteorological field (#9). This figure also shows the method used to produce the ensemble mean of the chemical field (#8).

We used two meteorological models, NHM (ver. 3.5) and the Weather Research and Forecasting (WRF) model (Skamarock et al., 2008; ver. 3.5.1) for the meteorological simulations. Both simulations #1 and #2 in Table 1 used NHM, but for #1, NHM was driven using the JMA's Meso-Regional Objective Analysis (MANAL) as the initial and boundary conditions, while for #2, the data assimilation system of NHM, using the local ensemble transform Kalman filter (LETKF), which was developed by Kunii (2013) and named NHM-LETKF, was used. For #1, the spectral nudging method (Nakano et al., 2012) was used to constrain the model forecast by the MANAL analysis. Spectral nudging was applied above a height of 7 km for the large-scale wave component (wavelength > 1,000 km) of horizontal momentums and potential temperature, with a weighting factor of 0.06. For #2, the simulation of NHM-LETKF itself is the reanalysis.

NHM was developed for the purpose of operational weather forecasting, and only a few combinations of physics modules (i.e., cloud microphysics, radiation, turbulence, and land surface processes) are available. Although the combination of modules was limited, each module has been extensively developed to achieve the best performance of weather prediction in Japan. On the other hand, the Advanced Research WRF was

Table 1
Meteorological Models and Physical Modules Compared in the Study

	Name	Analysis	Data assimilation	Cloud microphysics	Planetary boundary layer
1	NHM[a]	MANAL[b]	Spectral nudging[c]	Six-category double moment[a]	MYNN30[d]
2	NHM-LETKF	—[e]	LETKF[f]	Six-category double moment[a]	MYNN30
3	WRF[g]-WSM6-MYJ	MANAL	Grid nudging	WSM6[h]	MYJ[i]
4	WRF-WDM6-MYJ	MANAL	Grid nudging	WDM6[j]	MYJ
5	WRF-MORR-MYJ	MANAL	Grid nudging	MORR[k]	MYJ
6	WRF-MORR-MYNN25	MANAL	Grid nudging	MORR	MYNN25[l]
7	WRF-MORR-MYNN30	MANAL	Grid nudging	MORR	MYNN30
9	Met_EnsMean[m]	-	-	-	-

[a]NHM: JMA's Nonhydrostatic Model (Saito et al., 2007; JMA [Japanese Meteorological Agency], 2008). [b]MANAL: JMA Meso-Regional Objective Analysis. [c]Nakano et al. (2012). [d]MYNN30: Mellor-Yamada-Nakanishi-Niino level 3.0 scheme (Nakanishi & Niino, 2006). [e]This is a meteorological analysis. [f]LETKF: Local ensemble transform Kalman filter (Kunii, 2013; Sekiyama et al., 2017). [g]WRF: Weather Research and Forecast model (Skamarock et al., 2008). [h]WSM6: six-category single moment cloud microphysics scheme (Lin et al., 1983). [i]MYJ: Mellor-Yamada-Janjic scheme (Janjic, 2002). [j]WDM6: six-category double moment cloud microphysics scheme (Lim & Hong, 2010). [k]MORR: Morrison's double moment cloud microphysics scheme (Morrison et al., 2009). [l]MYNN25: Mello-Yamada-Nakanishi-Niino level 2.5 scheme (Nakanishi & Niino, 2006). [m]Met_EnsMean: Meteorological model ensemble mean ([1] + [2] + ([3] + [4] + ([5] + [6] + [7])/3)/3)/3.

developed for research purposes; thus, a number of physics modules have been implemented and can be compared.

From #3 to #7, in order to evaluate the sensitivity of the physics modules, we conducted multimodule simulations of WRF using three different cloud microphysics modules (Lin et al., 1983; Lim & Hong, 2010; Morrison et al., 2009, denoted as WSM6, WDM6, and MORR, respectively) and three different planetary boundary layer (PBL) physics modules (Janjic, 2002, and level 2.5 and level 3 of Nakanishi & Niino, 2006, denoted as MYJ, MYNN25, and MYNN30, respectively). Instead of comparing all nine combinations, five were selected for comparison, using MORR-MYJ as a control run: the combination of WSM6-MYJ, WDM6-MYJ, and MORR-MYJ was selected for the comparison of cloud microphysics modules, and the combination of MORR-MYJ, MORR-MYNN25, and MORR-MYNN30 was selected for the comparison of

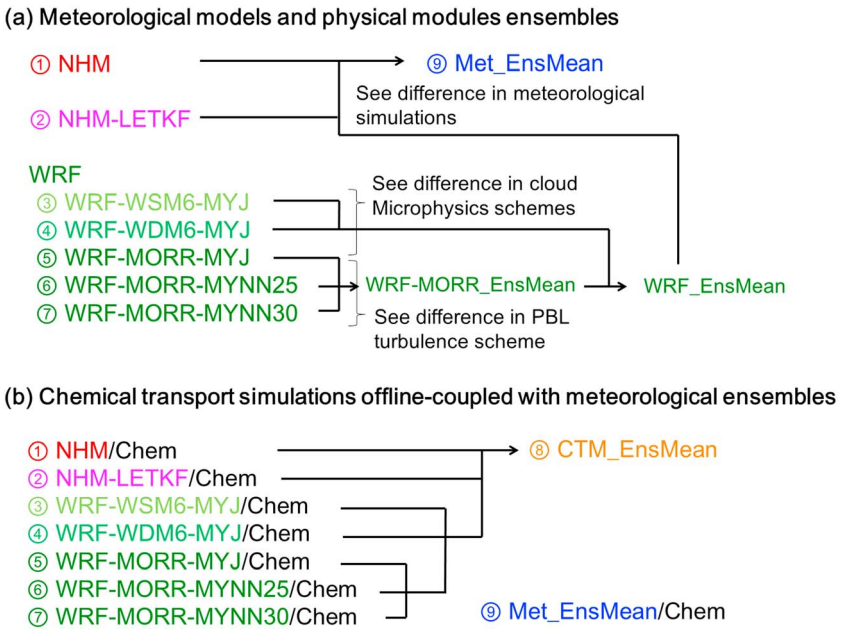

Figure 1. Meteorological models, meteorological model ensembles, and chemical transport simulations together with its ensemble, used and compared in the study. NHM = Nonhydrostatic Model; LETKF = local ensemble transform Kalman filter; WRF = Weather Research and Forecasting; CTM = chemical transport model; PBL = planetary boundary layer.

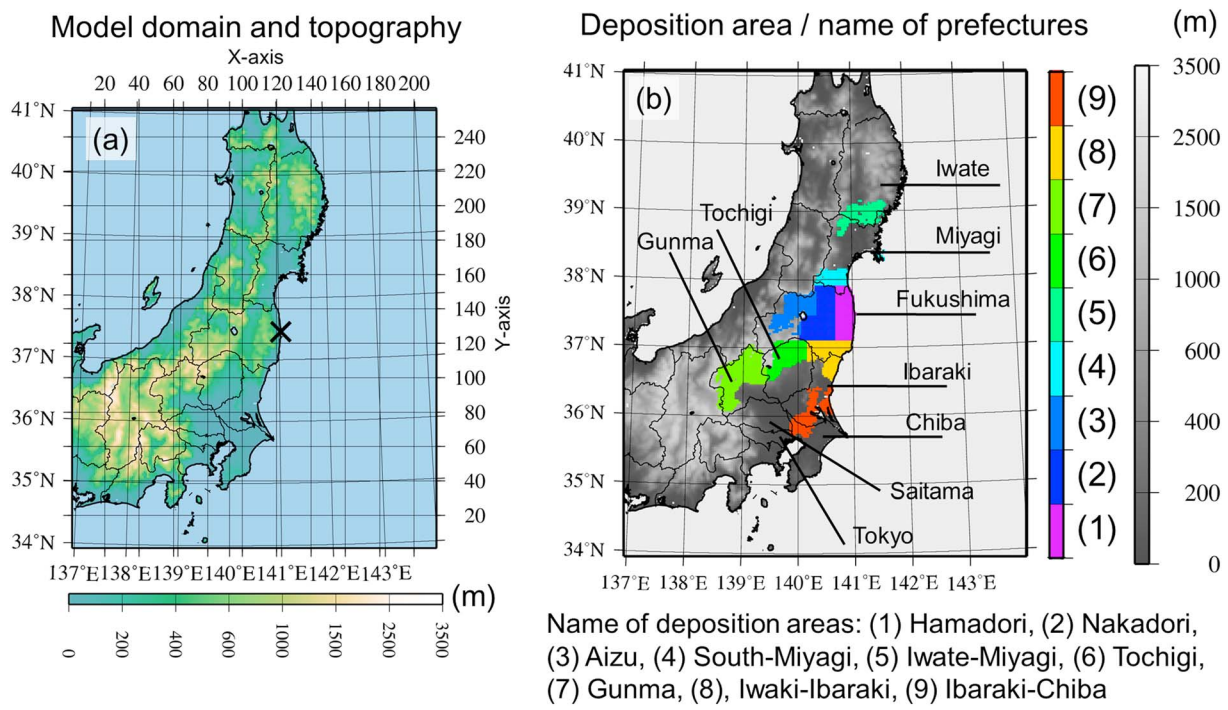

Figure 2. (a) Model domain and topographic height. (b) Deposition area defined in the study.

PBL modules, as shown in Figure 1a. MANAL was also used as the initial and boundary conditions, as well as for the grid nudging. Grid nudging was applied for horizontal wind speed, temperature, and water vapor, with a nudging factor of 0.0003, only above the PBL.

Instead of equally averaging the seven meteorological simulations, the following averaging was performed to produce the meteorological ensemble mean (#9, Met_EnsMean): Met_EnsMean is an average of NHM, NHM-LETKF, and WRF_EnsMean; WRF_EnsMean is an average of WRF-WSM6-MYJ, WRF-WDM6-MYJ, and WRF-MORR_EnsMean; and WRF-MORR_EnsMean is an average of WRF-MORR-MYJ, WRF_MORR-MYNN25, and WRF_MORR-MYNN30. The ensemble mean of the seven transport simulations, #8 CTM_EnsMean, was obtained in the same manner, as is shown in Figure 1b. The unweighted average is significantly biased toward the meteorological fields produced by the WRF simulations because all of the WRF simulations were predicted by a common dynamic core and constrained to MANAL. Even though the NHM simulation was also constrained to MANAL, the simulations of NHM were significantly different from those performed by WRFs, because the dynamic cores of the models and their methods of constraint were different (i.e., grid nudging vs. spectral nudging). Although the dynamic cores of NHM and NHM-LETKF were similar, the two simulations were significantly different due to the differences in their initial and boundary conditions. This feature is obviously found in the surface concentrations, as shown later in Figure 4 (see the differences in mean bias [*MB*] and the shapes of scatter diagrams between NHM, NHM-LETKF and WRFs).

Overall, we used eight meteorological model variations and nine chemical model variations for the current comparison study.

2.3. Simulation Settings

As shown in Figure 2a, the simulation domain and grid resolution are the same as those used in our previous studies (Adachi et al., 2013; Sekiyama et al., 2015, 2017). There are 213 × 257 horizontal grid cells with a 3-km grid resolution on the Lambert conformal coordinate. There are 48 vertical layers reaching up to approximately 22 km above sea level (ASL) for NHM and 27 layers reaching up to 100 hPa for WRF, which are reduced to 19 layers reaching up to 10 km ASL for the CTM on the terrain-following coordinate with vertically stretched grids (with more grids at lower levels to resolve the dynamics within the PBL). The latest version of the Japan Atomic Energy Agency's (JAEA) emission scenario, as established by Katata et al. (2015),

was selected for all simulations. The meteorological simulation was conducted from 00 UTC on March 11 to 00 UTC on 1 April, with a spin-up period of 20 hr: Katata et al.'s (2015) emission was initiated at 20 UTC on 11 March.

In the current simulation, as mentioned earlier, all of the radio-Cs nuclides were carried by sulfate aerosols, as inferred by Kaneyasu et al. (2012) and assumed by all simulations except for those of Adachi et al. (2013) and Kajino, Sekiyama, et al. (2018). In terms of the physical parameters of Cs-carrying sulfate during the emission (although sulfate is clearly "not" directly emitted from the reactor, it is assumed that the emitted Cs was mixed with environmental sulfate aerosols immediately after its emission from the reactor), we used a number-equivalent geometric mean dry diameter of 102 nm, a geometric standard deviation of 1.6, a particle density of 1.83 g/cm^3, and a hygroscopicity κ of 0.4 (see Adachi et al., 2013).

2.4. Observation Data

The JMA Radar/rain gauge-Analyzed Precipitation (RAP) data were used for the validation of the simulated precipitation amount. Since the RAP data provide 1-hr precipitation data with 30-min resolutions starting from 0 and 30 min, only data starting from 0 min were used in the study. The aircraft measurement data of NRA (2012) were interpolated to the model domain and used for the validation of the simulated deposition amount of ^{137}Cs. The simulated surface concentrations of ^{137}Cs were validated by the hourly observation data of 99 stations obtained by Tsuruta et al. (2014) and Oura et al. (2015).

2.5. Deposition Areas

The deposition areas used for the process analysis of this study are shown in Figure 2b. The deposition areas were selected where the grid mean (3-km) deposition of the aircraft measurement (NRA, 2012) exceeded 10 kBq/m^2, as shown later in Figure 5. These areas were divided into nine subareas based on the geography (mainly mountains), prefectures, and possible deposition processes (or events), which are also summarized in Morino et al. (2013) and Mathieu et al. (2018). The observed total deposition amount of ^{137}Cs over the entire land area of Japan (denoted as Area 0) was 2.59 PBq. Hamadori (Area 1) is a coastal area of Fukushima prefecture where FDNPS is located and bordered by the Abukuma Highlands, which are moderately high mountains (~1,000 m). The largest amount of deposition, 1.4 PBq, occurred in this area, which amounted to 53.4% of the total land deposition (as shown later in Table 3). Nakadori (Area 2), which is located next to Hamadori, is a valley between the Abukuma Highlands and the Ou Mountains, a high mountain chain (1,000~2,000 m). The second-largest amount of deposition occurred in this area, 0.44 PBq, which is 17.1% of the total land deposition. The major amounts of deposition in Hamadori and Nakadori were caused by light precipitation, which was lower than the detection limit of rain-gauge measurement (0.5 mm) or dry deposition (Mathieu et al., 2018). A total of 70% of deposition occurred in these two areas. Aizu (Area 3), which is located next to Nakadori, is located west of the dividing Ou Mountains; thus, it was less contaminated compared to the rest of Fukushima prefecture (0.076 PBq, 2.9%). South Miyagi (Area 4; 0.047 PBq, 1.8%) and Iwate-Miyagi (Area 5; 0.038 PBq, 1.4%) are located in the northern region of Fukushima prefecture. The Iwate-Miyagi area is isolated; thus, its contamination is presumed to have occurred due to air-aloft processes, that is, in-cloud scavenging. In Tochigi (Area 6) and Gumma (Area 7) prefectures, contamination occurred mainly over mountainous regions, and the importance of fog deposition (or cloud deposition) was inferred by Hososhima and Kaneyasu (2015), Katata et al. (2015), Sanada et al. (2018), and this study. The deposition of ^{137}Cs over both areas totaled 0.21 PBq, which represented 7.9% of the total land deposition. (Area 8) Iwaki-Ibaraki and (Area 9) Ibaraki-Chiba are located in the southern region of Fukushima prefecture; their ^{137}Cs depositions were 0.11 PBq (4.3%) and 0.044 (1.7%), respectively. The deposition amount for the remaining land areas, that is, areas with <10 kBq/m^2, or Area 0 minus the sum of Areas 1 to 9, was 0.24 PBq (9.4%).

3. Results

3.1. Comparison of Precipitation Fields

Throughout the paper, we only focus on ^{137}Cs because the atmospheric behavior and radioactivity of ^{134}Cs should be almost the same as those of ^{137}Cs for the current analysis. Certainly, the slight difference in the activities of ^{134}Cs and ^{137}Cs was essentially important for the analysis of their origins, as conducted by Satou et al. (2018). Thus, the simulation results of all radio-Cs can be obtained by doubling the results of ^{137}Cs.

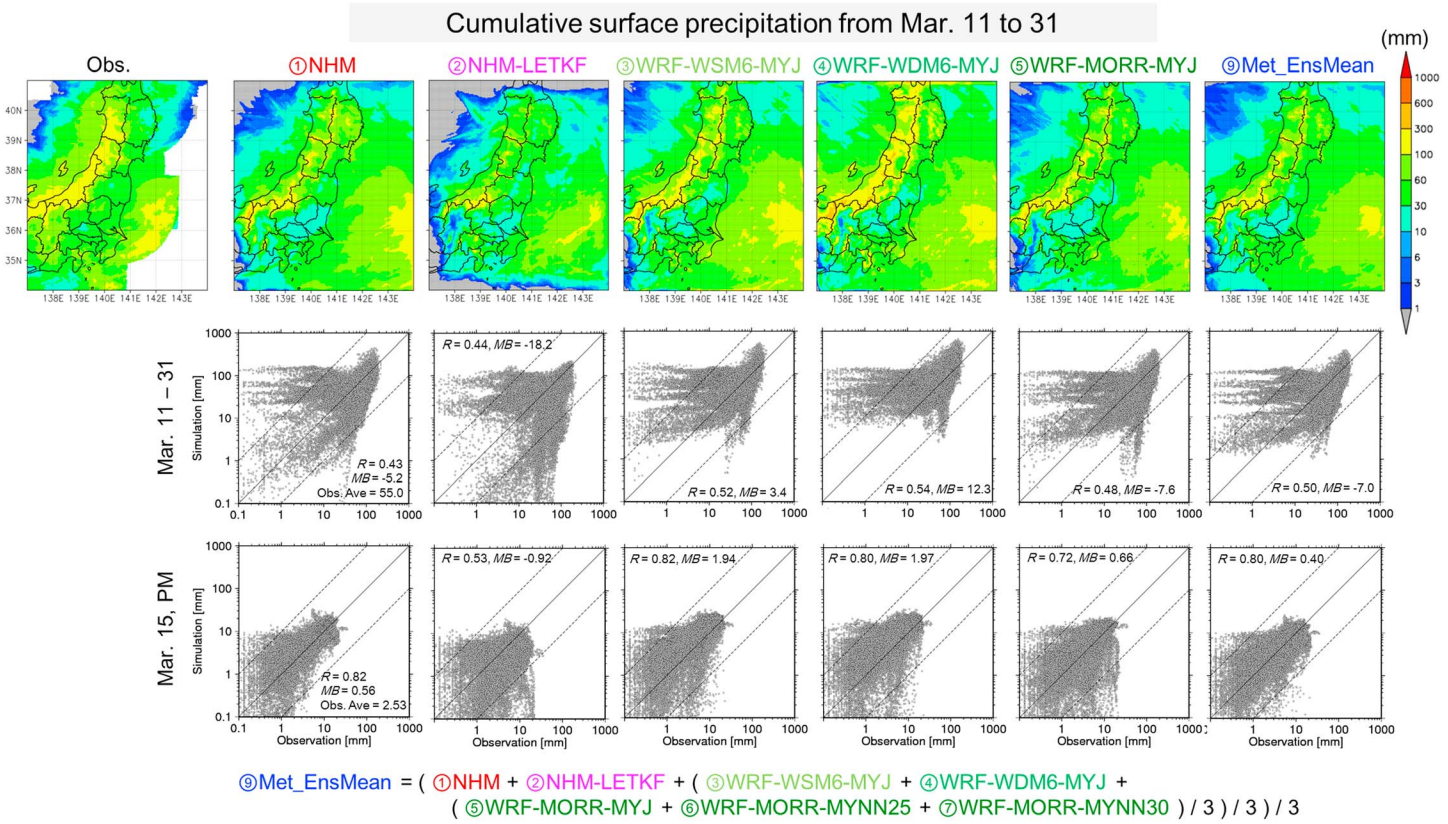

Figure 3. (upper panel) Horizontal distributions of observed and simulated cumulative precipitation from 11 to 31 March. (middle and lower panel) Scattergrams between observation and simulations for the whole period (middle) and for the afternoon (12–24 LT) of 15 March, when the most serious contamination occurred over the land of Japan. The correlation coefficient *R*, observed areal average, and mean bias (*MB*) values are embedded in the panels. NHM = Nonhydrostatic Model; LETKF = local ensemble transform Kalman filter; WRF = Weather Research and Forecasting.

Figure 3 shows the observed and simulated horizontal distributions of the cumulative precipitation from 11 to 31 March over the model domain in the upper panels. The middle and lower panels show the scattergram between the observed and simulated precipitation for the whole period and that during the afternoon of 15 March, respectively. The RAP data below the detection limit (0.5 mm/hr) were not added to the cumulative amount. The horizontal average of the RAP data (with a resolution of approximately 1 km) was made to match the model grids (Δx = 3 km) in order to directly compare the simulated and observed values. Due to the horizontal averaging, there are observed values below 0.5 mm in the scattergrams. Note that 10 grids from the lateral boundaries of the model domain were excluded from the comparison scattergrams. The observed areal average (obs. ave. = 55.0 mm), correlation coefficient *R*, and mean bias (*MB*) are embedded in the panels. Note that *R* is the linear-linear correlation despite the log-log plot of the scattergrams. Additionally, the RAP has a larger uncertainty for light precipitation due to the detection limits of the small droplet size (such as drizzle) for the C-band radar and the precipitation amount of the rain gauge (0.5 mm).

In terms of the cumulative precipitation from 11 to 31 March, WRF-WDM6 predicted the largest precipitation (*MB* = 12.3 mm), especially over the mountainous regions located at the center of the Japan Archipelago, where the cumulative precipitation exceeded 300 mm. WRF-WSM6 also overestimated precipitation, but to a lower degree (*MB* = 3.4). Despite the common dynamic core used, WRF-MORR did not show any overestimation over the mountainous regions and underestimated the values for the whole region (*MB* = −7.6). These data indicate that the selection of cloud microphysics modules is essentially important for the prediction of precipitation. They also indicate that the precipitation was well predicted by the WRF ensembles because the observed values fell between the minimum and maximum estimates, that is, the observed values were within the uncertainty of the cloud microphysics modules. Both NHM models

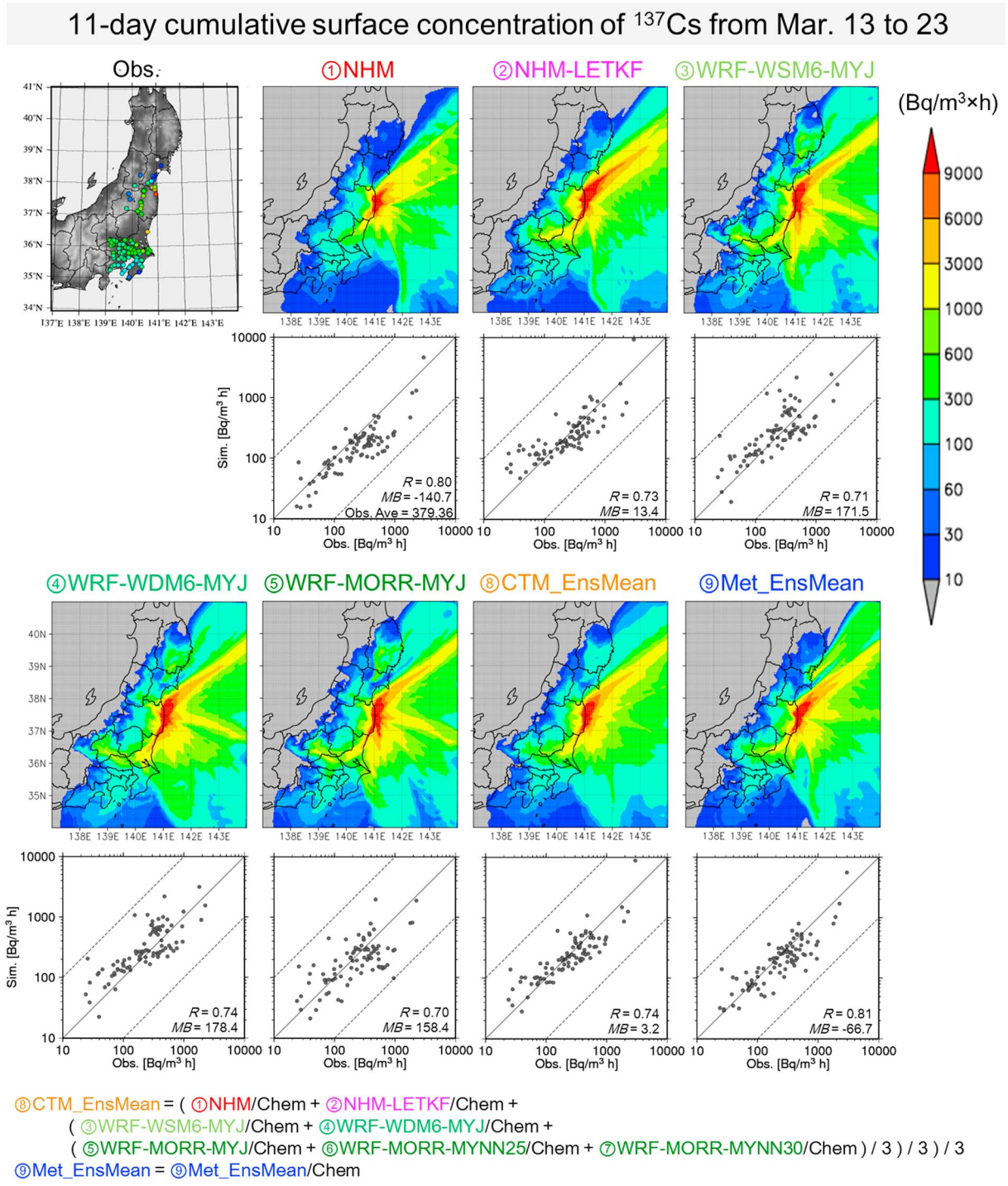

Figure 4. Horizontal distributions of observed and simulated cumulative surface concentrations from 13 to 23 March and scattergrams between observations and simulations. The correlation coefficient *R*, observed areal average, and mean bias (*MB*) values are embedded in the panels. The observation data in each model grid were averaged and used for the comparison. NHM = Nonhydrostatic Model; LETKF = local ensemble transform Kalman filter; WRF = Weather Research and Forecasting; CTM = chemical transport model.

underestimated the observations, but the underestimation of NHM-LETKF (*MB* = −18.2) was greater than that of NHM (*MB* = −5.2) due to the different treatments of their lateral boundary conditions. The lateral boundary of NHM contained hydrometeors, while that of NHM-LETKF did not (it only contains water vapor). Although 10 grids from the lateral boundaries were excluded in this comparison, the lateral

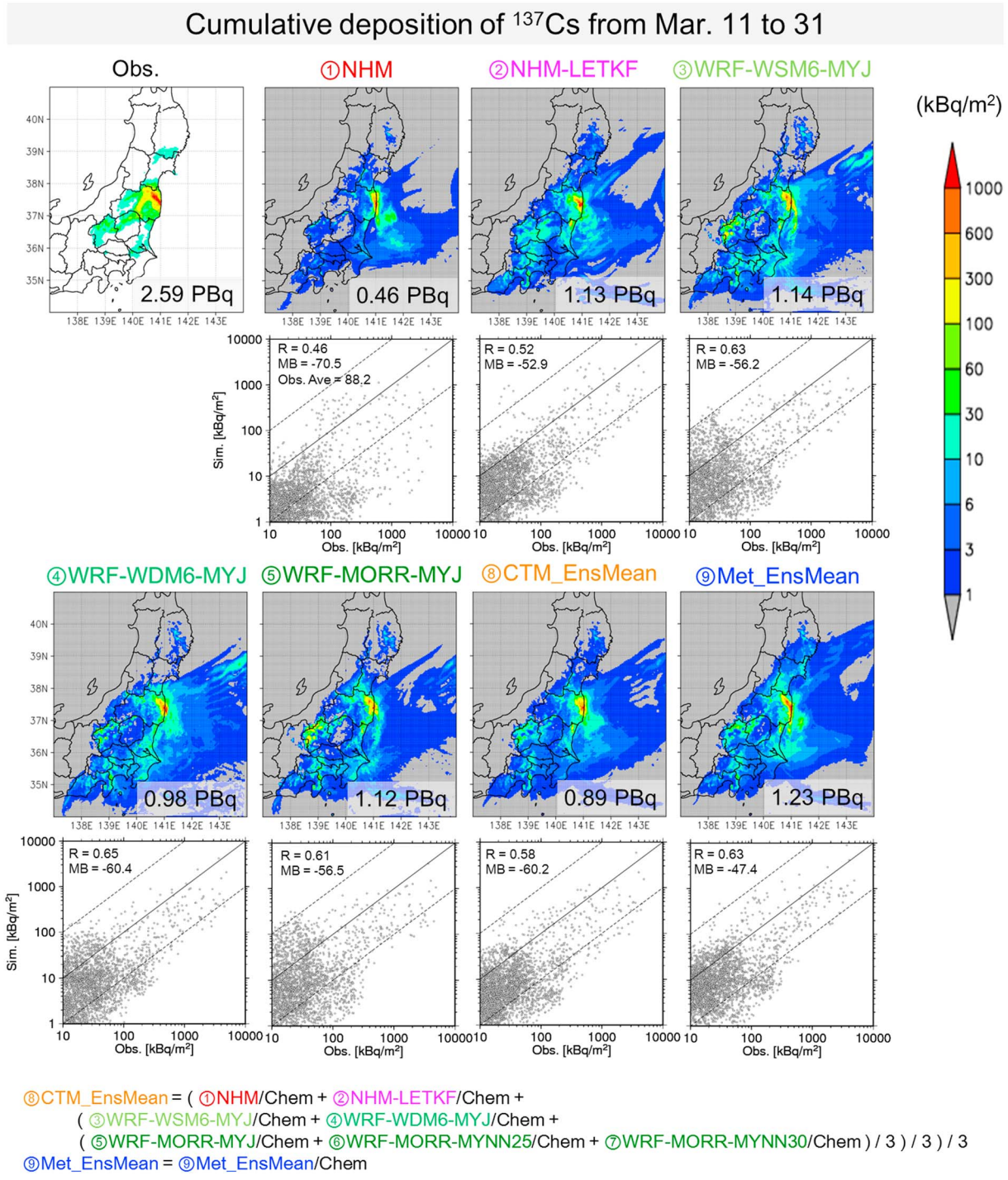

Figure 5. Horizontal distributions of observed and simulated cumulative deposition of ^{137}Cs from 11 to 31 March and scattergrams between observations and simulations. The gross deposition amounts, correlation coefficient *R*, observed areal average, and mean bias (*MB*) values are embedded in the panels.
NHM = Nonhydrostatic Model; LETKF = local ensemble transform Kalman filter; WRF = Weather Research and Forecasting; CTM = chemical transport model.

boundary conditions affected this analysis. Nevertheless, the artifact of the lateral boundary conditions is minor because the major deposition areas (e.g., Figure 2b) are well centered in the model domain. It is also noted here that the radioactive plumes were blocked by the high mountain chains; thus, the overestimation of precipitation over mountainous areas predicted by WRF-WSM6 and WRF-WDM6

should not deteriorate the model performances in the prediction of the wet deposition of ^{137}Cs. The correlation coefficients were not very different between the models, as they ranged from 0.43 (NHM) to 0.54 (WRF-WDM6). Although they are not shown here, the differences in the PBL turbulence schemes (WRF-MORR-MYJ, WRF-MYNN25, and WRF-MYNN30) were not significant for the predictions of precipitation (R: 0.48–0.48, MB: −9.8 to −7.6). Again, the precipitation was well predicted by the current meteorological model ensembles because the observed values fell between the minimum (NHM-LETKF) and maximum estimates (WRF-WDM6).

The simulated precipitation of Met_EnsMean was successful in reducing variance, yielding a higher R (0.50) value than the lowest one of NHM (0.43) and a lower absolute value of MB (7.0) than those of NHM-LETKF (18.2) and WRF-WDM6 (12.3).

In terms of the cumulative precipitation on the afternoon of 15 March, a similar conclusion was inferred as in the case of the entire simulation period: overestimation by WRF-WDM6 (MB = 1.97) and WSM6 (MB = 1.94) and underestimation by NHM-LETKF (−0.92). The precipitation was well predicted by the current meteorological model ensembles because the observed values fell within the minimum (NHM-LETKF) and maximum estimates (WRF-WDM6). Here NHM, the operational forecast model of the JMA, performed best in this case (yielding the highest R, lowest absolute value of MB, and narrowest aggregation of plots). The Met_EnsMean was successful, yielding a high R (0.80) close to the highest values (0.82 of NHM and WRF-WSM6) and showing the lowest absolute value of MB (0.40).

3.2. Comparison of ^{137}Cs Surface Concentration Fields

Figure 4 shows the observed and simulated horizontal distributions of the cumulative concentration (Bq·m^{-3}·hr) from 13 to 23 March. The observation data were averaged to the model 3-km grids and then compared with the simulated data. Still, however, the values in this comparison are biased toward the data of areas, where the observation sites are densely situated, that is, Tokyo and the surrounding areas. The observed areal average (obs. ave. = 379 Bq·m^{-3}·hr), correlation coefficient R, and mean bias (MB) values are embedded in the panels. The WRF simulations overestimated the observed values (MB = 158–178 Bq·m^{-3}·hr), the NHM simulations underestimated them (MB = −140.7), and the NHM-LETKF yielded the best MB value (13.4). Same as in the precipitation prediction, the surface activity concentration was also well predicted by the current meteorological model ensembles because the observed values fell within the minimum (NHM) and maximum (WRF-WDM6) estimates.

Because all the models used a common horizontal diffusion scheme, the differences in model performance were mainly due to vertical diffusion and horizontal advection. Since both the NHM and NHM-LETKF also employ the same Mellor-Yamada-type PBL scheme (MYNN30) as the WRF simulations, the differences in the simulated surface air concentrations due to differences in vertical diffusivities were not significant. Within the PBL, all of the simulations were not assimilated to the meteorological analysis data, except for NHM-LETKF: the surface wind data of the JMA's Automated Meteorological Data Acquisition System at more than 200 stations in the model domain were assimilated to the simulation (Sekiyama et al., 2017). This partly explains why NHM-LETKF-Chem performed best in the quantitative simulation of the surface activity concentrations of ^{137}Cs. The correlation coefficients obtained in all simulations were very similar to each other (R = 0.70–0.81). The CTM_EnsMean was successful in reducing variance, yielding a higher R (0.74) value than the lowest one of WRF-MORR (0.70) and showing the lowest absolute value of MB (3.2) compared to any other simulations.

The CTM simulation performed by Met_EnsMean (denoted as Met_EnsMean) was shown to perform well in the simulation of concentrations, showing the highest R (0.81) value and lower absolute value of MB (66.7) compared to the largest one of WRF-WDM6 (178.4). It is not surprising that the performance of CTM_EnsMean was good, but it is not necessary that the performance of Met_EnsMean-Chem was good. This is one of the major implications of the current study.

The simulated concentration of WRF-WDM6 was the largest, although the simulated precipitation of this model was also the largest. This appears to be contradictory, as precipitation removes aerosols. However, this result is still not surprising because below-cloud scavenging was not a controlling factor of the prediction of surface concentration, as is discussed extensively in sections 4.1 and 4.2.

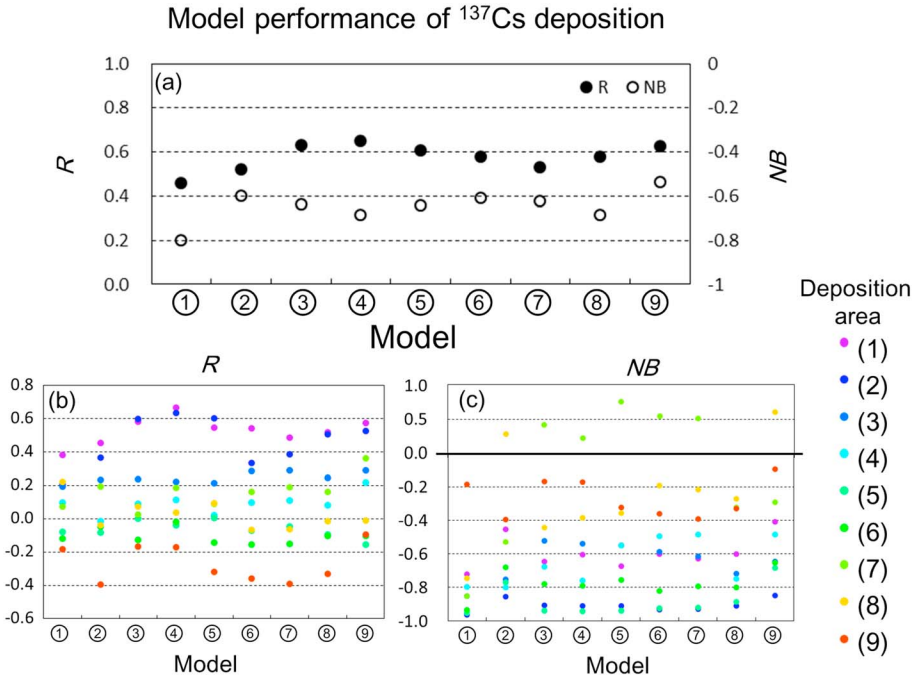

Figure 6. (a) The correlation coefficient *R* and normalized mean bias (*NB*) values of the cumulative ^{137}Cs deposition between the observed and simulated values by the nine models over the entire land area of Japan (Area 0). (b, c) Same as (a) but for (b) *R* and (c) *NB* over the nine deposition areas as defined in Figure 1.

3.3. Comparison of ^{137}Cs Deposition Fields Over Deposition Regions

Figure 5 shows the observed and simulated horizontal distributions of the cumulative deposition (kBq/m^2). The total land deposition (PBq), observational areal average (obs. ave. = 88.2 kBq/m^2), correlation coefficient *R*, and mean bias (*MB*) values are embedded in the panels. Note that *R* represents the linear-linear correlation between the data above the observational detection limit (10 kBq/m^2). The simulated *R*s of the ^{137}Cs depositions ($R = 0.46$–0.65) were not as large as those obtained in previous studies ($R > 0.7$–0.8; e.g., Draxler et al., 2015; Morino et al., 2013), but they were similar to those of simulated precipitation for the whole period ($R = 0.43$–0.54) and significantly lower than those of the cumulative concentrations ($R = 0.70$–0.81). The *R* and normalized bias values (*NB*; *MB* divided by the observational mean) over the entire land area (Area 0) and the nine depositional areas of the nine simulations are shown in Figure 6. All of the values of *R* and *NB* are listed in Tables 2 and 3, respectively.

In contrast to the precipitation and surface concentration simulations, all of the simulations underestimated the observations. The reason for this is discussed later in section 4.2.1. As shown in Figure 5, NHM significantly underestimated the ^{137}Cs deposition ($MB = -70.5$), whereas the underestimations of the other simulations were similar to each other: The largest deposition was simulated by NHM-LETKF ($MB = -52.9$), and the smallest deposition after NHM was simulated by WRF-WDM6 (−60.4). In terms of *R*, the WRF simulations showed better agreements with the observed ^{137}Cs deposition ($R = 0.61$–0.65), as they could successfully reproduce the general features of the deposition map: The most contaminated regions extended toward the northwest direction from the FDNPS (Area 1, 53.4% of total land deposition), the second-most contaminated regions were in the Nakadori valley (Area 2, 17.1%), and the third-most contaminated regions occurred over the mountain regions of Tochigi and Gunma prefectures (Area 6 + Area 7, 7.9%), the regions south of FDNPS and the Kanto plain (Area 8 + Area 9, 6.0%; see Figure 5). In fact, because *R* was obtained from the linear-linear relationship, the *R* values over the entire land region were determined by the magnitudes of *R* over Areas 1 and 2 (Figures 6a and 6b). The *R* of NHM was lowest (0.46) because it did not reproduce the northwest direction of the highest contamination over Area 1 and the deposition amounts over Nakadori (Area 2) and Tochigi and Gunma (Area 6 + Area 7) were significantly underestimated. Although NHM-LETKF the showed best quantity over Area 1, it significantly underestimated the

Table 2
Correlation Coefficients (R) Between Simulated and Observed Cumulative Depositions of Radio-Cesium for Each Deposition Area and Combination of Numerical Models, as Shown in Figures 6a and 6b

Model/deposition area	1 NHM	2 NHM-LETKF	3 WRF-WSM6-MYJ	4 WRF-WDM6-MYJ	5 WRF-MORR-MYJ	6 WRF-MORR-MYNN25	7 WRF-MORR-MYNN30	8 CTM_EnsMean	9 Met_EnsMean	Average of R[a]
0 = (entire land)	0.46	0.52	0.63	0.65	0.61	0.58	0.53	0.58	0.63	0.58
1 (Hamadori)	0.38	0.45	0.57	0.60	0.56	0.55	0.48	0.50	0.57	0.52
2 (Nakadori)	0.19	0.37	0.58	0.64	0.60	0.38	0.46	0.53	0.59	0.48
3 (Aizu)	0.21	0.24	0.24	0.24	0.21	0.28	0.28	0.25	0.27	0.25
4 (South Miyagi)	0.14	−0.07	0.16	0.41	0.06	0.15	0.15	0.16	0.28	0.16
5 (Iwate-Miyagi)	−0.09	−0.06	0.01	−0.02	0.02	−0.07	−0.05	−0.08	−0.17	−0.06
6 (Tochigi)	−0.11	0.00	−0.13	−0.04	−0.14	−0.15	−0.15	−0.08	−0.06	−0.10
7 (Gunma)	0.07	0.26	0.03	0.03	0.09	0.17	0.20	0.14	0.36	0.15
8 (Iwaki-Ibaraki)	0.17	−0.04	0.02	0.10	0.05	−0.07	−0.06	−0.03	0.17	0.03
9 (Ibaraki-Chiba)	−0.18	−0.39	−0.23	−0.18	−0.37	−0.36	−0.40	−0.34	−0.10	−0.28
Average of R[b]	0.12	0.13	0.19	0.24	0.17	0.15	0.15	0.16	0.25	

[a]Statistically nonsensical but useful measure to compare the mean predictability over different deposition areas. [b]Statistically nonsensical but useful measure to compare the mean predictability of different models.

deposition amounts over Nakadori (Area 2; Figure 6c). In Tochigi and Gunma prefectures, simulated depositions were found over the plain areas rather than in the mountain areas, in contrast to the aircraft observation.

The CTM_EnsMean was successful: Its R (0.58) was higher than the lowest one (0.46) predicted by NHM, and its absolute value of MB (60.2) was lower than the highest one (70.5) predicted by NHM. Because the performance of NHM was the worst in both aspects (R and MB), the performances of single WRF simulations were better than or as good as those of the CTM_EnsMean. NHM performed very well in terms of precipitation and NHM-LETKF performed best in the simulations of concentrations, whereas WRF simulations were better in terms of the simulations of ^{137}Cs deposition. This appears to be contradictory; the reason for this disparity is briefly discussed later in section 4.2.2.

It appears surprising that the Met_EnsMean-Chem performed significantly well in the simulation of ^{137}Cs deposition: Its R (0.63) was as large as the largest R (0.65) predicted by WRF-WDM6, and its MB (−47.4) was the best of all the simulations (−70.5 to −52.9). This is due simply to the enhancement of precipitation areas by the ensemble mean. Because precipitation areas are spatially sporadic and not continuous, using the ensemble mean of different precipitation fields should enlarge the precipitation area and decrease the spatial peaks. Contamination was caused by light precipitation after the FDNPS accident; thus, the enhanced light precipitation areas resulted in the enhancement of the simulated total ^{137}Cs deposition.

4. Discussion

4.1. Dominant Deposition Processes

Figure 7 shows (upper panel) the observed and simulated deposition amounts and (lower panel) contributions of deposition processes simulated by the nine models of the entire land area (Area 0) and the nine deposition areas. All of the models generally underestimated the observed deposition amounts, except in Gunma (Area 7), where the observed value fell within the range of uncertainty in the simulations. The underestimation was not very significant in the southern direction of FDNPS, that is, Area 8 and Area 9. The simulated values of NHM-LETKF and WRF-WDM6 were sufficiently close to the observed values for Area 8 and Area 9, respectively (also see Table 3). The underestimation of the simulation over the entire land was approximately 1.5 PBq, except in NHM, where it was approximately 2.0 PBq. Except for NHM, out of the 1.5 PBq of underestimation, 1 PBq was found in Hamadori (Area 1), and the other 0.5 PBq originated from Nakadori (Area 2).

The current ensemble study indicated that in-cloud scavenging (both solid and liquid precipitations) was the most dominant mechanism of the ^{137}Cs deposition; the next most dominant mechanisms were dry deposition and fog deposition, depending on the simulations and deposition regions. From southern to northern

Journal of Geophysical Research: Atmospheres

10.1029/2018JD028998

Table 3
Same as Table 2 but for Normalized Bias (NB), as Shown in Figures 6b and 6b

Model/deposition area	1 NHM	2 NHM-LETKF	3 WRF-WSM6-MYJ	4 WRF-WDM6-MYJ	5 WRF-MORR-MYJ	6 WRF-MORR-MYNN25	7 WRF-MORR-MYNN30	8 CTM_EnsMean	9 Met_EnsMean	Average of *NB*[a]	Observed ^{137}Cs deposition (PBq) and contribution to the whole area (%)
0 (entire land)	−0.80	−0.60	−0.64	−0.68	−0.64	−0.61	−0.62	−0.68	−0.54	−0.65	2.6
1 (Hamadori)	−0.72	−0.53	−0.65	−0.67	−0.69	−0.62	−0.64	−0.64	−0.47	−0.63	1.4 (53.4)
2 (Nakadori)	−0.97	−0.86	−0.92	−0.91	−0.91	−0.93	−0.93	−0.92	−0.87	−0.91	0.44 (17.1)
3 (Aizu)	−0.89	−0.77	−0.55	−0.57	−0.56	−0.60	−0.62	−0.74	−0.67	−0.66	0.076 (2.9)
4 (South Miyagi)	−0.81	−0.82	−0.68	−0.65	−0.56	−0.52	−0.52	−0.75	−0.54	−0.65	0.047 (1.8)
5 (Iwate-Miyagi)	−0.96	−0.78	−0.94	−0.95	−0.94	−0.93	−0.93	−0.89	−0.69	−0.89	0.038 (1.4)
6 (Tochigi)	−0.95	−0.68	−0.78	−0.85	−0.76	−0.82	−0.79	−0.81	−0.61	−0.78	0.088 (3.4)
7 (Gunma)	−0.87	−0.55	0.42	−0.20	0.75	0.55	0.52	−0.38	−0.28	−0.01	0.12 (4.5)
8 (Iwaki-Ibaraki)	−0.78	−0.07	−0.50	−0.60	−0.45	−0.25	−0.29	−0.44	−0.21	−0.40	0.11 (4.3)
9 (Ibaraki-Chiba)	−0.18	−0.39	−0.23	−0.18	−0.37	−0.36	−0.40	−0.34	−0.10	−0.28	0.044 (1.7)
Average of *NB*[b]	−0.79	−0.60	−0.54	−0.62	−0.50	−0.50	−0.51	−0.65	−0.49		
Land except areas 1–9 (PBq) and contribution to the simulated entire land deposition (%)	0.11 (23.1)	0.28 (25.0)	0.36 (31.3)	0.32 (32.1)	0.35 (30.9)	0.28 (25.8)	0.27 (25.9)	0.24 (26.8)	0.31 (25.8)		0.24 (9.4)

[a]Statistically nonsensical but useful measure to compare the mean predictability over different deposition areas. [b]Statistically nonsensical but useful measure to compare the mean predictability of different models.

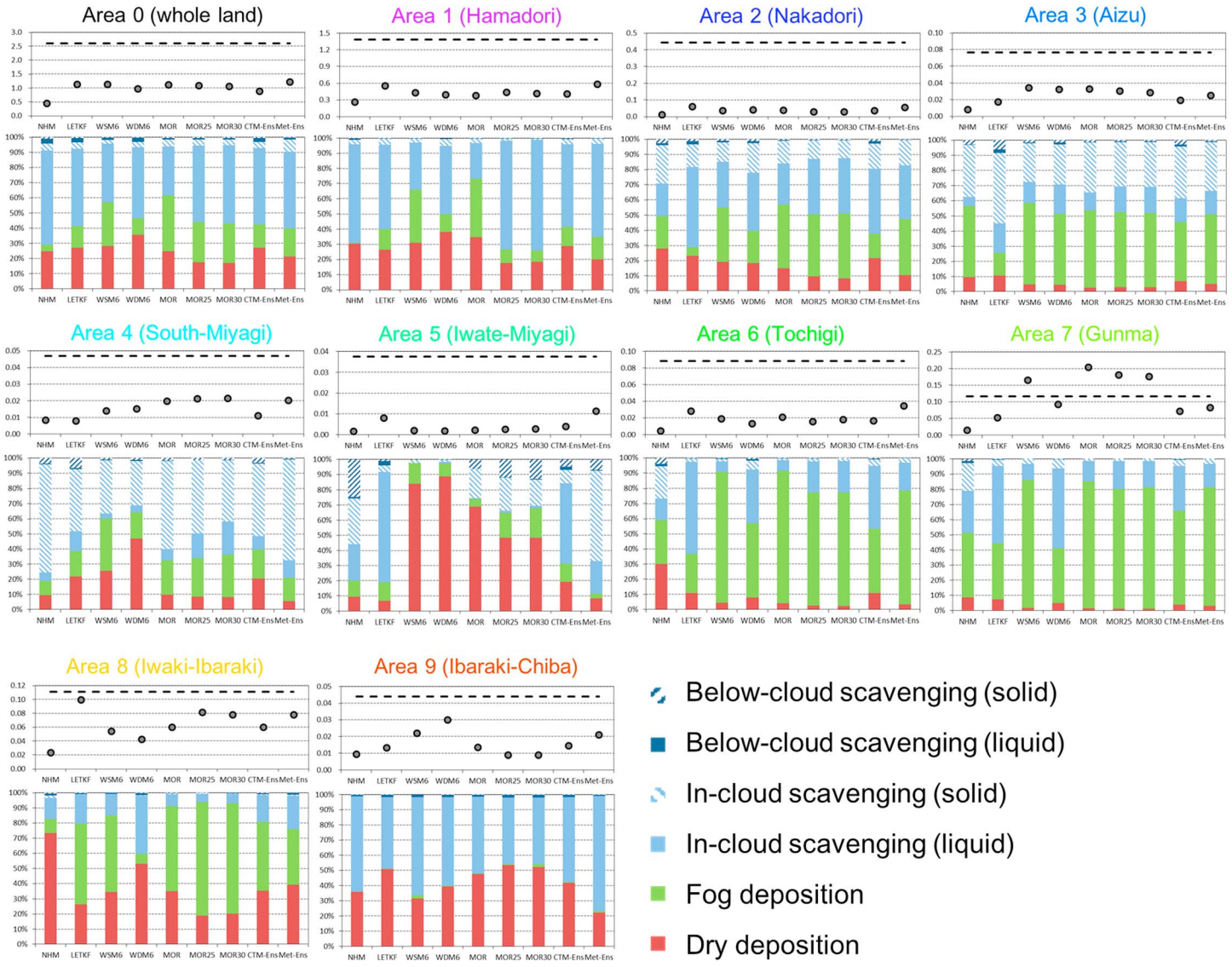

Figure 7. (upper panels) The observed (dashed line) and nine-model simulated (circles) gross deposition of ^{137}Cs (PBq) for the entire land area of Japan (denoted as Area 0) and the nine deposition areas as defined in Figure 1. (lower panels) The simulated contributions of each deposition process to the total deposition: (red) dry deposition, (green) fog deposition, (sky blue/solid) in-cloud scavenging by liquid precipitation, (sky blue/hatched) in-cloud scavenging by solid precipitation, (navy/solid) below-cloud scavenging by liquid precipitation, and (navy/hatched) below-cloud scavenging by solid precipitation. NHM = Nonhydrostatic Model; LETKF = local ensemble transform Kalman filter.

and lower- to higher-altitude areas, the snow (or solid precipitation) contribution increased (from Areas 1 to 4). As indicated by previous studies, fog deposition was the major process in Tochigi (Area 6) and Gunma (Area 7) prefectures. Because the major part of the Japan Archipelago was covered by mountainous forests, the contribution of fog (or cloud reaching to ground surface of mountains) was ubiquitous, except in Area 9, which is located over the Kanto plain. Different models gave different answers for Area 5: Some said they were dry, while others said they were wet. Additionally, some said they were liquid, while others said they were solid. This deposition area was isolated and located further north of the FDNPS. By assuming isentropic transport, the radioactive plumes that caused deposition over Area 5 could have been aloft; thus, in-cloud scavenging could have been a major process. Among the deposition processes, in-cloud scavenging can be the most difficult to simulate because a number of elemental processes are involved, and each process has its own uncertainty. The offline coupling itself has an inherent limitation in the in-cloud scavenging modeling, as discussed in Kajino, Deushi, et al. (2018); thus, the deposition modeling over Area 5 was also difficult to simulate using the current offline coupling framework.

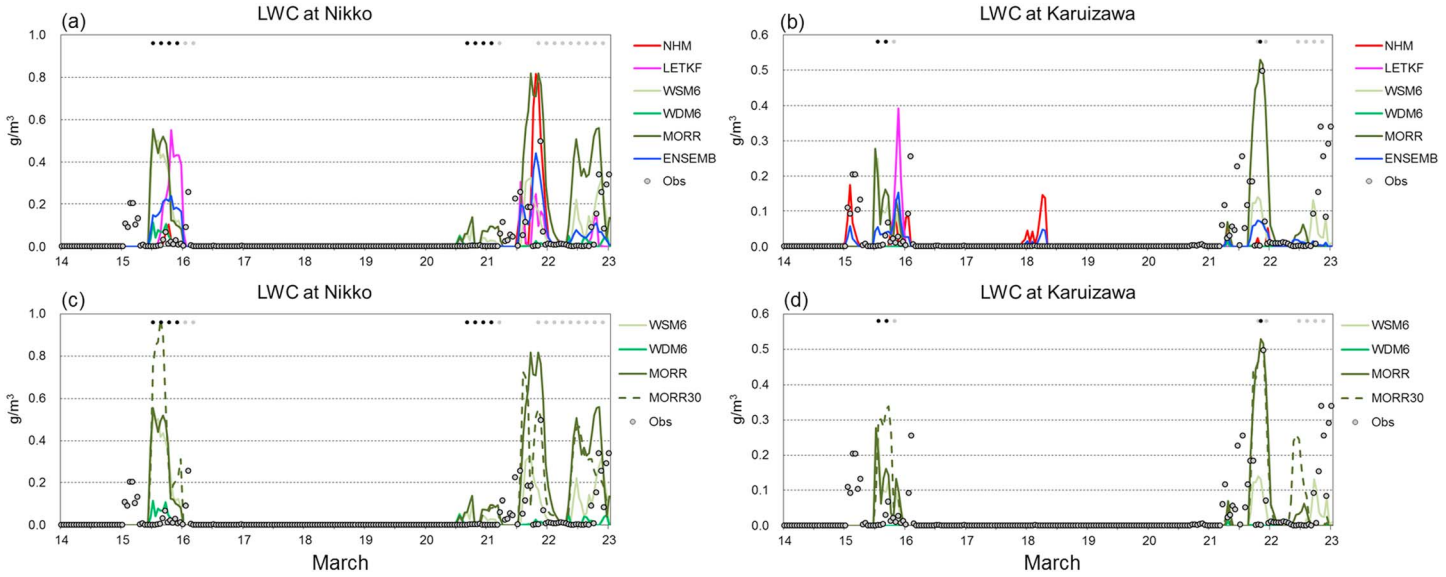

Figure 8. Time series of observed (open circles) and simulated (lines) LWC at Nikko and Karuizawa. The observed liquid water content (LWC) was estimated from the observed visibility. The black and gray dots near the top of each panel indicate the simulated ^{137}Cs concentrations by Met_EnsMean above 1 and 0.1 Bq/m^3, respectively.

The current simulations indicated the importance of fog deposition, which was not considered in previous modeling studies, except for that of Katata et al. (2015). However, there are significant differences in the contributions of fog between the models. Generally, NHM produced less fog deposition. The fog contribution of NHM over Areas 0 and 1 and that of NHM-LETKF over Area 2 were negligibly small. The WRF simulations tended to produce more fog deposition, except for WRF-WDM6, which produced as little fog deposition as NHM and NHM-LETKF. Differences in the selection of the PBL turbulence schemes (MORR-MYJ and MORR-MYNNs) caused significant differences in the fog contribution, especially over Area 1. Figure 8 shows the comparisons of the time series of fog water content at the two mountainous sites at Nikko (Tochigi, Area 6) and Karuizawa in Nagao (next to Gunma, Area 7). Both of these sites belong to the JMA's Automated Meteorological Data Acquisition System, where visibility data were available. The observed visibility data were converted to fog water content by using the formula of Stoelinga and Warner (1999) and compared with the simulations. The black and gray dots at the tops of the panels indicate that the ^{137}Cs concentrations simulated by Met_EnsMean exceeded 1 and 0.1 Bq/m^3, respectively. From 15 and 16 March and 20–23 March, the fog occurrence coincided with the transport of the radioactive plumes, which were well predicted by the simulations. However, the amount of fog water content varied significantly between the simulations. Although NHM and NHM-LETKF could not predict the fog deposition over Areas 6 and 7 (Figure 5), they actually produced fog but did not coincide with the transport of radioactive plumes (Figures 8a and 8b). On the other hand, the lower fog contribution of WRF-WDM6 (Figure 7) was probably due to the significant underestimation of the fog water content (Figures 8a–8d). Since the difference between the MORR-MYNN25 and MORR-MYNN30 was small, only MORR-MYNN30 is shown in Figures 8c and 8d. These data show that the selection of the PBL schemes sometimes caused significant differences in the prediction of fog water content.

There is an argument for the importance of the threshold of the fog water content. In the deposition module of Katata et al. (2015) used in this study, as follows:

$$V_{df} = R_{LUC} A_c U_{10}, \tag{1}$$

where V_{df} is the fog deposition velocity and R_{LUC} is the ratio of V_{df} for each land use category (LUC) to that for coniferous forest and set 1, 0.2, and 0.1 for forest, short vegetation, and smooth surfaces, respectively. A_c is the function of leaf area index (LAI) or LAI and the canopy height h (see Equation A12 of Katata et al., 2015) and U_{10} is the 10-m wind speed. Because h data were not available for the whole model domain, we used the function of LAI as follows:

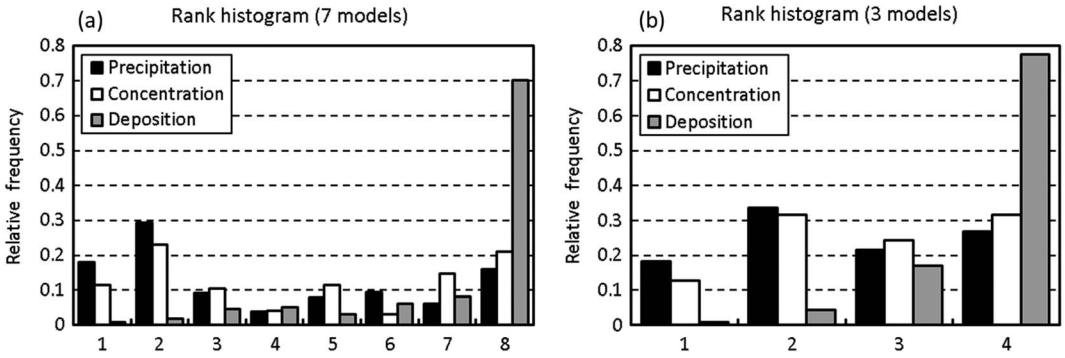

Figure 9. (a) Rank histograms of simulations with the seven meteorological models (NHM, NHM-LETKF, and the five WRFs) for (black) cumulative precipitation for the afternoon (12–24 LT) of 15 March (data used only observed values above 0.1 mm), (white) cumulative ^{137}Cs concentration from 13 to 23 March, and (gray) cumulative ^{137}Cs deposition from 11 to 31 March. (b) Same as (a) but for simulations with the three meteorological models (NHM, NHM-LETKF, and WRF_EnsMean).

$$A_c = 0.0095\,\mathrm{LAI}^3 - 0.05\,\mathrm{LAI}^2 + 0.0916\,\mathrm{LAI} + 0.0082 \quad (2)$$

Tav (2017) and Tav et al. (2018) indicated that fog deposition can only be detected with fog water mixing ratios of larger than 10^{-4} kg/kg under calm wind conditions. Nevertheless, it is not accurate to set the threshold value as 10^{-4} kg/kg for the simulation because no fog deposition will occur when the simulated fog mixing ratio is slightly lower than the threshold, such as 0.99×10^{-4} kg/kg. Therefore, the threshold was set as 10^{-5} kg/kg in the current study, thus reflecting the possibility of the underestimation of simulated fog by a factor of 10. In addition, in the presence of stronger surface wind, fog deposition could be enhanced, even in the case of thinner fog. To evaluate the sensitivity of the data to the threshold values, we conducted the simulation by Met_EnsMean with the threshold of 10^{-4} kg/kg to provide a minimum estimate of the fog deposition. The result is shown in Appendix A. Also, the fog deposition velocity should be proportional to fog mixing ratio, because the size (and the inertia) of fog droplets is generally larger as the mixing ratio is higher. This effect was not considered in the simulation.

4.2. Implications From the Multimeteorological Model Ensembles

4.2.1. Underestimation of Deposition Efficiencies

The simulated precipitations and cumulative concentrations of ^{137}Cs obtained by the meteorological model ensembles either overestimated or underestimated the observed values. Their simulated spatial distributions agreed well with the observations. These indicated that the simulations of wind fields and precipitations and the source term used in this study (Katata et al., 2015) were probably realistic. On the other hand, all of the simulated depositions of ^{137}Cs were underestimated. This feature is readily observed in Figure 9, which shows the rank histograms of (black) the cumulative precipitation for the afternoon of 15 March, when the most serious contamination occurred over the land of Japan (corresponding to the lower panel of Figure 3), (white) the cumulative concentration of ^{137}Cs (corresponding to Figure 4), and (gray) the cumulative deposition of ^{137}Cs (corresponding to Figure 5). The relative frequencies of the precipitation and concentration data in Figure 9 are enough close to each other, whereas the ensemble showed significant underestimation for the deposition. Because the behaviors of the five WRF simulations were relatively similar, compared to those of NHM and NHM-LETKF in Figure 9a, data in Figure 9a were biased toward the five WRF simulations. As the result, the relative frequencies of the precipitation and concentration data in Figure 9b (an ensemble of NHM, NHM-LETKF, and WRF_EnsMean) were more close to each other than those of Figure 9a. Therefore, Figure 9b also shows the validity of the current way of ensemble mean (CTM_EnsMean and Met_EnsMean): This three-member ensemble had the average spread in terms of the precipitation and the concentration data.

Combining these facts, it is safe to presume that the depositional efficiencies of CTM were underestimated: without the current multimeteorological model analysis, the reason for this could not be identified. Certainly, wrong patterns of simulated precipitation and/or wind fields could also lead to such a situation. Therefore, this conclusion is supported not only by the fact that the ensembles showed the average spread

but also by the fact that they showed good spatial agreements with the observations as presented in sections 3.1 and 3.2.

NHM-Chem considers four types of deposition mechanisms, that is, dry deposition, in-cloud scavenging, below-cloud scavenging, and fog deposition. Each process contains large uncertainties. The dry deposition efficiency is determined by the ^{137}Cs-carrying aerosol size distribution and the ground surface conditions. The below-cloud scavenging efficiency is determined by the size distribution of aerosols and hydrometeors. The state of hydrometeors is also important because most solid hydrometeors are very nonspherical, and their gravitational velocities and collection efficiencies are different than those of spheres. In-cloud scavenging and fog deposition consist of two processes, that is, "CCN activation" and "microphysical deposition." CCN activation is determined by the size and hygroscopicity of the carrier aerosols and the supersaturation of the air, both for in-cloud scavenging and fog deposition (the supersaturation of cloud formation, ~0.1–1%, is one to 2 orders of magnitude larger than that of fog formation, ~0.01–0.1%). For the microphysical deposition part of in-cloud scavenging, a number of elemental processes, that is, so-called cloud microphysical processes, are involved in the evolution of cloud droplets that form liquid or solid hydrometeors and settle to the ground. During the deposition process of fog deposition, the mechanism is the same as that of dry deposition: The deposition efficiency is determined by the ^{137}Cs-carrying fog size distribution and the ground surface conditions. Uncertainties in all of these parameters can contribute to the underestimation of deposition efficiencies; thus, it is difficult to identify the reason for this underestimation.

Nevertheless, several issues need to be investigated to identify the cause of this underestimation and improve the deposition modeling of radio-Cs by the current CTM:

1. In terms of the underestimation of dry deposition, Cs-ball should be considered. The sizes of Cs-ball range from one to several hundred micrometers in diameter, such that the dry deposition velocities of Cs-ball should be significantly larger than those of submicron carrier aerosols, as assumed in the simulation. The consideration of Cs-ball will certainly improve the underestimation of ^{137}Cs deposition. It is noted here that an aircraft survey could underestimate the ^{137}Cs deposition of Cs-ball, depending on the areal density: Doses from sporadic sources on the ground could be lower than those from homogeneously contaminated surfaces.
2. It has been well accepted and thus studied that the theoretical efficiencies of below-cloud scavenging are sometimes 1 to 2 orders of magnitude smaller than the experimental efficiencies for approximately 1-μm size ranges (e.g., Wang et al., 2010; Zhang et al., 2013). In addition, radioactive aerosols could be highly charged, such that their efficiencies could be enhanced due to electrostatic forces. Applying empirical efficiencies and/or considering the electric charges due to radioactive decay will certainly improve the underestimation of ^{137}Cs deposition.
3. There could be another solution to improve deposition modeling: a statistical approach. As performed by Toyoda et al. (2013), optimizing the four types of deposition efficiencies using a Greens' function approach toward the observed ^{137}Cs deposition with the current sets of the meteorological ensembles can help identify the cause of underestimation in the deposition modeling of ^{137}Cs.
4. Discrepancy in the deposition schemes can be assessed by using the Cs/Xe ratio. Xe is a noble gas so the Cs/Xe ratio in atmospheric concentrations only changes due to dry and wet removal of Cs during the transport, except radioactive decay. The discrepancy in the deposition schemes caused larger impacts on concentrations over further downwind regions. Therefore, the current and improved deposition processes should be evaluated by the Cs/Xe ratios analysis over further downwind regions such as North America and Europe.

4.2.2. Contradictory Performances in Meteorological and Deposition Modeling

As mentioned in section 3.3, NHM performed very well in terms of precipitation and NHM-LETKF performed best in terms of simulated concentrations, whereas WRF simulations were generally better in terms of the simulation of ^{137}Cs deposition. These results appear to be contradictory. One reason for this appears to be the inconsistency in in-cloud scavenging modeling. In-cloud scavenging is one of the major processes of ^{137}Cs deposition. In-cloud scavenging involves the vertical motion of air, cloud formation and evolution, and precipitation, but the simulated vertical profiles of ^{137}Cs and hydrometeors were not evaluated. If the simulated vertical profiles of ^{137}Cs and hydrometeors by the NHM and NHM-LETKF meteorological fields were farther from reality than those simulated by the WRF fields, it would be natural that the performances of the deposition modeling of the WRF simulations would be better than those of NHM and NHM-LETKF. The

observed vertical profiles of ^{137}Cs are limited. Fukushima University initiated radioactivity sonde observations from April 2011 (the data are available at http://www.sss.fukushima-u.ac.jp/sonde_data/, last access: 7 April 2018). Although most land surface contamination observations were made in March, the model performance of the simulated vertical distribution of ^{137}Cs can be evaluated using the radioactivity sonde data. The better performance in the simulation of precipitation does not necessarily ensure a better performance in the simulation of hydrometeors. The simulated spatial distributions of hydrometeors should be evaluated by radar observations for the further analysis of in-cloud scavenging modeling.

There is another difficulty in evaluating the in-cloud scavenging modeling of ^{137}Cs. The majority of land surface contamination was caused by light precipitation (or fog) events (<0.5 mm). Meteorological models and observations have been designed to study heavy precipitation. The radars used for the operational weather monitoring networks (C-band or S-band) cannot detect such small sizes of droplets (cloud, fog, and drizzle), and rain gauges cannot detect precipitation until it accumulates to 0.5 mm. The meteorological models used for the operational weather forecast, which employ "bulk" cloud microphysics modules, were not designed to predict light precipitation events, and their simulated light precipitation cannot be evaluated by the measurements. The current case study should be revisited in the future to evaluate a number of similar future light precipitation events in the region under similar pressure patterns as that in March 2011, using different models and observations that are designed to study light precipitation.

5. Conclusions

Meteorological model and module ensemble analysis with a single CTM (NHM-Chem) was conducted for the simulation of the transport and deposition of radio-Cs released in association with the FDNPS accident in March 2011 with a horizontal grid resolution of 3 km over the eastern and northern part of the main island of the Japan Archipelago. A total of eight meteorological fields were compared: seven from NHM, NHM-LETKF, five combinations of modules with WRF (different cloud microphysics and PBL modules), and the meteorological ensemble mean. Then, we obtained a total of nine CTM simulation results: seven by using the seven meteorological simulations, the ensemble mean of the seven simulations, and a simulation using the meteorological ensemble mean. Strictly speaking, the variables of the meteorological ensemble mean violate the physical consistency, but the current study proved that it was practically applicable. The three-member ensemble (NHM, NHM-LETKF, and WRF_EnsMean) was shown to have average spread in terms of the precipitation and the surface concentration data.

Whereas several multimodel ensemble studies were performed in previous studies, the current ensemble type (one CTM with several meteorological fields) was applied here for the first time. The current approach was found to be a useful way to evaluate the uncertainty in each component of CTM. The current analysis could successfully deduce that the underestimation of the deposition efficiencies of CTM was the reason for the underestimation of simulated radio-Cs deposition, whereas the simulated precipitation and estimated source term were all reasonable: All of the simulations underestimated the deposition amount, whereas some underestimated but others overestimated the simulated precipitation and radio-Cs air concentrations and the simulated spatial distributions of precipitation and concentrations were well correlated with the observations. The simulated total deposition amounts of ^{137}Cs ranged from 0.46–1.23 PBq, while the observed amount was 2.59 PBq (except in areas 3 km from the FNDPS). The *MB* values of simulated cumulative precipitation from 11 to 31 March ranged from −18.2 to 12.3 mm, and the observed average value was 55.0 mm. The *MB* values of the cumulative ^{137}Cs surface concentrations from 13 to 23 March ranged from −137.7 to 174.2 Bq·m^{-3}·hr, and the observed average value was 376.12 Bq·m^{-3}·hr. It was also found that the CTM simulation using the meteorological ensemble was successful in reducing variance and they gave reasonable results. The simulated deposition using the meteorological ensemble yielded the largest quantity (1.23 PBq). This occurred because the light precipitation areas were enlarged by the ensemble mean of meteorological fields and because the contamination was caused by light precipitation after the FDNPS accident.

Another target of this study was to reveal the dominant processes of the deposition of radio-Cs over each deposition region of the simulation land area and to show how they vary depending on meteorological fields. The simulated area was divided into nine areas, namely, Hamadori, Nakadori, Aizu, South Miyagi, Iwate-Miyagi, Tochigi, Gunma, Iwaki-Ibaraki, and Ibaraki-Chiba. The magnitudes of their contributions varied depending on the simulations, but the current ensemble study showed that in-cloud scavenging was the

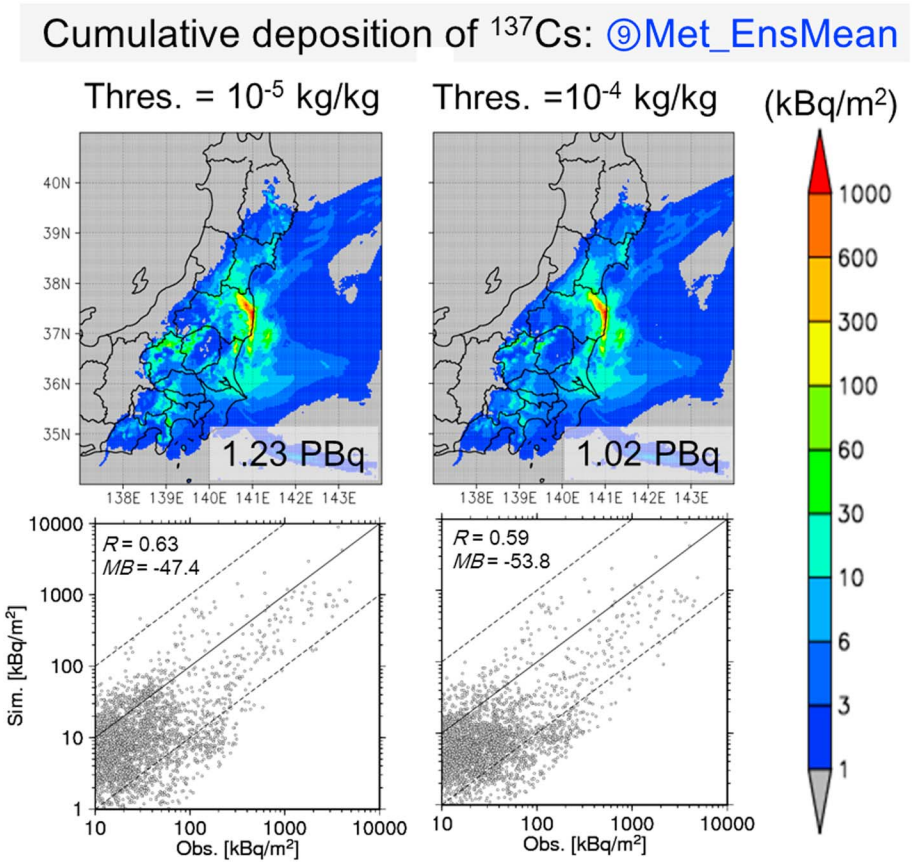

Figure A1. Same as Figure 5 but simulated by Met_EnsMean with different thresholds of fog water mixing ratio applied to the fog deposition scheme of 10^{-5} and 10^{-4} (kg/kg), respectively.

most dominant mechanism (40–65%) for the entire land region, followed by dry deposition (15–35%) or fog deposition (5–35%). The contribution of below-cloud scavenging was the least significant (<5%) for all simulations. These contributions also varied in the deposition areas. In Fukushima and Miyagi prefectures, from the coastal to mountain areas and from the southern to northern areas, the contributions of solid precipitation increased: More than 90% of contributions were liquid over Hamadori, but 70–90% were solid over South Miyagi. Because most Japanese land is covered with mountain forests, the contribution of fog deposition was ubiquitous everywhere except in Ibaraki-Chiba, which is located in the Kanto plain and includes no mountain areas. As suggested by Hososhima and Kaneyasu (2015) and Sanada et al. (2018), fog deposition was the major process in Tochigi, as well as in Gunma (30–85%). It was quite hard for the models to simulate deposition over Iwate-Miyagi, as the most dominant processes over the area were totally different between the models.

In inverse modeling, the simulated concentrations and/or depositions are used for the source term estimation (Saunier et al., 2013, 2016; Winiarek et al., 2014; Yumimoto et al., 2016). In the study, we showed that the simulated concentrations and depositions could vary by more than twofold, depending on the selection of the meteorological field, which could contribute to the uncertainty in the source term estimation. In the future, the source term estimation with a single CTM, a single inversion method, and the different meteorological fields should be made to evaluate the meteorological uncertainty in the estimated source term.

It should be noted here that the radio-Cs was assumed to be carried by hygroscopic submicron aerosols, as inferred by Kaneyasu et al. (2012). On the other hand, Adachi et al. (2013) found other types of the carrier aerosols, named Cs-ball, which differ significantly in terms of their size and hygroscopicity, and thus atmospheric behaviors. Adachi et al. (2013) also performed a sensitivity simulation of the size and hygroscopicity of the carrier aerosols for a limited period using limited knowledge about the production and emission

mechanisms of Cs-ball. Since then, the microphysical and chemical properties of Cs-ball have been extensively studied by Abe et al. (2014), Yamaguchi et al. (2016), Satou et al. (2016), and Higaki et al. (2017), and much knowledge has been accumulated. Recently, the Cs-balls found in the environment were successfully linked to the accidental sequences of FDNPS by Satou et al. (2018); thus, it is now necessary to resimulate the atmospheric behavior of Cs-ball and to show their differences compared to hygroscopic submicron aerosols. The sensitivity of simulated dispersion and deposition with respect to the properties of Cs-ball will be assessed in our next paper.

Appendix A: Sensitivity of Fog Deposition to the Threshold of Fog Water Content

Figures A1 and A2 show the differences in the simulated deposition and contributions of deposition processes obtained by using the different thresholds of fog water content. For simplicity, only the CTM

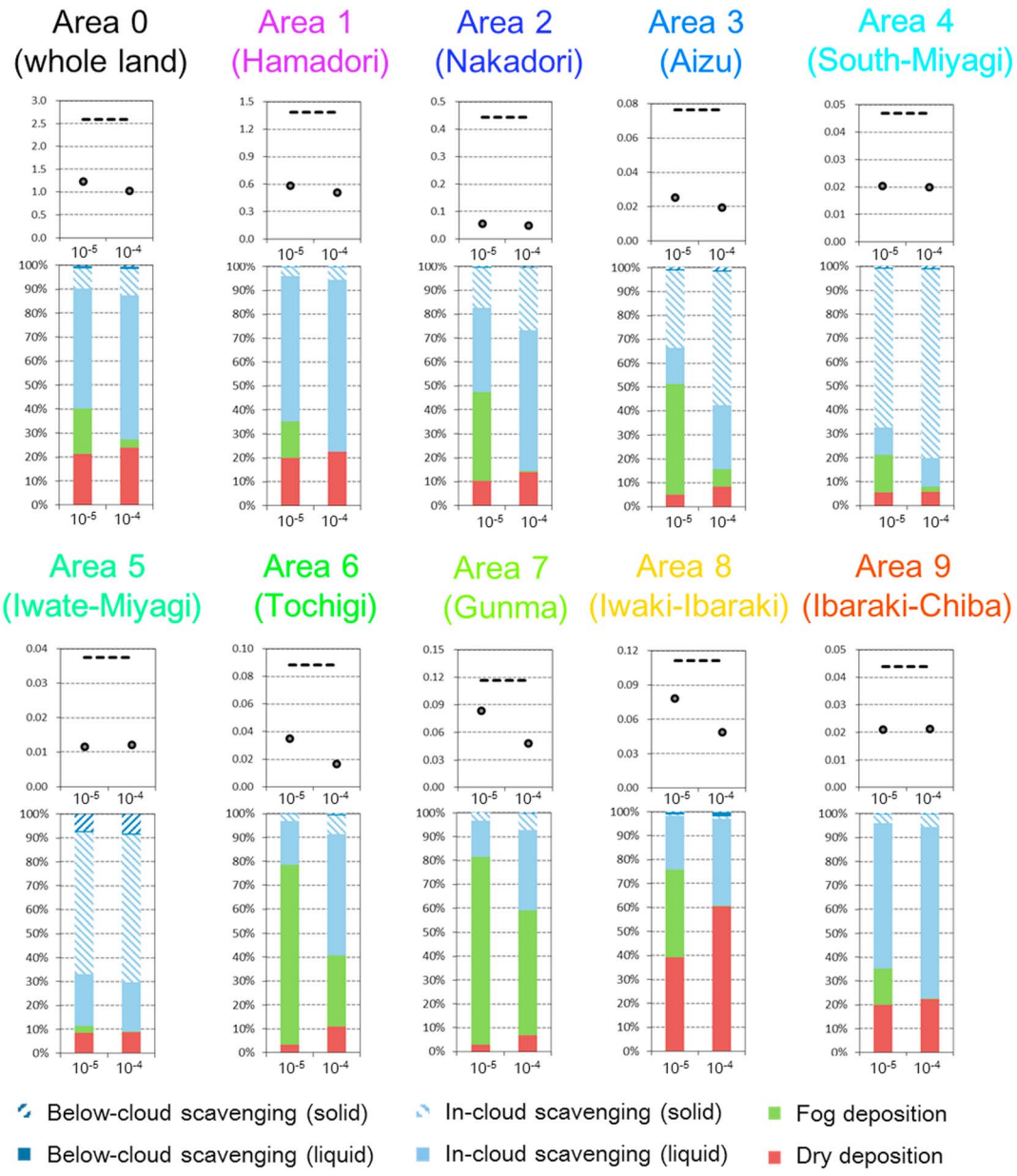

Figure A2. Same as Figure 7 but simulated by Met_EnsMean with different thresholds of fog water mixing ratio applied to the fog deposition scheme of 10^{-5} and 10^{-4} (kg/kg), respectively.

simulation obtained with Met_EnsMean was compared and shown. The simulation performed with a threshold fog water content of 10^{-4} kg/kg resulted in significantly less deposition over the mountainous regions over Nakadori, Tochigi, and Gunma. There were almost no contributions of fog, except in Tochigi and Gunma prefectures. As discussed previously, the simulation with 10^{-4} kg/kg could yield the lowest estimate, but the selection of the threshold value was also shown to be an important factor for the prediction of fog deposition. The accurate prediction of fog and its deposition was indispensable for the prediction of FDNPS-derived radio-Cs deposition over the mountainous areas of Japan.

Acknowledgments
This research was mainly supported by Grants-in-Aid for Scientific Research on Innovative Areas 24110002 and 24110003 of the Ministry of Education, Culture, Sports, Science and Technology (MEXT). It was partly supported by the Japanese Radioactivity Survey from the NRA, Japan, and also supported by the Japan Society of the Promotion of Science (JSPS) and Ministère des Affaires Étrangères et du Développement International (MAEDI) under the Japan-France Integrated Action Program (SAKURA) and by KAKENHI Grant JP15K16121, JP15H02811, JP24340115, and JP16KK0018 of JSPS. The issues presented in this paper were extensively discussed with Drs. Anne Mathieu, Arnaud Quérel, Denis Quélo, Olivier Saunier, and Damien Didier of l'Institut de Radioprotection et de Sûreté Nucléaire (IRSN). The authors feel obliged to their useful comments on the fog deposition mechanism by Dr. Olivier Masson of IRSN, the uncertainty in aircraft observations by Prof. Michio Aoyama of Fukushima University; the radar and precipitation observation products by Drs. Nobuhiro Nagumo, Takeshi Iriguchi, Hiroshige Tsuguti, and Ahoro Adachi of MRI; the optimization method by Dr. Takahiro Toyoda of MRI; the effects of electric charge due to radioactive decay by Dr. Pascal Lemaitre of IRSN; and the pros and cons of ensemble analysis by Drs. Makoto Deushi and Keiichi Kondo of MRI. The authors are deeply grateful for the support of Mr. Yuki Kobayashi of University of Tsukuba for his analysis of the visibility data. The simulated and observed data used in all figures are available at https://mri-2.mri-jma.go.jp/owncloud/index.php/s/CwFDOmEPCOlABbW (last access: 8 January 2019). In terms of the raw observation data sets, the surface activity concentration data are available at Appendix A of Oura et al. (2015; http://www.radiochem.org/en/j-online152.html; last access: 2 October 2018), the activity deposition data are available at https://emdb.jaea.go.jp/emdb/en/portals/b1010301/ (last access: 2 October 2018), and the RAP data are provided by Japan Meteorological Business Support Center for a charge.

References

Abe, Y., Iizawa, Y., Terada, Y., Adachi, K., Igarashi, Y., & Nakai, I. (2014). Detection of uranium and chemical state analysis of individual radioactive microparticles emitted from the Fukushima nuclear accident using multiple synchrotron radiation X-ray analyses. *Analytical Chemistry*, *86*(17), 8521–8525. https://doi.org/10.1021/ac501998d

Adachi, K., Kajino, M., Zaizen, Y., & Igarashi, Y. (2013). Emission of spherical cesium-bearing particles from an early stage of the Fukushima nuclear accident. *Scientific Reports*, *3*(1), 2554. https://doi.org/10.1038/srep02554

Doi, T., Masumoto, K., Toyoda, A., Tanaka, A., Shibata, Y., & Hirose, K. (2013). Anthropogenic radionuclides in the atmosphere observed at Tsukuba: Characteristics of the radionuclides derived from Fukushima. *Journal of Environmental Radioactivity*, *122*, 55–62. https://doi.org/10.1016/j.jenvrad.2013.02.001

Draxler, R., Arnold, D., Chino, M., Galmarini, S., Hort, M., Jones, A., et al. (2015). World Meteorological Organization's model simulations of the radionuclide dispersion and deposition from the Fukushima Daiichi nuclear power plant accident. *Journal of Environmental Radioactivity*, *139*, 172–184. https://doi.org/10.1016/j.jenvrad.2013.09.014

Girard, S., Korsakissok, I., & Mallet, V. (2014). Screening sensitivity analysis of a radionuclides atmospheric dispersion model applied to the Fukushima disaster. *Atmospheric Environment*, *95*, 490–500. https://doi.org/10.1016/j.atmosenv.2014.07.010

Girard, S., Mallet, V., Korsakissok, I., & Mathieu, A. (2016). Emulation and Sobol' sensitivity analysis of an atmospheric dispersion model applied to the Fukushima nuclear accident. *Journal of Geophysical Research: Atmospheres*, *121*, 3484–3496. https://doi.org/10.1002/2015JD023993

Groëll, J., Quélo, D., & Mathieu, A. (2014). Sensitivity analysis of the modelled deposition of ^{137}Cs on the Japanese land following the Fukushima accident. *International Journal of Environment and Pollution*, *55*(1/2/3/4), 67–75. https://doi.org/10.1504/IJEP.2014.065906

Higaki, S., Kurihara, Y., Yoshida, H., Takahashi, Y., & Shinohara, N. (2017). Discovery of non-spherical heterogeneous radiocesium-bearing particles not derived from unit 1 of the Fukushima Dai-ichi Nuclear Power Plant, in residences five years after the accident. *Journal of Environmental Radioactivity*, *177*, 65–70. https://doi.org/10.1016/j.jenvrad.2017.06.006

Hososhima, M., & Kaneyasu, N. (2015). Altitude-dependent distribution of ambient gamma dose rates in a mountainous area of Japan caused by the Fukushima nuclear accident. *Environmental Science and Technology*, *49*(6), 3341–3348. https://doi.org/10.1021/es504838w.

Igarashi, Y., Kajino, M., Zaizen, Y., Adachi, K., & Mikami, M. (2015). Atmospheric radioactivity over Tsukuba, Japan: A summary of three years of observations after the FDNPP accident. *Progress in Earth and Planetary Science*, *2*(1), 44. https://doi.org/10.1186/s40645-015-0066-1

Iwagami, S., Onda, Y., Tsujimura, M., & Abe, Y. (2016). Contribution of radioactive ^{137}Cs discharge by suspended sediment, coarse organic matter, and dissolved fraction from a headwater catchment in Fukushima after the Fukushima Dai-ichi Nuclear Power Plant accident. *Journal of Environmental Radioactivity*, *166*(3), 466–474.

Janjic, Z. I. (2002). Nonsingular implementation of the Mellor-Yamada level 2.5 scheme in the NCEP Meso model. Office Note, 437 (61 pp.). Camp Springs, MD: Natl. Cent. For Environ. Predict.

Japanese Meteorological Agency (2008). Japan Meteorological Agency's non-hydrostatic model II [in Japanese]. Suchi Yohoka Hokoku Bessatsu (Additional Volume to Report of Numerical Prediction Division), 54 (265 pp.).

Kajino, M., Deushi, M., Sekiyama, T. T., Oshima, N., Yumimoto, K., Tanaka, T. Y., et al. (2018). NHM-Chem, the Japan Meteorological Agency's regional meteorology—Chemistry model (v1.0): Model description and aerosol representations. *Geoscientific Model Development Discussion*, 1–45. https://doi.org/10.5194/gmd-2018-128

Kajino, M., Deushi, M., Sekiyama, T. T., Oshima, N., Yumimoto, K., Tanaka, T. Y., et al. (2019). NHM-Chem, the Japan Meteorological Agency's regional meteorology—Chemistry model: Model evaluations toward the consistent predictions of the chemical, physical, and optical properties of aerosols. *Journal of the Meteorological Society of Japan*, *97*. https://doi.org/10.2151/jmsj.2019-020

Kajino, M., Inomata, Y., Sato, K., Ueda, H., Han, Z., An, J., et al. (2012). Development of the RAQM2 aerosol chemical transport model and predictions of the Northeast Asian aerosol mass, size, chemistry, and mixing type. *Atmospheric Chemistry and Physics*, *12*(24), 11,833–11,856. https://doi.org/10.5194/acp-12-11833-2012

Kajino, M., Ishizuka, M., Igarashi, Y., Kita, K., Yoshikawa, C., & Inatsu, M. (2016). Long-term assessment of airborne radiocesium after the Fukushima nuclear accident: Re-suspension from bare soil and forest ecosystems. *Atmospheric Chemistry and Physics*, *16*(20), 13,149–13,172. https://doi.org/10.5194/acp-16-13149-2016

Kajino, M., Sekiyama, T. T., Mathieu, A., Korsakissok, I., Périllat, R., Quélo, D., et al. (2018). Lessons learned from atmospheric modeling studies after the Fukushima nuclear accident: Ensemble simulations, data assimilation, elemental process modeling, and inverse modeling. *Geochemical Journal*, *52*(2), 85–101. https://doi.org/10.2343/geochemj.2.0503

Kaneyasu, N., Ohashi, H., Suzuki, F., Okada, T., & Ikemori, F. (2012). Sulfate aerosol as a potential transport medium of radiocesium from the Fukushima nuclear accident. *Environmental Science and Technology*, *46*(11), 5720–5726. https://doi.org/10.1021/es204667h

Katata, G., Chino, M., Kobayashi, T., Terada, H., Ota, M., Nagai, H., et al. (2015). Detailed source term estimation of the atmospheric release for the Fukushima Daiichi Nuclear Power Station accident by coupling simulations of an atmospheric dispersion model with an improved deposition scheme and oceanic dispersion model. *Atmospheric Chemistry and Physics*, *15*(2), 1029–1070. https://doi.org/10.5194/acp-15-1029-2015

Kitayama, K., Morino, Y., Takigawa, M., Nakajima, T., Hayami, H., Nagai, H., et al. (2018). Atmospheric modeling of 137Cs plumes from the Fukushima Daiichi Nuclear Power Plant—Evaluation of the model intercomparison data of the Science Council of Japan. *Journal of Geophysical Research: Atmospheres*, *123*, 7047–7796. https://doi.org/10.1029/2017JD028230

Kristiansen, N. I., Stohl, A., Olivie, D. J. L., Croft, B., Sovde, O. A., Klein, H., et al. (2016). Evaluation of observed and modelled aerosol lifetimes using radioactive tracers of opportunity and an ensemble of 19 global models. *Atmospheric Chemistry and Physics*, *16*(5), 3525–3561. https://doi.org/10.5194/acp-16-3525-2016

Kunii, M. (2013). Mesoscale data assimilation for a local severe rainfall event with the NHM-LETKF system. *Weather and Forecasting*, *29*(5), 1093–1105. https://doi.org/10.1175/WAF-D-13-00032.1

Leadbetter, S. J., Hort, M. C., Jones, A. R., Webster, H. N., & Draxler, R. R. (2015). Sensitivity of the modelled deposition of Caesium-137 from the Fukushima Dai-ichi nuclear power plant to the wet deposition parameterization in NAME. *Journal of Environmental Radioactivity*, *139*, 200–211. https://doi.org/10.1016/j.jenvrad.2014.03.018

Lim, K.-S., & Hong, S.-Y. (2010). Development of an effective double-moment cloud microphysics scheme with prognostic cloud condensation nuclei (CCN) for weather and climate models. *Monthly Weather Review*, *138*(5), 1587–1612. https://doi.org/10.1175/2009MWR2968.1

Lin, Y.-L., Farley, R. D., & Orville, H. D. (1983). Bulk parameterization of the snow field in a cloud model. *Journal of Applied Meteorology and Climatology*, *22*(6), 1065–1092. https://doi.org/10.1175/1520-0450(1983)022<1065:BPOTSF>2.0.CO;2

Masson, O., Ringer, W., Mala, H., Rulik, P., Dlugosz-Lisiecka, M., Eleftheriadis, K., et al. (2013). Size distributions of airborne radionuclides from the Fukushima nuclear accident at several places in Europe. *Environmental Science and Technology*, *47*(19), 10,995–11,003. https://doi.org/10.1021/es401973c

Mathieu, A., Kajino, M., Korsakissok, I., Périrat, R., Quélo, D., Quérel, A., et al. (2018). Fukushima Daiichi-derived radionuclides in the atmosphere, transport and deposition in Japan: A review. *Applied Geochemistry*, *91*, 122–139. https://doi.org/10.1016/j.apgeochem.2018.01.002

Morino, Y., Ohara, T., Watanabe, S., Hayashi, S., & Nishizawa, M. (2013). Episode analysis of deposition of radiocesium from the Fukushima Daiichi Nuclear Power Plant accident. *Environmental Science and Technology*, *47*(5), 2314–2322. https://doi.org/10.1021/es304620x

Morrison, H., Thompson, G., & Tatarskii, V. (2009). Impact of cloud microphysics on the development of trailing stratiform precipitation in a simulated squall line: Comparison of one- and two-moment schemes. *Monthly Weather Review*, *137*(3), 991–1007. https://doi.org/10.1175/2008MWR2556.1

Nakajima, T., Misawa, S., Morino, Y., Tsuruta, H., Goto, D., Uchida, J., et al. (2017). Model depiction of the atmospheric flows of radioactive cesium emitted from the Fukushima Daiichi Nuclear Power Station accident. *Progress in Earth and Planetary Science*, *4*(1), 1–18. https://doi.org/10.1186/s40645-017-0117-x

Nakanishi, M., & Niino, H. (2006). An improved Mellor-Yamada level-3 model: Its numerical stability and application to a regional prediction of advection fog. *Boundary-Layer Meteorology*, *119*(2), 397–407. https://doi.org/10.1007/s10546-005-90308

Nakano, M., Kato, T., Hayashi, S., Kanada, S., Yamada, Y., & Kurihara, K. (2012). Development of a 5-km-mesh cloud-system-resolving regional climate model at the Meteorological Research Institute. *Journal of the Meteorological Society of Japan*, *90A*, 339–350. https://doi.org/10.2151/jmsj.2012-A19

Nuclear Regulation Authority (2012). Airborne monitoring results in each prefecture. Retrieved from http://radioactivity.nsr.go.jp/en/list/203/list-1.html, (last access: 12 February 2018).

Oura, Y., Ebihara, M., Tsuruta, H., Nakajima, T., Ohara, T., Ishimoto, M., et al. (2015). A database of hourly atmospheric concentration of radiocesium (^{134}Cs and ^{137}Cs) in suspended particulate matter collected in March 2011 at 99 air pollution monitoring stations in Eastern Japan. *Journal of Nuclear and Radiochemical Sciences*, *15*(2), 15–26.

Quérel, A., Roustan, Y., Quélo, D., & Benoit, J.-P. (2015). Hints to discriminate the choice of wet deposition models applied to an accidental radioactive release. *International Journal of Environment and Pollution*, *58*(4), 268–279. https://doi.org/10.1504/IJEP.2015.077457

Saito, K., Ishida, J., Aranami, K., Hara, T., Segawa, T., Narita, M., & Honda, Y. (2007). Nonhydrostatic atmospheric models and operational development at JMA. *Journal of the Meteorological Society of Japan*, *85B*, 271–304. https://doi.org/10.2151/jmsj.85B.271

Sanada, Y., Katata, G., Kaneyasu, N., Nakanishi, C., Urabe, Y., & Nishizawa, Y. (2018). Altitudal characteristics of atmospheric deposition of aerosols in mountainous regions: Lessons from the Fukushima Daiichi Nuclear Power Station accident. *Science of the Total Environment*, *618*, 881–890. https://doi.org/10.1016/j.scitotenv.2017.08.246

Satou, Y., Sueki, K., Sasa, K., Adachi, K., & Igarashi, Y. (2016). First successful isolation of radioactive particles from soil near the Fukushima Daiichi Nuclear Power Plant. *Anthropocene*, *14*, 71–76. https://doi.org/10.1016/j.ancene.2016.05.001

Satou, Y., Sueki, K., Sasa, K., Yoshikawa, H., Nakama, S., Minowa, H., et al. (2018). Analysis of two forms of radioactive particles emitted during the early stages of the Fukushima Dai-ichi Nuclear Power Station accident. *Geochemical Journal*, *52*(2), 137–143. https://doi.org/10.2343/geochemj.2.0514

Saunier, O., Mathieu, A., Didier, D., Tombette, M., Quélo, D., Winiarek, V., & Bocquet, M. (2013). An inverse modeling method to assess the source term of the Fukushima Nuclear Power Plant accident using gamma dose rate observations. *Atmospheric Chemistry and Physics*, *13*(22), 11,403–11,421. https://doi.org/10.5194/acp-13-11403-2013

Saunier, O., Mathieu, A., Sekiyama, T., Kajino, M., Adachi, K., Bocquet, M., et al. (2016). A new perspective on the Fukushima released brought by newly available ^{137}Cs air concentration observations and reliable meteorological fields. Proc. International Conference on Harmonisation within Atmospheric Dispersion Modelling for Regulatory Purposes (HARMO) 17th (7 pp.).

Science Coucil of Japan (2014). A review of the model comparison of transportation and deposition of radioactive materials released to the environment as a result of the Tokyo Electric Power Company's Fukushima Daiichi Nuclear Power Plant accident (36 pp.). Retrieved from http://www.scj.go.jp/ja/info/kohyo/pdf/kohyo-22-h140902-e1.pdf, (last access: April 17, 2018).

Sekiyama, T. T., Kajino, M., & Kunii, M. (2017). The impact of surface wind data assimilation on the predictability of near-surface plume advection in the case of the Fukushima nuclear accident. *Journal of the Meteorological Society of Japan*, *95*(6), 447–454. https://doi.org/10.2151/jmsj.2017-025

Sekiyama, T. T., Kunii, M., Kajino, M., & Shimbori, T. (2015). Horizontal resolution dependence of atmospheric simulations of the Fukushima nuclear accident using 15-km, 3-km, and 500-m grid models. *Journal of the Meteorological Society of Japan*, *93*(1), 49–64. https://doi.org/10.2151/jmsj.2015-002

Skamarock, W. C., Klemp, J. B., Dudhia, J., Gill, D. O., Barker, D. M., Duda, M. G., et al. (2008). A description of the advanced research WRF version 3. Technical Note, NCAR/TN-475+STR (125 pp.). Natl. Cent. for Atmos. Res., Boulder, CO.

Stoelinga, M. T., & Warner, T. T. (1999). Nonhydrostatic, mesobeta-scale model simulations of cloud ceiling and visibility for an East Coast winter precipitation event. *Journal of Applied Meteorology*, *38*(4), 385–404. https://doi.org/10.1175/1520-0450(1999)038<0385:NMSMSO>2.0.CO;2

Tav, J. (2017). Etude du dépôt de radionucléides par les gouttelettes de brouillard sur les végétaux. (PhD thesis), l'Institut de Radioprotection et de Sûreté Nucléaire (in French).

Tav, J., Masson, O., Burnet, F., Paulat, P., Bourrianne, T., Conil, S., & Pourcelot, L. (2018). Determination of fog-droplet deposition velocity from a simple weighing method. *Aerosol and Air Quality Research*, *18*(1), 103–113. https://doi.org/10.4209/aaqr.2016.11.0519

Torii, T., Sanada, Y., Sugita, T., Kondo, A., Shikaze, Y., Takahashi, M., et al. (2012), Investigation of radionuclide distribution using aircraft for surrounding environmental survey from Fukushima Dai-ichi Nuclear Power Plant [in Japanese with English abstract]. Japan Atomic Energy Agency (182 pp.).

Toyoda, T., Awaji, T., Masuda, S., Sugiura, N., Igarashi, H., Sasaki, Y., et al. (2013). Improved state estimations of lower trophic ecosystems in the global ocean based on a Green's function approach. *Progress in Oceanography*, *119*, 90–107. https://doi.org/10.1016/j.pocean.2013.08.008

Tsuruta, H., Oura, Y., Ebihara, M., Ohara, T., & Nakajima, T. (2014). First retrieval of hourly atmospheric radionuclides just after the Fukushima accident by analyzing filter-tapes of operational air pollution monitoring stations. *Scientific Reports*, *4*(1), 6717. https://doi.org/10.1038/srep06717

Wang, X., Zhang, L., & Moran, M. D. (2010). Uncertainty assessment of current size-resolved parameterizations for below-cloud particle scavenging by rain. *Atmospheric Chemistry and Physics*, *10*(12), 5685–5705. https://doi.org/10.5194/acp-10-5685-2010

Winiarek, V., Bocquet, M., Duhanyan, N., Roustan, Y., Saunier, O., & Mathieu, A. (2014). Estimation of the caesium-137 source term from the Fukushima Daiichi nuclear power plant using a consistent joint assimilation of air concentration and deposition observations. *Atmospheric Environment*, *82*, 268–279. https://doi.org/10.1016/j.atmosenv.2013.10.017

Yamaguchi, N., Mitome, M., Akiyama-Hasegawa, K., Asano, M., Adachi, K., & Kogure, T. (2016). Internal structure of cesium-bearing radioactive microparticles released from Fukushima nuclear power plant. *Scientific Reports*, *6*(1), 20548. https://doi.org/10.1038/srep20548

Yumimoto, K., Morino, Y., Ohara, T., Oura, Y., Ebihara, M., Tsuruta, H., & Nakajima, T. (2016). Inverse modeling of the ^{137}Cs source term of the Fukushima Dai-ichi Nuclear Power Plant accident constrained by a deposition map monitored by aircraft. *Journal of Environmental Radioactivity*, *164*, 1–12. https://doi.org/10.1016/j.jenvrad.2016.06.018

Zhang, L., Wang, X., Moran, M. D., & Feng, J. (2013). Review and uncertainty assessment of size-resolved scavenging coefficient formulations for below-cloud snow scavenging of atmospheric aerosols. *Atmospheric Chemistry and Physics*, *13*(19), 10,005–10,025. https://doi.org/10.5194/acp-13-10005-2013

BUNSEKI KAGAKU Vol. 68, No. 10, pp. 757–768（2019）

年間特集「粒」：アナリティカルレポート

福島第一原子力発電所事故により1号機から放出された放射性エアロゾルの物理・化学的性状の解明

小野﨑晴佳[1]，阿部　善也*[1]，中井　泉[1]，足立　光司[2]，五十嵐康人[3,4]，大浦　泰嗣[5]，海老原　充[5,6]，宮坂　貴文[2,7,8]，中村　尚[7]，末木　啓介[9]，鶴田　治雄[10]，森口　祐一[11]

1　緒　　言

2011年3月11日に発生した東日本大震災に伴って福島第一原子力発電所事故が発生し，膨大な量の放射性物質が環境中へと放出された．事故直後の3月に福島第一原発から大気中へ放出された^{137}Csは，およそ10 PBqに及ぶと推測されている[1)2)]．4月以降は原子炉からの放射性物質の一次放出は格段に減少し，その後の環境中における放射能の増減には，事故直後の段階で放出されていた放射性物質の環境中での循環や再飛散が関係する．このとき，放射性物質自体の持つ物理・化学的性状が，環境中での安定性や沈着挙動を大きく左右する．すなわち，放射性核種は単体で放出されることもあるが，多くの場合他の物質と混合した状態で放出される．そのため，事故影響の全貌を理解するためには，放出された放射性核種の種類や全量だけではなく，どういった性状を持つ物質として放出されたかを正しく理解することが不可欠である．

事故由来の放射性物質の物質同定を目的とした研究は数多く行われており，特に事故の初期段階に炉内で生成され，直接的に環境中へと放出されたと考えられる微小な粒子状物質に関する多くの報告がある[3)]．こうした粒子は比較的高濃度の放射性Csを含むために「CsMP（radiocesium-bearing microparticle）」，あるいは球状粒子の発見例が多いため「Csボール」などの名称で呼ばれる．Igarashiら[3)]は物理・化学的性状に基づきCsMPを「Type A」と「Type B」の2種類に大別できることを指摘しており，本稿でもこの名称を用いる．「Type A」とされるCsMPの最初の発見は，2013年に報告されたAdachiら[4)]による研究である．この研究において，2011年3月14日夜から15日朝にかけて茨城県つくば市の気象研究所で捕集された大気粉塵フィルター上から，高濃度の^{134}Cs及び^{137}Csを含む水に不溶性の放射性粒子が初めて発見された．Abeら[5)]はType AのCsMPに対して放射光X線マイクロビームを用いた複合分析を実施し，その主成分が核燃料及びその核分裂生成物に帰属可能な様々な重元素を含有したケイ酸塩ガラスであることを明らかにした．またYamaguchiら[6)]やKogureら[7)]により，Type AのCsMPについてナノオーダーの内部構造が調査され，詳細な元素分布やガラス相中のナノパーティクルの存在が明らかとなり，生成過程の考察が進んだ．Type AのCsMPは，2016年に大熊町と双葉町で行われた屋内掃除の際に使用されたマスクからも発見されており[8)]，事故直後に大気中へ放出されたものが屋内環境中に残留し，掃除により再飛散したものであると考えられる．2014年及び2015年に福島県内の河川で採取された堆積物中からもType AのCsMPが発見されており[9)]，水中で長期的な安定性を持つことが懸念される一方，海水中では溶解が進行しやすいとする最近の報告もある[10)]．Type AのCsMPはいずれも直径数μmで，その多くが球状粒子であった．また放射性粒子の分析には，各原子炉が運転履歴や燃料タイプの違いによって異なる^{134}Cs/^{137}Cs放射能比を持つことから，同比を用いた放出炉の推定が行われているが，Type AのCsMPはすべて福島第一原発2号機の推定値（1.08）[11)]に近い値を持つことが報告されている．

福島第一原発由来と考えられるCsMPは，福島県内，特に原発周辺地域で採取された土壌からも相次いで発見されている[12)〜16)]．そのなかには，上述したような2号機由来と考えられるType AのCsMPのほかに，1号機の推定値（0.94）[11)]と近い^{134}Cs/^{137}Cs放射能比を持つ「Type B」のCsMPも存在する[13)14)]．Type BのCsMPは，上述したType AのCsMPとは異なり，数十〜数百μmと大きく，形状も

* E-mail：y.abe@rs.tus.ac.jp
[1] 東京理科大学理学部：162-8601　東京都新宿区神楽坂1-3
[2] 気象研究所：305-0052　茨城県つくば市長峰1-1
[3] 京都大学複合原子力科学研究所：590-0494　大阪府泉南郡熊取町朝代西2丁目
[4] 茨城大学理学部：310-8512　茨城県水戸市文京2-1-1
[5] 首都大学東京理学研究科：192-0397　東京都八王子市南大沢1-1
[6] 早稲田大学教育学部：169-8050　東京都新宿区西早稲田1-6-1
[7] 東京大学先端科学技術研究センター：153-8904　東京都目黒区駒場4-6-1
[8] 気象業務支援センター：305-0052　茨城県つくば市長峰1-1
[9] 筑波大学数理物質研究科：305-8571　茨城県つくば市天王台1-1-1
[10] 一般財団法人リモート・センシング技術センター：105-0001　東京都港区虎ノ門3-17-1
[11] 東京大学工学系研究科：113-8656　東京都文京区本郷7-3-1

球形，繊維状，あるいは歪(いびつ)なものまで様々である．その詳細な物理・化学的性状に関して，小野[14]らが放射光X線等を用いた分析を実施しており，ケイ酸塩ガラスを母体として，放射性Cs以外にも核燃料の核分裂生成物に帰属される様々な重元素を含有していたと報告している．これらの元素は粒子内で不均一に存在しており，また2号機由来とされるType AのCsMPに比べて，還元雰囲気下で揮発性が高くなるBaやSrを多く含む．1号機は3月12日15:36頃に大規模な水素爆発を起こし，0.04 PBqの^{137}Csを放出したと推測されており[1)2)]，原発周辺の土壌から発見されている1号機由来とされるType BのCsMPはこのタイミングで生成・放出されたものと考えられる．その一方で，これまでに環境中から発見されている福島第一原発事故由来の放射性粒子のなかで，^{134}Cs/^{137}Cs放射能比によって1号機由来であると推定されたものは，上述したような粗大な粒子のみである．これは，1号機由来とされるType BのCsMPは，2号機由来とされるType AのCsMPに比べて体積あたりの比放射能が低いために[12)]，オートラジオグラフィー等によって粒子の放射能を追跡する現在の粒子分離法では，微小な粒子を発見しづらいためと考えられる．また，事故後数年が経過してから採取された土壌では，先述した水素爆発のような事故事象と関連付けない限り，放射性粒子が生成・放出されたタイミングを特定することはできない．一方で，Ouraら[17)]やTsurutaら[18)19)]は，事故当時に10 μm以下の大気粉塵を捕集していたSPM（Suspended Particulate Matter）計テープろ紙に着目して，その放射能測定と放射性プルームの時空間分布を再現しており，原発の北約25 kmの測定局において，1号機の水素爆発の数時間後から^{137}Cs濃度が急激に上昇していることを報告している．また，原発から約3 kmのSPM計測定局のテープろ紙の分析による^{134}Cs/^{137}Cs放射能比から，2011年3月12～13日のプルームは，すべて1号機由来だったと報告している[19)]．これらの結果は，1号機からも2号機と同様に，原発由来のCsをはじめ放射性核種を含む微小なエアロゾルが放出されていたことを示すものである．

そこで本研究では，福島第一原発1号機由来の放射性エアロゾルをSPM計テープろ紙から単離し，その詳細な物理・化学的性状を解明して，これまでに報告されているType A及びType BのCsMPと比較することを目的とした．Tsurutaらの先行研究[18)]で水素爆発直後に放射能の上昇を捉えた測定局のSPM計テープろ紙から，事故由来の放射性エアロゾルを1粒子レベルで単離し，大型放射光施設SPring-8におけるマイクロビーム複合X線分析を中心とした1粒子単位でのキャラクタリゼーションを行った．

2 実　　験

2･1 分析試料及び分離方法

対象としたSPM計テープろ紙は，事故直後に原発から北方向約25 kmに位置する測定局で採取されたものである．石英繊維製のテープ状のろ紙の上に1時間単位でSPMが捕集されており，このテープろ紙から各時間に円状（直径11 mm）に捕集されたSPMをろ紙とともに切り抜いたものをスポットと呼ぶ．本研究では2011年3月12日20～21時と同13日0～1時に捕集された2枚のスポットを対象とした．2枚のスポットの^{134}Cs及び^{137}Cs放射能は以下のとおりである[17)]: 12日20～21時は^{134}Cs 258±5 Bq/m^{3}及び^{137}Cs 283±5 Bq/m^3，13日0～1時は^{134}Cs 285±5 Bq/m^{3}及び^{137}Cs 310±6 Bq/m^3．さらに，これら2枚のスポットの^{134}Cs/^{137}Cs放射能比は，それぞれ0.91と0.92だった[17)]．これら2枚のスポットから，放射性粒子の単離を試みた．粒子の分離手順は以下に示す手法で行った[4)]．まずイメージングプレート（IP）に各スポットを密着露光させ，オートラジオグラフィー（GE measurement & control製CR×25P CRスキャナー）により放射性物質の分布を可視化した．そこから粒子状の放射性物質が確認された部分をカッターナイフで切り抜き，カーボンテープを貼り付けたスライドガラスにフィルター繊維を崩しながら広げた．その後，IPを用いたオートラジオグラフィーあるいはGe半導体検出器（セイコーEG&G製）を用いたガンマ線スペクトル測定による放射性粒子の追跡と，マイクロマニピュレーター（マイクロサポート製AP-xy-01）による分画作業を数回にわたって繰り返し，最終的に1粒子レベルまで単離した．12日20～21時のスポットからは大きさ数百 nm～数μmの粒子が複数発見された．このうち2点を単離して分析試料とし，それぞれ「FH 12-a」「FH 12-b」とした．13日0～1時のスポットからは1粒子が単離され，こちらは「FH 13」とした．

なお本稿では，2号機由来とされるType AのCsMPと，1号機由来とされるType BのCsMPの分析結果についても，比較用試料として適宜参照する．前者は2011年3月14日夜から15日朝にかけて気象研究所において捕集され，Abeらの先行研究[5)]で分析された「Particle A」である．本稿ではこの粒子を「CsMP-A」と称する．後者は小野らの先行研究[14)]で分析されたもので，福島県内の帰還困難区域において採取した土壌より分離された7点のCsMPのうちの「Particle 1」である．本稿ではこの粒子を「CsMP-B」と称する．

2･2 分析方法

2･2･1 形態観察及び放射能測定　SPM計テープろ紙より切り抜いた2枚のスポットから単離された放射性エア

ロゾル3粒子をスライドガラスに載せ，低真空型走査電子顕微鏡（SEM: 日立ハイテクノロジーズ製 SU3500）を用いて，蒸着等の前処理を行わずに形態観察を行った．そしてSEMに接続したエネルギー分散型X線検出器（EDS: 堀場製作所製 X-max）により，加速電圧15 kVでEDSスペクトルの測定を行った．

さらに，Ge半導体検出器（CANBERRA製 GC4018）を用いたガンマ線スペクトル測定によって，単離した試料1粒子ごとに，^{134}Csと^{137}Csの放射能測定を行った．^{134}Csは日本アイソトープ協会製の点線源用標準線源を，^{137}Csについてはアマーシャム製の点線源用標準線源を用いて，検出器の上部中心に置いて測定した．なお，標準線源の放射性同位体は表面から1 mm内側に装着されている．後述するように放射性エアロゾルは放射光実験用にカプトンテープ上に固定されているので，標準線源と測定条件が揃うよう，スライドガラスを用いて1 mm離した位置に来るよう調整した．標準線源と放射性エアロゾルが同一条件で測定できていると仮定し，標準線源の放射線計測量との比較により，放射能の絶対値と統計誤差を算出した．得られた各放射能は2011年3月11日14:46当時の値になるよう減衰補正を行った．各粒子について^{134}Cs/^{137}Cs放射能比を算出し，事故当時の福島第一原発1～3号機の核燃料組成から求められた推定値[11]と比較して放出炉を推定した．

2･2･2　放射光マイクロビーム複合X線分析　穴をあけたアクリル製の支持板にカプトンテープ（寺岡製作所650S #25）を貼り付け，粘着面に放射性エアロゾルを1粒子ずつスライドガラス上から転写し，放射光実験用試料とした．放射光マイクロビーム複合X線分析は，SPring-8の分光分析ビームラインであるBL37XUにて行った．このビームラインでは，アンジュレータから発生した硬X線領域のX線を二結晶モノクロメータで単色化後，Kirkpatrick-Baezミラー集光素子によって縦横約1 μmにまで集光することができる．この単色X線マイクロビームをプローブとして，各粒子について放射光マイクロビーム蛍光X線分析（SR-μ-XRF）及びイメージング，X線吸収端近傍構造解析（SR-μ-XANES），粉末X線回折分析（SR-μ-XRD）を行った．

測定に際し，各粒子はアクリルホルダーごと実験ハッチ内のX-Yステージに固定した．用いた入射X線のエネルギーは7.0 keVから37.5 keVまでと幅広いため，測定を高エネルギー用（17.1～37.5 keV）と低エネルギー用（7.0～15.0 keV）の2回のビームタイムに分けて行った．なお，試料によって光学系の細部及び実験ハッチが異なる．FH 13及び比較用試料2点については，先行研究[5)14)]と同じ光学系及び測定条件として，BL37XUの第1ハッチにて実験を実施した．この光学系では，高エネルギー用のビームタイムにおいては散乱角90°の位置にCANBERRA製Si（Li）半導体検出器を，低エネルギー用のビームタイムにおいてはシリコンドリフト検出器（SDD: Röntec製 Xflash 2000）を設置した．FH 12-a及びFH 12-bについてはBL37XUの第3ハッチにて実験を行い，こちらは高エネルギー用と低エネルギー用の双方のビームタイムで共通して4素子シリコンドリフト検出器（日立ハイテクサイエンス製 Vortex-ME4）を試料の左右2方向に設置した．これらの検出器を用いて試料由来の蛍光X線及び散乱X線信号を検出し，SR-μ-XRF及び蛍光法のSR-μ-XANESを行った．また，二つの実験ハッチで共通して，低エネルギー用ビームタイムにおいて，試料の後方200 mmの位置にCMOSフラットパネルセンサーを設置して，透過型デバイ・シェラー法のSR-μ-XRDを行った．

SR-μ-XRFは高エネルギー用ビームタイムにて行った．入射X線のエネルギーをBa-K吸収端（37.4 keV）まで励起可能な37.5 keVに単色化し，各粒子に含まれる微量重元素に着目した化学組成の分析を行った．SR-μ-XRFイメージングにより粒子の位置を特定し，SR-μ-XRFスペクトル測定を行った．積算時間は300秒とした．スペクトル上に検出された元素について，SR-μ-XRFイメージングにより元素分布を可視化した．イメージングのステップ幅は0.5 μm（第1ハッチ）または0.2 μm（第3ハッチ）とし，1点あたりの積算時間は3秒とした．

SR-μ-XRFで検出された金属元素のうち，Fe，Zn，Mo，Snの4元素についてK吸収端のSR-μ-XANESを行った．Fe及びZnは低エネルギー用，Mo及びSnについては高エネルギー用ビームタイムでそれぞれ分析した．各元素のK吸収端の前後約100 eVの範囲について，ステップ幅1 eVで蛍光法によりSR-μ-XANESスペクトルを測定した．1点あたりの積算時間は，SR-μ-XRFイメージングで検出されていたカウント強度に応じ，1～3秒で設定した．参照試料として，先行研究[5)14)]と同様に各元素の金属粉末，酸化物，塩化物と，各元素を含有するガラス試料を測定した．SR-μ-XRDは低エネルギー用ビームタイムで実施し，入射X線は15.0 keVに単色化し，1回440ミリ秒の測定を100回積算した．参照試料としてSi粉末（NIST製 SRM 640c）をカプトンテープ上に貼り付けたものを同様に測定した．これらの実験はすべて大気中で行われた．

2･3　流跡線解析

気象庁メソスケールモデル（MSM）から得られた風の場に基づいて，10分ごとに気塊の位置を評価する目的で流跡線解析を行った．MSM分析は21800 mまでの50層で，水平分解能0.0625×0.05度を有している．地表面データは3時間の解析値と1時間の予報値を，モデル面データは3時間の解析値を用いた．流跡線解析の初期高度は地表50～1000 mに50 m間隔で設置した．なお，気塊が地表面より下に移動した場合は計算を停止した．

Table 1 Decay-corrected activities (as of 14:46 JST, 11st March 2011) of ^{134}Cs, ^{137}Cs, and ^{134}Cs/^{137}Cs (± statistical error) of individual particles

	FH 12-a	FH 12-b	FH 13
^{134}Cs (Bq)	3.67 ± 0.09	4.62 ± 0.11	8.92 ± 0.22
^{137}Cs (Bq)	3.91 ± 0.13	4.93 ± 0.17	9.68 ± 0.33
^{134}Cs/^{137}Cs	0.94 ± 0.04	0.94 ± 0.04	0.92 ± 0.04

3 結果と考察

3·1 放射性エアロゾルの放射能及び形態

2011年3月12日20～21時のスポットより分離されたFH 12-aとFH 12-b，同13日0～1時のスポットより分離されたFH 13について，ガンマ線スペクトル測定により得られた1粒子レベルでの^{134}Cs及び^{137}Csの各放射能（2011年3月当時に減衰補正）と，^{134}Cs/^{137}Cs放射能比をTable 1にまとめた．いずれの粒子も^{134}Cs/^{137}Cs放射能比は約0.9となり，福島第一原発の2号機（1.08）や3号機（1.05）よりも1号機（0.94）の推定値[11]に近い結果となった．また，前述したスポット全体の平均的な放射能比とほぼ同じだった．捕集されたタイミングと観測された放射能比より，これらの粒子は福島第一原発1号機由来であると考えられる．1号機由来の微小な放射性エアロゾルを環境試料から単離することに成功した例は本研究が初めてである．これら3粒子のSEM像をFig. 1a～dに示す．比較のため，Fig. 1e及びFig. 1fにCsMP-A及びCsMP-BのSEM像を示してある．

FH 12-a（Fig. 1a）は直径2 μm程度の粒子であり，気体が凝集したような形状をしている．FH 12-bは，まとまった状態で発見された数百nm～数μmの粒子（Fig. 1b）の中から，最も大きい直径2 μm弱の1点（Fig. 1c）とした．FH 13（Fig. 1d）は5～10 μmの歪な形状をした粒子であり，他の2粒子に比べると大きいが，EDSマッピングによると主成分はCであり，その中に後述するような重元素を含む数百nmの微小粒子が複数個埋まっている状態であると考えられる．ここでSEM像（Fig. 1f）を示したCsMP-B以外にも，土壌より発見された1号機の水素爆発由来とされるType BのCsMPは少なくとも50 μmを超える大きさである[13,14]．しかしながら，本研究で発見された放射性エアロゾルは1号機由来であるにもかかわらず，いずれも数μmオーダーと小さく，これは2号機由来とされるType AのCsMP（Fig. 1e）と同程度である．

Type AのCsMPは直径数μm前後の粒子に0.1～1 Bqオーダー（2011年3月当時）の^{134}Cs及び^{137}Csを含む[4,5]．一方，1号機の水素爆発由来とされるType BのCsMPについては，先述したようにType AのCsMPよりも体積比放射能が低いことが指摘されている[13]．この特徴が1号機由来の放射性エアロゾルにも適用されるならば，Type AのCsMPと同程度の大きさ（直径数μm）のときには，その放射能は0.1 Bqあるいはそれ以下になるはずである．しかしながらTable 1に示したとおり，本研究で発見された放射性エアロゾルは，直径数μm以下という小ささにもかかわらず4～10 Bqという比較的高い放射能を有しており，2号機由来とされるType AのCsMPに匹敵する値であった．この結果は，これらの放射性エアロゾルは^{134}Cs/^{137}Cs放射能比から1号機由来であると推定されたものの，これまでに土壌中から発見されていたType BのCsMPがただ微細化しただけではなく，明らかに異なる物理・化学的性状を有していることを意味している．

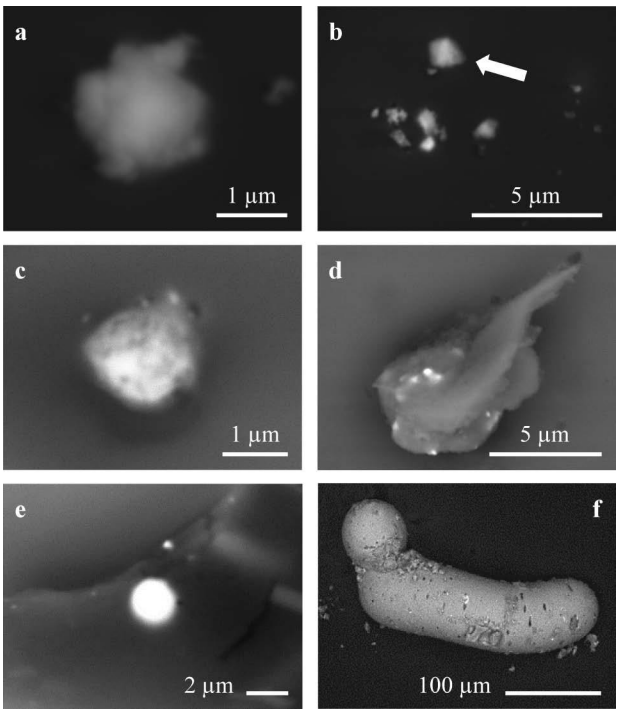

Fig. 1 SEM images of radioactive aerosols emitted by the FDNPP accident

(a) FH 12-a, (b, c) FH 12-b, and (c) FH 13 emitted from the FDNPP Reactor 1, (e) CsMP-A[5] and (f) CsMP-B[14] for the comparison.

3·2 化学組成及び元素の起源

本研究で発見された放射性エアロゾル3粒子（FH 12-a, FH 12-b, FH 13）について，代表的なEDSスペクトルをFig. 2にまとめて示した．FH 12-aのEDSスペクトルは粒子の中央付近で得られたものであり，Cs-L線が検出されたほか，Cr，Mn，Fe及びZnのK線も検出された．また，この粒子ではCl-K線もはっきりと検出されている．FH 12-bについても，粒子の中央付近で測定されたEDSスペクトルを示している．FH 12-aと同様にCs-L線，Fe及びZnのK

線が検出されたほか，FH 12-a ほどではないものの Cl-K 線も検出された．なお，FH 12-b とともにまとまった状態で発見された数百 nm ～数 μm の粒子（Fig. 1b）については，すべてから Cs-L 線及び Cl-K 線が検出された．FH 13 については，複数点の分析を行ったなかで最も明瞭な Cs-L 線が検出された点のスペクトルを Fig. 2 に示している．この点では Ca，Cr，Mn，Fe，Zn の K 線と Sn-L 線，さらに微弱ながら Cl-K 線も検出された．なお，Fig. 2 に示した 3 点の EDS スペクトルでは共通して Si と O の K 線が検出されているが，本研究の EDS はスライドガラス上に載せた状態で測定を行っているために，これらの元素が粒子中にどの程度含まれているかは判断できない．

続いて，本研究で発見された放射性エアロゾル 3 粒子の SR-μ-XRF スペクトルを Fig. 3 に示した．比較のために，先行研究[5)14)]で報告された CsMP-A 及び CsMP-B のスペクトルについても合わせて示してある．FH 12-a 及び FH 12-b については粒子の中央付近，FH 13 については後述する SR-μ-XRF イメージングにより，Cs-K 線が最も強く検出された部分で得られたものである．CsMP-A 及び CsMP-B のスペクトルは先行研究[5)14)]で示したものと同一である．なお，先述したとおり FH 13，CsMP-A，CsMP-B の 3 点（第 1 ハッチ，Si（Li）検出器を使用）と，FH 12-a 及び FH 12-b の 2 点（第 3 ハッチ，SDD を使用）とで，測定時の光学系が異なることに注意されたい．光学系の変化に伴って，33 ～ 35 keV の範囲に検出されているコンプトン散乱のエネルギーが変わっているほか，エネルギー分解能は SDD で測定したものの方が優れている．一方，素子厚の薄い SDD では，Si（Li）検出器に比べて高エネルギー領域の X 線の検出能力に劣る．そのため，Fig. 3 に示した 5 点の SR-μ-XRF スペクトルについて，検出されたピーク強度から粒子間で重元素組成を定量的に比較することは困難である．よって本稿では SR-μ-XRF の結果について，定性的な組成の議論のみを行う．

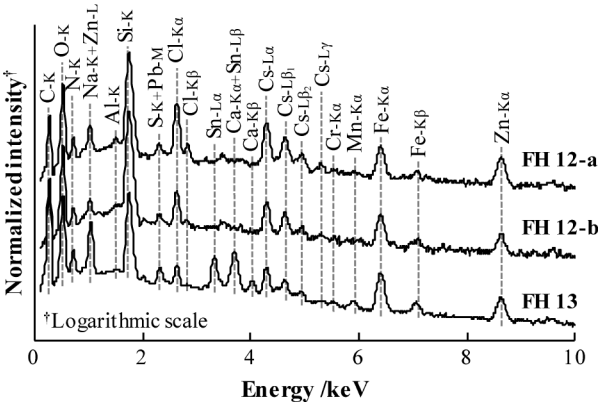

Fig. 2　Comparison of SEM-EDS spectra of the three radioactive aerosols emitted from the FDNPP Reactor 1

37.5 keV 励起の SR-μ-XRF によって，本研究で発見された放射性エアロゾル 3 粒子から，EDS では検出されなかった様々な重元素が検出された．以下の 14 元素は 3 粒子で共通して検出された：Fe，Zn，Br，Rb，Mo，Ag，Cd，In，Sn，Sb，Te，Cs，Ba，Pb．これらの元素のほかに，FH 12-a と FH 12-b から共通して Mn，Ni，Sr，Zr，Pd，U が検出された．FH 12-a と FH 12-b は全体的なスペクトル形状が似ており，検出された元素も共通しているが，FH 12-b の方が Br，Rb，Cs の強度が明らかに弱い．FH 13 はこれら 2 粒子とは異なる光学系で測定されたものであるが，光学系の違いによる感度の差を考慮しても，他の粒子とはやや異なる組成的特徴を示している．なお，これまで行われた CsMP に関する研究で，Br の存在を指摘した例はない[3)]．

SR-μ-XRF で検出された元素のうち，3 粒子で共通して検出された Fe，Zn，Br，Rb，Mo，Sn，Cs，Ba の 8 元素に着目して，SR-μ-XRF イメージングによってこれらの Kα 線の強度分布を可視化した．FH 12-a，FH 12-b，FH 13 につ

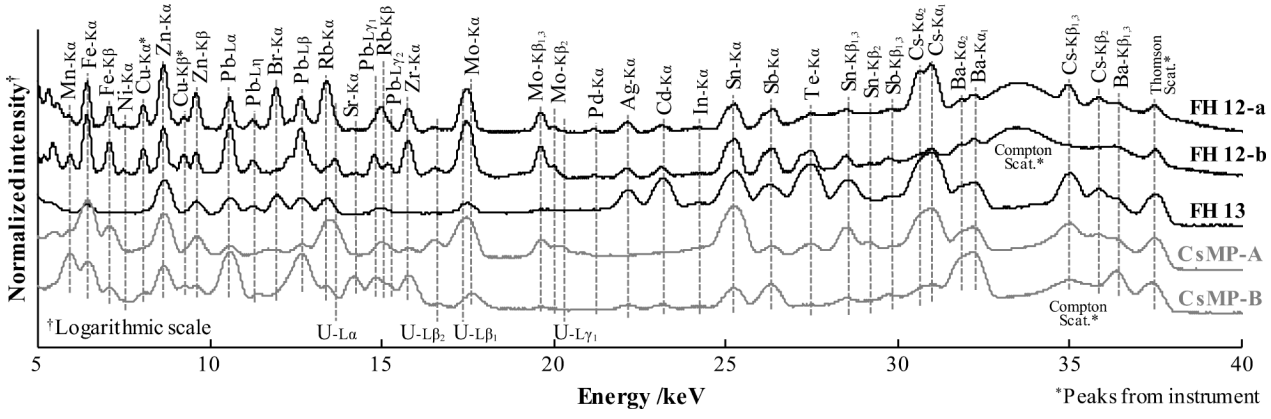

Fig. 3　Comparison of SR-μ-XRF spectra (excited by 37.5 keV X-ray) of the three radioactive aerosols emited from the FDNPP Reactor 1, CsMP-A (radioacrive particle believed to be emitted from the FDNPP Reactor 2)[5)], and CsMP-B (radioactive particle believed to be emitted by the hydrogen explosion of the FDNPP Reactor 1)[14)]

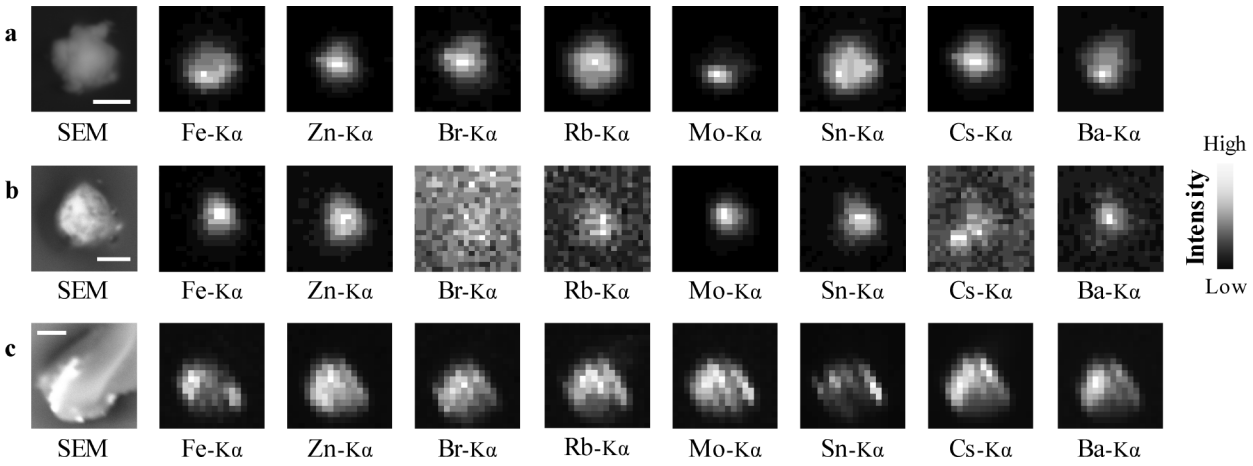

Fig. 4 Distribution of eight representative elements in the three radioactive aerosols obtained by SR-μ-XRF imaging and SEM images corresponding to the imaging region
(a) FH 12-a, (b) FH 12-b, and (c) FH 13. Scale bars in SEM images show 1 μm.

いて得られたSR-μ-XRFイメージング結果と，イメージング範囲に対応したSEM像をFig. 4a-cに示した．元素による明確な傾向はないものの，粒子内で重元素が不均一に存在していることが明らかとなった．例えばFig. 4aに示したFH 12-aのSR-μ-XRFイメージング結果において，RbやSnなどは粒子の全体から検出されているのに対し，Moは粒子の右下部分に偏在していることがわかる．同様にFH 13のイメージング結果（Fig. 4b）においても，SnとCsの分布に明らかな差が見られる．なおFig. 4bに示したFH 12-bのイメージング結果のうち，スペクトル（Fig. 3）上で極めて微弱に検出されていたBr，Rb，Csの3元素については，他の元素に比べてノイズによる影響が激しい．2号機由来とされるType AのCsMPについては，nmレベルのインクルージョンの存在がいくつかの研究[6)7)16)]で指摘されているものの，ここで見られたようなμmレベルの元素の偏在は確認されていない．一方，1号機の水素爆発で生成されたとされるType BのCsMP[13)14)]については，粒子自体の大きさがそもそも大きいせいもあり，粒子内にμmレベルでの元素の偏在が見つかっている．こうした粒子内での元素の均一性の違いは，粒子の生成過程を強く反映しているものと考えられる．本研究のSR-μ-XRFイメージングは透過力の高いX線を用いているため，深さ方向の信号が積算されてしまう．また，今回分析した粒子に対してビームサイズが大きいこともあり，Fig. 4に示したイメージング結果のみからでは，粒子内における元素の分布状態を正しく把握することは困難であった．CsMPに関するいくつかの研究[6)7)16)]で導入されているように，破壊分析にはなってしまうものの，集束イオンビームで粒子内部を切り出してSEMや透過電子顕微鏡による観察を行うことで，より詳細な元素分布や内部構造が明らかになると期待される．

EDS及びSR-μ-XRFによって検出された元素について，先行研究[5)14)]を参考にしながら，その由来を考察した．FH 12-a及びFH 12-bで検出されたUは核燃料，Brから Baまでの14元素（Br，Rb，Sr，Zr，Mo，Pd，Ag，Cd，In，Sn，Sb，Te，Cs，Ba）は，その核分裂生成物に帰属可能である．ただしZrとSnについては，燃料被覆管のZr-Sn合金に由来する可能性もある．Pbは格納容器内側の放射線遮蔽用のPb板に由来すると考えられる．Cr，Mn，Fe，Ni，Znについては原子炉の構成材料に由来するものと考えられ，特にCr，Fe，Niは一般的なステンレス鋼の主成分であり，これにMoを加えたSUS316やSUS316Lは耐腐食性に優れるとされる．またMn，Ni，Moの3元素については，圧力容器に使用されたMo-Mn-Ni鋼に由来する可能性も考えられる．EDSで検出されたO，Na，Al，Si，Caについては，断熱材やコンクリートに由来する可能性もあるが，先述したように下地のスライドガラスの成分が検出されている可能性もあるため，特定が困難であった．興味深いのが，本研究で発見された放射性エアロゾルから共通して検出されたClとBrである．これらは原子炉の緊急冷却用に注入された海水に由来する可能性があり，詳しくは後述する．なお，同じくハロゲン元素であるIについては，その$K\alpha$線（$K\alpha_1$：28.61 keV）が比較的高濃度で含有されているSnの$K\beta$線（$K\beta_1$：28.49 keV）と重複してしまい，本分析手法ではその存在を確認できなかった．以上のように，本研究で発見された放射性エアロゾル3粒子について，EDS及びSR-μ-XRFによって検出された元素は事故当時炉内に存在した物質に由来する可能性が示唆された．

3・3 粒子の化学状態

本研究で発見された放射性エアロゾル3粒子について，Fe，Zn，Mo，SnのK吸収端SR-μ-XANESスペクトルを測定した．ここではMo-K及びZn-K吸収端SR-μ-XANESの結果

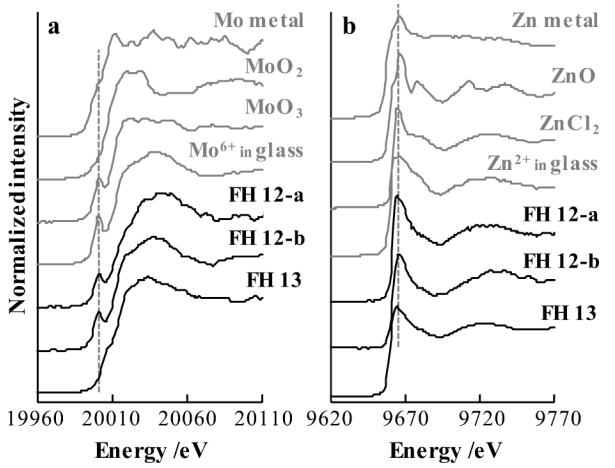

Fig. 5　Results of SR-μ-XANES analyses

Compasirion of (a) Mo-K edge and (b) Zn-K edge SR-μ-XANES spectra of the three radioactive aerosols emitted from the FDNPP Reactor 1 and reference materials.

について，参照試料のスペクトルと共にそれぞれ Fig. 5a b に示した．SR-μ-XANES スペクトルの測定箇所は SR-μ-XRF と同一である．

まず Mo-K 吸収端（Fig. 5a）に関して，Mo が酸化数＋6 で存在する場合には，図中に破線で示したような pre-edge ピークが検出される．そこで本研究で発見された放射性エアロゾル 3 粒子について見てみると，FH 12-a 及び FH 12-b では Mo^{6+} に帰属される pre-edge が検出された．さらに，これら 2 点についてスペクトルの形状を参照試料と比較すると，酸化物 MoO_3 よりも Mo^{6+} イオンを含むガラスのものに近いことがわかる．一方，FH 13 については pre-edge ピークは検出されておらず，より低い酸化数で存在する可能性が示唆された．ここで先行研究[5]を見ると，2 号機由来とされる Type A の CsMP では，本研究の FH 12-a や FH 12-b と同様に，ガラス相中に Mo^{6+} イオンの形で存在していることが，本研究と同じ SR-μ-XANES によって明らかになっている．一方，土壌から分離された 1 号機の水素爆発由来とされる Type B の CsMP においては，一つの粒子内でガラス中の Mo^{6+} イオンとして存在している部分と，より低い酸化数の状態で存在する部分が混在していた[14]．ただし，還元雰囲気下で生成した粒子であっても，長期間環境中にさらされることで部分的に酸化するとの指摘もあり[20]，高い酸化状態が生成時の酸化雰囲気を示唆するかどうかは現時点では断定できない．

続いて Zn-K 吸収端（Fig. 5b）を見ると，放射性エアロゾル 3 粒子のいずれにおいても，Zn は酸化数＋2 の状態で存在していることがわかった．特に FH 13 については，参照試料として測定した Zn^{2+} イオンを含むガラスのものとスペクトル形状が比較的類似していた．しかしながら，FH 12-a 及び FH 12-b においては，緩やかなガラスのスペクトルに比べて吸収の最大点（ホワイトライン）がシャープである．他の参照試料のスペクトルと比較した結果，これらの粒子中では Zn の一部が $ZnCl_2$ の形で存在すると推定された．先に示した EDS スペクトル（Fig. 2）においても，これら 2 粒子からは Cl の K 線が強く検出されており，この推定が支持される．CsMP に関する先行研究のなかで，SR-μ-XANES[5)14)] によって $ZnCl_2$ の存在が示された例はないが，高角度散乱暗視野法走査型透過電子顕微鏡（HAADF-STEM）を用いた研究[16]により，Type A の CsMP の内部に $ZnCl_2$ のナノスケールのインクルージョンが存在しているとする報告がある．

ここで示していない 2 元素については，まず Sn-K 吸収端 SR-μ-XANES ではホワイトラインの位置から 3 粒子とも酸化数＋4 の状態で Sn を含有していることが明らかになった．なお，酸化数＋4 の参照試料として酸化物 SnO_2 と，Sn^{4+} を含むガラスを測定しているが，放射性エアロゾル中の Sn がこれらのどちらに近いかはスペクトル形状から判断できなかった．Fe-K 吸収端 SR-μ-XANES については，FH 12-a と FH 12-b については Fe が酸化数＋3 で存在すると推定されたのに対し，FH 13 では吸収端エネルギーがやや低エネルギーに位置したため，還元的な形態が混在している可能性が示された．なお Fe についても SR-μ-XANES により具体的な存在状態は特定されなかった．

また，本研究で発見された放射性エアロゾル 3 粒子について SR-μ-XRD を行ったが，いずれにおいても回折ピークは得られなかった．Type A の CsMP についても，同手法で回折ピークは得られていないが[5]，先述したように粒子内にナノサイズの結晶性物質の存在が指摘されている[6)7)16)]．一方，Type B の CsMP[14]においては，粒子の母体は結晶性を持たないケイ酸塩ガラスであったが，粒子内部に Fe を主成分とする酸化物が存在していることが，本研究と同じ SR-μ-XANES 及び SR-μ-XRD によって同定されている．

以上の化学状態に関する分析結果をまとめると，SPM 計テープろ紙より切り抜いた 2 枚のスポットより単離された放射性エアロゾル 3 粒子については，比較的酸化的な状態で金属元素を含有しており，一部は塩化物の形になっている可能性が示された．また，一部の金属元素についてはガラス相中に金属イオンの形で存在する場合と SR-μ-XANES スペクトルが類似していたが，本研究で発見された放射性エアロゾルが先行研究[5)14)]で報告された CsMP と同様に，ケイ酸塩ガラスを母体としているかは現時点では判断できない．ただし SR-μ-XRD で回折ピークが検出されなかったことから，非晶質あるいは結晶性の低い物質を母体として，SR-μ-XANES で見られた塩化物はインクルージョンのような形態と推定される．同様の粒子がこれまで原発周辺で採取された土壌から発見されていなかったことを考慮す

ると，これらの放射性エアロゾルに含まれる放射性核種は可溶性である可能性が高い．

3･4 粒子の生成過程に関する考察

ここで，本研究で発見された放射性エアロゾル3粒子について，先行研究[5)14)]で報告されたCsMP-A及びCsMP-Bの化学組成を比較しながら，その生成過程を考察してみた．

まず，2号機由来とされるCsMP-Aと1号機の水素爆発由来とされるCsMP-Bの組成の違いについて，小野ら[14)]は前者がRbとCsに富み，後者がSrとBaに富むことが大きな特徴であると指摘している．小野ら[14)]は，本稿で示したCsMP-Bを含めて計4点のType BのCsMPについてEDSスペクトル及びSR-μ-XRFスペクトルを報告しているが，その4点に共通する特徴としてCsはEDSの検出限界以下の濃度であり，またSR-μ-XRFスペクトル上ではCs-K線よりBa-K線の方が強く検出された．さらにSR-μ-XRFでRbがほとんど検出されなかった一方で，2号機由来とされるType AのCsMPには見られないSr-K線が特徴的に検出された．Rbは酸化雰囲気，Sr及びBaは還元雰囲気において揮発性が高くなることが知られているため[21)]，小野ら[14)]は2号機由来とされるType AのCsMPと1号機由来とされるType BのCsMPは生成時の炉内状況に差があり，後者が水素爆発のタイミングで生成・放出されたことを示す根拠だと指摘している．そこで，本研究で分析した3粒子のSR-μ-XRFスペクトル（Fig. 3）を上記の元素に着目すると，FH 12-aとFH 13ではCs-K線の方がBa-K線より強く検出されており，FH 12-bでは同程度であった．また，1号機の水素爆発由来とされる粒子（CsMP-B）ではほとんど検出されないRbについても，本研究で発見された放射性エアロゾルから共通して検出されており，特にFH 12-aとFH 13においてRb-K線がはっきりと検出された．その一方で，本研究で発見された放射性エアロゾル3粒子からは，Srはほとんど検出されなかった．よってRb，Sr，Cs，Baという4元素に着目した場合，今回分析した3粒子のうちFH 12-aとFH 13については，1号機の水素爆発由来とされるType BのCsMPよりも，2号機由来とされるType AのCsMPに近い．すなわち，小野ら[14)]の指摘する揮発性の違いに関連付けるとすれば，FH 12-aとFH 13は還元雰囲気中ではなく，酸化雰囲気中で生成された可能性が高いということになる．残る1粒子のFH 12-bについては上記の4元素がほとんど検出されていないが，これは「FH 12-aからRbとCsが欠損した組成」と考えるのが適当であると考える．ここでSR-μ-XANESの結果と併せて考えると，FH 13では還元的な状態の金属が混在しているものの，1号機の水素爆発由来とされるType BのCsMP[14)]に比べて金属元素が酸化的な状態になっており，先述した可能性とよく対応している．

ここで着目したいのが，本研究で発見された放射性エアロゾル3粒子で共通して検出されたClおよびBrの存在である．2号機由来とされるType AのCsMPの研究において，EDS[7)]やHAADF-STEM[16)]を用いた分析によって微量なClの存在が指摘されており，その由来は冷却のために炉内に注入された海水と推定されている．さらに，2011年3月12日における1号機の冷却及び水素爆発に関する推移[22)]を見ると，12日5:46から14:53まで行われた原子炉への淡水注入のあと，15:36頃に水素爆発が発生した．19:04より海水注入が開始され，19:25に一旦停止したのち，20:20から海水及びホウ酸水による注水が開始された．すなわち，水素爆発を起こした時点で1号機において海水注入は行われていなかった．換言すれば，本研究で発見された放射性エアロゾルに含まれるClおよびBrが海水に由来するものであり，かつ放出から捕集までの間に大気中で付着した海塩によるものでないとすれば，これらの粒子が生成されたのは1号機への海水注入が行われたあとということになる．小野ら[14)]が指摘しているとおり，12日の水素爆発は炉心ではなく原子炉建屋で発生したものであるため，Type BのCsMPの生成がこの爆発のみで引き起こされたとは判断できないが，先述したような還元雰囲気下で揮発性の高くなる元素の存在や，50 μmを超える大きさ，あるいは歪な形状などを考慮すると，その主要な生成・放出要因は水素爆発であった可能性が高い．一方，本研究で発見された放射性エアロゾルについては，この水素爆発の段階で生成されたのではなく，海水注入に伴い揮発性の高いハロゲン化物が生成されたことが，その生成に大きく関係しているものと考察する．SR-μ-XRFイメージング（Fig. 4参照）によって粒子中にμmレベルの元素の不均一性が見られた点も，これらの粒子が高温で熔融したものではなく，揮発及び凝結によって生成されたものであった可能性を支持する．さらに，本研究で発見された放射性エアロゾルが比較的酸化的な雰囲気で生成されたという本研究の分析結果は，その生成当時，炉内に酸素が流入するような損傷が生じていたか，炉内で酸素が発生するような事象が生じていたことを示唆する．一方で，本研究で対象としたSPM計測定局は海岸地点に位置し，浮遊中に付着した海塩粒子に由来する可能性も十分に考慮する必要がある．今回発見された放射性エアロゾルについて，より詳細な内部構造が明らかになることで，ClおよびBrの由来が明らかになるものと期待される．

これまでに発見，報告された1号機由来とされる放射性粒子，すなわちType BのCsMPは，すべて事故後数年が経過したあとに採取された環境試料から分離されたものであった[13)14)]．これらの粒子はガラスを母体としているため，水に対して不溶または難溶と考えられ，環境中に数年間置かれていた間に部分的な溶出や酸化が生じることは

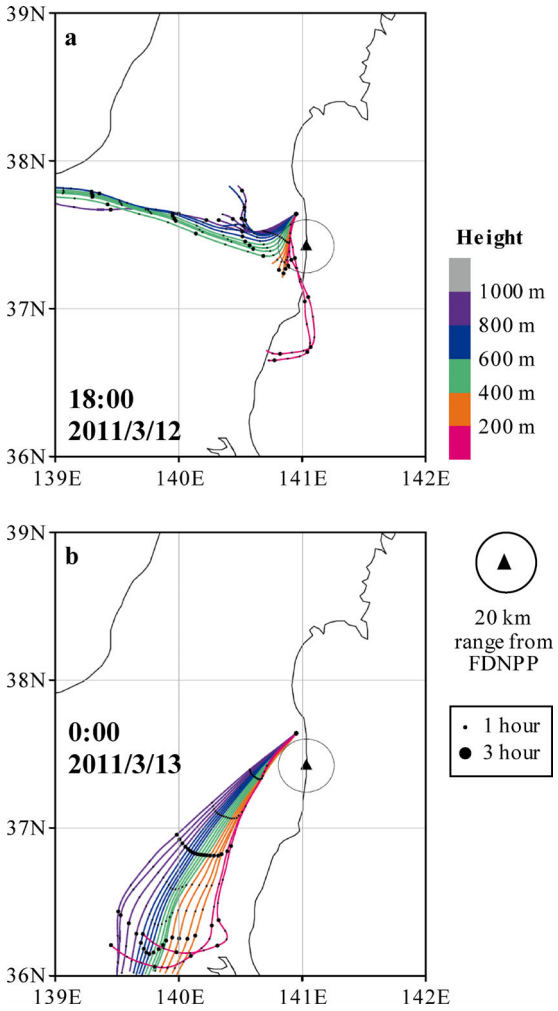

Fig. 6　Backward trajectories calculated for air parcels placed above the SPM monitoring site at (a) 20:00 JST 12th March 2011 and (b) 0:00 JST 13th March 2011

The trajectories are color-coded to distinguish heights (m) of the parcels at the monitoring station. Small and large dots on the trajectories indicate intervals of every hour and three hours since the calculation start time, respectively.

あっても，粒子自体が完全に消失することはない．しかしながら，今回SPM計テープろ紙から切り抜いたスポットより分離された放射性エアロゾル3粒子については，少なからず放射性核種を水溶性物質として含有している可能性がある．水溶性の放射性エアロゾルは事故当時の炉内環境を推測するうえで重要な情報を含んでいるが，こういったエアロゾルは大気中への放出後にすぐ変化・溶解してしまうため，その性状を長期間野外環境にさらされた試料から調査することは極めて難しい．本研究では，原発から極めて近い距離において事故直後の大気粉塵を捕集したSPM計テープろ紙を対象とし，さらにこの時間帯では近隣のAMeDAS地点で降水が観測されておらず，雨による変質を受けていなかったことで，これまでに発見されていなかった水溶性の放射性核種を含む放射性エアロゾルを発見・単離することができ，その具体的な物理・化学的性状を1粒子レベルで初めて明らかにした．また，これまで1号機由来のCsMP（Type B）と2号機由来のCsMP（Type A）は粒径や形状，あるいは体積比放射能などの物理・化学的性状に明確な違いがあると考えられてきたが，本研究で発見された1号機由来の放射性エアロゾルは，Type BのCsMPとは明らかに異なる性状を有していた．事故由来の放射性物質について放出源を推定するためには，大きさや形状のみを指標とするのではなく，やはり1粒子レベルで^{134}Cs/^{137}Cs放射能比を算出することが望ましい．

3・4　流跡線解析

本研究で対象としたSPM計テープろ紙より切り抜いた2枚のスポットは，捕集された場所（測定局）と日時が明らかで，さらに1時間単位という高い時間分解能を持つ試料である．これらの情報とMSMで得られた風の場の情報を使用した流跡線解析によって，捕集されたエアロゾルの飛散経路を見積もった．各スポットの捕集開始時間である2011年3月12日20時と13日0時（ともに日本標準時，JST）における，測定局からの後方流跡線解析の結果をFig. 6a及びbに示した．各気塊の流跡線は1時間ごとにマーカーを付し，3時間おきにマーカーを大きくしてある．また，流跡線の色は計算の始点，すなわち測定局上空到達時における，各気塊の高度を表している．

Fig. 6aより，12日20時に測定局の上空に存在した気塊のうち，上空400 m以高のものについては1時間前，低高度のものについても2時間前には福島第一原発の上空に位置していたことが示された．この結果は，FH 12-a及びFH 12-bが福島第一原発から放出されたものであったと仮定した場合，推定される放出時間は早くても18時であったということになる．この結果は，これらの放射性エアロゾルが15:36頃に発生した水素爆発により生成・放出されたものではなく，19:04より開始された海水注入の影響を受けて生成されたとする，先述の考察を支持するものである．続いて，Fig. 6bに示した13日0時の測定局における後方流跡線解析の結果については，測定局と原発の距離（約25 km）であれば1時間以内で移動可能であるとする結果であった．しかしながら，計算された各高度の流跡線のなかに，原発周辺20 km圏の上空を通過するものはなかった．ただし，今回の流跡線解析で用いたデータでは，特に地表付近で当時の気塊の動きを十分に再現できていない可能性が考えらえる．当時の風速が弱かったことを考慮すると，接地逆転層が形成されていた可能性もあり，それが再現を困難にする一因になった可能性がある．よってFH 13については，FH 12-a及びFH 12-bと同様のタイミングで生成・放出されたものが地表付近を通過して13日0～1時に

測定局に飛来した可能性と，1号機からの放射性エアロゾルの放出が少なくとも13日0時頃まで継続していた可能性の双方が推定される．

いずれにせよ，本研究でSPM計テープろ紙より単離された放射性エアロゾルは，$^{134}Cs/^{137}Cs$放射能比から推定されたとおり福島第一原発1号機に由来するものと考えられるが，その生成・放出の直接的要因は水素爆発ではなく，その後の海水注入に伴い揮発性の高いハロゲン化物が生成されたことが大きく影響している可能性が考えられる．

4 結　　言

2011年3月12日15時36分に発生した福島第一原子力発電所1号機の水素爆発のあとに，北方向約25 kmに設置されていた測定局で捕集されたSPM計テープろ紙から，12日20～21時及び13日0～1時に捕集された2枚のスポットを切り抜いた．各スポットから放射性エアロゾルを単離し，放射光マイクロビーム複合X線分析を含む1粒子レベルでのキャラクタリゼーションを実施した．本研究で発見された放射性エアロゾル3粒子は，$^{134}Cs/^{137}Cs$放射能比から1号機由来であることが確かめられた．しかしながらその形状や大きさは，先行研究[14]で原発周辺の土壌から発見されていた1号機の水素爆発由来とされるType BのCsMPとは明らかに異なっていた．また，EDSによってすべての粒子から共通してClが検出され，これは冷却のために注入された海水に由来するものであると考えられる．SR-μ-XRFの結果，本研究で発見された放射性エアロゾル3粒子から，核燃料由来と考えられるUをはじめとして，その核分裂生成物に帰属される重元素，さらには原子炉の構成材料と考えられる金属元素が検出されたが，これらの元素は粒子内で不均一に存在していた．Type BのCsMPが還元雰囲気下で揮発性が高くなるSrやBaを多く含んでいたのに対し，本研究で発見された放射性エアロゾルはこれらの元素を含まず，2号機由来とされるType AのCsMPと同様に，酸化雰囲気下で高揮発性となるRbを含んでいた．また，これまでCsMPの分析では報告例のないBrを含有していることが明らかになった．SR-μ-XANESでは，これらの放射性エアロゾルに含まれる金属元素が比較的酸化的な状態で存在し，さらにその一部が塩化物になっていることが示された．また，SR-μ-XRDにより粒子の母体が非晶質または結晶性の低い物質であることが示された．水素爆発由来とされるType BのCsMPとの物理・化学的性状の違い，さらにはCl及びBrを含むという組成的特徴から，本研究で発見された放射性エアロゾルは12日15:36頃に発生した水素爆発によって生成・放出されたものではなく，その後の19:04から開始された海水注入に伴い，揮発性の高いハロゲン化物が生成したことが，放射性エアロゾルの生成の要因の一つになった可能性が考えられる．こうした物理・化学的性状は，これまでに発見・報告されていたType A及びType Bという2種類のCsMPとは明らかに異なるものであり，本研究によって新たなタイプのCsMPが発見されたと言える．

事故から年月が経つにつれて，短半減期の放射性核種の検出は困難になる．それに伴い，事故による放射性粒子そのものを分析する研究例は減少していくだろう．しかし，こうした事故由来の放射性粒子は当時の炉内環境を保存し，多くの情報を内包している貴重な「試料・資料」であることに変わりはなく，それらの分析手法も多角化している．今後もCsMPをはじめとした放射性粒子を対象とした研究が発展し，事故事象解明の足がかりになることを期待したい．

謝　　辞

本研究の一部は，「科研費新学術領域研究2409（領域代表：恩田裕一）」，「同15H00978（代表：中井 泉）」，「平成30年度放射性物質環境動態・環境および生物への影響に関する学際共同研究（代表：阿部善也）」，「平成30年度英知を結集した原子力科学技術・人材育成推進事業（国際共同型，代表：五十嵐康人）」及び「環境再生保全機構の環境研究総合推進費5-1501（代表：森口祐一）及び1-1802（代表：山澤弘実）」の支援により実施されました．記して謝意を表します．

本研究の放射光実験は，高輝度光科学研究センターSPring-8一般利用課題（課題番号：2016A1705）及び社会・文化利用課題（課題番号：2016B1811，2017A1719，2017B1757，2018A1704，2018B1748）として行われました．測定でご指導いただきました寺田靖子氏，新田清文氏，関澤央輝氏に厚く謝礼申し上げます．

（平成30年10月25～26日，第54回X線分析討論会において，一部発表）

文　　献

1) TEPCO： Tokyo Electric Power Company Holdings, <http://www.tepco.co.jp/index-j.html>, (accessed 2019-9-21).
2) MEXT： Japanese Ministry of Education, Culture, Sports, Science and Technology, <http://www.mext.go.jp/>, (accessed 2019-9-21).
3) Y. Igarashi, T. Kogure, Y. Kurihara, H. Miura, T. Okumura, Y. Satou, Y. Takahashi, N. Yamaguchi： *J. Environ. Radioact.*, **205–206**, 101 (2019).
4) K. Adachi, M. Kajino, Y. Zaizen, Y. Igarashi： *Sci. Rep.*, **3**, 2554 (2013).
5) Y. Abe, Y. Iizawa, Y. Terada, K. Adachi, Y. Igarashi, I. Nakai： *Anal. Chem.*, **86**, 8521 (2014).
6) N. Yamaguchi, M. Mitime, K. Akiyama-Hasegawa, M. Asano, K. Adachi, T. Kogure： *Sci. Rep.*, **6**, 20548 (2016).
7) T. Kogure, N. Yamaguchi, H. Segawa, H. Mukai, S. Motai, K. Akiyama-Hasegawa, T. Yaita： *Microscopy*, **65**, 451 (2016).
8) S. Higaki, Y. Kurihara, H. Yoshida, Y. Takahashi, N. Shinohara： *J. Environ. Radioact.*, **177**, 65 (2017).

9) H. Miura, Y. Kurihara, A. Sakaguchi, K. Tanaka, N. Yamaguchi, S. Higaki, Y. Takahashi : *Geochem. J.*, **52**, 145 (2018).
10) T. Okumura, N. Yamaguchi, T. Dohi, K. Iijima, T. Kogure : *Sci. Rep.*, **9**, 3520 (2019).
11) 西原健司，岩元大樹，須山賢也：JAEA-Data/Code 2012-018 (2012).
12) Y. Satou, K. Sueki, K. Sasa, K. Adachi, Y. Igarashi : *Anthoropocene*, **14**, 71 (2016).
13) Y. Satou, K. Sueki, K. Sasa, H. Yoshikawa, S. Nakama, H. Minowa, Y. Abe, I. Nakai, T. Ono, K. Adachi, Y. Igarashi : *Geochem. J.*, **52**, 137 (2018).
14) 小野貴大，飯澤勇信，阿部善也，中井　泉，寺田靖子，佐藤志彦，末木啓介，足立光司，五十嵐康人：分析化学 (*Bunseki Kagaku*), **66**, 251 (2017).
15) S. Motai, H. Mukai, T. Watanuki, K. Ohwada, T. Fukuda, A. Machida, C. Kuramata, R. Kikuchi, T. Yaita, T. Kogure : *J. Mineral. Petrol. Sci.*, **111**, 5 (2016).
16) G. Furuki, J. Imoto, A. Ochiai, S. Yamasaki, K. Nanba, T. Ohnuki, B. Grambow, R. C. Ewing, S. Utsunomiya : *Sci. Rep.*, **7**, 42731 (2018).
17) Y. Oura, M. Ebihara, H. Tsuruta, T. Nakajima, T. Ohara, M. Ishimoto, H. Sawahata, Y. Katsumura, W. Nitta : *J. Nucl. Radiochem. Sci.*, **15**, 1 (2015).
18) H. Tsuruta, Y. Oura, M. Ebihara, T. Ohara, T. Nakajima : *Sci. Rep.*, **4**, 6717 (2014).
19) H. Tsuruta, Y. Oura, M. Ebihara, Y. Moriguchi, T. Ohara, T. Nakajima : *Geochem. J.*, **52**, 103 (2018).
20) 三浦　輝，栗原雄一，山本政義，山口紀子，坂口綾，桧垣正吾，高橋嘉夫：日本地球惑星科学連合2018年大会にて発表 (2018).
21) Y. Pontillon, G. Ducros, P. P. Malgouyres : *Nucl. Eng. Des.*, **240**, 1843 (2010).
22) TEPCO : “各種操作実績取り纏め”, (2011) <http://www.tepco.co.jp/nu/fukushima-np/plant-data/f1_7_Sousajisseki.pdf>, (accessed 2019-9-21).

Investigation of Physical and Chemical Characteristics of Radioactive Aerosols Emitted From Reactor Unit 1 by Fukushima Daiichi Nuclear Power Plant Accident

Seika ONOZAKI[1], Yoshinari ABE*[1], Izumi NAKAI[1], Kouji ADACHI[2], Yasuhito IGARASHI[3,4], Yasuji OURA[5], Mitsuru EBIHARA[5,6], Takafumi MIYASAKA[2,7,8], Hisashi NAKAMURA[7], Keisuke SUEKI[9], Haruo TSURUTA[10] and Yuichi MORIGUCHI[11]

* E-mail : y.abe@rs.tus.ac.jp

[1] Department of Applied Chemistry, Faculty of Science, Tokyo University of Science, 1-3, Kagurazaka, Shinjuku-ku, Tokyo 162-8601
[2] Meteorological Research Institute, 1-1, Nagamine, Tsukuba-shi, Ibaraki 305-0052
[3] Institute for Integrated Radiation and Nuclear Science, Kyoto University, 2, Asashiro-Nishi, Kumatori-cho, Sennan-gun, Osaka 590-0494
[4] College of Science, Ibaraki University, 2-1-1, Bunkyo, Mito-shi, Ibaraki 310-8512
[5] Graduate School of Science, Tokyo Metropolitan University, 1-1, Minami-Osawa, Hachioji-shi, Tokyo 192-0397
[6] Department of Earth Sciences, School of Education and Integrated Arts & Sciences, Waseda University, 1-6-1, Nishi-waseda, Shinjuku-ku, Tokyo 169-8050
[7] Research Center for Advanced Science and Technology, The University of Tokyo, 4-6-1, Komaba, Meguro-ku, Tokyo 153-8904
[8] Japan Meteorological Business Support Center, 1-1, Nakamine, Tsukuba-shi, Ibaraki 305-0052
[9] Faculty of Pure and Applied Sciences, University of Tsukuba, 1-1-1, Tennodai, Tsukuba-shi, Ibaraki 305-8571
[10] Remote Sensing Technology Center of Japan, 3-17-1, Toranomon, Minato-ku, Tokyo 105-0001
[11] School of Engineering, The University of Tokyo, 7-3-1, Hongo, Bunkyo-ku, Tokyo 113-8656

(Received June 7, 2019; Accepted July 7, 2019)

Three radioactive microparticles were separated from particles on filter tape samples collected hourly at a suspended particulate matter (SPM) monitoring site located at ~25 km north of the Fukushima Daiichi Nuclear Power Plant (FDNPP), after the hydrogen explosion of reactor 1 on 12th March 2011. The $^{134}Cs/^{137}Cs$ radioactivity ratios of the three radioactive aerosol particles showed that they were derived from the FDNPP reactor 1, rather than reactors 2 or 3. The physical characteristics of these particles with < 10 μm in diameter and non-uniform shape are clearly different from those of radioactive particles generated by the hydrogen explosion of the FDNPP reactor 1. A significant amount of Cl was detected by energy dispaersive X-ray spectrometery. Synchrosron radiation microbeam (SR-μ-) X-ray fluoresence (XRF) analysis showed that these particles contain a series of heavy elements related to the nuclear fules and their fission products with a non-homogeneous distribution within the particles. In addition, the SR-μ-XRF identified trace amounts of Br in these particles; the element has firstly been found in radioactive particles derived by the FDNPP accident. In contrast to the hydrogen explosion-generated radioactive particles containing Sr and Ba, both of which are easily volatile under a reduction atmosphere, these elements were not rich in the particles found in this study. By the SR-μ-X-ray absorption near edge structure analysis and SR-μ-X-ray powder diffraction, it was found that these particles consist of an amorphous (or low crystalline) matrix containing metal elements with chemical states in a comparatively high state of oxidation or chloride. Based on these physical and chemical characteristics and a trajectory analysis of air parcels that passed over the SPM monitoring site, we concluded that these radioactive particles were generated and emitted into the atomosphere at the time of seawater injection for cooling the reactor after the hydrogen explosion.

Keywords: Fukushima Daiichi Nuclear Power Plant Accident; aerosol particle; synchrotron radiation X-ray analysis; radioactive material.

4. Publication list 1954-2021

論文リスト（英文誌）1954-2021

2021

1. Abe, Y., Onozaki, S., Nakai, I. et al. Widespread distribution of radiocesium-bearing microparticles over the greater Kanto Region resulting from the Fukushima nuclear accident. Prog Earth Planet Sci 8, 13 (2021). https://doi.org/10.1186/s40645-020-00403-6
2. Kajino, M., Adachi1, K., Igarashi,Y., Satou,Y., Sawada, M., Sekiyama, T,T., Zaizen, Y., Saya, A., Tsuruta, H., and Moriguchi, Y. Deposition and Dispersion of Radio-Cesium Released due to the Fukushima Nuclear Accident: 2. Sensitivity to Aerosol Microphysical Properties of Cs-Bearing Microparticles (CsMPs) Journal of Geophysical Research: Atmospheres, Volume 126, Issue 1. doi: 10.1029/2020JD033460
3. Kajino, M., Watanabe, A., Ishizuka,M., Kita, K., Zaizen, Y., Kinase, T., Hirai, R., Konnai, K., Saya, A., Shiroma, Y., Hasegawa, H., Akata, N., Hosoda, M., Tokonami, S. and Igarashi,Y. Re-assessment of radiocesium resuspension flux from contaminated ground surface in East Japan. https://doi.org/10.5194/acp-2021-687
4. Sekiyama, T. T. and M. Kajino (2021) Performance of a 250-m grid Eulerian dispersion simulation evaluated at two coastal monitoring stations in the vicinity of the Fukushima Daiichi Nuclear Power Plant, J. Meteor. Soc. Japan, 99, doi:10.2151/jmsj.2021-052
5. Sekiyama, T, T., Kajino, M., and Kunii, M. Ensemble Dispersion Simulation of a Point-Source Radioactive Aerosol Using Perturbed Meteorological Fields over Eastern Japan. Atmosphere 2021, *12*(6), 662; https://doi.org/10.3390/atmos12060662
6. Watanabe, A., Kajino, M., Ninomiya, K., Nagahashi1, Y. and Shinohara, A. Eight-year variations in atmospheric radiocesium in Fukushima city. Atmospheric Chemistry and Physics. doi.org/10.5194/acp-2021-591
7. Ohno, T., Sato, N., Shikimori, J., Ijichi, Y., Fukami, Y., & Igarashi, Y. (2021). Temporal change of 236U/238U and 235U/238U isotopic ratios in atmospheric deposition in Tokyo and Akita from 1963 to 1979. Science of The Total Environment, 151292.

2020

1. Kinase, T., Adachi, K., Sekiyama, T.T. et al. Temporal variations of 90Sr and 137Cs in atmospheric depositions after the Fukushima Daiichi Nuclear Power Plant accident with long-term observations. Sci Rep 10, 21627 . https://doi.org/10.1038/s41598-020-78312-3
2. Kita, K., Igarashi, Y., Kinase, T. et al. Rain-induced bioecological resuspension of radiocaesium in a polluted forest in Japan. Sci Rep 10, 15330. https://doi.org/10.1038/s41598-020-72029-z
3. Sekiyama, T. T. and Kajino, M., Reproducibility of Surface Wind and Tracer Transport Simulations over Complex Terrain Using 5-, 3-, and 1-km-Grid Models. Journal of Applied Meteorology and Climatology. Volume 59. 937-952 doi: https://doi.org/10.1175/JAMC-D-19-0241.1

2019

1. Igarashi, Y., K., Kita, T., Maki, T., Kinase, N., Hayashi, K., Hosaka, K., Adachi, M., Kajino, M., Ishizuka, T. T., Sekiyama, Y., Zaizen, C., Takenaka, K., Ninomiya, H., Okochi, A., Sorimachi, Fungal spore involvement in the resuspension of radiocaesium in summer. Scientific Reports 9:1954, 2019.
2. Iwasaki, T., Sekiyama, T. T., Nakajima, T., Watanabe, A., Suzuki, Y., Kondo, H., Morino, Y., Terada, H., Nagai, H., Takigawa, M., Yamazawa, H., Quélo, D., and Mathieu, A. Intercomparison of numerical atmospheric dispersion prediction models for emergency response to emissions of radionuclides with limited source information in the Fukushima Dai-ichi Nuclear Power Plant accident. Atmospheric Environment, Volume 214, 2019, Article 116824
3. Kajino, M., Sekiyama, T, T., Igarashi, Y., Katata, G., Sawada, M., Adachi, K., Zaizen, Y., Tsuruta, H., and Nakajima, T., Deposition and Dispersion of Radio-Cesium Released Due to the Fukushima Nuclear Accident: Sensitivity to Meteorological Models and Physical Modules. Journal of Geophysical Research: Atmospheres, 124, 1823-1845.doi: 10.1029/2018JD028998.

2018

1. Hirose, K., Kikawada, Y., Igarashi, Y., Fujiwara, H., Jugder, D., Matsumoto, Y., Oi, T., and Nomura, M. Plutonium, ^{137}Cs and uranium isotopes in Mongolian surface soils, Journal of Environmental Radioactivity, 166, 97-103, 2017. http://dx.doi.org/10.1016/j.jenvrad.2016.01.007
2. Igarashi, Y., Kita., K., Maki, T., Kinase, T., Hyashi, N., Hotaka, K., Adachi, K., Kajino, M., Ishizuka, M., Sekiyama, T., T., Zaizen, Y., Takenaka, C., Ninomiya, K., Okochi, H., and Sorimachi, A. Fungal spore involvement in the resuspension of radiocaesium in summer, Scientific Reports, 9:1-10, 2019. 2019. DOI:10.1038/s41598-018-37698-x
3. Iwagami, S., Tsujimura, M., Onda, Y., Nishino, M., Konuma, R., Abe, Y., Hada, M., Pun, I., Sakaguchi, , A., Kondo, H., Yamamoto, M., Miyata, Y., and Igarashi, Y. Temporal changes in dissolved ^{137}Cs concentrations in groundwater and stream water in Fukushima after the Fukushima Dai-ichi Nuclear Power Plant accident. Journal of Environmental Radioactivity, 166, 458-465, 2017. http://dx.doi.org/10.1016/j.jenvrad.2015.03.025
4. Kajino, M.., Sekiyama, T. T., Mathieu, A,. Korsakissok, I., Périllat, R., Quélo, D., Quérel, A., Saunier, O., Adachi, K., Girard, S., Maki, T., Yumimoto, K., Didier, D., Masson, O., and Igarashi, Y., Lessons learned from atmospheric modeling studies after the Fukushima nuclear accident: Ensemble simulations, data assimilation, elemental process modeling, and inverse modeling, Geochemical Journal, Vol. 52, 2018.
5. Kinase, T., Kita, K., Igarashi, I., Adachi, K., Ninomiya, K., Shinohara, A., Okochi, H., Ogata, H., Ishizuka, M., Toyoda, S., Yamada, K., Yoshida, N., Zaizen, Y., Mikami, M,. Demizu, H., and Onda, Y., The seasonal variations of atmospheric 134,137Cs activity and possible host particles for their resuspension in the contaminated areas of Tsushima and Yamakiya, Fukushima, Japan, Progress in Earth and Planetary Science, 5:12, 2018.
6. Satou, Y., Sueki, K., Sasa, K., Yoshikawa, H., Nakama, S., Minowa, H., Abe, Y., Nakai, I., Ono, T., Adachi, K., and Igarashi, Y., Analysis of two forms of radioactive particles emitted during the early stages of the Fukushima Dai-ichi Nuclear Power Station accident, Geochemical Journal, Vol. 52, 137-143, 2018. doi:10.2343/geochemj.2.0514.
7. Sekiyama, T. T. and T. Iwasaki, Mass flux analysis of ^{137}Cs plumes emitted from the Fukushima Daiichi Nuclear Power Plant, Tellus B, 70(1), 1–11, doi:10.1080/16000889.2018.1507390, 2018.

2017

1. Iwagami, S., Tsujimura, M., Onda, Y., Nishino, M., Konuma, R., Abe, Y., Hada, M., Pun, I., Sakaguchi, A., Kondo, H., Yamamoto, M., Miyata, Y., and Igarashi, Y., Temporal changes in dissolved ^{137}Cs concentrations in groundwater and stream water in Fukushima after the Fukushima Dai-ichi Nuclear Power Plant accident, Journal of Environmental Radioactivity,166, 458-465, 2017.
2. Hirose, K., Kikawada, Y., Igarashi, Y., Fujiwara, H., Jugder, D., Matsumoto, Y., Oi, T., Nomura, M., Plutonium, ^{137}Cs and uranium isotopes in Mongolian surface soils, Journal of Environmental Radioactivity, 166, 97-103, 2017.
3. Sekiyama, T. T., Kajino, M., and Kunii, K., The Impact of Surface Wind Data Assimilation on the Predictability of Near-Surface Plume Advection in the Case of the Fukushima Nuclear Accident, Journal of the Meteorological Society of Japan, Vol. 95, 447-454, 2017. doi: 10.2151/jmsj.2017-025.

2016

1. Kajino, M., Ishizuka, M., Igarashi, Y., Kita, K., Yoshikawa, C., and Inatsu, M., Long-term assessment of airborne radiocerium after the Fukushima nuclear accident: re-suspension from bare soil and forest ecosystems, Atmos. Chem. Phys, 16, 13149-13172, 2016.
2. Satou,Y., Sueki, K., Sasa, K., Adachi, K., and Igarashi, Y., First successful isolation of radioactive particles from soil near the Fukushima Daiichi Nuclear Power Plant, Anthropocene, 14, 71-76, 2016.
3. Yamaguchi, N., Mitome, M., Kotone, A-H., Asano, M., Adachi, K., and Kogure, T., Internal structure of cesium-bearing radioactive microparticles released from Fukushima nuclear power plant. Scientific Reports. 6, 20548, 2016.

2015

1. Igarashi, Y., Kajino, M., Zaizen, Y., Adachi, K., and Mikami, M., Atmospheric radioactivity over Tsukuba, Japan: a summary of three years of observations after the FDNPP accident, Progress in Earth and Planetary Science 2:44, 2015. doi: 10.1186/s40645-015-0066-1.
2. Kajino, M., G-3. NHM-Chem: Sensitivity of Cs deposition to the size and hygroscopicity of Cs-bearing aerosols, Technical Reports of the Meteorological Research Institute, 76, 132–142, 2015.
3. Sekiyama, T. T., Kunii, M., Kajino, M., and Shinbori, T., Horizontal Resolution Dependence of Atmospheric Simulations of the Fukushima Nuclear Accident Using 15-km, 3-km, and 500-m Grid Models, J. Meteorol. Soc. Jpn., 93B, 49–64, 2015.

2014

1. Abe, Y., Iizawa, Y., Terada, Y., Adachi, K., Igarashi, Y., and Nakai, I., Detection of uranium and chemical state analysis of individual radioactive microparticles emitted from the Fukushima nuclear accident using multiple synchrotron radiation X-ray analyses, Analytical Chemistry, 86, 8521-8525, 2014.

2013

1. Aoyama, M., Uematsu, M., Tsumune, D., and Hamajima, Y., Surface pathway of radioactive plume of TEPCO Fukushima NPP1 released ^{134}Cs and ^{137}Cs, Biogeosciences, 10, 3067-3078, 2013. doi: 10.5194/bg-10-3067-2013.
2. Tsumune, D., Tsubono, T., Aoyama, M., Uematsu, M., Misumi, K., Maeda, Y., Yoshida, Y., and Hayami, H., One-year, regional-scale simulation of ^{137}Cs radioactivity in the ocean following the Fukushima Daiichi Nuclear Power Plant accident, Biogeosciences, 10, 5601-5617, 2013.
3. Povinec, P.P., Aoyama, M., Biddulph, D., Breier, R., Buesseler, K., Chang, C., Golser, R., Hou, X., Ješkovský, M., and Jull, A., Cesium, iodine and tritium in NW Pacific waters-a comparison of the Fukushima impact with global fallout. Biogeosciences, 10, 5481-5496. 2013.
4. Kumamoto, Y., Murata, A., Kawano, T., and Aoyama, M., Fukushima-derived radiocesium in the northwestern Pacific Ocean in February 2012, Applied Radiation and Isotopes, 81, 335-339, 2013. doi: 10.1016/j.apradiso.2013.03.085.
5. Toyama, C., Muramatsu, Y., Igarashi, Y., and Aoyama, M., Atmospheric fallout of ^{129}I in Japan before the Fukushima accident: Regional and global contributions, 1963-2005, Environmental Science & Technology, 47(15), 8383-8390, 2013. doi: 10.1021/es401596z.
6. Adachi, K., Kajino, M., Zaizen, Y., and Igarashi, Y., Emission of spherical cesium-bearing particles from an early stage of the Fukushima nuclear accident. Scientific Reports, 3, Article number 2554, 2013. doi:10.1038/srep02554.

2012

1. Toyama, C., Muramatsu, Y., Uchida, Y., Igarashi, Y., Aoyama, M., and Matsuzaki, H., Variations of ^{129}I in the atmospheric fallout of Tokyo, Japan 1963-2003, Journal of Environmental Radioactivity, 113, 116-122, 2012. doi: 10.1016/j.jenvrad.2012.04.014.
2. Inomata, Y., Aoyama, M., Tsumune, D., Motoi, T., and Nakano, H., Optimum interpolation analysis of basin-scale ^{137}Cs transport in surface seawater in the North Pacific Ocean, Journal of Environmental Monitoring, 14, 3146-3155, 2012. doi: 10.1039/C2EM30707C.
3. Aoyama, M., Tsumune, D., Uematsu, M., Kondo, F., and Hamajima, Y., Temporal variation of ^{134}Cs and ^{137}Cs activities in surface water at stations along the coastline near the Fukushima Dai-ichi Nuclear Power Plant accident site, Japan. Geochem. J, 46, 321-325, 2012.
4. Aoyama, M., Tsumune, D., and Hamajima, Y., Distribution of ^{137}Cs and ^{134}Cs in the North Pacific Ocean: impacts of the TEPCO Fukushima-Daiichi NPP accident, Journal of Radioanalytical and Nuclear Chemistry, 1-5, 2012. doi: 10.1007/s10967-012-2033-2.
5. Honda, M. C., Aono, T., Aoyama, M., Hamajima, Y., Kawakami, H., Kitamura, M., Masumoto, Y., Miyazawa, Y., Takigawa, M., and Saino, T., Dispersion of artificial caesium-134 and-137 in the western North Pacific one month after the Fukushima accident, Geochem. J, 46, e1-e9, 2012.

6. Povinec, P. P., Hirose, K., and Aoyama, M., Radiostrontium in the Western North Pacific: characteristics, behavior, and the Fukushima impact, Environmental Science & Technology, 46, 10356-10363, 2012. doi: 10.1021/es301997c.
7. Tsumune, D., Tsubono, T., Aoyama, M., and Hirose, K., Distribution of oceanic ^{137}Cs from the Fukushima Dai-ichi Nuclear Power Plant simulated numerically by a regional ocean model, Journal of Environmental Radioactivity, 111, 100-108, 2012.

2011

1. Aoyama, M., Fukasawa, M., Hirose, K., Hamajima, Y., Kawano, T., Povinec, P.P., and Sanchez-Cabeza, J. A., Cross Equator transport of ^{137}Cs from North Pacific Ocean to South Pacific Ocean, BEAGLE2003 cruises, Progress in Oceanography, 89, 7-16, 2011. doi:10.1016/j.pocean.2010.12.003.
2. Buesseler, K., Aoyama, M., and Fukasawa, M., Impacts of the Fukushima nuclear power plants on marine radioactivity. Environmental Science & Technology, 45(23), 9931-9935, 2011. doi: 10.1021/es202816c.
3. Povinec, P. P., Aoyama, M., Fukasawa, M., Hirose, K., Komura, K., Sanchez-Cabeza, J.A., Gastaud, J., Jeskovsky, M., Levy, I., and Sykora, I., ^{137}Cs water profiles in the South Indian Ocean - an evidence for accumulation of pollutants in the subtropical gyre. Progress in Oceanography, 89 , 17-30, 2011. doi:10.1016/j.pocean.2010.12.004.
4. Gastaud, J., Povinec, P.P., Aoyama, M., Hirose, K., Sanchez-Cabeza, J.A., Levy, I., Roos, P., Eriksson, M., Bosc, E. and Rezzoug, S., Transport and scavenging of Pu in surface waters of the Southern Hemisphere Oceans, Progress in Oceanography, 89, 92-100, 2011. doi:10.1016/j.pocean.2010.12.009.
5. Hirose, K., Kim, C.S., Yim, S.A., Aoyama, M., Fukasawa, M., Komura, K., Povinec, P.P., and Sanchez-Cabeza, J.A., Vertical profiles of plutonium in the central South Pacific, Progress in Oceanography, 89, 101-107, 2011. doi:10.1016/j.pocean.2010.12.010.
6. Tsumune, D., Aoyama, M., Hirose, K., Bryan, F., Lindsay, K. and Danabasoglu, G., Transport of ^{137}Cs to the Southern Hemisphere in an Ocean General Circulation Model, Progress in Oceanography, 89, 38-48, 2011. doi:10.1016/j.pocean.2010.12.006.
7. Sanchez-Cabeza, J.A., Levy, I., Gastaud, J., Eriksson, M., Osvath, I., Aoyama, M., Povinec, P.P. and Komura, K., Transport of North Pacific ^{137}Cs labeled waters to the south-eastern Atlantic Ocean. Progress in Oceanography, 89, 31-37, 2011. doi:10.1016/j.pocean.2010.12.005.
8. Levy, I., Povinec, P.P., Aoyama, M., Hirose, K., Sanchez-Cabeza, J.A., Comanducci, J-F., Gastaud, J., Eriksson, M., Hamajima, Y., Kim, C.S., Komura, K., Osvath, I., Roos, P. and Yim, S.A., Marine anthropogenic radiotracers in the Southern Hemisphere: new sampling and analytical strategies, Progress in Oceanography, 89, 120-133, 2011. doi:10.1016/j.pocean.2010.12.012.

2010

1. Inomata,Y., Igarashi, Y., Yoshioka, K., Tanaka, T. Y., and M, Chiba., Temporal variation of ^{222}Rn at the summit of Mt. Fuji associated with the Asian continental outflow, Atmospheric Environment, 44,3856-3865, 2010.
2. Nakano, H., Motoi, T., Hirose, K., and Aoyama, M., Analysis of ^{137}Cs concentration in the Pacific using a Lagrangian approach. Journal of Geophysical Research, 115, C06015, 2010. doi:10.1029/2009JC005640.
3. Hirose, K., Igarashi, Y., Aoyama, M., and Inomata, Y., Depositional behaviors of plutonium and thorium isotopes at Tsukuba and Mt. Haruna in Japan indicate the sources of atmospheric dust. Journal of Environmental Radioactivity, 101,106-112, 2010.
4. Zhang, Y., Zeng, J., Yamada, M., Wu, F., Igarashi, Y., and Hirose, K., Characterization of Pu concentration and its isotopic composition in a reference fallout material. Science of the Total Environment, 408(5), 1139-1144, 2010.

2009

1. Aoyama, M., Hamajima, Y., Fukasawa, M., Kawano, T., and Watanabe, S., Ultra low level deep water ^{137}Cs activity in the South Pacific Ocean, Journal of Radioanalytical and Nuclear Chemistry, 2009. doi:10.1007/s10967-009-0253-x.
2. Hirose, K., Aoyama, M., and Povinec, P.P., $^{239, 240}Pu$ /^{137}Cs ratios in the water column of the North Pacific: a proxy of biogeochemical processes, Journal of Environmental Radioactivity, 100, 258-262, 2009.
3. Igarashi, Y., Inomata, Y., Aoyama, M., Hirose, K., Takahashi, H., Shinoda, Y., Sugimoto, N., Shimizu, A., and Chiba, M., Possible change in Asian dust source suggested by atmospheric anthropogenic radionuclides during the 2000s, Atmospheric Environment, 43, 2971-2980, 2009.
4. Inomata, Y., Aoyama, M., and Hirose, K., Analysis of 50-y record of surface ^{137}Cs concentrations in the global ocean using the HAM-global database, Journal of Environmental Monitoring, 11(1), 116-125, 2009. doi: 10.1039/b811421h.
5. Hirose, K., Igarashi, Y., Aoyama, M., and Inomata, Y., Depositional behaviors of plutonium and thorium isotopes at Tsukuba and Mt.Haruna in Japan indicate the sources of atmospheric dust, Journal of Environmental Radioactivity, 101(2), 106-112, 2009. doi:10.1016/j.jenvrad.2009.09.003.
6. Igarashi Y., Kikawada, Y., Oda, K., Yamauchi, R., Nomura, M., Honda, T., Oi, T., and Hirose, K., Anomalous Uranium Isotope Ratio in Atmospheric Deposits in Japan, Journal of Nuclear Science and Technology, 46(12), 1094-1098. 2009.

2008

1. Aoyama, M., Hirose, K., Nemoto, K., Takatsuki, Y., and Tsumune, D., Water masses labeled with global fallout ^{137}Cs formed by subduction in the North Pacific, Geophysical Research Letters, 35, L01604, 2008. doi:10.1029/2007GL031964.
2. Hirose, K., Igarashi, Y., and Aoyama, M., Analysis of the 50-year records of the atmospheric deposition of long-loved radionuclides in Japan, Applied Radiation and Isotopes, 66, 1675-1678, 2008.
3. Hirose, K., Aoyama, M., Igarashi, Y., and Komura, K., Improvement of ^{137}Cs analysis in small Volume seawater samples using the Ogoya underground facility, Journal of Radioanalytical and Nuclear Chemistry, 276,3,795-798, 2008.
4. Aoyama, M., Hirose, K., Nemoto, K., Takatsuki, Y., and Tsumune, D., Water masses labeled with global fallout ^{137}Cs formed by subduction in the North Pacific, Geophysical Research Letters, 35, L01604, 2008. doi:10.1029/2007GL031964.

2007

1. Hirose, K., Aoyama, M., and Kim, C.S., Plutonium in Seawater of the Pacific Ocean, Journal of Radioanalytical and Nuclear Chemistry, 274 No. 3, 635-638, 2007.
2. Hirose, K., Igarashi, Y., and Aoyama, M., 50 years records of atmospheric deposition of long-lived anthropogenic radionuclides in Japan, International Conference on Environmental Radioactivity: From Measurements and Assessments to Regulation, IAEA-CN-145, 95-96, 2007.
3. Hirose, K., Igarashi, Y., and Aoyama, M., Recent trends of plutonium fallout observed in Japan: Comparison with natural lithogenic radionuclides, thorium isotopes, Journal of Radioanalytical and Nuclear Chemistry, 273 No.1, 115-118, 2007.
4. Hirose, K., Aoyama, M., Fukasawa, M., Kim, C. S., Komura, K., Povinec, P. P., and Sanchez-Cabeza, J. A., Plutonium and ^{137}Cs in surface water of the South Pacific Ocean, Science of the Total Environment, 381, 243-255, 2007.

2006

1. Yamamoto, M., Sakaguchi, A., Sasaki, K., Hirose, K., Igarashi, Y., and Kim, C.K., Seasonal and spatial variation of atmospheric ^{210}Pb and ^{7}Be deposition: features of the Japan Sea side of Japan, Journal of Environmental Radioactivity, 86, 110-131, 2006.

2. Hirose, K., Aoyama, M., Kim, C.S., Kim, C.K., and Povinec, P.P., Plutonium isotopes in seawater of the North Pacific: effects of close-in fallout, INTERNATIONAL CONFERENCE ON ISOTOPES AND ENVIRONMENTAL STUDIES. Eds. P. Povinec, J.A. Sanchez-Cabeza. Vol. 8 of Radioactivity in the Environment, Elsevier, London, 2006.
3. Aoyama, M., Hirose, K., and Igarashi, Y., Re-construction and updating our understanding on the global weapons tests ^{137}Cs fallout, Journal of Environmental Monitoring, 8, 431-438, 2006.
4. Aoyama, M., Fukasawa, M., Hirose, K., Mantoura, R.F.C., Povinec, P.P., Kim, C.S., and Komura, K., Southern Hemisphere Ocean Tracer Study (SHOTS): An overview and preliminary results, INTERNATIONAL CONFERENCE ON ISOTOPES AND ENVIRONMENTAL STUDIES. Eds. P. Povinec, J.A. Sanchez-Cabeza, Vol. 8 of Radioactivity in the Environment, Elsevier, London, 2006.Inoue, H.Y., Matsueda, H., Igarashi, Y., Sawa, Y., Wada, A., Nemoto, K., Sartorius, H., and Schlosser, C., Seasonal and long-term variations in atmospheric CO_2 and ^{85}Kr in Tsukuba, Central Japan, Journal of the Meteorological Society of Japan, 84/6, 959-968, 2006.

2005

1. Hirose, K., Aoyama, M., Igarashi, Y., and Komura, K., Extremely low background measurements of ^{137}Cs in seawater samples using an underground facility (Ogoya), Journal of Radioanalytical and Nuclear Chemistry, 263, 349-353, 2005.
2. Povinec, P.P., Aarkrog, A., Buesseler, K.O., Delfanti, R., Hirose, K., Hong, G.H., Ito, T., Livingston, H.D., Nies, H., Noshkin, V.E., Shima, S., and Togawa, O., ^{90}Sr, ^{137}Cs and ^{239,240}Pu concentration surface water time series in the Pacific and Indian Oceans- WOMARS results, Journal of Environmental Radioactivity, 81, 63-87, 2005.
3. Igarashi, Y., Aoyama, M., Hirose, K., Povinec, P.P., and Yabuki, S., What anthropogenic radionuclides (^{90}Sr and ^{137}Cs) in atmospheric deposition, surface soils and Aeoliandusts suggest for dust transport over JAPAN, Water, Air, and Soil Pollution: Focus, 5, 51-69, 2005.

2004

1. Hirose, K., Kim, C.K., Kim, C.S., Chang, B.W., Igarashi, Y., and Aoyama, M., Wet and dry depositions of plutonium in Daejeon, Korea, The Science of the Total Environment, 332, 243-252, 2004.
2. Povinec, P.P., Hirose, K., Honda, T., Ito, T., MarianScott, E., and Togawa, O., Spatial distribution of ^{3}H, ^{90}Sr, ^{137}Cs and ^{239,240}Pu in surface waters of the Pacific and Indian Oceans - GLOMARD database, Journal of Environmental Radioactivity, 76, 113-137, 2004.
3. Aoyama, M., and Hirose, K., Artificial Radionuclides database in the Pacific Ocean: Ham database, TheScientificWorldJOURNAL, 4, 200-215, 2004.
4. Hirota, M., Nemoto, K., Wada, A., Igarashi, Y., Aoyama, M., Matsueda, H., Hirose, K., Sartorius, H., Schlosser, C., Schmid, S., Weiss, W., and Fujii, K., Spatial and Temporal Variations of Atmospheric ^{85}Kr Observed During 1995-2001 in Japan: Estimation of Atmospheric ^{85}Kr inventory in the Northern Hemisphere, Journal of Radiation Research, 45, 405-413, 2004.
5. Hirose, K., Chemical Speciation of Thorium in Marine Biogenic Particulate matter, The Scientific World JOURNAL 4, 67-76, 2004.

2003

1. Hirose, K., and Aoyama, M., Analysis of ^{137}Cs and ^{239,240}Pu concentrations in surface waters of the Pacific Ocean, Deep-Sea Research II, 50, 2675-2700, 2003.
2. Hirose, K., Aoyama, and Povinec, P.P., Concentration of particulate plutonium in surface and deep-water, samples collected during the IAEA'97 expedition, Deep-Sea Research II, 50, 2639-2647, 2003.
3. Povinec, P.P., Livingston, H.D., Shima, S., Aoyama, M., Gastaud, J., Goroncy, I., Hirose, K., Huynh-Ngoc, L., Ikeuchi, Y., Ito, T., Rosa, J.L., Kwong, L.L.W., Lee, S.H., Moriya, H., Mulsow, S., Oregioni, B., Pettersson, H., and Togawa, O., IAEA'97 expedition to the NW Pacific Ocean-Results of oceanographic and radionuclide investigations of the water column, Deep-Sea Research II, 50,2607-2637, 2003.

4. Ito, T., Povinec, P.P., Togawa, O., and Hirose, K., Temporal and Spatial variation of anthropogenic radionuclides in seawater of the Japan Sea, Deep-Sea Research II, 50, 2701-2711, 2003.
5. Tsumune, D., Aoyama, M., and Hirose, K., Behavior of ^{137}Cs and concentrations in the North Pacific in an ocean general circulation model, Journal of Geophysical Research, 108, C8, 3262, 2003.
6. Hirose, K., and Aoyama, M., Present Background Levels of Surface ^{137}Cs and $^{239, 240}$Pu Concentrations in the Pacific, Journal of Environmental Radioactivity, 69(1-2), 53-60, 2003.
7. Tsumune, D., M. Aoyama, and K. Hirose, Numerical simulation of ^{137}Cs and $^{239, 240}$Pu concentrations by an ocean general circulation model, Journal of Environmental Radioactivity, 69(1-2), 61-84, 2003.
8. Aoyama, M., and Hirose, K., Temporal variation of ^{137}Cs water column inventory in the North Pacific since the 1960s, Journal of Environmental Radioactivity, 69(1-2),107-117, 2003.
9. Hirose, K., Igarashi, Y., Aoyama, M., Kim, C.K., Kim, C.S., Chang, B.W., Recent trends of plutonium fallout observed in Japan: plutonium as a proxy for desertification, J. Environ. Monit, 5, 302-307, 2003.
10. Igarashi, Y., Aoyama, M., Hirose, K., Miyao, T., Nemoto, K., Tomita, M., and Fujikawa, T., Resuspension: Decadal Monitoring Time Series of the Anthropogenic Radioactivity Deposition in Japan, Journal of Radiation Research, 44, 319-328, 2003.
11. Kim, C.K., Kim, C.S., Chang, B.U., Choi, S.W., Chung, C.S., Hong, G.H., Hirose, K., and Igarashi, Y., Plutonium isotopes in seas around the Korean Peninsula, The Science of the Total Environment, 318, 197-209, 2003.
12. Kim, C.K., Kim, C.S., Chang, B.U., Choi, S.W., Chung, C.S., Hong, G.H., Hirose, K., and Pettersson, H.B.L., ^{240}Pu /^{239}Pu atom ratios in the bottom sediments of the NW Pacific Ocean, Journal of Radioanalytical and Nuclear Chemistry, 258(2), 265-268, 2003.
13. Lee, H.N., Tanaka, T., Chiba, M., and Igarashi, Y., Long range transport of Asian dust from dust storms and its impact on Japan, Water, Air, and Soil Pollution, 3, 231-243, 2003
14. Hirose, K., Implication of POC/^{234}Th ratios in oceanic particulate matter: an approach to particle aggregation, Papers of Meteorology and Geophysics, 53, 4, 109-118, 2003.

2002

1. Hirose, K., Miyao, T., Aoyama, M., and Igarashi, Y., Plutonium isotopes in the Sea of Japan, Journal of Radioanalytical and Nuclear Chemistry, 252, 293-299, 2002.
2. Hirose, K., and Aoyama, M., Chemical speciation of plutonium in seawater, Analytical and Bioanalytical Chemistry, 372, 418-420, 2002.
3. Hong, G.H., Kim, Y.I., Lee, S.H., Cooper, L.W., Choe, S.M., Tkalin, A.V., Lee, T., Kim, S.H., Chung, C.S., and Hirose, K., $^{239+240}$Pu and ^{137}Cs concentrations for zooplankton and nekton in the Northwest Pacific and Antarctic Oceans 1993-1996, Marine Pollution Bulletin, 44, 660-665, 2002.

2001

1. Igarashi, Y., Aoyama, M., Nemoto, K., Hirose, K., Miyao, T., Fushimi, K., Suzuki, M., Yasui, S., Asai, Y., Aoki, I., Fujii, K., Yamamoto, S., Sartorius, H., and Weiss, W., ^{85}Kr measurement system for continuous monitoring at Meteorological Research Institute, Japan, Journal of Environmental Monitoring, 3, 688-696, 2001.
2. Igarashi, Y., Aoyama, M., Hirose, K., Miyao, T., and Yabuki, S., Is it Possible to use ^{90}Sr and ^{137}Cs as tracers for the aeolian transport?, Water. Air. And Soil Pollution, 130, 349-354, 2001
3. Hirose, K., Igarashi, Y., Aoyama, M., and Miyao, T., Long-term trends of plutonium fallout observed in Japan, In Plutonium in the Environment, 251-266, 2001.
4. Aoyama, M., Hirose, K., Miyao, T., Igarashi, Y., and Povinec, P.P., ^{137}Cs activity in surface water in the western North Pacific, J. Radioanal. Nucl. Chem., 248, 3, 789-793, 2001.
5. Aoyama, M., Hirose, K., Miyao, T., Igarashi, Y., and Povinec, P.P., Temporal variation of ^{137}Cs inventory in the western North Pacific, J Radioanal Nucl Chem, 248, 3, 785-787, 2001

6. Hirose, K., Aoyama, M., Miyao, T., and Igarashi, Y., Plutonium in seawaters on the western North Pacific, J Radioanal Nucl Chem, 248, 3, 771-776, 2001.
7. Tsumune. D., Aoyama, M., Hirose, K., Maruyama, K., and Nakashiki, N., Caluculation of Artificial Radionuclides in the Ocean by an Ocean General Circulation Model, J Radioanal Nucl Chem, 248, 3, 777-783, 2001.

2000

1. Shiraishi, K., Kimura, S., Yonehara, H., Takada, J., Ishikawa, M., Igarashi, Y., Aoyama, M., Komura, K., and Nakazima, T., Survey of external dose around the JCO facility using sugar samples and ESR method, Adv. ESR Appl, 16, 9-14, 2000.
2. Komura, K, Yamamoto, M., Muroyama, T., Murata, Y., Nakanishi, T., Hoshi, M., Takada, J., Ishikawa, M., Kitagawa, K., Suga, S., Endo, A., Tozaki, N., Mitsugashira, T., Hara, M., Hashimoto, T., Takano, M., Yanagawa, Y., Tsuboi, T., Ichimasa, M., Ichimasa, Y., Imura, H., Sasajima, E., Seki, R., Saito, Y., Kondo, M., Kojima, S., Muramatsu, Y., Yoshida, S., Shibata, S., Yonehara, H., Watanabe, Y., Kimura, S., Shiraishi, K., Bannai, T., Sahoo, S.K., Igarashi, Y., Aoyama, M., Hirose, K., Uehiro, M., Doi, T., and Matsuzawa, T., The JCO criticality accident at Tokai-mura, Japan: an overview of the sampling campaign and preliminary results, J. Environ. Radioactivity, 50, 3-14, 2000.
3. Igarashi, Y., Miyao, T., Aoyama, M., Hirose, K., Sartorius, H., and Weiss, W., Radioactive noble gases in the surface air monitored at MRI, Tsukuba, before and after the JCO accident, J. Environ. Radioactivity, 50, 107-118, 2000.
4. Miyao, T., Hirose, K., Aoyama, M., and Igarashi, Y., Trace of the recent deep water formation in the Japan Sea deduced from historical ^{137}Cs data, Geophys. Res. Lett., 27, 22, 3731-3734, 2000.
5. Aoyama, M., Hirose, K., Miyao, T., and Igarashi, Y., Low level ^{137}Cs measurements in deep seawater samples, Appl. Radiat. Isot, 53, 159-162, 2000.
6. Igarashi, Y., Sarutorius, H., Miyao, T., Weiss, W., Fushimi, K., Aoyama, M., Hirose, K., and Inoue, H.Y., ^{85}Kr and ^{133}Xe monitoring at MRI, Tsukuba and its importance, J. Environ. Radioactivity, 48, 191-202, 2000.

1999

1. Hirose, K., Amano, H., Baxter, M.S., Chaykovskaya, E., Chumichev, V.B., Hong, G.H., Isogai, K., Kim, C.K., Kim, S.H., Miyao, T., Morimoto. T, Nikitin, A., Oda, K., Pettersson, H.B.L., Povinec, P.P., Seto, Y., Tkalin, A., Togawa, O., and Veletova, N.K., Anthropogenic radionuclides in seawater in the East Sea/Japan Sea: Results of the first-stage Japanese-Korean-Russian expedition, J. Environ. Radioactivity, 43, 1-13, 1999.
2. Igarashi, Y., Aoyama, M., Miyao, T., Hirose, K., Komura, K., and Yamamoto, M., Air concentration of radiocaesium in Tsukuba, Japan following the release from the Tokai waste treatment plant: comparisons of observations with predictions, Applied Radiation and Isotopes, 50, 1063-1073, 1999.
3. Igarashi, Y., Aoyama, M., Miyao, T., Hirose, K., and Tomita, M., Anomalous ^{90}Sr deposition during the fall, 1995 at MRI, Tsukuba, Japan, J. Radioanal. Nucl. Chem, 239(3), 539-542, 1999.
4. Ikeuchi, Y., Amano, H., Aoyama, M., Berezhnov, V.I., Chaykovskaya, E., Chumichev, V.B., Chung, C.S., Gastaud, J., Hirose, K., Hong, G.H., Kim, C.K., Kim, S.H., Miyao, T., Morimoto, T., Nikitin, A., Oda, K., Pettersson, H.B.L., Povinec, P.P., Tkalin, A., Togawa, O., and Veletova, N.K., Anthropogenic radionuclides in seawater of the Far Eastern Seas, Sci. Total Environ., 237/238, 203-212, 1999.
5. Pettersson, H.B.L., Amano, H., Berezhnov, V.I., Chaykovskaya, E., Chumichev, V.B., Chung, C.S., Gastaud, J., Hirose, K., Hong, G.H., Kim, C. K., Lee, S.H., Morimoto, T., Nikitin, A., Oda, K., Povinec, P.P., Suzuki, E., Tkalin, A., Togawa, O., Veletova, N.K., Volkov, Y., and Yoshida, K., Anthropogenic radionuclides in sediments in the NW Pacific Ocean and its marginal seas:results of the 1994-1995 Japanese-Korean-Russian expeditions, Sci. Total Environ, 237/238, 213-224, 1999.

1998

1. Igarashi, Y., Hirose, K., and Otsuji-Hatori, M., Beryllium-7 Deposition and Its Relation to Sulfate Deposition, J. Atmos. Chem, 29, 217-231, 1998.
2. Miyao, T., Hirose, K., Aoyama, M., and Igarashi, Y., Temporal variation of ^{137}Cs and $^{239, 240}Pu$ in the sea of Japan, J. Environ. Radioactivity, 40, 239-250, 1998.

1997

1. Hirose, K., Complexation-scavenging of plutonium in the ocean, Radioprotection - Colloq, 32, C2-225 - C2-230, 1997.

1996

1. Igarashi, Y., Otsuji-Hattori, M., and Hirose, K., Recent deposition of ^{90}Sr and ^{137}Cs observed in Tsukuba, J. Environ. Radioactivity, 31, 157-169, 1996.
2. Otsuji-Hatori. M., Igarashi, Y., and Hirose, K., Preparation of a Reference Fall out Material for Activity Measurements, J. Environ Radioactivity, 31, 2, 143-155, 1966.

1995

1. Aoyama, M., and Hirose, K., The temporal and spatial variation of ^{137}Cs concentration in the western North Pacific and its marginal seas during the period from 1979 to 1988, J. Environ. Radioactivity, 29, 57-74, 1995.
2. Hirose, K., Geochemical studies on the Chernobyl radioactivity in environmental samples, J. Radioanal. Nucl. Chem., Articles, 197, 315-335, 1995.

1994

1. Hirose, K., Takatani, S., and Aoyama, M., Deposition of ^{90}Sr and plutonium isotopes derived from the Chernobyl accident in Japan, J. Radioanal. Nucl. Chem., Articles, 182, 349-358, 1994.

1993

1. Hirose, K., and Sugimura, Y., Chemical speciation of particulate ^{238}U, $^{239, 240}Pu$ and Th isotopes in seawater, Sci. Total Environ., 130/131, 517-524, 1993.
2. Hirose, K., Takatani, S., and Aoyama, M., Wet deposition of radionuclides derived from the Chernobyl accident, J. Atmos. Chem., 17, 61-71, 1993.
3. Shiraishi, K., Igarashi, Y., Yamamoto, M., and Nakajima, T., Concentrations of thorium and uranium in freshwater samples collected in the former USSR, J. Radioanal. Nucl. Chem., 185,157-165, 1993.

1992

1. Aoyama, M., Hirose, K., and Takatani, S., Particle size dependent dry deposition velocity of the Chernobyl radioactivity, In Precipitation Scavenging and Atmosphere - Surface Exchange.Volume 3, The 22e Summers olume: Application and Appraisals. Coordinated by S.E. Schwartz and W.G.N. Slinn. Hemisphere Publishing Corporation, Washington, 1581-1593, 1992.
2. Hirose, K., Sugimura, Y., and Aoyama, M., Plutonium and ^{137}Cs in the western North Pacific: estimation of residence time of plutonium in surface water, Appl. Radiat. Isot, 43, 349-359, 1992.

1991

1. Aoyama, M., Hirose, K., and Sugimura, Y., The temporal variation of stratospheric fallout derived from the Chernobyl accident, J. Environ. Radioactivity, 13, 103-115, 1991.
2. Hirose, K., and Sugimura, Y., Chemical speciation of particulate uranium in seawater, J. Radioanal. Nucl. Chem., Articles, 149, 83-96, 1991.

1990

1. Hirose, K., and Sugimura, Y., Plutonium isotopes in the surface air in Japan: effect of Chernobyl accident, J. Radioanal. Nucl. Chem., Articles, 138, 127-138, 1990.

2. Hirose, K., Aoyama, M., and Sugimura, Y., Plutonium and cesium isotopes in river waters in Japan, J. Radioanal. Nucl. Chem., Articles, 141, 191-202, 1990.
3. Hirose, K., Aoyama, M., and Sugimura, Y., Short and long term effects of Chernobyl radioactivity on deposition and air concentrations in Japan, IAEA-SM 306/129, 141-149, 1990.

1988

1. Aoyama, M., Evidence of stratospheric fallout of caesium isotopes from Chernobyl accident, Geophys. Res. Lett., 15, 327-330, 1988.
2. Miyake, Y., Saruhashi, K., Sugimura, Y., Kanazawa, T., and Hirose, K., Contents of ^{137}Cs, plutonium and americium isotopes in the southern ocean waters, Pap. Met. Geophys, 39, 95-113, 1988.

1987

1. Aoyama, M., Hirose, K., and Sugimura, Y., Deposition of gamma-emitting nuclides in Japan after the reactor-IV accident at Chernobyl, J. Radioanal. Nucl. Chem., Articles, 116, 291-306, 1987.
2. Hirose, K., Aoyama, M., Katsuragi, Y., and Sugimura, Y., Annual deposition of Sr-90, Cs-137 and Pu-239, 240 from the 1961-1980 nuclear explosions: a simple model, J. Meteor. Soc. Japan, 65, 259-277, 1987.

1986

1. Aoyama, M., Hirose, K., Suzuki, Y., and Sugimura, Y., High level radioactive nuclides in Japan in May, Nature, 321, 819-820, 1986.
2. Hirose, K., Sugimura, Y., and Katsuragi, Y., ^{90}Sr and $^{239+240}Pu$ in the surface air in Japan: their concentrations and size distributions, Pap. Met. Geophys, 37, 255-269, 1986.
3. Katsuragi, Y., and Aoyama, M., Seasonal variation of Sr-90 fallout in Japan through the end of 1983, Pap. Met. Geophys., 37, 15-36, 1986.
4. Suzuki, Y., Inoue, H., Katsuragi, Y., and Sugimura, Y., The distribution of 85Krin the air over the North and South Pacific Ocean Mem., Natl. Inst. Polar Res., Spec. Issue, 40, 462-466, 1986.

1985

1. Hirose, K., and Sugimura, Y., A new method of plutonium speciation in seawater, J. Radioanal. Nucl. Chem, Articles, 92, 363-369, 1985.

1984

1. Hirose, K., and Sugimura, Y., Plutonium in the surface air in Japan, Health Phys., 46, 1281-1285, 1984.
2. Inoue, H., Katsuragi, Y., and Shigehara, K., Tritiated water vapor in the surface air at Tokyo, Pap. Met. Geophys, 35, 11-20, 1984.

1983

1. Katsuragi, Y., A study of ^{90}Sr fallout in Japan, Pap. Met. Geophys., 33, 277-291, 1983.
2. Katsuragi, Y., Kawamura, K., and Inoue, H., Tritium fallout in Tokyo, Pap. Met. Geophys, 34, 21-30, 1983.

1982

1. Inoue, H., and Katsuragi, Y., A study of tritium fallout in Japan, Pap. Met. Geophys, 32, 21-28, 1982.
2. Katsuragi, Y., Hirose, K., and Sugimura, Y., A study of plutonium fallout in Japan, Pap. Met. Geophys, 33, 85-93, 1982.

1981

1. Hirose, K., and Sugimura, Y., Concentration of Uranium and the activity ratio of ^{234}U /^{238}U in surface air-effect of atmospheric burn-up of cosmos-954, Pap. Met. Geophys., 32, 317-322, 1981.
2. Hirose, K., and Sugimura, Y., Plutonium content of river water in Japan, Pap. Met. Geophys, 32, 301-305, 1981.

3. Sugimura, Y., and M. Mayeda, An improved method of analysis of uranium in sea water using chelating resin, Pap. Met. Geophys, 32, 167-171, 1981.

1980

1. Sugimura, Y., The uranium content and the activity ratio ^{234}U /^{238}U in sea water in the Pacific ocean, Isotope Marine Chemistry, 211-246, 1980.

1979

1. Sugiura, Y., Saruhashi, K., and Miyake, Y., Evaluation on the disposal of radioactive wastes into the North Pacific. - the effect of steady flow and up - welling, Proc. The 3rd NEA Seminar on Marine Radioecology, 1979.

1978

1. Miyake, Y., Nuclear weapons and radioactive pollution of the earth's environment, In, Proc. Internal Symp. On the damage and after-effects of the atomic bombing of Hiroshima and Nagasaki July 21-Aug., 9, 1977, Tokyo, 164-188, 1978.

1976

1. Miyake, Y., and Saruhashi, K., A critical study on the IAEA definition of high level radioactive waste unsuitable for dumping at sea, Pap. Met. Geophys. 27, 75-80, 1976.
2. Miyake, Y., and Saruhashi, K., Disposal of radioactive waste into deep seas, J. Radiat. Res., 17, 42-43, 1976.
3. Miyake, Y., and Sugimura, Y., The plutonium content in the Pacific Ocean waters, Proc. of Symp. on Transuranium Nuclides in the Environment, San Francisco, 17-21 Nov. 1975, USERDA and IAEA, IAEA-SM-199/22, 91-105,1976.
4. Sugimura, Y., Symposium II plutonium in environment, II-1.Distribution and behavior of plutonium in the global environments, J. Radiat. Res., 17, 4-5, 1976.
5. Sugiura, Y., Saruhashi, K., and Miyake, Y., Evaluation on the disposal of radioactive wastes into the North Pacific, Pap. Met. Geophys, 27, 81-87, 1976.

1975

1. Miyake, Y., Shimada, T., Kawamura, K., Sugimura, Y., Shigehara, K., and Saruhashi, K., Distribution of tritium in the Pacific ocean, Rec. Oceanogr. Works Japan, 13, 17, 1975.
2. Miyake, Y., Katsuragi, Y., and Sugimura, Y., Plutonium fallout in Tokyo, Pap. Met. Geophys, 26, 1-8, 1975.
3. Miyake, Y., Sugimura, Y., and Hirao, Y., Uranium, thorium and potassium contents in granitic and basaltic rocks in Japan, In, The Natural Radiation Environment II, II, Proc. 2nd Intnl. Symp. On Natural Radiation Environment, Aug. 7-11, 1972, Houston, Texas, USA, ed. J. A. S. Adams, W. M. Lowder, T. F. Gesell, 535-558,1975.
4. Saruhashi, K., I-1 The global radioactive contamination due to nuclear weapon testings, J. Radiat. Res., 16, 47, 1975.
5. Saruhashi, K., Katsuragi, Y., Kanazawa, T., Sugimura, Y., and Miyake, Y., ^{90}Sr and ^{137}Cs in the Pacific waters, Rec. Oceanogr. Works Japan, 13, 1-15, 1975.

1973

1. Miyake, Y., and Saruhashi, K., The radio-carbon model of the ocean, Pap. Met. Geophys, 24, 263-271, 1973.
2. Miyake, Y., Saruhashi, K., and Sugimura, Y., The isotopic ratio ^{234}U /^{238}U in sea water and its bearings on the isotopic ratio in river waters, Oceanogr. Works Japan, 12, 23-25, 1973.
3. Miyake, Y., Sugimura, Y., and Saruhashi, K., Content of plutonium in river water in Japan, Pap. Met. Geophys, 24, 75-78, 1973.
4. Miyake, Y., Sugimura, Y., and Yasujima, T., Thorium isotope content in river water in Japan, Pap. Met. Geophys, 24, 67-73, 1973.

1972

1. Miyake, Y., Sugimura, Y., and Uchida, T., A new method of spectrophotometric determination of uranium in sea water and uranium content with ^{234}U /^{238}U ratio in the Pacific water, Rec. Oceanogr. Works Japan, 11, 53-63, 1972.

1970

1. Miyake, Y., Katsuragi, Y., and Sugimura, Y., A study on plutonium fallout, J. Geophys. Res., 75, 2329-2330, 1970.
2. Miyake, Y., Sugimura, Y., and Mayeda, M., The uranium content and the activity ratio ^{234}U /^{238}U in marine organisms and sea water in the western North Pacific, J. Oceanogr. Soc. Japan, 26, 123-129, 1970.

1969

1. Miyake, Y., Radioactive contamination of the ocean, Bull. Jpn. Soc. Fisheries Oceanogr., Nov., 1969, 1969.

1968

1. Miyake, Y., and Sugimura, Y., Plutonium content in the western North Pacific waters, Pap. Met. Geophys, 19, 481-485, 1968.
2. Miyake, Y., Katsuragi, Y., and Sugimura, Y., Deposition of plutonium in Tokyo through the end of 1966, Pap. Met. Geophys, 19, 267-276, 1968.

1967

1. Miyake, Y., and Kanazawa, T., Atmospheric ozone and radioactive fallout, Pap. Met. Geophys., 18, 311-326, 1967.
2. Miyake, Y., Radioactive contamination of the ocean, J. Radiat. Res., 8, 1, 1967.
3. Miyake, Y., Sea, radioactivity in, International Dictionary of Geophysics, 1-7, 1967.

1966

1. Miyake, Y., and Saruhashi, K., On the radio-carbon age of the ocean waters, Pap. Met. Geophys., 17, 218-223, 1966.
2. Miyake, Y., and Sugimura, Y., Ratio ^{234}U /^{238}U and the uranium concentration in seawater in the western North Pacific, J. Geophys. Res., 71, 3083-3087, 1966.

1965

1. Kuroda, P. K., Miyake, Y., and Nemoto, J., Strontium isotopes Global circulation after the Chinese nuclear explosion of 14 May 1965, Science, 150, 1289-1290, 1965.
2. Miyake, Y., Saruhashi, K., Katsuragi K., and Kanazawa, T., Radioactivity of dust and rain - the ratio of Cs-137 and Sr-90 in the radioactive fallout, Proc. Internl. Conf. On Cloud Physics,Tokyo, IAMAP, 395-399, 1965.
3. Park, K., George, M.J., Miyake, Y., Saruhashi, K., Katsuragi, Y., and Kanazawa, T., Strontium-90 and caesium-137 in Columbia river plume, July 1964, Nature, 208, 1084-1085, 1965.

1964

1. Miyake, Y., and Sugimura, Y., Uranium and radium in the western North Pacific waters, Studies on Oceanography, Prof. K. Hidaka Sixtieth Birthday Commemorative Volume, Univ. of Tokyo Press, Tokyo, 274-278, 1964.
2. Miyake, Y., and Ohtsuka, Y., Beryllium-7 in rain water, Pap. Met. Geophys, 15, 89-92, 1964.
3. Miyake, Y., A sequential procedure for the radiochemical analysis of marine material, Annex to safety series 11."Method of surveying and monitoring marine radioactivity, IAEA, Vienna, 26, 1964.
4. Miyake, Y., Atomic weapons and the pollution of the sea, The East, 3, 64-68, 1964.

5. Miyake, Y., Saruhashi, K., Katsuragi, Y., Kanazawa, T., and Sugimura, Y., Uranium, radium, thorium, Ionium, strontium 90 and cesium 137 in coastal waters of Japan, In, Recent Researches in the Fields of Hydrosphere, Atmosphere and Nuclear Geochemistry, published by Editorial Committee of Sugawara Festival Volume, Maruzen Co. Ltd., 127-141, 1964.
6. Miyake, Y., Sugimura, Y., and Tsubota, H., Content of uranium, radium, and thorium in river waters in Japan, In, The Natural Radiation Environment, ed. By J. A. S. Adams and W. M. Lowder, Univ. of Chicago Press, Chicago, Rice Univ. Semicentennial Series, 219-225, 1964.
7. Sugimura, Y., Torii, T., and Murata, S., Uranium distribution in drake passage waters, Nature, 204, 464-465, 1964.

1963

1. Folsom, T.R., and Saruhashi, K., A comparison of analytical techniques used for determination of fallout cesium in sea water for oceanographic purpose, J. Radiat. Res., 4, 39-53, 1963.
2. Miyake, Y., and Tsubota, H., Estimation of the direct contribution of meteoric water to river waters by means of fall-out radio-cesium and radiostrontium, "Radioisotopes in Hydrology" Proc. IAEA Symp., Tokyo. IAEA, Vienna, 425-431, 1963.
3. Miyake, Y., Artificial radioactivity in the Pacific ocean, IUGG Monograph, 20 Radioactive traces in oceanography, 1963.
4. Miyake, Y., Saruhashi, K., Katsuragi, K., and Kanazawa, T., Deposition of Cs-137 and Sr-90 in Tokyo through the end of July 1963, Pap. Met. Geophys, 13, 180-181, 1963.
5. Miyake, Y., Saruhashi, K., Katsuragi, Y., Kanazawa, T., and Tsunogai, S., Deposition of ^{90}Sr and ^{137}Cs in Tokyo through the end of July 1963, Pap. Met. Geophys, 14, 58-65, 1963.
6. Miyake, Y., Sugiura, Y., and Tsubota, H., II. Contents of uranium, radium, and thorium in river waters in Japan, The Natural Radiation Environment, RICE Univ. semicentennial Pub, 1963.

1962

1. Miyake, Y., Saruhashi, K., Katsuragi, Y., and Kanazawa, T., Seasonal variation of radioactive fallout, J. Geophys. Res., 67, 189-193, 1962.
2. Miyake, Y., Saruhashi, K., Katsuragi, Y., and Kanazawa, T., Penetration of ^{90}Sr and ^{137}Cs in deep layers of the Pacific and vertical diffusion rate of deep water, J. Radiat. Res., 3, 141-147, 1962.
3. Miyake, Y., Saruhashi, K., Katsuragi, Y., and Kanazawa, T., The peak in radioactive fallout in the temperate zone of the northern hemisphere, J. Radiat. Res., 3,148-152, 1962.
4. Sugimura, Y., and Sugimura, T., Uranium in recent Japanese sediments, Nature, 194, 568-569, 1962.

1961

1. Miyake, Y., Saruhashi, K., Katsuragi, Y., and Kanazawa, T., Cesium 137 and strontium 90 in sea water, J. Radiat. Res., 2 25-28, 1961.
2. Miyake, Y., Saruhashi, K., Katsuragi, Y., and Kanazawa, T., Cesium 137 and strontium 90 in sea water, Pap. Met. Geophys., 12, 85-88, 1961.

1960

1. Miyake, Y., and Saruhashi, K., Vertical and horizontal mixing rates of radioactive material in the ocean, Disposal of Radioactive wastes IAEA Vienna, 167-173, 1960.
2. Miyake, Y., and Katsuragi, Y., Strontium 90 in western North Pacific surface waters, Pap. Met. Geophys., 11, 188-190, 1960.
3. Miyake, Y., Saruhashi, K., Katsuragi, Y., and Kanazawa, T., Radioactive fallout in Japan and its bearings on meteorological conditions, Pap. Met. Geophys., 11, 151-158, 1960.

1959

1. Miyake, Y., Saruhashi, K., and Katsuragi, Y., The Sr-90 fallout and the air motion, Pap. Met. Geophys., 9, 172-176, 1959.
2. Miyake, Y., Special committee on oceanic research, Working Group on Radioactivity in the Ocean, 1959.

1958

1. Miyake, Y., and Saruhashi, K., Distribution of man-made radio-activity in the North Pacific through summer 1955, J. Mar. Res., 17, 383-389, 1958.
2. Miyake, Y., and Sugiura, Y., The method of measurement of radioactivity in sea water, Pap. Met. Geophys., 9, 48-50, 1958.
3. Miyake, Y., Hazards to human health of radioactive dust, Radio Japan, 2, 3-5, 1958.
4. Miyake, Y., The distribution of artificial radioactivity in the equatorial region in the Pacific in the summer of 1956, The Proc. 9th Pacific Science Congress, 16, 227, 1958.

1957

1. Miyake, Y., and Saruhashi, K., The world-wide strontium 90 deposition during the period from 1951 to the fall of 1955, Pap. Met. Geophys., 8, 241-243, 1957.
2. Miyake, Y., The biological effects of nuclear tests - warning by Japanese scientists, Radio Japan, 1, 3-5, 1957.
3. Miyake, Y., XI. Methods for the measurement of radioactivity in sea water, Annuals of International Geophysical Year, 5, 1957.
4. Miyake, Y., XII. Radioactivity as a tracer of air motions in the atmosphere, Symp. On radioactivity, IGY, Utrecht, 360, 1957.
5. Miyake, Y., Sugiura, Y., Saruhashi, K., and Kanazawa, T., The estimation of the amount of Sr-90 deposition and the external infinite gamma does in Japan due to man-made radioactivity, Pap. Met. Geophys., 8, 222-231, 1957.

1956

1. Miyake, Y., On the distribution of radioactivity in the North Pacific ocean in 1954-1955, Internl. Conf. For Peaceful Uses of Atomic Energy in Geneva, August 1955, 13, pp.381-384, 1956.
2. Miyake, Y., Radioactivity in rain water and air, Proc. Internl. Conf. For Peaceful Uses of Atomic Energy in Geneva, August 1955, 13, 345-349, 1956.
3. Sugiura, Y., and Kanazawa, T., On the radioactive fallout collected in Tokyo on 26th November, 1955, Pap. Met. Geophys., 7, 128-135, 1956.

1955

1. Miyake, Y., and Sugiura, Y., Radiochemical analysis of radio-nuclides in sea water collected near BIKINI atoll, Pap. Met. Geophys., 6, 90-92, 1955.
2. Miyake, Y., Effects of atomic explosions on the atmosphere and sea, The research in the effects and influences of the nuclear bomb text explosions, 1-6, 1955.
3. Miyake, Y., Kigoshi, K., and Saruhashi, K., Radiochemical analysis of fission products contained in the soil collected at Tokyo, May, 1954, Pap. Met. Geophys., 6, 1, 93-94, 1955.
4. Miyake, Y., The artificial radioactivity in rain water observed in Japan, 1954-1955, Research in the Effects and Influences of the Nuclear Bomb Test Explosions Science, 151-159, 1955.
5. Miyake, Y., The artificial radioactivity in rain water observed in Japan, from autumn 1954 to spring 1955, Pap. Met. Geophys., 6, 26-32, 1955.
6. Miyake, Y., Sugiura, Y., and Kameda, K., On the artificial radioactivity in the sea near Japan, Pap. Met. Geophys., 6, 90-92, 1955.
7. Miyake, Y., Sugiura, Y., and Kameda, K., On the distribution of radioactivity in the sea around Bikini atoll in June, 1954, Pap. Met. Geophys., 5, 253-262, 1955.
8. Miyake, Y., Sugiura, Y., and Kameda, K., Research in the effects and influence of the nuclear bomb test explosions, Soc. For Promotion of Science, 415-417, 1955.

1954

1. Miyake, Y., Kigoshi, K., Sugiura, Y., and Saruhashi, K., A study on the productivity in coastal waters by means of the radio-carbon, Pap. Met. Geophys., 5, 89-94, 1954.
2. Miyake, Y., The artificial radioactivity in rain water observed in Japan from May to August, 1954, Pap. Met. Geophys, 5, 173-177, 1954.

5. Publication list (in Japanese) 1954-2019

論文リスト（和文誌）1954-2019

2019

1. 小野﨑 晴佳, 阿部 善也, 中井 泉, 足立 光司, 五十嵐 康人, 大浦 泰嗣, 海老原 充, 宮坂 貴文, 中村 尚, 末木 啓介, 鶴田 治雄, 森口 祐一: 福島第一原子力発電所事故により 1 号機から放出された放射性エアロゾルの物理・化学的性状の解明, 分析化学, 68, 757-768, 10.2116/bunsekikagaku.68.757, 2019.

2017

2. 足立光司, 福島原子力発電所事故で放出された不溶性放射性粒子の形態と組成, エアロゾル研究, 32-4,255–260, 2017.
3. 五十嵐康人, 放射性物質の大気沈着・拡散および陸域からの再浮遊について, Proceedings of the 17th Workshop Environmental Radioactivity. KEK Proceedings, 2017-6, 50-55, 2017.
4. 小野貴大, 飯澤勇信, 阿部善也, 中井 泉, 寺田康子, 佐藤志彦, 末木啓介, 足立光司, 五十嵐康人, 福島第一原子力発電所事故により 1 号機から放出された放射性粒子の放射光マイクロビーム X 線分析を用いる化学性状の解明, 分析化学 66（4）, 2017.
5. 梶野瑞王, 大気エアロゾルの環境動態シミュレーション,安全工学, 57-6, 433-441, 2018
6. 木村徹, 五十嵐康人, 財前祐二, ガンマ線スペクトル解析ソフト P-SCAN を用いた高精度な Cs^{134}/Cs^{137} 放射能比の導出, Proceedings of the 17th Workshop Environmental Radioactivity. KEK Proceedings, 2017-6, 262-266, 2017.

2016

1. 木村徹, 五十嵐康人, 財前祐二, 2016: IAEA-TEL-2015-03 Proficiency Test 試料の測定, Proceedings of the 17th Workshop Environmental Radioactivity. KEK Proceedings, 2016-8, 228-231.

2015

1. 足立光司, 電子顕微鏡がとらえた放射性粒子, 地球化学, 49,185–193, 2015.
2. 木村徹, 五十嵐康人,「大気降下物試料の放射能分析の品質管理」, Proceedings of the 16th Workshop Environmental Radioactivity. KEK Proceedings 2015-4 , 23-27, 2015.

2014

1. 青山道夫, 東電福島原発事故後の海洋での放射能汚染の推移 （With English Abstract）. YAKUGAKU ZASSHI, Journal of the Pharmaceutical Society of Japan. 2014.

2013

1. 青山道夫, 極低レベル放射能測定：少量表層海水および極深層海水試料への応用.放射線, 39(1), 17-20, 2013.

2012

1. 青山道夫, 福島第一原子力発電所から放出された放射性セシウム同位体の北太平洋における総量と分布, 日本原子力学会誌, 54, 780-783, 2012.
2. 青山道夫, 五十嵐康人, 1957 年から始まる気象研究所における環境放射能研究の歴史, 放射線, 38(3), 123-128, 2012.
3. 青山道夫, 海洋に放出された放射性物質の長期地球規模での挙動, 検証！福島第一原発事故-放射性物質の実際と科学者たちの活動の記録（化学 4 月号別冊）. 4, 33-38, 2012.
4. 青山道夫, 五十嵐康人, 広瀬勝己, 月間降下物測定 660 ヶ月が教えること-^{90}Sr, ^{137}Cs および Pu 降下量 1957 年 4 月～2012 年 3 月-. 科学, 82(4), 0442-0457, 2012.

2011

1. 青山道夫, 福島原子力発電所事故による海洋汚染. 理大科学フォーラム, 11(通 巻 329 号), 42-45, 2011.
2. 津旨大輔, 坪野考樹, 青山道夫, 廣瀬勝巳, 福島第一原子力発電所から漏洩した ^{137}Cs の海洋拡散シミュレーション(With English Abstract). 電力中央研究所報告書, V11002, PP.18, 2011.

2009

1. 五十嵐康人, 放射性同位体分析, In 岩坂泰信, 西川雅高, 山田丸, 洪天祥（編）, 黄砂, 古今書院, pp81-87, 東京, 2009.
2. Igarashi, Y., Anthropogenic Radioactivity in Aerosol -A Review Focusing on Studies during the 2000s-, 保健物理, 44(3), 2009.
3. 猪股弥生, 五十嵐康人, 千葉長, 青山道夫, 廣瀬勝己, 再現期間を用いた降水時における高ガンマ線線量率の異常値判定. Radioisotopes, 58, 37-42, 2009.

2007

1. 三浦誓也, 貝森優希, 工藤英嗣, 野呂幸男, 時枝隆之, 廣瀬勝己, 青森県における大気中クリプトン-85 濃度調査, 青森県原子力センター所報, 1, 43-44, 2007.
2. 廣瀬勝己, 青山道夫, Kim、S.A. Kim, 太平洋の海水中のプルトニウムの挙動について, 日本放射化学会誌 別冊, 8 supplement, 103, 2007.

2006

1. 青山道夫, 大気と海洋深層における核実験起源放射性降下物の超低レベル放射能測定, ADIOISOTOPES, 55, 429-438, 2006.
2. 小村和久, 青山道夫, 秋山正和, 氏平祐輔, 大田裕二, 大塚良仁, 大西勝基, 櫻井敬久, 篠原伸夫, Ge 検出器の使用状況に関するアンケート報告, RADIOISOTOPES, 55, 699-707,2006.

2004

1. 廣瀬勝己, 化学トレーサーを利用した海洋変動の研究, 測候時報第 71 巻特別号, 71, S81-S86, 2004.
2. 五十嵐康人, 廣瀬勝己, 放射性降下物標準試料の調製を通じた ^{90}Sr, ^{137}Cs,プルトニウムなどの人工放射性核種分析の相互比較と参照値の決定, 放射化分析, No. 17, 39-42, 2004.

2002

1. 五十嵐康人, ^{90}Sr と ^{137}Cs を用いたダスト輸送過程と再飛散, エアロゾル研究, 12, 17(4), 252, 2002.

1986

1. 鈴木款, 井上久幸, 杉村行勇, 大気中の放射性クリプトンの分布, 地球化学, 20, 106-108, 1986.

1978

1. 葛城幸雄, 人工放射性物質, 天気, 25, 第 11 号, 20-23, 1978.
2. 猿橋勝子, 海洋中の放射性物質を指標とした物質の移動・拡散, 水汚染の機構と解析－環境科学持論－, 日本地球化学編, 東京, 産業図書, 271-287, 1978.
3. 三宅泰雄, 猿橋勝子, 杉村行勇, 葛城幸雄, 金沢照子, 核兵器と地球環境の放射能汚染, 被爆の実相と被爆者の実情 －1977 年 NGO 被爆問題シンポジウム報告書, ISDA－ JNPC 編集, 朝日イブニングニュース社発行, 182-212, 1978.

1976

1. 葛城幸雄, 日本における放射性降下物, 天気, 23, No. 7, 333-345, 1976.
2. 杉村行雄, 環境のなかのプルトニウム, 自然, 3 月号, 1976.

1975

1. 三宅泰雄, 島田利夫, 川村清, 重原好次, 地上大気のトリチウム含量と気象との関係, 日本地球化学会 “環境問題特別号”, 131-135, 1975.

1974

1. 三宅泰雄, 葛城幸雄, 最近の ^{90}Sr 降下物の起源, 天気, 21, 639-644, 1974.

1971

1. 葛城幸雄, 人工放射能による大気汚染, 気象研究ノート, 107, 258-282, 1971

1970

1. 三宅泰雄, 葛城幸雄, 最近の日本における放射性塵の降下, 天気, 17, 593-598, 1970.

1965

1. 葛城幸雄, 日本における Cs-137 および Sr-90 降下について(I), 天気, 12, 323-328, 1965.
2. 葛城幸雄, 日本における Cs-137 および Sr-90 降下について(II) "成層圏における人工放射性物質の滞留時間の推定", 天気, 12, 377-384, 1965.

1964

1. 三宅泰雄, 葛城幸雄, 金沢照子, 放射性降下物の現状と将来, 科学, 34, 142-148, 1964.

1963

1. 三宅泰雄, 放射性降下物の気象学の側面, 天気, 9, No. 1, 1962.

1962

1. 三宅泰雄, 放射性降下物の気象学的側面, 天気, 9, 1-6, 1962.
2. 三宅泰雄, 猿橋勝子, 放射能による水の汚染, 水利科学, 23, 1-14, 1962.

1958

1. 三宅泰雄, 猿橋勝子, 放射化学と海洋, 科学, 28, 510-513, 1958.

1956

1. 三宅泰雄, 杉浦吉雄, 葛城幸雄, 1955 年 4 月旭川地方に降った放射性の落下塵,気象集誌, 第 2 号, 34, 226-230, 1956.

1955

1. 三宅泰雄, 放射能雨の性格, 測候時報, 22, 196-202, 1955.
2. 三宅泰雄, 日本に降った人工放射性雨・雪[II]9 月～12 月, 天文と気象, 21, 1-8, 1955.
3. 三宅泰雄, 杉浦吉雄, 亀田和久, 日本近海の海水放射能について, 昭和 29 年度海洋資源開発調査報告（黒潮班）, 81-82, 1955.
4. 三宅泰雄, 放射能雨の性格, 測候時報, 22, No. 7, 196-202, 1955.

1954

1. 三宅泰雄, 日本に降った人工放射性雨(1954 年 5-7 月), 天文と気象, 20, 1-8, 1954.
2. 三宅泰雄, 杉浦吉雄,亀田和久, ビキニ海域における人工放射能の分布とその海洋学的考察" ビキニ灰とそれによる傷害 第三", 科学, 24, 601-605, 1954.
3. 三宅泰雄, 有住直介, 磯野謙治, 田島英三, ビキニの灰とそれによる傷害（つづき）日本に降った放射能雨, 科学, 24, No. 8, 405-409, 1954.

年代・雑誌名不明

1. 三宅泰雄, 放射能とその作用, 遺伝,（1975？）
2. 三宅泰雄, 第 II 編 環境の放射能汚染と化学分析,（1970？）
3. 三宅泰雄, 猿橋勝子, 杉村行勇, 海洋における放射性核種, 海洋化学講座, 第 6 巻, 海洋無機化学, 第 4 章, 109-170,（1969？）
4. 三宅泰雄, 田島英三, 日米放射能会議, 8-18,（1954？）

6. History of the studies at the Meteorological Research Institute

表：研究の歴史

研究の歴史

放射能調査研究費以前および、放射能調査研究費での研究

西暦	年度	予算項目	予算項目							
				課題名	課題名	課題名	課題名	課題名	課題名	課題名
1954	昭和29年									
1955	S30	北太平洋観測（日・米・加）								
1956	S31	北太平洋赤道海域観測（日・米・仏）								
1957	S32	国際地球観測年事業費								
1958	S33	国際地球観測年事業費	放射能調査研究費	放射化学分析(落下塵・降水・海水中の放射性物質の研究)		深海水の循環に関する研究（以下深海水）				
1959	S34		放射能調査研究費	放射化学分析		深海水				
1960	S35	国際原子力機関委託研究	放射能調査研究費	放射化学分析		深海水				
1961	S36	国際原子力機関委託研究	放射能調査研究費	放射化学分析		深海水				
1962	S37	国際インド洋観測（日・米・ソ・英・仏）	放射能調査研究費	放射化学分析		深海水				
1963	S38	国際インド洋観測（日・米・ソ・英・仏）	放射能調査研究費	放射化学分析		深海水				
1964	S39	オレゴン州立大学との共同研究	放射能調査研究費	放射化学分析		深海水				
1965	S40		放射能調査研究費	放射化学分析	海洋中の放射性廃棄物のモニタリングの測定法に関する研究（以下海洋廃棄物モニタリング）	深海水		海水中における放射廃棄物の化学的挙動の研究(以下廃棄物化学的挙動）		
1966	S41		放射能調査研究費	放射化学分析	海洋廃棄物モニタリング	深海水		廃棄物化学的挙動		
1967	S42		放射能調査研究費	放射化学分析	海洋廃棄物モニタリング	深海水		廃棄物化学的挙動		
1968	S43		放射能調査研究費	放射化学分析	海洋廃棄物モニタリング	深海水		廃棄物化学的挙動		
1969	S44		放射能調査研究費	放射化学分析		深海水		廃棄物化学的挙動		
1970	S45		放射能調査研究費	放射化学分析		深海水		廃棄物化学的挙動		
1971	S46		放射能調査研究費	放射化学分析		深海水		廃棄物化学的挙動		

放射能調査研究費以前および、放射能調査研究費での研究

西暦	年度	予算項目	予算項目							
				課題名	課題名	課題名	課題名	課題名	課題名	課題名
1972	S47		放射能調査研究費	放射化学分析				放射性固体廃棄物の海洋処分に伴う鉛直拡散に関する研究(以下廃棄物鉛直拡散)		
1973	S48		放射能調査研究費	放射化学分析				廃棄物鉛直拡散		
1974	S49		放射能調査研究費	放射化学分析				廃棄物鉛直拡散	大気中におけるKr-85およびH-3挙動と蓄積に関する調査研究(以下Kr-85／H-3)	
1975	S50		放射能調査研究費	放射化学分析				廃棄物鉛直拡散	Kr-85／H-3	
1976	S51		放射能調査研究費	放射化学分析				廃棄物鉛直拡散	Kr-85／H-3	
1977	S52		放射能調査研究費	放射化学分析				数種の放射性核種の同時測定による深海拡散の研究(以下深海拡散)	原子力施設に由来する放射性気体の広域分布に関する調査研究(以下放射性気体)	
1978	S53		放射能調査研究費	放射化学分析				深海拡散	放射性気体	環境における超ウラン元素の分布と挙動に関する研究(以下超ウラン元素)
1979	S54		放射能調査研究費	放射化学分析				深海拡散	放射性気体	超ウラン元素
1980	S55		放射能調査研究費	放射化学分析				深海拡散	放射性気体	超ウラン元素
1981	S56		放射能調査研究費	放射化学分析				深海拡散	放射性気体	超ウラン元素
1982	S57		放射能調査研究費	放射化学分析				深海拡散	放射性気体	超ウラン元素
1983	S58		放射能調査研究費	放射化学分析				深海拡散	放射性気体	超ウラン元素
1984	S59		放射能調査研究費	放射化学分析				深海拡散	放射性気体	超ウラン元素
1985	S60		放射能調査研究費	放射化学分析				深海拡散	放射性気体	超ウラン元素
1986	S61		放射能調査研究費	放射化学分析				深海拡散	放射性気体	超ウラン元素
1987	S62		放射能調査研究費	放射化学分析				深海拡散	放射性気体	超ウラン元素
1988	S63		放射能調査研究費	放射化学分析				深海拡散	放射性気体	超ウラン元素
1989	H1		放射能調査研究費	放射化学分析				深海拡散	放射性気体	超ウラン元素
1990	H2		放射能調査研究費	放射化学分析				深海拡散	放射性気体	超ウラン元素
1991	H3		放射能調査研究費	放射化学分析				深海拡散	放射性気体	超ウラン元素
1992	H4		放射能調査研究費	放射化学分析	海洋における放射性核種の挙動に関する調査研究(以下海洋放射性核種)				放射性気体	超ウラン元素
1993	H5		放射能調査研究費	放射化学分析	海洋放射性核種				放射性気体	超ウラン元素
1994	H6		放射能調査研究費	放射化学分析	海洋放射性核種				放射性気体	超ウラン元素
1995	H7		放射能調査研究費	放射化学分析	海洋放射性核種				放射性気体	超ウラン元素

放射能調査研究費以前および、放射能調査研究費での研究

西暦	年度	予算項目	予算項目							
				課題名	課題名	課題名	課題名	課題名	課題名	課題名
1996	H8		放射能調査研究費	大気圏の放射性核種の動態に関する研究（以下大気圏放射性核種）	海洋環境における放射性核種の挙動に関する研究（以下海洋環境放射性核種）					
1997	H9		放射能調査研究費	大気圏放射性核種	海洋環境放射性核種					
1998	H10		放射能調査研究費	大気圏放射性核種	海洋環境放射性核種					
1999	H11		放射能調査研究費	大気圏放射性核種	海洋環境放射性核種					
2000	H12		放射能調査研究費	大気圏放射性核種	海洋環境放射性核種					
2001	H13		放射能調査研究費	大気圏の放射性核種の長期的動態に関する研究(以下大気圏放射性核種）	海洋環境における放射性核種の長期挙動に関する研究(以下海洋環境放射性核種）				大気中の放射性気体の実態把握に関する研究　（以下放射性気体）	
2002	H14		放射能調査研究費	大気圏放射性核種	海洋環境放射性核種				放射性気体	
2003	H15		放射能調査研究費	大気圏放射性核種	海洋環境放射性核種				放射性気体	
2004	H16		放射能調査研究費	大気圏放射性核種	海洋環境放射性核種				放射性気体	
2005	H17		放射能調査研究費	大気圏放射性核種	海洋環境放射性核種				放射性気体	
2006	H18		放射能調査研究費	放射性降下物の長期変動と再浮遊に関する研究（以下放射性降下物）	海洋環境における放射性核種の長期挙動に関する研究(以下海洋環境放射性核種）					
2007	H19		放射能調査研究費	放射性降下物	海洋環境放射性核種					
2008	H20		放射能調査研究費	放射性降下物	海洋環境放射性核種					
2009	H21		放射能調査研究費	放射性降下物	海洋環境放射性核種					
2010	H22		放射能調査研究費	放射性降下物	海洋環境放射性核種					

放射能調査研究費以前および、放射能調査研究費での研究

西暦	年度	予算項目	予算項目							
				課題名	課題名	課題名	課題名	課題名	課題名	課題名
2011	H23(8月から)		放射能調査研究費	「大気を通じた人工放射性核種の陸圏・水圏への沈着およびその後の移行過程の解明研究（以下陸圏水圏人工放射性核種）」						
2012	H24		放射能調査研究費	陸圏水圏人工放射性核種						
2013	H25		放射能調査研究費	陸圏水圏人工放射性核種						
2014	H26		放射能調査研究費	陸圏水圏人工放射性核種						
2015	H27(4月から)		放射能調査研究費	「人工放射性核種のバックグラウンド大気監視と数値解析に関する研究（以下BG放射性核種）」						
2016	H28		放射能調査研究費	BG放射性核種						
2017	H29		放射能調査研究費	BG放射性核種						
2018	H30		放射能調査研究費	BG放射性核種						
2019	R01		放射能調査研究費	BG放射性核種						
2020	R02（4月から）		放射能調査研究費	「人工放射性核種の大気長期変動監視と変動メカニズム解析に関する研究」						
2021	R03（4月から）		放射能調査研究費	「人工放射性核種の大気長期変動監視に関する研究」						

表紙の図説明

2021 年 3 月までの ^{90}Sr および ^{137}Cs 月間降下量

福島第一原発事故後の大気の放射能汚染の実態把握を継続しています。2011 年3 月の事故以降に確定できた^{90}Srおよび^{137}Cs月間降下量を対数軸で誤差と併せてプロットしています。^{134}Cs は事故直後には ^{137}Cs とほぼ等量降下していますから、放射性セシウム全体ではこのプロットのほぼ倍量となります。ただし、^{90}Sr、^{137}Cs はどちらもおよそ 30 年の半減期で減衰しますが、^{134}Cs はおよそ 2 年で半減します。図示した誤差は計測の統計誤差で、1 シグマです。測定誤差は本来全ての測定値につき表示すべきですが、グラフが見づらくなるため、従来はあえて表示してきませんでした。また、数十年前のデータについては誤差データが伝えられていません。

福島第一原発事故以前に採取され、分析や前処理途上だった試料については、事故の汚染によって実験室環境および測定室環境、測定機器のバックグラウンドなどが大幅に上昇したため、蒸発濃縮工程においても試料の汚染（コンタミネーションと言います）の問題が発生します。そのため、観測値を求めること自体が困難になっていましたが、試料を汚染の水準の低い関西にて分析しこの問題の回避に努めました。しかし、細心の注意と努力にもかかわらず、2010 年の後半および 2011 年初のデータは欠測となってしまいました。

徐々に実験環境の除染や測定機器の入れ替えなどを実施して事故以前のきれいな実験環境を追求し、データを求めるように努めています。また、IAEA が実施した分析相互比較に参画するなどし、その精度の維持管理に努めていますので、現状のデータの信頼性は担保できていると考えています。

7. A caption of the cover art

Monthly depositions of ^{90}Sr and ^{137}Cs before March 2018.

We have been monitoring the deposition amounts for the purpose of understanding the actual condition of radioactive pollution after the accident of Fukushima Daiichi Nuclear Power Plant (FDNPP). The monthly deposition amounts of both ^{90}Sr and ^{137}Cs, which were successfully fixed values after the accident in March 2011, are shown in logarithmic axis with error widths. Since the deposition amounts of ^{134}Cs were nearly equal to those of ^{137}Cs, the total amounts of radioactive cesium were approximately two times of the values in this figure. We would like to note that the half-lives of ^{90}Sr and ^{137}Cs are approximately 30 years, however, ^{134}Cs decays to half in about 2 years. The error widths are one sigma in statistical error of measurements. Although the error widths of all measurement values were better to be shown, error values used to be not shown on purpose to avoid busy figure in the former versions. In addition, error data before several decades are not handed down.

For the analysis of samples collected before the accident of FDNPP and not measured then, significant increase of background values were severe problem, because environments including laboratories and instruments were polluted, and it was also problem that samples could have been polluted in the operations of concentration or other preprocesses (contamination problem). We overcame the difficulty by carrying the analysis out in western Japan (Kansai area) where the pollution level was low, however, the data during the latter part of 2010 and the former part of 2011 were lacked in spite of our efforts.

We are making efforts to recover clean working environment as before the accident, by cleaning of the environments, exchanging instruments, etc. for the purpose of acquire the correct data. In addition, we maintain the precision of the data, for example, by participating inter-comparison programs performed by IAEA, so that, the credibility of the data are assured (please refer to the section: quality control of radioactive analysis of atmospheric deposition samples).